

**ALMA MATER STUDIORUM – UNIVERSITÀ DI BOLOGNA**

---

**DOTTORATO DI RICERCA**

in

**INGEGNERIA CIVILE, CHIMICA, AMBIENTALE E DEI MATERIALI**

Ciclo XXXII

Settore Concorsuale: 08/B3 Tecnica delle Costruzioni

Settore Scientifico Disciplinare: ICAR 09

**SEISMIC FRAGILITY ASSESSMENT OF  
UNREINFORCED MASONRY AGGREGATE  
BUILDINGS**

Candidata

**Lidia Battaglia**

Supervisore

**Prof. Ing. Marco Savoia**

Coordinatore Dottorato

**Prof. Ing. Luca Vittuari**

Co-supervisori

**Prof. Ing. Paulo J. B. B. Lourenço**

**Prof. Ing. Nicola Buratti**

**Dott. Ing. Tiago M. Ferreira**

Esame finale anno 2020



## ABSTRACT

The historical and cultural heritage of historic buildings is very often the result of an uncontrolled urban growth, due to the need to fill all possible urban spaces. For this reason, aggregate masonry buildings have been generated over the years, allowing the interaction of different aggregated inhomogeneous structural units under seismic action. Therefore, the seismic analysis of the aggregate structures cannot ignore the inevitable interactions resulting from structural contiguity between adjacent buildings.

The main goal of this thesis is the seismic vulnerability and fragility assessment of different classes of unreinforced masonry buildings, through the individuation of some prototypes having similar characteristics and representative of those classes of buildings, starting from the idea that buildings located in similar geotechnical conditions and with similar geometrical and structural properties are expected to have similar seismic performances. Thus, since the common simplification in civil engineering field to consider a building belonging to an aggregate structure as isolated, the selected classes of masonry buildings were at first considered as isolated structural units and then belonging to aggregations in row of those similar (or identical) structural units.

The first part of this work is focused on the seismic vulnerability and fragility assessment of clay brick masonry buildings, sited in Bologna (Italy), with reference, at first, to single isolated structural units. In order to account for some variabilities and uncertainties involved in the problem, the Response Surface statistical method is used, where the expected value of a response parameter (the peak ground acceleration ( $PGA_C$ ) corresponding to the attainment of the life safety limit state) is approximated through a polynomial function of a set of chosen variables. The Response Surface model is calibrated through numerical data obtained by non-linear static analyses and used to determine the fragility curves, by applying full Monte Carlo simulations. The seismic action was defined by means of a group of selected registered accelerograms, in order to analyse the effect of the variability of the earthquakes, also considering two different and orthogonal directions of the seismic action.

Identical structural units chosen by the Response Surface generated simulations are then aggregated in row, in order to compare the collapse PGA referred to the isolated structural unit and the one referred to the entire aggregate structure.

Afterwards, this work aims to assess the seismic vulnerability and fragility of unreinforced masonry aggregates in row, considering structural units along the aggregate with geometrical differences each other, generated starting from the medium values of the variables used to study the masonry aggregates with identical structural units in row, following the rules of the Response Surface (RS) statistical method. The goal is to show how the relative differences between the structural units in row affect the seismic response and to compare their seismic behaviour with those obtained aggregating identical structural units in row.

The second part of this thesis is focused on the seismic vulnerability and fragility assessment of stone masonry structures, sited in Seixal (Portugal), applying a methodology similar to that used for the masonry buildings sited in Bologna. Since the availability of several information on the buildings present in the historic centre of Seixal, the analyses involved the assessment of the most prevalent structural typologies in the study area, considering the variability of a set of structural and geometrical parameters. The variation of such parameters has allowed the individuation of different structural configurations, whose seismic performance behaviours were studied by means of non-linear static analyses. Based on the seismic performance analysis, the PGA corresponding to the attainment of the life safety limit state were obtained, considering the variation of the seismic action referred to a group of selected registered accelerograms, representing previous earthquakes and the fragility curves were plotted. Furthermore, the seismic behaviour of these structural configurations, analysed as isolated structural units, is also compared with their structural performance when enclosed in aggregate.

The results have highlighted the importance of the statistic procedures as method able to consider the variabilities and the uncertainties involved in the problem of the fragility of unreinforced masonry structures, in absence of accurate investigations on the structural typologies of the site, as in the Seixal case study. Furthermore, it was showed that the structural units along the unreinforced clay brick or stone masonry aggregates cannot be analysed as isolated, as they are affected by the effect of the aggregation with adjacent structural units, according to the different directions of the seismic action considered and to their different position along the row aggregate.

## ACKNOWLEDGEMENTS

*I would like to express my great and sincere gratitude to my supervisor, prof. Marco Savoia, for the full dedication, support and guidance during these years, in which I learnt a lot also because of his teachings.*

*I would like to acknowledge prof. Nicola Buratti, my co-supervisor, for the guidance offered to my work; his support was fundamental to solve most of the technical issues arisen during my research activity.*

*I would also like to acknowledge prof. Claudio Mazzotti; even if he did not directly follow my work, his mental and technical support helped me to face the research activity with serenity.*

*I would like to express my sincere gratitude to Prof. Paulo Lourenço, my supervisor in Portugal, for his dedication, guidance, suggestions and scientific support during my abroad period in Guimarães.*

*I would also like to acknowledge Dott. Tiago Miguel Ferreira, my co-supervisor in Portugal, for the technical support that was very useful to carry out my research activity in Guimarães.*

*I also want to acknowledge prof. Andrea Penna and Dott. Stefano Bracchi, as technical referents of “TreMuri” software; I really appreciated their help and suggestions to solve the problems arisen in the use of the software.*

*One of the biggest acknowledgements goes to my family: my parents, for always believing in me, for the psychological and economical support on the choice to leave my hometown and for the constant affection they show me every day; my brother Fabrizio, who was always present in my life despite the distance with his affection, support and love, representing a “referent point” for me. I also want to acknowledge my grandparents, always giving me their love, my hunts Gaspare and Gabriella and my cousins Giulia and Giuseppe, for being my big family always sustaining me since I was young.*

*I want to express my gratitude to my boyfriend Davide, for being on my side all these years, for giving me his love and affection, for his help to get up in difficult moments, for supporting all my choices, but also for the several funny moments spent together.*

*I want to acknowledge my dear and best friends Andrea, Luca and Viviana for their constant presence since we were young and for offering me their friendship, representing one of the most precious things I have; but also thanks to Bianca, Daniele, Dorotea, Marco, Maurizio, Roberta A., Roberta L., Roberta S. and Roberto for standing by me with their affection during these years.*

*A big acknowledgment goes to my flatmates Giulia and Ilaria, for the lovely time spent together at home and outside and becoming dear friends I had the luck to find.*

*One of the great acknowledgments for these 3 years goes to Clementina: we shared all the moments of our PhD, supporting each other and facing together all the difficult moments; in these years she became more than a simply colleague, now she is a dear friend, always standing by me and with whom I collected a lot of lovely memories I will ever remember with affection.*

*A big acknowledgement goes to my colleagues Said and Vittoria, always present in my PhD life, becoming friends out of the university and whose presence made special these years. I also want to acknowledge all my colleagues Cristiano, Diego, Elena, Francesca, Giacomo, Jessica, Lucia, Marco, Marta, Matteo, Milena, Mirco, Noemi, Silvia, Simonetta, for sharing with me these amazing years in the University.*

*My acknowledgements finally go to the colleagues and friends known during my abroad period in Portugal. In particular Antonio M., Antonio R., Nicola and Nicoletta, who made me feel like at home since the first days, giving me their support and making me aware that special friendships can be born even in a short time.*

*I will never forget all the moments spent together with the guys known in Portugal, Abide, Alban, Alberto, Alessandro, Beatrice, Claudia, Claudio, Elesban, Elixabete, Fabio, Francesco, Gianpaolo, Jennifer, Leslie, Luis, Maria Carla, Maria Jose, Maria Pia, Maxime, Meera, Pilar, Rafael, Reza, Telma, Thomas and Xinyu, making that experience unforgettable.*

## List of contents

List of Figures .....	i
List of Tables.....	xiii
1. INTRODUCTION .....	1
1.1 Motivation .....	2
1.2 Research problem: the aggregate buildings.....	5
1.3 Goals, methodology and outlines .....	8
2. SEISMIC FRAGILITY .....	13
2.1 Introduction .....	14
2.2 Failure probability .....	15
2.3 Evaluation of the seismic fragility.....	16
2.4 The fragility curves.....	18
2.5 Damage levels .....	25
3. PROBABILITY COMPUTATION METHODS THROUGH SIMULATIONS.....	27
3.1 Introduction .....	28
3.2 Monte Carlo simulations .....	29
3.3 Response Surface method.....	30
3.3.1 Standard Response Surface .....	31
3.3.1.1 Ordinary least square method.....	33
3.3.2 Random block effects.....	35
3.3.3 Design of the experiments theory.....	37
3.3.3.1 Central composite design .....	38
3.3.3.2 Design for mixed model.....	40
4. MODELLING AND ANALYSIS OF URM BUILDINGS.....	41
4.1 Introduction .....	42
4.2 Mechanical behaviour of the masonry walls .....	43
4.2.1 Out-of-plane behaviour .....	44
4.2.2 In-plane behaviour.....	46
4.3 Existing URM buildings.....	51
4.4 Numerical modelling.....	55
4.5 The macro-element modelling: TreMuri software .....	58
4.6 Non-linear static analysis according to the Italian Code .....	61
4.7 The N2 method .....	63
5. SEISMIC FRAGILITY ASSESSMENT OF MASONRY STRUCTURES .....	69
5.1 The methodology.....	70

5.2	Selection of the parameters defining a set of different structural models.....	73
5.3	Non-linear static analyses of the different structural models.....	74
5.4	Definition of the seismic action .....	75
5.5	Evaluation of the peak ground acceleration corresponding to the structural failure .....	80
5.6	Definition of the seismic fragility .....	82
6.	SEISMIC FRAGILITY OF CLAY BRICK MASONRY STRUCTURES: CASE STUDIES IN BOLOGNA, ITALY .....	85
6.1	Introduction.....	86
6.2	The isolated structural units .....	86
6.2.1	The structure .....	86
6.2.2	Selection of the variables .....	88
6.2.3	Push-over analyses.....	93
6.2.4	Response Surface models .....	100
6.2.5	Fragility curves .....	107
6.3	Comparison between the isolated structural units and the aggregations of identical structural units in row.....	108
6.3.1	Introduction.....	108
6.3.2	The aggregation of identical structural units in row .....	109
6.3.3	Selection of the variables .....	110
6.3.4	Push-over analyses.....	112
6.3.5	Response Surface models .....	120
6.3.6	Fragility curves .....	127
6.4	Aggregations of different structural units in row.....	128
6.4.1	Introduction.....	128
6.4.2	RS model: definition of the structural units along the aggregates.....	129
6.4.3	Push-over analyses.....	135
6.4.4	Response Surface models .....	138
6.4.5	Fragility curves .....	151
6.4.6	Comparison between the aggregate with different structural units and the aggregate with identical structural units in row .....	152
7.	SEISMIC FRAGILITY OF STONE MASONRY STRUCTURES: CASE STUDIES IN SEIXAL, PORTUGAL.....	167
7.1	Introduction.....	168
7.2	Identification of the structural typologies .....	169
7.3	Numerical modelling of the structures.....	174
7.3.1	Mechanical and geometrical properties of the masonry walls.....	175

7.3.2 Mechanical and geometrical properties of the slabs .....	176
7.4 Push-over analyses .....	177
7.5 Fragility curves.....	192
8. CONCLUSIONS.....	199
8.1 Summary.....	200
8.2 Future works.....	203
References .....	205
Appendix A.....	215
Appendix B .....	237
Appendix C .....	251



## List of Figures

Figure 3.1: Design of experiment with (a) 2 variables and (b) 3 variables.....	38
Figure 3.2: Example of a cuboidal region of the Central Composite Design. ....	39
Figure 4.1: Collapse of a masonry building having steel ties combined to poor masonry (a) Amatrice, Petrana; (b) Arquata d/T, Piazza Umberto I (Sorrentino et al., 2018). ....	44
Figure 4.2: Typical out-of-plane local mechanisms (ReLUIS - Dipartimento di Protezione Civile, 2009).....	45
Figure 4.3: Typical in-plane failure modes of masonry piers (Calderini et al., 2009): (a) flexural-rocking; (b) shear failure (sliding along the bed joints); (c) shear failure (diagonal cracking). ....	46
Figure 4.4: Parabolic domain relating the axial compressive action and the ultimate bending moment (adapted from Lagomarsino et al, 2008). ....	47
Figure 4.5: Different bending moment variation and failure mechanism due to different grades of coupling provided by the spandrels in masonry walls: weak (a), intermediate (b) and strong (c) spandrels (Graziotti et al., 2012). ....	50
Figure 4.6: Definition of the knowledge levels according to the geometry, the details and the materials. ....	52
Figure 4.7: Masonry modelling strategies: (a) masonry sample; (b) detailed micro-modelling; (c) simplified micro-modelling; (d) macro-modelling (Lourenço, 1996). ....	56
Figure 4.8: Examples of analytical models for the seismic analysis of URM buildings: (a) FE model, macro-modelling approach (Mendes, 2012); (b) DE model, micro-modelling approach (Alexandris et al., 2004); (c) structural component model by macroblocks (Orduña, 2003). ....	57
Figure 4.9: URM wall idealization according to the equivalent frame models (adapted from Lagomarsino et al. (2013)). ....	59
Figure 4.10: Non-linear beam degrading behaviour (Lagomarsino et al., 2008). ....	60
Figure 4.11: Determination of the capacity curve.....	62
Figure 4.12: Passage from the MDOF system to the SDOF system, through $\Gamma$ . ....	63
Figure 4.13: (a) Capacity curve for the MDOF system; (b) capacity curve for the SDOF equivalent system.....	64
Figure 4.14: Definition of the bilinear equivalent curve from the SDOF system.....	65
Figure 4.15: Use of the displacement spectrum to find the displacement demand $d_{max}^*$ . ....	66
Figure 4.16: Definition of the displacement demand: (a) for $T^* \geq T_C$ ; (b) for $T^* < T_C$ (NTC, 2018). ...	67
Figure 5.1: Comparison between the isolated structural unit considered as isolated and that enclosed in a row aggregate. ....	70
Figure 5.2: Steps of the applied procedure, starting from the definition of the models to the plotting of the fragility curves. ....	72
Figure 5.3: Example of an ISU and an AS with the considered reference axes.....	75
Figure 5.4: Scaling factors used to scale the accelerograms of Bologna. ....	77

Figure 5.5: (a) Group of 48 acceleration spectra and (b) displacement spectra for the site of Bologna. ....	78
Figure 5.6: Scaling factors used to scale the accelerograms of Seixal. ....	79
Figure 5.7: (a) Group of 50 acceleration spectra and (b) displacement spectra for the site of Seixal. ....	79
Figure 5.8: Example of three (a) displacement spectra and (b) displacement scaled spectra. ....	81
Figure 5.9: Example of three (a) acceleration spectra and (b) acceleration scaled spectra. ....	81
Figure 5.10: Example of non-regular shape of the fragility curves. ....	82
Figure 5.11: Procedure to plot the fragility curves, using Monte Carlo simulations for the case studies in Bologna. ....	83
Figure 5.12: Procedure to plot the fragility curves, using Monte Carlo simulations for the case studies in Seixal. ....	84
Figure 6.1: (a) Architectural ground floor plan and (b) sections of the prototype building. ....	87
Figure 6.2: (a) Plan of the structural ground floor and (b) tri-dimensional view of the isolated structural unit. ....	88
Figure 6.3: Normal distributions adopted for the (a) variable $\tau$ , (b) variable $E_1$ and (c) variable $d$ . ....	89
Figure 6.4: Cuboidal region of interest for the 3 coded variables $x_i$ . ....	91
Figure 6.5: Definition of the implicit variable $\delta_{sis}$ , by means of $\mu_d$ and $s$ . ....	92
Figure 6.6: Capacity curves from the analyses with (a) positive forces ( $+ F_x$ ) and (b) negative forces ( $- F_x$ ). ....	93
Figure 6.7: (a) Indication of the masonry walls in x-direction; (b) Point of the capacity curve ( $+ F_x$ ) related to the collapse of the spandrels E13 and E9 of the panel P3. ....	95
Figure 6.8: Failure mechanisms of the masonry walls considering a seismic action in x-direction ( $+ F_x$ ). ....	95
Figure 6.9: (a) Indication of the masonry walls in x-direction; (b) Point of the capacity curve ( $- F_x$ ) in correspondence of the point in Figure 6.7(b). ....	96
Figure 6.10: Failure mechanisms of the masonry walls considering a seismic action in x-direction ( $- F_x$ ). ....	96
Figure 6.11: Capacity curves from the analyses with (a) positive forces ( $+ F_y$ ) and (b) negative forces ( $- F_y$ ). ....	97
Figure 6.12: (a) Indication of the masonry walls in y-direction; (b) Point of the capacity curve ( $+ F_y$ ) related to the same displacement in Figure 6.14(b). ....	98
Figure 6.13: Failure mechanisms of the masonry walls considering a seismic action in y-direction ( $+ F_y$ ). ....	98
Figure 6.14: (a) Indication of the masonry walls in y-direction; (b) Point of the capacity curve ( $- F_y$ ) related to the collapse of the panels P5 and P7. ....	99
Figure 6.15: Failure mechanisms of the masonry walls considering a seismic action in y-direction ( $- F_y$ ). ....	99

Figure 6.16: (a) Axial and central region and (b) factorial region of the isolated structural unit quadratic RS sections obtained varying $\tau$ , considering the seismic forces $+ F_x$ .	102
Figure 6.17: (a) Axial and central region and (b) factorial region of the isolated structural unit quadratic RS sections obtained varying $d$ , considering the seismic forces $+ F_x$ .	102
Figure 6.18: (a) Axial and central region and (b) factorial region of the isolated structural unit quadratic RS sections obtained varying $\tau$ , considering the seismic forces $- F_x$ .	103
Figure 6.19: (a) Axial and central region and (b) factorial region of the isolated structural unit quadratic RS sections obtained varying $d$ , considering the seismic forces $- F_x$ .	103
Figure 6.20: (a) Axial and central region and (b) factorial region of the isolated structural unit quadratic RS sections obtained varying $\tau$ , considering the seismic forces $+ F_y$ .	104
Figure 6.21: (a) Axial and central region and (b) factorial region of the isolated structural unit quadratic RS sections obtained varying $d$ , considering the seismic forces $+ F_y$ .	104
Figure 6.22: (a) Axial and central region and (b) factorial region of the isolated structural unit quadratic RS sections obtained varying $\tau$ , considering the seismic forces $- F_y$ .	105
Figure 6.23: (a) Axial and central region and (b) factorial region of the isolated structural unit quadratic RS sections obtained varying $d$ , considering the seismic forces $- F_y$ .	105
Figure 6.24: 3D Response Surfaces for (a) the positive ( $+ F_x$ ) and (b) negative ( $- F_x$ ) x-direction of the seismic action.	106
Figure 6.25: 3D Response Surfaces for (a) the positive ( $+ F_y$ ) and (b) negative ( $- F_y$ ) y-direction of the seismic action.	106
Figure 6.26: Fragility curves obtained for the isolated structural units in x- and y-direction of the seismic action.	108
Figure 6.27: Model of the 3D masonry aggregate structure.	109
Figure 6.28: Plan of the structural ground floor of the masonry aggregate structure.	110
Figure 6.29: Normal distribution adopted for the variable $s$ .	111
Figure 6.30: Capacity curves from the analyses in x-direction: (a) isolated structural units and (b) aggregate structures.	113
Figure 6.31: Deformed configuration of the model with $s = 0.30$ m, considering a seismic action in x-direction ( $+ F_x$ ).	113
Figure 6.32: Mechanisms of the walls of the model with $s = 0.30$ m, considering a seismic action in x-direction ( $+ F_x$ ): (a) P3 and (b) P8; (c) P36 and (e) P37 Unit 1; (d) P35 Unit 2.	114
Figure 6.33: Mechanisms of the walls of the model with $s = 0.30$ m, considering a seismic action in x-direction ( $- F_x$ ): (a) P3 and (b) P8; (c) P36 and (e) P37 Unit 1; (d) P35 Unit 2.	115
Figure 6.34: Capacity curves from the analyses in y-direction: (a) isolated structural units and (b) aggregate structures.	117
Figure 6.35: Deformed configuration of the model with $s = 0.30$ m, considering a seismic action in y-direction ( $+ F_y$ ).	117
Figure 6.36: Mechanisms of the walls of the model with $s = 0.30$ m, considering a seismic action in y-direction ( $+ F_y$ ): (a) P33 Unit 1; (b) P31 Unit 2; (c) P22 Unit 3 and (d) P21 Unit 4.	118

Figure 6.37: Capacity curves from the analyses in $y$ -direction ( $+ F_y$ ) over the attainment of the LS limit state. ....	118
Figure 6.38: Mechanisms of the walls of the model with $s = 0.30$ m, considering a seismic action in $y$ -direction ( $- F_y$ ): (a) P33 Unit 1; (b) P31 Unit 2; (c) P22 Unit 3 and (d) P21 Unit 4.....	119
Figure 6.39: Capacity curves from the analyses in $y$ -direction ( $- F_y$ ) over the attainment of the LS limit state. ....	119
Figure 6.40: Relation between $s$ and $PGA_C$ , considering 6 different accelerograms for each value of $s$ : (a) seismic forces $+ F_x$ and (b) seismic forces $- F_x$ .....	121
Figure 6.41: Relation between $s$ and $PGA_C$ , considering 6 different accelerograms for each value of $s$ : (a) seismic forces $+ F_y$ and (b) seismic forces $- F_y$ .....	121
Figure 6.42: Relation between $s$ and $PGA_C$ , considering all the accelerograms for each value of $s$ : (a) seismic forces $+ F_x$ and (b) seismic forces $- F_x$ .....	122
Figure 6.43: Relation between $s$ and $PGA_C$ , considering all the accelerograms for each value of $s$ : (a) seismic forces $+ F_y$ and (b) seismic forces $- F_y$ .....	122
Figure 6.44: Response Surface sections for (a) the ISU and (b) the AS, considering the seismic forces $+ F_x$ .....	124
Figure 6.45: Response Surface sections for (a) the ISU and (b) the AS, considering the seismic forces $- F_x$ . ....	124
Figure 6.46: Response Surface sections for (a) the ISU and (b) the AS, considering the seismic forces $+ F_y$ .....	125
Figure 6.47: Response Surface sections for (a) the ISU and (b) the AS, considering the seismic forces $- F_y$ . ....	125
Figure 6.48: RS sections for (a) the Unit 3 and (b) the Unit 4, considering the seismic forces $+ F_y$ . ....	126
Figure 6.49: RS sections for (a) the Unit 3 and (b) the Unit 4, considering the seismic forces $- F_y$ . ....	126
Figure 6.50: Fragility curves considering (a) the $x$ -direction and (b) the $y$ -direction of the seismic action.....	128
Figure 6.51: Model of the 3D masonry aggregate with different structural units. ....	129
Figure 6.52: Plan of the structural ground floor of the masonry aggregate with different structural units.....	130
Figure 6.53: Region of interest for the 2 coded variables $x_i$ .....	131
Figure 6.54: Gaussian distributions defined for the 5 distances between walls in $x$ -direction (d)..	132
Figure 6.55: Groups of $s$ for the definition of the blocks $\delta_s$ .....	132
Figure 6.56: Numeration of the structural units along the aggregate. ....	133
Figure 6.57: Capacity curves from the analyses in $x$ -direction: seismic forces (a) $+ F_x$ and (b) $- F_x$ . ....	136

Figure 6.58: Capacity curves from the analyses in y-direction: seismic forces (a) + $F_y$ and (b) - $F_y$ . .....	137
Figure 6.59: Capacity curves from the analyses in y-direction (+ $F_y$ ) over the attainment of the LS limit state. ....	137
Figure 6.60: Capacity curves from the analyses in y-direction (- $F_y$ ) over the attainment of the LS limit state. ....	138
Figure 6.61: Relations between the 200 values of d and s, randomly selected. ....	139
Figure 6.62: (a) Axial and central region and (b) factorial region of the AS quadratic RS sections obtained varying $\tau$ , considering the seismic forces + $F_x$ . ....	141
Figure 6.63: (a) Axial and central region and (b) factorial region of the AS quadratic RS sections obtained varying d, considering the seismic forces + $F_x$ . ....	141
Figure 6.64: (a) Axial and central region and (b) factorial region of the AS quadratic RS sections obtained varying $\tau$ , considering the seismic forces - $F_x$ . ....	142
Figure 6.65: (a) Axial and central region and (b) factorial region of the AS quadratic RS sections obtained varying d, considering the seismic forces - $F_x$ . ....	142
Figure 6.66: (a) Axial and central region and (b) factorial region of the AS quadratic RS sections obtained varying $\tau$ , considering the seismic forces + $F_y$ . ....	143
Figure 6.67: (a) Axial and central region and (b) factorial region of the AS quadratic RS sections obtained varying d, considering the seismic forces + $F_y$ . ....	143
Figure 6.68: (a) Axial and central region and (b) factorial region of the AS quadratic RS sections obtained varying $\tau$ , considering the seismic forces - $F_y$ . ....	144
Figure 6.69: (a) Axial and central region and (b) factorial region of the AS quadratic RS sections obtained varying d, considering the seismic forces - $F_y$ . ....	144
Figure 6.70: (a) Axial and central region and (b) factorial region of the Unit 3 quadratic RS sections obtained varying $\tau$ , considering the seismic forces + $F_y$ , over the attainment of the LS limit state. ....	145
Figure 6.71: (a) Axial and central region and (b) factorial region of the Unit 3 quadratic RS sections obtained varying d, considering the seismic forces + $F_y$ , over the attainment of the LS limit state. .....	145
Figure 6.72: (a) Axial and central region and (b) factorial region of the Unit 3 quadratic RS sections obtained varying $\tau$ , considering the seismic forces - $F_y$ , over the attainment of the LS limit state. ....	146
Figure 6.73: (a) Axial and central region and (b) factorial region of the Unit 3 quadratic RS sections obtained varying d, considering the seismic forces - $F_y$ , over the attainment of the LS limit state. ....	146
Figure 6.74: (a) Axial and central region and (b) factorial region of the Unit 4 quadratic RS sections obtained varying $\tau$ , considering the seismic forces + $F_y$ , over the attainment of the LS limit state. ....	147
Figure 6.75: (a) Axial and central region and (b) factorial region of the Unit 4 quadratic RS sections obtained varying d, considering the seismic forces + $F_y$ , over the attainment of the LS limit state. .....	147
Figure 6.76: (a) Axial and central region and (b) factorial region of the Unit 4 quadratic RS sections obtained varying $\tau$ , considering the seismic forces - $F_y$ , over the attainment of the LS limit state. ....	148

Figure 6.77: (a) Axial and central region and (b) factorial region of the Unit 4 quadratic RS sections obtained varying $d$ , considering the seismic forces - $F_y$ , over the attainment of the LS limit state.	148
Figure 6.78: 3D Response Surfaces for the AS with different structural units, considering (a) the seismic forces + $F_x$ and (b) the seismic forces - $F_x$ .	149
Figure 6.79: 3D Response Surfaces for the AS with different structural units, considering (a) the seismic forces + $F_y$ and (b) the seismic forces - $F_y$ .	149
Figure 6.80: 3D Response Surfaces for the Unit 3, considering (a) the seismic forces + $F_y$ and (b) the seismic forces - $F_y$ , over the attainment of the LS limit state.	150
Figure 6.81: 3D Response Surfaces for the Unit 4, considering (a) the seismic forces + $F_y$ and (b) the seismic forces - $F_y$ , over the attainment of the LS limit state.	150
Figure 6.82: Fragility curves of the masonry aggregate structures with different structural units in row.	152
Figure 6.83: Example of comparison between an AS - D and the correspondent AS - I.	153
Figure 6.84: Example of comparison between the AS - D configuration 1 and the correspondent AS - I.	155
Figure 6.85: Comparison between the AS - D, the AS - I and the ISU for the group $\tau_1$ - $d_3$ - $s_3$ .	155
Figure 6.86: Comparison between the AS - D, the AS - I and the ISU for the group $\tau_2$ - $d_2$ - $s_2$ .	156
Figure 6.87: Comparison between the AS - D, the AS - I and the ISU for the group $\tau_2$ - $d_4$ - $s_4$ .	156
Figure 6.88: Comparison between the AS - D, the AS - I and the ISU for the group $\tau_3$ - $d_1$ - $s_1$ .	157
Figure 6.89: Comparison between the AS - D, the AS - I and the ISU for the group $\tau_3$ - $d_3$ - $s_3$ .	157
Figure 6.90: Comparison between the AS - D, the AS - I and the ISU for the group $\tau_3$ - $d_5$ - $s_5$ .	158
Figure 6.91: Comparison between the AS - D, the AS - I and the ISU for the group $\tau_4$ - $d_2$ - $s_2$ .	158
Figure 6.92: Comparison between the AS - D, the AS - I and the ISU for the group $\tau_4$ - $d_4$ - $s_4$ .	159
Figure 6.93: Comparison between the AS - D, the AS - I and the ISU for the group $\tau_5$ - $d_3$ - $s_3$ .	159
Figure 6.94: Fragility curves in x-direction (+ $F_x$ ): comparison between (a) the AS-D and the 9 AD-I groups and (b) the AS-D and the AS-I.	162
Figure 6.95: Fragility curves in x-direction (- $F_x$ ): comparison between (a) the AS-D and the 9 AD-I groups and (b) the AS-D and the AS-I.	162
Figure 6.96: Fragility curves in y-direction (+ $F_y$ ): comparison between (a) the AS-D and the 9 AD-I groups and (b) the AS-D and the AS-I.	163
Figure 6.97: Fragility curves in y-direction (- $F_y$ ): comparison between (a) the AS-D and the 9 AD-I groups and (b) the AS-D and the AS-I.	163
Figure 6.98: Fragility curves in y-direction (+ $F_y$ ) over the attainment of the LS limit state (Unit 3): comparison between (a) the AS-D and the 9 AD-I groups and (b) the AS-D and the AS-I.	164
Figure 6.99: Fragility curves in y-direction (- $F_y$ ) over the attainment of the LS limit state (Unit 3): comparison between (a) the AS-D and the 9 AD-I groups and (b) the AS-D and the AS-I.	164

Figure 6.100: Fragility curves in y-direction (+ $F_y$ ) over the attainment of the LS limit state (Unit 4): comparison between (a) the AS-D and the 9 AD-I groups and (b) the AS-D and the AS-I. ....	165
Figure 6.101: Fragility curves in y-direction (- $F_y$ ) over the attainment of the LS limit state (Unit 4): comparison between (a) the AS-D and the 9 AD-I groups and (b) the AS-D and the AS-I. ....	165
Figure 7.1: Architectural plans and front views of some “narrow front buildings” (adapted from Santos et al. (2013)). ....	170
Figure 7.2: (a) Architectural ground floor plan, (b) architectural first floor plan and (c) Section A-A’. ....	170
Figure 7.3: External aspect of some of the most common limestone masonry walls in Seixal (Ferreira et al., 2016). ....	172
Figure 7.4: Internal masonry tabique walls: (a) “narrow front building” in Seixal (Ferreira et al., 2016) and (b) “Pombalino” building in Lisbon (Appleton, 2003; Lopes et al., 2014). ....	172
Figure 7.5: Logic-tree diagram built used to obtain the 36 different structural typologies analysed. ....	173
Figure 7.6: (a) Structural ground floor plan of the model “2-2.7-T-B” and (b) 3D structure of the model “2-2.7-T-B”. ....	174
Figure 7.7: (a) Structural ground floor plan of the aggregate model “2-2.7-T-B” and (b) 3D structure of the aggregate model “2-2.7-T-B”. ....	175
Figure 7.8: x-direction push-over curves of the buildings with 2 floors and timber slabs: (a) Isolated structural units and (b) Aggregate structures. ....	178
Figure 7.9: x-direction push-over curves of the buildings with 2 floors and concrete slabs: (a) Isolated structural units and (b) Aggregate structures. ....	179
Figure 7.10: (a) Indication of the masonry walls in x-direction; (b) Point of the capacity curve (+ $F_x$ ) related to the collapse of the walls P5 and P7 for the “2-2.7-T-B” model. ....	180
Figure 7.11: Failure mechanisms of the masonry walls considering a seismic action in x-direction (+ $F_x$ ) for the “2-2.7-T-B” model. ....	180
Figure 7.12: (a) Indication of the masonry walls in x-direction; (b) Point of the capacity curve (+ $F_x$ ) related to the collapse of the wall P2 for the “2-2.7-C-B” model. ....	181
Figure 7.13: Failure mechanisms of the masonry walls considering a seismic action in x-direction (+ $F_x$ ) for the “2-2.7-C-B” model. ....	181
Figure 7.14: x-direction push-over curves of the buildings with timber slabs: (a) Isolated structural units and (b) Aggregate structures. ....	183
Figure 7.15: x-direction push-over curves of the buildings with concrete slabs: (a) Isolated structural units and (b) Aggregate structures. ....	183
Figure 7.16: y-direction push-over curves of the buildings with 2 floors and timber slabs: (a) Isolated structural units and (b) Aggregate structures. ....	184
Figure 7.17: y-direction push-over curves of the buildings with 2 floors and concrete slabs: (a) Isolated structural units and (b) Aggregate structures. ....	184

Figure 7.18: (a) Indication of the masonry walls in $y$ -direction; (b) Point of the capacity curve ( $+ F_y$ ) related to the collapse of the wall P3 for the “2-2.7-T-B” model.....	186
Figure 7.19: Failure mechanisms of the masonry walls considering a seismic action in $y$ -direction ( $+ F_y$ ) for the “2-2.7-T-B” model.....	186
Figure 7.20: (a) Indication of the masonry walls in $y$ -direction; (b) Point of the capacity curve ( $+ F_y$ ) related to the collapse of the walls P6 and P8 for the “2-2.7-C-B” model.....	187
Figure 7.21: Failure mechanisms of the masonry walls considering a seismic action in $y$ -direction ( $+ F_y$ ) for the “2-2.7-C-B” model.....	187
Figure 7.22: $y$ -direction push-over curves of the buildings with timber slabs: (a) Isolated structural units and (b) Aggregate structures.....	188
Figure 7.23: $y$ -direction push-over curves of the buildings with concrete slabs: (a) Isolated structural units and (b) Aggregate structures.....	188
Figure 7.24: Deformed shape of the “2-2.7-C-B” aggregate model.....	189
Figure 7.25: Deformed shape of the “2-2.7-T-B” aggregate model.....	190
Figure 7.26: Pushover curves of the AS with concrete slabs: analyses over the attainment of the LS limit state.....	191
Figure 7.27: Pushover curves of the AS with timber slabs: analyses over the attainment of the LS limit state.....	192
Figure 7.28: Deformed shape of the “2-2.7-C-B” aggregate sub-models.....	192
Figure 7.29: Fragility curves of all the models in $x$ -direction, distinguished according the type of slabs: (a) actual PGA; (b) Monte Carlo method.....	194
Figure 7.30: Fragility curves of all the models in $x$ -direction using Monte Carlo method: (a) distinguished according the number of floors; (b) distinguished according the type of internal walls.....	194
Figure 7.31: Fragility curves of all the models in $y$ -direction, distinguished according the type of slabs: (a) actual PGA; (b) Monte Carlo method.....	195
Figure 7.32: Fragility curves of all the models in $y$ -direction using Monte Carlo method: (a) distinguished according the number of floors; (b) distinguished according the type of internal walls.....	195
Figure 7.33: Fragility curves of the AS using Monte Carlo method: analyses over the LS limit state in buildings with (a) concrete slabs and (b) timber slabs.....	197
Figure A.1.1: Accelerogram 1 – Bologna.....	216
Figure A.1.2: Accelerogram 2 – Bologna.....	216
Figure A.1.3: Accelerogram 3 – Bologna.....	216
Figure A.1.4: Accelerogram 4 – Bologna.....	217
Figure A.1.5: Accelerogram 5 – Bologna.....	217
Figure A.1.6: Accelerogram 6 – Bologna.....	217
Figure A.1.7: Accelerogram 7 – Bologna.....	217

Figure A.1.8: Accelerogram 8 – Bologna. ....	217
Figure A.1.9: Accelerogram 9 – Bologna. ....	218
Figure A.1.10: Accelerogram 10 – Bologna. ....	218
Figure A.1.11: Accelerogram 11 – Bologna. ....	218
Figure A.1.12: Accelerogram 12 – Bologna. ....	218
Figure A.1.13: Accelerogram 13 – Bologna. ....	218
Figure A.1.14: Accelerogram 14 – Bologna. ....	219
Figure A.1.15: Accelerogram 15 – Bologna. ....	219
Figure A.1.16: Accelerogram 16 – Bologna. ....	219
Figure A.1.17: Accelerogram 17 – Bologna. ....	219
Figure A.1.18: Accelerogram 18 – Bologna. ....	219
Figure A.1.19: Accelerogram 19 – Bologna. ....	220
Figure A.1.20: Accelerogram 20 – Bologna. ....	220
Figure A.1.21: Accelerogram 21 – Bologna. ....	220
Figure A.1.22: Accelerogram 22 – Bologna. ....	220
Figure A.1.23: Accelerogram 23 – Bologna. ....	220
Figure A.1.24: Accelerogram 24 – Bologna. ....	221
Figure A.1.25: Accelerogram 25 – Bologna. ....	221
Figure A.1.26: Accelerogram 26 – Bologna. ....	221
Figure A.1.27: Accelerogram 27 – Bologna. ....	221
Figure A.1.28: Accelerogram 28 – Bologna. ....	221
Figure A.1.29: Accelerogram 29 – Bologna. ....	222
Figure A.1.30: Accelerogram 30 – Bologna. ....	222
Figure A.1.31: Accelerogram 31 – Bologna. ....	222
Figure A.1.32: Accelerogram 32 – Bologna. ....	222
Figure A.1.33: Accelerogram 33 – Bologna. ....	222
Figure A.1.34: Accelerogram 34 – Bologna. ....	223
Figure A.1.35: Accelerogram 35 – Bologna. ....	223
Figure A.1.36: Accelerogram 36 – Bologna. ....	223
Figure A.1.37: Accelerogram 37 – Bologna. ....	223
Figure A.1.38: Accelerogram 38 – Bologna. ....	223
Figure A.1.39: Accelerogram 39 – Bologna. ....	224
Figure A.1.40: Accelerogram 40 – Bologna. ....	224
Figure A.1.41: Accelerogram 41 – Bologna. ....	224

Figure A.1.42: Accelerogram 42 – Bologna.....	224
Figure A.1.43: Accelerogram 43 – Bologna.....	224
Figure A.1.44: Accelerogram 44 – Bologna.....	225
Figure A.1.45: Accelerogram 45 – Bologna.....	225
Figure A.1.46: Accelerogram 46 – Bologna.....	225
Figure A.1.47: Accelerogram 47 – Bologna.....	225
Figure A.1.48: Accelerogram 48 – Bologna.....	225
Figure A.2.1: Accelerogram 1 – Seixal. ....	227
Figure A.2.2: Accelerogram 2 – Seixal. ....	227
Figure A.2.3: Accelerogram 3 – Seixal. ....	227
Figure A.2.4: Accelerogram 4 – Seixal. ....	227
Figure A.2.5: Accelerogram 5 – Seixal. ....	227
Figure A.2.6: Accelerogram 6 – Seixal. ....	228
Figure A.2.7: Accelerogram 7 – Seixal. ....	228
Figure A.2.8: Accelerogram 8 – Seixal. ....	228
Figure A.2.9: Accelerogram 9 – Seixal. ....	228
Figure A.2.10: Accelerogram 10 – Seixal. ....	228
Figure A.2.11: Accelerogram 11 – Seixal. ....	229
Figure A.2.12: Accelerogram 12 – Seixal. ....	229
Figure A.2.13: Accelerogram 13 – Seixal. ....	229
Figure A.2.14: Accelerogram 14 – Seixal. ....	229
Figure A.2.15: Accelerogram 15 – Seixal. ....	229
Figure A.2.16: Accelerogram 16 – Seixal. ....	230
Figure A.2.17: Accelerogram 17 – Seixal. ....	230
Figure A.2.18: Accelerogram 18 – Seixal. ....	230
Figure A.2.19: Accelerogram 19 – Seixal. ....	230
Figure A.2.20: Accelerogram 20 - Seixal.....	230
Figure A.2.21: Accelerogram 21 – Seixal. ....	231
Figure A.2.22: Accelerogram 22 – Seixal. ....	231
Figure A.2.23: Accelerogram 23 – Seixal. ....	231
Figure A.2.24: Accelerogram 24 – Seixal. ....	231
Figure A.2.25: Accelerogram 25 – Seixal. ....	231
Figure A.2.26: Accelerogram 26 – Seixal. ....	232
Figure A.2.27: Accelerogram 27 – Seixal. ....	232

Figure A.2.28: Accelerogram 28 – Seixal.....	232
Figure A.2.29: Accelerogram 29 – Seixal.....	232
Figure A.2.30: Accelerogram 30 – Seixal.....	232
Figure A.2.31: Accelerogram 31 – Seixal.....	233
Figure A.2.32: Accelerogram 32 – Seixal.....	233
Figure A.2.33: Accelerogram 33 – Seixal.....	233
Figure A.2.34: Accelerogram 34 – Seixal.....	233
Figure A.2.35: Accelerogram 35 – Seixal.....	233
Figure A.2.36: Accelerogram 36 – Seixal.....	234
Figure A.2.37: Accelerogram 37 – Seixal.....	234
Figure A.2.38: Accelerogram 38 – Seixal.....	234
Figure A.2.39: Accelerogram 39 – Seixal.....	234
Figure A.2.40: Accelerogram 40 – Seixal.....	234
Figure A.2.41: Accelerogram 41 – Seixal.....	235
Figure A.2.42: Accelerogram 42 – Seixal.....	235
Figure A.2.43: Accelerogram 43 – Seixal.....	235
Figure A.2.44: Accelerogram 44 – Seixal.....	235
Figure A.2.45: Accelerogram 45 – Seixal.....	235
Figure A.2.46: Accelerogram 46 – Seixal.....	236
Figure A.2.47: Accelerogram 47 – Seixal.....	236
Figure A.2.48: Accelerogram 48 – Seixal.....	236
Figure A.2.49: Accelerogram 49 – Seixal.....	236
Figure A.2.50: Accelerogram 50 – Seixal.....	236
Figure C.1: $x$ -direction ( $- F_x$ ) push-over curves of the buildings with 2 floors and timber slabs: (a) Isolated structural units and (b) Aggregate structures.....	251
Figure C.2: $x$ -direction ( $- F_x$ ) push-over curves of the buildings with 2 floors and concrete slabs: (a) Isolated structural units and (b) Aggregate structures.....	251
Figure C.3: $x$ -direction ( $- F_x$ ) push-over curves of the buildings with timber slabs: (a) Isolated structural units and (b) Aggregate structures. ....	252
Figure C.4: $x$ -direction ( $- F_x$ ) push-over curves of the buildings with concrete slabs: (a) Isolated structural units and (b) Aggregate structures. ....	252
Figure C.5: $y$ -direction ( $- F_y$ ) push-over curves of the buildings with 2 floors and timber slabs: (a) Isolated structural units and (b) Aggregate structures.....	253
Figure C.6: $y$ -direction ( $- F_y$ ) push-over curves of the buildings with 2 floors and concrete slabs: (a) Isolated structural units and (b) Aggregate structures.....	253

Figure C.7: $y$ -direction ( $- F_y$ ) push-over curves of the buildings with timber slabs: (a) Isolated structural units and (b) Aggregate structures.....	254
Figure C.8: $y$ -direction ( $- F_y$ ) push-over curves of the buildings with concrete slabs: (a) Isolated structural units and (b) Aggregate structures.....	254
Figure C.9: Pushover curves of the AS with concrete slabs: analyses over the attainment of the LS limit state ( $- F_y$ ).....	255
Figure C.10: Pushover curves of the AS with timber slabs: analyses over the attainment of the LS limit state ( $- F_y$ ).....	255
Figure C.11: Fragility curves of all the models in $x$ -direction ( $- F_x$ ), distinguished according the type of slabs: (a) actual PGA; (b) Monte Carlo method.....	256
Figure C.12: Fragility curves of all the models in $x$ -direction ( $- F_x$ ) using Monte Carlo method: (a) distinguished according the number of floors; (b) distinguished according the type of internal walls. ....	256
Figure C.13: Fragility curves of all the models in $y$ -direction ( $- F_y$ ), distinguished according the type of slabs: (a) actual PGA; (b) Monte Carlo method.....	257
Figure C.14: Fragility curves of all the models in $y$ -direction ( $- F_y$ ) using Monte Carlo method: (a) distinguished according the number of floors; (b) distinguished according the type of internal walls. ....	257
Figure C.15: Fragility curves of the AS using Monte Carlo method: analyses ( $- F_y$ ) over the LS limit state in buildings with (a) concrete slabs and (b) timber slabs.....	258

## List of Tables

Table 2.1: Classification of the damage levels referred to masonry buildings. ....	26
Table 3.1: Example of a factorial design with 3 variables. ....	39
Table 3.2: Example of a central composite design with 17 simulations. ....	40
Table 3.3: Example of a central composite design with 17 simulations and 3 blocks. ....	40
Table 4.1: Knowledge levels and confidence factors. ....	52
Table 4.2: Reference values of mechanical parameters (minimum and maximum) and mean self-weight for different masonry typologies, referred to weak mortar, uncoursed masonry, absent connections between wall leaves, texture following the “rule of the art” in case of regular elements: $f_m$ = mean compressive strength of masonry; $\tau_0$ = mean shear strength of masonry; $E$ = mean value of the elastic modulus; $G$ = mean value of the shear modulus; $w$ = mean self-weight of masonry. (Commentary to the NTC 2008 – Table C8A.2.I). ....	54
Table 4.3: Corrective coefficients of the mechanical parameters indicated in Table 4.2 to be applied in presence of: high-quality mortar, thin mortar joints, transversal connections between wall leaves, poor internal core, strengthening interventions such as mortar injections or reinforced plaster (Commentary to the NTC 2008 – Table C8A.2.2). ....	54
Table 5.1: Parameters defined the group of accelerograms in Bologna, Italy. ....	77
Table 5.2: Parameters defined the group of accelerograms in Seixal, Portugal. ....	78
Table 6.1: Structural properties of the masonry walls. ....	88
Table 6.2: Structural properties of the diaphragms. ....	88
Table 6.3: Definition of the normal distributions adopted for the explicit variables. ....	89
Table 6.4: Relations between masonry properties and masonry shear strength ( $\tau$ ). ....	90
Table 6.5: Relations between slab properties and slab elastic modulus ( $E_1$ ). ....	90
Table 6.6: Values assumed by the variable $X_i$ in the defined normal distributions. ....	90
Table 6.7: Definition of the group of 17 simulations using the coded variables $x_i$ . ....	91
Table 6.8: Values assumed by the thickness of the walls $s$ and correspondent blocks. ....	92
Table 6.9: Regression parameters and standard deviations of the isolated structural unit, considering the seismic forces + $F_x$ . ....	102
Table 6.10: Regression parameters and standard deviations of the isolated structural unit, considering the seismic forces - $F_x$ . ....	103
Table 6.11: Regression parameters and standard deviations of the isolated structural unit, considering the seismic forces + $F_y$ . ....	104
Table 6.12: Regression parameters and standard deviations of the isolated structural unit, considering the seismic forces - $F_y$ . ....	105
Table 6.13: Values assumed by the thickness of the walls $s$ . ....	110
Table 6.14: Definition of the normal distribution adopted for the explicit variable $s$ . ....	111

Table 6.15: Groups of the 6 accelererograms and the correspondent simulations (Table B.2) for each of the thicknesses $s$ .	121
Table 6.16: Regression parameters and standard deviations of the ISU and AS RS models, considering the seismic forces $+ F_x$ .	124
Table 6.17: Regression parameters and standard deviations of the ISU and AS RS models, considering the seismic forces $- F_x$ .	124
Table 6.18: Regression parameters and standard deviations of the ISU and AS RS models, considering the seismic forces $+ F_y$ .	125
Table 6.19: Regression parameters and standard deviations of the ISU and AS RS models, considering the seismic forces $- F_y$ .	125
Table 6.20: Regression parameters and standard deviations of the Unit 3 and Unit 4 RS models, considering the seismic forces $+ F_y$ .	126
Table 6.21: Regression parameters and standard deviations of the Unit 3 and Unit 4 RS models, considering the seismic forces $- F_y$ .	126
Table 6.22: Definition of the group of 11 simulations using the coded variables $x_i$ .	131
Table 6.23: Definition of the aggregate configurations.	134
Table 6.24: Regression parameters and standard deviations of the AS with different structural units, considering the seismic forces $+ F_x$ .	141
Table 6.25: Regression parameters and standard deviations of the AS with different structural units, considering the seismic forces $- F_x$ .	142
Table 6.26: Regression parameters and standard deviations of the AS with different structural units, considering the seismic forces $+ F_y$ .	143
Table 6.27: Regression parameters and standard deviations of the AS with different structural units, considering the seismic forces $- F_y$ .	144
Table 6.28: Regression parameters and standard deviations of the Unit 3, considering the seismic forces $+ F_y$ , over the attainment of the LS limit state.	145
Table 6.29: Regression parameters and standard deviations of the Unit 3, considering the seismic forces $- F_y$ , over the attainment of the LS limit state.	146
Table 6.30: Regression parameters and standard deviations of the Unit 4, considering the seismic forces $+ F_y$ , over the attainment of the LS limit state.	147
Table 6.31: Regression parameters and standard deviations of the Unit 4, considering the seismic forces $- F_y$ , over the attainment of the LS limit state.	148
Table 6.32: 9 type of comparisons carried out between the AS - D and the AS - I.	154
Table 6.33: Expected and the actual behaviours on the variation of the $PGA_C$ for the group $\tau_1$ -d <sub>3</sub> -s <sub>3</sub> .	155
Table 6.34: Expected and the actual behaviours on the variation of the $PGA_C$ for the group $\tau_2$ -d <sub>2</sub> -s <sub>2</sub> .	156
Table 6.35: Expected and the actual behaviours on the variation of the $PGA_C$ for the group $\tau_2$ -d <sub>4</sub> -s <sub>4</sub> .	156

Table 6.36: Expected and the actual behaviours on the variation of the $PGA_C$ for the group $\tau_3-d_1-s_1$ . .....	157
Table 6.37: Expected and the actual behaviours on the variation of the $PGA_C$ for the group $\tau_3-d_3-s_3$ . .....	157
Table 6.38: Expected and the actual behaviours on the variation of the $PGA_C$ for the group $\tau_3-d_5-s_5$ . .....	158
Table 6.39: Expected and the actual behaviours on the variation of the $PGA_C$ for the group $\tau_4-d_2-s_2$ . .....	158
Table 6.40: Expected and the actual behaviours on the variation of the $PGA_C$ for the group $\tau_3-d_4-s_4$ . .....	159
Table 6.41: Expected and the actual behaviours on the variation of the $PGA_C$ for the group $\tau_5-d_3-s_3$ . .....	159
Table 6.42: Number of the cases where the $PGA_C$ has a variation different from what is expected. .....	160
Table 6.43: Comparison between the AS - D and the AS - I according to the variation of d and s between the structural units along the AS. ....	161
Table 7.1: Variation considered for the structural and geometrical properties. ....	171
Table 7.2: Mechanical and geometrical properties of the masonry walls. ....	176
Table 7.3: Mechanical and geometrical properties of the slabs. ....	177
Table A.1: Ground-motion selections for the site of Bologna. ....	215
Table A.2: Ground-motion selections for the site of Seixal. ....	226
Table B.1: Design matrix of the Isolated Structural Unit RS model in Section 6.2. ....	237
Table B.2: Design matrix of the Response Surface models in Section 6.3. ....	241
Table B.3: Design matrix of the Response Surface models in Section 6.3. ....	247



# **1. INTRODUCTION**

---

## 1.1 Motivation

Among the actions soliciting the buildings during their nominal life, earthquakes are one of the most dangerous and devastating events in terms of number of victims and damages. The seismic actions determine dynamic stress regimes comparable to those generated by systems of horizontal forces, varying in time. The earthquakes, and in particular the assessment of the seismic vulnerability, represent a topic of particular relevance in the world scenario; Italy is one of the countries with the highest seismic risk in the Mediterranean area, due to the great occurrence frequency and intensity of the earthquakes (Barbieri et al., 2013). The historical and architectural heritage safeguard, aimed to preserve the buildings over the time, is therefore a necessary requirement for the preservation of the cultural identity of the places.

The assessment of the seismic risk is very important to determine the safety level of the structures, both to perform studies at the territorial scale, identifying the buildings most at risk, and to direct the first aid after the seismic event to the most vulnerable areas. The seismic risk results from the combination of three components: the hazard, the exposure and the vulnerability (McGuire, 2004; Vicente et al., 2011).

The seismic hazard indicates the quantitative estimate of the occurrence of earthquakes, in a given area. It represents the probability of exceeding a certain intensity of a seismic event and its evaluation is a prevision tool of the degree of severity of expected earthquakes. This severity can be measured using instrumental scales, providing objective measures of the seismic action, or macro-seismic scales, based on subjective measures of the effects produced by the earthquake. The seismic exposure indicates the value of what can be damaged due to a seismic event, i.e. people, buildings, infrastructures. The estimate of the exposure corresponds, therefore, to the quantification of those parameters, as well as to the evaluation of their reaction capacity. The seismic vulnerability is the propensity of a structure to suffer damages, modifications or losses, against a seismic event of a given intensity.

In other words, the seismic risk is strongly influenced by the location, the quality and the value of the assets and activities present on the territory that can be directly or indirectly influenced by the seismic event (settlements, buildings, economic-productive activities, infrastructures, assets of historical and cultural value, population density). Any intervention aimed at the reduction of the risk should be carried out on the parameters just described. Actually, while the hazard is a value that cannot be modified, since it is a characteristic of the

territory subject to seismic events, and the exposure is a parameter that can only be modified with appropriate management policies, vulnerability is the parameter on which it is possible to intervene with greater incisiveness, according to the codes and undertaking structural or non-structural improvement interventions (Tyagunov et al., 2004; Birkmann, 2007; Hajibabaei et al., 2012).

The assessment of the seismic vulnerability can be carried out at different levels of scale, from the territorial to the one of the block and the single building. Regarding the territorial analyses, it is necessary to identify some typological classes, referring to buildings characterized by similar behaviours under the action of an earthquake, to which associate vulnerability levels (Giovinazzi and Lagomarsino, 2001). Furthermore, it is necessary to take into account the extension and the consistency of the heritage to be assessed, as well as the economic and time effort, and the reliability of the information to be acquired through survey campaigns. This process involves greater difficulties, mostly linked to the big variety of the typologies, characterizing an entire municipal area (Borri et al., 2007; Ceroni et al., 2013).

The most common methods of vulnerability assessment, proposed in the past, can be divided into three main categories: empirical/statistical methods, analytical/mechanical methods and methods based on the judgment of the experts (Calvi et al., 2006).

The empirical or statistical methods represent the approach based on the statistical analysis of the damages of the earthquakes; usually, the buildings are classified according to the materials and the structural techniques and to the previous observed damages on buildings of the same typologies. These methods are based on information obtaining through quick survey procedures and on correlations between the typological characteristics and the expected damage in the presence of seismic events of predetermined intensity. The correlations between the structural typology and the damage are usually obtained from the statistical processing of the data obtained through survey sheets of the earthquake effects, providing as results the vulnerability index and the vulnerability class of the building.

The analytical or mechanical methods use mechanical models reproducing the main characteristics of the buildings to be evaluated, on which the damages caused by simulated earthquakes are studied and evaluated completely in an analytical and mechanical way. Usually non-linear analyses of the structure are performed, referred to a set of samples, reduced with respect to the set of buildings whose vulnerability must be assessed. The damage

is associated to the attainment of a limit state, which can be identified by the achievement of a limit rotation or a collapse mechanism of the structure, while the seismic action is generally expressed in terms of spectral quantities, such as the PGA.

The methods based on the judgment of the experts are based on expert judgments to assess the seismic behaviour and the vulnerability of some structural typologies, or to identify the factors influencing the seismic vulnerability of the buildings.

The assessment of the seismic vulnerability, either through empirical approaches or through more accurate mechanical models, cannot ignore the knowledge, as accurate as possible, of the peculiar characteristics of the buildings, obtaining through survey campaigns. In particular, with regard to the seismic behaviour of the historic masonry buildings, there is a strong dependence on the structural details relating to vertical connections and to the connections between the slabs and the vertical panels, ensuring the box-like behaviour, which is an indispensable requirement for an effective limitation of the seismic vulnerability, and avoiding the activation of overturning mechanisms for out-of-plane actions. The absence of these precautions allows the activation of collapse mechanisms in the plane orthogonal to the individual panel; in this case, it would be necessary to perform analyses relating to the various structural elements with local models.

A further complication is generated by the mutual interactions between the individual structural units that are generated when, as common in most of the buildings in the historic centres, the structure is located within a structural aggregate. The masonry aggregate buildings represent a considerably widespread structural typology in the Italian historical centres and they are often the result of an unplanned urban development (Formisano et al., 2010). The research of the last twenty years has shown that the seismic analysis of these structural complexes cannot ignore the inevitable interactions deriving from the structural contiguity between adjacent buildings, connected or simply juxtaposed (Lagomarsino et al., 2014).

Sometimes, it is a common simplification in civil engineering practice to analyse the seismic behaviour of a building considering it as an isolated structural unit, even when it belongs to an aggregation of buildings. This simplification certainly leads to approximations and incorrect predictions of the seismic response, ignoring the interactions with the adjacent buildings. If an engineer has to perform a seismic analysis of a masonry structure enclosed in

an aggregation of buildings, he cannot ignore the contribute of the adjacent structures, because all these buildings are part of a complex and each one of them concurs to the seismic response. The awareness of this common simplification in civil engineering is the main motivation that led to the study of the seismic vulnerability and fragility of masonry aggregate buildings, present in this thesis.

## **1.2 Research problem: the aggregate buildings**

Masonry is the oldest and simplest building technique and it has a history as long as the history of constructions. The assessment of the structural safety of existing masonry buildings is a current and a critical issue; the situation is even more critical when dealing with old masonry constructions, either built without a proper seismic design or subjected to damages and degradation through years and, therefore, particularly vulnerable to horizontal actions. The safety assessment of historical constructions is affected by their geometrical complexity, the variability of materials and the building techniques adopted, the poor knowledge on past events which might have affected the current condition of the constructions and the lack of design codes.

The majority of the masonry structures are unreinforced masonry (URM) and they not contain reinforcing (FEMA, 2009). The seismic response of URM buildings is mainly affected by the mechanical properties of the masonry, the geometry of the element, the type of slabs and roofs and the construction details (Lourenço et al. 2011; Cattari and Lagomarsino 2013; Penna et al. 2014).

Usually, URM buildings present higher seismic vulnerability with respect to other structural typologies, but some precautions can ensure a global box-type behaviour, where the seismic response is mainly governed by the in-plane capacity of the walls and the in-plane stiffness of horizontal diaphragms. However, the lower mechanical properties, the presence of flexible diaphragms, the irregular distribution of mass and stiffness in plan and elevation, and the lack of proper connection between orthogonal walls and between walls and slabs/roofs are the reasons of a higher vulnerability, where the local seismic behaviour of the single walls can occur (Shawa et al., 2012; Prajapati et al., 2015).

Masonry buildings in Italy represent the majority of the historical and cultural heritage and they are very often the result of an unbridled urban growth, carried out without accuracy in the design, filling all possible urban spaces. For this reason, aggregate masonry buildings

have been generated over the years, allowing the aggregations of different inhomogeneous buildings, arranged along the years and strictly linked to a historical planning system. They may be formed by one or more buildings, aggregated by means of a contact, or a link, more or less effective, between buildings with generally different constructive characteristics (Formisano et al., 2010; Lagomarsino et al., 2014). The buildings of the aggregate, which have been subjected to the generation process, interact between themselves under a seismic action or a general dynamic action, giving the aggregate different characteristics from the individual element components (Maio, 2013).

An aggregate structure causes a series of problems: a) the non-homogeneity of the masonry bearing structures, as the result of the "assembly" process of different structural units interacting each others, b) the coexistence of different materials, often with very different stiffness and strengths properties and c) the correct and univocal knowledge of the structural model characterizing the masonry aggregate (Battaglia et al., 2019).

Within the structural aggregates the buildings have to be identified, defined as homogeneous structural units from the bottom to the top, in general, distinguishable from the adjacent ones by at least one of the following characteristics that identifies a distinct dynamic behaviour: structural typology, differences in elevation, irregularity plan with some parts not effectively connected, age of construction, different heights of the slabs, renovation from the bottom to the top. Nevertheless, in the aggregates of the historical centres, complex situations are present and the identification of the structural units is not always univocal.

Among the procedures of seismic vulnerability assessment, most used in the literature, there are the approaches outlined by the Italian codes, which have formalized some aspects related to aggregate buildings. Thus, the "Norme Tecniche per le Costruzioni" (NTC) in DM 17.01.2018 (NTC, 2018) and, in particular, the commentary of the NTC, "Istruzioni per l'applicazione delle Norme Tecniche delle Costruzioni" (Commentary to the NTC 2018, 2019) includes instructions which should be followed in the study of aggregate buildings.

In particular, as it is shown in the NTC, it is preliminarily fundamental to determine the Structural Unit (S.U.) to consider in the study, namely those portions of the building to which corresponds a uniform behaviour. The entire aggregate should be analysed, identifying the fundamental spatial connections, with attention to overlapping and juxtaposition mechanisms, and taking into account that these aggregate portions must show an unified structural

behaviour against static and dynamic actions. The S.U. must have continuity from the summit to the base, both if it is composed of one or more building units, as regards the flow of the vertical loads and, normally, it can be delimited by open spaces, structural joints or contiguous buildings with different characteristics.

The conservation and the renovation of ancient buildings belonging to the culture heritage, preserving their main architectural features, are becoming a very sensitive problem in Italy as in other Countries (Barbieri et al., 2013). Most of the historical heritage consists of masonry buildings and most of them are enclosed in aggregations. They are generally affected by a high seismic vulnerability in relation to the construction techniques developed over the years and to the frequent lack of an adequate structural conception, aimed to defend against the seismic action. In fact, masonry structures were generally built in times when the absence of codes, specific methodologies and calculation tools led to a design approach based more on intuition and experience than on a structural conception well defined and justified.

Therefore, the vulnerability assessment of an aggregate should start from a first cognitive phase, necessary to develop the successive phases of analysis (Ramos and Lourenço, 2004). The cognitive process has as its fundamental presupposition the identification of the aggregate in the environmental and urban context in which it is located, in order to formulate hypotheses on its formation and evolution process and it is conducted through geometrical and structural surveys.

The techniques that allow, from the data acquired in the first cognitive phase, the evaluation of the seismic safety and the possible design of the interventions will be then analysed. The analysis should be conducted examining the procedures for the global or local assessment of the vulnerability of the aggregate. In existing masonry buildings subjected to seismic actions, both global and local mechanisms can occur. The global mechanisms are those affecting the entire structure and involving the walls mainly in their plane. The global seismic analysis should consider, as far as possible, the real structural system of the construction, with particular attention to the stiffness and the strength of the floors and all the efficiency of the connections of the structural elements. With this kind of structures, the methods of general use verification for new buildings (linear analyses most of the times) may not be adequate. In the analyses (the most appropriate are the non-linear ones) of a building belonging to an aggregate, it will be necessary to take into account all the possible interactions deriving from

the structural contiguity with adjacent buildings. Therefore, the structural unit, object of the study, must be taken into consideration, highlighting the actions that can derive from the adjacent structural units (Commentary to the NTC 2018, 2019).

However, the aggregate buildings of the historical centres often undergo transformations over time such as to make uncertain and inadequate an analysis conducted in terms of global response. In these buildings, it is necessary to consider the presence of the characteristic elements of vulnerability linked to: the quality of the connection between the walls and the slabs; the quality of the walls; the iterations with the other elements of the structure and with the adjacent buildings. Thus, it is possible to hypothesize, according to the knowledge of the seismic behaviour of analogous structures, the local mechanisms considered significant. The local mechanisms involve single walls or larger portions of the building and they are facilitated by the absence or the ineffectiveness of the connections between walls and slabs and in the intersections between the walls.

The structural analysis of the entire aggregate, global or local, allows to define the structural seismic capacity that, compared with the seismic demand, allows to establish the vulnerability of the aggregate. The assessment of the vulnerability and of the fragility is defined relating to the limit states that can occur during the nominal life of the aggregate, in such a way to identify the performances to be guaranteed for different return periods of the earthquake, by means of structural analysis methods, at local or global level.

### **1.3 Goals, methodology and outlines**

Since the common simplification in civil engineering to analyse a structure as isolated, even if it belongs to an aggregation of buildings, the starting point of this thesis is the study of the seismic vulnerability and fragility of a masonry structural unit, conceived as belonging to an aggregate but studied, at first, as isolated structural unit (ISU). The goal is to show that the seismic analysis cannot ignore the inevitable contribution of the adjacent structural units.

The vulnerability assessment of the masonry buildings is carried out by means of the comparison between the seismic structural capacity and the seismic demand. But masonry structures can fail through a large variety of modes and their structural capacity is characterized by many structural and geometrical variabilities and uncertainties (Franchin et al., 2004). For this reason, it is convenient to use statistical and probabilistic approaches for the evaluation of the seismic structural capacity, not considering some characteristics of the

structure in a deterministic way, but as probabilistic variables in defined ranges. The statistical study allows to perform parametric analyses that, considering a certain number of variables and uncertainties, let to consider different simulations referred to different buildings, changing according to the choice of the variables. This leads to obtain results referring to different classes of buildings, subjected to studies of seismic fragility.

Therefore, the first purpose of this thesis is to analyse a masonry single structural unit, taking into account some geometrical and structural variabilities and the uncertainties involved in the problem, using statistical methods, in order to highlight which are the mechanical and geometrical parameters most affecting the seismic response. The analysis of the single unit allows to face the main purpose of this thesis which is focused on the comparison between the isolated structural units and some aggregations of identical structural units in row.

Since the lack of knowledge and past studies on the subject in the literature and considering the difficulty inherent in the study of the seismic vulnerability of this type of buildings, as a starting point, it is convenient to analyse one of the simplest kind of aggregate present in Italian territories: the masonry aggregates in row composed by identical structural units.

The comparison should be carried out considering two orthogonal directions of the seismic action: the one following the development of the aggregate and the orthogonal one. This allows to evaluate all the possible advantages and disadvantages deriving from the aggregation process and the variation on the seismic behaviour when the single structural unit is located in different positions within the aggregate. The comparison in statistical terms allows to study the seismic vulnerability, deriving the fragility curves referred to the isolated structural units and to the aggregations of identical structural units in row, considering two different directions of the seismic action.

The assessment of the seismic vulnerability and fragility, through the comparison between the single structural units and the row aggregations, is at first carried out on one of the most diffused typological masonry in northern Italy, the clay brick masonry and, in a second moment, on one of the most common typological masonry in the south of Portugal, the limestone masonry.

A further objective of this thesis is to analyse aggregations of structural units in row, generated starting from the aggregates obtained considering the medium values of the considered variables and changing the values of those variables in predetermined ranges.

This approach lets to generate aggregates with different structural units, to compare them with the single structural units and with the aggregations of identical structural units and to analyse which variables, characterizing the differences within the aggregate, most influence the seismic response.

The buildings object of this work are analysed with their global behaviour, assuming that the orthogonal masonry walls and the slabs and the walls are well-connected. As a first part of the study, the activation of local mechanisms is neglected and just the in plane behaviour of the masonry panels is considered.

In order to achieve these objectives, the thesis is organized in eight Chapters and three Annexes. The main tasks and methodologies are described below:

**1. Introduction:** this chapter presents the main motivations, the research problem object of this thesis, highlighting the goals, the methodologies and the outlines proposed to evaluate the seismic fragility and vulnerability of unreinforced masonry aggregate buildings.

**2. Seismic fragility:** this chapter presents an introduction of the structural reliability problem, with particular focus on seismic reliability of structures. The analysis of the failure probability, by means of the fragility curves is then examined, presenting and discussing some different approaches present in the literature.

**3. Probability computation methods through simulations:** this chapter gives the main simulation methods used to estimate the failure probability  $P_F$ , focusing among them on the Response Surface statistical method, used in this thesis for the fragility analyses. The definition of the statistical model, the regression methods and the definition of the variables involved in the problem are detailed.

**4. Modelling and analysis of URM buildings:** this chapter provides a general description of the crucial aspects characterizing the modelling and the seismic analysis of existing Unreinforced Masonry Buildings (URM), object of this thesis, detailing the out-of-plane and in-plane behaviour of their resisting walls, the main numerical modelling to be adopted for their complex structure, with particular focus on the macro-element modelling with TreMuri software adopted in this thesis, and the application of the non-linear static analysis as method to perform the structural capacity of these types of structures.

**5. Seismic fragility assessment of masonry structures:** this chapter defines the general methodology applied to assess the seismic fragility of unreinforced clay brick (Bologna) and

stone (Seixal) masonry structures: starting from the selection of the parameters defining different structural models (representative of different classes of buildings) a set of non-linear static analyses was performed to obtain the structural capacities to be compared with the structural demands, defined by means of the variation of the seismic action in the site (different registered accelerograms), in order to plot the fragility curves.

**6. Seismic fragility of clay brick masonry structures: case studies in Bologna, Italy:** in this Chapter the criteria to select the explicit and implicit variables defining the masonry structures, the numerical models used to perform the non-linear static analyses, the RS models and the fragility curves obtained are described, referring as first step, to the isolated structural units and then to aggregations of identical structural units in row, in order to analyse advantages and disadvantages obtained in the aggregation process. Finally, the seismic fragility of aggregate structures with geometrical differences between the structural units in row is compared with that referred to the previous aggregate structures with identical structural units.

**7. Seismic fragility of stone masonry structures: case studies in Seixal, Portugal:** this Chapter aims to assess the seismic vulnerability and fragility of stone masonry structures sited in Seixal, a small city in the south of Lisbon, in Portugal. A methodology similar to those applied in Chapter 6 allowed to define the most prevalent structural typologies in the study area, considering the variability of a set of structural and geometrical properties and to perform a set of non-linear static analyses, in order to obtain the fragility curves referred to the selected structural typologies. This application also provided the comparison between the masonries as isolated structural units and as aggregations of identical structural units in row.

**8. Conclusions:** the main conclusions from the work developed and the identification of the issues that need further future developments are herein presented.

**Appendix A:** this Appendix gives two Tables showing all the data related to the recordings of the selected earthquakes for the site of Bologna and for the site of Seixal and all the plots of the two groups of accelerograms.

**Appendix B:** this Appendix gives the 3 design matrices containing the definition of the simulations of the 3 Response Surface models defined in Chapter 6.

**Appendix C:** since in Chapter 7 only the results related to the application of the positive actions ( $+F_x$  and  $+F_y$ ) of the seismic action are showed, this Appendix gives the results related to the negative actions ( $- F_x$  and  $- F_y$ ) for the masonry buildings sited in Seixal.

## **2. SEISMIC FRAGILITY**

---

## 2.1 Introduction

The field of civil engineering is subjected to a large number of uncertainties and variabilities, especially when dealing with seismic engineering (Der Kiureghian, 1996). The evaluation of the structural reliability against earthquakes is one of the most studied topics in seismic engineering, especially in the research field (Wen, 2001). In order to take into account a set of uncertainties and to carry out quantitative assessments of structural safety, the use of probabilistic methods is recommended. They allow to consider, for example, the randomness of earthquake events, the great uncertainty in predicting the intensity of ground motions and the difficulty of accurately assessing the structural capacity of structures subjected to cyclic loads, such as earthquakes (Buratti, 2008).

In the past, the main known types of uncertainties and variabilities in structural and seismic engineering were (Der Kiureghian, 1996): (1) the inherent randomness, related to the inherent variability in materials and in environmental effects, such as loads and support movements; (2) the statistical uncertainty, which occurs during the estimation of the parameters of probability distributions from observational samples of limited size; and (3) the model uncertainty, related to the imperfection of mathematical models used to describe complex physical phenomena, such as models describing loads and capacities of soils or structures. Only the uncertainty due to inherent randomness results to be irreducible, while the statistical uncertainty can be reduced by collecting a greater number of samples and model uncertainty by using more accurate models.

Lately, a more detailed list of sources of uncertainties was proposed by Der Kiureghian and Ditlevsen (2009): (1) uncertainty intrinsic in the basic random variables, such as the uncertainty inherent in material property constants and load values, which can be directly measured; (2) uncertain model error resulting from selection of the form of the probabilistic sub-model used to describe the distribution of basic variables; (3) uncertain modelling errors resulting from selection of the physical sub-models used to describe the derived variables; (4) statistical uncertainty in the estimation of the parameters of the probabilistic sub-model; (5) statistical uncertainty in the estimation of the parameters of the physical sub-models; (6) uncertain errors involved in measuring of observations, including errors involved in indirect measurement; (7) uncertainty modelled by the random variables corresponding to the derived

variables, which may include, in addition to all the above uncertainties, uncertain errors resulting from computational errors, numerical approximations or truncations.

The above list categorizes the sources of possible uncertainties, but the uncertainties themselves are distinguished into aleatory or epistemic (Casti, 1990). The aleatory uncertainty is due to the innate and intrinsic variability of some parts of the considered model or to the randomness and natural unpredictability of a phenomenon. The epistemic uncertainty is caused by lack of sufficient data to have a reliable knowledge, by imperfections in the data acquisition phase or imperfections in the process of knowledge. The epistemic uncertainty can be reduced by increasing the knowledge on the considered physical phenomenon, while the aleatory one can often be better characterized by additional studies allowing an estimate more accurate, but it is not reducible through acquisitions of new knowledge (Rathje et al., 2010; Rodriguez-Marek et al., 2014).

Therefore, it is convenient to introduce the categorization of uncertainties into aleatory and epistemic on the use of probabilistic models. The advantage of distinction of the uncertainties is the clarification on which uncertainties can be reduced and which uncertainties are less inclined to reduction. The categorization of uncertainties is a choice that must be made by the model builder, and generally depends on the context and application (Buratti, 2008).

## 2.2 Failure probability

The consideration of uncertainties and variabilities in seismic engineering studies is carried out by means of probabilistic methods. The starting point is the probability integral, representing the essence of the structural reliability problem (Der Kiureghian, 1996):

$$P_F = \int_F f(\mathbf{x}) d\mathbf{x} \quad (2.1)$$

where  $P_F$  is the failure probability,  $f(\mathbf{x})$  is the probability density function (PDF) of a vector of random variables  $\mathbf{x}$ , representing time-invariant uncertain quantities influencing the state of the structure under consideration and  $F$  is a subset of the outcome space where failure occurs. By failure, usually the exceedance of a prescribed serviceability or safety limit is implied. For mathematical analysis, it is necessary to describe the failure domain  $F$  in an analytical form. Usually this is done in terms of a performance function, i.e.:

$$F = \{\mathbf{x} : g(\mathbf{x}) \leq 0\} \quad (2.2)$$

where  $g(\mathbf{x})$  is the limit state function. The boundary of  $F$  is defined by  $g(\mathbf{x}) = 0$  and it is known as the limit-state surface. The safe set is defined by  $g(\mathbf{x}) > 0$ .

A reliability problem is said to be time-variant when the limit-state function depends on time,  $t$ . One important case is when some of the uncertain variables are stochastic in nature, as in  $g(\mathbf{x}, \mathbf{y}(t))$ , where  $\mathbf{y}(t)$  is a vector of stochastic processes. For example,  $\mathbf{x}$  may be uncertain mass, stiffness, strength, uncertain on the geometry of the structure or uncertain on damping properties, which are usually time-invariant, and  $\mathbf{y}(t)$  may denote ground acceleration processes at the support points of the structure. For this class of reliability problems, the failure event constitutes the out-crossing of the vector process  $\mathbf{y}(t)$  through the limit-state surface  $g(\mathbf{x}, \mathbf{y}) = 0$ . Usually it is necessary to solve this problem by conditioning on  $\mathbf{x}$ , i.e.:

$$P_F = \int P\left(\min_{0 \leq t \leq T} (g(\mathbf{x}, \mathbf{y}(t))) \leq 0 \mid \mathbf{x}\right) f(\mathbf{x}) d\mathbf{x} \quad (2.3)$$

where  $T$  represents the structure lifetime. The conditioned failure probability for given  $\mathbf{x}$  is solved by the methods of stochastic process theory, evaluating the integral of the failure probability. Some of these methods, based on classical random approaches, are provided by Pinto et al. (2004).

Among the procedures developed for the estimation of  $P_F$ , the simulation methods are the most used. Further details on these methods can be found in Chapter 3.

### 2.3 Evaluation of the seismic fragility

The terms “fragility” means the probability of exceeding a given state of structural performance (for example a limit state) and it is usually evaluated as a function of parameters describing the intensity of the ground motion, generally the peak ground acceleration (PGA) corresponding to the attainment of a certain failure of the structure.

In the field of seismic engineering the use of the limit state function allows to establish the probability of attainment defined failures and therefore to establish the fragility of the structures. Failures are generally established by the limit states.

The limit state refers to specific requirements a structure has to respect to and it is defined as the state in which the structure is at the point of not satisfying those requirements; if the structure exceeds that state, it means that the requirements for which it was designed are no

longer respected. Generally, the requirements are defined using mathematical models describing the geometrical and mechanical properties of the structure. These properties can also be described using geometrical and structural variables and to each choice of variable values corresponds a uniquely defined structure with uniquely defined loads. This structure with its loads is a pure mathematical object that does or does not satisfy a given limit state requirement (Buratti, 2008).

The most used is the life safety (LS) limit state, associated to the maximum value of the structural capacity or to other forms of structural failure endangering the safety of people. The LS limit state represents a situation where the structure is at the point of losing its integrity, passing into an irreversible state that may have a catastrophic nature and from which the structure only recovers by repair or reconstruction.

The limit state identification requires a complete understanding of the behaviour of the safety of systems, especially for the role of structural components and systems in ensuring adequate behaviour of such systems (Wen et al., 2004).

If the limit state (LS) is identified, its probability is defined as:

$$P(LS) = \sum P(LS | IM = im) P(IM = im) \quad (2.4)$$

where  $IM$  is a random variable (or vector) describing the intensity of the demand (ground motion in this case) on the system,  $im$  is the value of the ground motion corresponding to the attainment of the LS,  $P(LS | IM = im)$  is the conditional limit state probability given that  $IM = im$ , and the summation is taken over all the possible values of  $IM$ . The conditional probability  $P(LS | IM = im) = F_{LS}(im)$  is the fragility. The probability  $P(IM = im)$  defines the hazard (in earthquake engineering, the seismic hazard is defined by the cumulative distribution function  $P(IM > im)$ ) (Buratti, 2008).

In a seismic reliability framework, the seismic fragility function is defined as the probability of failure of a structure conditional to the ground-motion intensity. Considering the LS limit state, the structural failure is attained when the limit state function, defined as the difference between the structural capacity ( $C$ ) and the demand ( $D$ ), both dependent on a set  $\mathbf{x}$  of random variables and time  $t$ , is less than or equal to zero (Buratti et al. , 2010):

$$g = \min_t [C(\mathbf{x}, t) - D(\mathbf{x}, t)] \leq 0 \quad (2.5)$$

In the field of seismic engineering, according to Casciati F. (1991) and Veneziano et al. (1983), in the definition of the limit state function in Equation 2.5, the explicit dependence on time is eliminated, because the minimum value over the entire ground-motion duration is taken.

The studies of the seismic fragility is usually carried out using the spectral accelerations; in this contest the quantities C and D can be expressed in terms on spectral acceleration, corresponding to the first natural period of the structure, and therefore, the limit state function can be rewritten:

$$g = S_{a,C}(\mathbf{x}) - S_{a,D} \quad (2.6)$$

where  $S_{a,C}$  is the capacity spectral acceleration and  $S_{a,D}$  is the demand spectral acceleration. Following this approach  $S_{a,D}$  is independent from the structural capacity, because the fragility is conditioned on this parameter, therefore it is independent from the selected variables  $\mathbf{x}$  (Buratti et al., 2010). As known, the seismic demand corresponds to the seismic action the structure is subjected to, thus it does not depend on the characteristics of the structure. On the other hand, the seismic structural capacity corresponds to the seismic action for which the structure failure (for example the attainment of a limit state) is reached, thus it depends on the characteristics of the structure and therefore it is dependent on the selected variables  $\mathbf{x}$ .

The evaluation of the seismic fragility by means of the spectral accelerations and depending on a set on  $\mathbf{x}$  variables, is the approach used in this thesis and depth in Chapter 6 and Chapter 7.

## 2.4 The fragility curves

The most used tool to express the seismic fragility is represented by the fragility curves, relating the probability of exceedance of multiple damage states to a parameter of ground motion severity and can therefore be regarded as a graphical representation of the seismic risk. In the case of building populations, the use of the fragility curves leads to a prediction of the proportion of the exposed stock in each damage state after an earthquake that causes a certain spatial distribution of ground motion severity (Rossetto and Elnashai, 2003).

In the literature, it is possible to find a high number of practical procedures and methods proposed for defining seismic fragility or to directly obtain failure probability. They can be classified in four group (Porter et al., 2007; Pitilakis et al., 2014): (1) empirical methods,

based on post-observations of damages caused by past earthquakes; (2) judgmental methods, based on the judgment of expert opinions; (3) simplified or detailed analytical methods, based on analytical simulations; (4) hybrid methods, derived from combinations of the previous.

Empirical curves use the building damage distributions reported in post-earthquake surveys as their statistical basis. This approach was used, for example, by Gülkan and Sözen (1999) and Yücemem et al., (2004), using some basic structural information (e.g., number of stories, structural system), material properties (e.g., in-situ concrete strength), apparent structural deficiencies (e.g., vertical and plan irregularities), and building site location were collected with damage data through a post-earthquake survey. This information was utilized to arrive at a rating score or index in which the numerical value usually determines whether the building is safe or unsafe, with respect to the traditional goal of assuring life safety. Other procedures utilized the collected information for developing seismic assessment tools in the form of fragility curves.

These curves are highly specific to a particular seismo-tectonic, geotechnical and built-environment (Rossetto and Elnashai, 2003). The reliability of these methods is achieved if the performance of a large number of structural systems is considered and if many reliable empirical data are used, considering a wide range of ground motions. Therefore, these results can only be achieved by combining data from different earthquakes and locations. However, the rare frequency of large seismic events on densely populated areas only allows the collection of scarce and concentrated observational data in the range of low seismic events, with low-damage and low-ground motion. The low level of refinement in terms of both structure and damage classification characterizing the statistics of post-earthquake surveys therefore represents a real obstacle to combining damage data for the populations of different composition.

In the most recent scenario, there are several works aimed to estimate fragility curves for historic masonry buildings present in Italian historic centres with empirical methods. Between these, Rosti et al. (2019) developed empirical fragility curves for residential masonry buildings, by statistically processing post-earthquake damage data collected after Italian seismic events in the time span 1980-2009, distinguishing 5 levels of damage and evaluating the PGA from shakemaps. Once some vulnerability classes of decreasing vulnerability were defined, starting from the typological classification of the masonry building stock,

empirically-derived fragility curves were then obtained and implemented in the Italian national platform for evaluating seismic risk at territorial scale and applied to the Tuscany region, as an example.

Furthermore, Cocco et al. (2019) proposed the application of two different seismic vulnerability methodologies on the historic centre of Campotosto, in Italy, which was hit by the last 2016 Central Italy earthquake. The first is an empirical method, applied considering a large stock of 130 buildings, which was calibrated by the authors after the 2009 L'Aquila earthquake for historical centres. The latter, is a method based on analytical formulations dealt with by the Vulnus software, developed at the University of Padua in Italy, which was used for evaluating the seismic vulnerability of an aggregate building, representative of the historic centre. Also Donà et al. (2019) used the Vulnus software to develop a methodology to estimate the fragility of the Italian masonry buildings stock grouped in macro-typologies ISTAT (National Institute of Statistics), i.e. defined by construction age and number of stories; judgments on the quality of information are also used to provide an upper and lower fragility limit.

The judgmental methods provide expert opinions of civil engineers with experience in the field of seismic engineering, in order to estimate the probable distributions of damage within classes of populations subject to earthquakes of different intensity. Probability distribution functions are fit to the expert predictions to represent the range of damage estimates at each intensity level. The probability of a specified damage state is derived from the resulting distributions and plotted against the corresponding ground motion level to obtain a set of vulnerability curves, and associated uncertainty bounds (Rossetto and Elnashai, 2003). Experts are asked to provide estimates of damage, without limitations on the number of structural types, so the curves can be easily obtained by including all the factors influencing the seismic response of different structures. Clearly, the reliability of these methods is very low because it is strongly influenced by the individual experience of the consulted experts. One of the first applications of this method to civil infrastructures subject to earthquakes was the ATC relied on expert opinion with limited observational data from the 1971 San Fernando earthquake when preparing the ATC-13 report (ATC, 1985). The reliability of the fragilities in ATC-13, which were identified in terms of damage state probability matrices, is

questionable in that the fragilities are subjective and the associated degree of conservatism is unknown (Rossetto and Elnashai, 2003).

Moreover, the well-known loss estimation software package, HAZUS, developed under the sponsorship of FEMA (FEMA, 2003), is mainly based on expert opinion. HAZUS incorporates fragilities for 36 categories of building and 4 damage states, where the fragilities are modelled by lognormal distributions with the distribution parameters based primarily on expert opinion. The methodology classifies the buildings in terms of building type on the basis of their height and structural system and seismic design level on the basis of the seismic standard used in their design, the seismic zones in which they are built, their design vintage, and their use (Kircher et al., 1997a). Based on this classification, building capacity is represented by a non-linear static push-over curves in terms of base shear and roof displacement, and building response to an input scenario earthquake, considering the local site conditions, is determined with the capacity spectrum method. The building response is then entered into the associated built-in fragility curves defined at the thresholds of four discrete damage states (slight, moderate, extensive, and complete), defined separately for the structural system and for drift and acceleration sensitive non-structural components, to perform the loss estimation calculations given the occupancy class of the building (e.g., residential, commercial) (Kircher et al., 1997b). Whitman et al. (1997) observed that the losses estimated using HAZUS should be viewed with caution since they may be off by a factor of two. But the most significant limitation is that, HAZUS does not provide for the analysis or propagation of uncertainty (Celik, 2007).

Analytical fragility curves adopt damage distributions simulated from the analyses of structural models with varying comprehensiveness, establishing the relation between structural response and earthquake ground motion intensity. Usually, these methods involve a considerable computational effort and present limitations in modelling capabilities. The choices made for the analysis method, structural idealisation, seismic hazard and damage models strongly influence the derived curves and have been seen to cause significant discrepancies in seismic risk assessments made by different authorities for the same location, structure type and seismicity (Priestley, 1998). Their application may therefore not be justified unless an appropriate degree of uncertainty in the structural models and ground motions are considered.

There are several methods available in the literature for the analytical derivation of fragility functions for building typologies.

One of the first procedure to evaluate fragility curves taking into account uncertainties in both ground-motion and structure was proposed by Hwang and Jaw (1990). Following this method, the uncertainty in each parameter defining the earthquake-structure system is characterized by numerous characteristic values selected taking into account the range of uncertainty of the parameter. Samples of structures and earthquake motions are considered from the combination of these representative values, and then the latin hypercube sampling technique is used to construct the samples of earthquake structure system. For each sample, the non-linear seismic analysis is performed to produce response data, analysed in a statistical way. Five limit states representing various degrees of structural damage are defined and the statistics of the structural capacity corresponding to each limit state can be established. The fragility curve is generated by evaluating the limit state probabilities at different levels of peak ground acceleration.

Singhal and Kiremidjian (1996) used Monte Carlo simulations, considering the uncertainty in structural capacity and demand, to develop fragility curves for low-, mid-, and high-rise RC frames, designed using seismic provisions. They applied non-linear time history analyses to frame models randomly associated to simulated ground motion records. The so-called stripe analyses (i.e. incremental dynamic analyses with ground motions scaled to different intensity levels (Vamvatsikos and Cornell, 2002)) allowed to find the relationships between the structural demand and the seismic intensity. The structural demand at each seismic intensity level was assessed using ground motions scaled to that particular intensity level and was represented by a lognormal probability density function. The lognormal model of demand was then utilized to compute fragility estimates (for the performance limits considered) at that particular level. Finally, fragility curves were represented by lognormal cumulative distribution functions that were fit to individual fragility estimates, computed at several seismic intensity levels.

Staying in the field of RC structures, Mosalam et al. (1997) developed fragility curves for RC frames with and without masonry infill walls. The models used single degree of freedom systems (SDOF) performing non-linear static push-over analyses of the frame models, which were generated using Monte Carlo simulations to take into account the uncertainty in

structural material properties. The structural responses of these SDOF models to each ground motion were used to determine the estimates of fragility and each model was paired with each ground motion rather than randomly.

Further analytical methods were developed using fragility curves obtained through a response surface with random block effects approach (Franchin et al., 2003a; Franchin et al., 2003b; Schotanus, et al., 2004). This procedure allows to take into account uncertainties in both ground-motion and structure and can be used in conjunction with finite element method (FEM) models. Structural capacity is approximated by a polynomial response surface as a function of the uncertain structural parameters. Uncertainty in ground-motion or other characteristics of the materials and the geometry are taken into account implicitly introducing random factors in the response surface model. Data required to calibrate the model are collected performing a set of non-linear incremental analysis planned according to the theory of the Design of Experiments (Buratti et al., 2006; Buratti et al., 2007). The response surface method with random block effects was also investigated by the author (Battaglia et al., 2018; Battaglia et al., 2019) and further details can be found in Chapter 3 and some case study applications in Chapter 6.

Recently other methods were proposed to compute fragility function taking in account different aspects involved in the reliability problem: for example, the possibility of multiple failure modes to occur and their reciprocal interaction, the uncertainty in structural capacity, the influence on dynamic response of the variability of system parameters (Gardoni et al., 2002; Gardoni et al., 2003; Lupoi et al., 2006).

Several methods applied to masonry buildings were developed during the past years (Lagomarsino and Cattari, 2014). Erberik (2008) proposed the generation of fragility functions for the masonry typologies in Turkey, taking into account structural variations within each building typology (e.g. number of storeys, load-bearing wall material, regularity in plan and the arrangement of walls). The mechanical properties of masonry were considered as aleatory variables and treated by the Latin Hypercube Sampling Method. The buildings capacity curves were obtained through non-linear static analyses. (Rota et al., 2010) proposed a methodology for the derivation of fragility functions for masonry buildings based on the convolution between the probability density function of specified damage limit states, determined based on non-linear static analyses, and the probability distribution of the seismic

demand obtained from non-linear dynamic time-history analyses. In this case, the mechanical properties of masonry were considered as aleatory variables and treated by the Monte Carlo Method.

Among the most recent analytical estimation of the fragility curves, several works developed fragility analyses on buildings sited in the Portuguese territory. Simões et al. (2015) derived fragility curves for four type of old masonry buildings in Lisbon, which are still used for housing and services: the buildings were modelled with the equivalent frame model approach and analysed with non-linear static analyses. Then, a probabilistic performance-based assessment was carried out and the fragility curves for each building type derived.

Lamego et al. (2017) and Milošević et al. (2019) performed non-linear dynamic and static analyses, respectively, to evaluate the structural capacity of old building stocks, consisting of existing mixed masonry-reinforced concrete structures, with application to a neighbourhood in Lisbon, using the equivalent frame method. The main strength of these procedures is the ability to explicitly quantify the various contributions of uncertainty to the dispersion, associated to those on the structural capacity (taking into account both aleatory and epistemic sources) and on the seismic input. Finally, fragility curves were computed according to the HAZUS methodology, with the seismic intensity being expressed in terms of spectral displacement.

Simões et al. (2019a and 2019b) derived fragility functions for unreinforced masonry buildings, with reference to a typical prototype building with five storeys high and to different classes of buildings, respectively, obtained starting from the prototype. Different approaches are considered for the generation of the corresponding fragility functions and for the evaluation of the propagation of uncertainties. The contributions for the dispersion of the fragility functions account for the variability in the definition of the capacity, the aleatory uncertainty in the definition of the seismic demand and the aleatory uncertainty in the definition of the modified/floor response spectrum, when the local mechanisms are located in the upper level of the building. In the end, the individual fragility curves are properly combined in order to define a single fragility curve for the class of buildings.

The hybrid methods try to compensate for the scarcity of observational data, subjectivity of judgemental data and modelling deficiencies of analytical procedures by combining data from the different sources. Existing examples of hybrid curves typically involve the modification

of analytical or judgement-based relationships with observational data. However, in most cases the data deriving from the additional sources are very limited in quantity and scope. In some cases, these data are further supplemented with experimental test results. However, due to the cost and time required for full-scale testing and since small-scale testing is non-definitive on similitude grounds, a very limited number of parameters can be investigated and parametric variations are not possible. Experimental data are therefore currently only used for verification purposes, rather than as an additional source of building damage statistics.

The above motioned application ATC-13 and the ATC-40 (ATC-40, 1995), though based heavily on expert opinion, also incorporate limited observational data from the San Fernando earthquake on 1971 and Northridge earthquake on 1994, respectively.

A further application by Singhal and Kiremidjian (1996) adopts a Bayesian technique to update analytical curves for low-rise frames with observational damage data from a tagging survey of only 84 buildings affected by the 1994 Northridge earthquake (Singhal and Kiremidjian, 1997). Observations taken from a single earthquake event will cover only a small range of ground motions. Nevertheless, their inclusion may have a significant influence on the vulnerability and it can lead to a greater uncertainty. Hence, the consideration of multiple data sources is necessary for the correct determination of vulnerability curve reliability.

Shinozuka et al. (2000) developed both empirical and analytical fragility curves for bridges. The empirical fragility curves are obtained using the observed bridge damage data from the 1995 Kobe earthquake. On the contrary, the analytical fragility curves are developed by means of data that were simulated from the non-linear time history analyses of stochastically generated models of two bridges, considering the uncertainty in structural material properties. Both fragility curves were represented by lognormal distribution functions with the distribution parameters estimated using the maximum likelihood method.

## 2.5 Damage levels

The fragility curves provide the probability of a structural system, subject to an assigned seismic input, to overcome certain damage levels. A fundamental step in defining the curves is the identification of the damage thresholds, which define the different damage levels. There are many ways in which it is possible to define the damage thresholds and they are not often directly related each other (Hill and Rossetto, 2008). Certainly, for each identified damage level a different fragility curve is identified. One of the most common and most used

classification of damage levels is that referred to European Macroseismic Scale (EMS 98) (Grünthal, 1998), defining 5 increasing damage levels from 1 (no structural damage, slight non-structural damage) to damage 5 (total or near total collapse), plus zero damage (0).

Since the way in which a building deforms under earthquake loading depends on the building type, the European Macroseismic Scale is distinguished between the case of masonry buildings and that of the reinforced concrete buildings. Table 2.1 shows the classification of the damage levels, defined in the European Macroseismic Scale, for masonry buildings, as in this work, the seismic fragility of unreinforced masonry buildings is investigated.

In this thesis the fragility curves are related to the attainment of the damage level 5, as the goal is the evaluation of the seismic fragility of unreinforced masonry buildings at the collapse (total or near).

Table 2.1: Classification of the damage levels referred to masonry buildings.

Classification of damage to masonry buildings	
	<b>Grade 1: Negligible to slight damage</b> (no structural damage, slight non-structural damage) Hair-line cracks in very few walls. Fall of small pieces of plaster only. Fall of loose stones from upper parts of buildings in very few cases.
	<b>Grade 2: Moderate damage</b> (slight structural damage, moderate non-structural damage) Cracks in many walls. Fall of fairly large pieces of plaster. Partial collapse of chimneys.
	<b>Grade 3: Substantial to heavy damage</b> (moderate structural damage, heavy non-structural damage) Large and extensive cracks in most walls. Roof tiles detach. Chimneys fracture at the roof line; failure of individual non-structural elements (partitions, gable walls).
	<b>Grade 4: Very heavy damage</b> (heavy structural damage, very heavy non-structural damage) Serious failure of walls; partial structural failure of roofs and floors.
	<b>Grade 5: Destruction</b> (very heavy structural damage) Total or near total collapse.

### **3. PROBABILITY COMPUTATION METHODS THROUGH SIMULATIONS**

---

### 3.1 Introduction

A large number of attempts to develop efficient algorithms for computing probability integrals in Equation 2.1 have been studied in these years by the researchers. A simple integration, analytic or numeric, usually is not possible because of the arbitrary nature of the integration domain and the typically high dimension of the problem. Often the size of  $\mathbf{x}$  is large and, consequently, indirect approaches for the evaluation of the integral are essential. Most of these methods need modification of the random variables in the original space  $\mathbf{x} \in \mathbb{R}^d$ , where  $d$  is the dimension of the problem, into the standard normal space,  $\mathbf{u} \in \mathbb{R}^d$ , where each component of the vector  $\mathbf{u}$  is associated to an independent central unit Gaussian standard distributions. The transformation, which is nonlinear for non-Gaussian random variables, is expressed as  $\mathbf{u} = \mathbf{u}(\mathbf{x})$ , where  $\mathbf{u}$  has the standard normal density. These transformations,  $\mathbf{u} = T_{xu}(\mathbf{x})$  and  $\mathbf{x} = T_{ux}(\mathbf{u})$ , are established by applying for example the Rosenblatt's or the Nataf's transformation (Ditlevsen and Madsen, 1996; Pinto et al., 2004).

Concerning the performance function  $g(\mathbf{x})$ , it can only be specified explicitly for simple and particular cases. However, in most cases of practical interest, the function  $g(\mathbf{x})$  is not known explicitly in terms on an analytically expression. In cases where a deterministic FEM analysis code is used to compute the structural response, the performance function is known only point wise, i.e. the performance  $g_i = g(\mathbf{x}^{(i)})$  can be computed for each vector  $\mathbf{x}^{(i)}$ . Using the transformations mentioned above, the performance function  $g_u$  defined in the standard normal space, can be determined as follows:

$$g_u(\mathbf{u}) = g(\mathbf{x}) = g(T_{ux}(\mathbf{u})) \quad (3.1)$$

In this way, the evaluation of the performance at a single point  $\mathbf{u}^{(i)}$  in the standard normal space requires a transformation into the original space, a complete run of the FEM model and the computation of the performance form the response. The computational cost of evaluating the failure probability is governed by the number of structural analyses that have to be carried out. Therefore, in view of practicability and efficiency Schuëller et al. (2004) suggested to determine the probability of failure within a specified confidence interval such that the number of required structural analyses is small, when the problem in structural reliability using deterministic FEM is studied.

### 3.2 Monte Carlo simulations

A role of great importance on the estimation of the  $P_F$  expressed in Equation 2.1 is held by the simulation methods and, among them, the ones based on traditional Monte Carlo sampling are the most used.

The Monte Carlo method is a wide class of computational methods based on random sampling to obtain numerical results. The method is used to derive estimates through simulations. It is based on an algorithm generating a series of uncorrelated numbers, which follow the probability distribution that is supposed to have the phenomenon to be investigated. The Monte Carlo simulation calculates a series of possible realizations of the phenomenon under examination, with the weight of the probability of this eventuality, trying to explore in a dense way the whole space of the parameters of the phenomenon. Once the random sample has been calculated, the simulation performs measurements of the quantities of interest on this sample. The Monte Carlo simulation is well performed if the average value of these measures on the realizations of the system converges to the true value.

For the estimate of the  $P_F$  an indicator function  $I_f(\mathbf{x})$  is introduced which assumes a value equal to 1 if  $\mathbf{x}$  is in the failure domain and equal to 0 otherwise; thus, then the Integral in Equation 2.1 can be rewritten as follows:

$$P_F = \int_{F \cup S} I_f(\mathbf{x}) f_{\mathbf{x}}(\mathbf{x}) d\mathbf{x} = E[I_f(\mathbf{x})] \quad (3.2)$$

where that failure probability is the expected value of the indicator function according to the probability density function  $f_{\mathbf{x}}(\mathbf{x})$ . Therefore, in Monte Carlo simulation an estimator of the form expressed in Equation 3.3 is used:

$$\hat{P}_F = \frac{1}{N} \sum_{i=1}^N I_f(\mathbf{x}^{(i)}) \quad (3.3)$$

where the samples  $\mathbf{x}^{(i)}$  in Equation 3.3 are independently identically distributed according to  $f(\mathbf{x})$ . It can be shown that the estimator in Equation 3.3 is unbiased (Pinto et al., 2004). The greatest advantage of Monte Carlo is its generality; in fact, it can be applied to almost any class of problems. Furthermore, in Monte Carlo simulation the convergence rate is independent of the dimensionality of the random vector  $\mathbf{x}$ . Its main disadvantage is its inefficiency in estimating small failure probabilities  $P_F$  due to the large number (proportional

to  $1/P_F$ ) of samples or equivalently system analyses needed to achieve an acceptable level of accuracy. Many variance reducing techniques have been proposed in the literature, e.g. importance sampling, directional sampling, importance sampling using design points, adaptive importance sampling, subset simulation, etc. (Buratti, 2008). It should be noted that some of these methods, directional simulation for example, are usually limited by the dimensionality of the problem.

### 3.3 Response Surface method

An alternative approach from computing probabilities of the type in Equation 2.1 is to substitute the integration boundary by an approximating response surface and then perform the integration by an appropriate means without engaging the actual limit state function. This approach is particularly useful when the limit state function is algorithmic and its gradient is difficult to compute. Typically, the response surface is constructed computing  $g(\mathbf{x})$  at a number of points and then a polynomial surface is fitted to the points by the least squares method.

The use of the response surface methodology is strongly influenced by the selection of the experiment points, which can be obtained following the theory of Design of Experiments, explained in the following. According to this method, the number of simulations needed to calibrate the model grows as the number of variables in the model increases. Hence, the model is not computationally efficient in very high dimensions. Nevertheless, this problem can be solved using response surfaces with random effects (Faravelli, 1989) allowing to take into account the effects of some of the variables involved in the problem implicitly. In this way, it is possible to greatly increase the computational efficiency but, the accuracy is reduced.

The Response Surface (RS) method is based on the definition of a statistical model expressing a structural response parameter as a function of a set of variables, called *factors* in the statistical language; the values assumed from the factors are called *levels*. The RS is typically based on a polynomial function, and it is possible to find many applications in different research fields (Box and Draper, 1987; Khuri and Cornell, 1996; Searle et al, 1992; Rajashekhar and Ellingwood, 1993).

### 3.3.1 Standard Response Surface

The response variable is the measured quantity the value of which is assumed to be dependent upon the levels of the factors. The true value of the response corresponding to any particular combination of the factor levels and in the absence of experimental error of any kind is denoted by  $\eta$ . The dependence of  $\eta$  on the factors can be written as:

$$\eta = \phi(x_1, x_2, \dots, x_k) \quad (3.4)$$

where  $\phi$  is an unknown function, called the true response function, and it is assumed to be continuous. Considering a Taylor series expansion as polynomial equation on the variables, the Equation 3.4 can be written as:

$$\eta = \beta_0 + \sum_{i=1}^k \beta_i x_i + \sum_{i=1}^k \sum_{j=1}^k \beta_{ij} x_i x_j \quad (3.5)$$

where the coefficients  $\beta_i$  are the values of the first order partial derivatives and the coefficients  $\beta_{ij}$  are the values of the second order partial derivatives.

A statistical model of this kind is called *fixed effect model* because the effects are related to a finite set of levels of the factors. The model in Equation 3.5 is non-linear as far as the  $x_i$  variables are concerned but is linear with regard to  $\beta$ . The latter are called regression coefficients or parameters. The coefficients  $\beta_i$  are the values of the first order partial derivatives and are referred to as first-order effects. The coefficients  $\beta_{ij}$  are defined as the values of the second order partial derivatives and are called second-order effects. The structural form of  $\eta$  is usually unknown and therefore an approximation is used through a polynomial or some type of empirical model equation. Furthermore, as far as experimental data is concerned, the real value of the response is not known and it is substituted by the expected values of the response parameter  $E(y)$ . The model in Eq. (3.5) can be rewritten as (Searle et al., 1992; Khuri and Cornell, 1996):

$$E(y) = \eta = \mathbf{f}(\mathbf{x})^T \boldsymbol{\beta} \quad (3.6)$$

where  $\mathbf{f}(\mathbf{x})$  is a vector of  $p$  monomials of  $\mathbf{x}$ :

$$\mathbf{f}(\mathbf{x}) = \left[ 1 \quad x_1 \quad \dots \quad x_k \quad x_1^2 \quad \dots \quad x_k^2 \quad x_1 \cdot x_2 \quad \dots \quad x_1 \cdot x_k \quad x_1 \cdot x_k \quad \dots \quad x_{k-1} \cdot x_k \right]^T \quad (3.7)$$

and  $\boldsymbol{\beta}$  is the vector of regression parameters:

$$\boldsymbol{\beta} = [\beta_0 \quad \beta_1 \cdots \beta_k \quad \beta_{11} \cdots \beta_{kk} \quad \beta_{12} \cdots \beta_{1k} \cdots \beta_{k-1,k}]^T \quad (3.8)$$

Considering  $n$  observations and the errors  $\varepsilon_i$  of  $E(y_i)$  respect to the observed response values:

$$\varepsilon_i = y_i - E(y_i) = y_i - \mathbf{f}(\mathbf{x}_i)^T \boldsymbol{\beta} \quad (i = 1, \dots, N) \quad (3.9)$$

Writing the equation of the model in matrix notation:

$$\mathbf{y} = \mathbf{X}\boldsymbol{\beta} + \boldsymbol{\varepsilon} \quad (3.10)$$

where  $\mathbf{y}$  is a  $l \times n$  vector collecting the observed response values

$$\mathbf{y} = [y_1 \cdots y_n]^T \quad (3.11)$$

$\mathbf{X}$  is a  $n \times p$  matrix, called *design matrix*, whose  $i$ -th row is the vector of monomials  $\mathbf{f}(\mathbf{x})^T$  referred to the values of the variables  $\mathbf{x}$  at the  $i$ -th trial

$$\mathbf{X} = \begin{bmatrix} \mathbf{f}(\mathbf{x}_1)^T \\ \vdots \\ \mathbf{f}(\mathbf{x}_n)^T \end{bmatrix} \quad (3.12)$$

and  $\boldsymbol{\varepsilon}$  is a  $l \times n$  vector collecting the errors with respect to  $E(y_i)$ :

$$\boldsymbol{\varepsilon} = [\varepsilon_1 \cdots \varepsilon_n]^T \quad (3.13)$$

As an example, if 2 factors and 6 experiments are considered, the model in Equation 3.10 can be written as:

$$\begin{bmatrix} y_1 \\ y_2 \\ y_3 \\ y_4 \\ y_5 \\ y_6 \end{bmatrix} = \begin{bmatrix} 1 & x_{1,1} & x_{2,1} & x_{1,1}^2 & x_{2,1}^2 & x_{1,1}x_{2,1} \\ 1 & x_{1,2} & x_{2,2} & x_{1,2}^2 & x_{2,2}^2 & x_{1,2}x_{2,2} \\ 1 & x_{1,3} & x_{2,3} & x_{1,3}^2 & x_{2,3}^2 & x_{1,3}x_{2,3} \\ 1 & x_{1,4} & x_{2,4} & x_{1,4}^2 & x_{2,4}^2 & x_{1,4}x_{2,4} \\ 1 & x_{1,5} & x_{2,5} & x_{1,5}^2 & x_{2,5}^2 & x_{1,5}x_{2,5} \\ 1 & x_{1,6} & x_{2,6} & x_{1,6}^2 & x_{2,6}^2 & x_{1,6}x_{2,6} \end{bmatrix} \begin{bmatrix} \beta_0 \\ \beta_1 \\ \beta_2 \\ \beta_{11} \\ \beta_{22} \\ \beta_{12} \end{bmatrix} + \begin{bmatrix} \varepsilon_1 \\ \varepsilon_2 \\ \varepsilon_3 \\ \varepsilon_4 \\ \varepsilon_5 \\ \varepsilon_6 \end{bmatrix} \quad (3.14)$$

where  $x_{i,j}$  is the  $j$ -th level of the  $i$ -th factor.

According to Khuri and Cornell (1996) Khuri and Searle et al. (1992) the errors are normally distributed with constant variance ( $\sigma^2_\varepsilon$ ). Usually, the regression parameters  $\beta$  and the variance  $\sigma^2_\varepsilon$  can be estimated by the ordinary least squares method (Buratti et al., 2010), described in the following paragraph.

### 3.3.1.1 Ordinary least square method

The ordinary least square method is one of the simplest in statistics and allows to estimate the regression coefficients, given a model in the form of Equation 3.10.

About the errors  $\varepsilon$ , some assumptions have to be follow:

1. Random errors have zero mean and common variance,  $\sigma^2$ ;
2. Random errors  $\varepsilon_i$  are mutually independent in the statistical sense;
3. Random errors  $\varepsilon_i$  are normally distributed.

The method of least squares selects as estimates for the unknown parameters in Equation 3.10, some values,  $b_0, b_1, \dots, b_k$ , which minimize the quantity:

$$R(\boldsymbol{\beta}) = \sum_{i=1}^n \varepsilon_i^2 = \boldsymbol{\varepsilon}^T \boldsymbol{\varepsilon} = (\mathbf{y} - \mathbf{X}\boldsymbol{\beta})^T (\mathbf{y} - \mathbf{X}\boldsymbol{\beta}) \quad (3.15)$$

Setting to zero the derivatives of (3.15) with respect to  $\boldsymbol{\beta}$  is obtained as follows:

$$\mathbf{X}^T \mathbf{X} \boldsymbol{\beta} - \mathbf{X}^T \mathbf{y} = \mathbf{0} \quad (3.16)$$

from which the estimates of the least squares estimates of the elements of  $\boldsymbol{\beta}$  can be obtained:

$$\mathbf{b} = (\mathbf{X}^T \mathbf{X})^{-1} \mathbf{X}^T \mathbf{y} \quad (3.17)$$

It is noted that this method does not require the value of the variance of the error to be known. The statistical properties of the estimator  $\mathbf{b}$  derive from the assumptions concerning the elements of  $\varepsilon$ . The expectation vector of  $\mathbf{b}$  is:

$$E(\mathbf{b}) = E\left[(\mathbf{X}^T \mathbf{X})^{-1} \mathbf{X}^T \mathbf{y}\right] = E\left[(\mathbf{X}^T \mathbf{X})^{-1} \mathbf{X}^T (\mathbf{X}\boldsymbol{\beta}) + \boldsymbol{\varepsilon}\right] = \boldsymbol{\beta} + E(\mathbf{X}^T \mathbf{X})^{-1} \mathbf{X}^T \boldsymbol{\varepsilon} = \boldsymbol{\beta} \quad (3.18)$$

Thus,  $\mathbf{b}$  is an unbiased estimator of  $\boldsymbol{\beta}$ . The variance-covariance matrix of the vector of the estimates is:

$$\mathbf{C}_{bb} = \text{var}(\mathbf{b}) = \text{var}\left[\left(\mathbf{X}^T \mathbf{X}\right)^{-1} \mathbf{X}^T \mathbf{y}\right] = \left(\mathbf{X}^T \mathbf{X}\right)^{-1} \mathbf{X}^T \text{var}(\mathbf{y}) \mathbf{X} \left(\mathbf{X}^T \mathbf{X}\right)^{-1} \quad (3.19)$$

and, since the covariance matrix of the vector  $\mathbf{y}$  can be written (accordingly to assumption 1) as follows:

$$\mathbf{C}_{YY} = \text{var}(\mathbf{y}) = E\left[(\mathbf{y} - \mathbf{X}\boldsymbol{\beta})(\mathbf{y} - \mathbf{X}\boldsymbol{\beta})^T\right] = E\left[\boldsymbol{\varepsilon}\boldsymbol{\varepsilon}^T\right] = \text{var}(\boldsymbol{\varepsilon}) = \mathbf{C}_{\varepsilon\varepsilon} = \sigma_{\varepsilon}^2 \mathbf{I}_n \quad (3.20)$$

the variance-covariance matrix of  $\mathbf{b}$  can be rewritten as:

$$\mathbf{C}_{bb} = \text{var}(\mathbf{b}) = \left(\mathbf{X}^T \mathbf{X}\right)^{-1} \sigma_{\varepsilon}^2 \quad (3.21)$$

Along the main diagonal of the matrix  $\mathbf{C}_{bb}$ , the  $ii$ -th element, is the variance of  $b_i$ . The  $ij$ -th element of  $\mathbf{C}_{bb}$  is the covariance between the elements  $b_i$  and  $b_j$  of  $\mathbf{b}$ . If the errors are jointly normally distributed, then  $\mathbf{b}$  is distributed as a normal multivariate:

$$\mathbf{b} \sim N\left[\boldsymbol{\beta} \left(\mathbf{X}^T \mathbf{X}\right)^{-1} \sigma_{\varepsilon}^2\right] \quad (3.22)$$

Another important property of the estimator  $\mathbf{b}$  is that it produces the minimum variance estimates of the elements of  $\boldsymbol{\beta}$ , therefore it is called best linear estimator of  $\boldsymbol{\beta}$ . One of the purposes in obtaining a fitted model is to use the model for predicting response values at points throughout the experimental region. Let  $\mathbf{x}$  denote a  $p \times 1$  vector the elements of which correspond to the elements of a row of the matrix  $\mathbf{X}$  in Equation 3.10. An expression for the predicted value of the response, at any point  $\mathbf{x}$  in the experimental region is:

$$\hat{y}(\mathbf{x}) = \mathbf{x}'\mathbf{b} \quad (3.23)$$

A measure of the precision of the prediction  $\hat{y}(\mathbf{x})$  is expressed as:

$$\text{var}(\hat{y}(\mathbf{x})) = \text{var}\left[\mathbf{f}(\mathbf{x})^T \mathbf{b}\right] = \mathbf{f}(\mathbf{x})^T \text{var}(\mathbf{b}) \mathbf{f}(\mathbf{x}) = \mathbf{f}(\mathbf{x})^T \left(\mathbf{X}^T \mathbf{X}\right)^{-1} \mathbf{f}(\mathbf{x}) \sigma_{\varepsilon}^2 \quad (3.24)$$

The variance of the prediction depends on  $\mathbf{x}$ , i.e. it is not constant throughout the experimental region. In Equation 3.19 for the variance-covariance matrix of  $\mathbf{b}$ , as well as in Equation 3.24 for the variance of  $\hat{y}(\mathbf{x})$ , the variance of errors  $\sigma_{\varepsilon}^2$  was assumed known. This assumption is seldom true and usually an estimate  $\hat{\sigma}_{\varepsilon}^2$  is needed. The estimate is obtained from the analysis

of the data values. For the general case where the fitted model contains  $p$  parameters and the total number of observations is  $n$  ( $n > p$ ), the estimate,  $s^2$ , is computed from:

$$s^2 = \frac{1}{n-p} \sum_{i=1}^n \varepsilon_i^2 = \frac{1}{n-p} (\mathbf{y} - \mathbf{X}\mathbf{b})^T (\mathbf{y} - \mathbf{X}\mathbf{b}) = \frac{1}{n-p} S(\mathbf{b}) = \frac{1}{n-p} SSE \quad (3.25)$$

where  $SSE$  is the sum of squared residuals. The divisor  $n - p$  is the degrees of freedom of the estimator  $s^2$ , which is an unbiased estimator of  $\sigma_\varepsilon^2$ .

### 3.3.2 Random block effects

The standard formulation of RS cannot be used for applications in earthquake engineering because not all the random variables on which the structural behaviour depends can be expressed in explicit form as reported in Equation 3.10. In fact, the evaluation of the seismic fragility requires to take the variability of the seismic action and mechanical parameters over the structure into account. As for the first aspect, the earthquake ground-motion is a non-stationary process, with amplitude and frequency content variable in time; therefore a fully probabilistic description of it would require a big amount of variables.

The Response Surface method provides good results only if the number of the variables involved in the problem is low (6-8 variables), in fact it is a valid alternative to Monte Carlo method, regarding the computational effort (Franchin et al., 2003a; Schotanus et al., 2004). Whereas, if the number of variables is high, a large amount of simulations is needed. In order to reduce the number of variables, they are divided in explicit ( $\mathbf{x}_E$ ), considered as random variables explicitly, and implicit ( $\mathbf{x}_I$ ), considered implicitly (Veneziano et al., 1983; Faravelli, 1989; Casciati and Faravelli, 1991).

The formulation of the model given in the previous Sections needs to be extended, in order to take into account the differences between fixed and random factors. The statistical model that also takes into account implicit variables is called *mixed model* and the effects of random variables ( $\mathbf{x}_I$ ) are considered in additive form (they do not interact with explicit variables) (Franchin et al., 2003b). Thus, according to Khuri and Cornell (1996) and Searle et al. (1992), the equation of the Response Surface is modified by adding the effect of the random implicit variables, through a set of *random factors*,  $\delta_j$  ( $j = 1, \dots, r$ ) (Buratti et al., 2010). The generic observation can be expressed as:

$$y = \mathbf{f}^T \boldsymbol{\beta} + \sum_j^r \delta_j + \varepsilon \quad (3.26)$$

Moreover, the hypothesis that  $\delta_j$  are independent random variables normally distributed with zero mean and variance  $\sigma_{\delta_j}^2$  was introduced (Franchin et al., 2003b).

The  $N$  observations were divided in  $b_j$  blocks, each corresponding to different values of the implicit variables  $\delta_j$ . The blocks are repeated  $n_j$  times until the number of observations  $N$  is reached; whenever the block is repeated, a different value of the variable  $\delta_j$  is considered. Thus, Equation 3.26 can be written in matrix form:

$$\mathbf{y} = \mathbf{X}\boldsymbol{\beta} + \mathbf{Z}\boldsymbol{\delta} + \boldsymbol{\varepsilon} \quad (3.27)$$

where  $\boldsymbol{\delta} = [\boldsymbol{\delta}_1^T \dots \boldsymbol{\delta}_r^T]^T$  contains as many vectors as the number ( $r$ ) of random variables; each vector  $\boldsymbol{\delta}_j$  is divided into blocks and each block corresponds to a different value of the variable  $\delta_j$ .

Instead  $\mathbf{Z}$  is a Boolean matrix ( $N \times \sum_{j=1}^r b_j$ ), containing value 1 every time the corresponding block is associated with the considered observation, and 0 in the opposite case.  $\mathbf{Z}$  can be considered as divided into  $r$  sub-matrices ( $\mathbf{Z} = [\mathbf{Z}_1 \dots \mathbf{Z}_r]$ ) where each  $\mathbf{Z}_j$  is a  $N \times b_j$  Boolean matrix. Thus, the term  $\mathbf{Z}\boldsymbol{\delta}$  can be written as:

$$\mathbf{Z}\boldsymbol{\delta} = [\mathbf{Z}_1 \dots \mathbf{Z}_r] \begin{bmatrix} \boldsymbol{\delta}_1 \\ \vdots \\ \boldsymbol{\delta}_r \end{bmatrix} = \sum_{i=1}^r \mathbf{Z}_i \boldsymbol{\delta}_i \quad (3.28)$$

Thus, Equation 3.27 can be rewritten as:

$$\mathbf{y} = \mathbf{X}\boldsymbol{\beta} + \sum_{i=1}^r \mathbf{Z}_i \boldsymbol{\delta}_i + \boldsymbol{\varepsilon} \quad (3.29)$$

As an example if 4 experiments and 2 random factor with 2 levels each are considered the vector  $\boldsymbol{\delta}$  and matrix  $\mathbf{Z}$  can be written as:

$$\boldsymbol{\delta} = [\delta_{1,1} \quad \delta_{1,2} \quad \delta_{2,1} \quad \delta_{2,2}]^T \quad (3.30)$$

$$\mathbf{Z}_1 = \begin{bmatrix} 1 & 0 \\ 1 & 0 \\ 0 & 1 \\ 0 & 1 \end{bmatrix} \quad \mathbf{Z}_2 = \begin{bmatrix} 1 & 0 \\ 0 & 1 \\ 1 & 0 \\ 0 & 1 \end{bmatrix} \quad \mathbf{Z} = \begin{bmatrix} 1 & 0 & | & 1 & 0 \\ 1 & 0 & | & 0 & 1 \\ 0 & 1 & | & 1 & 0 \\ 0 & 1 & | & 0 & 1 \end{bmatrix} \quad (3.31)$$

### 3.3.3 Design of the experiments theory

A set of numerical simulations is needed to obtain the data to calibrate the Response Surface; usually, in the seismic engineering field, each simulation corresponds to a different structural analysis; in this work, the simulations are non-linear static analyses of masonry structures subjected to seismic actions.

The Design of Experiment Theory (Box and Draper, 1987; Khuri and Cornell, 1996) allows to define the criteria necessary to establish the number of simulations (each simulation is referred to a different analysis) and the region of interest for the explicit variables influencing the response, selecting the range of values and the number of the values of each variable. Typically, this region is cuboidal or spherical. All the variables are given by normal distributions, from which the values of the variables are defined.

The use of coded variables in place of the input variables facilitates the construction of the experimental designs. Coding removes the units of measurements of the input variables and consequently the distances measured along the axes of the coded variables in a  $k$ -dimensional space are standardized. A convenient coding formula for defining the *coded variables*  $x_i$  is (Box and Draper, 1987):

$$x_i = \frac{2X_i - (X_{iL} + X_{iH})}{X_{iH} - X_{iL}} \quad (3.32)$$

where  $X_{iL}$  and  $X_{iH}$  are the low and high levels of the factor  $X_i$ , respectively. If only two levels are considered for a factor, Equation 3.32 gives the notation  $\pm 1$ . The region defined by those two levels is a cuboidal region in a  $k$ -dimensional space. Geometrically, the cuboidal region has  $2^k$  vertices where each vertex is defined by the coordinate  $\pm 1$  settings in  $x_1, x_2, \dots, x_k$ . When a factor has three levels and the mid-level is in the middle between the lower and upper levels, the coding formula in Equation 3.32 produces the coded levels  $x_i = -1, 0, +1$  associated with the low, middle and high values of  $X_i$ , respectively. When all factors have

three levels, again the region in the coded variables is a  $k$ -dimensional cuboidal region. However, the number of factor combinations is now  $3^k$  and  $2^k$  of the combinations are the vertices of the  $k$ -dimensional cuboidal region, the remaining  $3^k - 2^k$  combinations define the centroids of all the lower dimensional boundaries of the  $k$ -dimensional cube along with the centroid, 0, of the cuboidal region. Figures 3.1(a) and (b) show two examples of designs with 3 levels for 2 and 3 factors respectively.

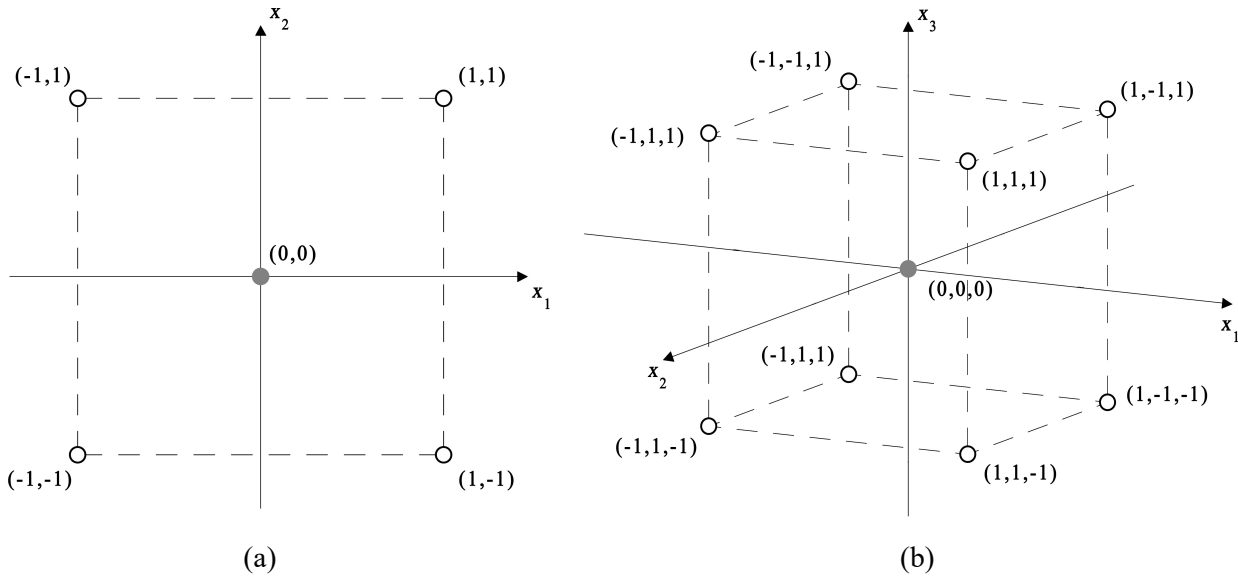


Figure 3.1: Design of experiment with (a) 2 variables and (b) 3 variables.

The use of coded variables rather than the original input variables when fitting polynomial models allows to have computational ease and to increase the accuracy in estimating the model coefficients and to improve the interpretability of the coefficient estimates.

### 3.3.3.1 Central composite design

Box and Wilson (1951) introduced the class of central composite designs (CCD) for problems involving response surfaces. A central composite design consist of:

- a  $2^k$  factorial design, where the factor levels are coded to the usual -1, +1 values. This is called factorial portion of the design;
- $n_0$  centre points;
- two axial points on the axes of each design variable at a distance of  $\alpha$  from the design centre. This is called axial portion of the design.

A  $2^k$  factorial design consists of all the  $2^k$  points with levels  $(x_1, x_2, \dots, x_k) = (\pm 1, \pm 1, \dots, \pm 1)$  where every possible combination of + and - signs is selected in turn. Table 3.1 shows an

example of factorial design with 3 variables ( $2^3 = 8$  simulations), expressed both with their real values and the coded values (according to the Equation 3.32).

Table 3.1: Example of a factorial design with 3 variables.

Real values			Coded values			Response
$X_1$	$X_2$	$X_3$	$x_1$	$x_2$	$x_3$	$y$
200	32	10	-1	-1	-1	0.15
150	32	10	1	-1	-1	0.23
200	46	10	-1	1	-1	0.06
150	46	10	1	1	-1	0.59
200	32	30	-1	-1	1	0.86
150	32	30	1	-1	1	0.78
200	46	30	-1	1	1	0.19
150	46	30	1	1	1	0.46

Figure 3.1(b) represents the factorial design with coded variables described in Table 3.1. However, a factorial design does not suffice in order to estimate all the parameters of a complete polynomial response surface of second degree. For this reason, in CCD, centre points and axial points are added to the factorial design. Figure 3.2 shows the points added to the  $2^k$  factorial design.

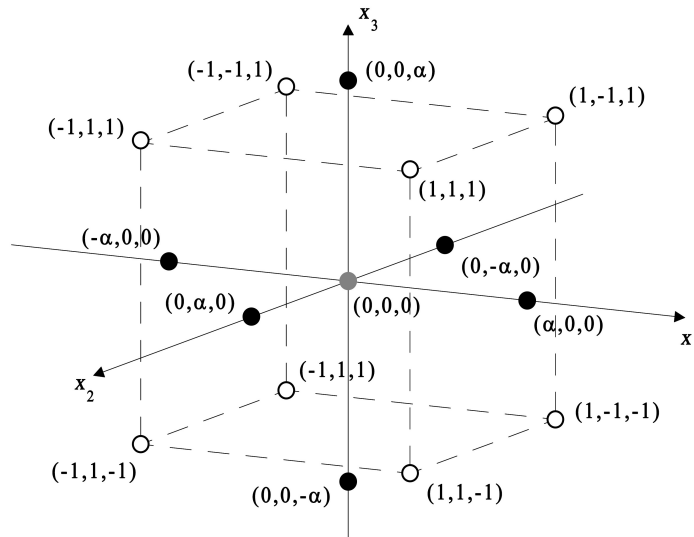


Figure 3.2: Example of a cuboidal region of the Central Composite Design.

The total number of experiments to run is therefore  $N = 2^k + 2k + n_0$ . Usually the amount of the central points  $n_0$  is set equal to the number of the variables (3 in this case) and the value of  $\alpha$  is greater than 1. As an example a design matrix with 3 ( $k$ ) variables and  $N = 17$  ( $2^k = 8$  variables,  $n_0 = 3$  and  $2k = 6$  axial points with  $\alpha = 1.4$ ) has the form:

Table 3.2: Example of a central composite design with 17 simulations.

$x_1$	-1	1	-1	1	-1	1	-1	1	1.4	-1.4	0	0	0	0	0	0	0
$x_2$	-1	-1	1	1	-1	-1	1	1	0	0	1.4	-1.4	0	0	0	0	0
$x_3$	-1	-1	-1	-1	1	1	1	1	0	0	0	0	-1.4	1.4	0	0	0

### 3.3.3.2 Design for mixed model

The central composite design, in its standard formulation, allows to take into account fixed effect only. For this reason, it needs to be modified in order to be used with mixed models. In fact, the central composite design must be partitioned in blocks to which different values of the random factors can be associated. A block is a homogenous group of simulations affected by the same value of the considered implicit variable. In order to ensure a good regression Box and Draper (1987) suggest some rules for the subdivision of the simulations into blocks. In general, it is convenient to distinguish the factorial part from the axial part.

For example, it is possible to consider one implicit variable with 3 values (accordingly 3 blocks are obtained). The general rule provides for the association of 2 blocks to the factorial part and 1 block to the axial part. Considering the example in Table 3.2, the associations of the blocks to the factorial part is such as to have one block (I) when the result of the product between the explicit variables is positive (+) and the other block (II) when the product is negative (-). The third block (III) is associated to the axial part and the central points are associated to all the 3 blocks (I, II, III), as shown in Table 3.3.

Table 3.3: Example of a central composite design with 17 simulations and 3 blocks.

$x_1$	-1	1	-1	1	-1	1	-1	1	1.4	-1.4	0	0	0	0	0	0	0
$x_2$	-1	-1	1	1	-1	-1	1	1	0	0	1.4	-1.4	0	0	0	0	0
$x_3$	-1	-1	-1	-1	1	1	1	1	0	0	0	0	-1.4	1.4	0	0	0
<i>BLOCK</i>	II	I	I	II	I	II	II	I	III	III	III	III	III	III	I	II	III

Then the group of 17 simulations will be repeat, always maintaining the same values of the explicit variables, according to the choice of the implicit variables and to the division in blocks, in order to obtain  $n$  simulations.

## **4. MODELLING AND ANALYSIS OF URM BUILDINGS**

---

## 4.1 Introduction

Masonry buildings represent one of the most common building typology and one of the most vulnerable too (Lagomarsino and Magenes, 2006). They are typically complex structures and there is lack of knowledge and information concerning the behaviour of their structural systems, particularly in what regards their seismic response. The structure is made of natural or artificial elements (that can be stone, brick, adobe etc.) over one another and usually connected in different way by mortar. Typically, these structures are more massive than today's structures and carry their actions primarily in compression.

In the unreinforced masonry buildings (URM) the structure is composed of load-bearing exterior and interior walls mostly bearing the weight and additional vertical loads, as well as the horizontal loads. Floors and roof in this building type are usually made of light material like wood, and sometimes they are Reinforced Concrete (RC) slabs, acting as flexible and rigid diaphragms, respectively. The vertical and horizontal actions are transmitted to the load-bearing walls by either floors/roof bond beams or contacting friction between the walls top surface and floors/roof components (i.e. without any additional connecting elements).

The behaviour of URM buildings can be classified into two main categories: buildings with and without box-behaviour. The term box-behaviour refers to a global seismic response of URM buildings that prevents the out-of-plane mechanisms of the walls. In the case of a building with box-behaviour, if disintegration of the masonry walls is prevented, the in-plane behaviour governs the global building response, because the walls are well-connected to the adjacent walls and the floor diaphragms. In other words, the assumptions are that the local out-of-plane behaviour of the walls and the local floor flexural response are negligible with respect to the global seismic response of the structure. In this context, the response of the structure is mainly governed by the in-plane capacity of the walls and by the in-plane stiffness of horizontal diaphragms that rules the distribution of the horizontal loads between vertical structural elements. However, the presence of flexible horizontal diaphragms (timber floors and roof) provides lower degree of coupling between walls, compromising the activation of the global box-type behaviour. It is noted that a building without box-type behaviour can be retrofitted to provide a box-type behaviour, by providing adequate connections.

## 4.2 Mechanical behaviour of the masonry walls

Masonry is a non-homogeneous, plastic and anisotropic material, characterized by high compressive strength and a very low tensile strength. It is usually described as a material exhibiting distinct directional properties due to the mortar joints, which act as planes of weakness (Lourenço, 1996). Clay bricks, stones, and mortar are quasi-brittle materials, which fail due to a process of progressive internal crack growth (Lourenço, 2014). The properties of the masonry walls depend on the inherent mechanical properties of the masonry materials, the geometry and the boundary condition of the walls, and the interaction between its different components (Lagomarsino, 2006).

The identification of the masonry quality is of essential importance, especially when dealing with existing buildings, since it is strongly correlated to the mechanical behaviour of the structural elements. It should be gained by diagnostic analyses, in which the characteristics of the materials should be investigated, as well as the characteristics of the masonry typology. The poor quality of the masonry can strongly affect its structural behaviour leading to phenomena of disintegration of the masonry walls, caused by the type of the resisting elements, the shape and the dimensions of the resisting elements, the type of mortar, the characteristics of the texture and the cohesion between the elements composing the masonry. For these reasons, the identification of the masonry quality is the first requirement for safety, because the disintegration of the masonry walls, due to the poor quality of the masonry, can occur before the activation of in-plane or out-of-plane mechanisms.

Figure 4.1 (Sorrentino et al., 2018) shows two examples of reinforced masonry with steel ties: it is possible to notice that when masonry has such a low strength and poor quality, even the systematic use of steel ties is ineffective. When combined with a reasonable quality masonry, steel ties certainly contributed to preventing collapse.

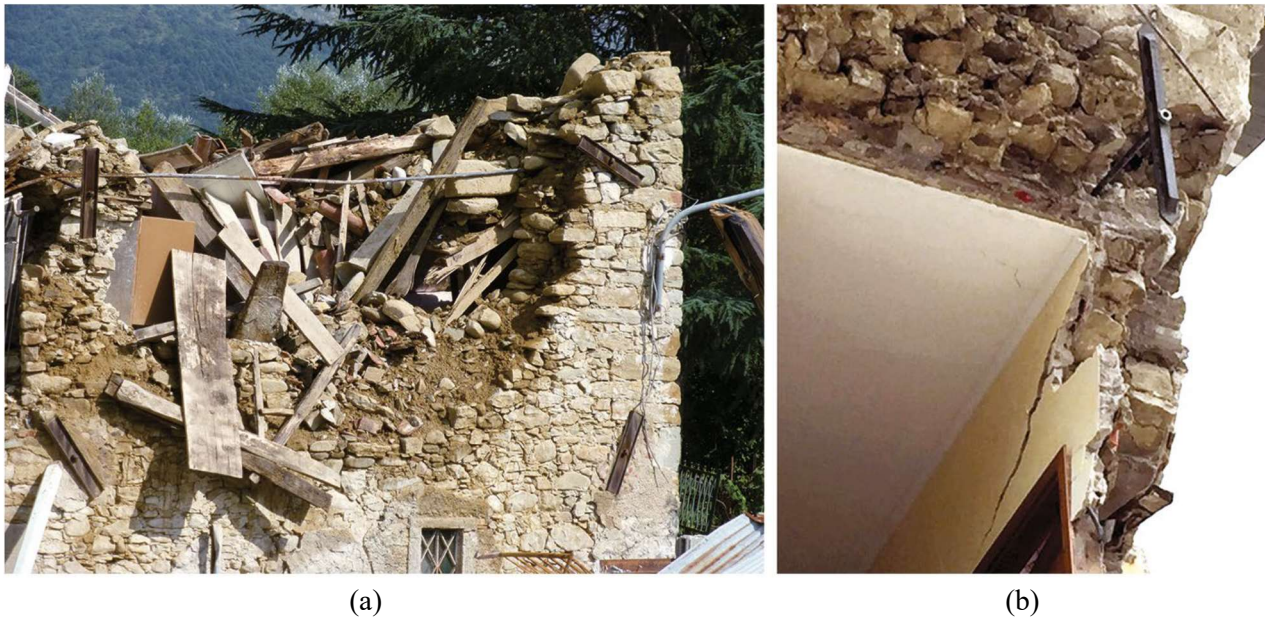


Figure 4.1: Collapse of a masonry building having steel ties combined to poor masonry (a) Amatrice, Petrana; (b) Arquata d/T, Piazza Umberto I (Sorrentino et al., 2018).

### 4.2.1 Out-of-plane behaviour

In the ancient masonry buildings some elements of connection between the walls, at level of the horizontal elements, are often absent; this implies possible local vulnerabilities, which may affect not only the collapse of individual walls out-of-plane, but larger parts of the building (overturning of entire walls not well-connected, overturning of summit walls in presence of buildings with different heights, partial collapses in the corner buildings of the building aggregates, etc.). The collapse mechanism of out-of-plane walls mainly depends on their boundary conditions, i.e. the connections between roof/floors diaphragms and the adjacent walls, or between orthogonal walls. Usually, as showed by the post-earthquake damage surveys, the local out-of-plane failure modes are the main sources of vulnerability for masonry structures (Magenes and Penna, 2009). Local mechanisms occur in masonry walls mainly for actions perpendicular to their plane and, in the case of systems of arches, also for actions in-plane. Due to the slenderness of the elements and the negligible tensile strength, the structures can lose static equilibrium for very low values of PGA. The out-of-plane behaviour is mainly related to the geometric stability of the part of the structure involved in the mechanism rather than to the strength of materials.

A possible model for this type of evaluation is the limit analysis of the equilibrium of masonry structures, according to the cinematic approach, based on the choice of the local mechanisms considered significant for the structure and on the evaluation of the horizontal action

activating these mechanisms. The kinematic approach also allows to determine the progressive horizontal action the structure is able to resist to as the mechanism evolves (Doherty et al., 2002). The obtained curve is expressed through a multiplier  $\alpha$ , ratio between the applied horizontal forces and the corresponding weights of the masses, represented as a function of the displacement of a reference point of the system; the curve is determined until the annulation of each resistance ability to the horizontal actions ( $\alpha = 0$ ).

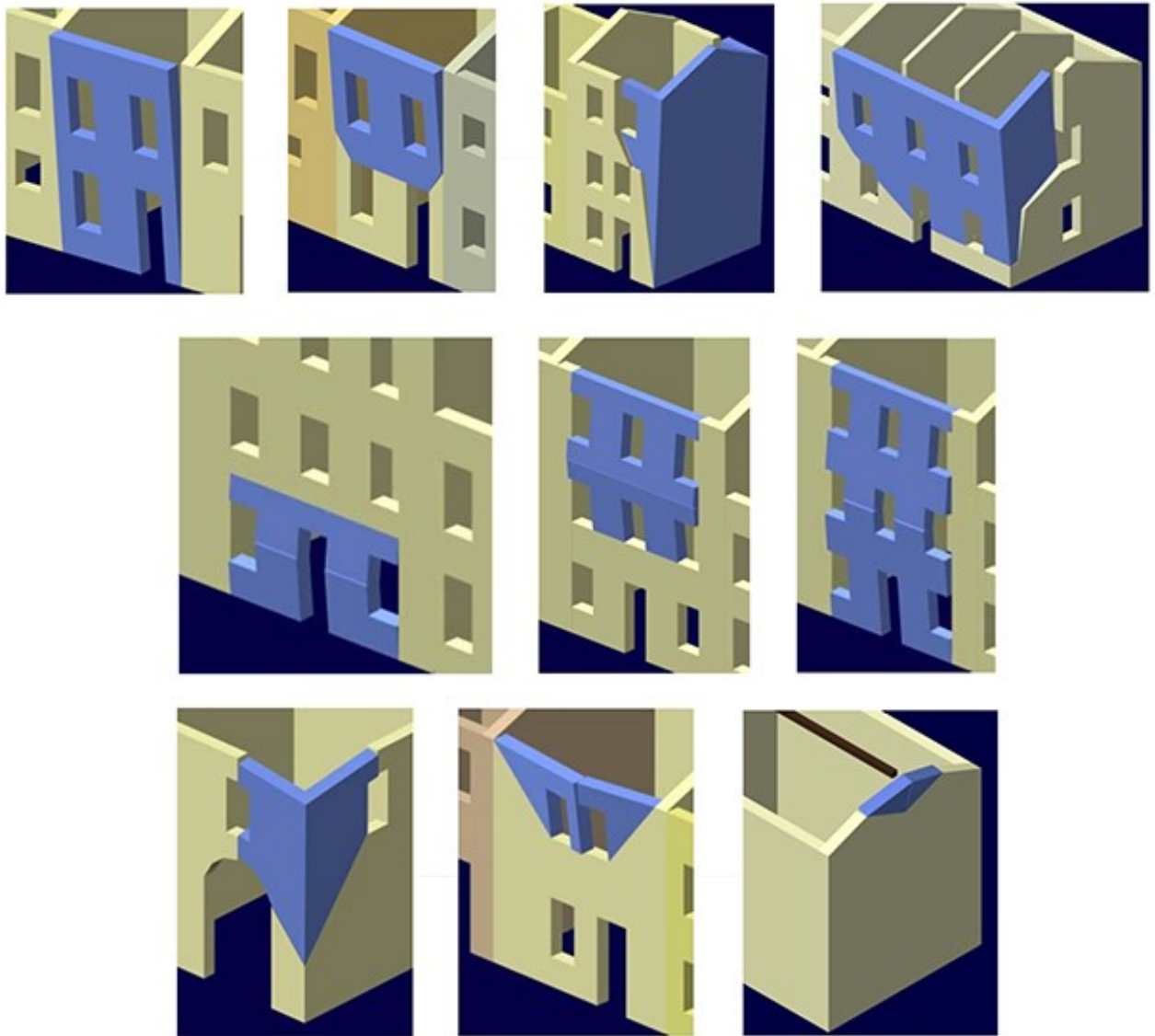


Figure 4.2: Typical out-of-plane local mechanisms (ReLUIS - Dipartimento di Protezione Civile, 2009).

### 4.2.2 In-plane behaviour

If the box behaviour is ensured and the walls and the slabs are well-connected, the in-plane behaviour governs the global building response. Masonry piers subjected to in-plane loading typically show three types of mechanisms, summarized in Figure 4.3: flexural-rocking, sliding and diagonal cracking (Calderini et al., 2009; Magenes and Calvi, 1997). The response of the panels depends on the geometry, the boundary conditions, the axial load, the mechanical properties of masonry and the type of masonry.

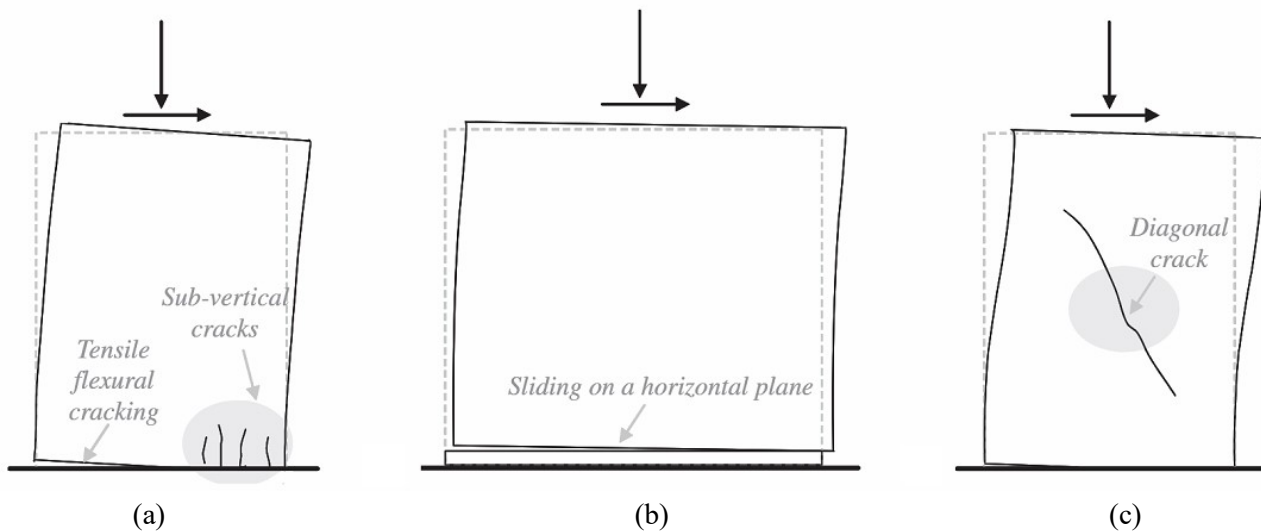


Figure 4.3: Typical in-plane failure modes of masonry piers (Calderini et al., 2009): (a) flexural-rocking; (b) shear failure (sliding along the bed joints); (c) shear failure (diagonal cracking).

The flexural behaviour of piers combines both rocking/bending and crushing/compression failure modes (Figure 4.3 (a)). In the former, under increasing displacement demand, the pier behaves as a nearly rigid body rotating around the toe, if the masonry compressive strength is high with respect to the induced vertical stresses: wide tensile flexural cracks develop at the corners of the pier. In the latter, usually after rocking deformations and under high levels of axial load, a compressive failure, called toe-crushing, with sub-vertical cracks occurs at the toe of the pier. Slender piers are generally prone to a predominant flexural-rocking behaviour. The flexural failure is described by the beam theory, following the common criteria proposed in the Italian code (Commentary to the NTC 2018, 2019) and defining a parabolic domain relating the axial compressive action and the ultimate bending moment (Figure 4.4). The ultimate bending moment, at the panel end section, is determined according to Equation 4.1, by neglecting the tensile strength of masonry and assuming a non-linear distribution of stresses at the compressed toe.

$$M_u = \frac{l^2 t \sigma_0}{2} \left( 1 - \frac{\sigma_0}{0.85 f_m} \right) = \frac{Nl}{2} \left( 1 - \frac{N}{N_u} \right). \quad (4.1)$$

where  $l$  is the width of the panel,  $t$  is the thickness,  $N$  is the axial compressive action,  $\sigma_0$  is the normal compressive stress on the whole area ( $\sigma_0 = N/lt$ ) and  $f_m$  is the average compressive strength. This approach is based on a no-tensile material where a non-linear reallocation of the stress is performed (rectangular stress-block with factor = 0.85).

In existing buildings the compressive strength  $f_m$  is to be divided by the “confidence factor”  $FC$  according to the structural knowledge level (further details can be found in the following paragraph 4.3).

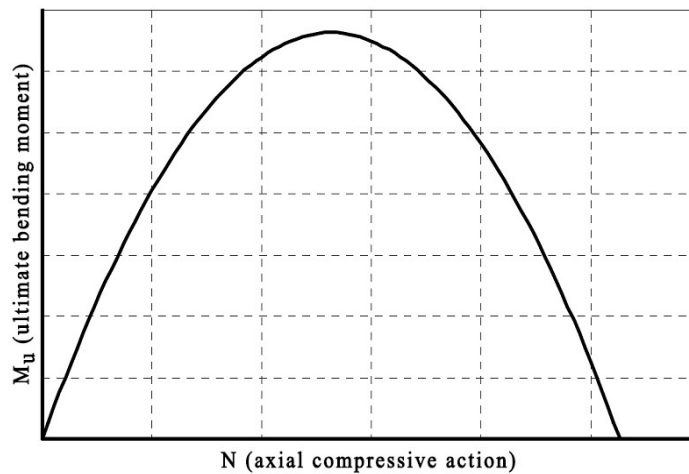


Figure 4.4: Parabolic domain relating the axial compressive action and the ultimate bending moment (adapted from Lagomarsino et al, 2008).

The sliding failure takes place along a mortar joint, usually at the bottom of squat masonry piers subjected to low compressive stress. This causes the formation of sliding shear cracks in the bed joint, usually observed at the end of the pier (see Figure 4.3(b)). Due to increasing uncompressed length of the end joint, the friction of mortar joint usually contributes to this failure mode alone. The failure is attained in case of low vertical load levels and/or low friction coefficients of the mortar joint.

The model describing the sliding failure is the Mohr-Coulomb’s model, in which the governing parameters of the phenomenon are the cohesion and the friction coefficient, according to the linear formulation:

$$\tau = c + \mu \sigma \quad (4.2)$$

where  $\tau$  is the shear strength,  $\sigma$  is the compressive stress,  $c$  is the cohesion and  $\mu$  is the friction coefficient. These latter parameters can be determined from slightly-destructive tests in which the sliding along a mortar joint is investigated, as will be shown in the followings. These parameters are defined globally for a whole masonry pier rather than locally for mortar joints. The most well-known formulation using this concept was developed by Mann and Muller (1982): differently from the model in Equation 4.2, where masonry is assumed to be elastic, homogeneous and isotropic until failure, they analysed masonry as a composite material. Therefore, they considered the possibility for the crack to develop according to the features of the constituents, and not rigidly along a principal stress direction.

The diagonal cracking failure mode, typical of moderately slender masonry panels with higher compressive stress applied, is characterized by the presence of diagonal cracks, generally developing from the centre of the panel and then propagating towards the corners. The failure criterion proposed for the interpretation of this mechanism is based on the assumption that the crack will appear in correspondence of the reaching of the masonry tensile strength in the centre of the panel, made of irregular units or characterized by not particularly resistant units. The shear behaviour may be governed by the diagonal cracking failure according to the criterion proposed by Turnšek and Čačovič (1971) and Turnšek and Sheppard (1980), defining a parabolic failure domain, in which the governing parameter is the diagonal tensile strength  $f_t$ :

$$\tau = lt \frac{f_t}{b} \sqrt{1 + \frac{\sigma_0}{f_t}} = lt \frac{1.5\tau_0}{b} \sqrt{1 + \frac{\sigma_0}{1.5\tau_0}} = lt \frac{1.5\tau_0}{b} \sqrt{1 + \frac{N}{1.5\tau_0 lt}} \quad (4.3)$$

where  $f_t$  is the tensile strength of masonry due to diagonal cracking,  $\tau_0$  is the equivalent shear strength of masonry, conventionally defined as  $\tau_0 = f_t / 1.5$ , and  $b$  is a corrective factor related to the distribution of the loads in the element:

$$b = \begin{cases} 1.5 & h/l > 1.5 \\ h/l & 1 \leq h/l \leq 1.5 \\ 1 & h/l < 1 \end{cases} \quad (4.4)$$

The shear strength can be obtained from the tests carried out on masonry wallets through diagonal compressive loading, which induces indirect tensile strength (Tomažević, 1999). In general, flexural-rocking, bed joint sliding and diagonal cracking propagating through the mortar bed joints and head joints are the failure mechanisms with large deformation capacity. Thus, these mechanisms are the most common for a pier under seismic action. The flexural-rocking failure mode has a ductile behaviour; on the contrary, the two failure modes of toe-crushing and diagonal cracking propagating through the units represent a brittle behaviour in which the damage to the units causes rapid strength deterioration of the masonry piers (Yi, 2004).

The term “masonry spandrel” (or masonry beam) defines the portion of wall that links two adjacent piers across an opening. Masonry spandrels result often damaged during a seismic event and in general they usually are the first structural components that crack in unreinforced masonry (URM) buildings (Graziotti et al., 2012). Masonry spandrels contribute to the wall in-plane behaviour, resisting against the seismic loads together with the masonry piers. Spandrels have a significant contribution to the global in-plane behaviour of the wall, increasing its stiffness and affecting the boundary conditions of piers. Thus, recognizing that the masonry piers are the most important elements both for vertical load carrying capacity and for the resistance to seismic action, it is nevertheless not generally correct to neglect the presence of the spandrels and their role in increasing stiffness. Figure 4.5 shows that a different degree of coupling offered by the spandrels may introduce a completely different structural behaviour in terms of shear, moment diagrams and collapse mechanism. In particular, the Figure shows the two extreme ideal and non-realistic conditions of infinitely flexible (a) and infinitely stiff (c) spandrels, corresponding to cantilever (i.e. a global flexural-rocking behaviour) and shear-type mechanisms, respectively. The most realistic situation appears to be in between these extreme conditions, as represented in the intermediate (b) configuration, in which the spandrel beams offer a limited degree of coupling to the vertical masonry piers (Graziotti et al., 2012).

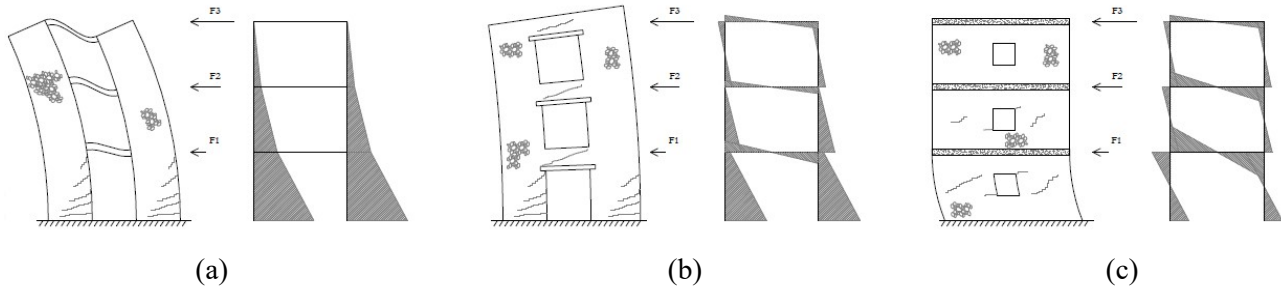


Figure 4.5: Different bending moment variation and failure mechanism due to different grades of coupling provided by the spandrels in masonry walls: weak (a), intermediate (b) and strong (c) spandrels (Graziotti et al., 2012).

The most observed in-plane failure modes of spandrels during past earthquakes are almost similar to those of piers. The main difference is related to the spandrel axis, which is horizontal (i.e. parallel to the bed joints) and not vertical as that of the piers.

The Italian Code (Commentary to the NTC 2019) defines the strength criterion to adopt for the masonry spandrels.

For the evaluations relating to the flexure (coupled with the axial stress) in the spandrels, a critical aspect is related to the evaluation of the axial action, influenced by the interaction with the horizontal diaphragms (in some models assumed to be rigid) and by the kinematic interaction between rotation and axial deformation in the spandrels. If there are horizontal elements with tensile strength, coupled to the spandrel, it is possible to evaluate the maximum bending moment ( $M_{u,spandrels}$ ) of the spandrels:

$$M_{u,spandrels} = \frac{hH_p}{2} \left[ 1 - \frac{H_p}{0.85f_h ht} \right] \quad (4.5)$$

where  $H_p$  is the minimum between the tensile strength of the horizontal element in the spandrels (for example a tie-rod or tie-beam) and  $0.4f_h ht$ , where  $f_h$  is the compression strength of the masonry in the horizontal direction in the plane of the wall;  $h$  is the height and  $t$  is the thickness of the spandrel.

Unlike the case of piers, the axial-bending strength domain for the spandrels can be determined taking into account the tensile strength ( $f_{td}$ ) that is generated in the end sections, due to the effect of the tothing with the adjacent masonry portions. The failure mechanisms can involve the tensile strength  $f_{td}$  of the blocks or occur by sliding along the horizontal joints; the horizontal tensile strength is, therefore, given by the expression:

$$f_{\text{fd}} = \min\left(\frac{f_{\text{btd}}}{2}; f_{\text{v0d}} + \frac{\mu\sigma_y}{\Phi}\right) \quad (4.6)$$

where  $\sigma_y$  is the medium normal stress on the horizontal joints in the end section;  $f_{\text{v0d}}$  is the shear strength in the absence of normal stress;  $\mu$  is the local friction coefficient of the joint;  $\Phi$  is the tothing coefficient. Without more accurate evaluations,  $\sigma_y$  can be assumed equal to the half of the medium normal stress  $\sigma_0$  on the adjacent piers. Once the tensile strength of the spandrel  $f_{\text{ft}}$  is evaluated, the domain M-N can be assumed with an adequate stress-deformation law. For compressive strength, it is necessary to evaluate that in the horizontal direction  $f_{\text{h}}$ , usually lower than that in the vertical direction.

For the evaluation related to the shear strength, both for the masonry piers and spandrels, the criteria to be adopted are the same explained above, following the Equations 4.2 or 4.3.

### 4.3 Existing URM buildings

The assessment of the seismic vulnerability on existing buildings is affected by a series of uncertainties and variabilities involving the knowledge of the building, leading to a great difficulty in the process of verification and, possibly, of the design of the strengthening interventions. The Eurocode 8, (2004) and NTC (2018) propose an approach of seismic vulnerability assessment based on the knowledge of the building under investigation.

The uncertainties may concern the geometry, the structural elements, the construction details, the type of masonry, the state of damage, the quality of the materials; these parameters can also have considerable variability within the same structure, and cannot be imposed as design data to be achieved in phase constructive, as a new design building. On the other hand, a correct and accurate evaluation reduces the uncertainties that, in a new construction, are inherent in the passage from the project data to the realization. The best possible knowledge of the building, which is the essential requirement for any type of structural analysis and for the seismic vulnerability assessment of existing structures, can be achieved by means of historical analysis, survey operations and experimental investigations, with different levels of detail (Ferretti, 2018).

In assessing the earthquake resistance of existing structures, the input data shall be collected

from a variety of sources, including: available documentation specific to the building in question, relevant generic data sources (e.g. contemporary codes and standards), field investigations and, in most cases, in-situ and laboratory tests.

For this reason the code introduces a category of factors, the "confidence factors" (Table 4.1), according to the "knowledge levels" (limited, extensive, exhaustive) achieved in the cognitive surveys.

Table 4.1: Knowledge levels and confidence factors.

Knowledge level	Confidence factor
Limited knowledge (KL1)	1.35
Extensive knowledge (KL2)	1.2
Exhaustive knowledge (KL3)	1.0

The confidence factors preliminary reduce the mechanical properties of the existing structure investigated, to derive the values to be adopted in the design or in the verification, and to be further reduced, when required, by the partial safety coefficients.

Figure 4.6 shows the definition of the knowledge levels according to the geometry, the details and the materials and that lower knowledge levels are associated to higher values of the confidence factors.

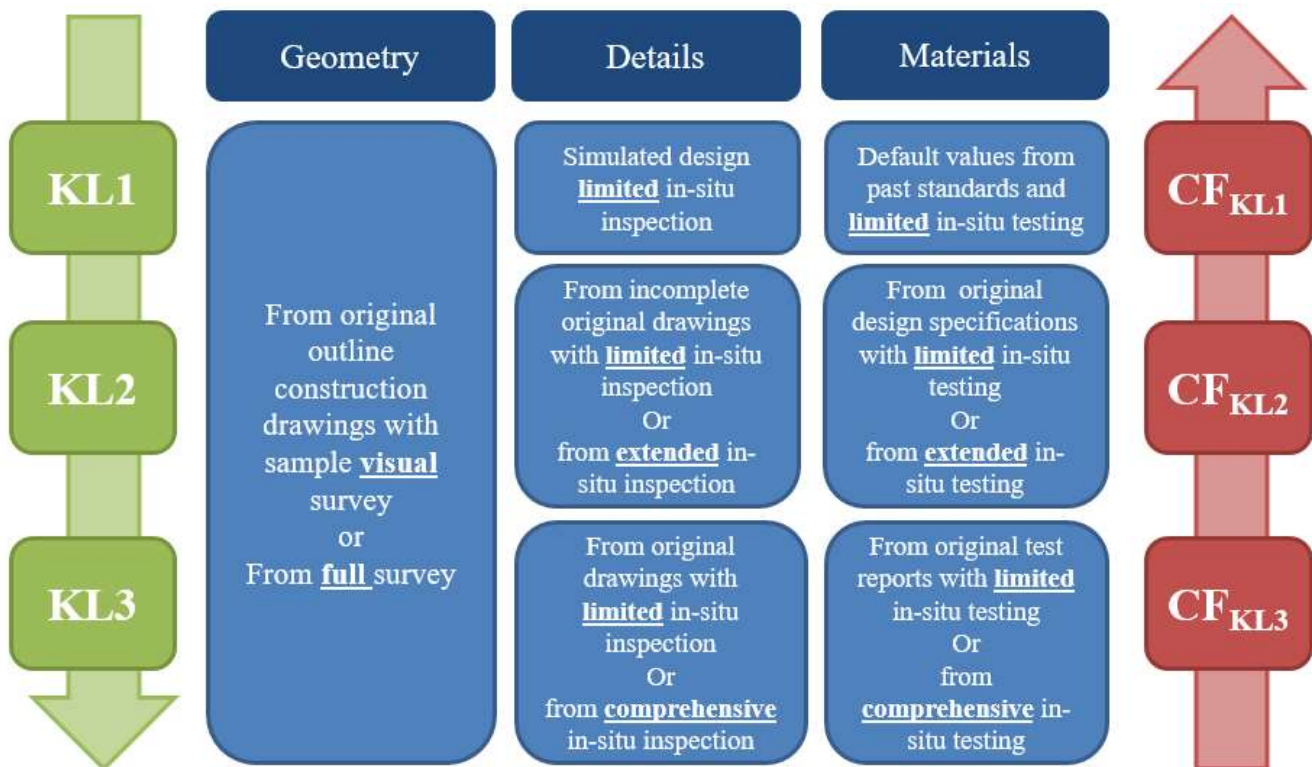


Figure 4.6: Definition of the knowledge levels according to the geometry, the details and the materials.

One of the most complex aspects concerns the evaluation of the mechanical characteristics of the masonry. The Italian code lists a series of tests that can be carried out on the masonry: non-destructive, slightly-destructive or destructive tests. However, the safeguarding of the building often leads to limitations on the number of tests to be carried out and therefore makes the mechanical characterization incomplete.

Limited indications can be found in the Building Codes regarding the type and number of tests which should be executed in order to reach a certain Knowledge Level. Nevertheless, when destructive tests are not performed, which is common in the engineering practice, the Italian Code (Commentary to the NTC 2008, 2009) provides values of the mechanical properties for different masonry typologies to be used for the structural verifications (Table 4.2). In particular, the values reported in Table 4.2 should be corrected with the coefficients of Table 4.3 if the characteristics of the investigated masonry are different from the ones to which Table 4.2 refers.

It was decided to report the Tables of the Italian Code 2008, instead of those of the more recent Italian Code 2018, because in this thesis the modelling of the structures started when the previous Code (2008) was in force.

Table 4.2: Reference values of mechanical parameters (minimum and maximum) and mean self-weight for different masonry typologies, referred to weak mortar, uncoursed masonry, absent connections between wall leaves, texture following the “rule of the art” in case of regular elements:  $f_m$  = mean compressive strength of masonry;  $\tau_0$  = mean shear strength of masonry; E = mean value of the elastic modulus; G = mean value of the shear modulus; w = mean self-weight of masonry. (Commentary to the NTC 2008 – Table C8A.2.I).

Tipologia di muratura	$f_m$	$\tau_0$	E	G	w ( $\text{kN/m}^3$ )
	( $\text{N/cm}^2$ )	( $\text{N/cm}^2$ )	( $\text{N/mm}^2$ )	( $\text{N/mm}^2$ )	
	Min-max	min-max	min-max	min-max	
Muratura in pietrame disordinata (ciottoli, pietre erratiche e irregolari)	100	2,0	690	230	19
	180	3,2	1050	350	
Muratura a conci sbozzati, con paramento di limitato spessore e nucleo interno	200	3,5	1020	340	20
	300	5,1	1440	480	
Muratura in pietre a spacco con buona tessitura	260	5,6	1500	500	21
	380	7,4	1980	660	
Muratura a conci di pietra tenera (tufo, calcarenite, ecc.)	140	2,8	900	300	16
	240	4,2	1260	420	
Muratura a blocchi lapidei squadriati	600	9,0	2400	780	22
	800	12,0	3200	940	
Muratura in mattoni pieni e malta di calce	240	6,0	1200	400	18
	400	9,2	1800	600	
Muratura in mattoni semipieni con malta cementizia (es.: doppio UNI foratura $\leq 40\%$ )	500	24	3500	875	15
	800	32	5600	1400	
Muratura in blocchi laterizi semipieni (perc. foratura < 45%)	400	30,0	3600	1080	12
	600	40,0	5400	1620	
Muratura in blocchi laterizi semipieni, con giunti verticali a secco (perc. foratura < 45%)	300	10,0	2700	810	11
	400	13,0	3600	1080	
Muratura in blocchi di calcestruzzo o argilla espansa (perc. foratura tra 45% e 65%)	150	9,5	1200	300	12
	200	12,5	1600	400	
Muratura in blocchi di calcestruzzo semipieni (foratura < 45%)	300	18,0	2400	600	14
	440	24,0	3520	880	

Table 4.3: Corrective coefficients of the mechanical parameters indicated in Table 4.2 to be applied in presence of: high-quality mortar, thin mortar joints, transversal connections between wall leaves, poor internal core, strengthening interventions such as mortar injections or reinforced plaster (Commentary to the NTC 2008 – Table C8A.2.2).

Tipologia di muratura	Malta buona	Giunti sottili (<10 mm)	Ricorsi o listature	Connessioni trasversale	Nucleo scadente e/o ampio	Iniezione di miscele leganti	Intonaco armato *
Muratura in pietrame disordinata (ciottoli, pietre erratiche e irregolari)	1,5	-	1,3	1,5	0,9	2	2,5
Muratura a conci sbozzati, con paramento di limitato spessore e	1,4	1,2	1,2	1,5	0,8	1,7	2
Muratura in pietre a spacco con buona tessitura	1,3	-	1,1	1,3	0,8	1,5	1,5
Muratura a conci di pietra tenera (tufo, calcarenite, ecc.)	1,5	1,5	-	1,5	0,9	1,7	2
Muratura a blocchi lapidei squadriati	1,2	1,2	-	1,2	0,7	1,2	1,2
Muratura in mattoni pieni e malta di calce	1,5	1,5	-	1,3	0,7	1,5	1,5

## 4.4 Numerical modelling

For the purpose of masonry analysis and design, an operationally simple strength criterion is essential, taking into account the many uncertainties of the problem. Systematic experimental and analytical investigations on the response of masonry and its failure modes have been conducted in the last decades.

Successful modelling of a masonry historical structure is a prerequisite for a reliable earthquake resistant design or assessment (Asteris et al., 2014). The main disadvantage of many existing criteria is that they ignore the distinct anisotropic nature of masonry and the problems arising from differences within its thickness. For modern structures, with new industrial materials (reinforced concrete, steel, etc.), the development of a reliable mathematical model is possible, due to the fact that materials and member characteristics are more uniform and mostly explicitly known. On the other hand, for the case of masonry, and especially for the traditional one, it seems that there is a lot to be done in this field, until engineers become more confident about the accuracy of the modelling.

Masonry modelling, which represents the material numerically, can address different levels of complexity and accuracy: modelling the masonry as a composite material or modelling each constitutive component individually. In either case, since the material without reinforcement (URM) is characterized by low tensile strength, non-linear constitutive models are essential to be adopted for reproducing the real seismic behaviour (Lourenço, 2014). Masonry modelling strategies can be categorized as follows based on the level of complexity and accuracy desired (Figure 4.7) (Lourenço et al., 1995):

- Detailed micro-modelling: continuum elements are adopted for the modelling of masonry units and mortar joints, whereas the masonry unit-mortar interface is modelled by discontinuous elements;
- Simplified micro-modelling: on the basis of a discrete approach, masonry units are represented by continuum elements, while the behaviour of the mortar joints and unit-mortar interface is lumped in discontinuous elements;
- Macro-modelling: masonry units, mortar and unit-mortar interface are smeared out in the continuum. In other words, masonry is considered as a homogeneous isotropic/orthotropic material.

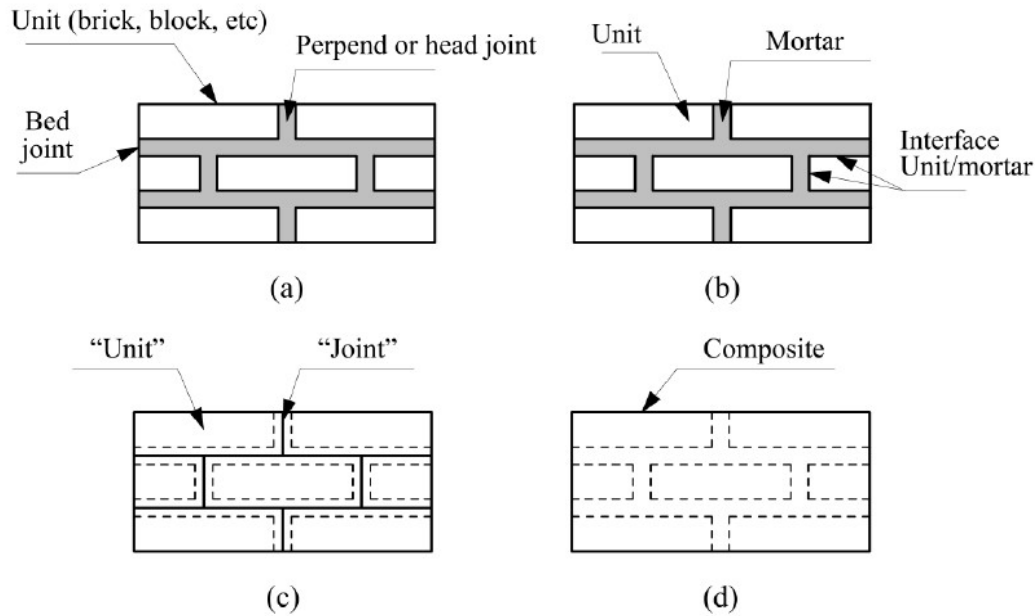


Figure 4.7: Masonry modelling strategies: (a) masonry sample; (b) detailed micro-modelling; (c) simplified micro-modelling; (d) macro-modelling (Lourenço, 1996).

Micro-modelling strategies (detailed or simplified) present an accurate behaviour of URM buildings using an intensive computational process. For this reason, the strategies are proper for the analysis of small masonry structures or elements and especially for simulating the behaviour of the masonry unit-mortar interface. The macro-modelling strategy is identified as the faster and less accurate method than the others and it is used for the modelling of large masonry structures. However, the methodology is still complex due to the brittle behaviour of masonry.

For the analysis of the complex masonry structures, a wide range of analytical models based on the aforementioned strategies are available in literature. The models having different levels of complexity can be summarized as follows (Lourenço, 2002).

- The macro-modelling, based on the identification of macroscopic structural elements, is the simplest approach; it is defined from a geometrical and kinematic point of view through finite elements (solid, shell or frame) and described from a static point of view by their internal generalized forces (Lagomarsino et al., 2013). The two most used structural component models in literature are the ones using several macroblocks and interfaces and those using macro-elements. The former can simulate the out-of-plane failure modes of walls, whereas the latter is adequate for masonry buildings with box behaviour.

The first type of structural component models is based on the assumption that the damaged URM building is composed by a number of discrete macroblocks and interfaces. The

macroblocks are infinitely rigid portions of the building with similar mechanical properties, while the interfaces are the failure lines representing the actual cracking pattern. The analysis is based on the equilibrium of the macroblocks through the limit analysis basic assumptions (Mendes, 2014) for analysing URM buildings as follows: masonry material has no tensile strength and infinitely compressive strength; sliding mechanism cannot happen; failure is exhibited under small displacements (Orduña, 2003).

The macro-element model, as the second type of structural component models, is based on the use of 1D or 2D macro-elements with macroscopic behaviour to simulate the subdivided parts of a masonry wall (piers and spandrels). These rather simple models approximate the actual geometry of the building in a reliable way. The non-linear response of the building under static and dynamic loads can be reproduced by these models using different analysis methods. Moreover, the models are capable of predicting evolution of predefined failure mechanisms in each structural component and global collapse as well.

- Finite Element (FE) structural models (macro and micro-modelling approach): these types of models refer to 2D or 3D finite element models with high accuracy, requiring higher computational effort rather than the structural component models. It makes the models ideal for a full (macro) or partial (micro-modelling) simulation of a masonry structure.

- Discontinuous structural models not using finite elements (micro-modelling approach): these sophisticated models are appropriate for small structures due to the detailed representation of the masonry units and mortar joints. These models are typically studied using the Discrete Element (DE) method (Lemos, 2007) and limit analysis concept.

Figure 4.8 shows an example of different analytical models for the seismic analysis of URM structures.

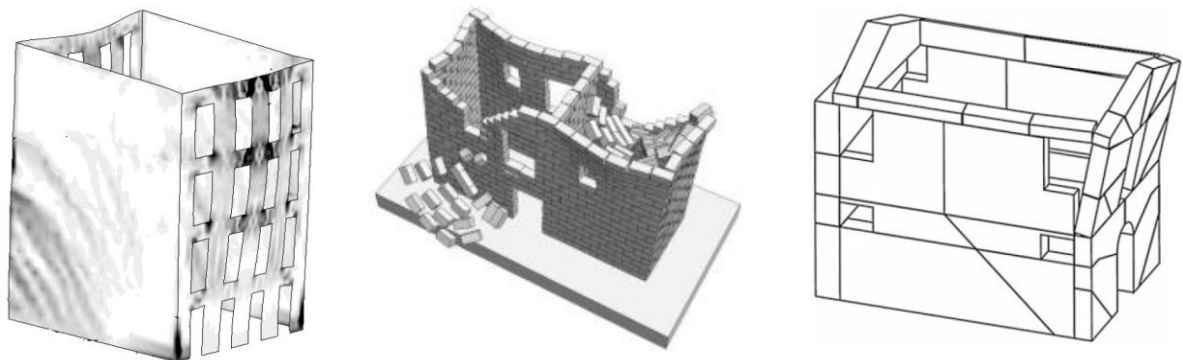


Figure 4.8: Examples of analytical models for the seismic analysis of URM buildings: (a) FE model, macro-modelling approach (Mendes, 2012); (b) DE model, micro-modelling approach (Alexandris et al., 2004); (c) structural component model by macroblocks (Orduña, 2003).

## 4.5 The macro-element modelling: TreMuri software

In this thesis, the masonry buildings are modelled using TreMuri program (Lagomarsino et al., 2013). The commercial version of the program, 3Muri release 11.5.0.4 (S.T.A. DATA, 2013), is used to generate the mesh of the elements, while the research version, TreMuriRicerca (Lagomarsino et al., 2008), is used to perform the non-linear analyses considering a more detailed force-deformation law for the characterization of the masonry elements.

The reference model for the modelling is the box-type, corresponding to a three-dimensional equivalent frame, in which the walls are interconnected by horizontal diaphragms (slabs).

The equivalent frame model approach comprehends the discretization of the masonry walls with openings into a set of panels (Figure 4.9): each wall of the building is subdivided into piers, which are the main vertical elements carrying both vertical and horizontal loads, and spandrels (modelled by non-linear beams), which are the horizontal elements coupling piers and limiting their end-rotations in case of horizontal loads, connected by rigid nodes (undamaged elements confined between piers and spandrels). Earthquake damage observations show, in fact, that only rarely (very irregular geometry or very small openings) cracks appear in these areas of the wall: because of this, the deformation of these regions is assumed to be negligible, relatively to the macro-element non-linear deformations governing the seismic response (Galasco et al., 2006).

The geometry of these panels is defined by the distribution of openings and by the damage observations in URM buildings after past earthquakes and experimental tests. The height of interior piers corresponds to the height of the openings. The height of exterior piers is assumed as the average between the height of the opening and the inter-storey height, considering the possible development of inclined cracks starting from the opening corners (identified as  $H_{\text{eff}}$  in Figure 4.9). The height and length of spandrels is defined by the vertical and horizontal alignment of openings.

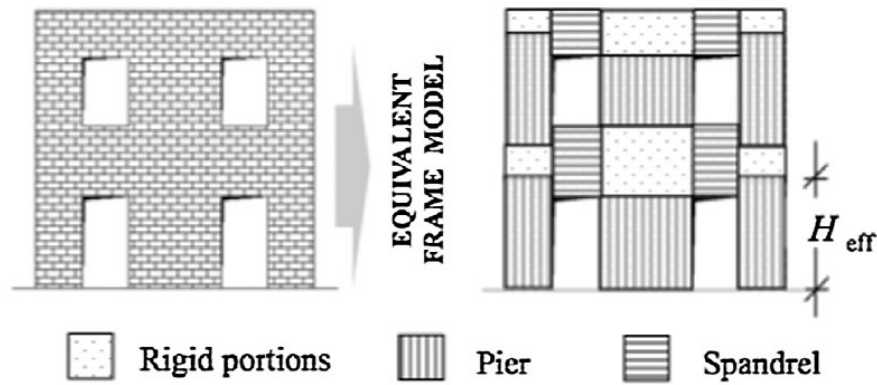


Figure 4.9: URM wall idealization according to the equivalent frame models (adapted from Lagomarsino et al. (2013)).

The 3-dimensional modelling of the whole URM buildings starts from some hypotheses on their structural and seismic behaviour: the bearing structure, both referring to vertical and horizontal loads, is identified with walls and floors (or vaults); the walls are the bearing elements, while the floors, apart from sharing vertical loads to the walls, are considered as planar stiffening elements (orthotropic 3-4 nodes membrane elements), on which the horizontal actions distribution between the walls depends; the local flexural behaviour of the floors and the wall out-of-plane response are not computed because they are considered negligible with respect to the global building response, which is governed by their in-plane behaviour (a global seismic response is possible only if vertical and horizontal elements are properly connected) (Galasco et al., 2006).

A non-linear beam element model has been implemented in the TreMuri program in together with the macro-element with additional degrees of freedom, described by:

- 1) initial stiffness given by elastic (cracked) properties;
- 2) bilinear behaviour with maximum values of shear and bending moment as calculated in ultimate limit states;
- 3) redistribution of the internal forces according to the element equilibrium;
- 4) detection of damage limit states considering global and local damage parameters;
- 5) stiffness degradation in plastic range;
- 6) secant stiffness unloading;
- 7) ductility control by definition of maximum drift ( $\delta_u$ ) (Equation 4.7) based on the failure mechanism, according to the Italian seismic code:

$$\delta_u = \frac{(u_j - u_i)}{h} + \frac{(\phi_j + \phi_i)}{2} = \begin{cases} 0.4\% & \text{shear} \\ 0.6\% & \text{bending} \end{cases} \quad (4.7)$$

8) element expiration at ultimate drift without interruption of global analysis (Figure 4.10).

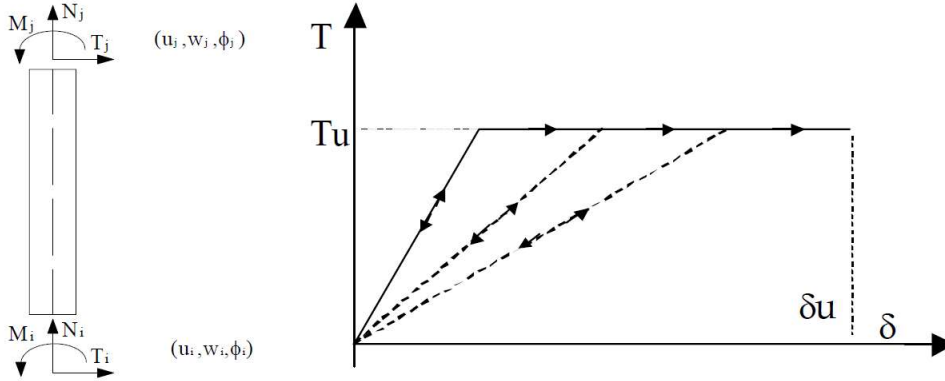


Figure 4.10: Non-linear beam degrading behaviour (Lagomarsino et al., 2008).

The elastic behaviour of this element is given by:

$$\begin{Bmatrix} T_i \\ N_i \\ M_i \\ T_j \\ N_j \\ M_j \end{Bmatrix} = \begin{bmatrix} \frac{12EJ}{h^3(1+\psi)} & 0 & -\frac{6EJ}{h^2(1+\psi)} & \frac{12EJ}{h^3(1+\psi)} & 0 & -\frac{6EJ}{h^2(1+\psi)} \\ 0 & \frac{EA}{h} & 0 & 0 & -\frac{EA}{h} & 0 \\ -\frac{6EJ}{h^2(1+\psi)} & 0 & \frac{EJ(4+\psi)}{h(1+\psi)} & \frac{6EJ}{h^2(1+\psi)} & 0 & \frac{EJ(2-\psi)}{h(1+\psi)} \\ \frac{12EJ}{h^3(1+\psi)} & 0 & \frac{6EJ}{h^2(1+\psi)} & \frac{12EJ}{h^3(1+\psi)} & 0 & \frac{6EJ}{h^2(1+\psi)} \\ 0 & -\frac{EA}{h} & 0 & 0 & \frac{EA}{h} & 0 \\ -\frac{6EJ}{h^2(1+\psi)} & 0 & \frac{EJ(2-\psi)}{h(1+\psi)} & \frac{6EJ}{h^2(1+\psi)} & 0 & \frac{EJ(4+\psi)}{h(1+\psi)} \end{bmatrix} \begin{Bmatrix} u_i \\ w_i \\ \phi_i \\ u_j \\ w_j \\ \phi_j \end{Bmatrix} \quad (4.8)$$

where:

$$\psi = 24 \left( 1 + \frac{E - 2G}{2G} \right) 1.2 \frac{b^2}{12h^2} = 1.2 \frac{E}{G} \frac{b^2}{h^2} \quad (4.9)$$

and  $T$ ,  $N$ ,  $M$  are, respectively, the acting shear force, axial force and bending moment at the element end nodes  $i$  and  $j$ ,  $E$  is the modulus of elasticity of masonry,  $J$  is the inertia of the element section,  $h$  is the height of the element,  $u$ ,  $w$  and  $\phi$  are, respectively, the horizontal displacement, vertical displacement and rotation at the element end nodes  $i$  and  $j$  and  $G$  is the shear modulus of masonry.

The non-linear behaviour is activated when one of the nodal generalized forces reaches its maximum value estimated according to minimum of the strength criteria (flexural-rocking, shear-sliding or diagonal shear cracking), already explained in Section 4.2.2, related to the in-plane behaviour of the masonry walls.

#### **4.6 Non-linear static analysis according to the Italian Code**

The Eurocode 8 (2004) and the NTC (2018) provide the possibility to perform two type of analyses: the linear ones (lateral force analysis and modal response spectrum analysis) and the non-linear ones (static push-over analysis and time-history dynamic analysis).

URM structures exhibit inelastic deformations and dissipate high levels of energy under cyclic loading. This results in a significant reserve of non-linear capacity. Thus, linear analysis techniques are not adequate for evaluating their seismic response. The best approach to the seismic analysis of URM buildings (for design or assessment purposes) is a non-linear analytical approach, considering the material and the geometrical non-linearity of the buildings.

The dynamic response of a system with multi degrees of freedoms (MDOF) can be described very accurately through the performing of non-linear dynamic analyses involving the direct integration of the equations of motion of the system, where a history of accelerations is applied to. However, this methodology presents several difficulties in its practical application, first of all the computational effort and therefore the time required to perform the analyses. It is also necessary to define, with accurate precision, a significant number of parameters, which are not easily estimable and regulating the hysteretic behaviour of materials and plasticization zones. The obtained dynamic response is also strongly dependent on the accelerogram, i.e. the earthquake chosen. To obtain reliable results it is therefore necessary to repeat the analyses for a number of accelerograms sufficiently representative of the seismicity of the site.

An alternative and simpler application approach, which has become widespread in the most recent period, is represented by the possibility of performing a non-linear static analysis, which consists in the application of a monotonically increasing lateral force (or displacement) profile and monitoring the response of the structure through a simple force-displacement relation. Therefore, the non-linear, or push-over static analysis, consists of an iterative incremental analysis in which the structure is pushed to a predetermined threshold of displacement or until its ultimate deformation capacity is reached.

The most commonly monitored parameters during the analysis are the base shear of the building and the displacement of a control point, generally taken at the centre of gravity of the highest slabs. The representation of the curve base shear-displacement provides what is called “capacity curve” of the structure (Figure 4.11).

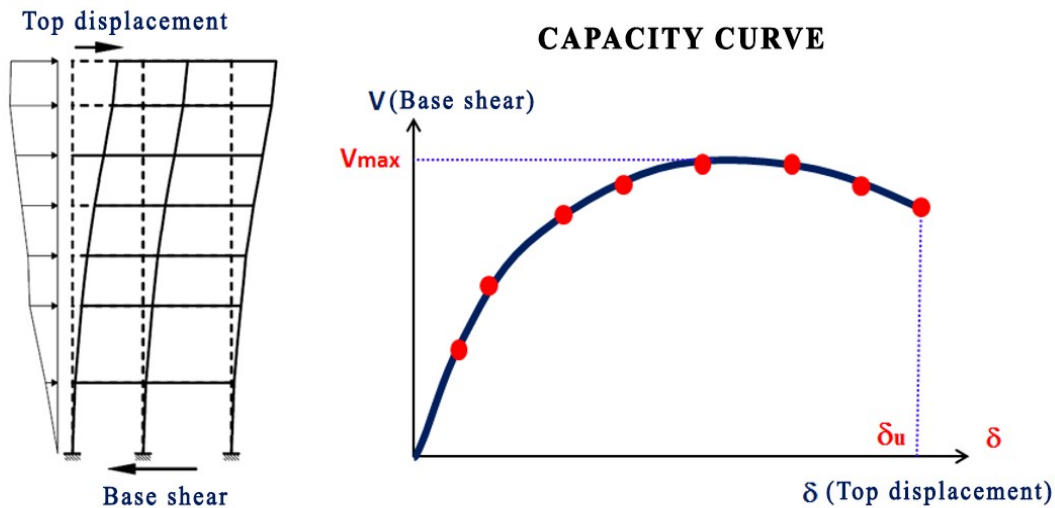


Figure 4.11: Determination of the capacity curve.

The push-over analysis is a simplification of the physical reality, constituted by a seismic phenomenon and therefore needs some applicative hypotheses to be able to be performed. In the first place, the structural seismic response is determined through a growing static application of a lateral force profile and therefore the effects due to the cyclical nature of the actions are disregarded. Secondly, the profile of the lateral forces should be proportional to the internal forces due to the effect of the seismic motion.

In the most simple case it is assumed that the forces are proportional to the eigenvector associated with the first mode and, for this reason, it is representative of inertia forces of the “non-damaged” structure, i.e. elastic (triangular distribution). The second possibility, proposed by the code, is a distribution of the forces proportional to the masses: it is representative of the inertia forces of the damaged structure, i.e. when relevant inelastic deformations were developed.

It is generally accepted that the real form of the distribution of the forces in each load phase is between the triangular one (typical of the equivalent static analysis) and the uniform one and that the verification of the displacement capacity in correspondence of these two limit distributions and in static conditions, is a guarantee of positive verification with respect to the actual forms of the force distributions.

## 4.7 The N2 method

The final objective is the assessment of the seismic vulnerability, which can be expressed in terms of ratio between the displacement capacity ( $d_u$ ) and the displacement demand ( $d_{max}$ ):

$$\mu_d = \frac{d_u}{d_{max}}. \quad (4.10)$$

According to the Italian Code (NTC, 2018) the capacity verification is satisfied when that ratio (expressing the structural ductility  $\mu_d$ ) is greater than or equal to 1, i.e. when the displacement capacity is greater than the displacement demand.

For the evaluation of the seismic displacement demand, the response spectra must necessarily be used. However, since these latter are defined starting from single degree of freedom (SDOF) systems, it is necessary that the response (capacity) obtained with the push-over analysis on an MDOF system is attributed to that of an equivalent SDOF system. Therefore, the verification of the displacement capacity is carried out by transforming the MDOF system into an equivalent SDOF system, using the properties of the response spectra.

According to Fajfar (2000) and the Codes (Eurocode 8, 2004; NTC, 2018) it is possible to determine the response in terms of base shear and top displacement starting from a MDOF system and then to relate them to a SDOF system, through the modal participation factor  $\Gamma$  (Equations 4.11 and 4.12), obtained in such a way as to normalize the eigenvector  $\Phi$  according to the distribution of the forces (Figure 4.12).

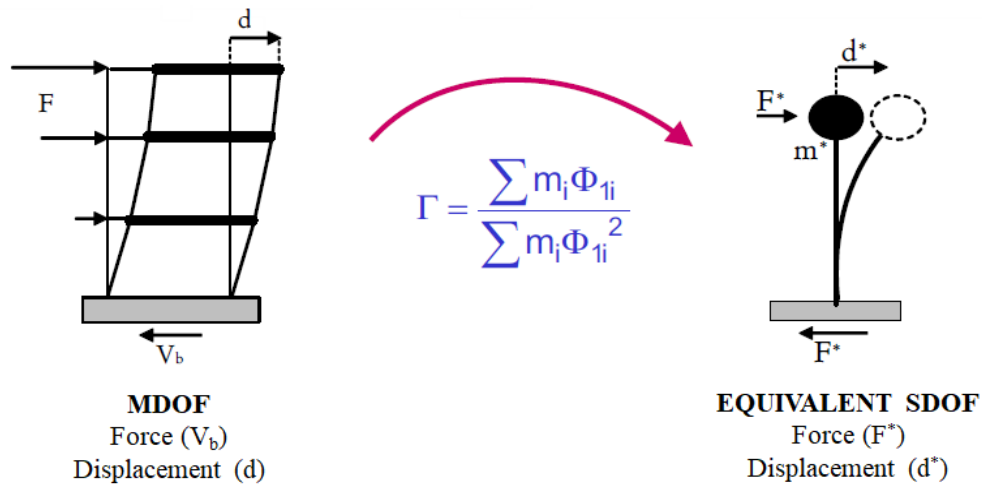


Figure 4.12: Passage from the MDOF system to the SDOF system, through  $\Gamma$ .

$$F^* = \frac{V_b}{\Gamma} \quad (4.11)$$

$$d^* = \frac{d}{\Gamma}. \quad (4.12)$$

As an example, Figure 4.13(a) shows the generic capacity curve for an MDOF system, characterized by the maximum shear base  $V_{bu}$  and the maximum displacement on the top  $d_u$ . The capacity curve of the equivalent SDOF (Figure 4.13(b)) is obtained starting from this by applying the Equations 4.11 and 4.12.

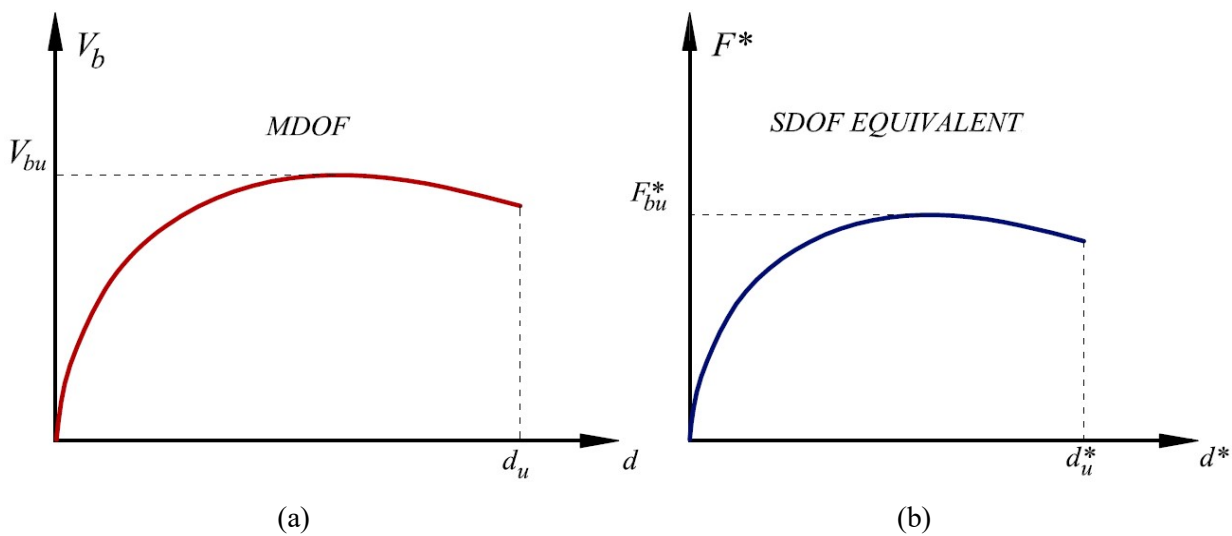


Figure 4.13: (a) Capacity curve for the MDOF system; (b) capacity curve for the SDOF equivalent system.

Since the objective is the assessment of the seismic vulnerability, it is possible to obtain the parameters to perform the capacity verification from the capacity curve of the SDOF system. It is necessary to identify the seismic demand, which depend on the seismicity of the site, but also on the mass and the stiffness of the system.

To evaluate the initial stiffness of the SDOF system it is necessary to perform a bilinearization of the capacity curve, i.e. to transform the capacity curve of the SDOF into an equivalent bilateral curve (Figure 4.14). This bilinearization can be performed according to different criteria. What follows is the one defined by the NTC (2018).

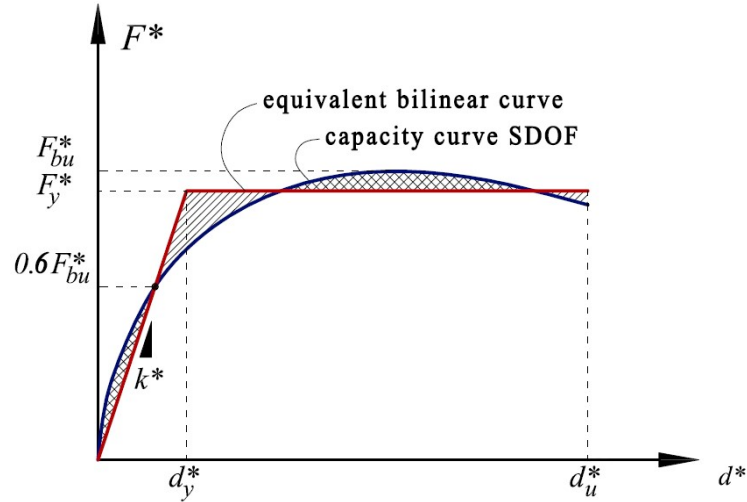


Figure 4.14: Definition of the bilinear equivalent curve from the SDOF system.

With reference to Figure 4.14, once the maximum value of the force associated to the SDOF system has been identified on the capacity curve, the first linear part intersects the capacity curve in the point characterized by the strength value equal to  $0.6F_{bu}^*$ . The value of the force  $F_y^*$ , identifying the yield of the bilinear system, is determined in such a way to have the equality of the area subtended by the capacity curve and that subtended by the bilinear curve. The stiffness ( $k^*$ ) of the SDOF is given by the ratio between the yielding force of the bilinear curve and its associated displacement ( $d_y^*$ ):

$$k^* = \frac{F_y^*}{d_y^*}. \quad (4.13)$$

The mass can be determined as:

$$m^* = \sum m_i \Phi_{1i} \quad (4.14)$$

and the associated period as:

$$T^* = 2\pi \sqrt{\frac{m^*}{k^*}}. \quad (4.15)$$

Once the period referred to the SDOF equivalent system is found, it is possible to use the response spectra to obtain the displacement demand  $d_{\max}^*$ , using the relation between the acceleration spectra and the displacement spectra:

$$S_{Ac}(T^*) = S_{De}(T^*) \omega^{*2} \quad (4.16)$$

where  $S_{Ae}(T^*)$  is the spectral acceleration, found using the acceleration spectra starting from the period  $T^*$ ,  $S_{De}(T^*)$  is the spectral displacement and  $\omega^{*2}$  is the square of the natural frequency of the SDOF equivalent system. Figure 4.15 shows the use of the displacement spectrum to find displacement demand  $d^*_{max}$ .

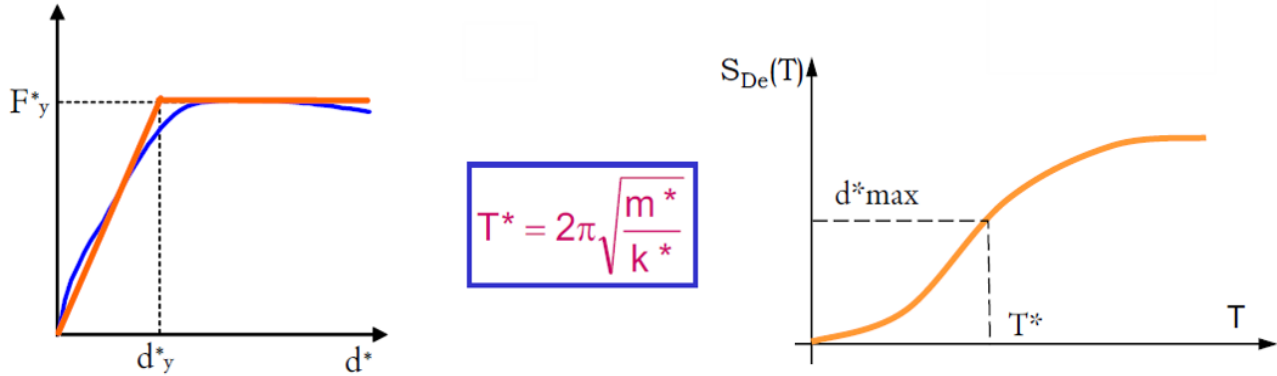


Figure 4.15: Use of the displacement spectrum to find the displacement demand  $d^*_{max}$ .

According to the Italian Code, the displacement demand depends on the value of the period  $T^*$ ; in particular if  $T^* \geq T_C$  the displacement demand  $d^*_{max}$  exactly corresponds to the elastic displacement demand, i.e. to the values of the spectral displacement  $S_{De}(T^*)$ :

$$d^*_{max} = d^*_{e,max} = S_{De}(T^*) \quad T^* \geq T_C. \quad (4.17)$$

On the contrary, if  $T^* < T_C$ :

$$d^*_{max} = \frac{d^*_{e,max}}{q^*} \left[ (q^* - 1) \frac{T_C}{T^*} + 1 \right] \quad T^* < T_C \quad (4.18)$$

where  $q^* = m^* S_{Ae}(T^*) / F^* y$ .

The Equations 4.17 and 4.18 are also reported in the NTC (2018). They express the displacement required to the equivalent SDOF as a function of its period  $T^*$  and of the factor  $q^*$  from which it is characterized according to the rules of the criterion of equal energies and equal displacements. Figure 4.16 graphically exemplifies what is expressed in the Equations 4.17 and 4.18. In particular, for periods greater than  $T_C$  the displacement demand for the non-linear system (inelastic demand) is equal to that would be required in the linear field if this were unlimitedly elastic (Figure 16(a)). For periods less than  $T_C$ , the non-linear displacement demand is different from the elastic one and in particular the displacement demand is greater

than the elastic one (Figure 16(b)). This refers to the well-known criterion of equal energies and equal displacements between linear and non-linear SDOF systems.

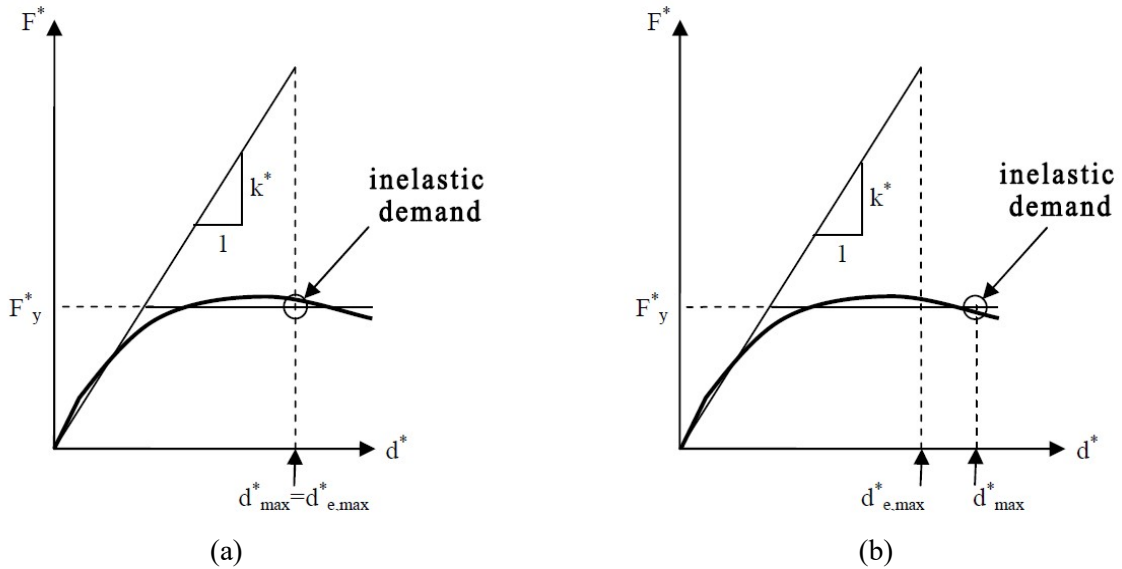


Figure 4.16: Definition of the displacement demand: (a) for  $T^* \geq T_c$ ; (b) for  $T^* < T_c$  (NTC, 2018).

Finally, it is necessary to pass again from the SDOF system to the MDOF system: it is sufficient to multiply the obtained displacement demand  $d_{\max}^*$ , referred to the SDOF system, for the modal participation factor  $\Gamma$  (defined in Figure 4.12):

$$d_{\max} = d_{\max}^* \Gamma. \quad (4.19)$$

The structural capacity is represented by the ultimate point of the push-over curve. The verification is satisfied if:

$$d_{\max} \leq d_u. \quad (4.20)$$

Recent studies have shown some limitations on the application of the N2 method, showing alternative methods that highlight some differences in the results obtained. In particular, some limitations have been found by Guerrini et al. (2017) for very rigid structures with a short period and by Marino et al. (2019) for buildings with some sources of irregularity, as in plan, in elevation and related to the decrease in stiffness of diaphragms. In the latter case, the applicability of the non-linear static procedure for the seismic assessment of irregular URM buildings has been investigated by a systematic comparison with the results provided by the

non-linear dynamic analyses, assumed as reference solution, focusing on the global response of URM buildings, i.e. based only on the in-plane response of URM walls. It was shown that the procedures of the N2 method, currently adopted in the European and the Italian codes, do not provide conservative results with respect to that proposed by Marino et al. (2019).

Since the several previous applications of the method in structures similar to those analysed in this thesis, the method is considered suitable for the study of seismic vulnerability and fragility of masonry aggregate buildings object of this study.

## **5. SEISMIC FRAGILITY ASSESSMENT OF MASONRY STRUCTURES**

---

## 5.1 The methodology

The development of detailed vulnerability models at territorial scale requires the identification of different building classes or typologies. This is supported on the idea that buildings with similar architectural and structural features and located in similar geotechnical conditions are expected to have similar seismic performances (Simões, 2018).

The general objective of this thesis is the assessment of the seismic vulnerability and fragility of classes of unreinforced masonry buildings, through the individuation of some prototypes having similar characteristics and representative of those classes of buildings. Particularly, these classes have been individuated considering buildings, especially present in historical centres, enclosed in aggregates. The individuated structures were at first considered as isolated structural units (ISU) and then belonging to aggregations in row of those similar (or identical) structures, in order to compare the different seismic responses and to show as it is no possible to perform seismic analysis of buildings considered as isolated, if they are enclosed in aggregate structures (AS), because the interaction with adjacent buildings significantly affects the seismic behaviour (Figure 5.1).

In this thesis, the aggregate masonry buildings are analysed considering the global behaviour: the local behaviour of the walls out-of-plane is not considered because it is considered negligible with respect to the global building response, which is governed by the in-plane behaviour of the masonry walls, in this type of structures.

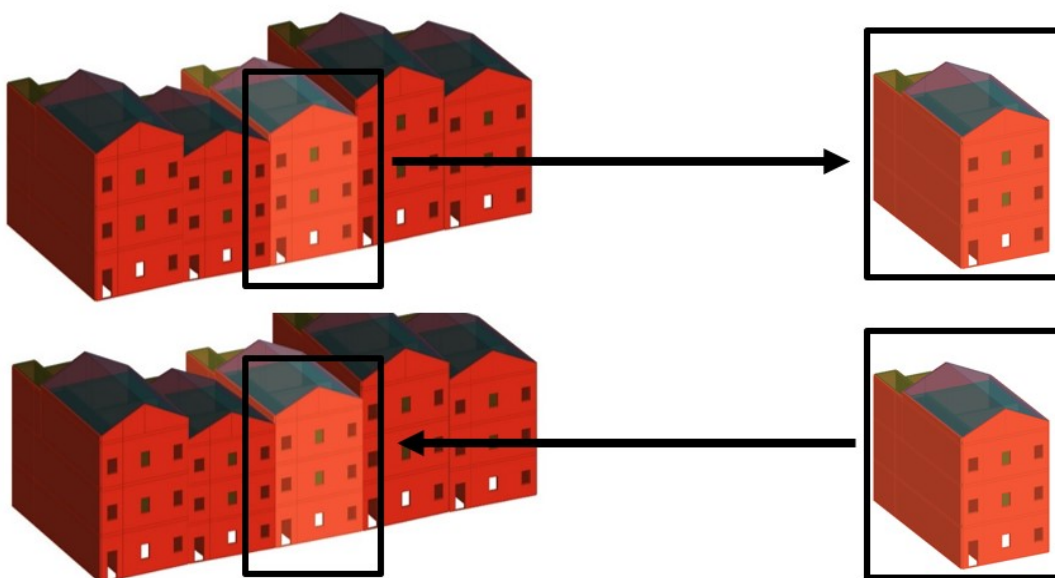


Figure 5.1: Comparison between the isolated structural unit considered as isolated and that enclosed in a row aggregate.

The first step is the definition of one (or more) class of buildings, in which it is possible to individuate some geometrical and structural similar characteristics. It is important to define which parameters characterize the different structural typologies of the class of buildings: the variation of these parameters in defined ranges allows the individuation of a set of different masonry buildings.

Thus, a set of different structural models was defined using TreMuri software, according to the choice of the variation of the parameters. The structural capacity of each model was obtained by means of non-linear static analyses (push-over), considering two different and orthogonal directions of the seismic action.

According to the Italian code (NTC, 2018), the seismic vulnerability is evaluated with the comparison between the structural capacity, in this case defined by the capacity curves, and the structural demand, defined by means of the definition of the seismic action soliciting the structures. In this work, the seismic action is defined through homogenous class of accelerograms, referred to previous earthquakes and representative of the possible variability of the seismic action in the considered site. For each accelerogram, the definition of the correspondent acceleration and displacement spectrum allows to obtain the seismic demand, in terms of acceleration and displacement, according to the intrinsic structural characteristics of the structures.

The ratio between the structural capacity and the structural demand defines the vulnerability of the building and, in this work, it is evaluated in correspondence of the peak ground acceleration (collapse PGA) corresponding to the attainment of the life safety (LS) limit state. Finally, the definition of a set of collapse PGA allows to obtain the condition probability of the structural failure (attainment of the LS limit state) for different values of the seismic demand, plotting the fragility curves, by means of the limit state function (Equation 2.5).

In this thesis, the explained methodology was applied in two different class of buildings: the first is related to clay brick masonry structures, sited in Bologna (Italy) and it is more detailed in Chapter 6; the second is related to stone masonry structures, sited in Seixal (Portugal) and it is more detailed in Chapter 7.

Figure 5.2 shows the steps of the procedure applied, starting from the definition of the models to the plotting of the fragility curves. The pictures in the figure below are just some examples, not referred to the case studies of this work.

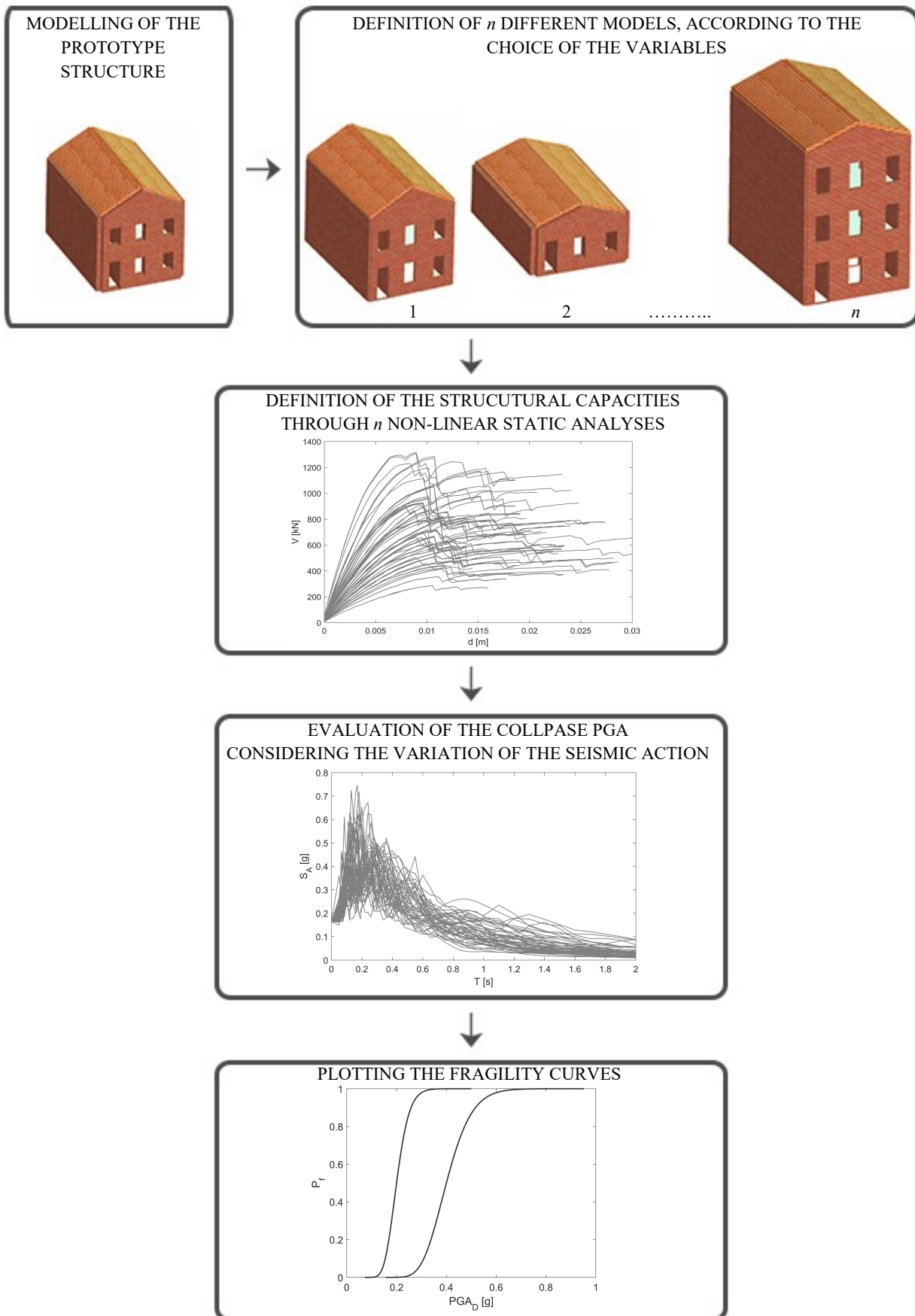


Figure 5.2: Steps of the applied procedure, starting from the definition of the models to the plotting of the fragility curves.

## **5.2 Selection of the parameters defining a set of different structural models**

One of the main difficulties when performing a seismic fragility analysis is related to the large number of variables required to describe the uncertainties affecting the structural behaviour and the complex modelling of the uncertainty related to the definition of the ground-motion. Thus, the first step concerns the definition of the models representing a class of buildings in the considered historic centre. This selection is made through the choice of the most significant geometrical and mechanical properties, also chosen according to the process of knowledge on the structural typologies or to data acquired from diagnostic investigations on the buildings. The definition of the variables involved in the problem can be made in a statistical or deterministic way.

The first part of this work, focused on the study of clay brick masonry buildings (Chapter 6), provides for a choice of the considered variables according to preliminary sensitivity analyses to understand which could be the parameters most influencing the seismic response. This approach was adopted due to a limited availability of the mechanical and geometrical characteristics of the structures in question; thus, the analyses were carried out with statistical procedures, taking into account the variabilities and uncertainties involved in the problem. Particularly, the Response Surface (RS) statistical method (Section 3.3) was adopted. According to the RS approach, the variables can be explicit or implicit and they are defined by means of Gaussian distributions, chosen in such way to have reliable ranges of variation of the variables.

In the second part of this work, focused on the study of stone masonry buildings (Chapter 7), the choice of the parameters, defining the different structural typologies, is based on deterministic data obtained from past investigative studies allowing a complete typological classification of the buildings in the historic centre of Seixal. Among the various classes of buildings identified, the most significant was chosen in this work, represented by a prototype model. According to the typological investigation in the historic centre, a set of different buildings is obtained through all the combinations of the chosen parameters. Thus, in this case it was not necessary to adopt statistical methodologies, as information on the geometrical and mechanical characteristics of the examined buildings were already available.

As for the variation of the seismic action, the approach was the same in the two case studies. A group of accelerograms compatible with the Bologna spectrum, defined by the Italian code, was chosen for the first part of the study and considered as implicit variable: the accelerograms were distributed on the various models according to the definition of the simulations of the Response Surfaces. Similarly, a group of accelerograms compatible with the spectrum of Seixal, defined by the Portuguese code, was chosen for the second part of the study: this time, the group of accelerograms is applied to each defined model, i.e. for each model a number of the collapse PGA equal to the number of the considered accelerograms was obtained.

### **5.3 Non-linear static analyses of the different structural models**

Once the values assumed by the variables are defined, the prototype buildings are modelled using the commercial version of 3Muri software (S.T.A. DATA, 2013) and the research version (Lagomarsino et al., 2008) allowed to automate the generation of all the models, according to the choice of the variables.

For both case studies (Chapters 6 and 7) the structural capacity of the models is obtained by means of non-linear static analyses. The mechanical and geometrical characteristics are considered in the software based on the initial choice of the parameters, that can be defined with fixed or variable values. According to the Italian Code (NTC, 2018), the loads are considered with a seismic combination obtained multiplying both structural and non-structural loads by 1 and the live loads by 0.3. Furthermore, a distribution of the forces proportional to the masses was applied, as it turns out to be more dangerous for the structure and because this distribution is more suitable for structures showing inelastic deformations. In both case studies, for each structure analysed, both isolated and aggregated, two different and orthogonal directions of the seismic action are considered, indicated as  $x$  and  $y$ .

The analyses are carried out considering the in-plan behaviour of the masonry walls, neglecting the activation of out-of-plane mechanisms. The global behaviour of the masonry walls is governed by the criteria explained in Section 4: the ultimate bending moment is defined as in the Equation 4.1 and the shear failure as in the Equation 4.3

The structures of the case studies have a plan shape similar to rectangular: referring to the isolated structural unit, the  $x$ -direction is the one assumed parallel to the shorter side of the rectangle, the  $y$ -direction is that parallel to the longer side of the rectangle. Without reference

to the structures object of the case studies, Figure 5.3 shows two examples of structures with rectangular plan, isolated structural unit and aggregation of identical structural units in a row, with the indication of the orthogonal axes: referring to the aggregate structure, the  $x$ -direction is that of extension of the aggregate, the  $y$ -direction is the perpendicular one.

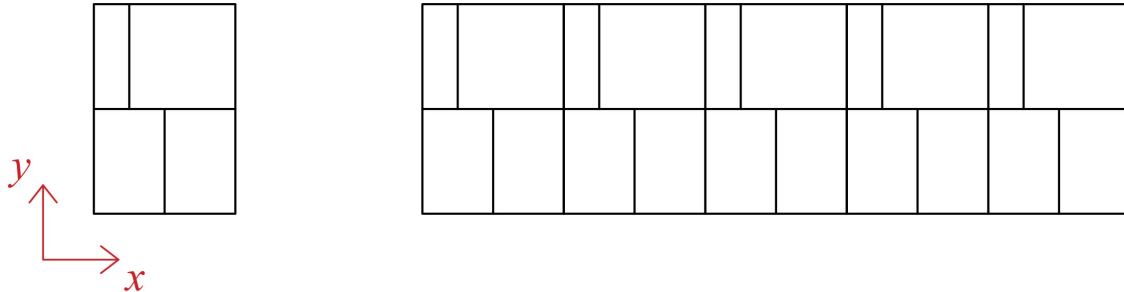


Figure 5.3: Example of an ISU and an AS with the considered reference axes.

The capacity curves represent the results of the push-over analyses, reported in terms of displacement of a control point (generally chosen on the top of the building) in abscissa ( $d$ ) and the total base shear in ordinate ( $V$ ); in order to compare the capacities obtained for the different models, it is possible to make the shear dimensionless, dividing it by the total mass ( $V/M$ ). As far as the displacement is concerned, in this work it was decided to return the average displacement, weighted on the masses, considering the nodes of the last floor of the building, so as to eliminate the dependence on the choice of the control point.

According to the Italian Code, the analyses are stopped when a value equal to 80% of the maximum shear is reached (20% decrease): the last point of the push-over curve represents the ultimate structural capacity, defined as the attainment of the LS limit state.

## 5.4 Definition of the seismic action

In order to assess the seismic vulnerability and fragility, it is necessary to compare the seismic capacity with the seismic demand. To obtain the latter, the seismic action soliciting the structure has to be defined. The codes (Eurocode 8, 2004; NTC, 2018) define the elastic response spectrum to determine the seismic forces to apply, expressed in terms of vibration periods and spectral accelerations (or displacements) and having a regular shape: each spectrum interval (delimited from two fixed period) is defined by means of an expression fixed by the code.

It is a simplified and conventional elastic response spectrum which encloses, in a simplified and precautionary way, the characteristics of the elastic response spectra of earthquakes that can occur in an assigned site.

In this work, in order to consider the possible variability of the seismic action in a site and the uncertainty related to the definition of the ground motion, a group of registered accelerograms referred to past earthquakes was considered. The accelerograms were chosen based on the data referred to previous earthquakes present in the PEER Ground Motion Database (<https://ngawest2.berkeley.edu>), created in collaboration with the NGA project (Power et al., 2006; Power et al., 2008).

The two case studies of this work are related to buildings sited respectively in Bologna (Italy) and in Seixal (Portugal). Thus, two different groups of accelerograms were chosen to have a sufficient number to define a reliable variability of the seismic action in the two sites:

- Bologna: 48 accelerograms;
- Seixal: 50 accelerograms.

With regard to the case studies in Bologna, the choice of the number of the accelerograms was affected by the Design of Experiments (Section 3.3.3) and the number of the simulations defined for the Response Surface models. However, the models referred to buildings sited in Seixal do not follow a particular definition of the simulations: each of the 50 accelerograms is considered for each defined model. The number 50 was just chosen to be comparable with the number of the accelerograms chosen for Bologna. In both cases the accelerograms were scaled to the same reference peak ground acceleration of the considered site ( $a_g$ ), imposing some limits to the scaling in such a way as to be compatible with the LS limit state spectrum in that site, in the range period between  $T = 0.1s$  and  $T = 1.0s$ , but also usable until  $T=3.0 s$ . Furthermore, the selection was done avoiding recordings with impulsive characteristics, considering fixed ranges of epicentral Joyner-Boore distance (distance between the considered point and the projection of the fault plane in the surface) and fixed ranges of the average shear wave velocity  $V_{s30}$  (Eurocode 8, 2004; NTC, 2018) in such a way to make the selections compatible with the considered site. All the parameters defined for the selection of the two groups of accelerograms are listed in the following.

The characteristics of the group of accelerograms referred to data of previous earthquakes in Bologna are showed in Table 5.1:

Table 5.1: Parameters defined the group of accelerograms in Bologna, Italy.

BOLOGNA (Italy)		
n° Accelerograms	48	
$a_g$ (g)	0.166	
Moment magnitude	$5 < M_w < 6.5$	
Period of compatibility (s)	$0.1 < T < 1.0$	
Epicentral Joyner-Boore distance (km)	$0 < D_{JB} < 30$	
$v_{s,30}$ (m/s)	$200 < v_{s,30} < 700$	
Scaling limit	MAX	4
	MIN	0.25

All the selected accelerograms of Bologna and the information related to the registrations are reported in Appendix A.

Figure 5.4 shows the scaling factors used to scale the accelerograms, in order to make them compatible with the code spectrum of Bologna.

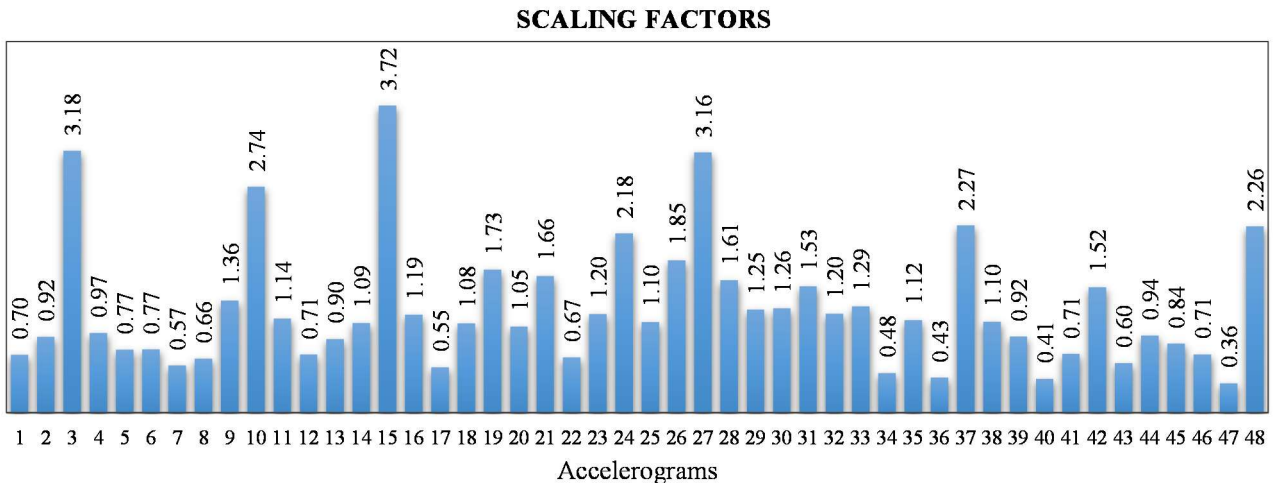


Figure 5.4: Scaling factors used to scale the accelerograms of Bologna.

Starting from the accelerograms the correspondent spectra were obtained: Figure 5.5(a) shows the group of 48 acceleration scaled spectra and Figure 5.5(b) shows the group of 48 displacement scaled spectra, obtained dividing the spectral accelerations for the frequency squared ( $\omega^2$ ). In the figures the acceleration and displacement spectra defined by the Italian Code (NTC, 2018) are also reported.

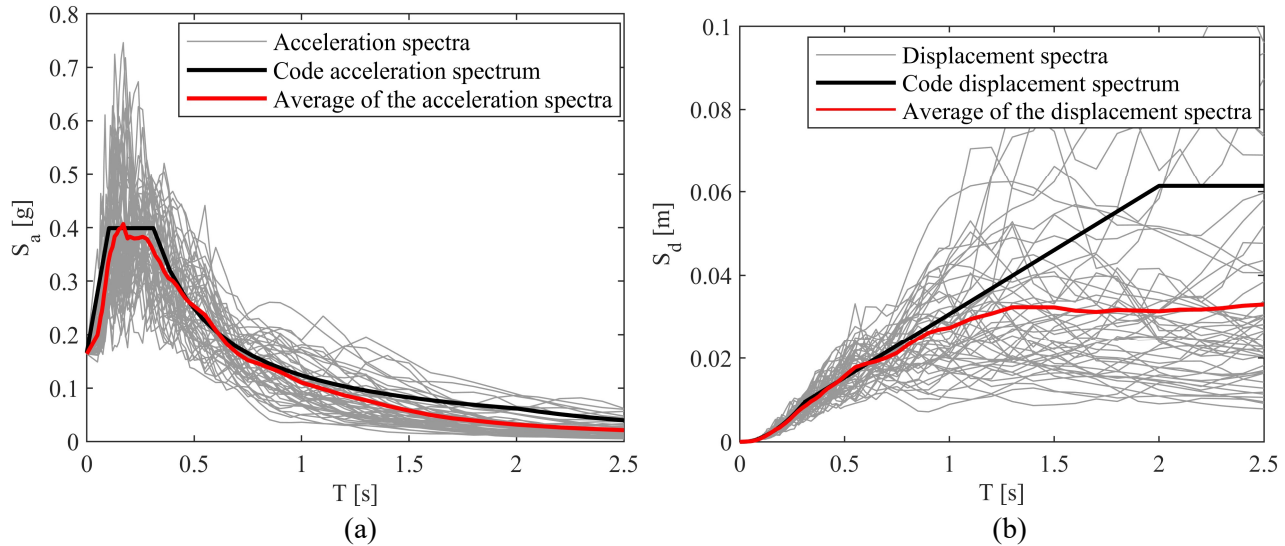


Figure 5.5: (a) Group of 48 acceleration spectra and (b) displacement spectra for the site of Bologna.

The characteristics of the group of accelerograms referred to data of previous earthquakes in Seixal are showed in Table 5.2, obtained according to the seismic hazard maps of Lisbon Metropolitan area (Carvalho et al., 2008; Laboratório Nacional de Engenharia Civil, 2012) and to the most recent geological maps of the area (<https://www.lneg.pt>).

Table 5.2: Parameters defined the group of accelerograms in Seixal, Portugal.

SEIXAL (Portugal)		
n° Accelerograms	50	
$a_g$ (g)	0.22	
Moment magnitude	$6.5 < M_w < 7$	
Period of compatibility (s)	$0.1 < T < 1.0$	
Epicentral Joyner-Boore distance (km)	$0 < D_{JB} < 60$	
$v_{s,30}$ (m/s)	$350 < v_{s,30} < 750$	
Scaling limit	MAX	1.5
	MIN	0.5

All the selected accelerograms of Seixal and the information related to the registrations are reported in Appendix A.

Figure 5.6 shows the scaling factors used to scale the accelerograms, in order to make them compatible with the code spectrum of Seixal.

## SCALING FACTORS

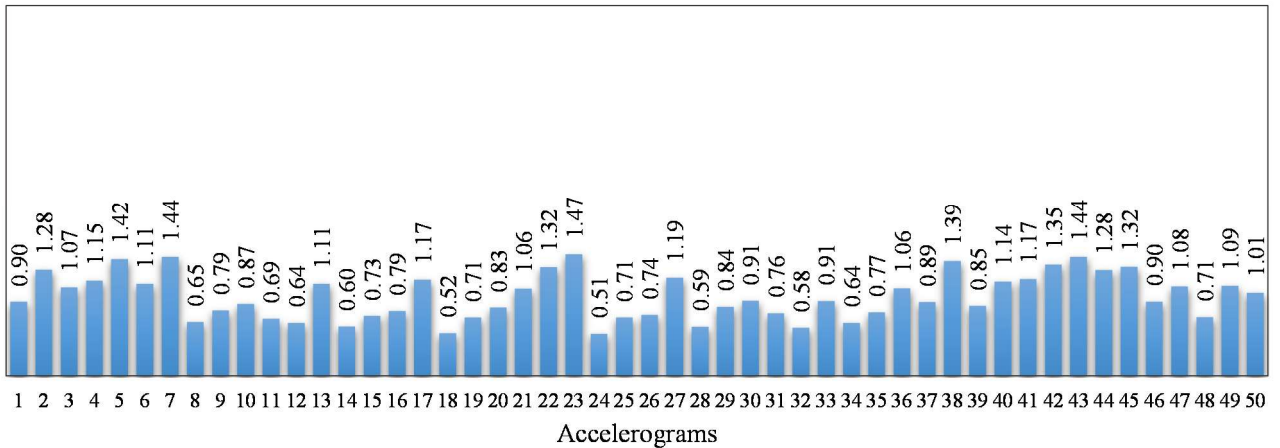


Figure 5.6: Scaling factors used to scale the accelerograms of Seixal.

Starting from the accelerograms the correspondent spectra were obtained: Figure 5.7(a) shows the groups of 50 acceleration scaled spectra and Figure 5.7(b) shows the groups of 50 displacement scaled spectra, obtained dividing the spectral accelerations for the frequency squared ( $\omega^2$ ). In the figures the acceleration and displacement spectra defined by the Portuguese National Annex of Eurocode 8 (Eurocódigo 8, 2009) are also reported. According to this code two scenarios can be considered for the definition of the seismic action: (1) a scenario labelled “seismic action 1”, characterizing earthquakes with their epicentres mainly offshore (moderate magnitude earthquake at close distance) and (2) a scenario labelled “seismic action 2”, referring to events with their epicentres mainly inland (greater magnitude earthquake at longer distance) (Campos Costa et al, 2008). Since the scenario 2 is the most representative of the earthquakes occurred in Seixal, in this work the spectra generated using the “seismic action 2” are used.

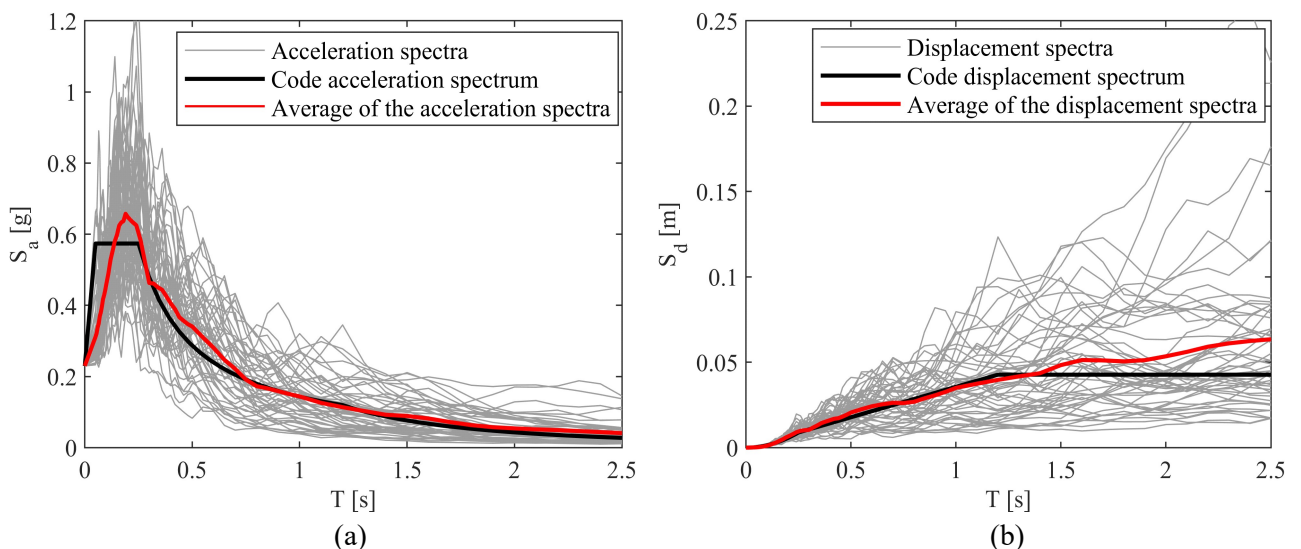


Figure 5.7: (a) Group of 50 acceleration spectra and (b) displacement spectra for the site of Seixal.

## 5.5 Evaluation of the peak ground acceleration corresponding to the structural failure

In this work, the structural failure (structural capacity) of the structures is defined in terms of peak ground acceleration corresponding to the attainment of the LS limit state ( $PGA_C$ ). The procedure adopted to obtain the  $PGA_C$  for each studied model is explained in the following.

The defined spectra allow the determination of the seismic action to apply on the structures and to find the seismic demand, in terms of displacement. For each push-over curve obtained, the last point corresponds to the ultimate displacement ( $d_u$ ) representing the structural capacity, i.e. the attainment of the LS limit state. The displacement capacity ( $d_u$ ) has to be compared with the displacement demand ( $d_{max}$ ), to be found using the spectra.

As already explained in the Section 4.7, the spectra are defined starting from a SDOF system. Thus, each of the models (MDOF systems) has to be transformed in a SDOF system, from which each equivalent period ( $T^*$ ) is obtained, using Equation 4.15.

Starting from the displacement spectra, the spectral displacements  $S_d(T^*)$  were found, according to the values of the equivalent periods ( $T^*$ ). Figure 5.8(a) shows, as an example, the adopted procedure to obtain three spectral displacements in a structure with equivalent period  $T^* = 0.45s$  and considering three different displacement spectra (i.e. three different seismic actions). The green and blue circles are related to two values of the spectral displacement demands less than the value of the spectral displacement capacity (black square), whereas the red circle indicates a value of the displacement demand greater than the value of the spectral displacement capacity.

Each spectral displacement demand obtained allows to find the correspondent displacement demand ( $d_{max}$ ), through the two relations 4.17 and 4.18 and according to the values of each equivalent period ( $T^*$ ) with respect to the defined value  $T_C$  of the code spectrum.

In order to find the  $PGA_C$ , the ratio  $d_u / d_{max}$  is used to scale the displacement and acceleration spectra (Figure 5.8(a) and Figure 5.9(a)), setting  $d_u = d_{max}$ . Figures 5.8(b) and Figure 5.9(b) show the displacement and acceleration spectra respectively, scaled of the ratio  $d_u / d_{max}$ .

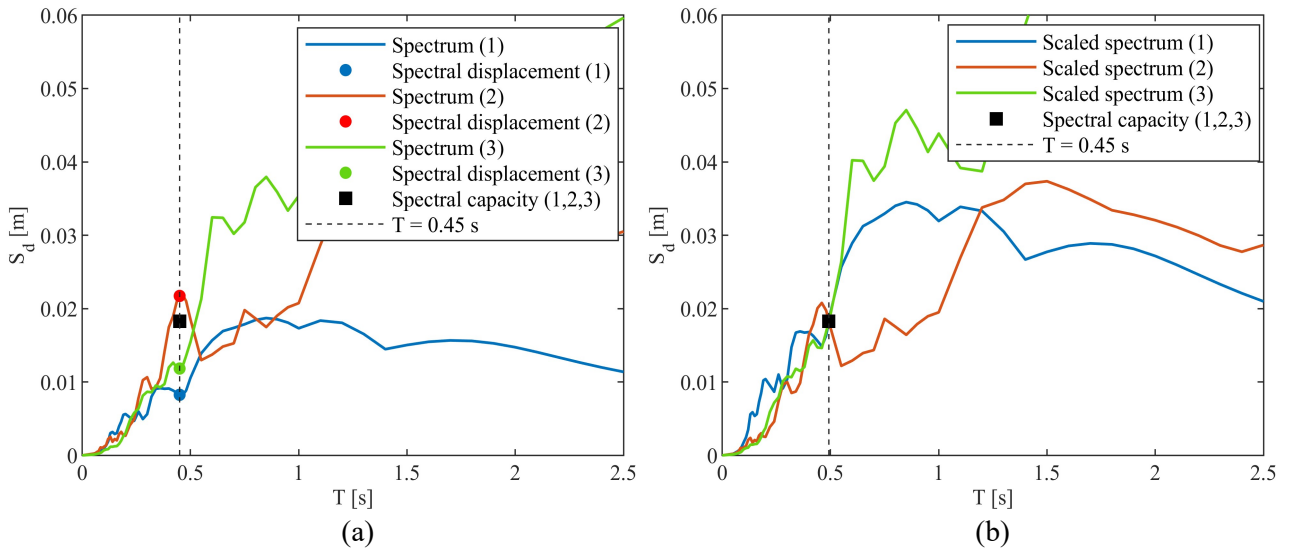


Figure 5.8: Example of three (a) displacement spectra and (b) displacement scaled spectra.

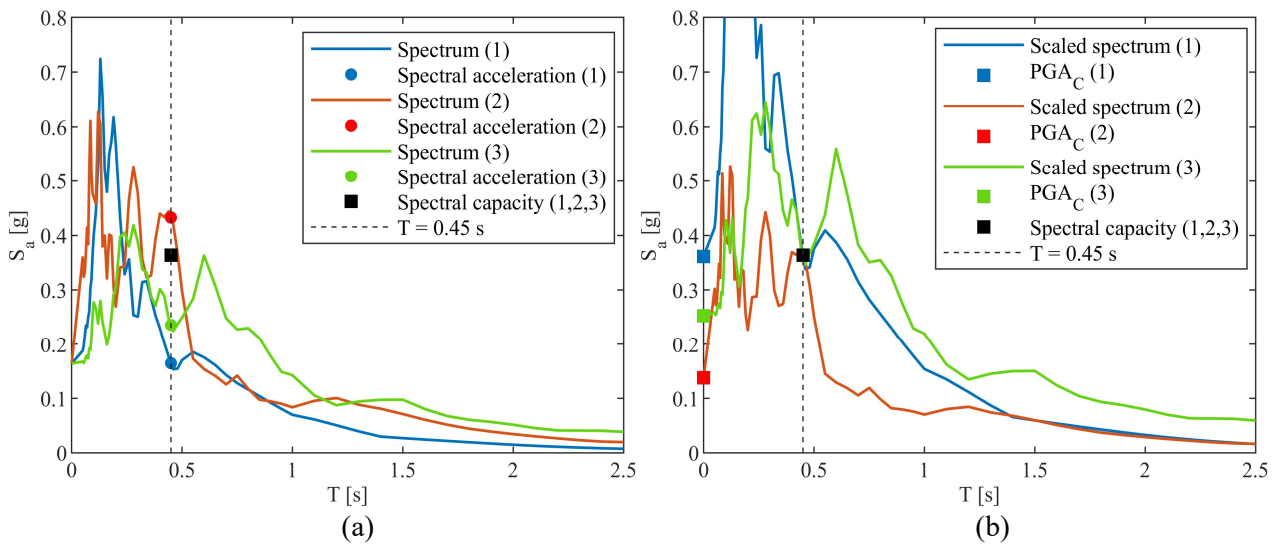


Figure 5.9: Example of three (a) acceleration spectra and (b) acceleration scaled spectra.

In these specific cases, since the values of the spectral demands (1) and (3) are less than the value of spectral capacity, the spectra (1) and (3) are scaled of a factor ( $d_u/d_{max}$ ) greater than 1; on the contrary, the spectrum (2) is scaled of a factor less than 1.

Finally, the sought values of the collapse PGA ( $PGA_C$ ) are those represented by the squares in the axis of the ordinates in Figure 5.9(b): they can be obtained multiplying the value of the peak ground acceleration ( $a_g$ ) of the site for the ratio  $d_u/d_{max}$ :

$$PGA_C = a_g \frac{d_u}{d_{max}} \quad (5.1)$$

## 5.6 Definition of the seismic fragility

Once the structural capacities ( $PGA_C$ ) for each model are defined, it is possible to determine the seismic fragility, obtaining the probability of failure ( $P_f$ ) for fixed values of the seismic acceleration demand ( $PGA_D$ ). This relation is figured through the plotting of the fragility curves.

As already explained in Section 2.3, the fragility is found using the limit state function (Equation 2.5): considering the LS limit state, the structural failure is attained when the difference between the structural capacity ( $PGA_C$ ) and the structural demand ( $PGA_D$ ) is less than or equal to zero.

In general, having a distribution of the  $PGA_C$  and fixing some values of  $PGA_D$ , the summation of the cases where the quantity ( $PGA_C - PGA_D$ ) is less than or equal to zero represents the number of the failures. Thus, the probability of failure ( $P_f$ ) is defined as the ratio between the number of the failures and the total number of the structural capacities ( $PGA_C$ ).

In this thesis, each structural analysis leads to the determination of a  $PGA_C$ , following the procedure explained in Section 5.5. The distribution of the obtained  $PGA_C$ , for each different type of analysis, allows the plotting of fragility curves with a non-regular shape, because they were obtained considering the actual obtained values from the analyses. Figure 5.10 shows an example of non-regular shape of fragility curves.

These non-regular curves were compared with those obtained using Monte Carlo simulations, leading to a more regular shape of the curves, because the number of the values of the generated  $PGA_C$  is higher.

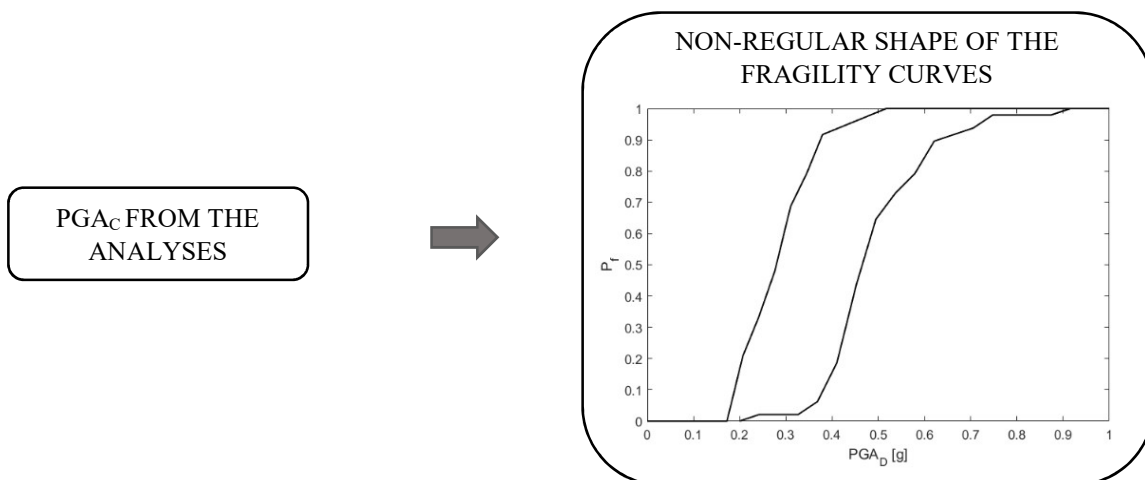


Figure 5.10: Example of non-regular shape of the fragility curves.

As regard the case studies in Bologna, the collapse  $PGA_C$  were obtained by means of the Response Surface simulations. Thus, to plot the fragility curves to compare with the non-regular ones, Monte Carlo was used to obtain a set ( $n$ , usually greater than  $10^3$ ) of values from the normal distributions defined for the variables (both explicit and implicit). However, to avoid the prediction of negative values of the structural capacity, the log-normal distributions were obtained from the defined normal distributions of the variables and the natural logarithm of the  $PGA_C$  ( $\log(PGA_C)$ ) is used as response parameter. Hence, starting from the  $n$  obtained values of each variable from the log-normal distributions, a distribution of  $n$   $PGA_C$ , found with the polynomial function of the RS model with the obtained regression parameters, was used to plot the fragility curves, having a regular shape. As an example, the procedure to plot the fragility curves, using Monte Carlo simulations for the case studies in Bologna, is shown in Figure 5.11.

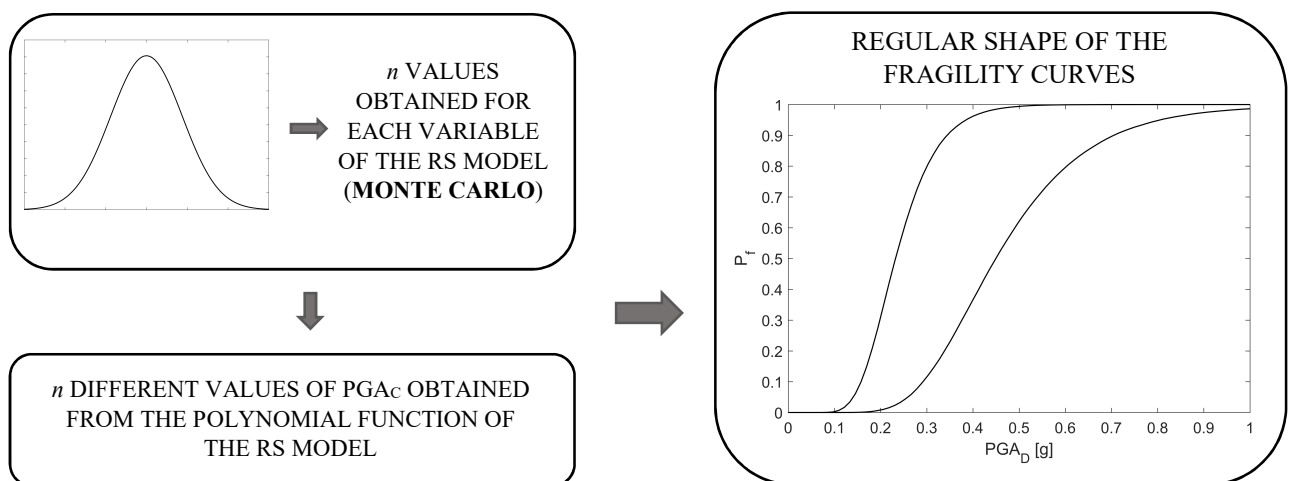


Figure 5.11: Procedure to plot the fragility curves, using Monte Carlo simulations for the case studies in Bologna.

As regard the case studies in Seixal, to each distribution of the  $PGA_C$  obtained from the analyses, a log-normal distribution was associated according to the medium value and the standard deviation of the distributions.  $n$  different values of the  $PGA_C$  were obtained using Monte Carlo, to plot the more regular fragility curves to be compared with the ones obtained using the actual values of the  $PGA_C$  from the analyses. As an example, the procedure to plot the fragility curves, using Monte Carlo simulations for the case studies in Seixal, is shown in Figure 5.12.

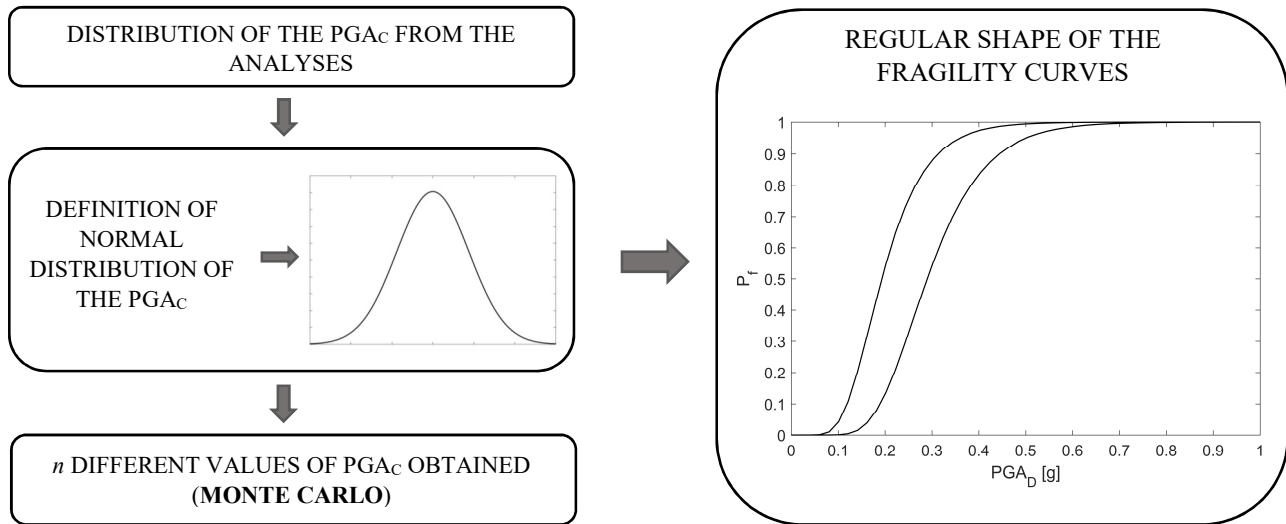


Figure 5.12: Procedure to plot the fragility curves, using Monte Carlo simulations for the case studies in Seixal.

## **6. SEISMIC FRAGILITY OF CLAY BRICK MASONRY STRUCTURES: CASE STUDIES IN BOLOGNA, ITALY**

---

## 6.1 Introduction

In this Chapter the seismic fragility analysis of clay brick masonry structures sited in Bologna is studied. Section 6.2 is focused on the analysis of the selected masonry structure, considered as isolated structural unit (ISU), as first step. In order to take into account some geometrical and structural variabilities involved in the problem, the Response Surface (RS) statistical method is used, allowing to determine which are the parameters most influencing the seismic response. In Section 6.3 the same structure was analysed, considering a simplified model of the RS, as the purpose is to compare the seismic fragility of the building considered as isolated structural unit and the one of the same building, belonging to an aggregation of identical structural units in row. Finally, in order to consider some differences between the structural units aggregated in row, Section 6.4 is focused on the seismic fragility analysis of aggregations in row of structural units with geometrical differences each other, to show how the variability of some parameters between the structural units along the aggregate affects the seismic response. Afterwards, the seismic fragility of the aggregate structures with different structural units is compared with those referred to the isolated structural units and to the previous aggregate structures with identical structural units.

The structures object of the study, the criteria to select the explicit and implicit variables, the numerical models used to perform the non-linear static analyses, the RS models and the fragility curves obtained are described in the following.

## 6.2 The isolated structural units

### 6.2.1 The structure

The structure is selected as representative of a class of buildings existing in Bologna, in Italy. It is not referred to a real case, but it was selected according to some common geometrical and structural properties belonging to existing masonry buildings in Bologna. Figure 6.1(a) shows the architectural ground floor plan and Figure 6.1(b) two perpendicular sections, referred to the prototype structure, whose geometrical and structural properties are fixed to the main values in the ranges of the chosen variables. It is a three-storeis masonry building (plus the roof storey) and it has a rectangular non-regular shape plan. All the dimensions in Figure 6.1 are reported in meters (m).

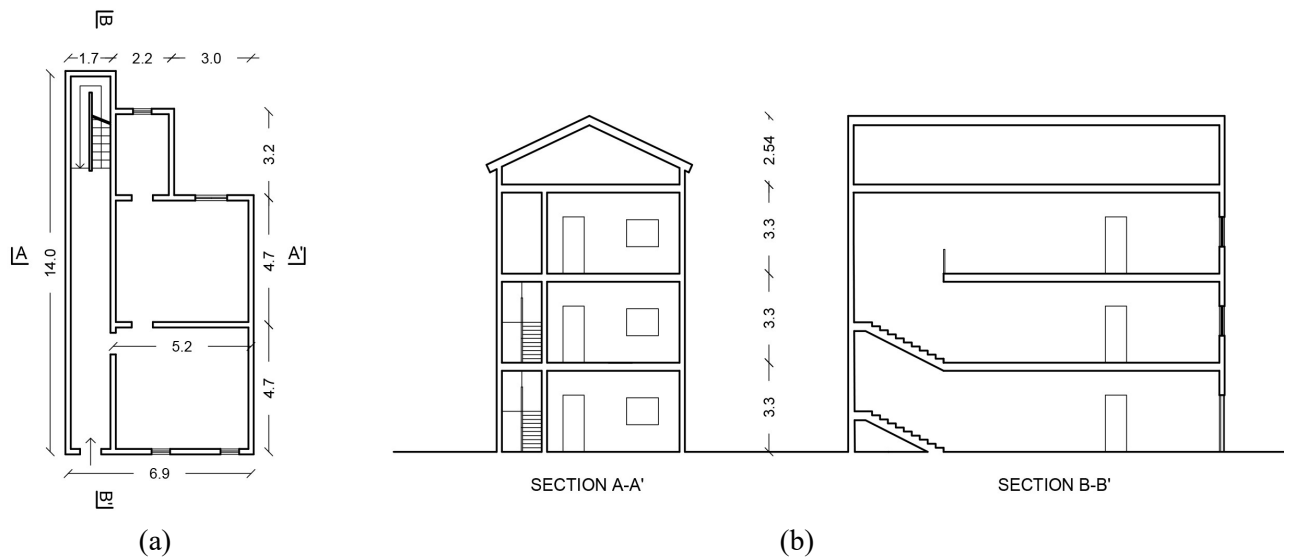


Figure 6.1: (a) Architectural ground floor plan and (b) sections of the prototype building.

The building was modelled using 3Muri software. The external and internal walls are defined with the same properties: masonry clay brick walls, characterized by a thickness equal to 0.25 m. The horizontal elements are selected as hollow-core concrete slabs, modelled considering reinforced concrete joists, alternated with perforated bricks and a continuous layer of concrete above and characterised by an equivalent thickness equal to 0.05 m, defined in the software. The load direction of the slabs is highlighted in Figure 6.2(a): they load the walls according that direction at 100%. Whereas, the pitched roof is made by timber beams with cross section 0.10 m x 0.10 m and spanned in 0.50 m, a timber plank above and it is covered by roof brick tiles. Figure 6.2(a) shows the plan of the structural ground floor and Figure 6.2(b) a tri-dimensional view of the single structural unit.

The structural properties of the masonry walls are chosen according to *Table C8A.2.1* of the Italian Code (NTC, 2008): Table 6.1 gives the values of the compressive strength ( $f_m$ ), the shear strength ( $\tau$ ), the elastic ( $E$ ) and shear ( $G$ ) modulus and the self-weight ( $w$ ) of the masonry walls. The value of the strengths reported in the Table 6.1 are already divided by the confidence factor (Section 4.3), set equal to 1.2 in this case. Table 6.2 gives the values of the main elastic modulus ( $E_1$ ), the secondary elastic modulus ( $E_2$ ) and the shear modulus ( $G_s$ ) of the diaphragms, chosen according to the common existing slabs and roofs in Bologna.

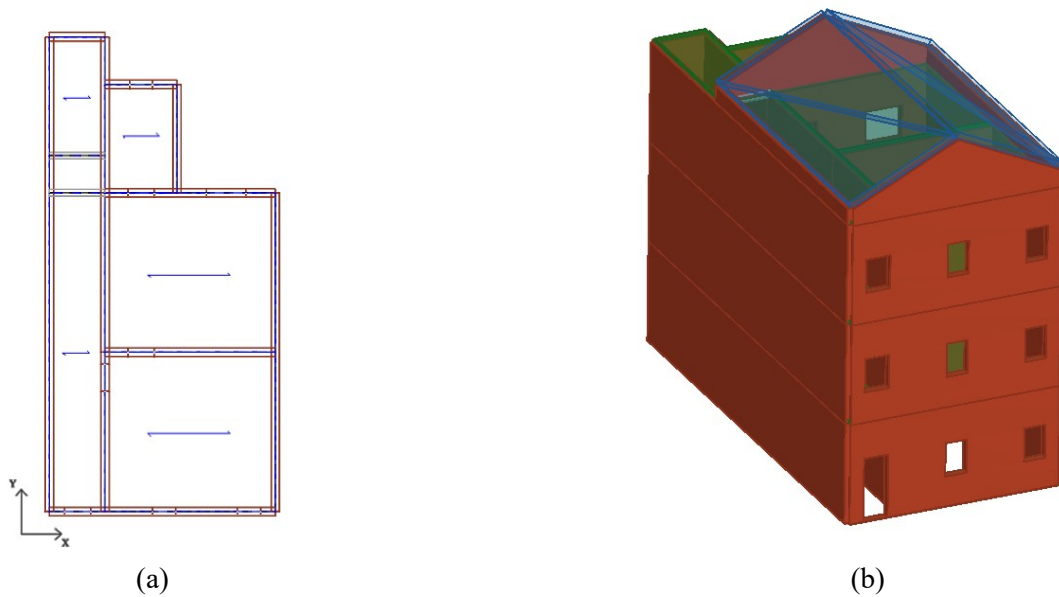


Figure 6.2: (a) Plan of the structural ground floor and (b) tri-dimensional view of the isolated structural unit.

Table 6.1: Structural properties of the masonry walls.

MASONRY WALLS	$f_m$ (MPa)	$\tau$ (MPa)	$E$ (GPa)	$G$ (GPa)	$w$ (kN/m <sup>3</sup> )
Clay brick walls	2.66	0.063	1.50	0.50	18.00

Table 6.2: Structural properties of the diaphragms.

DIAPHRAGMS	$E_1$ (GPa)	$E_2$ (GPa)	$G_s$ (GPa)
Hollow-core concrete slab	31.50	15.75	13.125
Pitched timber roof	7.00	3.50	0.035

## 6.2.2 Selection of the variables

As already mentioned, this first part of the work was carried out by means of the Response Surface (RS) statistical method, detailed in Section 3.3, in order to take account some variabilities and uncertainties and to highlight which are the parameters most influencing the seismic behaviour. According to the RS method, the selected variables are divided in explicit and implicit. The former are accounted for explicitly as random variables in the RS model, allowing to define for each one a regression coefficient ( $\beta$ ) expressing the relation with the response parameter; the latter are considered implicitly and their effect is assumed in additive form in the polynomial function of the RS model.

- *Explicit variables*

According to the RS model, an explicit variable is defined starting from a selected normal distribution. As a first step, the choices of one explicit variable related to the structural properties of the walls, one to the structural properties of the slabs and one to the geometrical properties of the walls, were assumed. Thus, the three explicit variables chosen are: the mean masonry shear strength ( $\tau$ ), the mean slab elastic modulus ( $E_1$ ), the mean distance between external walls in  $x$ -direction ( $d$ ) (in Figure 6.1(a) the mean value of “ $d$ ” is equal to 6.90 m). Their normal distributions are given in Figure 6.3. Table 6.3 gives the parameters defining the normal distributions for each variable, i.e. the mean value ( $\mu$ ), the coefficient of variation (COV) and the standard deviation ( $\sigma$ ).

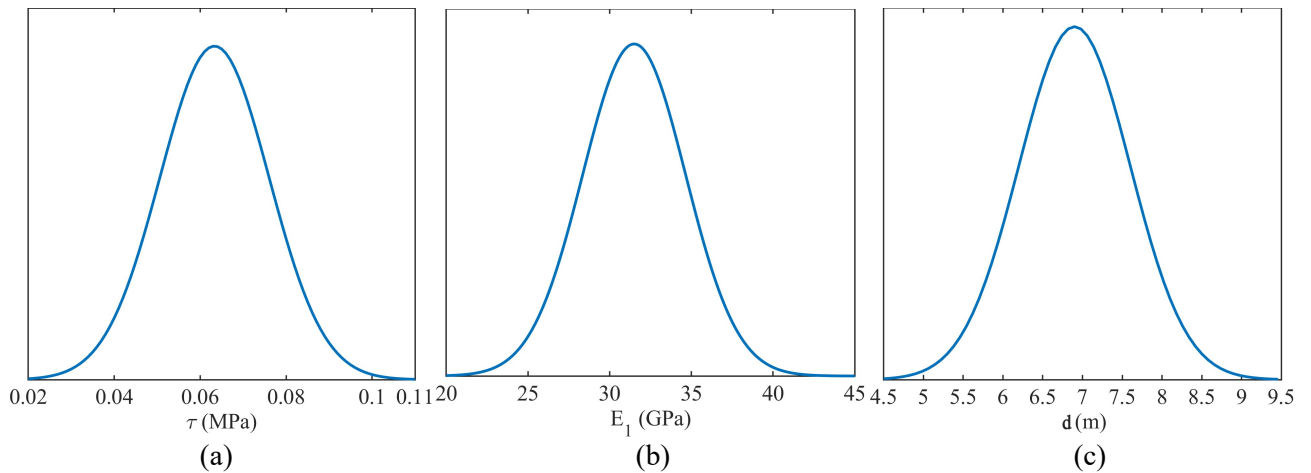


Figure 6.3: Normal distributions adopted for the (a) variable  $\tau$ , (b) variable  $E_1$  and (c) variable  $d$ .

Table 6.3: Definition of the normal distributions adopted for the explicit variables.

Variable ( $X_i$ )	Distribution	$\mu$	COV	$\sigma$
$\tau$	N	0.063 (MPa)	0.2	0.012
$E_1$	N	31.50 (GPa)	0.1	3.150
$d$	N	6.90 (m)	0.1	0.690

The variation of the distance ( $d$ ) is carried out maintaining the same ratio between the internal distances in  $x$ -direction. The other structural masonry properties (masonry compressive strength ( $f_m$ ), masonry elastic ( $E$ ) and shear ( $G$ ) modulus) are direct function of  $\tau$  according to the values reported in *Table C8A.2.1* of the Italian Code. Thus, it is possible to find a relation between  $\tau$  (variable in this work) and the other three masonry properties, in such a way to make their variability direct function of  $\tau$ . As for the slab properties,  $E_2$  (secondary

slab elastic modulus) and  $G_s$  (slab shear modulus) are direct function of  $E_1$ . The adopted relations between the variables are shown in Table 6.4 and Table 6.5.

Table 6.4: Relations between masonry properties and masonry shear strength ( $\tau$ ).

Masonry Property	Relation with $\tau$
Compressive Strength ( $f_m$ )	$f_m = 50 \tau - 0.5$
Elastic Modulus (E)	$E = 11250 \tau + 37.5$
Shear Modulus (G)	$G = 3750 \tau + 12.5$

Table 6.5: Relations between slab properties and slab elastic modulus ( $E_1$ ).

Slab property	Relation with $E_1$
Secondary Elastic Modulus ( $E_2$ )	$E_2 = 0.5 E_1$
Shear Modulus ( $G_s$ )	$G = 0.4166 E_1$

As mentioned before, the variable values are selected following the Design of Experiment Theory (Section 3.3.3) to calibrate the RS model. Therefore, using Equation 3.32 and according to the Central Composite Design the simulations are defined as following:

- $2^3$  simulations, considering all the combinations of the three explicit coded variables ( $X_i = \mu \pm 1.5\sigma \rightarrow x_i = \pm 1$ );
- 2 axial points for each variables ( $X_i = \mu \pm 2\sigma \rightarrow x_i = \pm 1.33$ );
- 3 central points ( $X_i = \mu \rightarrow x_i = 0$ ).

Thus, the total number of a group of simulations is 17; it is repeated several times, according to the definition of the blocks for the implicit variables.

Tables 6.6 shows the values assumed by the variables ( $X_i$ ) in the defined normal distributions according to the Design of Experiment rules.

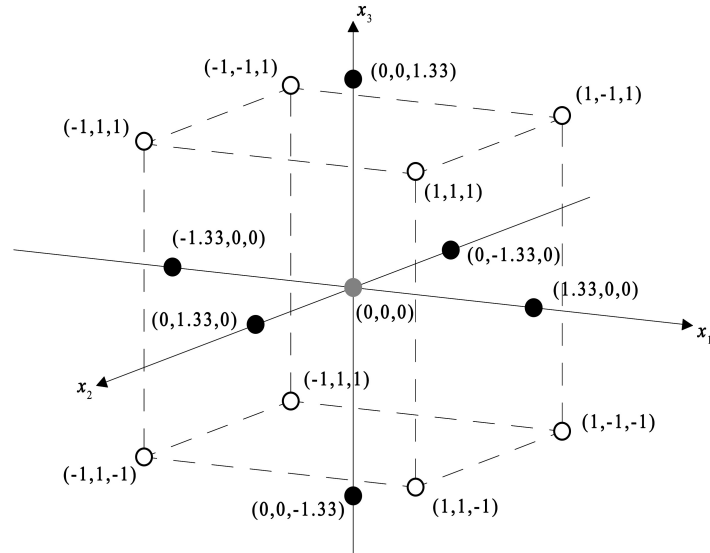
Table 6.6: Values assumed by the variable  $X_i$  in the defined normal distributions.

$X_i$	$\tau$ (MPa)	$E_1$ (GPa)	$d$ (m)
$2\sigma$	0.088	37.80	8.30
$1,5\sigma$	0.082	36.22	7.95
$\mu$	0.063	31.50	6.90
$-1,5\sigma$	0.044	26.77	5.85
$-2\sigma$	0.038	25.20	5.50

Table 6.7 gives the definition of the group of 17 simulations, setting the coded variables as  $x_1 = \tau$ ,  $x_2 = E_1$ ,  $x_3 = d$  and Figure 6.4 shows the cuboidal region of interest for the three selected coded variables.

Table 6.7: Definition of the group of 17 simulations using the coded variables  $x_i$ .

$x_1$	1	-1	-1	1	1	-1	1	-1	1.33	-1.33	0	0	0	0	0	0
$x_2$	1	-1	1	-1	1	-1	-1	1	0	0	1.33	-1.33	0	0	0	0
$x_3$	1	1	1	1	-1	-1	-1	-1	0	0	0	0	1.33	-1.33	0	0

Figure 6.4: Cuboidal region of interest for the 3 coded variables  $x_i$ .

In this thesis, it was decided to neglect the contribute of some variabilities related to the parameters of the analyses, such as the drift for piers and spandrels, as only the geometrical and mechanical properties of the masonry are varied in prescribed ranges. Despite recent statistical elaborations of experimental data (Morandi et al. 2019; Vanin et al. 2017) show how the dispersion related to the drifts is significant, the maximum drifts in case of shear and flexural failure are fixed according to the Equation 4.7.

#### - *Implicit variables*

The choice of the implicit random variables is very important because it influences the partition in blocks. They are selected as normally distributed variables with zero mean. In this work, two implicit variables were chosen: the uncertainty of the seismic action ( $\delta_{\text{sis}}$ ) and the uncertainty of some geometrical properties of the walls ( $\delta_{\text{geom}}$ ).

As far as  $\delta_{\text{sis}}$  is concerned, the group of 48 accelerograms defined in Section 5.4 was used in order to consider the variability of the seismic action. For each of the 17 simulations, according to the Design of Experiment Theory, 2 accelerograms were associated to the factorial region and 1 accelerogram was associated to the axial and central points. Thus, each

group of 17 simulations is related to 3 blocks  $\delta_{\text{sis}}$  and it is repeated 16 times (the total number of blocks is 48).

As for  $\delta_{\text{geom}}$ , two different uncertainties of geometrical properties were chosen: the variability of the thickness of all the walls ( $s$ ) and the variability of the position of the central wall in  $x$ -direction ( $\mu_d$ ), with respect to the position of the parallels external walls. Both  $s$  and  $\mu_d$  vary together in the same block. 8 blocks were chosen for  $\delta_{\text{geom}}$ : each block is associated to 34 simulations (2 groups of 17 simulations).

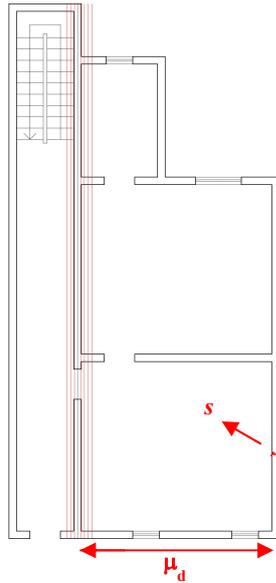


Figure 6.5: Definition of the implicit variable  $\delta_{\text{sis}}$ , by means of  $\mu_d$  and  $s$ .

The values assumed for  $s$  and  $\mu_d$  change together, in such a way to have greater distances  $\mu_d$  with greater thicknesses  $s$ . Figure 6.5 shows the indication of the thickness of the walls  $s$ , assuming the 8 values reported in Table 6.8, and the variation of  $\mu_d$ , obtained moving the internal wall about 1.5% (on the right and on the left) of the medium distance  $\mu_d$  (red lines in Figure 6.5). The values of  $s$  in Table 6.8 were chosen according to realistic cases of clay brick wall thickness existing in the Italian historic centres; each value corresponds to a different block of the RS simulation.

Table 6.8: Values assumed by the thickness of the walls  $s$  and correspondent blocks.

$s$	0.125 m	0.15 m	0.20 m	0.25 m	0.30 m	0.375 m	0.40 m	0.50 m
<b>BLOCK</b>	8	7	6	5	4	3	2	1

Summarizing, the division in blocks for the implicit variables is obtained as following:

- 48 blocks of  $\delta_{\text{sis}}$ , divided in 16 groups of 3 blocks for a set of 17 simulations;
- 8 blocks of  $\delta_{\text{geom}}$ , divided in 8 groups of 1 block for a set of 34 (17x2) simulations.

The partition in blocks, associated to the groups of explicit variables, generates 272 simulations in total. Table B.1 in Appendix B gives the design matrix containing the 272 simulations with the combinations of the explicit and implicit variables, according to the Design of Experiment Theory and the division in blocks.

### 6.2.3 Push-over analyses

Once the simulations are defined, the data required to calibrate the Response Surface models were obtained by means of non-linear static analyses (push-over), performed using TreMuri software, following the procedure in Section 5.3.

Two orthogonal directions ( $x$  and  $y$ ) of the seismic action are considered (Figure 5.3) and the distribution of the forces applied (proportional to the masses) was considered with both signs ( $+F$  and  $-F$ ). Each of this case generates 272 capacity curves; the types of performed analyses for the masonry isolated structural units, object of this Section, are defined as follows:

- 272  $x$ -direction analyses with applied forces  $+F_x$ ;
- 272  $x$ -direction analyses with applied forces  $-F_x$ ;
- 272  $y$ -direction analyses with applied forces  $+F_y$ ;
- 272  $y$ -direction analyses with applied forces  $-F_y$ .

The results related to the two different directions are shown in the following.

-  $x$ -direction

Figures 6.6(a) and 6.6(b) show the capacity curves obtained from the analyses considering the  $x$ -direction with positive forces ( $+F_x$ ) and negative forces ( $-F_x$ ) respectively.

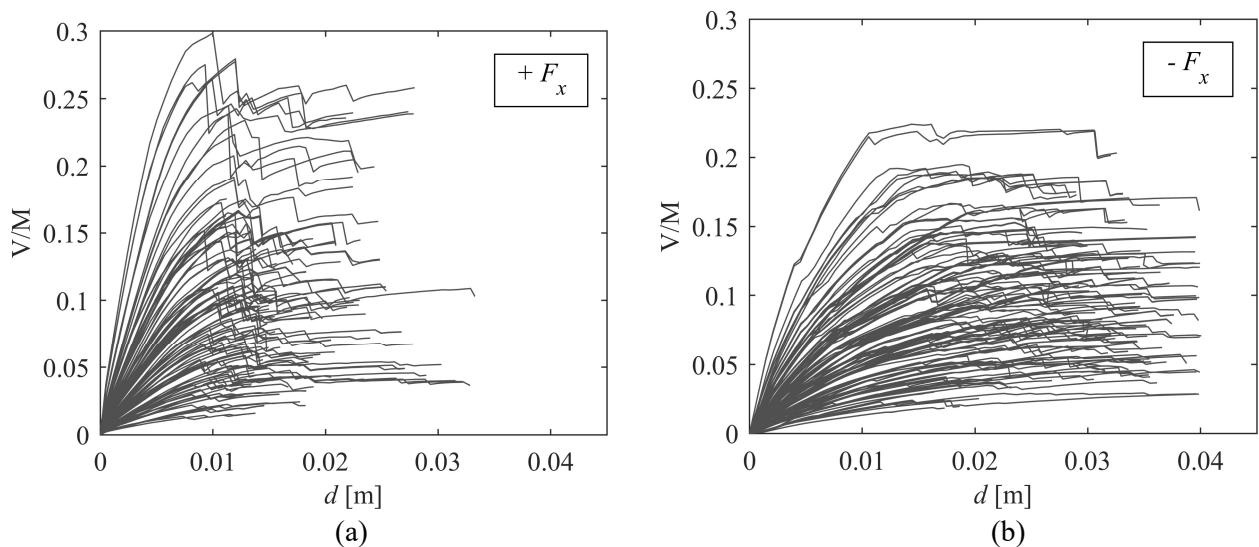


Figure 6.6: Capacity curves from the analyses with (a) positive forces ( $+F_x$ ) and (b) negative forces ( $-F_x$ )

These curves highlight different behaviour of the structures when the seismic forces are considered with different sign (+ or -). Even if the curves (+  $F_x$ ) in Figure 6.6(a) show higher capacity with respect to those (-  $F_x$ ) in Figure 6.6(b), the ultimate displacements reached are lower, because of the progressive decrement of the capacity in the case of positive forces (+  $F_x$ ). The loss of capacity is due to the configuration of the resisting masonry walls in  $x$ -direction P1, P3, P6, P8, P10 (Figures 6.7(a) and 6.9(a)). To explain the differences, Figures 6.7(b) and 6.8 and Figures 6.9(b) and 6.10 are referred to the model of the simulations 217, 218, 219, 234, 235, 236 having the shear strength ( $\tau$ ) and the distance ( $d$ ) fixed to the mean values and a thickness of the walls ( $s$ ) equal to 0.15 m. Figures 6.8 and 6.10 show the failure mechanisms referred to the walls in  $x$ -direction, in correspondence of a displacement ( $d$ ) equal to 0.011 m (Figures 6.7(b) and 6.9(b)), highlighting that the main failure mechanism in this direction is the flexural one. Looking at the geometrical configuration of the walls in Figures 6.8 and 6.10, the left-sides are the weaker due to a greater presence of the openings (in particular for the panels P3, P8, P10). Thus, if the forces +  $F_x$  are considered those weaker portions of the walls are the most solicited, causing the progressive decrement of the total capacity of the building. On the contrary, if the forces -  $F_x$  are considered the most solicited portions of the walls are on the right-side, where the reduced presence of openings allows to experience a more gradual loss of capacity with the attainment of higher displacements (Figure 6.9(b)).

The point of the capacity curve indicated in Figure 6.7(b) is related to the collapse of the spandrels E13 and E9 of the panel P3 (Figure 6.9); however, in correspondence of the same displacement reached considering the forces -  $F_x$  (Figure 6.9(b)), most of the piers and spandrels are still in the elastic or plastic phase.

These results highlight how the geometrical configuration of the walls, in particular the presence of the openings, substantially affects the seismic response. In this specific case, the geometrical properties of the walls make the building weaker to the positive seismic action in  $x$ -direction (+  $F_x$ ). Thus, considering this latter case, lower values of the collapse PGA are expected, with respect to the negative seismic action in  $x$ -direction (-  $F_x$ ), i.e. higher seismic fragility.

In general, the showed seismic behaviour of the masonry panels has been found for all the 272 simulations referred to different structural models.

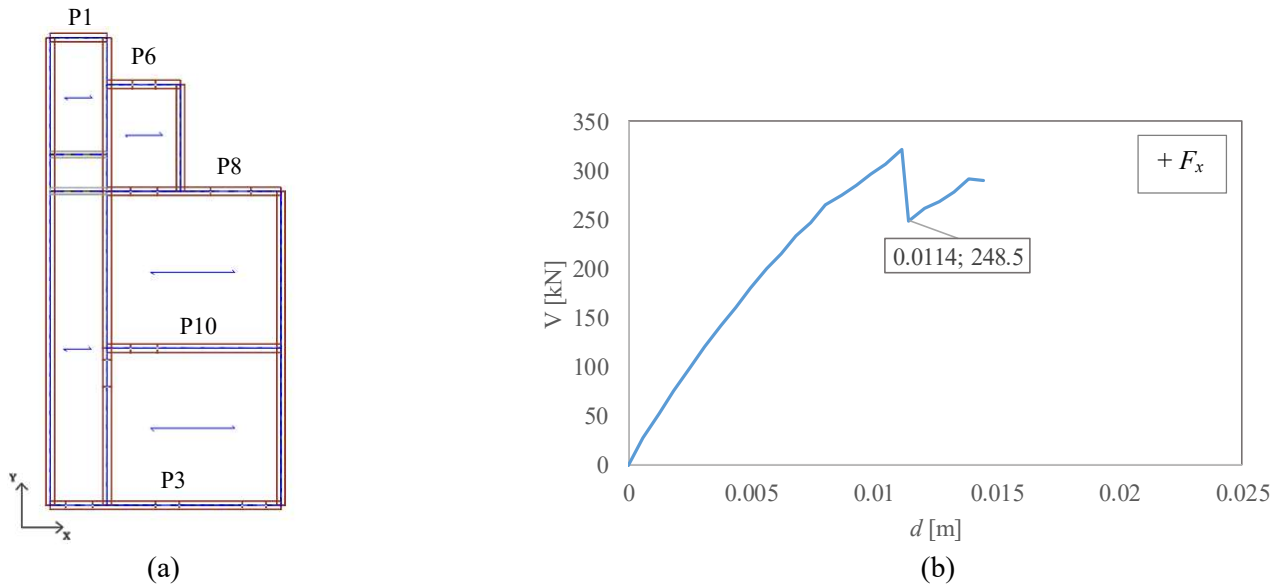


Figure 6.7: (a) Indication of the masonry walls in  $x$ -direction; (b) Point of the capacity curve ( $+F_x$ ) related to the collapse of the spandrels E13 and E9 of the panel P3.

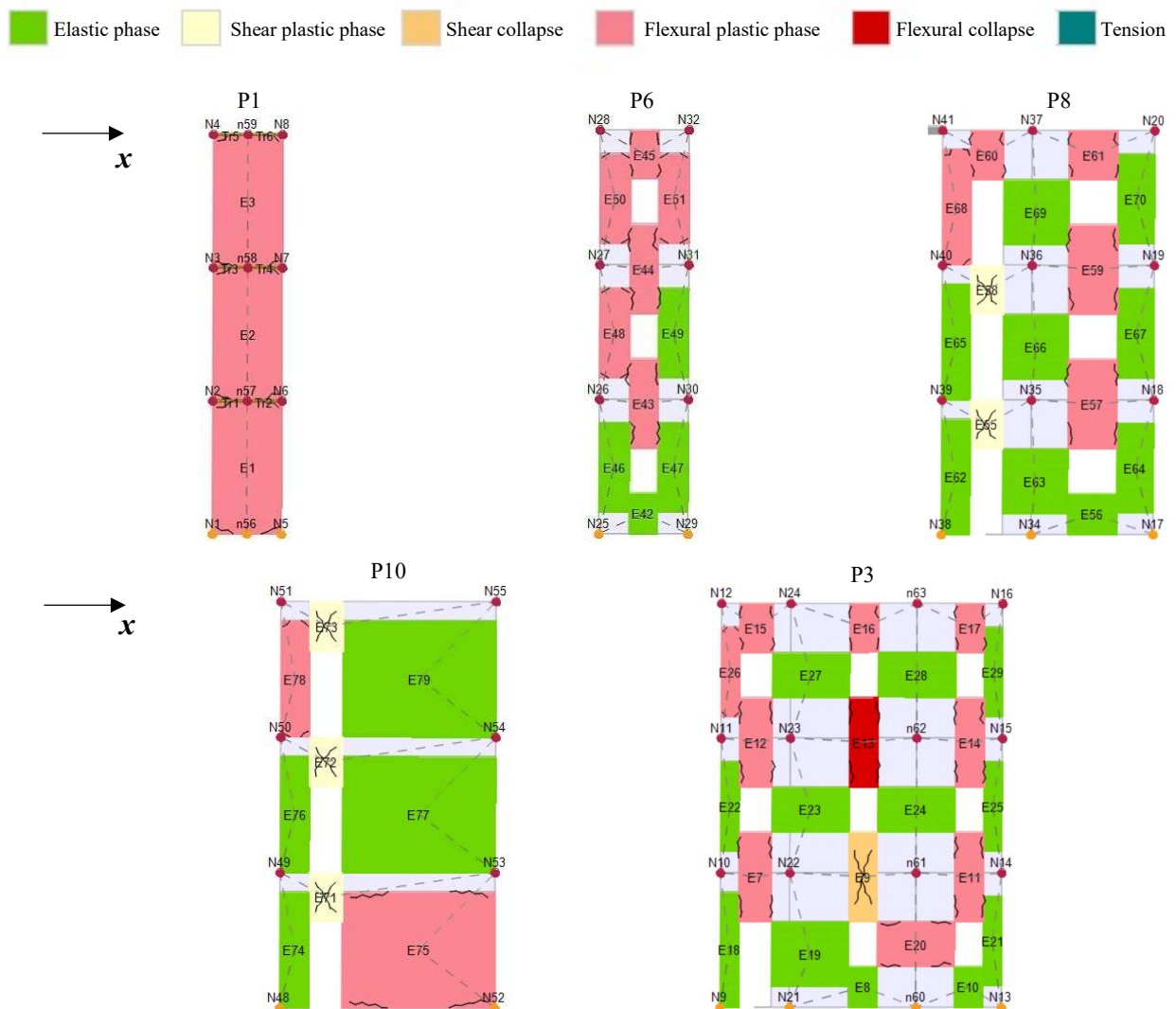


Figure 6.8: Failure mechanisms of the masonry walls considering a seismic action in  $x$ -direction ( $+F_x$ ).

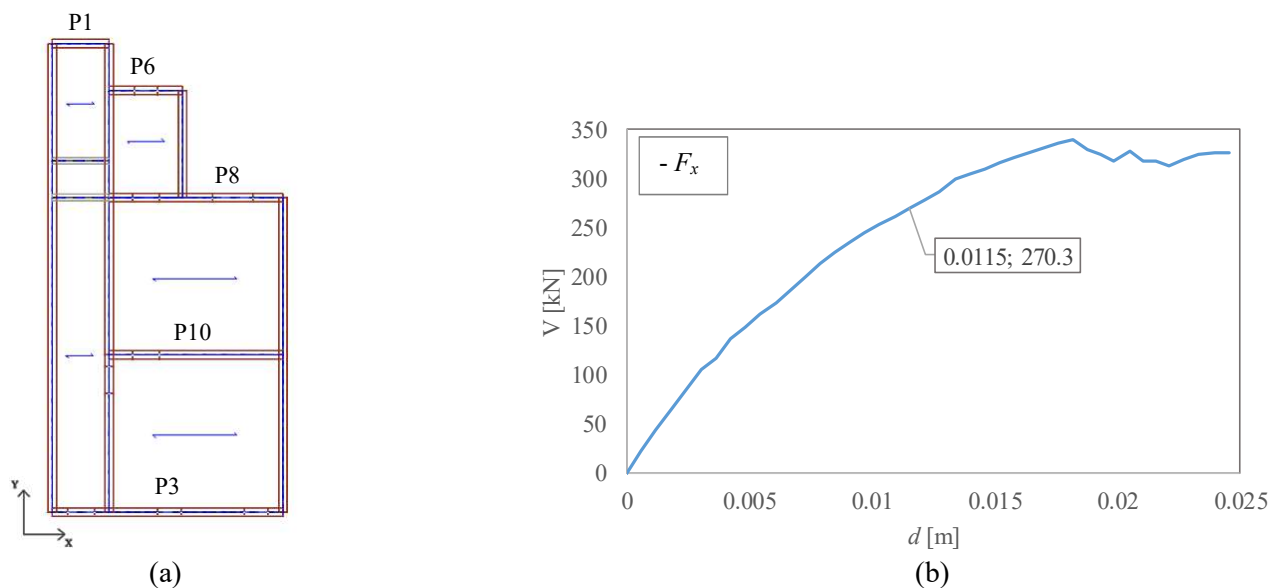


Figure 6.9: (a) Indication of the masonry walls in  $x$ -direction; (b) Point of the capacity curve ( $-F_x$ ) in correspondence of the point in Figure 6.7(b).

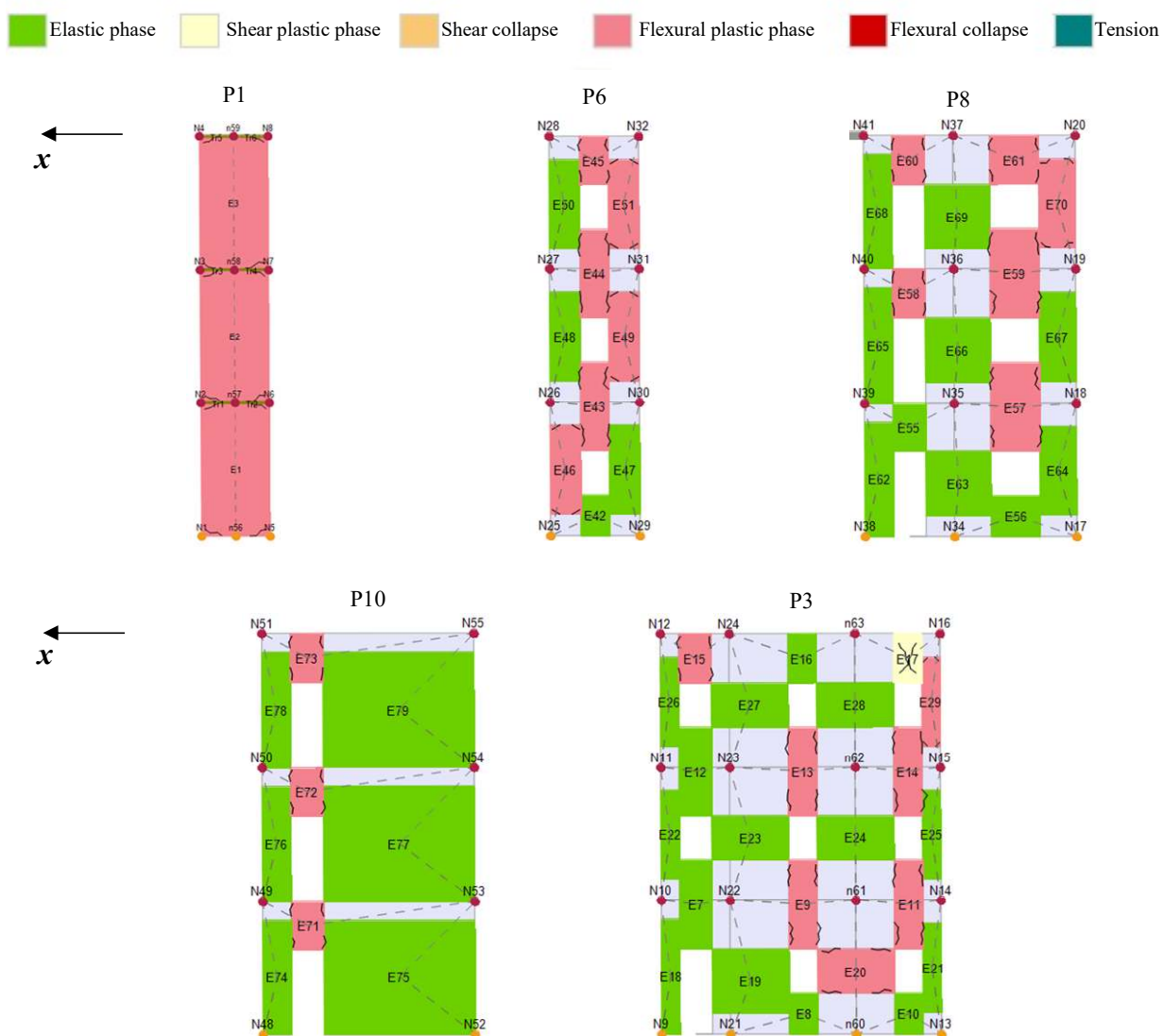


Figure 6.10: Failure mechanisms of the masonry walls considering a seismic action in  $x$ -direction ( $-F_x$ ).

*y-direction*

Figures 6.11(a) and (b) show the capacity curves obtained from the analyses considering the *y*-direction of the seismic action with positive ( $+F_y$ ) and negative forces ( $-F_y$ ) respectively.

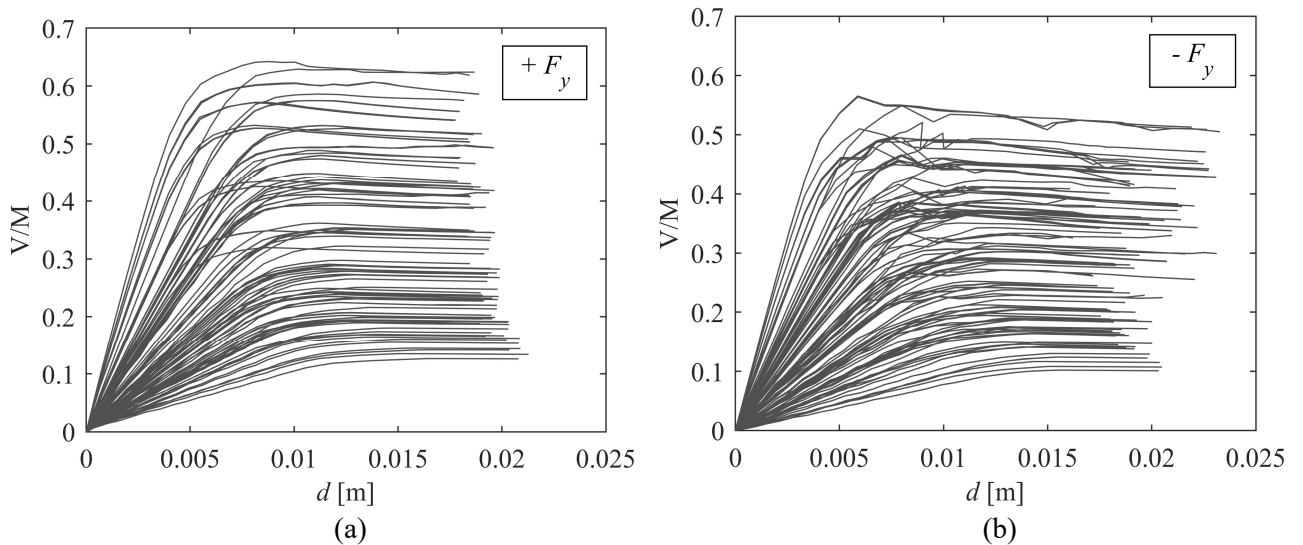


Figure 6.11: Capacity curves from the analyses with (a) positive forces ( $+F_y$ ) and (b) negative forces ( $-F_y$ ).

The same buildings referred to the 272 simulations exhibit greater capacity in *y*-direction, due to the arrangement and the geometry of the walls in this direction: they have a greater length and most of them are without openings. Also for the *y*-direction, the same model is used as an example to show the results. The indication of the resisting masonry walls in *y*-direction (P2, P4, P5, P7) is shown in Figures 6.12(a) and 6.14(a). Figures 6.13 and 6.15 show the failure mechanisms referred to the walls in *y*-direction, in correspondence of a displacement ( $d$ ) equal to 0.018 m (Figures 6.12(b) and 6.14(b)), highlighting that the main collapse mechanism in this direction is the shear one. In this case, the two behaviours are very similar, due to the presence of the openings just in the panel P5. Considering the non-regularity in plan, the building results to be weaker to the negative seismic action in *y*-direction ( $-F_y$ ), as the activation of flexural mechanisms in the spandrels of the panel P5 and in the ground-floor-pier of the smaller panel P7, due to the torsional effects more accentuated in this case depending on the asymmetry resulted in the upper part (in plan) of the model. However, in correspondence of the same displacement reached considering the forces  $+F_y$  (Figure 6.12(b)), most of the panels are still in the elastic or plastic phase. Thus, considering this latter case, higher values of the collapse PGA are expected, with respect to the negative seismic action in *y*-direction ( $-F_y$ ), i.e. lower seismic fragility.

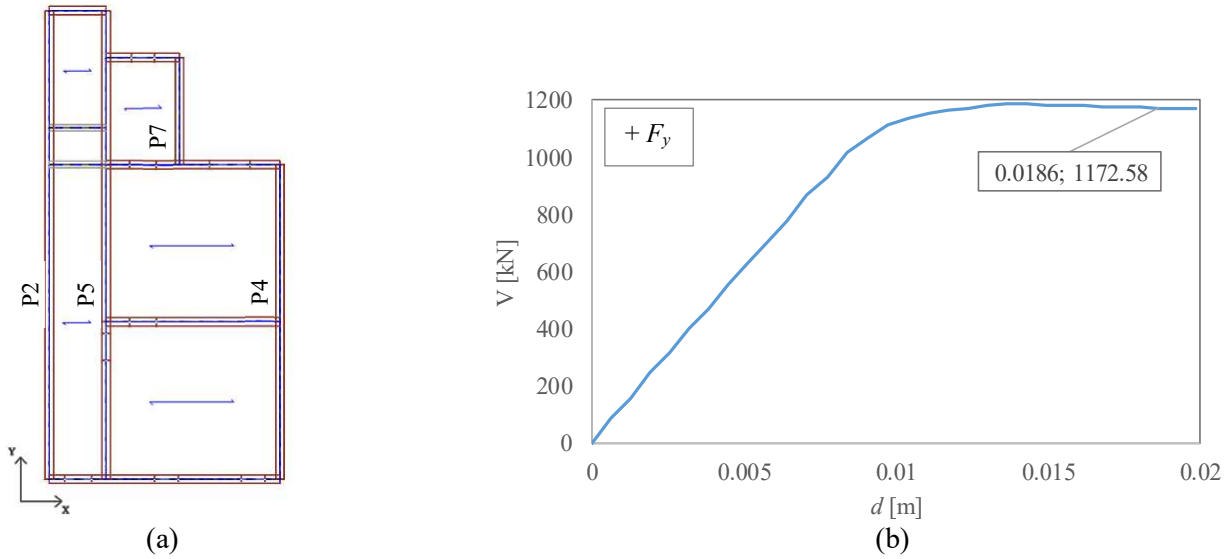


Figure 6.12: (a) Indication of the masonry walls in  $y$ -direction; (b) Point of the capacity curve ( $+F_y$ ) related to the same displacement in Figure 6.14(b).

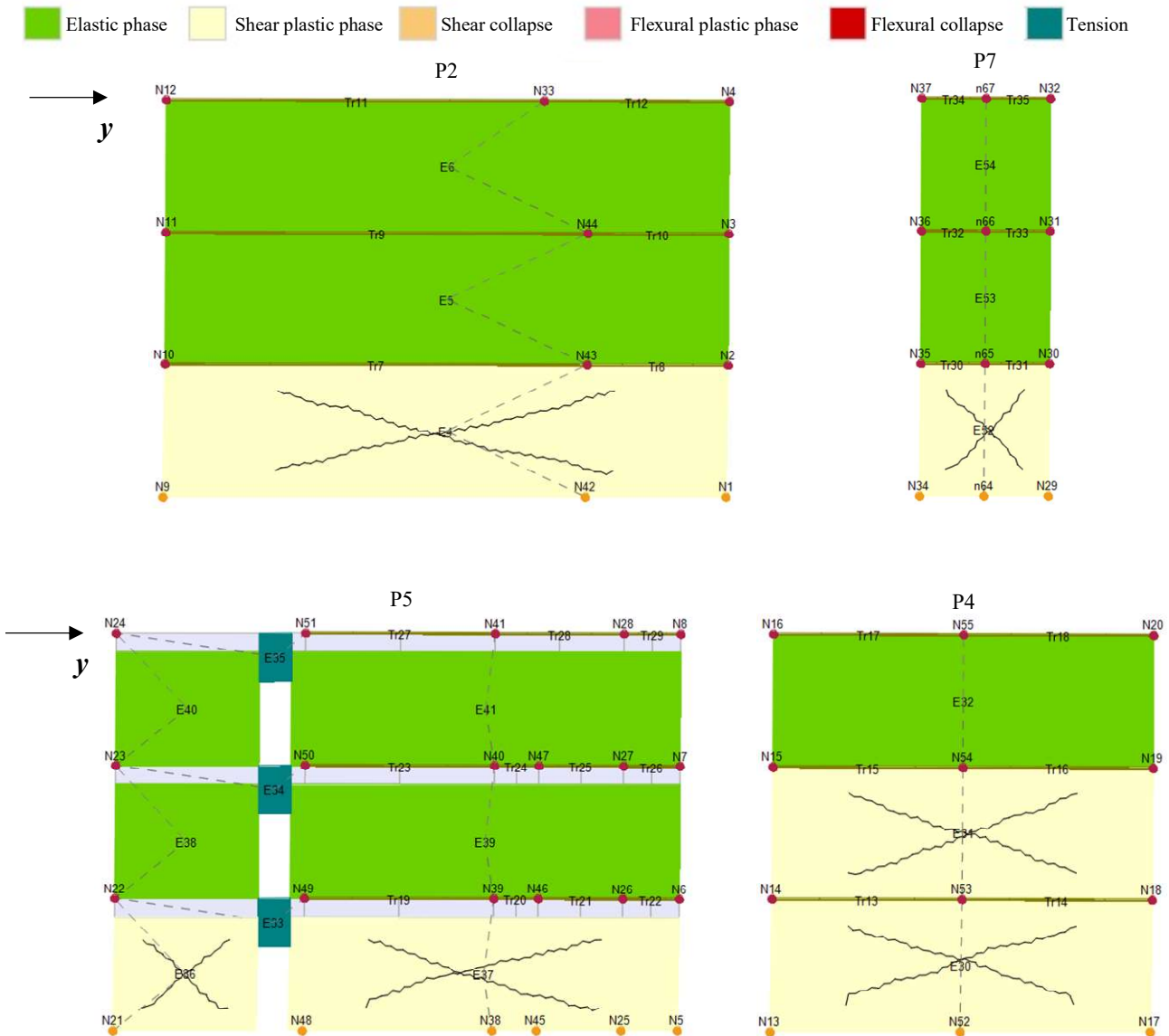


Figure 6.13: Failure mechanisms of the masonry walls considering a seismic action in  $y$ -direction ( $+F_y$ ).

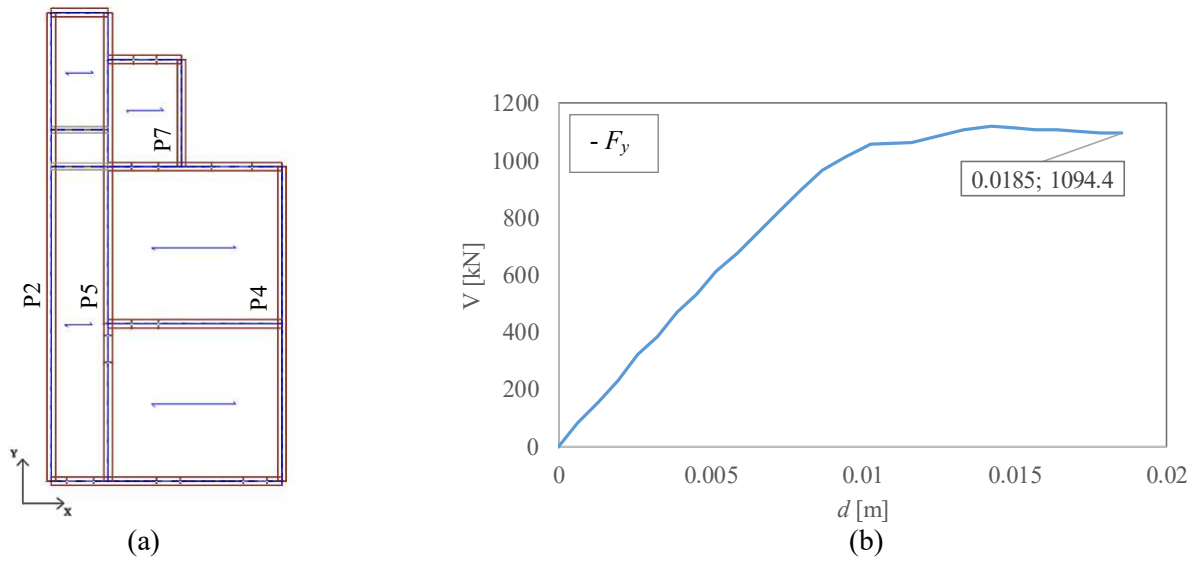


Figure 6.14: (a) Indication of the masonry walls in  $y$ -direction; (b) Point of the capacity curve ( $-F_y$ ) related to the collapse of the panels P5 and P7.

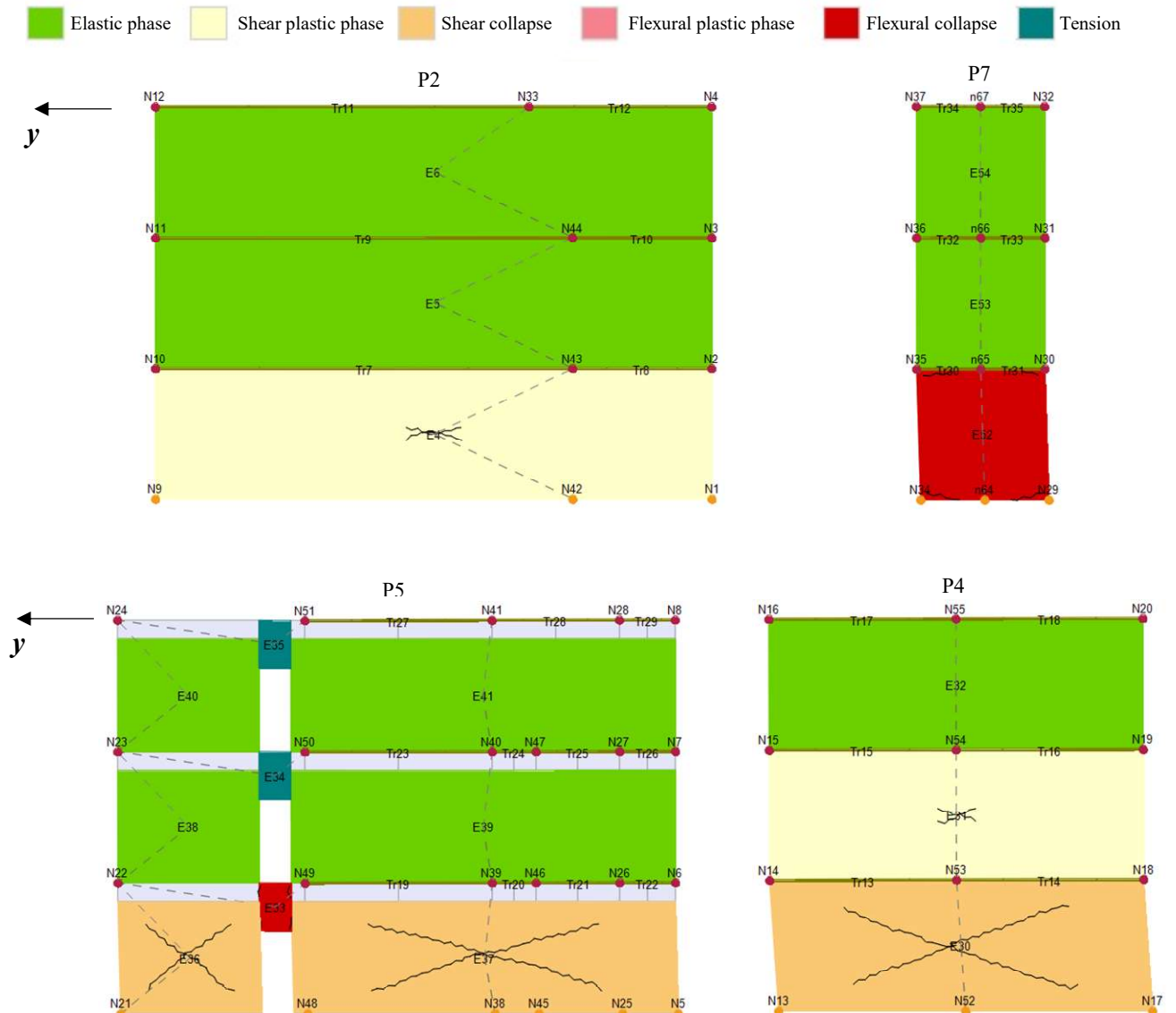


Figure 6.15: Failure mechanisms of the masonry walls considering a seismic action in  $y$ -direction ( $-F_y$ ).

## 6.2.4 Response Surface models

The capacity curves represent the structural capacities of the models, from which the ultimate displacements ( $d_u$ ) were obtained. Following the procedure in Section 5.5 the displacement demands ( $d_{max}$ ), to be compared with  $d_u$ , were evaluating, in order to obtain all the PGA corresponding to the attainment of the LS limit state ( $PGA_C$ ), representing the response parameter used to calibrate the Response Surface (RS) models. However, since Monte Carlo was used (Section 3.2), in order to avoid the prediction of negative values of the variables from the distributions, the natural logarithm of  $PGA_C$  ( $\log(PGA_C)$ ) was used as response parameter for the calibration. Thus, the correspondent log-normal distributions were obtained from the selected normal distributions used for the variables (Section 6.2.2).

A quadratic polynomial was then chosen for the RS, but with only one quadratic term producing significant effects in the response ( $x^2_1$ ). Thus, the equation describing the RS models used to study the clay brick isolated structural unit is set as:

$$\log(PGA_{C,i,j,k}) = \beta_0 + \beta_1 x_{1,i} + \beta_2 x_{2,i} + \beta_3 x_{3,i} + \beta_4 x^2_{1,i} + \delta_{sis,j} + \delta_{geom,k} + \varepsilon_{i,j,k} \quad (6.1)$$

where  $i$  stands for the  $i$ -th simulation,  $j$  for the  $j$ -th  $\delta_{sis}$  block,  $k$  for the  $k$ -th  $\delta_{geom}$  block and  $\varepsilon$  represents the errors. The regression is obtained through the Ordinary Least Squares method (Section 3.3.1.1), approximating the structural response by the polynomial function defined in Equation 6.1.

In the following the results referred to the 4 seismic action cases ( $+F_x$ ,  $-F_x$ ,  $+F_y$ ,  $-F_y$ ) are given. Since the contribute of the variable  $x_2 = E_1$  is negligible, the RS models just show the relation of the response parameter ( $\log(PGA_C)$ ) with the other two explicit variables  $\tau$  and  $d$ . The results of the RS allow to show how the parameters chosen as variables affect the seismic response of the selected masonry isolated structural units, also highlighting the differences considering two orthogonal directions of the seismic action.

Tables 6.9, 6.10, 6.11 and 6.12 give the regression parameters obtained for each explicit variable ( $\tau$ ,  $E_1, d$ ,  $\tau^2$ ) and the standard deviations related to the implicit variables ( $\delta_{sis}$ ,  $\delta_{geom}$  and the random error  $\varepsilon$ ). Regarding the  $x$ -direction, the regression parameters ( $\beta_i$ ) related to the variables  $\tau$  and  $d$  are always positive: as expected, the value of the  $PGA_C$  increases as the values of the two variables increase. The values of the regression parameters  $\beta_1$  and  $\beta_4$  indicate that the shear strength ( $\tau$ ) is the variable most influencing the response; the value of

the variable  $d$  (mean distance of the masonry walls in  $x$ -direction) is also affecting the  $PGA_C$ , but through a smaller regression parameter  $\beta_3$ . This latter parameter is positive as expected, because since the main failure mechanism is the flexural one (Section 6.2.3) if  $d$  increases, the length of the walls in  $x$ -direction increases, and the structure can better withstand the seismic action in  $x$ -direction.

As for the  $y$ -direction, the RS indicates a qualitatively similar relationship between the response parameter and the explicit variables, except for the variable  $d$ : if  $d$  increases, the length of the wall in  $x$ -direction increases, implying an increment of the slab length in the same direction. As a consequence, the capacity of the walls in  $y$ -direction against a seismic action in  $y$ -direction decreases, leading to lower values of the  $PGA_C$ .

Figures 6.16, 6.18, 6.20 and 6.22 show the sections of the RS models obtained setting the distance  $d$  to the fixed values chosen to calibrate the RS (Table 6.6) and changing the values of the shear strength  $\tau$ ; on the contrary, Figures 6.17, 6.19, 6.21 and 6.23 show the sections of the RS models obtained setting the shear strength  $\tau$  to the fixed values chosen to calibrate the RS (Table 6.6) and changing the values of the distance  $d$ . In these figures the sections are divided between the factorial values of the variable (pink and blue continuous lines) and the central and axial points (black, green and red continuous lines); the dashed lines (--) indicate the section models obtained adding and subtracting the RS variance  $\sigma = \sqrt{\sigma_{\varepsilon}^2 + \sigma_{sis}^2 + \sigma_{geom}^2}$ ; the points are those corresponding to the various simulations used to calibrate the RS models.

The section of the RS models obtained varying  $\tau$  (both for  $x$ - and  $y$ -direction) have a greater slope because the shear strength is the variable most influencing the  $PGA_C$ , but they are closer each other because they are referred to the five values of  $d$ , having reduced effect on the response. For this latter motivation, the section of the RS models obtained varying  $d$  (both for  $x$ - and  $y$ -direction) have a minor slope, but they are more spaced each other because they are referred to the five values of  $\tau$ , having a significant effect on the response.

The results also confirm those obtained in terms of capacity: in  $x$ -direction the weaker direction is the positive ( $+F_x$ ), in  $y$ -direction is the negative one ( $-F_y$ ).

In the Figures below, representing the RS models, the values of the  $PGA_C$  are reported in a logarithmic scale.

- *x*-direction (+  $F_x$ )

Table 6.9: Regression parameters and standard deviations of the isolated structural unit, considering the seismic forces +  $F_x$ .

Variable	$\beta_i$	Variable	$\sigma$
$x_1 (\tau)$	12.19	$\delta_{\text{sis}}$	0.1883
$x_2 (E_1)$	0.0001667	$\delta_{\text{geom}}$	0.239
$x_3 (d)$	0.03705	$\varepsilon$	0.2929
$x_1 (\tau^2)$	29.43		

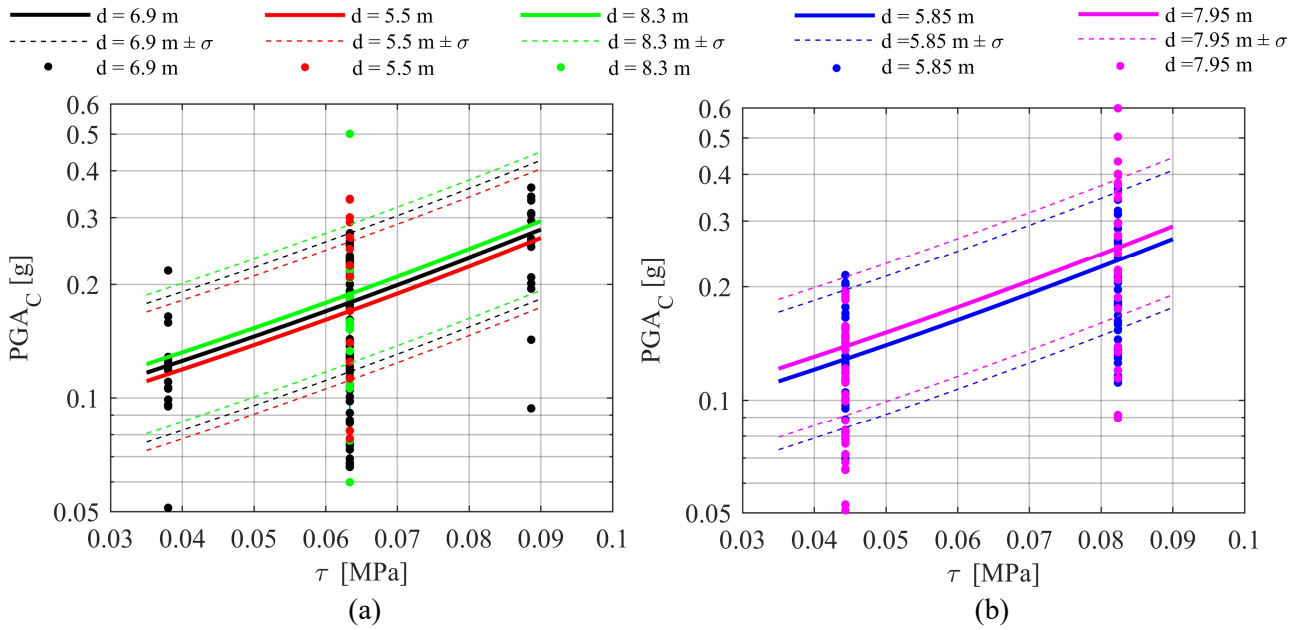


Figure 6.16: (a) Axial and central region and (b) factorial region of the isolated structural unit quadratic RS sections obtained varying  $\tau$ , considering the seismic forces +  $F_x$ .

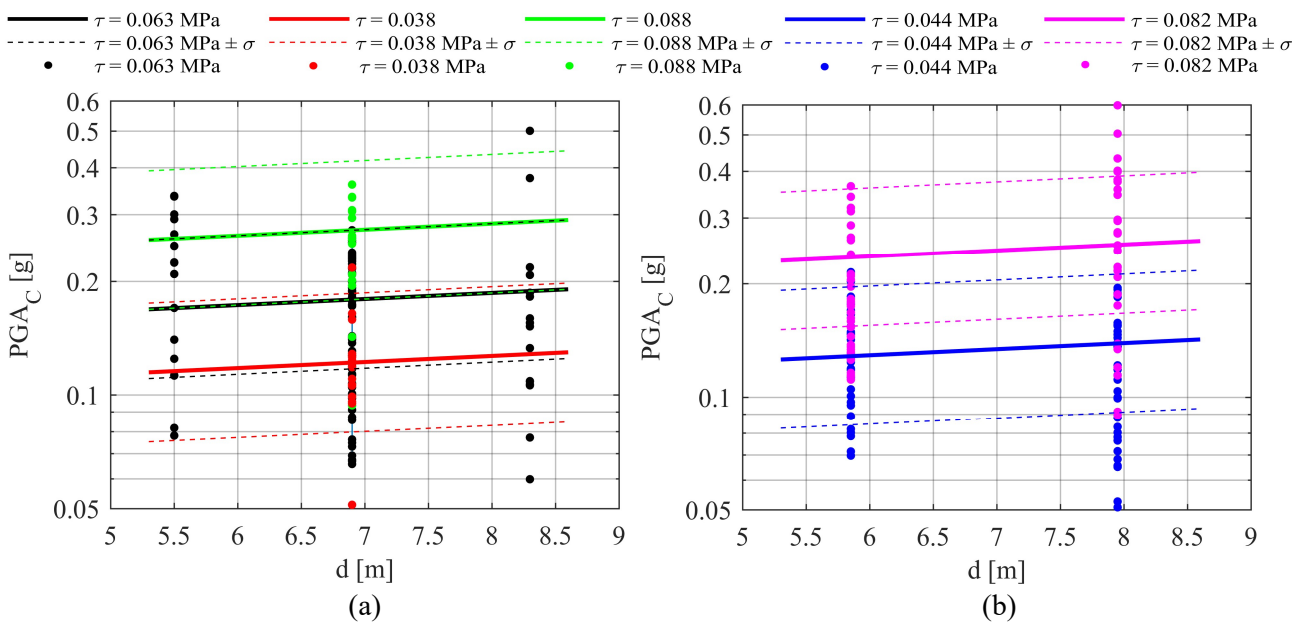


Figure 6.17: (a) Axial and central region and (b) factorial region of the isolated structural unit quadratic RS sections obtained varying  $d$ , considering the seismic forces +  $F_x$ .

-  $x$ -direction ( $-F_x$ )

Table 6.10: Regression parameters and standard deviations of the isolated structural unit, considering the seismic forces  $-F_x$ .

Variable	$\beta_i$	Variable	$\sigma$
$x_1 (\tau)$	1.377	$\delta_{\text{sis}}$	0.2341
$x_2 (E_1)$	0.0001444	$\delta_{\text{geom}}$	0.1565
$x_3 (d)$	0.07699	$\varepsilon$	0.2527
$x_1 (\tau^2)$	46.28		

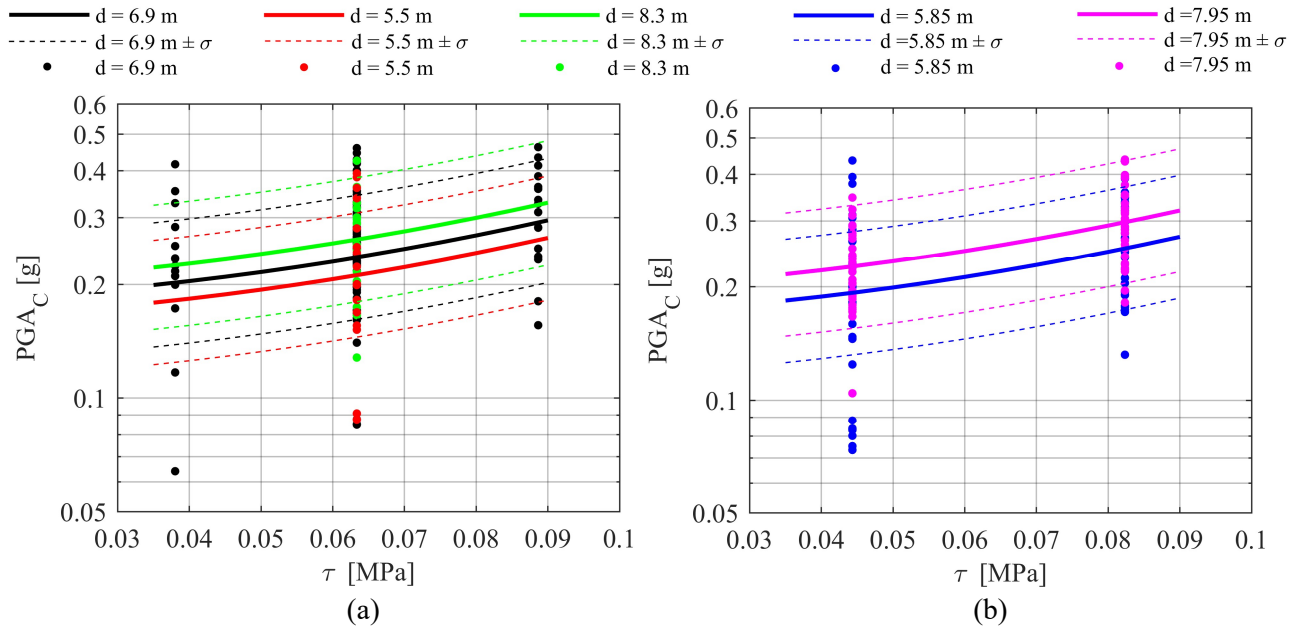


Figure 6.18: (a) Axial and central region and (b) factorial region of the isolated structural unit quadratic RS sections obtained varying  $\tau$ , considering the seismic forces  $-F_x$ .

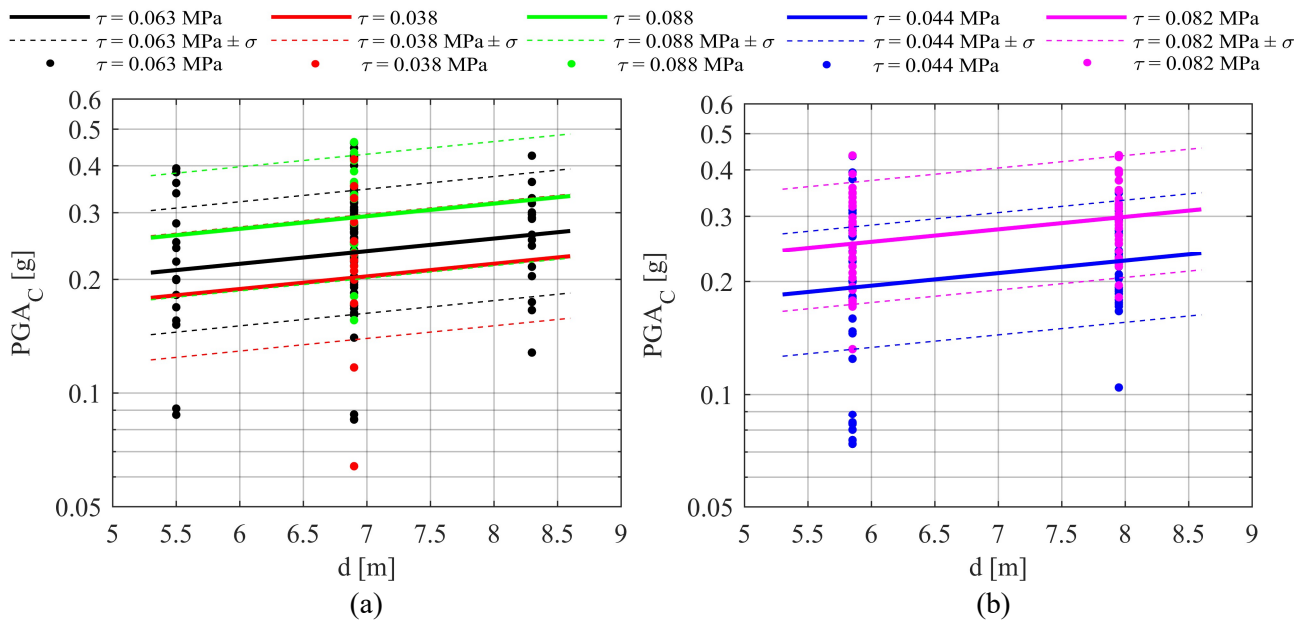


Figure 6.19: (a) Axial and central region and (b) factorial region of the isolated structural unit quadratic RS sections obtained varying  $d$ , considering the seismic forces  $-F_x$ .

*y*-direction (+  $F_y$ )

Table 6.11: Regression parameters and standard deviations of the isolated structural unit, considering the seismic forces +  $F_y$ .

Variable	$\beta_i$	Variable	$\sigma$
$x_1 (\tau)$	4.19	$\delta_{sis}$	0.1649
$x_2 (E_1)$	0.0004991	$\delta_{geom}$	0.1592
$x_3 (d)$	-0.07605	$\varepsilon$	0.1576
$x_1 (\tau^2)$	51.21		

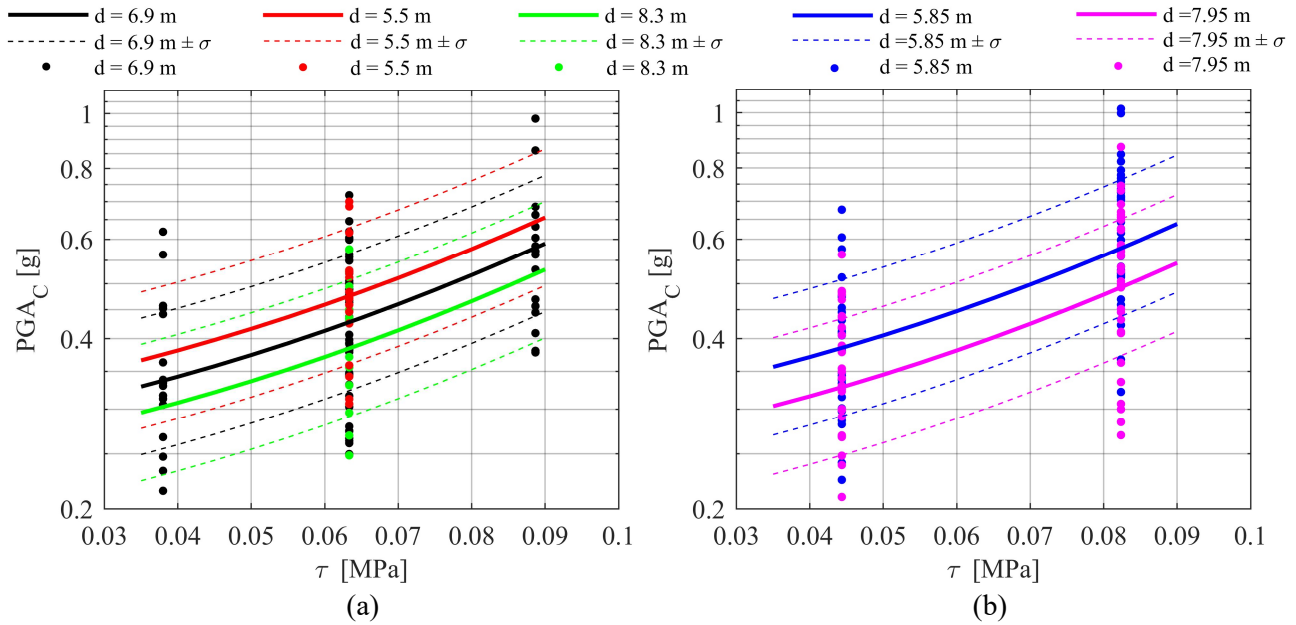


Figure 6.20: (a) Axial and central region and (b) factorial region of the isolated structural unit quadratic RS sections obtained varying  $\tau$ , considering the seismic forces +  $F_y$ .

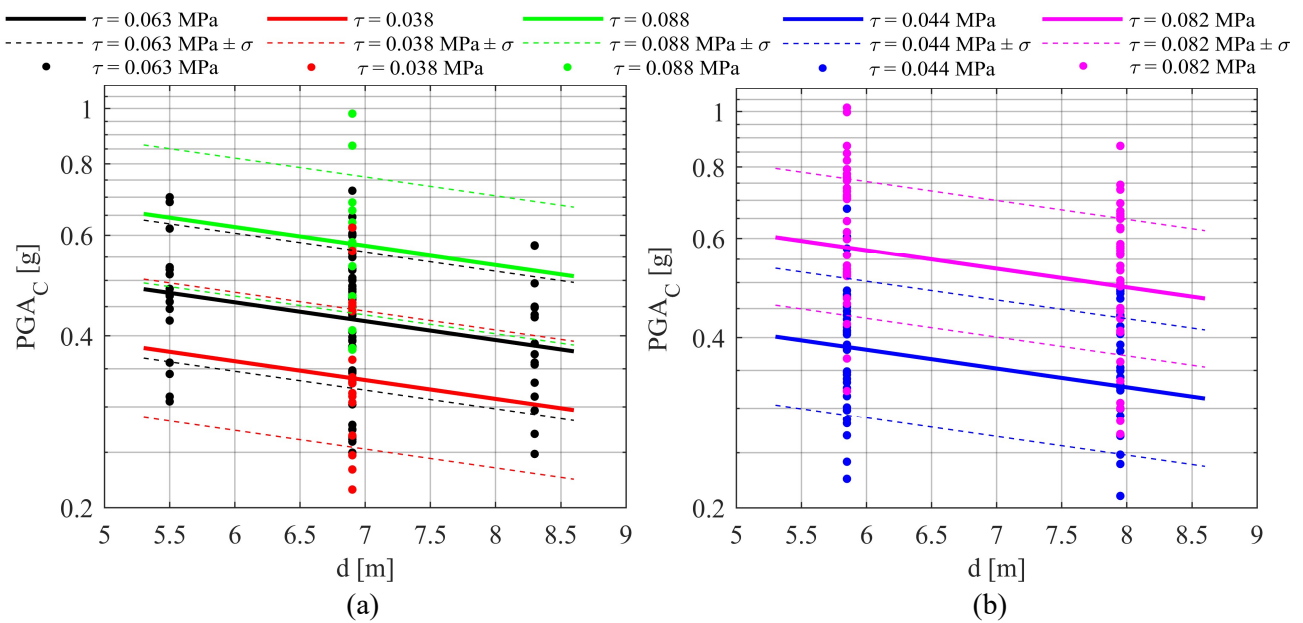


Figure 6.21: (a) Axial and central region and (b) factorial region of the isolated structural unit quadratic RS sections obtained varying  $d$ , considering the seismic forces +  $F_y$ .

- *y*-direction (-  $F_y$ )

Table 6.12: Regression parameters and standard deviations of the isolated structural unit, considering the seismic forces -  $F_y$ .

Variable	$\beta_i$	Variable	$\sigma$
$x_1$ ( $\tau$ )	2.81	$\delta_{\text{sis}}$	0.1646
$x_2$ ( $E_1$ )	0.0001477	$\delta_{\text{geom}}$	0.2166
$x_3$ ( $d$ )	-0.06113	$\varepsilon$	0.1832
$x_1$ ( $\tau^2$ )	78.37		

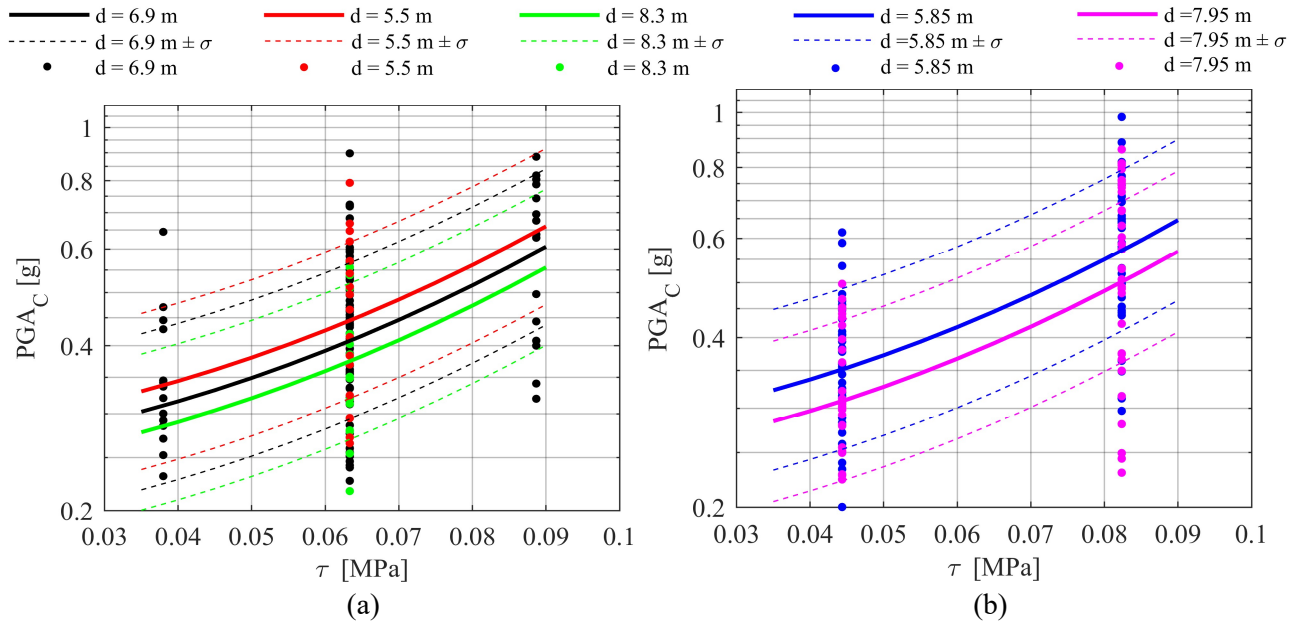


Figure 6.22: (a) Axial and central region and (b) factorial region of the isolated structural unit quadratic RS sections obtained varying  $\tau$ , considering the seismic forces -  $F_y$ .

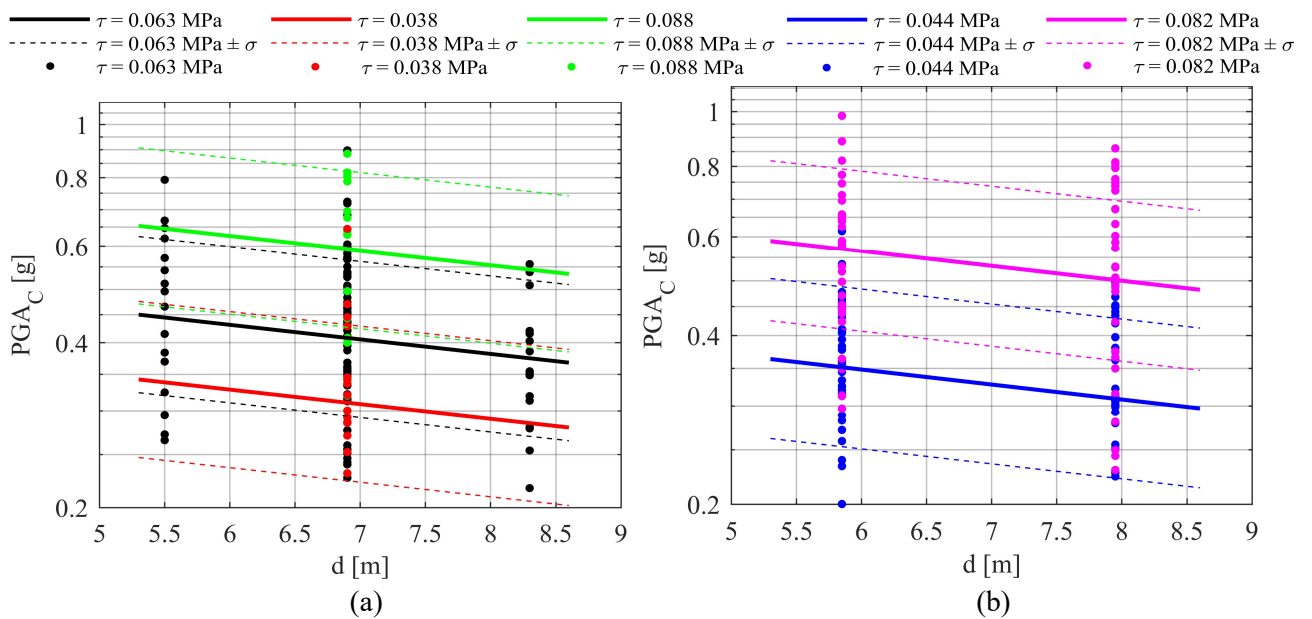


Figure 6.23: (a) Axial and central region and (b) factorial region of the isolated structural unit quadratic RS sections obtained varying  $d$ , considering the seismic forces -  $F_y$ .

Finally, the results are reported by means of the 3D Response Surfaces. Figures 6.24(a) and (b) show the 3D Response Surfaces referred to the positive ( $+F_x$ ) and negative ( $-F_x$ )  $x$ -direction of the seismic action, respectively; Figures 6.25(a) and (b) show the 3D Response Surfaces referred to the positive ( $+F_y$ ) and negative ( $-F_y$ )  $y$ -direction of the seismic action, respectively. The black surfaces are obtained considering  $\tau$  and  $d$  as variables, with  $E_1$  fixed to its mean value; the grey surfaces are obtained adding and subtracting the RS variance

$$\sigma = \sqrt{\sigma_\varepsilon^2 + \sigma_{sis}^2 + \sigma_{geom}^2}.$$

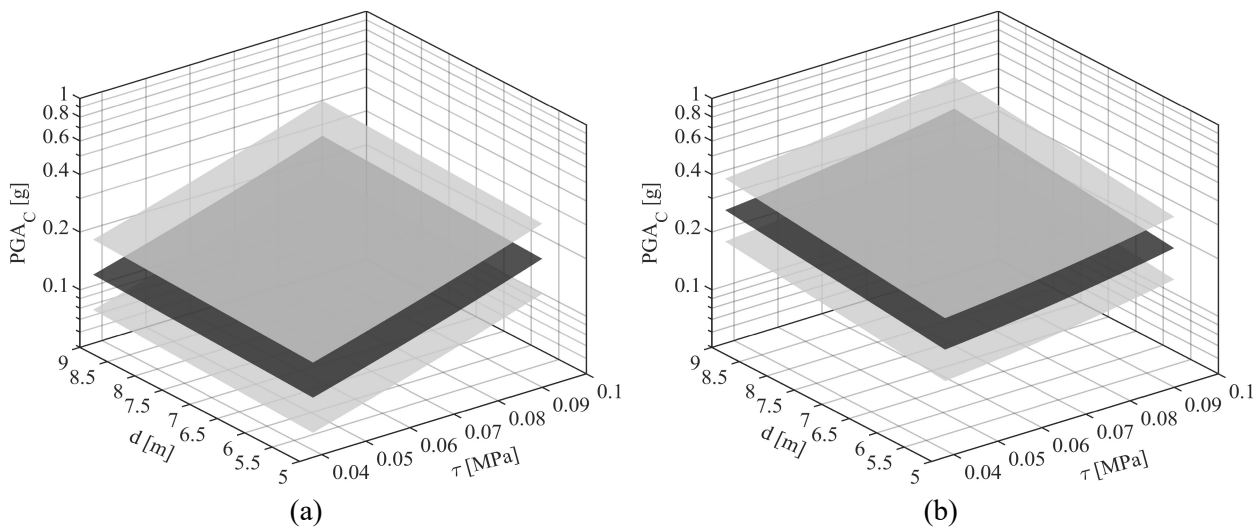


Figure 6.24: 3D Response Surfaces for (a) the positive ( $+F_x$ ) and (b) negative ( $-F_x$ )  $x$ -direction of the seismic action.

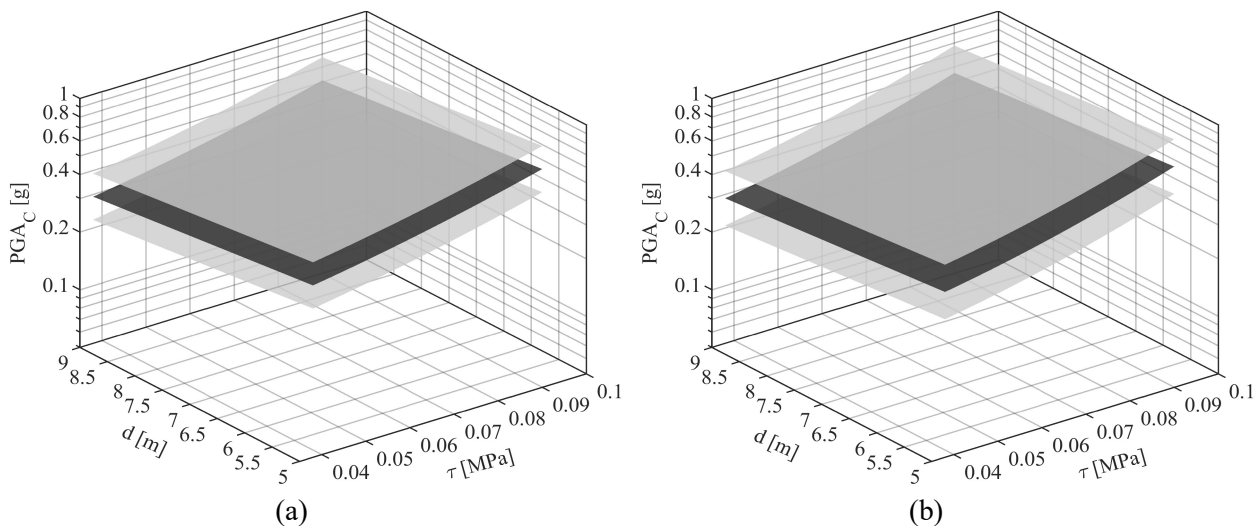


Figure 6.25: 3D Response Surfaces for (a) the positive ( $+F_y$ ) and (b) negative ( $-F_y$ )  $y$ -direction of the seismic action.

### 6.2.5 Fragility curves

The obtained RS models were used to estimate the fragility curves of the masonry isolated structural units. The fragility analysis was assessed adopting the limit state function in Equation 2.5, rewritten in the form:

$$\begin{aligned} g(\mathbf{x}_E, \beta, \varepsilon, \delta_{\text{sis}}, \delta_{\text{geom}} | \text{PGA}_D) &= \log(\text{PGA}_C) - \log(\text{PGA}_D) = \\ &= \beta_0 + \beta_1 x_1 + \beta_2 x_2 + \beta_3 x_3 + \beta_4 x_1^2 + \delta_{\text{sis}} + \delta_{\text{geom}} + \varepsilon - \log(\text{PGA}_D) \end{aligned} \quad (6.2)$$

Four fragility curves were then obtained for seismic action in  $x$ - and  $y$ -direction (Figure 6.26). They give the conditional probability of the structural failure ( $P_f$ ) for different values of the structural demand ( $\text{PGA}_D$ ). Thus, once obtained the collapse  $\text{PGA}_C$ , fixed  $\text{PGA}_D$  and being the behaviour of the structures non-linear, in order to solve the Equation 6.2, Monte Carlo method was used, as explained in Section 5.6.

As expected, the fragility curves for the seismic action in  $x$ -direction reach higher values of the conditional probability of the structural failure ( $P_f$ ) for smaller values of  $\text{PGA}_D$  if compared to the seismic action in  $y$ -direction. These results confirm that the masonry structural units, object of study, is more vulnerable against the seismic action in  $x$ -direction because of the geometry, the number of openings and the arrangement of the resisting walls in the same direction. Instead, the resisting walls in  $y$ -direction have a considerable length and a reduced number of openings; thus, the values of the spectral acceleration corresponding to the attainment of the building failure ( $\text{PGA}_C$ ) are greater.

Moreover, if the  $x$ -direction of the seismic action is considered, the differences between the fragility curve related to the application of the positive forces  $+F_x$  (continuous red line) and that related to the application of the negative forces  $-F_x$  (dash dot red line), are significant because of the consideration on the geometrical properties of the resisting walls in  $x$ -direction already explained in Section 6.2.3. In  $y$ -direction, the two blue curves give almost the same fragility, as the resisting walls in this direction do not exhibit substantial differences between the case of the application of positive forces  $+F_y$  (continuous blue line) and that related to the application of the negative forces  $-F_y$  (dash dot blue line), due to their geometrical configuration with a reduced presence of the openings, making them stockier.

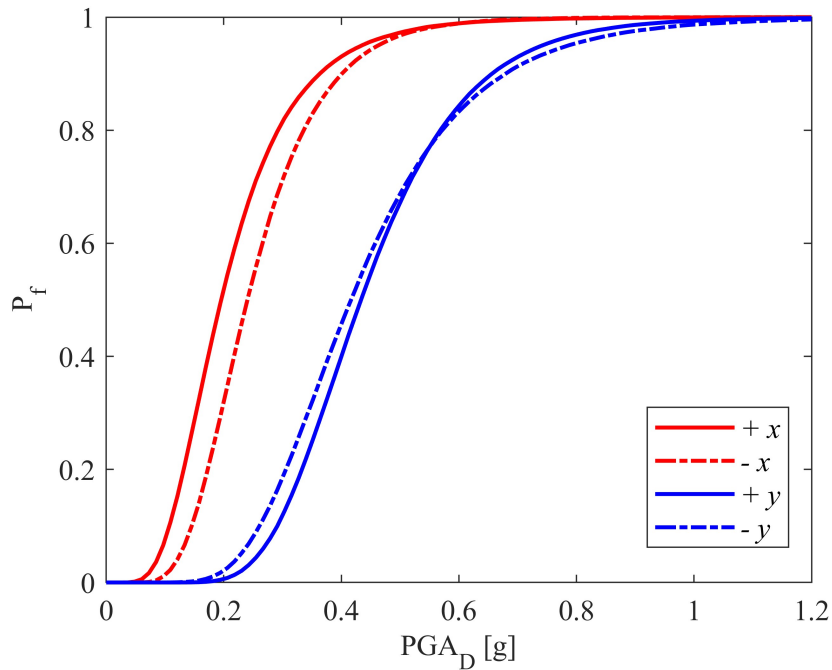


Figure 6.26: Fragility curves obtained for the isolated structural units in  $x$ - and  $y$ -direction of the seismic action.

## 6.3 Comparison between the isolated structural units and the aggregations of identical structural units in row

### 6.3.1 Introduction

The main purpose of this work is the seismic fragility assessment of the masonry aggregate buildings. Thus, once the masonry isolated structural unit (ISU) was studied to analyse which are the parameters most influencing the seismic response, in this Section it was compared with an aggregation in row of 5 structural units (AS). As a first step, in order to start from a simplified structure object of the study, it was decided to consider the structural units along the masonry aggregate identical each other. Moreover, it is very common to find aggregations of identical or similar structural units in the Italian historic centre, as very often they were built in the same historic period, characterized by the use of similar materials and construction techniques.

Thus as a first step, the isolated structural unit studied in Section 6.2 was analysed with a simplified Response Surface, to compare its seismic behaviour with the one of an aggregation of the same identical structural units in row. The purpose is to show how a masonry structural unit cannot be studied as isolated if it belongs to an aggregation of structures, as the adjacent buildings affect its behaviour against the seismic action.

The comparison involves both  $x$ - and  $y$ -direction of the seismic action (Figure 5.3), to analyse the differences on the global seismic behaviour due to the different geometrical configurations of the resisting masonry walls in the two directions. Furthermore, the comparison was made considering the masonry structural units in different positions along the row aggregate, as differences in the seismic response are expected if the structural unit is externally located in the corners of the row or internally between adjacent structural units.

### 6.3.2 The aggregation of identical structural units in row

The modelling of the aggregation of identical structural units in row uses the same structural and geometrical properties of the model analysed in Section 6.2. Figure 6.27 shows a tri-dimensional view of the masonry aggregate and Figure 6.28 shows the plan of the structural ground floor, referring to a model with all the medium values of the explicit variables ( $\tau$ ,  $E_1$ ,  $d$ ) used for the RS model in Section 6.2 and with a thickness of the walls equal to 0.30 m, as an example. Even if it is not very common in existing masonry aggregates, the thickness of the common walls between two adjacent buildings is twice as that of the other walls, to ensure that the aggregate structure is a combination of identical structural units (Figure 6.28).

Since the thickness of the adjacent walls is twice and the same orientation of the slabs was maintained, the masonry walls in  $y$ -direction are loaded in the same way than those of the isolated structural unit in the same direction.

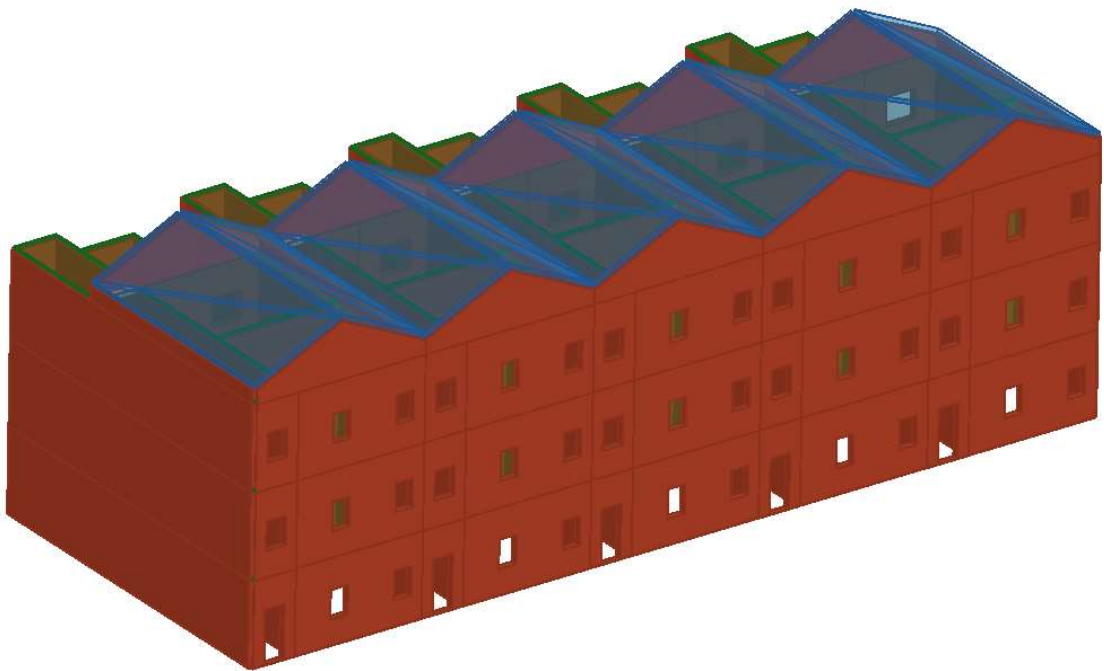


Figure 6.27: Model of the 3D masonry aggregate structure.

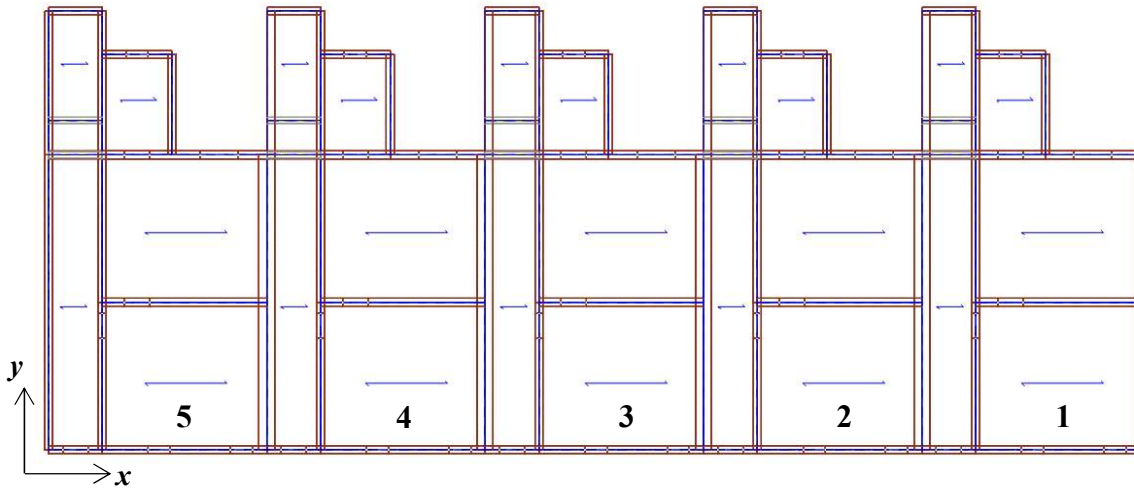


Figure 6.28: Plan of the structural ground floor of the masonry aggregate structure.

### 6.3.3 Selection of the variables

The variables are chosen according to the Response Surface model defined in Section 6.2. Since the purpose of this work is to compare the seismic fragility of the isolated structural unit to that of an aggregate structure, a reduced number of variables is first selected.

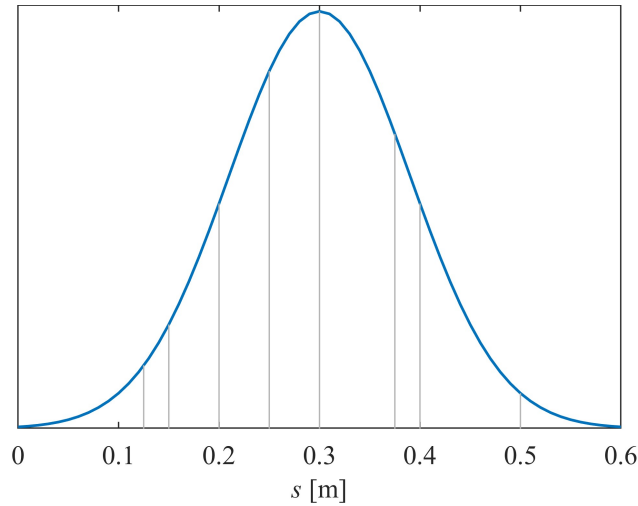
- *Explicit variables*

The thickness ( $s$ ) of the resisting walls was chosen as explicit variable, as in the RS of the Section 6.2 it was considered as implicit variable: the assumption of  $s$  as explicit variable allows to obtain a direct relation with the collapse PGA ( $PGA_C$ ) referred to the attainment of the LS limit state, representing the response parameter used to calibrate the RS model. In this way, the RS is simplified, but a large number of simulations was considered, compared to that reported in Section 6.2.

In order to consider realistic cases of thickness ( $s$ ) of the walls in civil applications, 8 different values are selected, taking into account the most common typologies of masonry structures in the Italian historic cities, following the same choice showed in Section 6.2. In addition, following the RS rules (Section 3.3) in order to define the statistical properties, the values of the thickness ( $s$ ) of the walls belong to a chosen normal distribution. Table 6.13 gives the 8 wall thicknesses selected for the simulations, Figure 6.29 shows the Gaussian distribution chosen, with the indication of the selected values of the thickness ( $s$ ) and Table 6.14 gives the parameters defining the normal distribution.

Table 6.13: Values assumed by the thickness of the walls  $s$ .

$s$	0.125 m	0.15 m	0.20 m	0.25 m	0.30 m	0.375 m	0.40 m	0.50 m
-----	---------	--------	--------	--------	--------	---------	--------	--------

Figure 6.29: Normal distribution adopted for the variable  $s$ .Table 6.14: Definition of the normal distribution adopted for the explicit variable  $s$ .

Variable ( $X_i$ )	Distribution	$\mu$	COV	$\sigma$
$s$	N	0.30 (m)	0.3	0.09

Since the RS is simplified in this Section, the Design of Experiment Theory was not adopted for the definition of the region of interest of the variables. Thus, 8 different structural models are defined, as the unique explicit variable is the thickness  $s$ , defined with 8 selected values.

- *Implicit variables*

As for the RS model adopted in Section 6.2, the uncertainty of the seismic action ( $\delta_{\text{sis}}$ ) was chosen as implicit variable, using the same group of 48 accelerograms defined in Section 5.4. However, in this application the division in blocks allows to associate each of the 48 accelerograms to each of the 8 simulations defined by the 8 values of the explicit variable  $s$ . Thus, the group of the 8 simulations is repeated 48 times, as the number of the selected accelerograms.

Summarizing, the division in blocks for the implicit variables is obtained as following:

- 48 blocks of  $\delta_{\text{sis}}$ , divided in 48 groups of 1 block for a set of 8 simulations.

The partition in blocks, associated to the groups of the explicit variable  $s$ , generates 384 simulations in total. Table B.2 in Appendix B gives the design matrix containing the 384 simulations with the combinations of the explicit and implicit variables, according to the selection of the values of the explicit variable ( $s$ ) and the division in blocks ( $\delta_{\text{sis}}$ ).

### 6.3.4 Push-over analyses

In this section the same procedure adopted in Section 6.2.3 was followed, performing non-linear static analyses (push-over), using TreMuri software to obtain the data required to calibrate the Response Surface models.

Two orthogonal directions ( $x$  and  $y$ ) of the seismic action are considered (Figure 5.3) and the distribution of the forces applied (proportional to the masses) was considered with both signs ( $+F$  and  $-F$ ), generating 384 capacity curves for each studied case. Since the analyses were performed both for the masonry isolated structural units and the row-aggregations of identical structural units, the number of the type of analyses doubles; furthermore, in  $y$ -direction the analyses over the attainment of the LS limit state were performed, to evaluate the collapse of the structural units in different positions along the aggregate (further details in the following). Thus, the type of performed analyses for the masonry isolated structural units and the aggregations of identical structural units in row, object of this Section, are listed as follows:

- 768 in  $x$ -direction with applied forces  $+F_x$  (384 for the ISU and 384 for the AS);
- 768 in  $x$ -direction with applied forces  $-F_x$  (384 for the ISU and 384 for the AS);
- 1536 in  $y$ -direction with applied forces  $+F_y$  (384 for the ISU and 1152 for the AS);
- 1536 in  $y$ -direction with applied forces  $-F_y$  (384 for the ISU and 1152 for the AS).

The results related to the two different directions of the seismic action are shown in the following.

#### - $x$ -direction

Figures 6.30(a) and (b) show the capacity curves obtained from the analyses considering the  $x$ -direction of the seismic action and referred to the isolated structural unit (ISU) and the aggregate structure (AS) respectively, showing the differences between the two cases in terms of capacity and ultimate displacements. The curves show a little increment of the capacity of the aggregate structures, as well as the attainment of larger ultimate displacements. Thus, since the length of the walls is about 5 times that of the walls of the isolated structural unit and the dominance of the flexure as main global failure mechanism (Figures 6.32 and 6.33), an increment of the collapse PGA is expected, if structural units in  $x$ -direction are aggregated. Furthermore, the curves in Figure 6.30 give the same differences between the seismic forces  $+F_x$  and  $-F_x$ , confirming the results obtained in Section 6.2 and showing that the geometrical

configuration of the masonry walls in this direction makes the structures more vulnerable to the application of the seismic forces  $+F_x$ .

As an example, Figure 6.31 gives the deformed configuration of the aggregate structure with 0.30 m of thickness considering a seismic action  $+F_x$ , showing the rigid movement of the structure due to the presence of rigid hollow-core concrete slabs. The deformed configuration referred to the seismic action  $-F_x$  was not reported because it almost shows the same rigid movement in the opposite side.

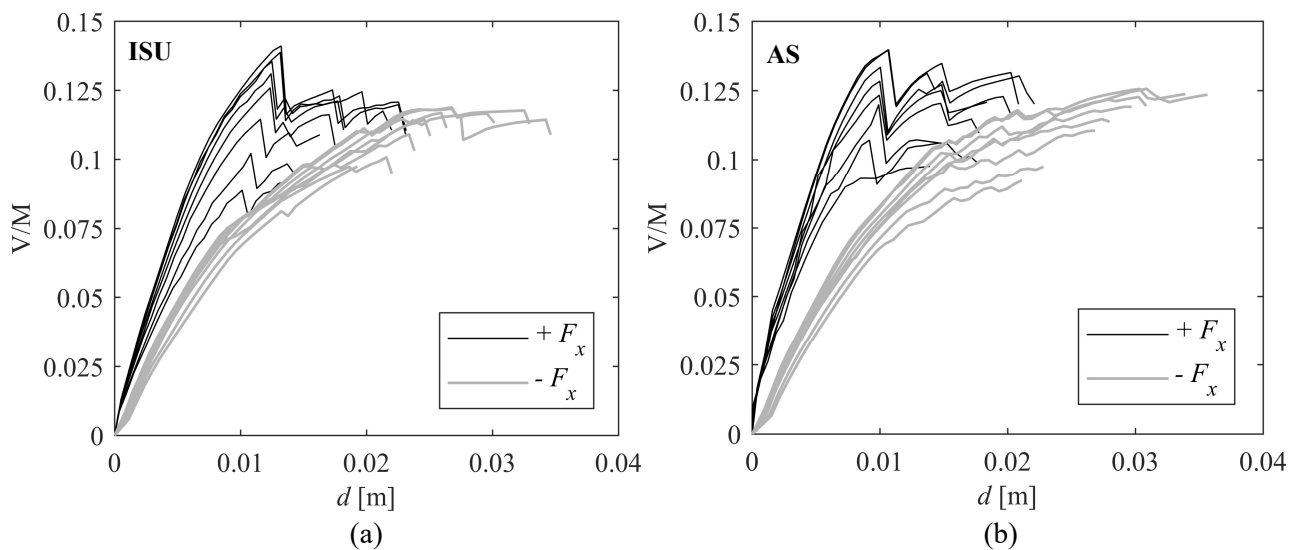


Figure 6.30: Capacity curves from the analyses in  $x$ -direction: (a) isolated structural units and (b) aggregate structures.

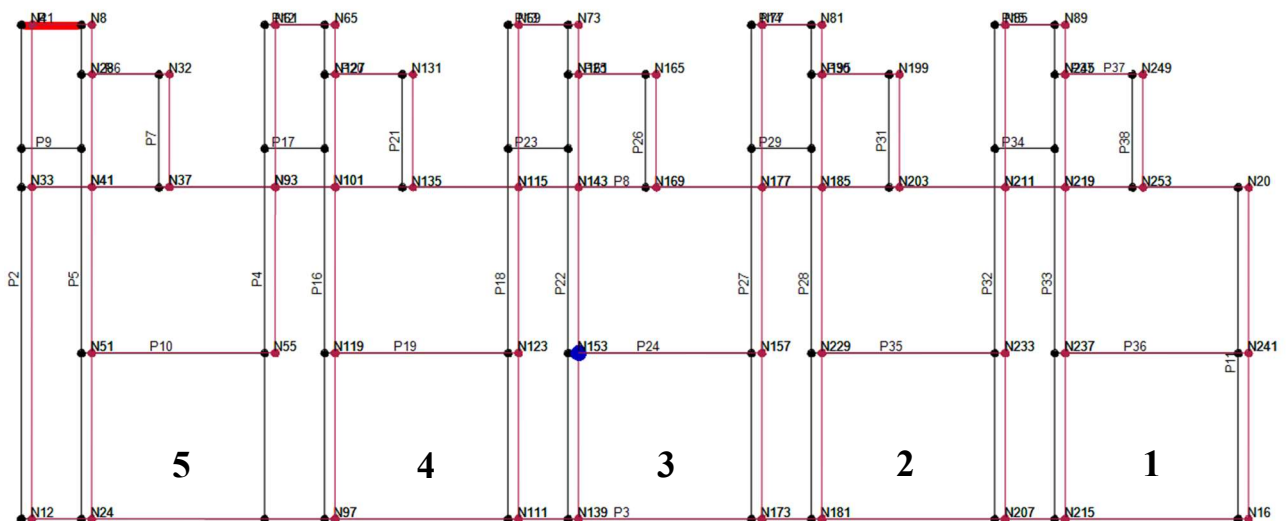


Figure 6.31: Deformed configuration of the model with  $s = 0.30$  m, considering a seismic action in  $x$ -direction ( $+F_x$ ).

Referring to the same model, Figure 6.32 and 6.33 show the more significant mechanisms of the walls corresponding to the last point of the capacity curves, i.e. to the attainment of the

LS limit state, referring to the seismic action +  $F_x$  and  $-F_x$  respectively: the masonry panels are mainly solicited to flexure and most of the piers and spandrels reach the flexural collapse, some of them reach the shear collapse.

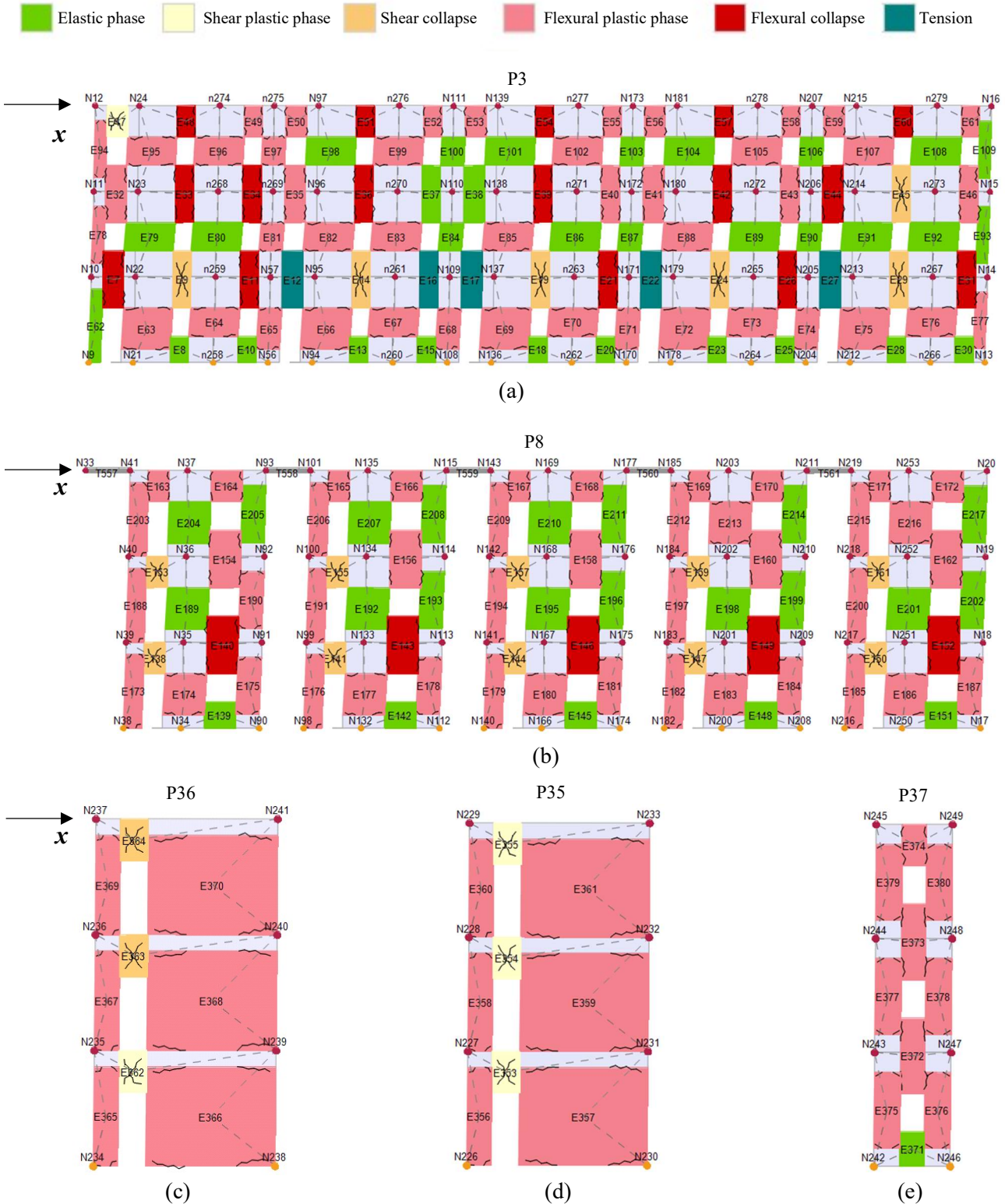


Figure 6.32: Mechanisms of the walls of the model with  $s = 0.30$  m, considering a seismic action in  $x$ -direction (+  $F_x$ ): (a) P3 and (b) P8; (c) P36 and (e) P37 Unit 1; (d) P35 Unit 2.

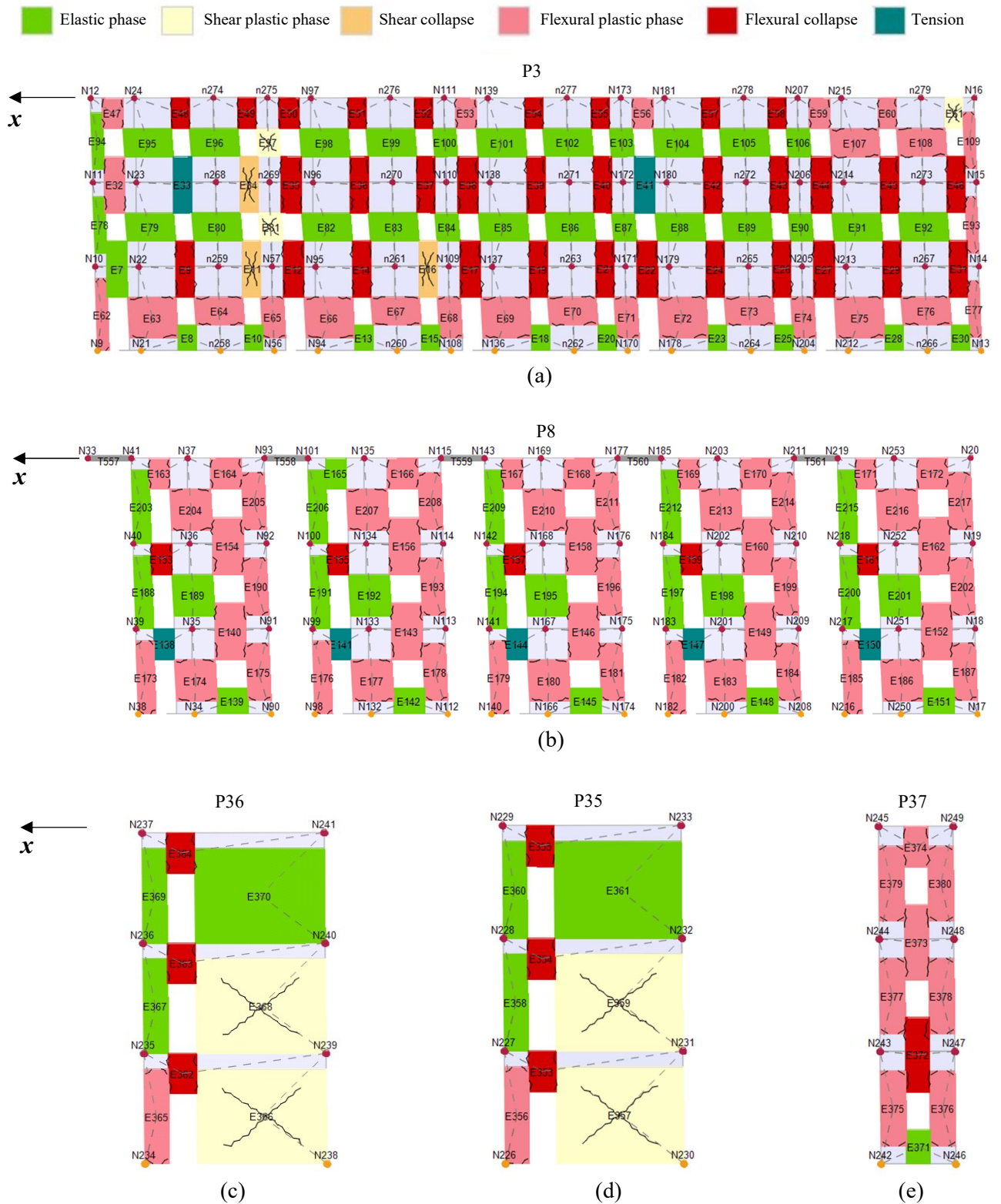


Figure 6.33: Mechanisms of the walls of the model with  $s = 0.30$  m, considering a seismic action in  $x$ -direction ( $-F_x$ ): (a) P3 and (b) P8; (c) P36 and (e) P37 Unit 1; (d) P35 Unit 2.

The masonry walls in Figure 6.33 results more damaged, but these failure mechanisms are reached for higher values of displacements (Figure 6.30(b)) with respect to the those attained considering the positive  $x$ -direction of the seismic action ( $+F_x$ ).

- *y-direction*

Figures 6.34(a) and (b) show the capacity curves obtained from the analyses considering the *y*-direction of the seismic action and referred to the isolated structural unit (ISU) and the aggregate structure (AS) respectively, showing the differences between the two cases in terms of capacity and ultimate displacements. The curves give the same differences between the seismic forces  $+F_y$  and  $-F_y$ , confirming the results obtained in Section 6.2 and showing that the geometrical configuration of the masonry walls in this direction makes the structures more vulnerable to the application of the seismic forces  $-F_y$ . Furthermore, due to the geometrical configuration and arrangement of the resisting walls in *y*-direction, the push-over curves in this direction exhibit higher capacity with respect to those in *x*-direction, as already shown in Section 6.2.

In *y*-direction, the aggregation of structural units leads to a different geometrical configuration, which causes it to exhibit different levels of vulnerability due to the torsional effects mainly affected the external units: the *y*-direction walls do not increase their length, as for the *x*-direction aggregation, and their seismic behaviour is affected by the action of the adjacent buildings. Therefore, the total displacement attained by the aggregate structure is smaller than that of the isolated structural unit, if the LS limit state is considered as the limit for the global seismic response of the aggregate structure. Thus, contrary to what happens in *x*-direction, a decrement of the collapse PGA is expected if the global seismic behaviour of the aggregate structures is compared with those of the isolated structural units.

As an example, Figure 6.35 shows the *y*-direction deformed configuration of the aggregate structure with  $s=0.30$  m at the end of the push-over analysis, considering the seismic forces  $+F_y$ . The deformed configuration referred to the seismic action  $-F_y$  was not reported because it almost shows the same rotation movement in the opposite side. Due to the torsional effects, the external Units 1 and 2 reach larger displacements with respect to units 3, 4 and 5. Nevertheless, only the resisting walls of the external Units 1-2 fail for shear or flexure (Figures 6.36(a) and (b) and Figures 6.38(a) and (b)), with all other resisting walls still belonging to the plastic field (Figures 6.36 (c) and (d) and Figures 6.38(c) and (d) ). Thus, the displacement can still increase until the walls of the other structural units experience the failure for shear. For this reason, the analyses over the attainment of the LS limit state were performed, to allow the resisting walls in *y*-direction of the other Units (3, 4 and 5) to reach

the shear collapse. Therefore, continuing the analyses over the attainment of the LS limit state allows to evaluate the different vulnerabilities of the masonry structural units along the aggregate structure. Figure 6.37 and 6.39 highlight the points on the push-over curves (over the attainment of the LS limit state) corresponding to the failure of the various structural Units, considering both  $+F_y$  and  $-F_y$  directions of the seismic action, respectively: middle Units 3 and 4 have larger values of displacement capacity, corresponding to the shear collapse of their masonry walls. The results referred to the external Unit 5 were neglected, as it is so stiff to reach values of ultimate displacements so large to make the results not reliable. For this reason, it was decided to preserve the reliability of the analyses.

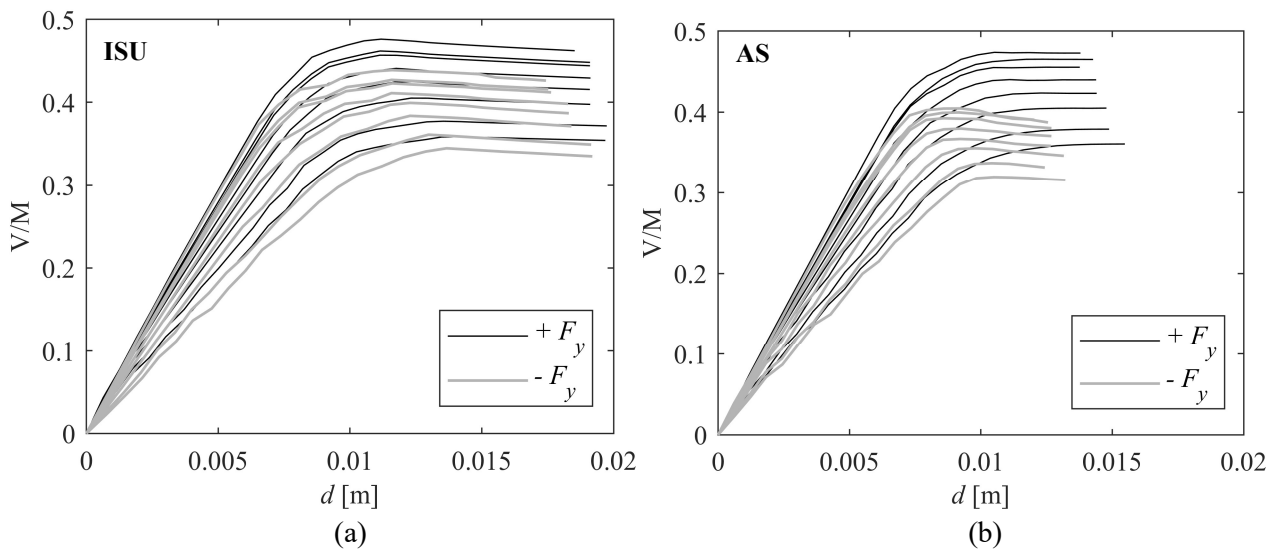


Figure 6.34: Capacity curves from the analyses in  $y$ -direction: (a) isolated structural units and (b) aggregate structures.

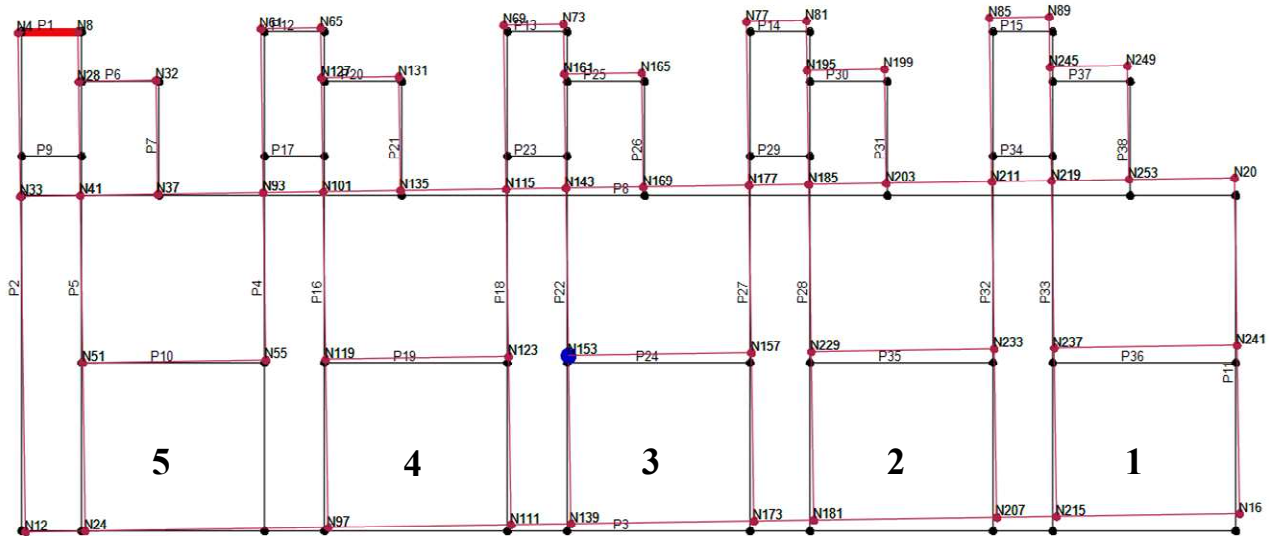


Figure 6.35: Deformed configuration of the model with  $s = 0.30$  m, considering a seismic action in  $y$ -direction ( $+F_y$ ).

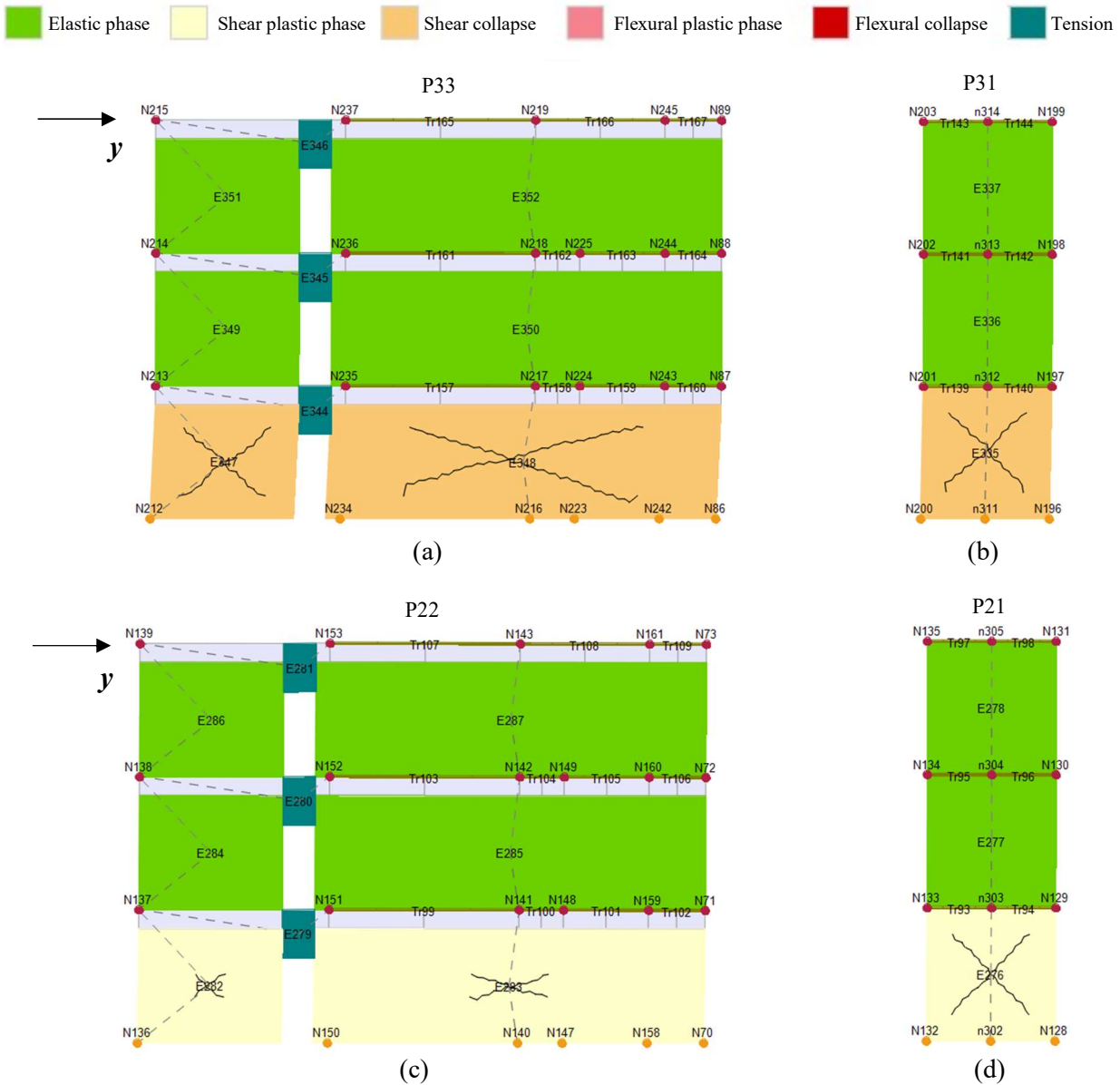


Figure 6.36: Mechanisms of the walls of the model with  $s = 0.30$  m, considering a seismic action in  $y$ -direction ( $+F_y$ ): (a) P33 Unit 1; (b) P31 Unit 2; (c) P22 Unit 3 and (d) P21 Unit 4.

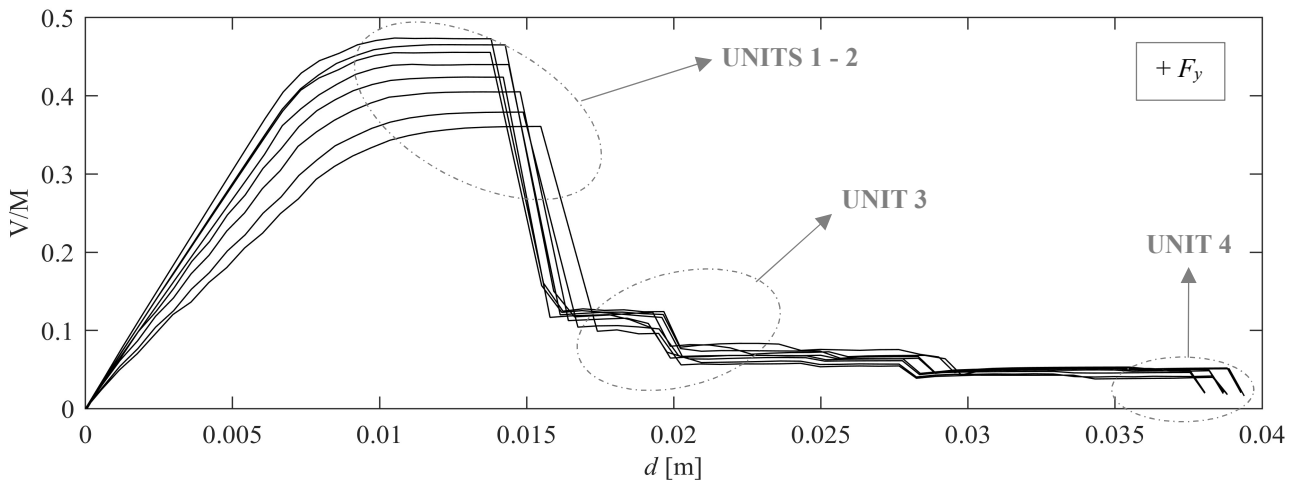


Figure 6.37: Capacity curves from the analyses in  $y$ -direction ( $+F_y$ ) over the attainment of the LS limit state.

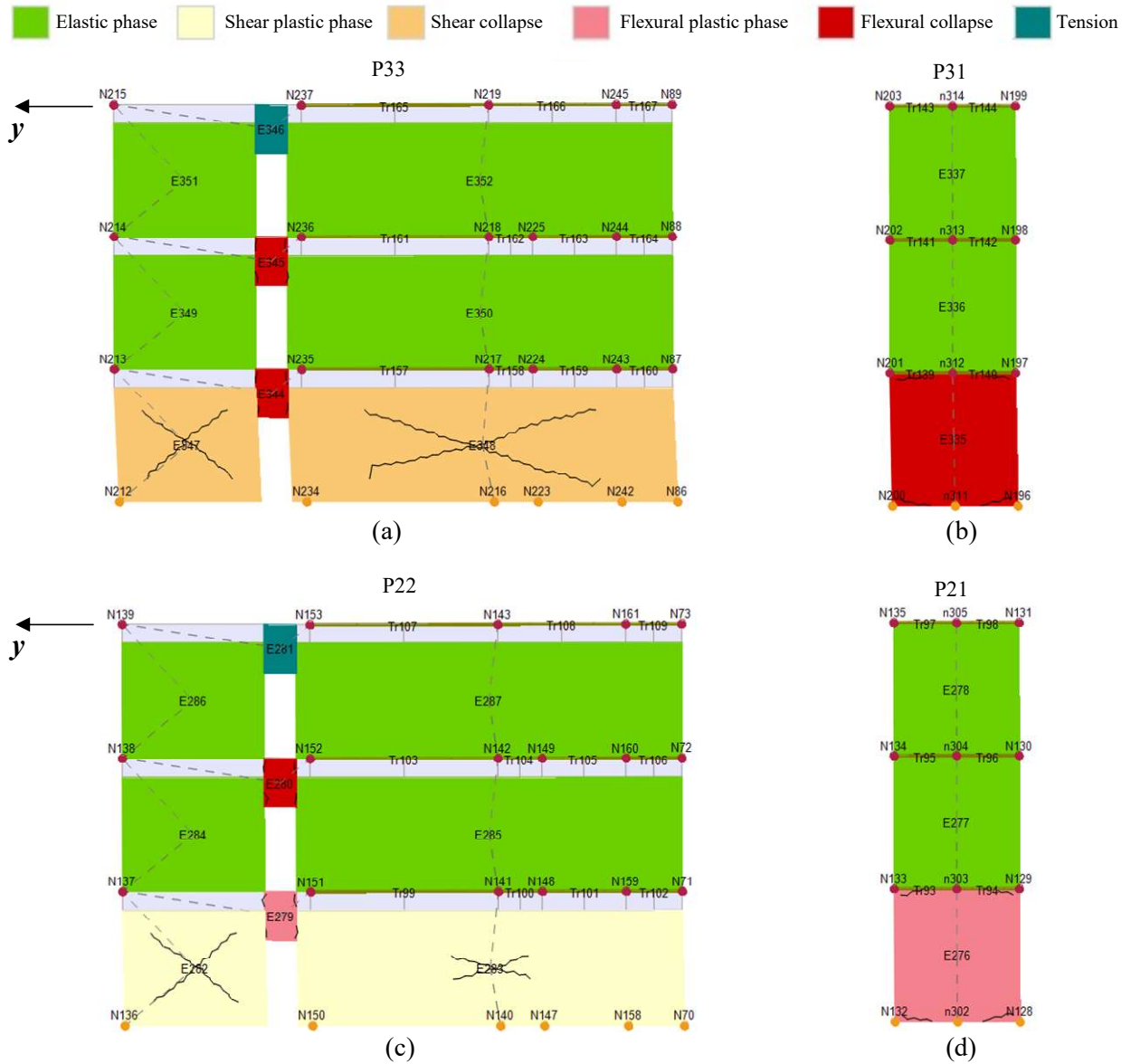


Figure 6.38: Mechanisms of the walls of the model with  $s = 0.30$  m, considering a seismic action in  $y$ -direction ( $-F_y$ ): (a) P33 Unit 1; (b) P31 Unit 2; (c) P22 Unit 3 and (d) P21 Unit 4.

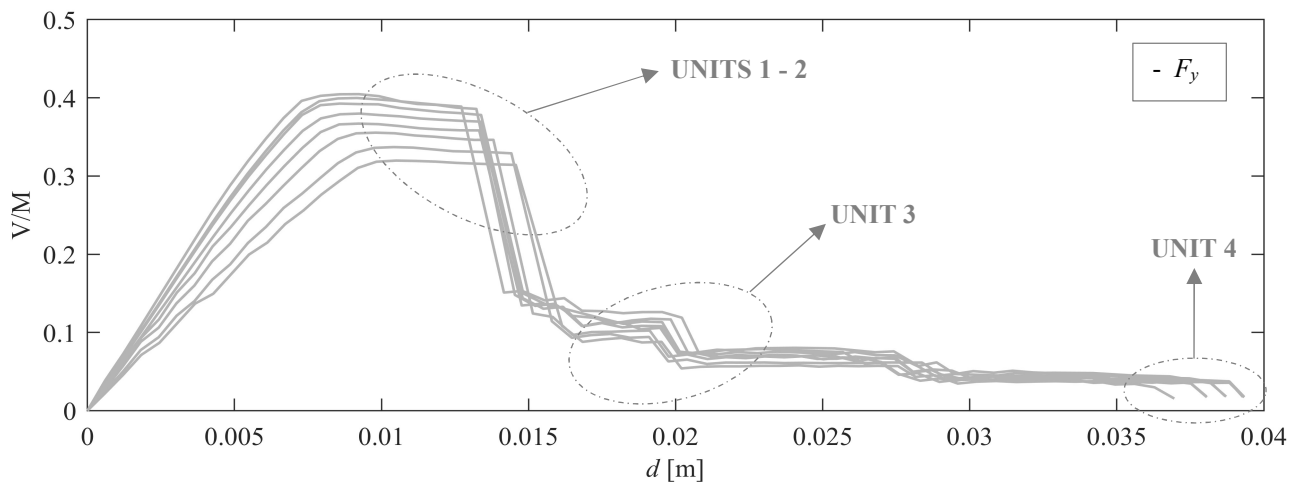


Figure 6.39: Capacity curves from the analyses in  $y$ -direction ( $-F_y$ ) over the attainment of the LS limit state.

### 6.3.5 Response Surface models

Once all the collapse PGA ( $PGA_C$ ) for each of the 8 structural models are evaluated, to calibrate the RS models, a comparison between the values referred to the isolated structural units and those referred to the aggregate structures was made, expressing them in function of the thickness of the walls ( $s$ ). In order to show the influence of the variability of the seismic action on the collapse PGA, Figures 6.40 and 6.41 show the relation between  $s$  and  $PGA_C$ , obtained evaluating for each value of  $s$  the average of the  $PGA_C$  found for 6 different accelerograms. Table 6.15 gives the group of 6 accelerograms used for each value of  $s$  and the correspondent simulations (Table B.2) from which the values of the  $PGA_C$  are obtained. The results highlight for both  $x$ - and  $y$ -direction of the seismic action, that there is not a progressive increment of the  $PGA_C$  if the value of the thickness of the walls  $s$  increases. This is due to the great variability of the earthquake considered, making the results different for each group of 6 different accelerograms. Furthermore, in this work real accelerograms are used and the spectra have an irregular shape: sometimes, the variation of the period may not correspond to the same variation (increase or decrease) of the  $PGA_C$ , obtained with the N2 method, that would occur with the use of the regular spectrum of the code. Thus, these motivations in some cases lead to a decrement of the value of  $PGA_C$  with the increment of the thickness  $s$ , considering different accelerograms.

Otherwise, Figures 6.42 and 6.43 show the relation between  $s$  and  $PGA_C$ , obtained evaluating for each value of  $s$  the contribute of all the accelerograms considered in this study: thus, each point of the Figures corresponds to the average of the values of the  $PGA_C$  obtained applying all the 48 seismic actions. The results highlight for both  $x$ - and  $y$ -direction of the seismic action, that there is a progressive increment of the  $PGA_C$  if the value of the thickness of the walls  $s$  increases, as expected. This is due to the fact that the comparisons between  $PGA_C$  corresponding to different thicknesses is made using the same groups of 48 accelerograms, differently from what has been done in the previous case. Furthermore, the results show that the aggregation of identical structural units in row leads to an increment of the  $PGA_C$  if the  $x$ -direction of the seismic action is considered and a decrement if the  $y$ -direction is considered, as expected from the consideration in terms of capacity discussed in Section 6.3.4. Moreover, considering this latter direction of the seismic action, the values of the collapse PGA increase if more internal structural units are considered (further details in the following).

Table 6.15: Groups of the 6 accelererograms and the correspondent simulations (Table B.2) for each of the thicknesses  $s$ .

$s$	Accelerograms	Simulations
0.50	1-2-3-4-5-6	1-9-17-25-33-41
0.40	7-8-9-10-11-12	50-58-66-74-82-90
0.375	13-14-15-16-17-18	99-107-115-123-131-139
0.30	19-20-21-22-23-24	148-156-164-172-180-188
0.25	25-26-27-28-29-30	197-205-213-221-229-237
0.20	31-32-33-34-35-36	246-254-262-270-278-286
0.15	37-38-39-40-41-42	295-303-311-319-327-335
0.125	43-44-45-46-47-48	344-352-360-368-376-384

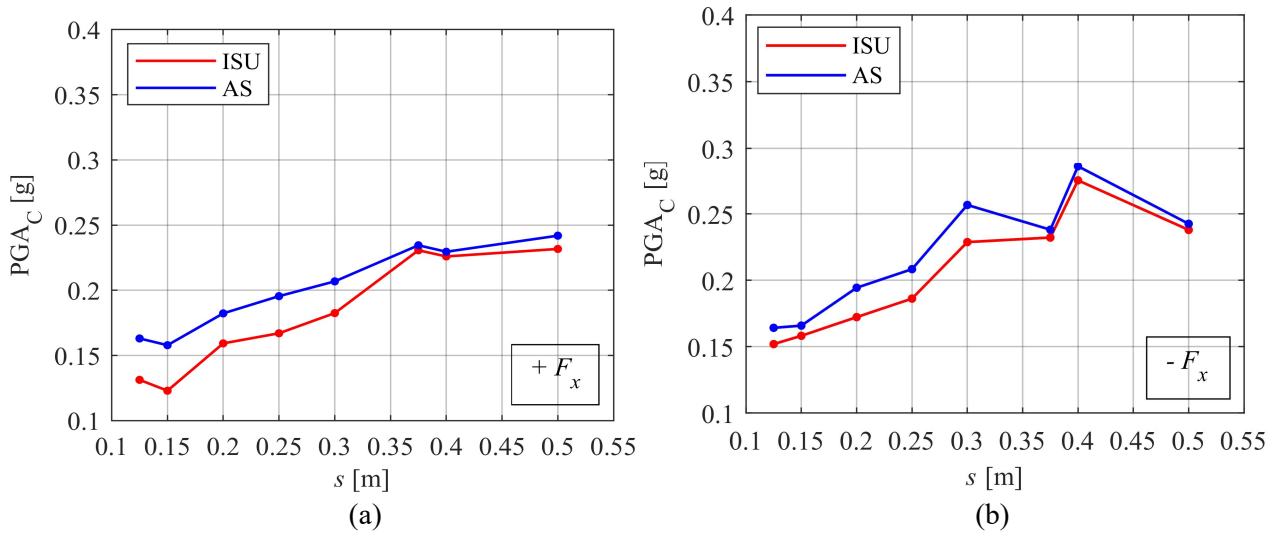


Figure 6.40: Relation between  $s$  and  $PGA_C$ , considering 6 different accelerograms for each value of  $s$ : (a) seismic forces  $+F_x$  and (b) seismic forces  $-F_x$ .

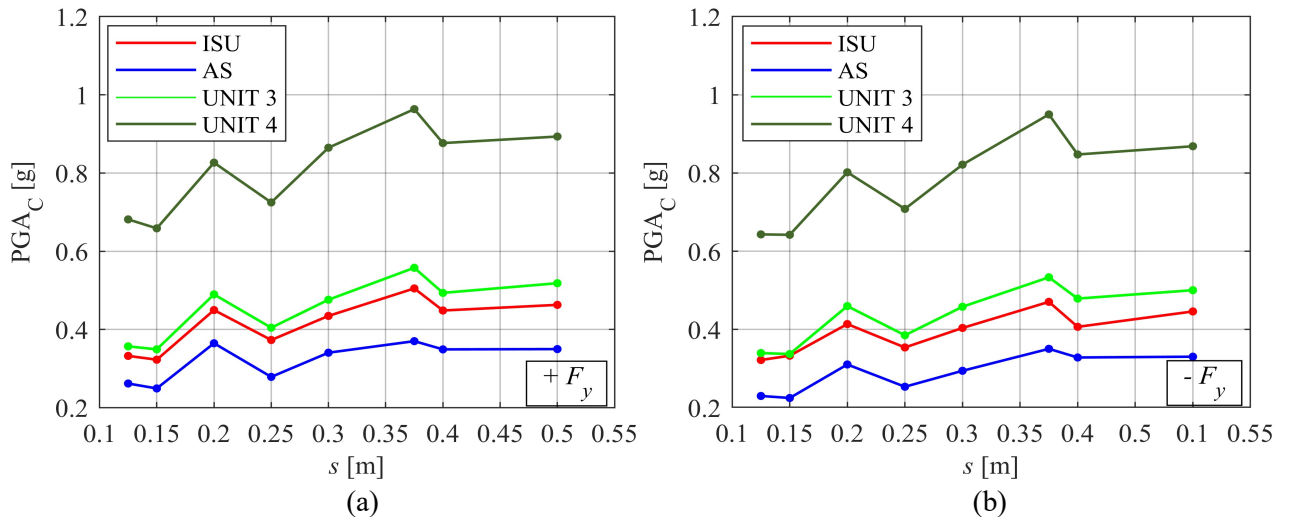


Figure 6.41: Relation between  $s$  and  $PGA_C$ , considering 6 different accelerograms for each value of  $s$ : (a) seismic forces  $+F_y$  and (b) seismic forces  $-F_y$ .

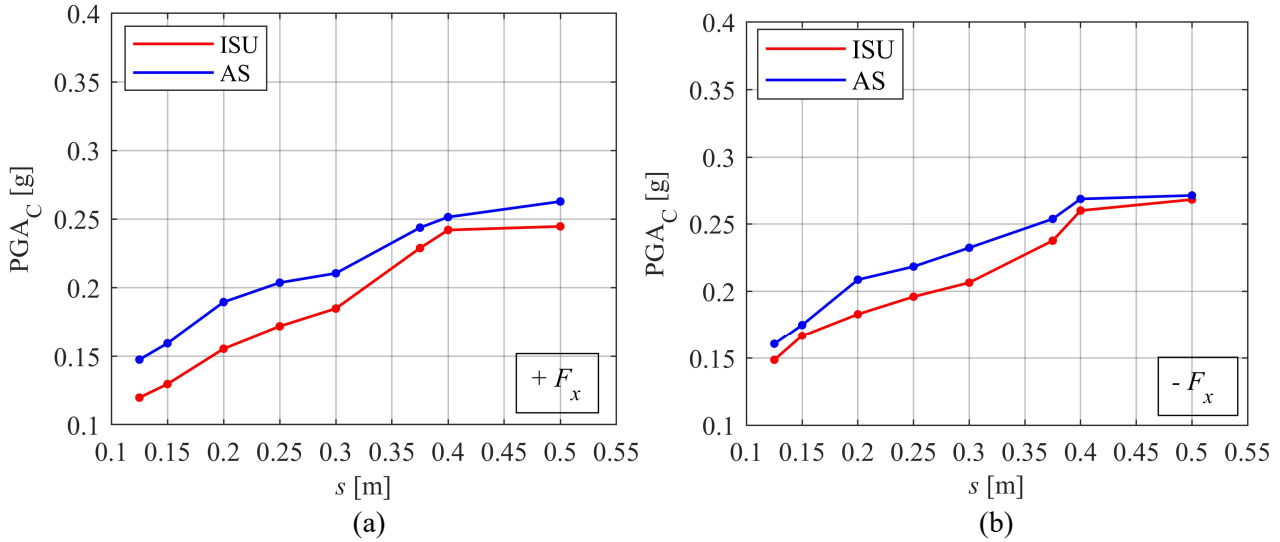


Figure 6.42: Relation between  $s$  and  $PGA_C$ , considering all the accelerograms for each value of  $s$ : (a) seismic forces  $+F_x$  and (b) seismic forces  $-F_x$ .

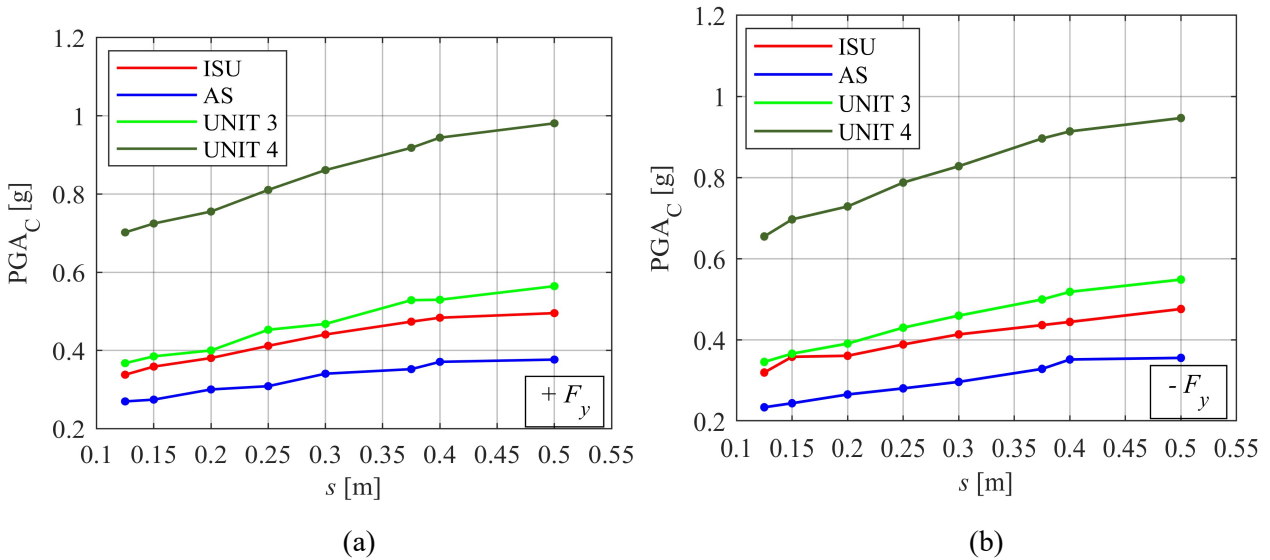


Figure 6.43: Relation between  $s$  and  $PGA_C$ , considering all the accelerograms for each value of  $s$ : (a) seismic forces  $+F_y$  and (b) seismic forces  $-F_y$ .

The simulations of this second application allow to generate a simplified Response Surface, defined by means of a quadratic polynomial, whose equation used to study the clay brick isolated structural unit and aggregate structure is set as:

$$\log(PGA_{C,i,j}) = \beta_0 + \beta_1 x_{1,i} + \beta_2 x_{1,i}^2 + \delta_{sis,j} + \varepsilon_{i,j} \tag{6.3}$$

where  $x_1$  is the selected explicit variable ( $s$ ),  $i$  stands for the  $i$ -th simulation,  $j$  for the  $j$ -th block and  $\varepsilon$  represents the errors. The regression is obtained through the Ordinary Least Squares method (Section 3.3.1.1), approximating the structural response by the polynomial function defined in Equation 6.3.

In the following the results referred to the 4 seismic action cases ( $+F_x$ ,  $-F_x$ ,  $+F_y$ ,  $-F_y$ ) are given. The RS models show the relation of the response parameter ( $\log(\text{PGA}_C)$ ) with the selected explicit variables  $s$ . The following Tables give the regression parameters obtained for each explicit variable ( $s$ ,  $s^2$ ) and the standard deviations related to the implicit variables ( $\delta_{\text{sis}}$  and the random error  $\varepsilon$ ). The following Figures show the sections of the RS models (continuous lines) obtained changing the values of the variable  $s$  and the sections (dashed lines) obtained adding and subtracting the RS variance  $\sigma = \sqrt{\sigma_{\varepsilon}^2 + \sigma_{\text{sis}}^2}$ ; the points are those corresponding to the various simulations used to calibrate the RS models.

Regarding the  $x$ -direction, the regression parameters  $\beta_1$  (Tables 6.16 and 6.17) related to the variable  $s$  are positive, for both the ISU and the AS: as expected, the value of the  $\text{PGA}_C$  increases as the values of the thickness of the walls increase. The comparison between the RS models referred to the ISU (Figures 6.44(a) and 6.45(a)) and those referred to the AS (Figure 6.44(b) and 6.45(b)) shows that the aggregation of identical structural units in row leads to a decrease of the vulnerability, due to the consideration on the geometrical properties of the walls discussed in Section 6.3.4.

For the seismic action in  $y$ -direction, the coefficients of the linear terms  $\beta_1$  are also positive (Tables 6.18, 6.19, 6.20 and 6.21). Figures 6.46(a) and 6.47(a) show the RS models obtained for the ISU and Figures 6.46(b) and 6.47(b) show those referred to the AS, which indicate a decrease of the collapse PGA, due to the torsional effects, when the aggregation is considered in  $y$ -direction.

As mentioned before, the failure of the aggregate structure is due to the shear failure of the masonry walls of Units 1 and 2. Figures 6.48 and 6.49 show the RS models obtained continuing the analysis over the attainment of the LS limit state, allowing to reach larger values of displacement, corresponding to the failure of the central Unit 3 and Unit 4, which are associated to higher values of the collapse PGA.

The results also confirm that the values of the collapse PGA for the  $y$ -direction are larger than those obtained for the  $x$ -direction, due to the different geometrical properties of the resisting walls in the two directions, and the results in terms of capacity are the same: in  $x$ -direction the weaker direction is the positive ( $+F_x$ ), in  $y$ -direction is the negative one ( $-F_y$ ).

- *x-direction*

Table 6.16: Regression parameters and standard deviations of the ISU and AS RS models, considering the seismic forces +  $F_x$ .

Structure	Variable	$\beta_i$	Variable	$\sigma$
ISU	$s$	4.761	$\delta_{sis}$	0.235
	$s^2$	-4.392	$\varepsilon$	0.117
AS	$s$	3.355	$\delta_{sis}$	0.214
	$s^2$	-3.011	$\varepsilon$	0.102

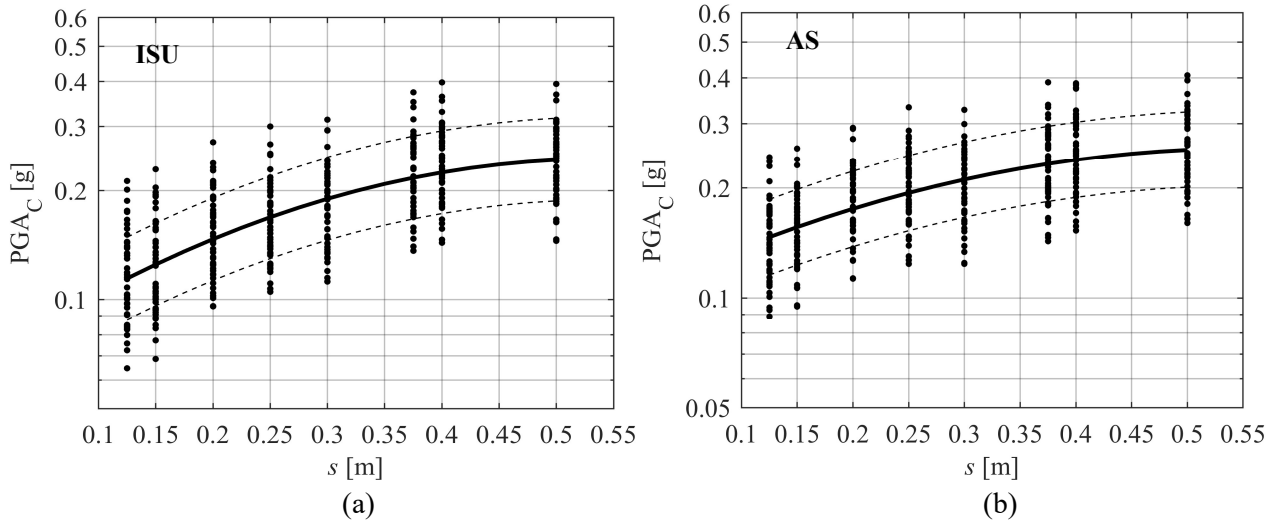


Figure 6.44: Response Surface sections for (a) the ISU and (b) the AS, considering the seismic forces +  $F_x$ .

Table 6.17: Regression parameters and standard deviations of the ISU and AS RS models, considering the seismic forces -  $F_x$ .

Structure	Variable	$\beta_i$	Variable	$\sigma$
ISU	$s$	2.853	$\delta_{sis}$	0.232
	$s^2$	-2.118	$\varepsilon$	0.076
AS	$s$	3.545	$\delta_{sis}$	0.230
	$s^2$	-3.599	$\varepsilon$	0.085

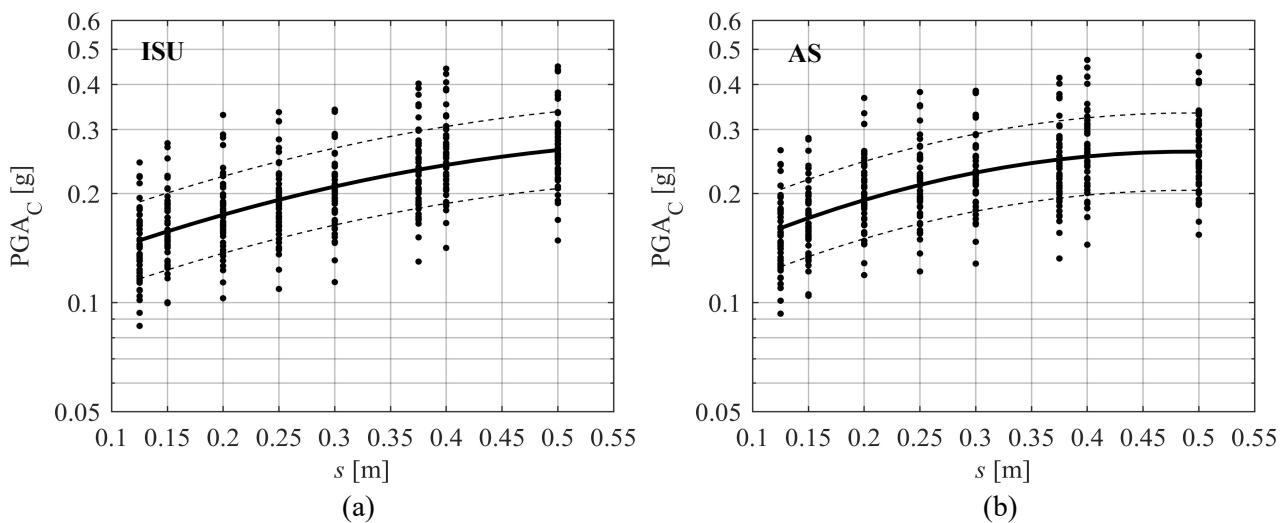


Figure 6.45: Response Surface sections for (a) the ISU and (b) the AS, considering the seismic forces -  $F_x$ .

- *y*-direction

Table 6.18: Regression parameters and standard deviations of the ISU and AS RS models, considering the seismic forces +  $F_y$ .

Structure	Variable	$\beta_i$	Variable	$\sigma$
ISU	$s$	2.514	$\delta_{\text{sis}}$	0.179
	$s^2$	-2.731	$\varepsilon$	0.130
AS	$s$	2.062	$\delta_{\text{sis}}$	0.180
	$s^2$	-1.790	$\varepsilon$	0.134

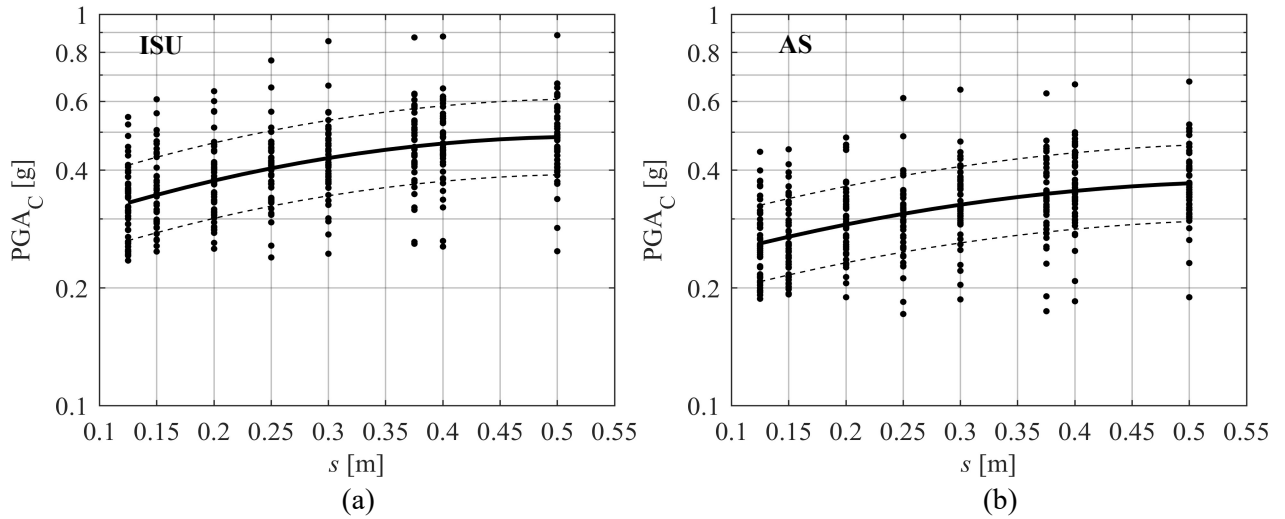


Figure 6.46: Response Surface sections for (a) the ISU and (b) the AS, considering the seismic forces +  $F_y$ .

Table 6.19: Regression parameters and standard deviations of the ISU and AS RS models, considering the seismic forces -  $F_y$ .

Structure	Variable	$\beta_i$	Variable	$\sigma$
ISU	$s$	1.811	$\delta_{\text{sis}}$	0.173
	$s^2$	-1.351	$\varepsilon$	0.151
AS	$s$	2.164	$\delta_{\text{sis}}$	0.184
	$s^2$	-1.590	$\varepsilon$	0.150

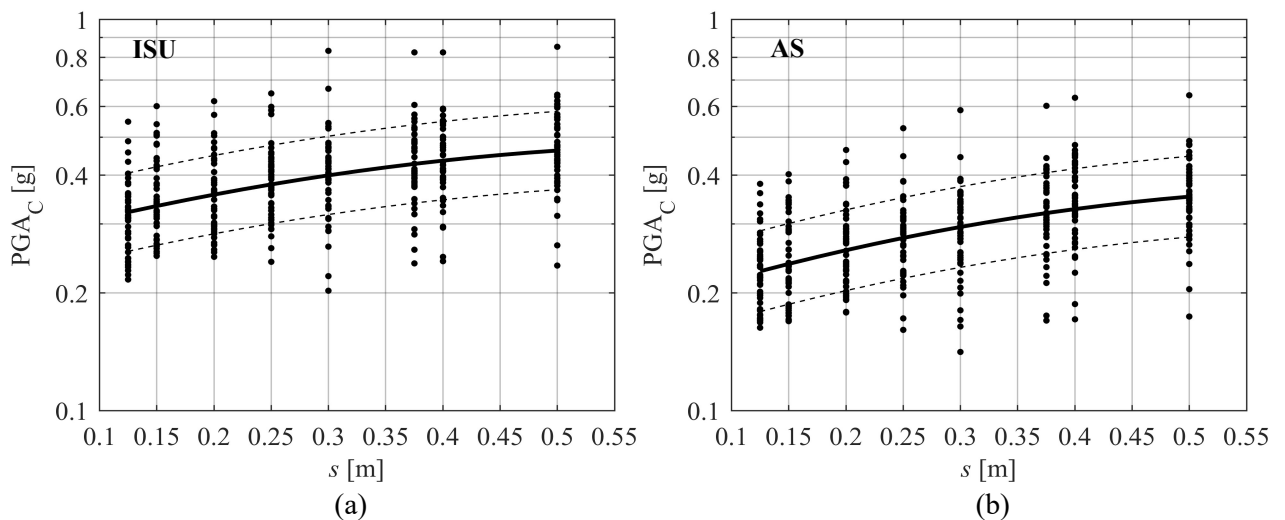


Figure 6.47: Response Surface sections for (a) the ISU and (b) the AS, considering the seismic forces -  $F_y$ .

- *y*-direction, over the attainment of the LS limit state

Table 6.20: Regression parameters and standard deviations of the Unit 3 and Unit 4 RS models, considering the seismic forces +  $F_y$ .

Structure	Variable	$\beta_i$	Variable	$\sigma$
UNIT 3	$s$	2.084	$\delta_{sis}$	0.199
	$s^2$	-1.457	$\varepsilon$	0.146
UNIT 4	$s$	1.702	$\delta_{sis}$	0.191
	$s^2$	-1.257	$\varepsilon$	0.139

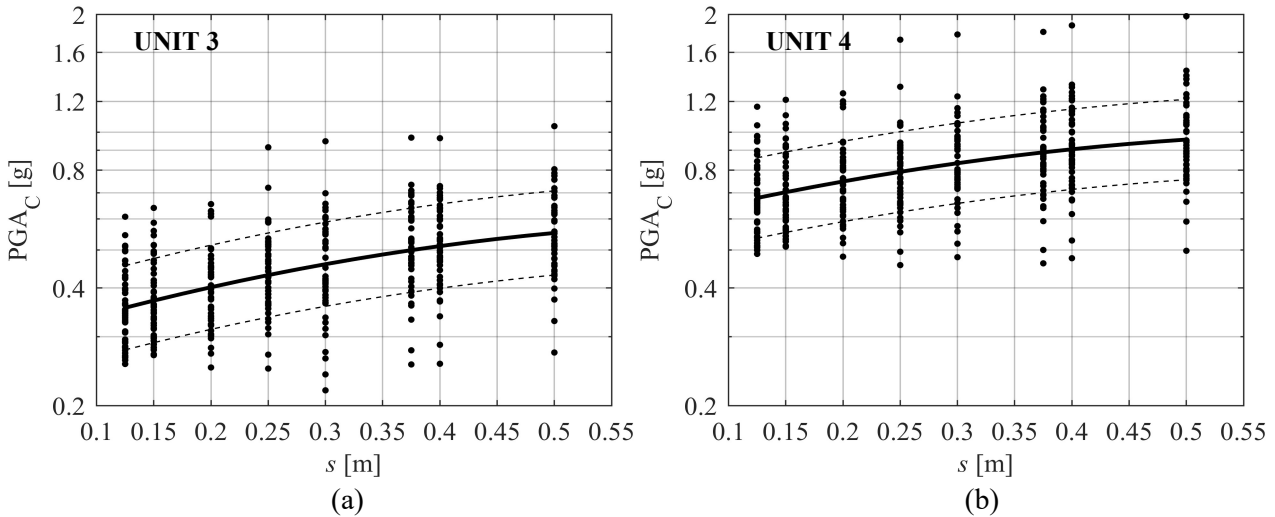


Figure 6.48: RS sections for (a) the Unit 3 and (b) the Unit 4, considering the seismic forces +  $F_y$ .

Table 6.21: Regression parameters and standard deviations of the Unit 3 and Unit 4 RS models, considering the seismic forces -  $F_y$ .

Structure	Variable	$\beta_i$	Variable	$\sigma$
UNIT 3	$s$	2.406	$\delta_{sis}$	0.189
	$s^2$	-1.894	$\varepsilon$	0.152
UNIT 4	$s$	2.097	$\delta_{sis}$	0.182
	$s^2$	-1.799	$\varepsilon$	0.147

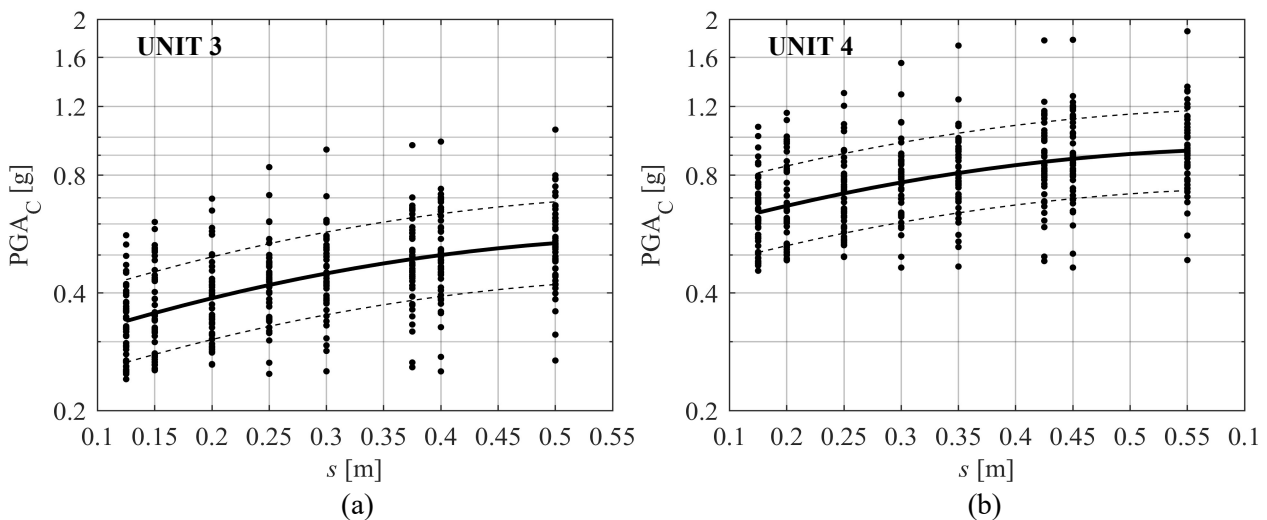


Figure 6.49: RS sections for (a) the Unit 3 and (b) the Unit 4, considering the seismic forces -  $F_y$ .

### 6.3.6 Fragility curves

The obtained RS models were used to estimate the fragility curves of the masonry isolated structural units and the masonry aggregate structures. The fragility analysis was assessed adopting the limit state function in Equation 2.5, rewritten in the form:

$$g(x_1, \beta_1, \varepsilon, \delta_{\text{sis}} | \text{PGA}_D) = \log(\text{PGA}_C) - \log(\text{PGA}_D) = \beta_0 + \beta_1 x_1 + \beta_2 x_1^2 + \delta_{\text{sis}} + \varepsilon - \log(\text{PGA}_D) \quad (6.4)$$

Four fragility curves were then obtained for the seismic action in  $x$ -direction (Figure 6.50 (a)) and eight for the  $y$ -direction (Figure 6.50 (b)), using the same procedure adopted in Section 6.2.5. For each direction the fragility curves are shown distinguishing the positive ( $+F_x$  and  $+F_y$ ) and negative ( $-F_x$  and  $-F_y$ ) seismic actions, highlighting the same considerations on the geometrical properties of the walls discussed in Section 6.2.3.

The curves indicate greater fragility for the seismic action in  $x$ -direction due to the geometry, the number of openings and the arrangement of the resisting walls in this direction. Moreover, in  $x$ -direction, aggregating identical structural units in a row decreases the fragility, compared with that of the isolated structural units. On the contrary, the fragility is higher in  $y$ -direction, due to the torsional effects affecting the external Unit 1 and Unit 2, decreasing the total collapse PGA, when referred to the first attainment of the displacement capacity. If, instead, higher values of the ultimate displacements are allowed, corresponding to the attainment of displacement capacity of the central Unit 3 and Unit 4, higher values of collapse PGA are obtained. In particular, a considerable difference it was found between Unit 4 and the other Units, due to the torsional effects more accentuated in the external Units (1-2-3): Figures 6.37 and 6.39 show that the displacement of the Unit 4 is almost twice that of the Unit 3.

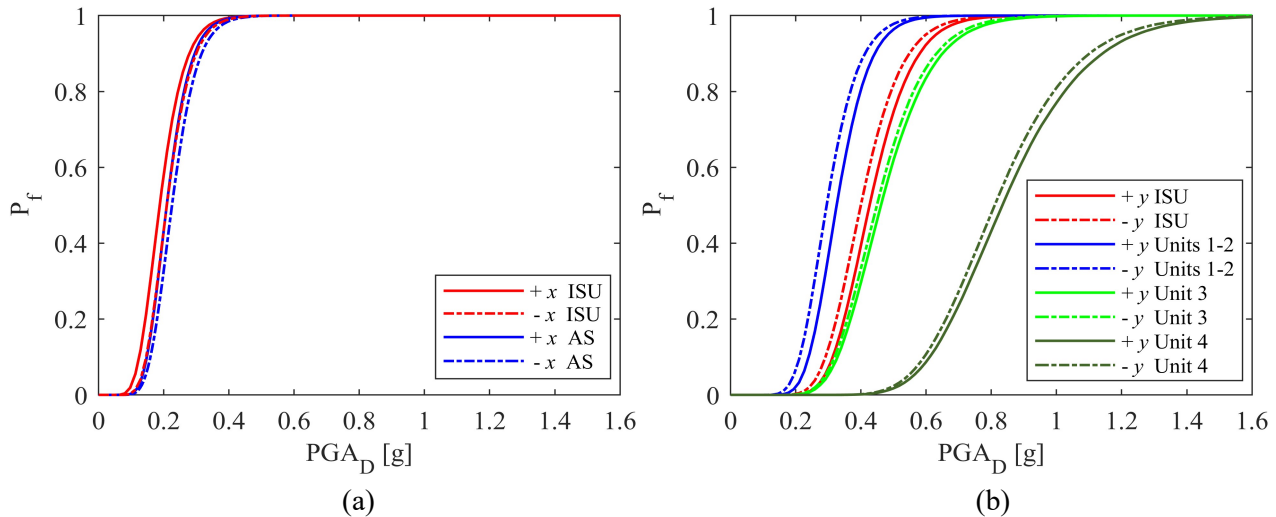


Figure 6.50: Fragility curves considering (a) the  $x$ -direction and (b) the  $y$ -direction of the seismic action.

## 6.4 Aggregations of different structural units in row

### 6.4.1 Introduction

Once the seismic fragility analyses of identical structural units aggregated in row were carried out in Section 6.3, the aggregate structures object of the current Section consider different structural units each other, aggregated in row. It is very common to find aggregations of different, but similar, masonry structural units in row in the Italian historic centres, commonly due to the urban growth characterized by the development of similar construction techniques in the same historic period.

Thus, this Section is focused on the study of unreinforced masonry aggregates in row, considering structural units differing each other along the aggregate structures, generated starting from the medium values of the variables used for RS models studied in Section 6.2 and 6.3. The same methodology was applied: once the simulations of the RS model were defined, a set of non-linear static analyses was performed using TreMuri software, considering two orthogonal directions of the seismic action; afterwards, the data obtained from the analyses were used to plot the fragility curves.

The purpose is to analyse how the considered differences affect the seismic response in the global behaviour of the aggregate structures, evaluating which are the parameters most influencing the seismic behaviour of the various structural units sited in different positions along the aggregates.

### 6.4.2 RS model: definition of the structural units along the aggregates

The masonry aggregate buildings object of this Section were generated starting from the same structural units analysed in Section 6.2 and 6.3: three-storeys masonry buildings, with clay brick walls, hollow-core concrete slabs and pitched roof made by timber beams. Figure 6.51 shows a tri-dimensional view of the masonry aggregate and Figure 6.52 shows the structural plan of the ground floor, referring to a model chosen as example of one of the row-aggregations of different structural units analysed in this Section. In Figure 6.52 the differences in terms of thickness of the walls and distance between the walls in  $x$ -direction are highlighted; as in Section 6.3 the thickness of the masonry walls between two adjacent buildings is equal to the summation of the two thicknesses, to ensure that the aggregate structure is a combination of the structural units.

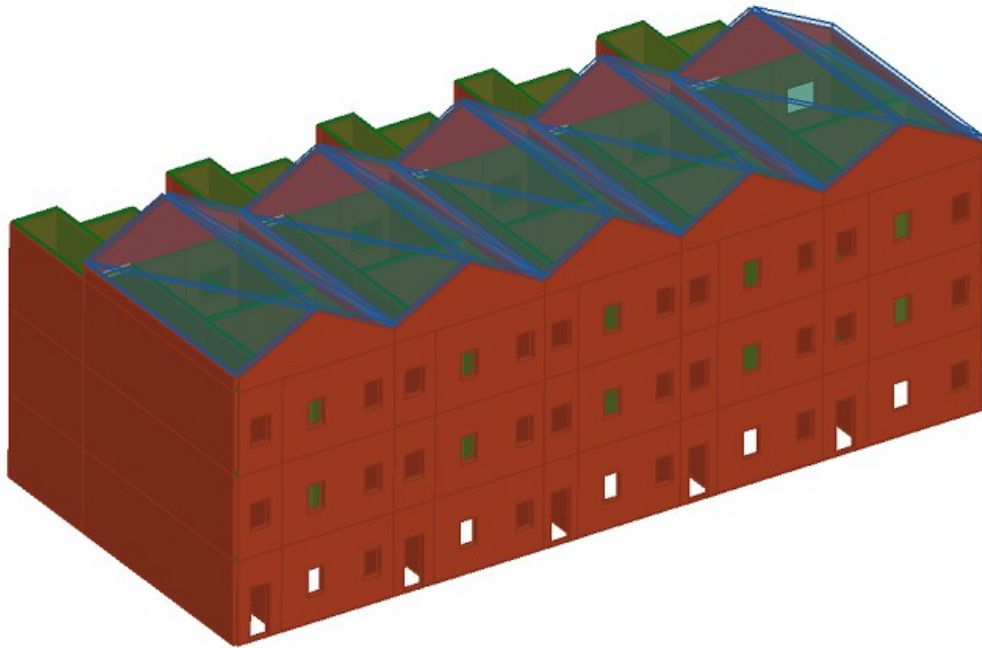


Figure 6.51: Model of the 3D masonry aggregate with different structural units.

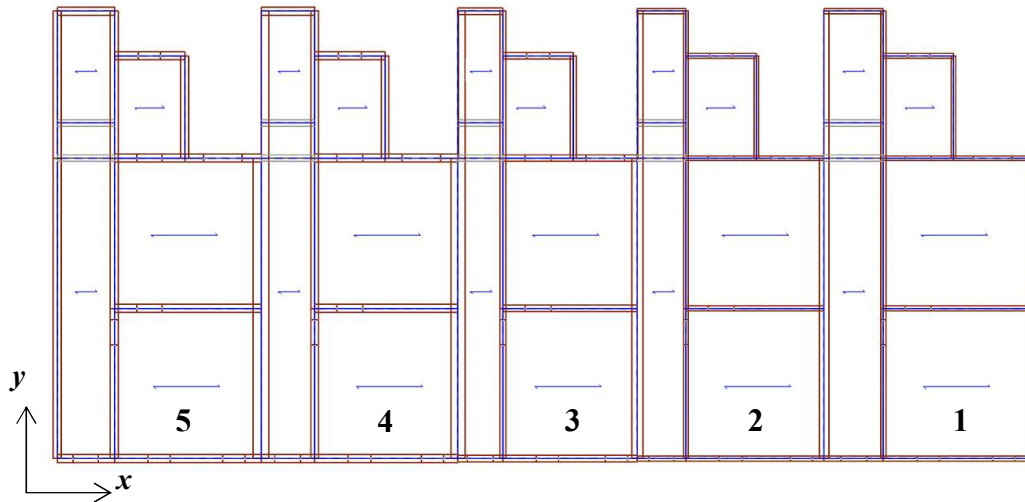


Figure 6.52: Plan of the structural ground floor of the masonry aggregate with different structural units.

As in the applications of the Sections 6.2 and 6.3, the definition of the simulations to calibrate the Response Surface model is carried out by means of the choice of the explicit and implicit variables.

- *Explicit variables*

In this application it was assumed the choice of the same explicit variables defined for the RS model in Section 6.2 (mean masonry shear strength ( $\tau$ ) and mean distance between external walls in  $x$ -direction ( $d$ )), except for the mean slab elastic modulus ( $E_1$ ), considered in this application in a deterministic way with a fixed value, as it was shown that it does not affect the seismic response. The two explicit variables ( $\tau$  and  $d$ ) were defined with the same normal distributions (Figures 6.3(a) and 6.3(c)) and the same assumption of the values (Table 6.6) adopted in Section 6.2.

As already mentioned, the variable values are selected following the Design of Experiment Theory (Section 3.3.3) to calibrate the RS model. Therefore, using Equation 3.32 and according to the Central Composite Design the simulations are defined as following:

- $2^2$  simulations, considering all the combinations of the two explicit coded variables ( $X_i = \mu \pm 1.5\sigma \rightarrow x_i = \pm 1$ );
- 2 axial points for each variables ( $X_i = \mu \pm 2\sigma \rightarrow x_i = \pm 1.33$ );
- 3 central points ( $X_i = \mu \rightarrow x_i = 0$ ).

Thus, the total number of a group of simulations is 11; it is repeated several times, according to the definition of the blocks for the implicit variables.

Table 6.22 gives the definition of the group of 11 simulations, setting the coded variables as  $x_1 = \tau$  and  $x_2 = d$ , and Figure 6.53 shows the region of interest for the two selected variables: since the variables are two, the region of interest is represented by 4 vertices defining a square.

Table 6.22: Definition of the group of 11 simulations using the coded variables  $x_i$ .

$x_1$	1	-1	1	-1	0	0	0	1.33	-1.33	0	0
$x_2$	1	1	-1	-1	0	0	0	0	0	1.33	-1.33

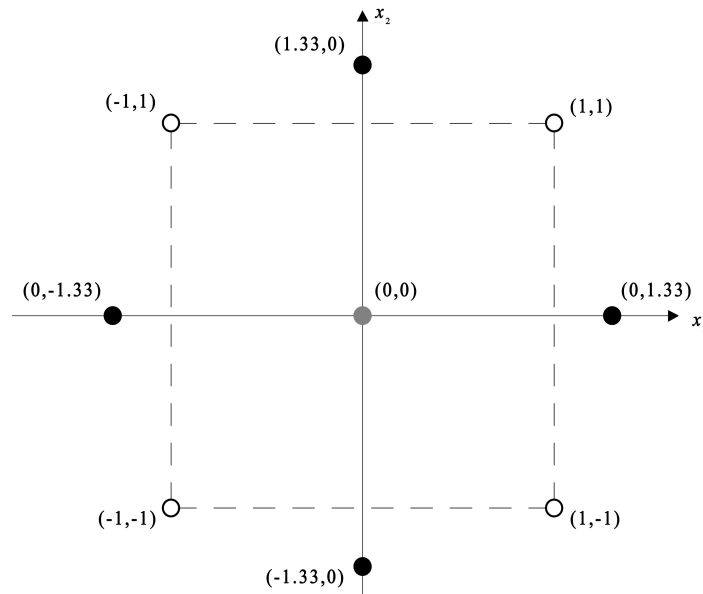


Figure 6.53: Region of interest for the 2 coded variables  $x_i$ .

#### - *Implicit variables*

In this application, three implicit variables were chosen: the uncertainty of the seismic action ( $\delta_{\text{sis}}$ ), the uncertainty of the distance between the walls in  $x$ -direction ( $\delta_d$ ) and the uncertainty of the thickness of the walls ( $\delta_s$ ).

As far as  $\delta_{\text{sis}}$  is concerned, the group of 48 accelerograms defined in Section 5.4 was used in order to consider the variability of the seismic action. For each of the 11 simulations, according to the Design of Experiment Theory, 2 accelerograms were associated to the factorial region and 1 accelerogram was associated to the axial and central points. Thus, each group of 11 simulations is related to 3 blocks  $\delta_{\text{sis}}$  and it is repeated 16 times (the total number of blocks is 48).

$\delta_d$  and  $\delta_s$  represent the implicit variables defining the different geometrical properties of the structural units along the aggregate.  $\delta_d$  is the uncertainty of the distance between the walls in  $x$ -direction ( $d$ ) and it allows to define a different value of  $d$  for each structural unit along the

aggregates. For each of the 5 values of  $d$  (Table 6.6) a normal distribution was defined and 8 groups of 5 values (5 as the number of the structural units in row) was randomly selected in the distributions: in total 40 groups  $\delta_d$  were selected, defining 40 different aggregate configurations. Figure 6.54 shows the 5 normal distributions used for each value of  $d$ .

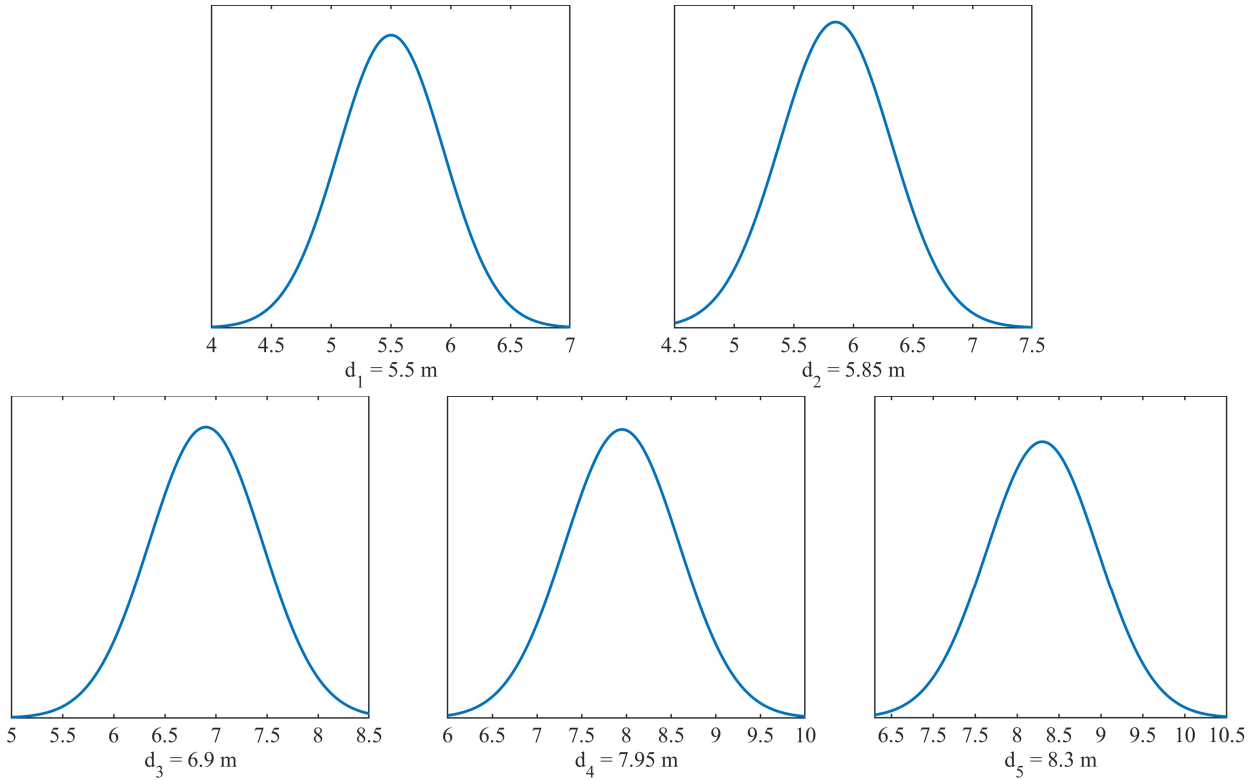


Figure 6.54: Gaussian distributions defined for the 5 distances between walls in  $x$ -direction ( $d$ ).

As far as  $\delta_s$  is concerned, the thickness of the walls  $s$  was considered as implicit variable and the variation of its values depends on the variation of the values of the distance  $d$ : each aggregate configuration was generated in such a way as to have greater  $s$  with greater  $d$ . The values of the thickness  $s$  are the same used in Table 6.13: in this application they were divided in 5 groups of 3 values (Figure 6.55), from  $s_1$  to  $s_5$ , and for each generated aggregate configuration 5 random values of  $s$  (5 as the number of the structural units in row) were obtained from the 5 groups of  $s$ .

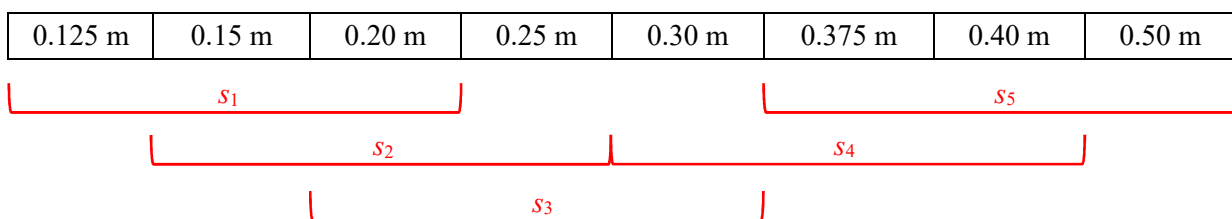


Figure 6.55: Groups of  $s$  for the definition of the blocks  $\delta_s$ .

Thus, each aggregate configuration was generated selecting every time 5 random different values of the distance ( $d$ ) from the correspondent distribution of  $d$  and 5 random values of  $s$  from the correspondent group of  $s$ , in such a way as to have the correspondence between  $d_i$  and  $s_i$  ( $i$  assumes values from 1 to 5). Table 6.23 gives the definition of the 40 aggregate configurations, obtained with the selections of  $d$  and  $s$  for each structural unit (from US1 to US5) along the aggregate structures (Figure 6.56). Each aggregate configuration is represented by a block  $\delta_d$  and a block  $\delta_s$  (the numeration of the blocks is indicated between the brackets in the column of the blocks). The values of  $d$  and  $s$  in Table 6.23 are given in meters.

Summarizing, the division in blocks for the implicit variables is obtained as following:

- 48 blocks of  $\delta_{sis}$ , divided in 16 groups of 3 blocks for a set of 11 simulations;
- 40 blocks of  $\delta_d$ , divided in 8 groups of 5 blocks for a set of 22 (11x2) simulations;
- 40 blocks of  $\delta_s$ , divided in 8 groups of 5 blocks for a set of 22 (11x2) simulations.

The partition in blocks, associated to the groups of explicit variables, generates 176 simulations in total. Table B.3 in Appendix B gives the design matrix containing the 176 simulations with the combinations of the explicit and implicit variables, according to the Design of Experiment Theory and the division in blocks.

Following these criteria, the structural units along each aggregate configuration differ each other just in the geometrical properties ( $d$  and  $s$ ); instead, the different aggregate configurations differ each other in both structural and geometrical properties ( $\tau$ ,  $d$  and  $s$ ), according to the definition of the RS simulations.

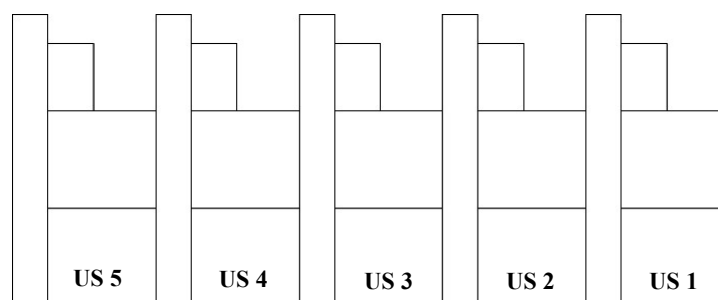


Figure 6.56: Numeration of the structural units along the aggregate.

Table 6.23: Definition of the aggregate configurations.

AGGREGATE CONFIGURATION	BLOCK	US 5	US 4	US 3	US 2	US 1
1	$\delta_{d1}$ (1)	5.11	5.89	5.76	5.35	5.50
	$\delta_{s1}$ (1)	0.2	0.2	0.125	0.15	0.125
2	$\delta_{d2}$ (2)	5.52	5.80	5.83	5.99	5.94
	$\delta_{s2}$ (2)	0.25	0.15	0.2	0.25	0.2
3	$\delta_{d3}$ (3)	7.59	7.04	7.25	6.91	5.95
	$\delta_{s3}$ (3)	0.2	0.3	0.3	0.2	0.25
4	$\delta_{d4}$ (4)	8.56	7.22	7.86	6.93	7.40
	$\delta_{s4}$ (4)	0.375	0.3	0.3	0.4	0.375
5	$\delta_{d5}$ (5)	8.24	8.27	7.62	8.36	7.59
	$\delta_{s5}$ (5)	0.375	0.5	0.5	0.5	0.4
6	$\delta_{d1}$ (6)	5.64	5.54	6.11	5.61	5.59
	$\delta_{s1}$ (6)	0.2	0.2	0.125	0.2	0.15
7	$\delta_{d2}$ (7)	5.99	6.21	5.27	5.86	6.30
	$\delta_{s2}$ (7)	0.25	0.15	0.15	0.25	0.15
8	$\delta_{d3}$ (8)	6.99	7.39	6.90	6.70	6.63
	$\delta_{s3}$ (8)	0.25	0.25	0.3	0.3	0.25
9	$\delta_{d4}$ (9)	7.17	7.69	8.84	7.82	7.45
	$\delta_{s4}$ (9)	0.375	0.375	0.4	0.375	0.4
10	$\delta_{d5}$ (10)	8.28	8.54	8.64	9.30	8.06
	$\delta_{s5}$ (10)	0.5	0.375	0.4	0.5	0.375
11	$\delta_{d1}$ (11)	5.79	5.25	6.31	5.63	5.32
	$\delta_{s1}$ (11)	0.15	0.125	0.2	0.2	0.15
12	$\delta_{d2}$ (12)	6.37	6.16	5.61	5.84	6.50
	$\delta_{s2}$ (12)	0.25	0.25	0.2	0.15	0.15
13	$\delta_{d3}$ (13)	6.93	6.44	6.45	6.55	7.49
	$\delta_{s3}$ (13)	0.2	0.2	0.25	0.2	0.2
14	$\delta_{d4}$ (14)	7.27	7.13	8.15	8.68	7.73
	$\delta_{s4}$ (14)	0.3	0.4	0.4	0.3	0.375
15	$\delta_{d5}$ (15)	8.43	7.79	8.33	9.49	8.93
	$\delta_{s5}$ (15)	0.4	0.5	0.375	0.375	0.5
16	$\delta_{d1}$ (16)	5.86	5.72	4.67	5.20	5.79
	$\delta_{s1}$ (16)	0.125	0.125	0.2	0.2	0.15
17	$\delta_{d2}$ (17)	5.64	6.03	6.00	5.85	5.41
	$\delta_{s2}$ (17)	0.15	0.25	0.2	0.15	0.15
18	$\delta_{d3}$ (18)	7.67	7.21	6.96	6.62	6.60
	$\delta_{s3}$ (18)	0.25	0.2	0.3	0.2	0.2
19	$\delta_{d4}$ (19)	8.11	8.00	7.61	8.37	8.36
	$\delta_{s4}$ (19)	0.375	0.4	0.375	0.375	0.4
20	$\delta_{d5}$ (20)	7.61	8.66	8.13	9.03	8.41
	$\delta_{s5}$ (20)	0.4	0.375	0.375	0.4	0.4
21	$\delta_{d1}$ (21)	5.50	5.29	4.72	5.14	5.60
	$\delta_{s1}$ (21)	0.15	0.125	0.2	0.125	0.2
22	$\delta_{d2}$ (22)	5.63	6.21	5.33	6.28	6.21
	$\delta_{s2}$ (22)	0.2	0.25	0.25	0.2	0.2
23	$\delta_{d3}$ (23)	5.92	7.71	7.01	6.42	7.88
	$\delta_{s3}$ (23)	0.2	0.2	0.3	0.3	0.25
24	$\delta_{d4}$ (24)	7.92	8.05	7.80	8.05	9.26
	$\delta_{s4}$ (24)	0.4	0.3	0.375	0.3	0.4
25	$\delta_{d5}$ (25)	8.65	8.05	7.94	8.08	8.46
	$\delta_{s5}$ (25)	0.375	0.4	0.5	0.375	0.4

26	$\delta_{d1}$ (26)	5.40	5.60	5.09	5.85	5.41
	$\delta_{s1}$ (26)	0.15	0.2	0.125	0.2	0.15
27	$\delta_{d2}$ (27)	5.18	6.56	6.07	5.81	5.96
	$\delta_{s2}$ (27)	0.25	0.15	0.2	0.15	0.2
28	$\delta_{d3}$ (28)	7.08	6.43	6.65	6.33	6.47
	$\delta_{s3}$ (28)	0.2	0.25	0.25	0.3	0.25
29	$\delta_{d4}$ (29)	7.49	8.38	7.61	9.09	8.46
	$\delta_{s4}$ (29)	0.4	0.375	0.4	0.3	0.375
30	$\delta_{d5}$ (30)	6.83	7.20	9.41	7.91	9.05
	$\delta_{s5}$ (30)	0.4	0.5	0.375	0.5	0.375
31	$\delta_{d1}$ (31)	5.79	5.84	4.70	5.33	5.48
	$\delta_{s1}$ (31)	0.2	0.125	0.2	0.15	0.2
32	$\delta_{d2}$ (32)	5.39	6.12	6.00	4.61	5.75
	$\delta_{s2}$ (32)	0.2	0.15	0.15	0.25	0.2
33	$\delta_{d3}$ (33)	6.32	6.35	6.28	7.60	6.48
	$\delta_{s3}$ (33)	0.3	0.3	0.3	0.25	0.2
34	$\delta_{d4}$ (34)	8.16	7.26	8.87	7.58	7.27
	$\delta_{s4}$ (34)	0.375	0.4	0.4	0.4	0.3
35	$\delta_{d5}$ (35)	8.37	8.09	9.08	8.80	8.46
	$\delta_{s5}$ (35)	0.4	0.5	0.5	0.375	0.5
36	$\delta_{d1}$ (36)	6.36	5.91	5.34	4.90	5.70
	$\delta_{s1}$ (36)	0.125	0.2	0.15	0.2	0.125
37	$\delta_{d2}$ (37)	6.13	6.05	5.90	5.62	5.86
	$\delta_{s2}$ (37)	0.2	0.2	0.15	0.15	0.2
38	$\delta_{d3}$ (38)	6.54	6.89	7.14	6.77	6.33
	$\delta_{s3}$ (38)	0.3	0.2	0.2	0.25	0.3
39	$\delta_{d4}$ (39)	8.43	8.14	7.62	8.11	7.82
	$\delta_{s4}$ (39)	0.3	0.4	0.3	0.3	0.375
40	$\delta_{d5}$ (40)	8.59	7.89	8.17	7.73	7.54
	$\delta_{s5}$ (40)	0.375	0.5	0.5	0.4	0.5

### 6.4.3 Push-over analyses

The aggregate configurations obtained were analysed performing non-linear static analyses (push-over), using TreMuri software, to obtain the data required to calibrate the Response Surface models. Two orthogonal directions ( $x$  and  $y$ ) of the seismic action are considered (Figure 5.3) and the distribution of the forces applied (proportional to the masses) was considered with both signs ( $+F$  and  $-F$ ), generating 176 capacity curves for each studied case; furthermore, in the  $y$ -direction the analyses over the attainment of the LS limit state were performed, to evaluate the collapse of the structural units in different positions along the aggregate.

#### - $x$ -direction

Figures 6.57(a) and (b) show the capacity curves obtained from the analyses in  $x$ -direction, considering the seismic forces  $+F_x$  and  $-F_x$  respectively. In terms of capacity and ductility,

the curves confirm what already discussed in the previous Sections: the geometrical arrangement and configuration of the masonry walls in  $x$ -direction makes the masonry aggregate structures weaker to the application of the forces  $+F_x$ , being the main collapse mechanism the flexural one. The curves in Figure 6.57(a) show the achievement of lower ultimate displacements, corresponding to the attainment of the LS limit state, and a progressive decrement of the total capacity allowing to reach the collapse of the  $x$ -direction walls before than that related to the case  $-F_x$ . Thus, an increment of the collapse PGA is expected if the application of the seismic forces  $-F_x$  is considered.

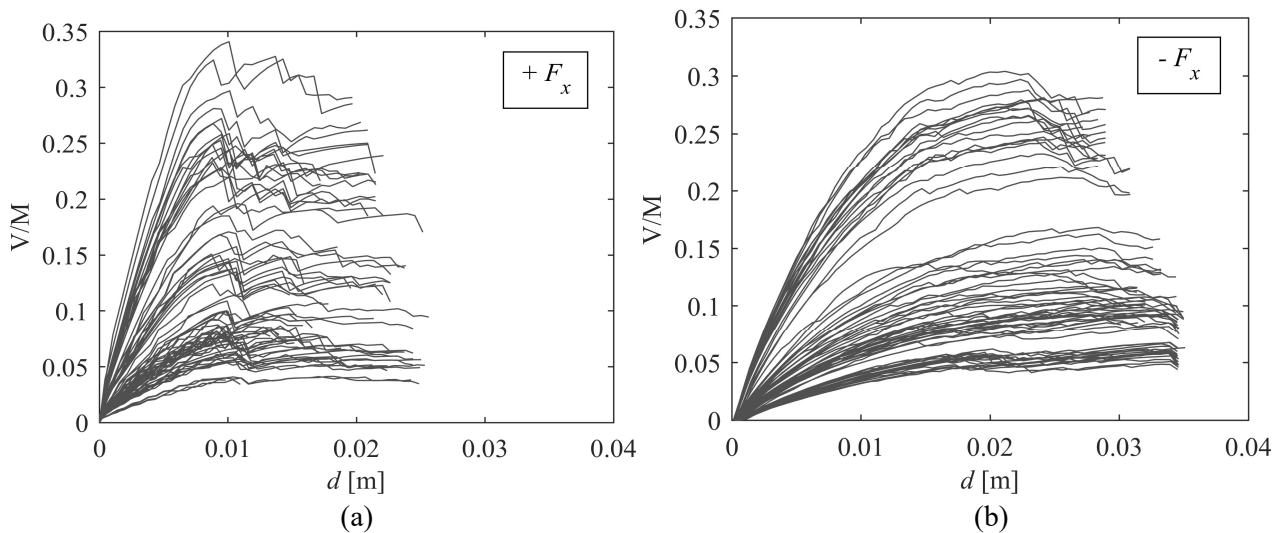


Figure 6.57: Capacity curves from the analyses in  $x$ -direction: seismic forces (a)  $+F_x$  and (b)  $-F_x$ .

#### - $y$ -direction

Figures 6.58(a) and (b) show the capacity curves obtained from the analyses in  $y$ -direction, considering the seismic forces  $+F_y$  and  $-F_y$  respectively. The curves show higher capacity with respect to the  $x$ -direction, due to the geometrical configuration of the walls in  $y$ -direction, being stocky and with a reduced quantity of openings. The seismic behaviours in terms of capacity and ductility are very similar and they are characterised by the shear failure mechanism; however, the aggregate structures show more weakness to the application of the seismic forces  $-F_y$ , due to the geometrical configuration of the walls making asymmetric the buildings and allowing the activation of torsional mechanisms, decreasing the total capacity. Thus, an increment of the collapse PGA is expected if the application of the seismic forces  $+F_y$  is considered.

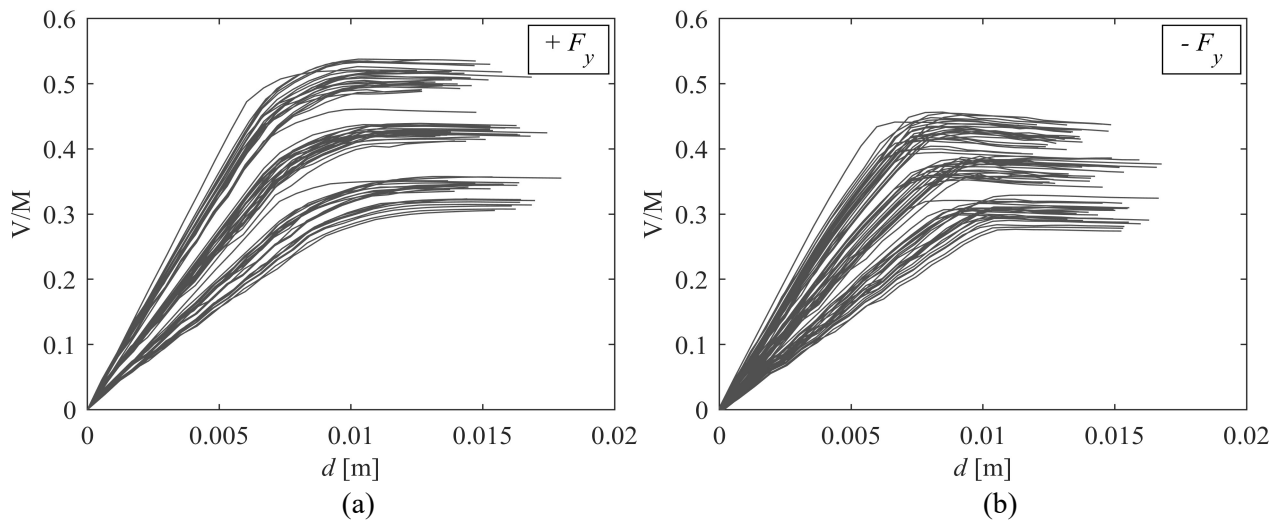


Figure 6.58: Capacity curves from the analyses in  $y$ -direction: seismic forces (a)  $+F_y$  and (b)  $-F_y$ .

-  $y$ -direction, over the attainment of the LS limit state

As for the application shown in Section 6.3, the analyses over the attainment of the LS limit state were carried out in this Section. If the LS limit state is considered as limit for the analyses, only the masonry walls belonging to the external Units 1 and 2 reach the collapse for shear, before than the walls of the other Units, due to the torsional effects affecting them. Thus, the analyses over the attainment of the LS limit state allowed the  $y$ -direction masonry walls to reach the collapse for shear and to define a hierarchy of collapse of the various structural Units along the aggregate structures, showed in Figures 6.59 ( $+F_y$ ) and 6.60 ( $-F_y$ ). The curves in the Figures highlight different levels of vulnerability between the structural units: larger values of the collapse PGA are expected for the structural units occupying the internal positions along the aggregate, being affect by lower torsional effects and showing a greater stiffness against the seismic action in  $y$ -direction.

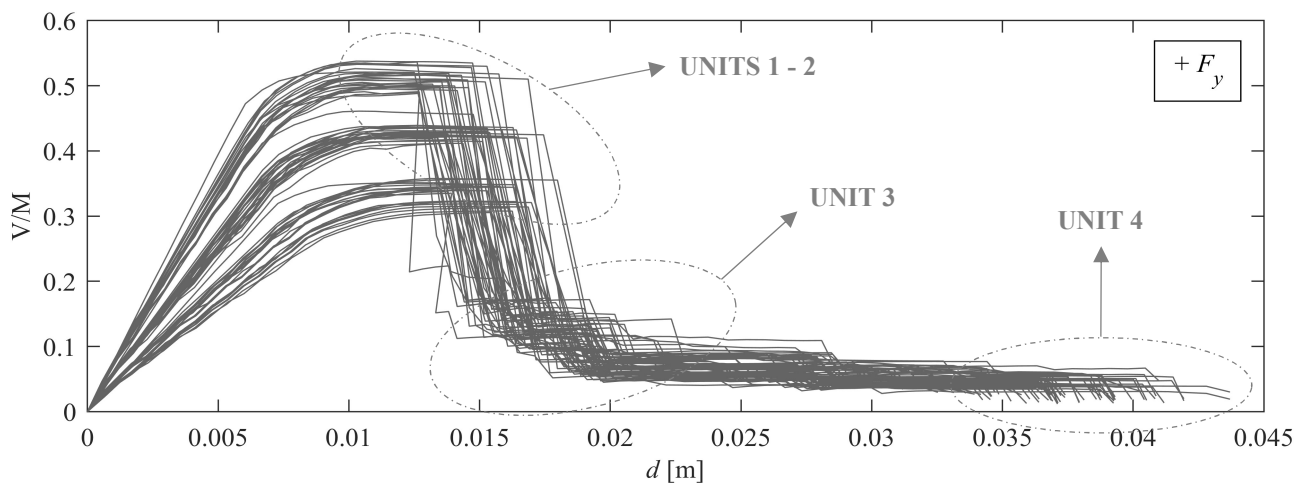


Figure 6.59: Capacity curves from the analyses in  $y$ -direction ( $+F_y$ ) over the attainment of the LS limit state.

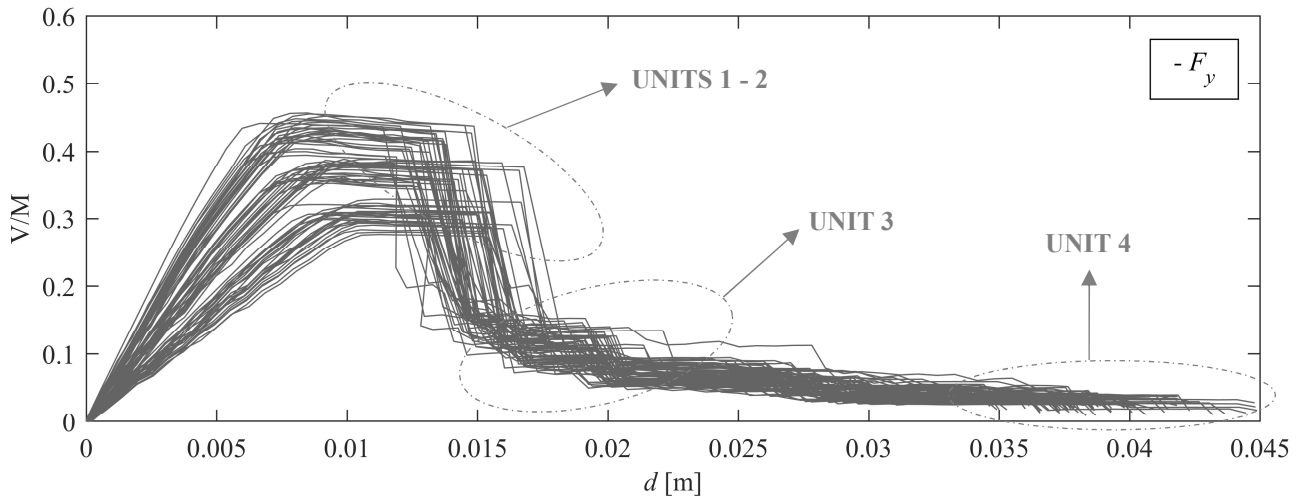


Figure 6.60: Capacity curves from the analyses in  $y$ -direction ( $-F_y$ ) over the attainment of the LS limit state.

#### 6.4.4 Response Surface models

The simulations of this application allow to calibrate the Response Surface models, defined by means of a quadratic polynomial, whose equation used to study the masonry aggregate structures with different structural units is set as:

$$\log(\text{PGA}_{C,i,j,k,l}) = \beta_0 + \beta_1 x_{1,i} + \beta_2 x_{2,i} + \beta_3 x_{1,i}^2 + \beta_4 x_{2,i}^2 + \delta_{sis,j} + \delta_{d,k} + \delta_{s,l} + \varepsilon_{i,j,k,l} \quad (6.5)$$

where  $i$  stands for the  $i$ -th simulation,  $j$  for the  $j$ -th  $\delta_{sis}$  block,  $k$  for the  $k$ -th  $\delta_d$  block,  $l$  for the  $l$ -th  $\delta_s$  block and  $\varepsilon$  represents the errors. The regression is obtained through the Ordinary Least Squares method (Section 3.3.1.1), approximating the structural response by the polynomial function defined in Equation 6.5.

In the following the results referred to the various seismic action cases are given. The results of the RS allow to show how the parameters chosen as variables affect the seismic response of the selected masonry aggregate structures with different structural units, also highlighting the differences considering two orthogonal directions of the seismic action.

Tables 6.24, 6.25, 6.26, 6.27, 6.28, 6.29, 6.30 and 6.31 give the regression parameters obtained for each explicit variable ( $\tau$ ,  $d$ ,  $\tau^2$ ,  $d^2$ ) and the standard deviations related to the implicit variables ( $\delta_{sis}$ ,  $\delta_d$ ,  $\delta_s$  and the random error  $\varepsilon$ ). As for the  $x$ -direction, the regression parameters related to the variables  $\tau$  and  $d$  are always positive: as expected, the value of the  $\text{PGA}_C$  increases as the values of the two variables increase, for the considerations already discussed in Section 6.2.

As for the  $y$ -direction, the RS indicates a qualitatively similar relationship between the response parameter and the explicit variables, also for the variable  $d$ , differently from what was shown in Section 6.2: in this application, if  $d$  increases the values of the  $PGA_C$  increases, as well. This is due to the fact that the relation between  $d$  and  $PGA_C$  is also influenced by the thickness of the walls ( $s$ ), whose values increase as the values of the distance ( $d$ ) increase. Conversely, in the definition of the RS of the Section 6.2 the association between  $d$  and  $s$  is more random and simulations with high values of  $d$  associated to low values of  $s$ , and vice versa, were obtained. Therefore, the trend to decrease of the  $PGA_C$ , if  $d$  increases, is mitigated by the effect of the thickness of the walls ( $s$ ), making the curves relating  $d$  and  $PGA_C$  flatter. According to these motivations, the relation between  $d$  and  $PGA_C$  depends on the ratio between the values of  $\delta_d$  and  $\delta_s$ , randomly selected to obtain the 40 aggregate configurations (Table 6.23). Figure 6.61 shows the 200 (5 structural units times the 40 aggregate configurations) relations between  $d$  and  $s$ , highlighting the trend to have greater values of  $d$  with greater values of  $s$ . In the Figure below the thicknesses  $s$  are divided according to the definition of the 5 groups of  $s$ , given in Figure 6.55.

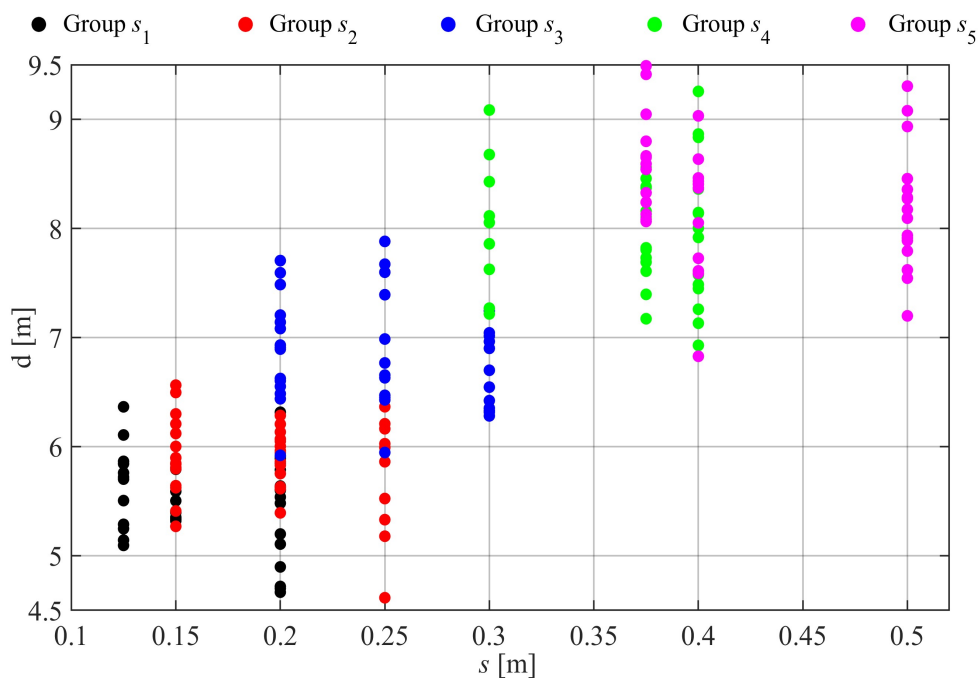


Figure 6.61: Relations between the 200 values of  $d$  and  $s$ , randomly selected.

Figures 6.62, 6.64, 6.66, 6.68, 6.70, 6.72, 6.74 and 6.76 show the sections of the RS models obtained setting the distance  $d$  to the fixed values chosen to calibrate the RS (Table 6.6) and changing the values of the shear strength  $\tau$ ; on the contrary, Figures 6.63, 6.65, 6.67, 6.69, 6.71, 6.73, 6.75, and 6.77 show the sections of the RS models obtained setting the shear strength  $\tau$  to the fixed values chosen to calibrate the RS (Table 6.6) and changing the values of the distance  $d$ . In these Figures the sections are divided between factorial values of the variable (pink and blue continuous lines) and central and axial points (black, green and red continuous lines); the dashed lines (--) indicate the section of the RS models obtained adding and subtracting the RS variance  $\sigma = \sqrt{\sigma_{\varepsilon}^2 + \sigma_{sis}^2 + \sigma_d^2 + \sigma_s^2}$ ; the points are those corresponding to the various simulations used to calibrate the RS models.

The section of the RS models obtained varying  $\tau$  confirm that the shear strength is the variable most influencing the  $PGA_C$ , having a greater slope and being closer each other because referred to the five values of  $d$ , having reduced effect on the response. For this latter motivation, the sections of the RS models obtained varying  $d$  have a minor slope, but they are more spaced each other because they are referred to the five values of  $\tau$ , having a significant effect on the response. The results also confirm those obtained in terms of capacity: in  $x$ -direction the weaker direction is the positive ( $+F_x$ ), in  $y$ -direction is the negative one ( $-F_y$ ). Furthermore, in this application the RS sections referred to the analyses in  $y$ -direction over the attainment of the LS limit state are reported, confirming the greater vulnerability of the external Units 1 and 2 with respect to the internal Units 3 and 4.

-  $x$ -direction ( $+ F_x$ )

Table 6.24: Regression parameters and standard deviations of the AS with different structural units, considering the seismic forces  $+ F_x$ .

Variable	$\beta_i$	Variable	$\sigma$
$x_1 (\tau)$	30.806	$\delta_{sis}$	0.176
$x_2 (d)$	0.587	$\delta_{\mu d}$	0.041
$x_1 (\tau^2)$	-168.20	$\delta_{\mu s}$	0.143
$x_2 (d^2)$	-0.029	$\epsilon$	0.220

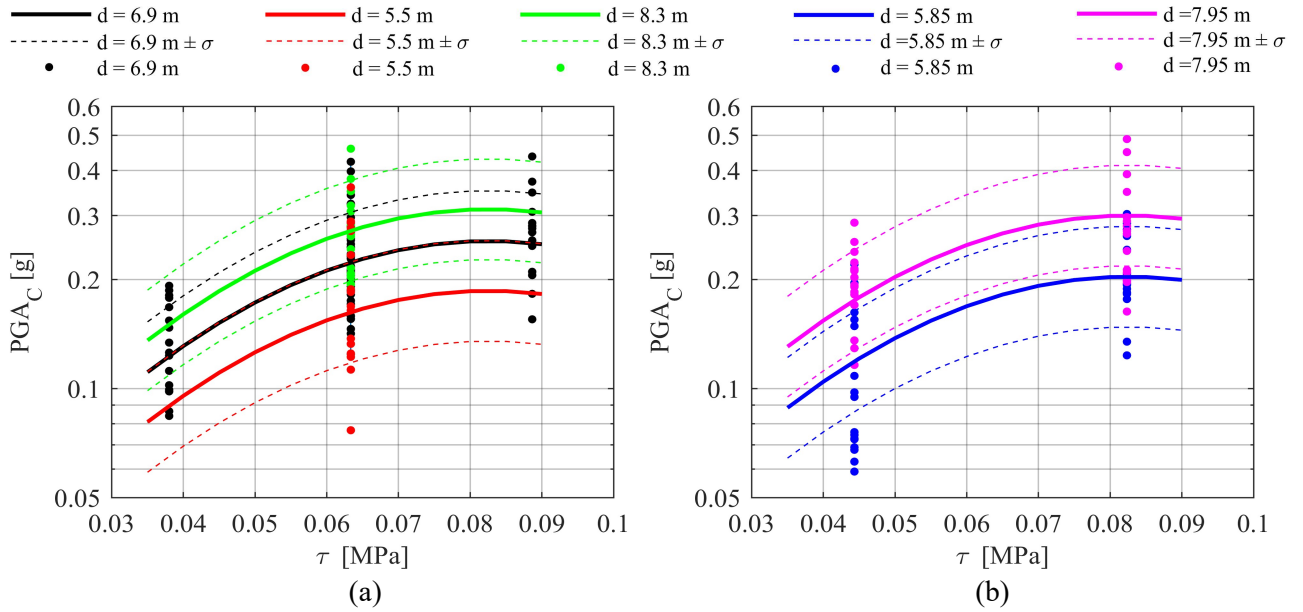


Figure 6.62: (a) Axial and central region and (b) factorial region of the AS quadratic RS sections obtained varying  $\tau$ , considering the seismic forces  $+ F_x$ .

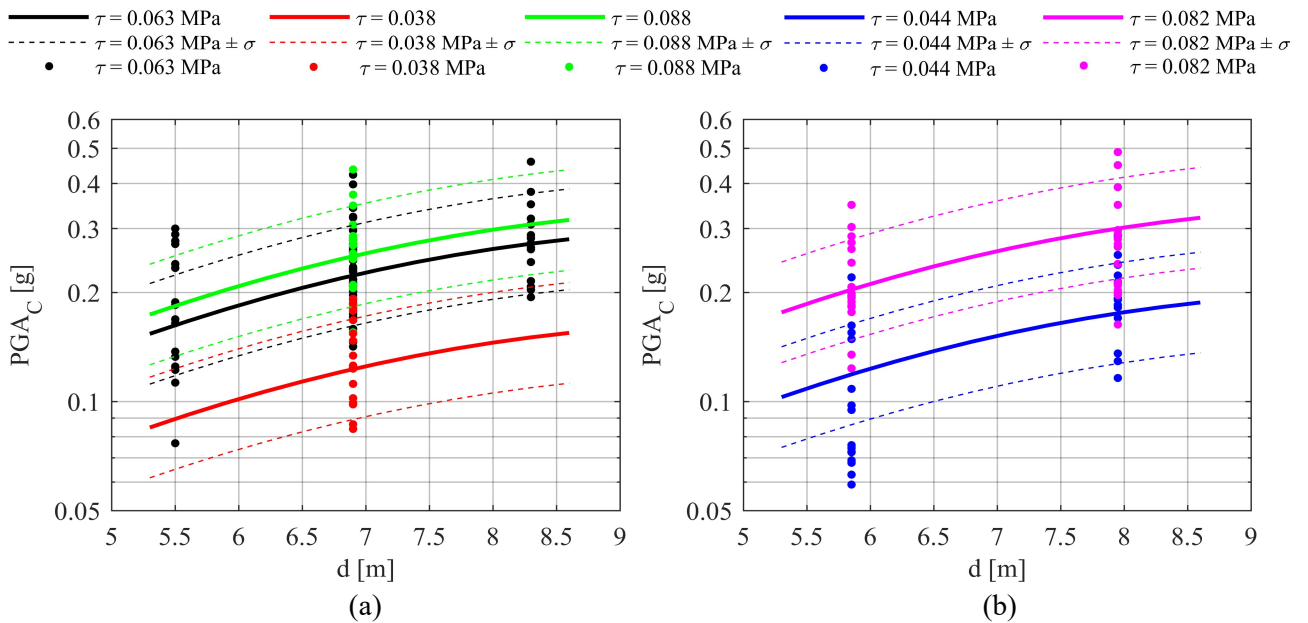


Figure 6.63: (a) Axial and central region and (b) factorial region of the AS quadratic RS sections obtained varying  $d$ , considering the seismic forces  $+ F_x$ .

- *x*-direction ( $-F_x$ )

Table 6.25: Regression parameters and standard deviations of the AS with different structural units, considering the seismic forces  $-F_x$

Variable	$\beta_i$	Variable	$\sigma$
$x_1 (\tau)$	14.144	$\delta_{sis}$	0.202
$x_2 (d)$	0.394	$\delta_{\mu d}$	0.019
$x_1 (\tau^2)$	-61.625	$\delta_{\mu s}$	0.010
$x_2 (d^2)$	-0.021	$\epsilon$	0.202

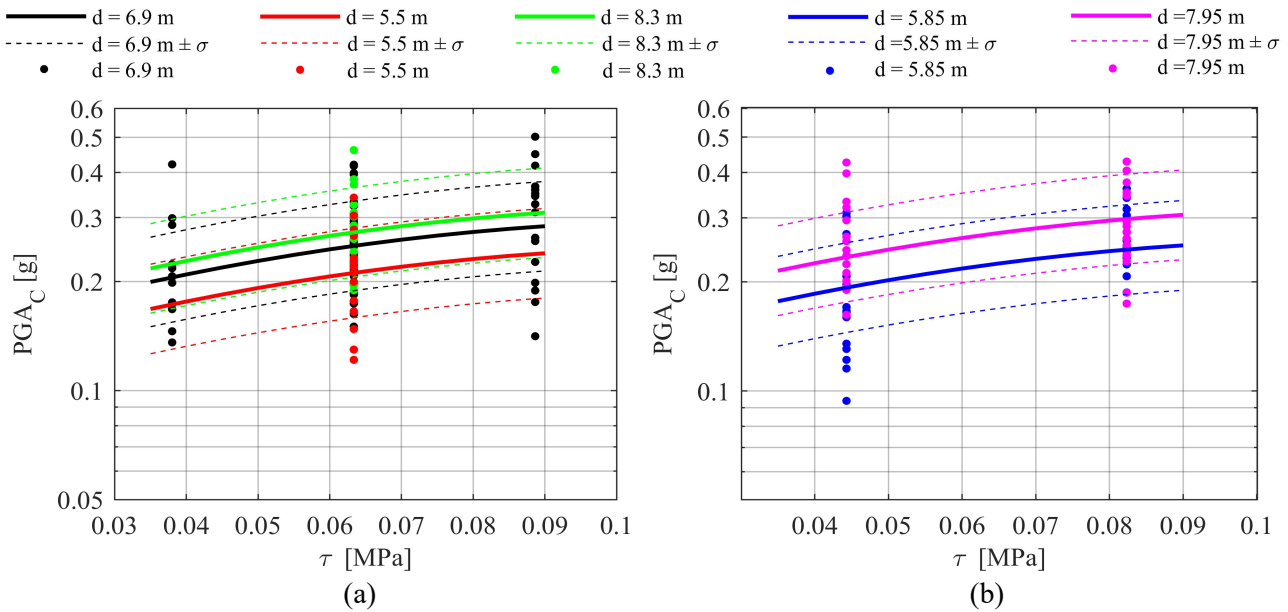


Figure 6.64: (a) Axial and central region and (b) factorial region of the AS quadratic RS sections obtained varying  $\tau$ , considering the seismic forces  $-F_x$ .

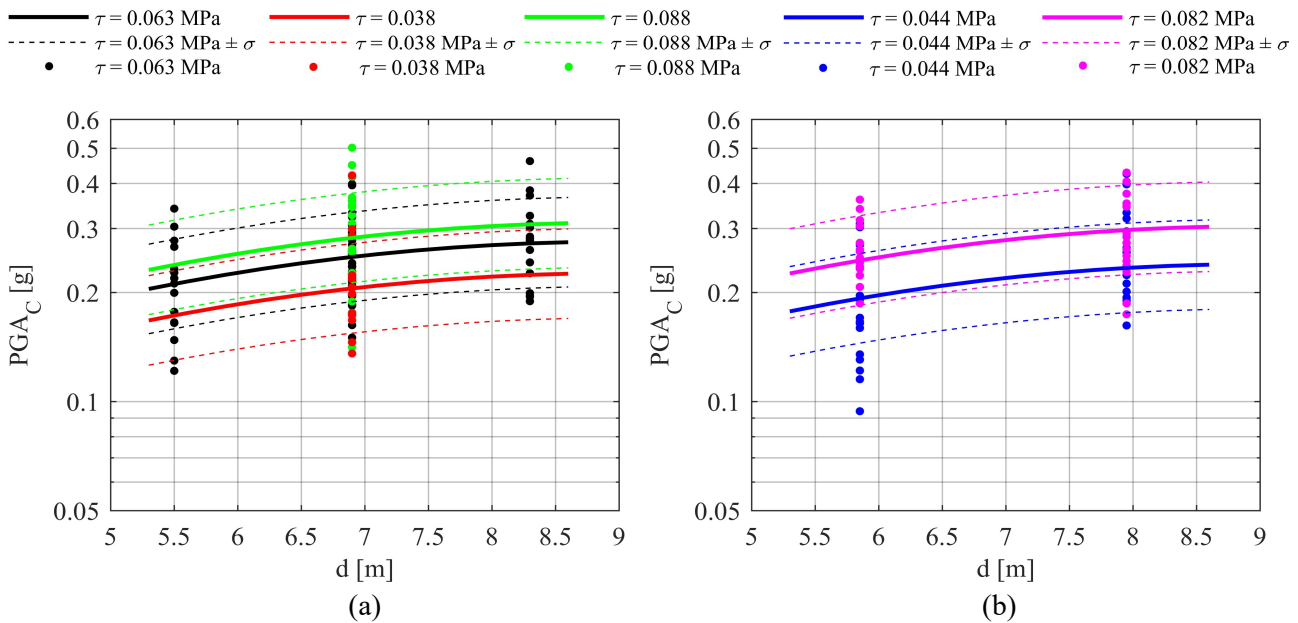


Figure 6.65: (a) Axial and central region and (b) factorial region of the AS quadratic RS sections obtained varying  $d$ , considering the seismic forces  $-F_x$ .

- *y*-direction (+  $F_y$ )

Table 6.26: Regression parameters and standard deviations of the AS with different structural units, considering the seismic forces +  $F_y$ .

Variable	$\beta_i$	Variable	$\sigma$
$x_1$ ( $\tau$ )	14.229	$\delta_{sis}$	0.142
$x_2$ (d)	0.168	$\delta_{\mu d}$	0.084
$x_1$ ( $\tau^2$ )	-16.537	$\delta_{\mu \tau}$	0.080
$x_2$ (d <sup>2</sup> )	-0.010	$\varepsilon$	0.193

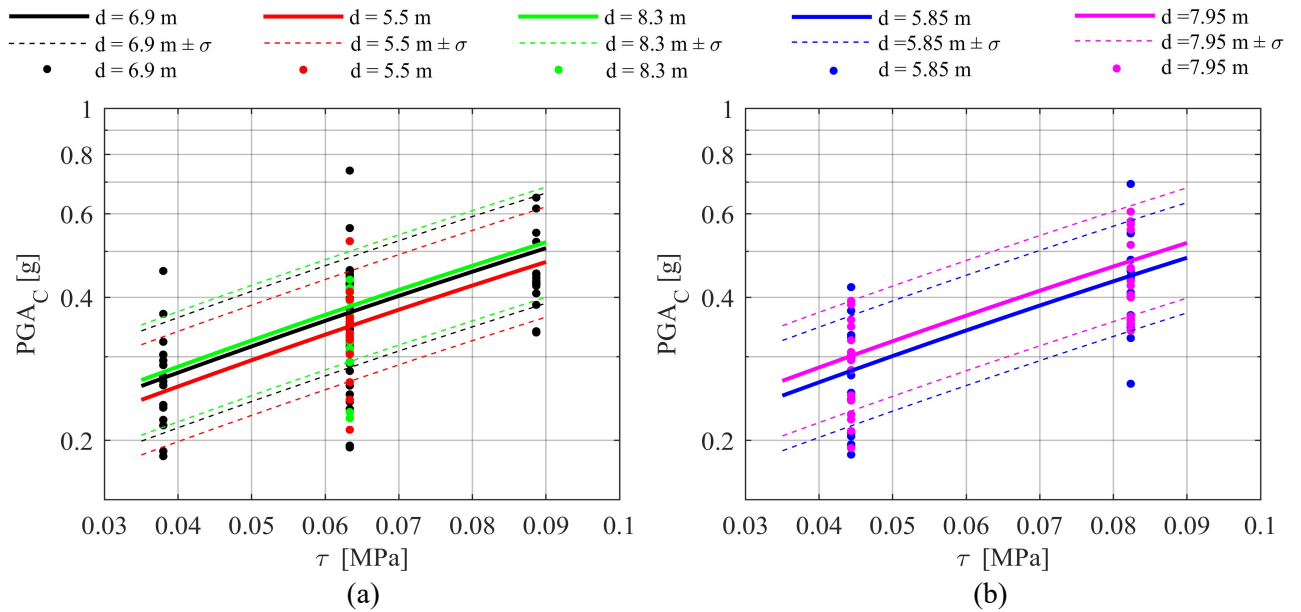


Figure 6.66: (a) Axial and central region and (b) factorial region of the AS quadratic RS sections obtained varying  $\tau$ , considering the seismic forces +  $F_y$ .

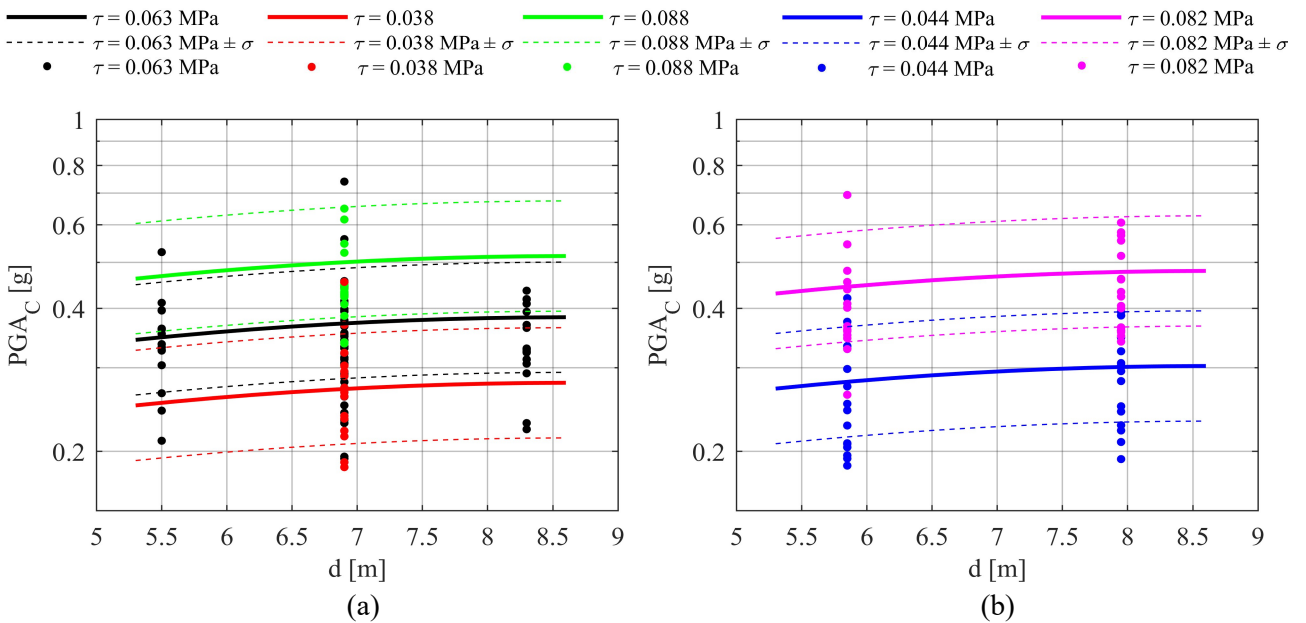


Figure 6.67: (a) Axial and central region and (b) factorial region of the AS quadratic RS sections obtained varying  $d$ , considering the seismic forces +  $F_y$ .

-  $y$ -direction ( $-F_y$ )

Table 6.27: Regression parameters and standard deviations of the AS with different structural units, considering the seismic forces  $-F_y$ .

Variable	$\beta_i$	Variable	$\sigma$
$x_1 (\tau)$	8.056	$\delta_{sis}$	0.130
$x_2 (d)$	0.168	$\delta_{\mu d}$	0.066
$x_1 (\tau^2)$	18.612	$\delta_{\mu s}$	0.040
$x_2 (d^2)$	-0.010	$\varepsilon$	0.175

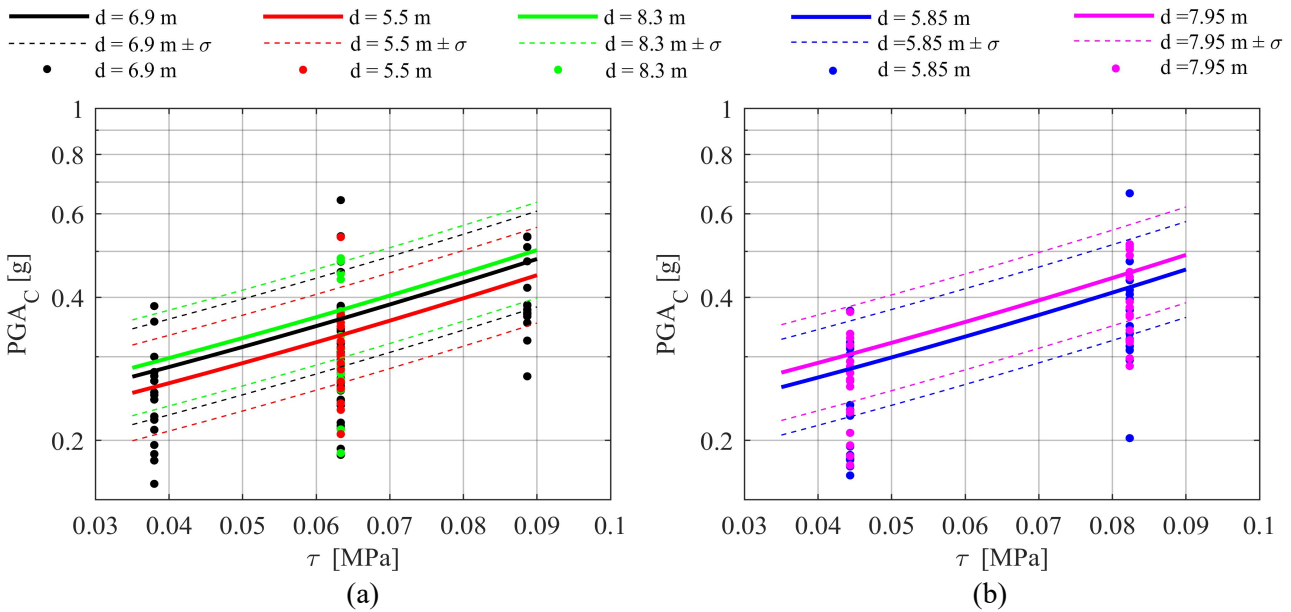


Figure 6.68: (a) Axial and central region and (b) factorial region of the AS quadratic RS sections obtained varying  $\tau$ , considering the seismic forces  $-F_y$ .

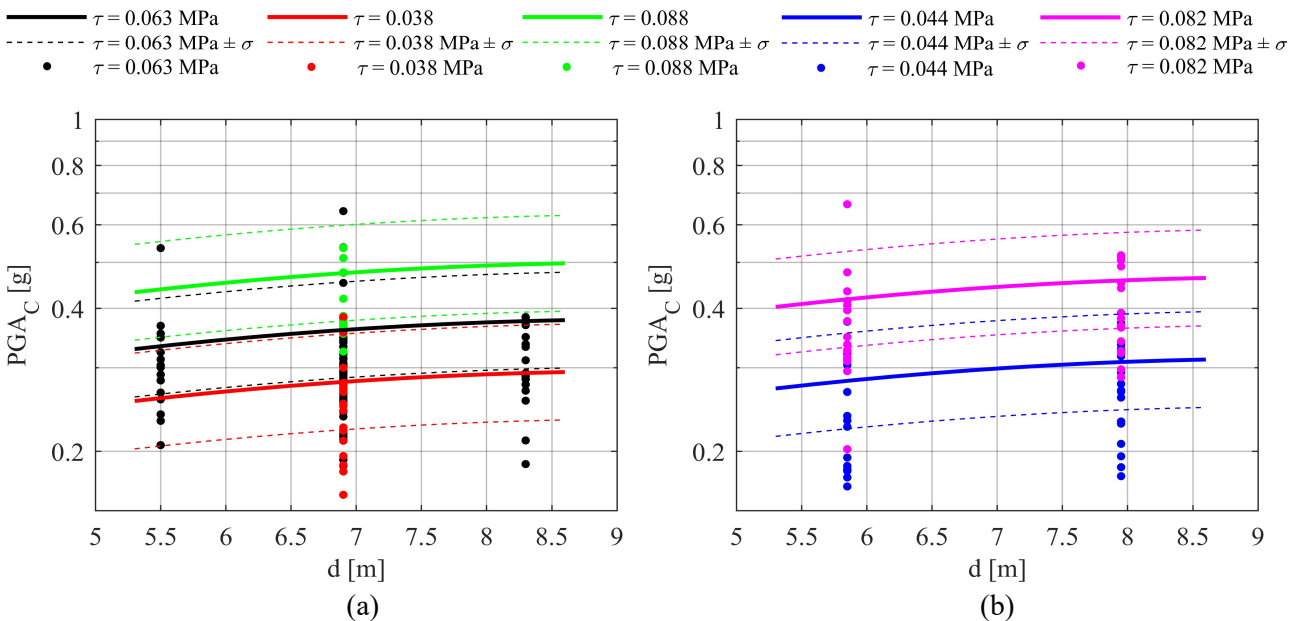


Figure 6.69: (a) Axial and central region and (b) factorial region of the AS quadratic RS sections obtained varying  $d$ , considering the seismic forces  $-F_y$ .

- *y*-direction (+  $F_y$ ), over the attainment of the LS limit state (Unit 3)

Table 6.28: Regression parameters and standard deviations of the Unit 3, considering the seismic forces +  $F_y$ , over the attainment of the LS limit state.

Variable	$\beta_i$	Variable	$\sigma$
$x_1$ ( $\tau$ )	3.689	$\delta_{sis}$	0.138
$x_2$ (d)	0.058	$\delta_{\mu d}$	0.072
$x_1$ ( $\tau^2$ )	72.212	$\delta_{\mu s}$	0.019
$x_2$ (d <sup>2</sup> )	0.003	$\varepsilon$	0.181

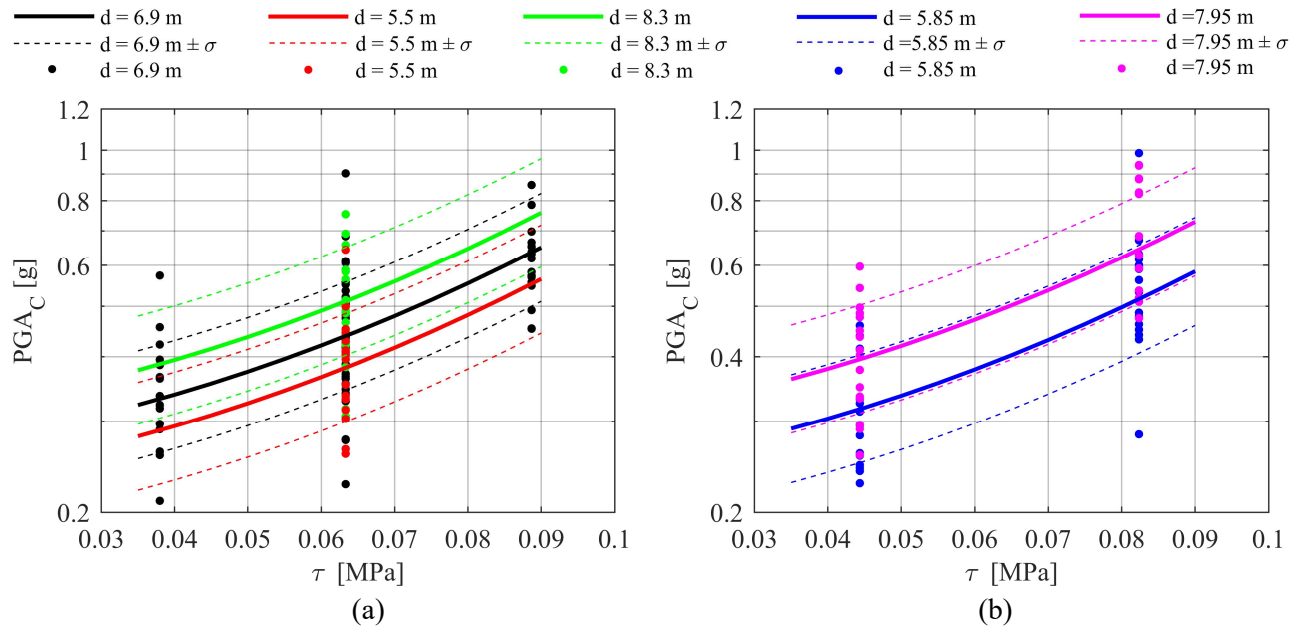


Figure 6.70: (a) Axial and central region and (b) factorial region of the Unit 3 quadratic RS sections obtained varying  $\tau$ , considering the seismic forces +  $F_y$ , over the attainment of the LS limit state.

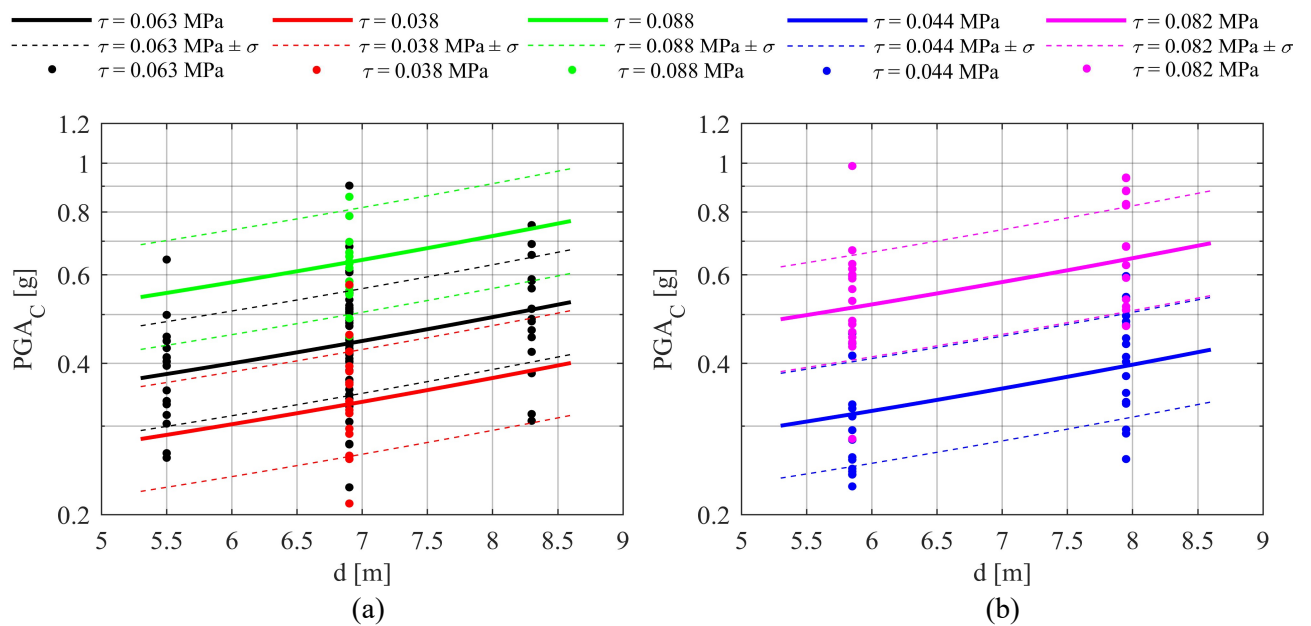


Figure 6.71: (a) Axial and central region and (b) factorial region of the Unit 3 quadratic RS sections obtained varying d, considering the seismic forces +  $F_y$ , over the attainment of the LS limit state.

-  $y$ -direction ( $-F_y$ ), over the attainment of the LS limit state (Unit 3)

Table 6.29: Regression parameters and standard deviations of the Unit 3, considering the seismic forces  $-F_y$ , over the attainment of the LS limit state.

Variable	$\beta_i$	Variable	$\sigma$
$x_1(\tau)$	5.738	$\delta_{sis}$	0.141
$x_2(d)$	0.113	$\delta_{\mu d}$	0.067
$x_1(\tau^2)$	44.958	$\delta_{\mu s}$	0.014
$x_2(d^2)$	0.013	$\epsilon$	0.182

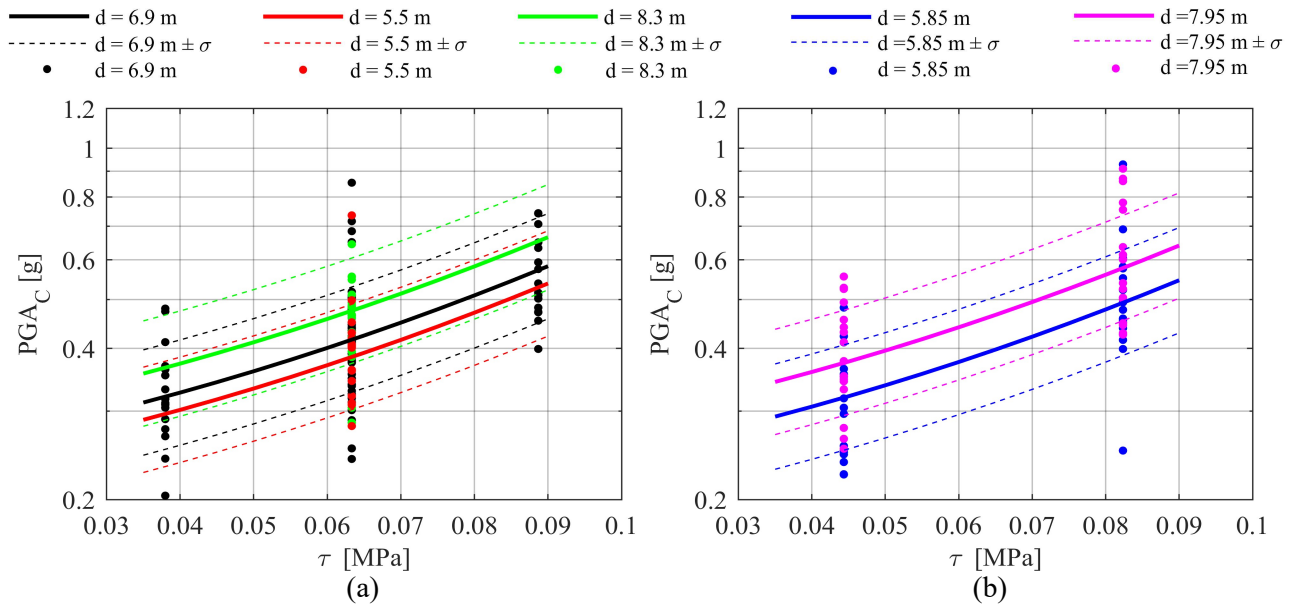


Figure 6.72: (a) Axial and central region and (b) factorial region of the Unit 3 quadratic RS sections obtained varying  $\tau$ , considering the seismic forces  $-F_y$ , over the attainment of the LS limit state.

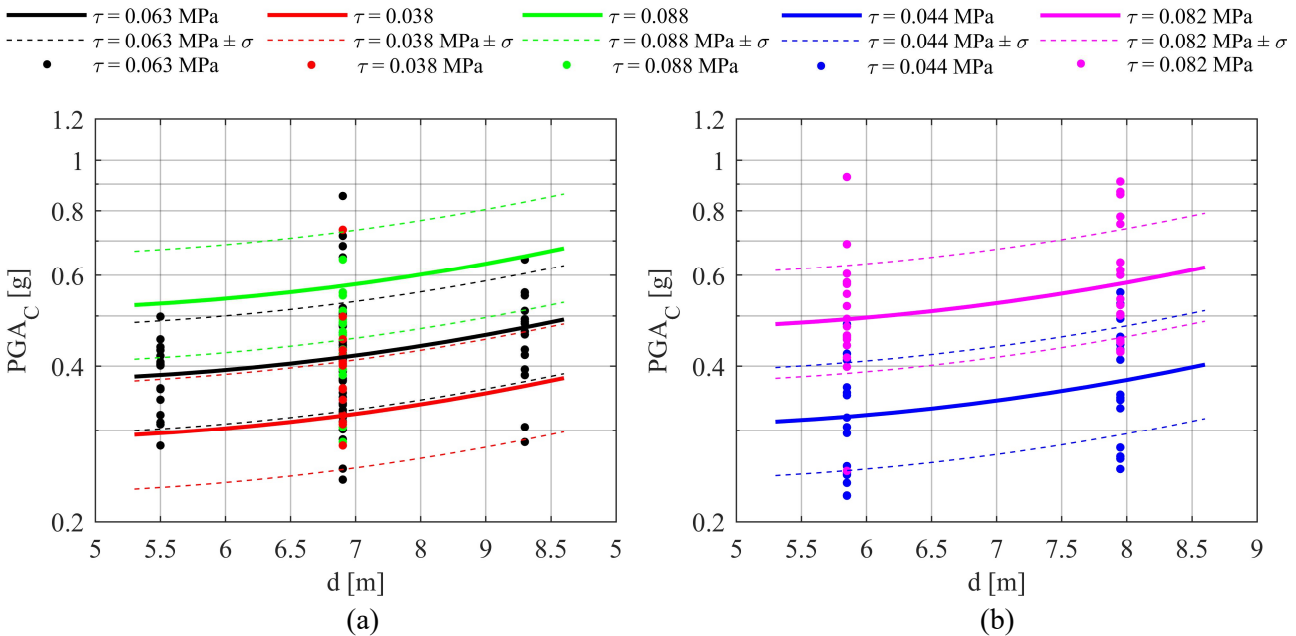


Figure 6.73: (a) Axial and central region and (b) factorial region of the Unit 3 quadratic RS sections obtained varying  $d$ , considering the seismic forces  $-F_y$ , over the attainment of the LS limit state.

-  $y$ -direction ( $+F_y$ ), over the attainment of the LS limit state (Unit 4)

Table 6.30: Regression parameters and standard deviations of the Unit 4, considering the seismic forces  $+F_y$ , over the attainment of the LS limit state.

Variable	$\beta_i$	Variable	$\sigma$
$x_1 (\tau)$	12.966	$\delta_{sis}$	0.138
$x_2 (d)$	0.378	$\delta_{\mu d}$	0.006
$x_1 (\tau^2)$	-19.642	$\delta_{\mu s}$	0.095
$x_2 (d^2)$	-0.0211	$\varepsilon$	0.180

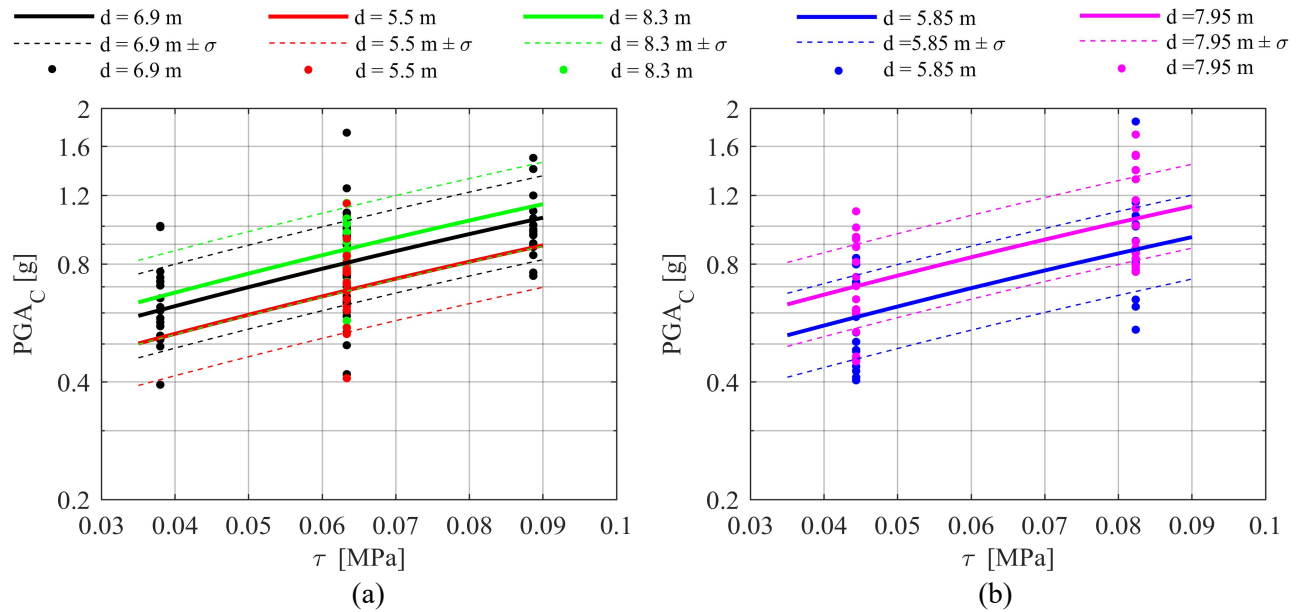


Figure 6.74: (a) Axial and central region and (b) factorial region of the Unit 4 quadratic RS sections obtained varying  $\tau$ , considering the seismic forces  $+F_y$ , over the attainment of the LS limit state.

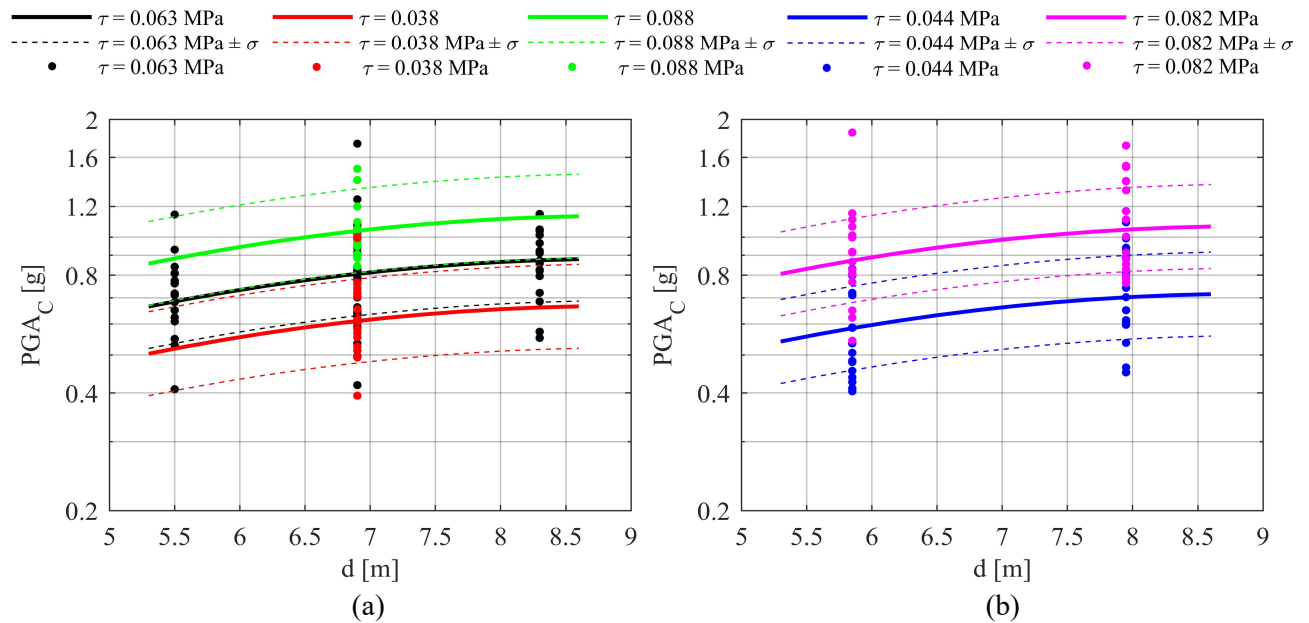


Figure 6.75: (a) Axial and central region and (b) factorial region of the Unit 4 quadratic RS sections obtained varying  $d$ , considering the seismic forces  $+F_y$ , over the attainment of the LS limit state.

-  $y$ -direction ( $-F_y$ ), over the attainment of the LS limit state (Unit 4)

Table 6.31: Regression parameters and standard deviations of the Unit 4, considering the seismic forces  $-F_y$ , over the attainment of the LS limit state.

Variable	$\beta_i$	Variable	$\sigma$
$x_1 (\tau)$	4.532	$\delta_{sis}$	0.136
$x_2 (d)$	0.244	$\delta_{\mu d}$	0.036
$x_1 (\tau^2)$	32.741	$\delta_{\mu s}$	0.083
$x_2 (d^2)$	-0.015	$\varepsilon$	0.178

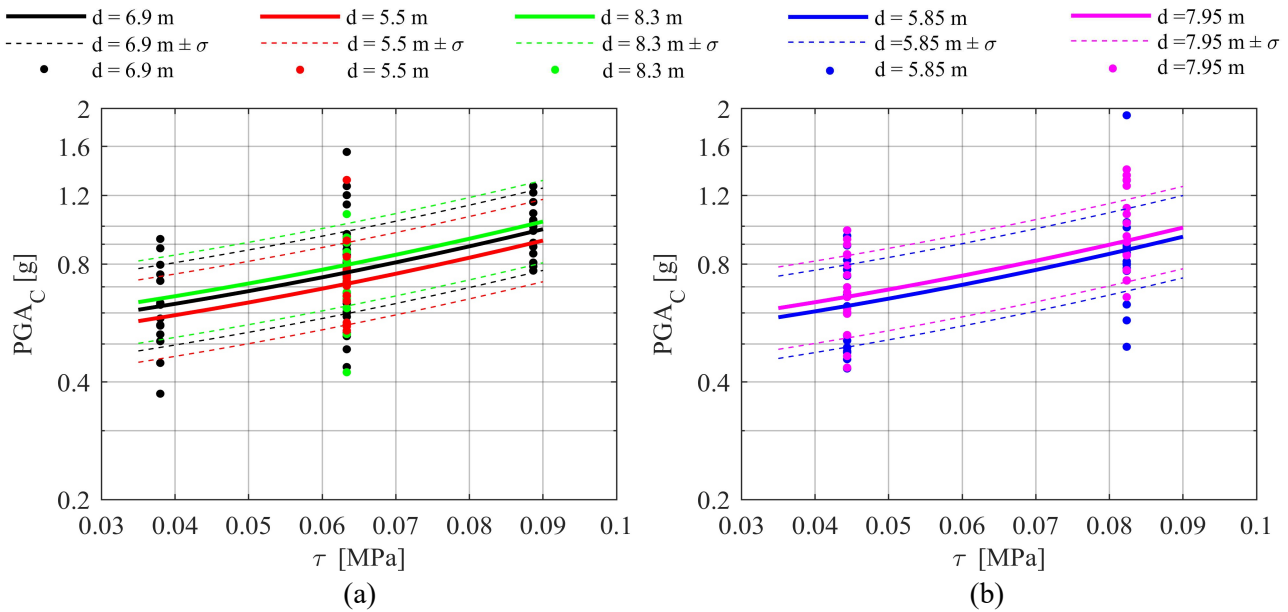


Figure 6.76: (a) Axial and central region and (b) factorial region of the Unit 4 quadratic RS sections obtained varying  $\tau$ , considering the seismic forces  $-F_y$ , over the attainment of the LS limit state.

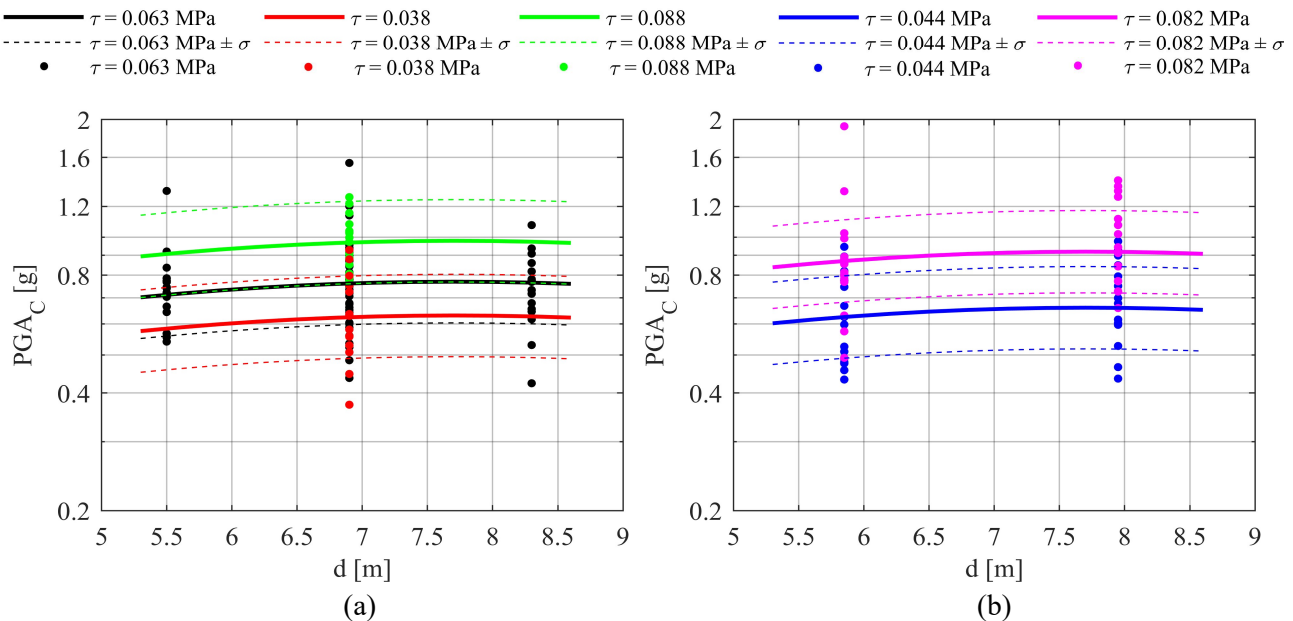


Figure 6.77: (a) Axial and central region and (b) factorial region of the Unit 4 quadratic RS sections obtained varying  $d$ , considering the seismic forces  $-F_y$ , over the attainment of the LS limit state.

As in Section 6.2, the results are reported by means of the 3D Response Surfaces. Figures 6.78(a) and (b) show the 3D Response Surfaces referred to the positive ( $+F_x$ ) and negative ( $-F_x$ )  $x$ -direction of the seismic action, respectively; Figures 6.79(a) and (b) show the 3D Response Surfaces referred to the positive ( $+F_y$ ) and negative ( $-F_y$ )  $y$ -direction of the seismic action, respectively. The black surfaces are obtained varying  $\tau$  and  $d$ , the grey surfaces are obtained adding and subtracting the RS variance  $\sigma = \sqrt{\sigma_\varepsilon^2 + \sigma_{sis}^2 + \sigma_d^2 + \sigma_s^2}$ .

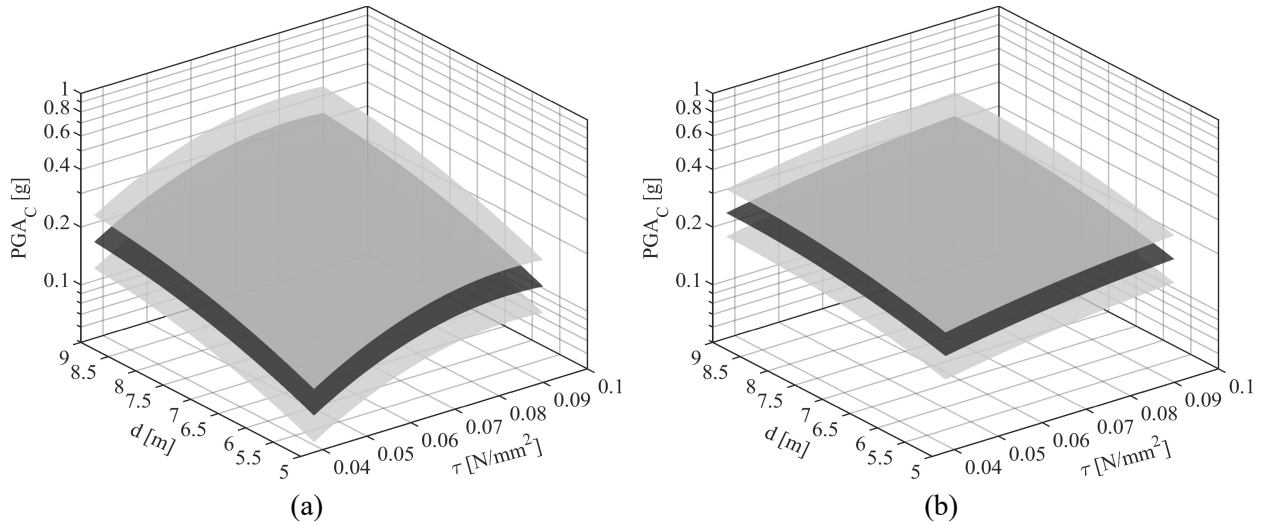


Figure 6.78: 3D Response Surfaces for the AS with different structural units, considering (a) the seismic forces  $+F_x$  and (b) the seismic forces  $-F_x$ .

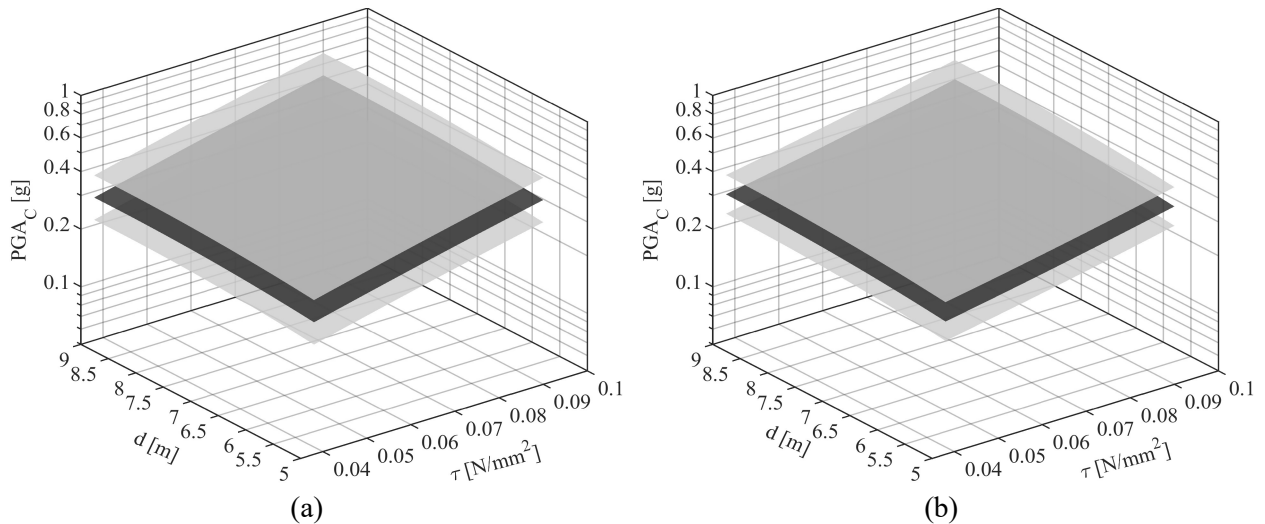


Figure 6.79: 3D Response Surfaces for the AS with different structural units, considering (a) the seismic forces  $+F_y$  and (b) the seismic forces  $-F_y$ .

The analyses over the attainment of the LS limit state allowed to obtain the following 3D Response Surfaces, referring to the collapse of the Unit 3 (Figures 6.80(a) and (b)) and of the Unit 4 (Figures 6.81(a) and (b)), confirming the attainment of higher values of the  $PGA_C$  if more internal structural units are considered.

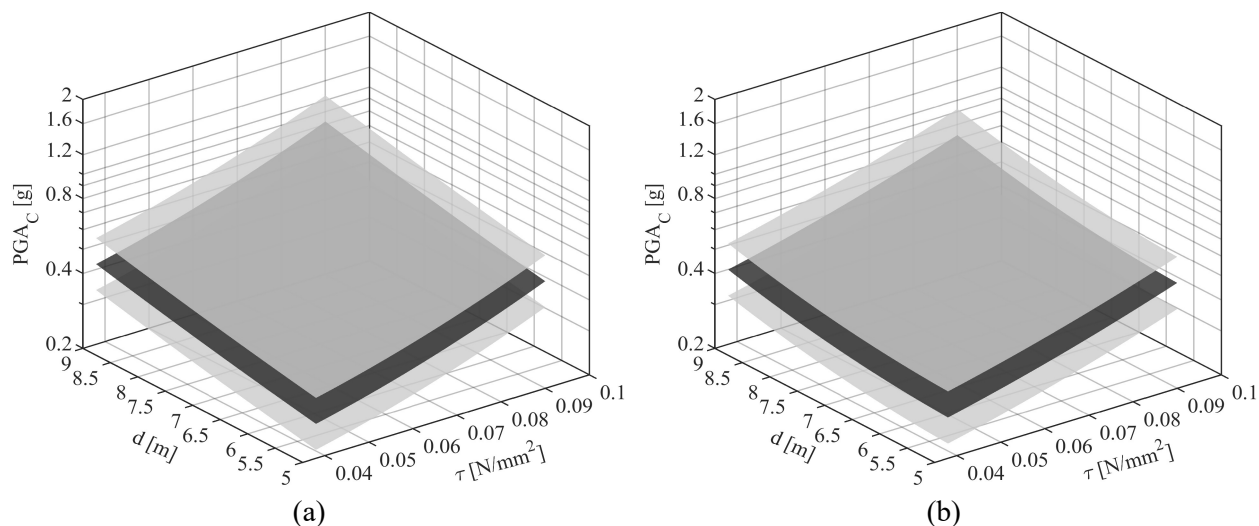


Figure 6.80: 3D Response Surfaces for the Unit 3, considering (a) the seismic forces  $+F_y$ , and (b) the seismic forces  $-F_y$ , over the attainment of the LS limit state.

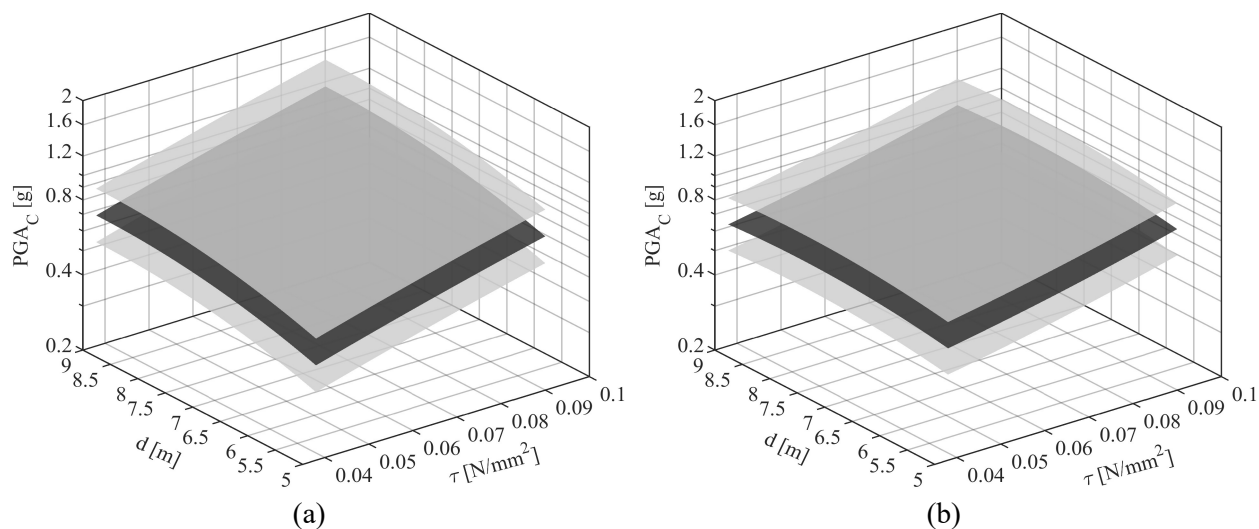


Figure 6.81: 3D Response Surfaces for the Unit 4, considering (a) the seismic forces  $+F_y$ , and (b) the seismic forces  $-F_y$ , over the attainment of the LS limit state.

### 6.4.5 Fragility curves

The obtained RS models were used to estimate the fragility curves of the masonry aggregate structures with different structural units in row. The fragility analysis was assessed using the same procedure of the previous Sections, adopting the limit state function in Equation 2.5, rewritten in the form:

$$\begin{aligned} g(\mathbf{x}_E, \beta, \varepsilon, \delta_{\text{sis}}, \delta_d, \delta_s | \text{PGA}_D) &= \log(\text{PGA}_C) - \log(\text{PGA}_D) = \\ &= \beta_0 + \beta_1 x_1 + \beta_2 x_2 + \beta_3 x_1^2 + \beta_4 x_2^2 + \delta_{\text{sis}} + \delta_d + \delta_s + \varepsilon - \log(\text{PGA}_D) \end{aligned} \quad (6.6)$$

Eight fragility curves were obtained for seismic action in  $x$ - and  $y$ -direction (Figure 6.82). They give the conditional probability of the structural failure ( $P_f$ ) for different values of the structural demand ( $\text{PGA}_D$ ). Thus, once obtained the collapse  $\text{PGA}_C$ , fixed  $\text{PGA}_D$  and being the behaviour of the structures non-linear, in order to solve the Equation 6.6, Monte Carlo method was used.

These curves confirm that the masonry aggregate structures, object of this Section, are more vulnerable against the seismic action in  $x$ -direction (red curves) because of the geometrical properties, which have already been discussed in the previous Sections, with respect to the curves obtained for the  $y$ -direction (blue curves) showing the attainment of the  $P_f$  for higher values of  $\text{PGA}_D$ . These latter curves give the fragility of the external Units 1 and 2, affecting by substantial torsional effects, decreasing the total  $\text{PGA}_C$ , referring to the attainment of the LS limit state for the global aggregate structures. However, continuing the analyses to allow the other structural units to reach the shear failure, the green curves give the fragility of the internal Unit 3 and Unit 4, showing their higher stiffness against the seismic action in  $y$ -direction, allowing them to attain the  $P_f$  for higher values of  $\text{PGA}_D$ .

In Figure 6.82 the continuous lines are related to the analyses carried out with the application of the positive seismic forces ( $+F_x$  or  $+F_y$ ), the dash dot lines to those with the application of the negative seismic forces ( $-F_x$  or  $-F_y$ ), highlighting that the presence of the openings and their positions in the masonry walls make the aggregate structure more fragile against the positive forces in  $x$ -direction and against the negative forces in  $y$ -direction.

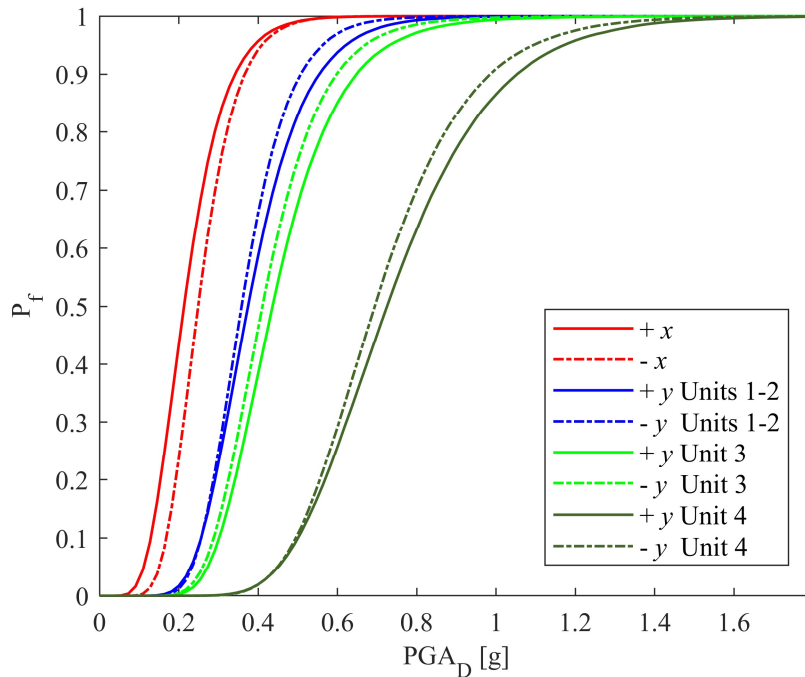


Figure 6.82: Fragility curves of the masonry aggregate structures with different structural units in row.

#### 6.4.6 Comparison between the aggregate with different structural units and the aggregate with identical structural units in row

The fragility of the masonry aggregates with different structural units (AS - D) was compared with the one of the aggregates with identical structural units (AS - I) and of the isolated structural units (ISU), generated using the medium values of the distributions of the chosen variables. The comparisons allow to analyse how the differences between structural units along the aggregate affect the seismic response and to show how the fragility of the AS - D differs from the one of the AS - I.

Since the simulations of the RS models are characterized by masonry aggregate structures with different structural and geometrical properties, the comparisons need to be made coherently. Thus, the aggregate structures with different structural units (AS - D) were compared with those with identical structural units (AS - I), having the same values of the shear strength ( $\tau$ ) and the values of the geometrical properties ( $d$  and  $s$ ) equal to the medium values of the distributions used to generate the AS - D (Section 6.4.2). Furthermore, the comparisons were carried out considering the same seismic action, i.e. the same accelerogram associated to each simulation of the RS model defined in this Section. Therefore, all the 48 accelerograms were applied to each AS - I, object of the comparison, and the  $PGA_C$  obtained

were compared with the correspondent  $PGA_C$  of the RS model simulations, having the same accelerograms, the same  $\tau$  and the comparable geometrical properties.

Figure 6.83 shows an example of comparison carried out in this application: the simulation 11 (Table B.3), is associated to the aggregate configuration n°1 (Table 6.23) with explicit variables  $\tau_3 = 0.063$  MPa and  $d_1 = 5.5$  m, implicit variables defined by the blocks  $\delta_{d1}$  and  $\delta_{s1}$  and whose  $PGA_C$  was obtained applying the accelerogram n°3 ( $\delta_{sis} = 3$ ). It was compared with the aggregate structure with identical structural units having the same values of the explicit variables ( $\tau_3$  and  $d_1$ ) for each structural unit and whose  $PGA_C$  was obtained applying the same accelerogram n°3.

SIMULATION	EXPLICIT VARIABLES				IMPLICIT VARIABLES			AGGREGATE CONFIGURATION
	$\tau$		$d$		$\delta_{sis}$	$\delta_d$	$\delta_s$	
11	$\tau_3$	0.063	$d_1$	5.5	3	$\delta_{d1}(1)$	$\delta_{s1}(1)$	1

AGGREGATE CONFIGURATION	BLOCK	US 5	US 4	US 3	US 2	US 1
1	$\delta_{d1}(1)$	5.11	5.89	5.76	5.35	5.50
	$\delta_{s1}(1)$	0.2	0.2	0.125	0.15	0.125

COMPARED WITH THE AGGREGATION OF IDENTICAL STRUCTURAL UNITS, WITH THE MEDIUM VALUES  $d_1$  AND  $s_1$ , THE SAME  $\tau$  AND THE SAME ACCELEROGRAM 3



AGGREGATE CONFIGURATION	BLOCK	US 5	US 4	US 3	US 2	US 1
IDENTICAL STRUCTURAL UNITS $d_1 - s_1$	$\delta_{d1}(1)$	5.50	5.50	5.50	5.50	5.50
	$\delta_{s1}(1)$	0.15	0.15	0.15	0.15	0.15

Figure 6.83: Example of comparison between an AS - D and the correspondent AS - I.

Since the aggregate configurations were divided in 5 groups (from  $d_1-s_1$  to  $d_5-s_5$ ), Table 6.32 gives the 9 type of comparisons carried out between the AS - D and the AS - I, according to the definition of the associations of  $\tau$  and the groups d-s defined in the RS model. Moreover, the two types of aggregate structures were compared with the isolated structural units, modelled with the same mechanical and geometrical properties of those belonging to the AS - I, expecting the results already discusses in Section 6.3: the increment of the  $PGA_C$  aggregating in  $x$ -direction and the decrement in  $y$ -direction.

Table 6.32: 9 type of comparisons carried out between the AS - D and the AS - I.

Shear strength	AS - D	AS - I	
$\tau_1$	group d <sub>3</sub> -s <sub>3</sub>	d <sub>3</sub> = 6.9 m	s <sub>3</sub> = 0.25 m
$\tau_2$	group d <sub>2</sub> -s <sub>2</sub>	d <sub>2</sub> = 5.85 m	s <sub>2</sub> = 0.20 m
$\tau_2$	group d <sub>4</sub> -s <sub>4</sub>	d <sub>4</sub> = 7.95 m	s <sub>4</sub> = 0.375 m
$\tau_3$	group d <sub>1</sub> -s <sub>1</sub>	d <sub>1</sub> = 5.5 m	s <sub>1</sub> = 0.15 m
$\tau_3$	group d <sub>3</sub> -s <sub>3</sub>	d <sub>3</sub> = 6.9 m	s <sub>3</sub> = 0.25 m
$\tau_3$	group d <sub>5</sub> -s <sub>5</sub>	d <sub>5</sub> = 8.3 m	s <sub>5</sub> = 0.40 m
$\tau_4$	group d <sub>2</sub> -s <sub>2</sub>	d <sub>2</sub> = 5.85 m	s <sub>2</sub> = 0.20 m
$\tau_4$	group d <sub>4</sub> -s <sub>4</sub>	d <sub>4</sub> = 7.95 m	s <sub>4</sub> = 0.375 m
$\tau_5$	group d <sub>3</sub> -s <sub>3</sub>	d <sub>3</sub> = 6.9 m	s <sub>3</sub> = 0.25 m

The results of the comparisons, showed in the Figures below, highlight how the geometrical properties affect the variation of the  $PGA_C$  between the AS - D and the AS - I. The regressions of the RS models showed that the increment of the values of  $d$  and  $s$  leads to an increment of the  $PGA_C$ : it is expected that the  $PGA_C$  increases as the ratio  $d/s$  decreases. Thus, this application provides a comparison between the AS - D and the AS - I, in terms of  $PGA_C$  mainly depending on the ratio  $d/s$ , being the parameter determining the differences between the two types of aggregate structures. In the following it is showed how the  $PGA_C$  referred to the AS - D varies with respect to that referred to the AS - I, highlighting that the general trend is characterized by an increment of the collapse  $PGA_C$  if the average of the ratio  $d/s$  of the different structural units along the AS - D is less than the ratio  $d/s$  of the identical structural unit along the AS - I.

Since in  $x$ -direction the global behaviour of the aggregates is studied, the ratio  $d/s$  is calculated considering the average of the 5 structural units; in  $y$ -direction, besides that of the 5 structural units, the ratio  $d/s$  considering only the average of the units involved in the collapse is calculated, since the local behaviour is considered. The cases taking into account the local behaviour of the various structural units along the aggregate in  $y$ -direction are listed in the following:

- Units 1-2: average of the ratio  $d/s$  of the Units 1-2;
- Unit 3: average of the ratio  $d/s$  of the Units 3-4-5 (as Units 1-2 are already collapsed);
- Unit 4: average of the ratio  $d/s$  of the Units 4-5 (as Units 1-2-3 are already collapsed).

Figure 6.84 gives an example of comparison between the aggregate configuration 1 and the correspondent aggregate with identical structural units.

AGGREGATE CONFIGURATION	BLOCK	US 5	US 4	US 3	US 2	US 1	
IDENTICAL STRUCTURAL UNITS $d_1 - s_1$	$\delta_{d1}(1)$	5.50	5.50	5.50	5.50	5.50	⇒ $d/s = 36.66$
	$\delta_{s1}(1)$	0.15	0.15	0.15	0.15	0.15	

AGGREGATE CONFIGURATION	BLOCK	US 5	US 4	US 3	US 2	US 1	
1	$\delta_{d1}(1)$	5.11	5.89	5.76	5.35	5.50	⇒ $d/s$ (average) = 36.16 $d/s$ (average US1 and US2) = 39.85
	$\delta_{s1}(1)$	0.2	0.2	0.125	0.15	0.125	

Figure 6.84: Example of comparison between the AS - D configuration 1 and the correspondent AS - I.

Following the example, if all the 5 units are considered, the average of the ratio  $d/s$  decreases and an increment of the collapse  $PGA_C$  is expected; if the Units 1-2 are considered for the  $y$ -direction the ratio  $d/s$  increases and a decrement of the collapse  $PGA_C$  is expected.

As an example, Figures 6.85, 6.86, 6.87, 6.88, 6.89, 6.90, 6.91, 6.92 and 6.93 show the 9 comparisons (Table 6.32), considering the seismic action in  $y$ -direction with negative forces ( $-F_y$ ) and reporting the values of the collapse  $PGA_C$  for each correspondent accelerogram applied. The dashed lines indicate the averages of the  $PGA_C$  values ( $\mu$ ), for each case. The comparisons are carried out between the AS - D, the AS - I and the ISU. Tables 6.33, 6.34, 6.35, 6.36, 6.37, 6.38, 6.39, 6.40 and 6.41 gives the comparisons between the expected behaviour of the variation of the  $PGA_C$  and the actual behaviour obtained, considering the average of the  $PGA_C$  related to the accelerograms applied to each aggregate configuration.

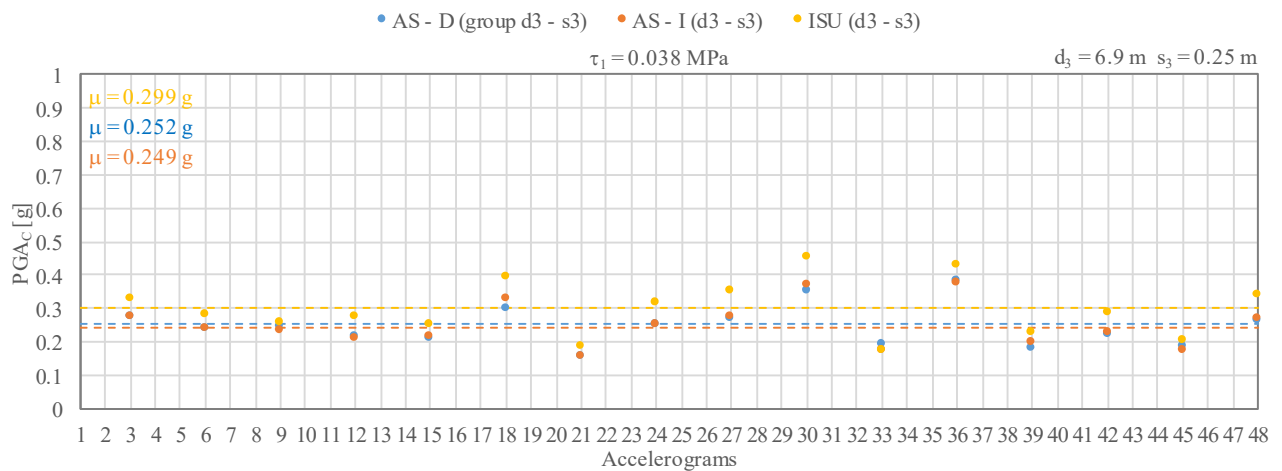


Figure 6.85: Comparison between the AS - D, the AS - I and the ISU for the group  $\tau_1$ - $d_3$ - $s_3$ .

Table 6.33: Expected and the actual behaviours on the variation of the  $PGA_C$  for the group  $\tau_1$ - $d_3$ - $s_3$ .

ACCELEROGRAMS	AGGREGATE CONFIGURATION	EXPECTED BEHAVIOUR ( $PGA_C$ )	ACTUAL BEHAVIOUR ( $PGA_C$ )
3 - 6	3	decrement	increment
9 - 12	8	increment	decrement
15 - 18	13	decrement	decrement
21 - 24	18	decrement	increment
27 - 30	23	increment	decrement
33 - 36	28	increment	increment
39 - 42	33	decrement	decrement
45 - 48	38	increment	increment

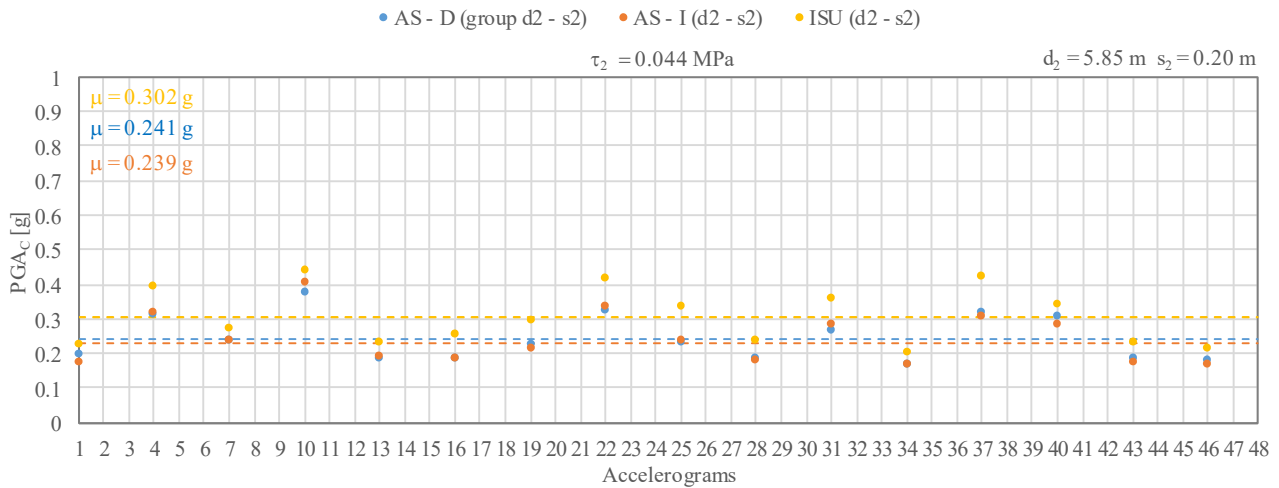


Figure 6.86: Comparison between the AS - D, the AS - I and the ISU for the group  $\tau_2$ - $d_2$ - $s_2$ .

Table 6.34: Expected and the actual behaviours on the variation of the  $PGA_C$  for the group  $\tau_2$ - $d_2$ - $s_2$ .

ACCELEROGRAMS	AGGREGATE CONFIGURATION	EXPECTED BEHAVIOUR ( $PGA_C$ )	ACTUAL BEHAVIOUR ( $PGA_C$ )
1 - 4	2	increment	increment
7 - 10	7	decrement	decrement
13 - 16	12	decrement	decrement
19 - 22	17	decrement	increment
25 - 28	22	decrement	increment
31 - 34	27	decrement	decrement
37 - 40	32	increment	increment
43 - 46	37	decrement	increment

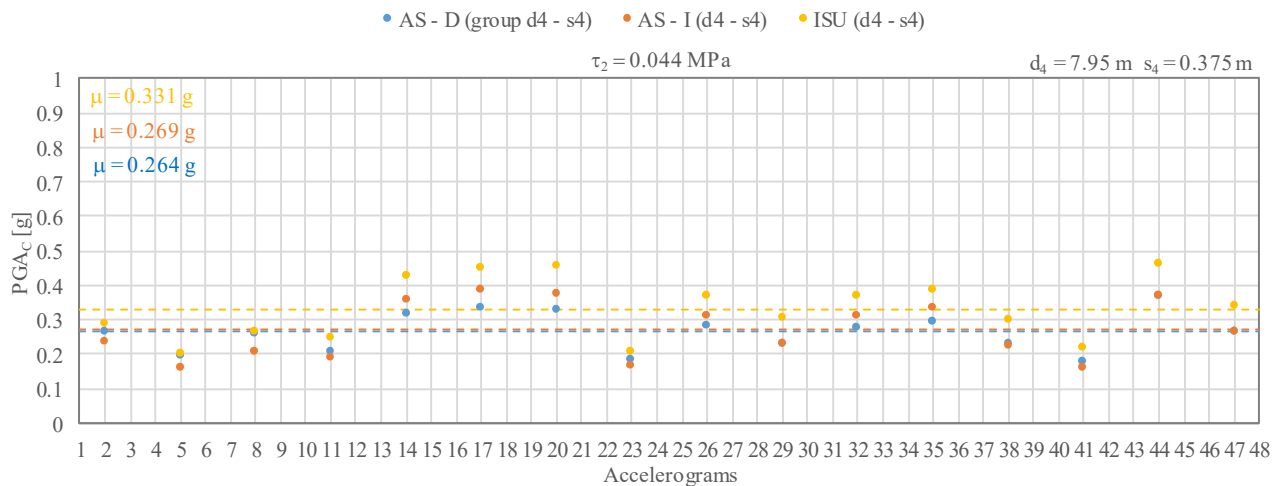


Figure 6.87: Comparison between the AS - D, the AS - I and the ISU for the group  $\tau_2$ - $d_4$ - $s_4$ .

Table 6.35: Expected and the actual behaviours on the variation of the  $PGA_C$  for the group  $\tau_2$ - $d_4$ - $s_4$ .

ACCELEROGRAMS	AGGREGATE CONFIGURATION	EXPECTED BEHAVIOUR ( $PGA_C$ )	ACTUAL BEHAVIOUR ( $PGA_C$ )
2 - 5	4	increment	increment
8 - 11	9	increment	increment
14 - 17	14	decrement	decrement
20 - 23	19	decrement	decrement
26 - 29	24	decrement	decrement
32 - 35	29	decrement	decrement
38 - 41	34	decrement	decrement
44 - 47	39	decrement	decrement

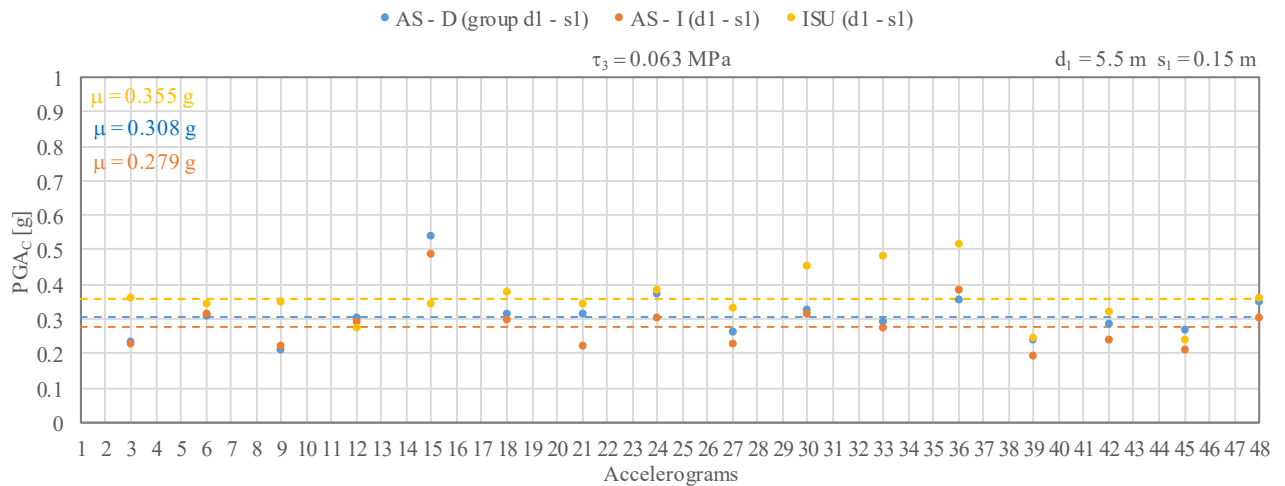


Figure 6.88: Comparison between the AS - D, the AS - I and the ISU for the group  $\tau_3$ -d<sub>1</sub>-s<sub>1</sub>.

Table 6.36: Expected and the actual behaviours on the variation of the PGAc for the group  $\tau_3$ -d<sub>1</sub>-s<sub>1</sub>.

ACCELEROGRAMS	AGGREGATE CONFIGURATION	EXPECTED BEHAVIOUR (PGAc)	ACTUAL BEHAVIOUR (PGAc)
3- 6	1	decrement	increment
9 - 12	6	increment	decrement
15 -18	11	increment	increment
21 -24	16	increment	increment
27 - 30	21	decrement	increment
33 - 36	26	increment	decrement
39 -42	31	decrement	increment
45 - 48	36	increment	increment

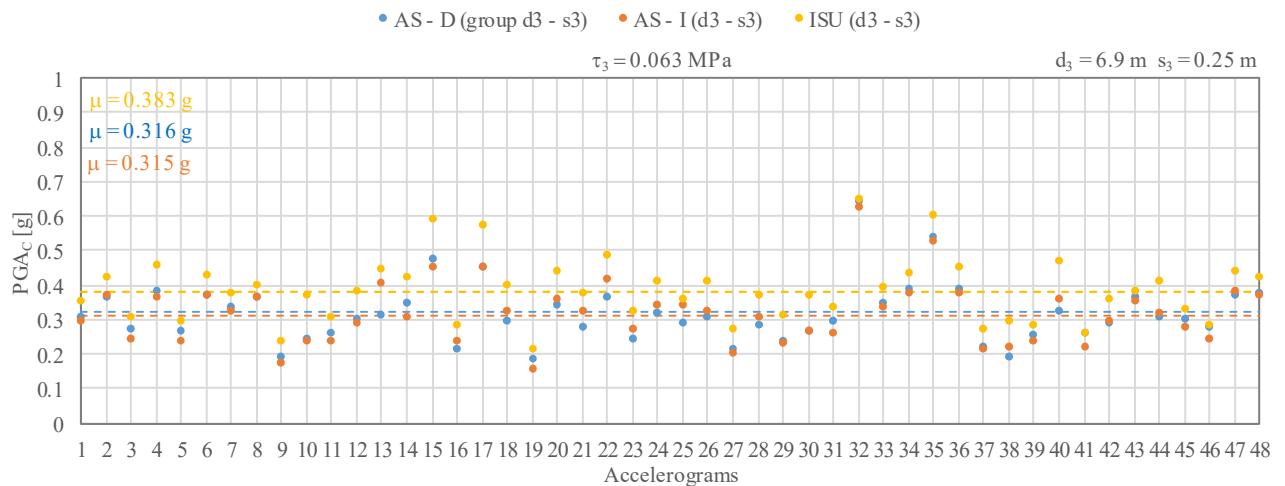


Figure 6.89: Comparison between the AS - D, the AS - I and the ISU for the group  $\tau_3$ -d<sub>3</sub>-s<sub>3</sub>.

Table 6.37: Expected and the actual behaviours on the variation of the PGAc for the group  $\tau_3$ -d<sub>3</sub>-s<sub>3</sub>.

ACCELEROGRAMS	AGGREGATE CONFIGURATION	EXPECTED BEHAVIOUR (PGAc)	ACTUAL BEHAVIOUR (PGAc)
1 - 2 -3 - 4 -5 - 6	3	decrement	increment
7 - 8 - 9 - 10 - 11 - 12	8	increment	increment
13 - 14 - 15 - 16 - 17 - 18	13	decrement	decrement
19 - 20 - 21 - 22 - 23 - 24	18	decrement	decrement
25 - 26 - 27 - 28 - 29 - 30	23	increment	decrement
31 - 32 - 33 - 34 - 35 - 36	28	increment	increment
37 - 38 - 39 - 40 - 41 - 42	33	decrement	decrement
43 - 44 - 45 - 46 - 47 - 48	38	increment	increment

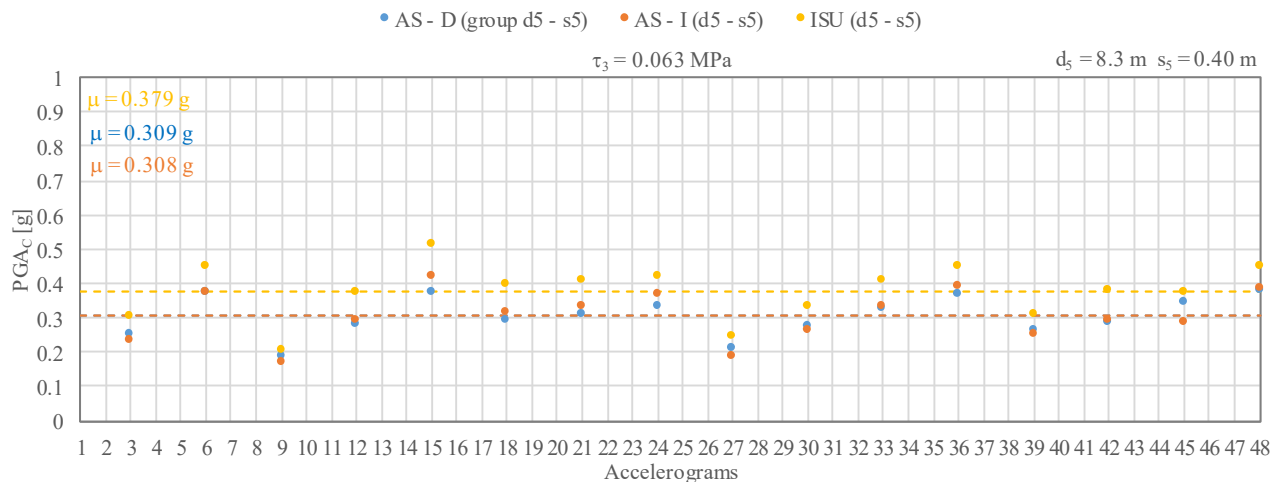


Figure 6.90: Comparison between the AS - D, the AS - I and the ISU for the group  $\tau_3$ - $d_5$ - $s_5$ .

Table 6.38: Expected and the actual behaviours on the variation of the  $PGA_C$  for the group  $\tau_3$ - $d_5$ - $s_5$ .

ACCELEROGRAMS	AGGREGATE CONFIGURATION	EXPECTED BEHAVIOUR ( $PGA_C$ )	ACTUAL BEHAVIOUR ( $PGA_C$ )
3- 6	5	increment	increment
9 - 12	10	increment	increment
15 -18	15	decrement	decrement
21 -24	20	decrement	decrement
27 - 30	25	decrement	increment
33 - 36	30	increment	decrement
39 -42	35	increment	increment
45 - 48	40	increment	increment

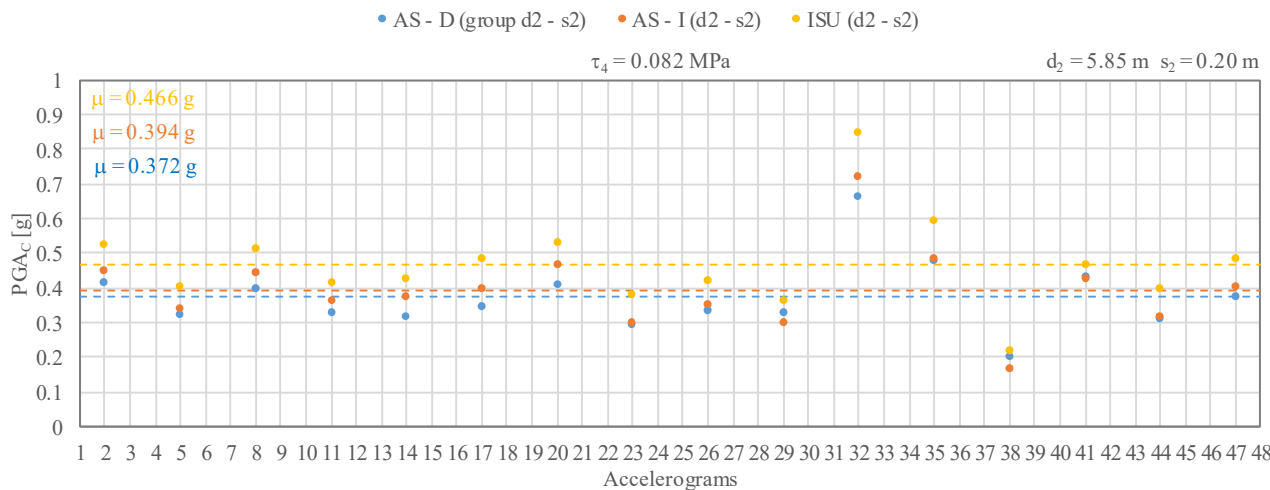


Figure 6.91: Comparison between the AS - D, the AS - I and the ISU for the group  $\tau_4$ - $d_2$ - $s_2$ .

Table 6.39: Expected and the actual behaviours on the variation of the  $PGA_C$  for the group  $\tau_4$ - $d_2$ - $s_2$ .

ACCELEROGRAMS	AGGREGATE CONFIGURATION	EXPECTED BEHAVIOUR ( $PGA_C$ )	ACTUAL BEHAVIOUR ( $PGA_C$ )
2 - 5	2	increment	decrement
8 - 11	7	decrement	decrement
14 - 17	12	decrement	decrement
20 - 23	17	decrement	decrement
26 - 29	22	decrement	increment
32 - 35	27	decrement	decrement
38 - 41	32	increment	increment
44 - 47	37	decrement	decrement

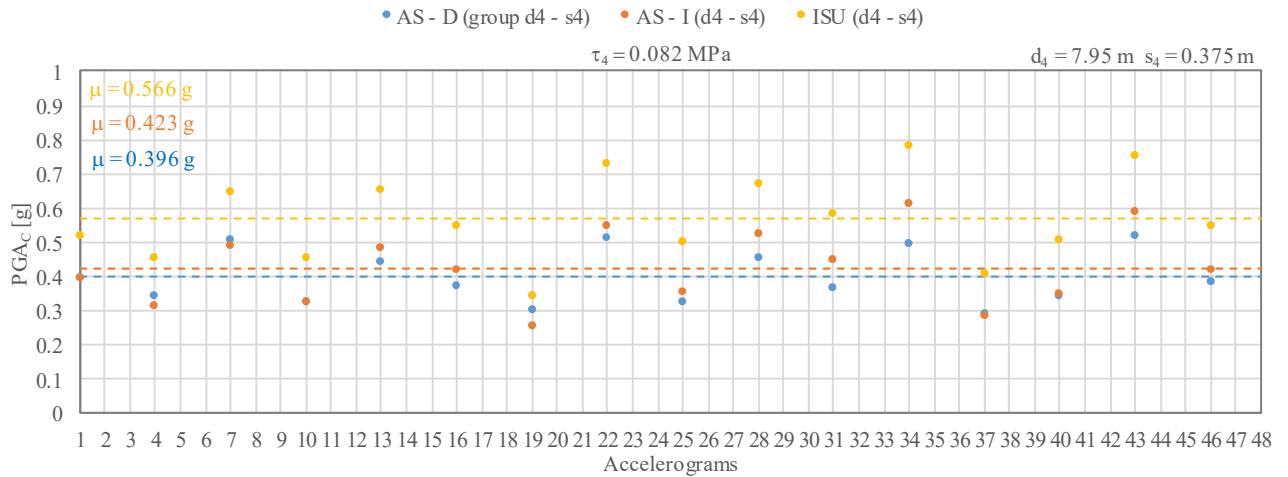


Figure 6.92: Comparison between the AS - D, the AS - I and the ISU for the group  $\tau_4$ - $d_4$ - $s_4$ .

Table 6.40: Expected and the actual behaviours on the variation of the  $PGAc$  for the group  $\tau_3$ - $d_4$ - $s_4$ .

ACCELEROGRAMS	AGGREGATE CONFIGURATION	EXPECTED BEHAVIOUR ( $PGAc$ )	ACTUAL BEHAVIOUR ( $PGAc$ )
1 - 4	4	increment	decrement
7 - 10	9	increment	decrement
13 - 16	14	decrement	decrement
19 - 22	19	decrement	decrement
25 - 28	24	decrement	decrement
31 - 34	29	decrement	decrement
37 - 40	34	decrement	decrement
43 - 46	39	decrement	decrement

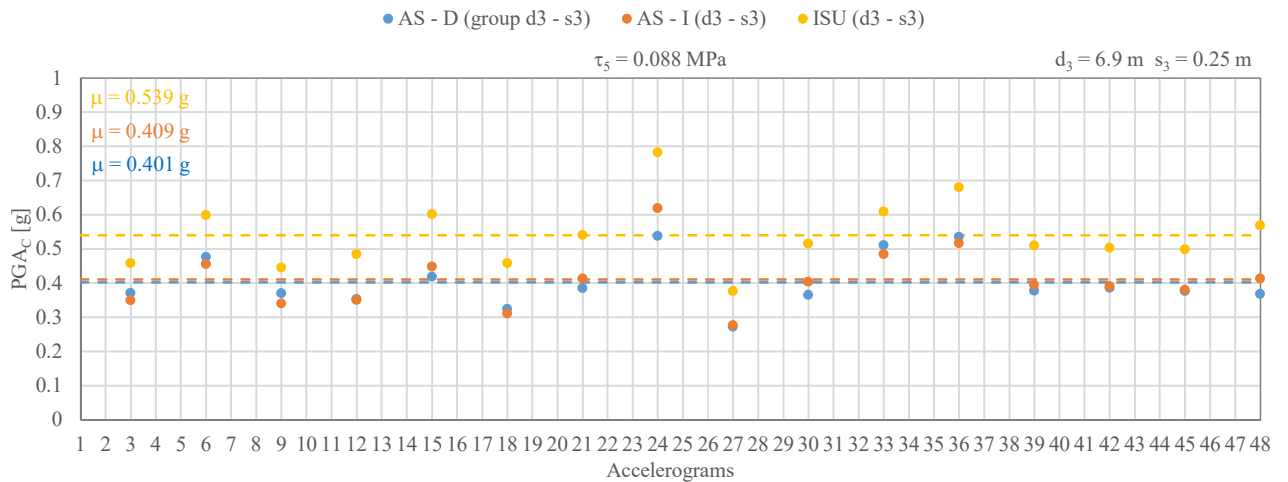


Figure 6.93: Comparison between the AS - D, the AS - I and the ISU for the group  $\tau_5$ - $d_3$ - $s_3$ .

Table 6.41: Expected and the actual behaviours on the variation of the  $PGAc$  for the group  $\tau_5$ - $d_3$ - $s_3$ .

ACCELEROGRAMS	AGGREGATE CONFIGURATION	EXPECTED BEHAVIOUR ( $PGAc$ )	ACTUAL BEHAVIOUR ( $PGAc$ )
3- 6	3	decrement	increment
9 - 12	8	increment	increment
15 - 18	13	decrement	decrement
21 - 24	18	decrement	decrement
27 - 30	23	increment	decrement
33 - 36	28	increment	increment
39 - 42	33	decrement	decrement
45 - 48	38	increment	decrement

In the Figures the average of the values of the  $PGA_C$  ( $\mu$ ) confirm that the aggregation of structural units in row in  $y$ -direction leads to a decrement of the vulnerability with respect to the isolated structural units (yellow lines) and that in most of the cases the AS - D models (blue lines) have an average of the  $PGA_C$  ( $\mu$ ) greater than that of the AS - I (orange lines). The results show that in the majority of the cases (50 on 72 total comparisons) the variation of the  $PGA_C$  referred to the AS - D with respect to the AS - I follows the expectations. The same methodology was applied to each of the cases differing for direction of the seismic action (positive and negative), collecting in total 1008 (14x72) comparisons. Table 6.42 gives the data referred to these 14 comparisons, highlighting the number of the cases where the  $PGA_C$  has a variation different from what is expected. With respect to the total comparisons, the cases with different behaviour are always under the 50%: the deviations from the expectative are, first of all, due to the variability of the seismic action and the irregular shape of the spectra, with respect to those of the code, but also is due to the fact that the ratio  $d/s$ , in this type of analyses, cannot be considered as the only parameters affecting the seismic response.

Table 6.42: Number of the cases where the  $PGA_C$  has a variation different from what is expected.

SEISMIC DIRECTION	TYPE OF COMPARISON	TOTAL CASES	DIFFERENT BEHAVIOUR
$x$	$d/s$ as average of the 5 Units	72	24
$x (-)$	$d/s$ as average of the 5 Units	72	29
$y$	$d/s$ as average of the 5 Units	72	31
	$d/s$ as average of the Units 1-2	72	19
$y (-)$	$d/s$ as average of the 5 Units	72	26
	$d/s$ as average of the Units 1-2	72	22
$y$ Unit 3	$d/s$ as average of the 5 Units	72	28
	$d/s$ as average of the Units 3-4-5	72	31
$y (-)$ Unit 3	$d/s$ as average of the 5 Units	72	27
	$d/s$ as average of the Units 3-4-5	72	33
$y$ Unit 4	$d/s$ as average of the 5 Units	72	33
	$d/s$ as average of the Units 4-5	72	32
$y (-)$ Unit 4	$d/s$ as average of the 5 Units	72	33
	$d/s$ as average of the Units 4-5	72	32

Finally, the 9 comparisons showed in Table 6.32 were carried out in terms of fragility curves, considering the 4 case analyses performed

- $x$ -direction (Figures 6.94 and 6.95);
- $y$ -direction (Figures 6.96 and 6.97);
- $y$ -direction, over the attainment of the LS limit state for the Unit 3 (Figures 6.98 and 6.99);

- $y$ -direction, over the attainment of the LS limit state for the Unit 4 (Figures 6.100 and 6.101).

In the Figures below, the red curves are those obtained in Figure 6.82 for the aggregate structures with different structural units (AS - D), using the data of the RS models and applying Monte Carlo simulations and the grey curves were obtained using all the actual  $PGA_C$  referred to the aggregate structures with identical structural units (AS - I). These latter curves group all the 9 coloured curves related to the 9 comparisons showed in Table 6.32, divided according the values of  $d$ ,  $s$  and  $\tau$ . In all the cases the blue curves, representing the group aggregates  $d_3-s_3-\tau_3$ , are in a median position between those having lower and higher values, respectively, of the parameters  $d$ ,  $s$ , and  $\tau$ .

The curves showed that, for these specific aggregate configurations, the fragility of the AS - I is higher than the fragility of the AS - D. Of course, these cannot be considered as general results, because they are affected by the randomly selections of the geometric parameters ( $d$  and  $s$ ), which led to generate aggregate structures with different structural units (AS - D) less fragile than those with identical structural units (AS - I). To confirm these results, all the values of  $d$  and  $s$  of the 200 structural units (5 units times 40 aggregate configurations) along the AS - D, were compared with the 40 values of  $d$  and  $s$  of the identical structural units along the AS - I. Table 6.43 shows that the aggregate configurations AS - D having structural units with  $d$  and  $s$  greater than those of the identical structural units along the AS - I are more than the 50% of the total cases. Since it was shown that greater values of  $d$  and  $s$  increase the collapse  $PGA_C$ , these percentages can justify the greater fragility of the AS - I with respect to the AS - D, affected by the differences in the geometrical properties.

Table 6.43: Comparison between the AS - D and the AS - I according to the variation of  $d$  and  $s$  between the structural units along the AS.

UNITS ALONG THE AS	AS - D THICKNESSES ( $s$ ) GREATER THAN AS - I THICKNESS ( $s$ )	AS - D DISTANCES ( $d$ ) GREATER THAN AS - I DISTANCE ( $d$ )
200	132	103

- *x*-direction

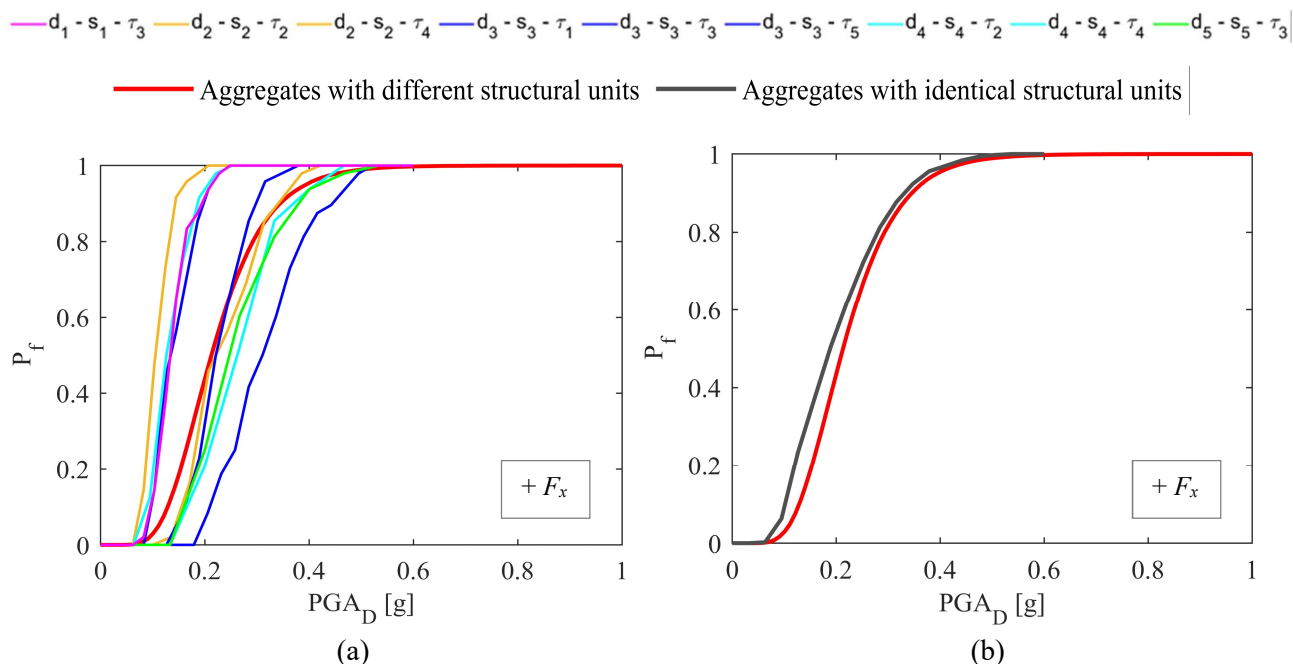


Figure 6.94: Fragility curves in *x*-direction (+ $F_x$ ): comparison between (a) the AS-D and the 9 AD-I groups and (b) the AS-D and the AS-I.

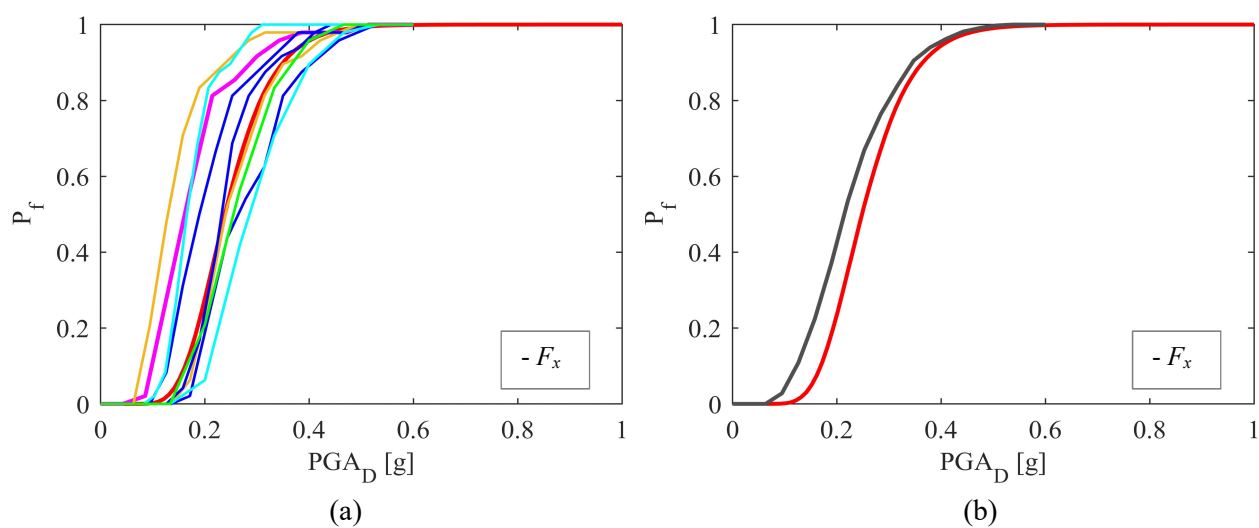


Figure 6.95: Fragility curves in *x*-direction (- $F_x$ ): comparison between (a) the AS-D and the 9 AD-I groups and (b) the AS-D and the AS-I.

- *y*-direction

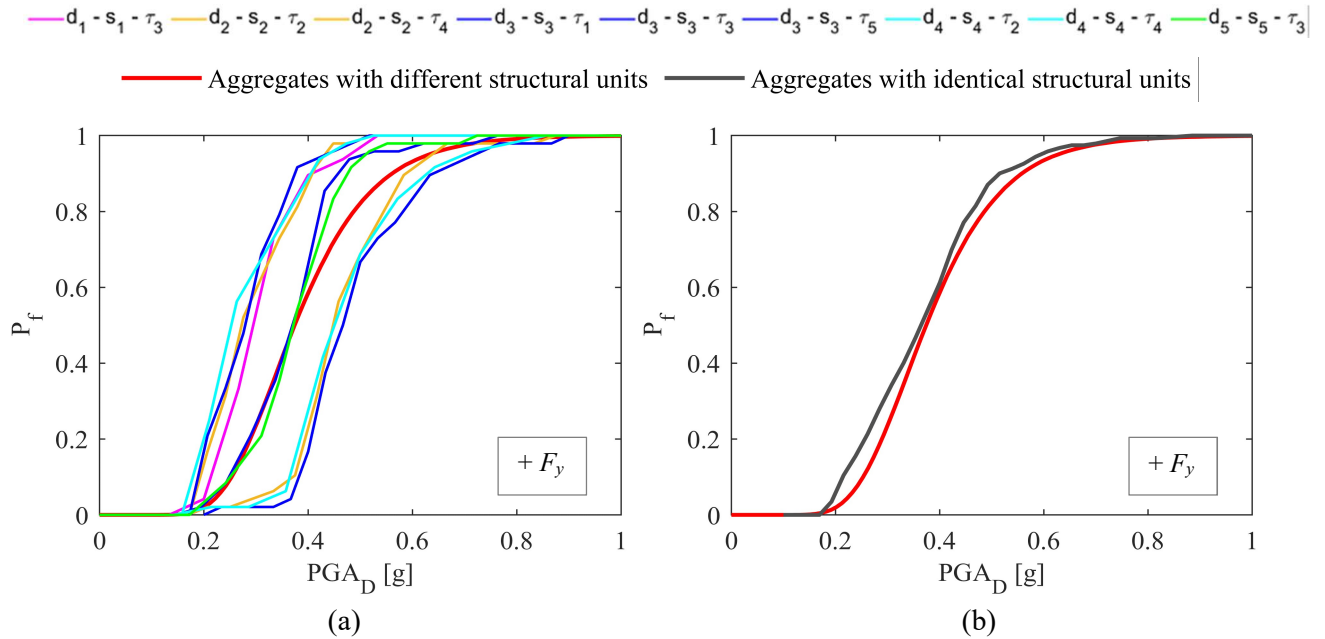


Figure 6.96: Fragility curves in *y*-direction (+  $F_y$ ): comparison between (a) the AS-D and the 9 AD-I groups and (b) the AS-D and the AS-I.

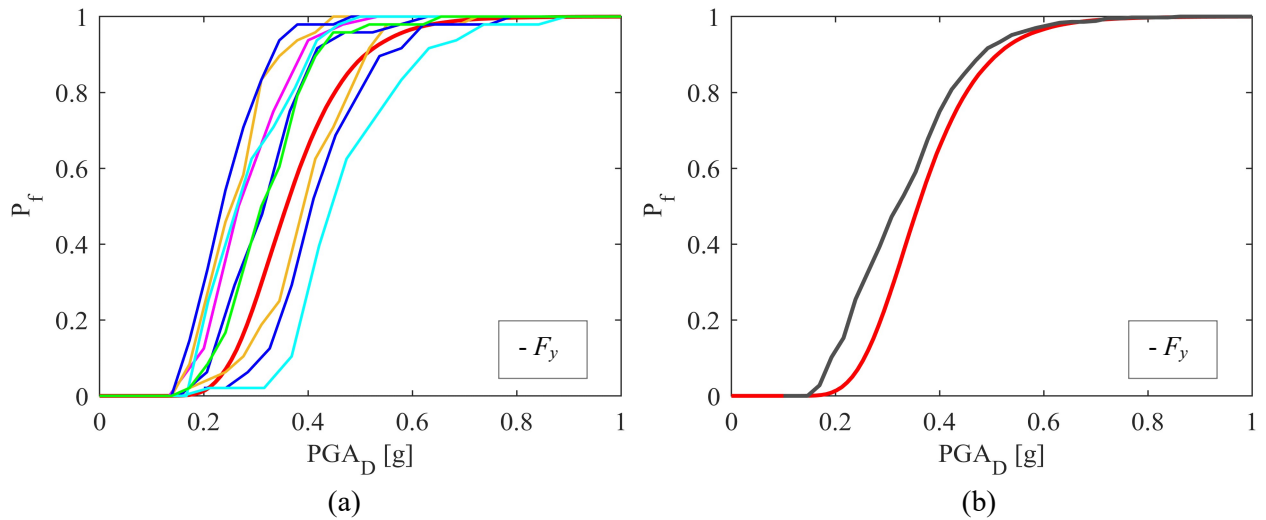


Figure 6.97: Fragility curves in *y*-direction (-  $F_y$ ): comparison between (a) the AS-D and the 9 AD-I groups and (b) the AS-D and the AS-I.

- *y*-direction, over the attainment of the LS limit state (Unit 3)

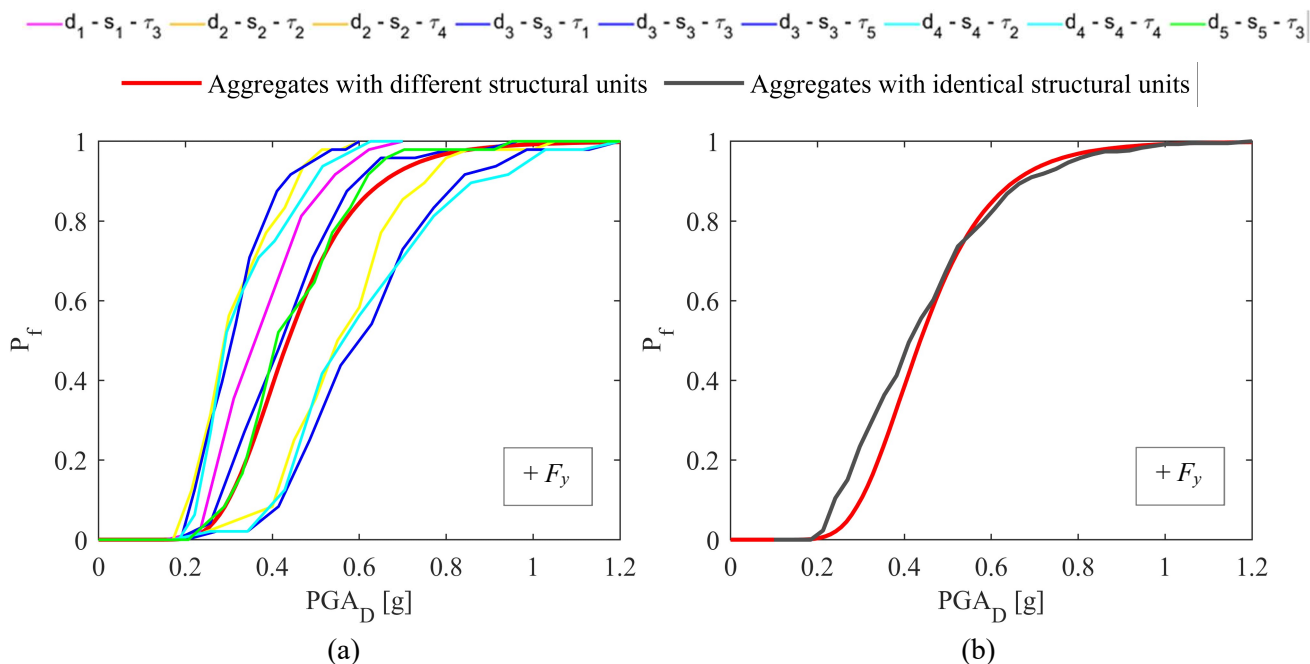


Figure 6.98: Fragility curves in *y*-direction (+  $F_y$ ) over the attainment of the LS limit state (Unit 3): comparison between (a) the AS-D and the 9 AD-I groups and (b) the AS-D and the AS-I.

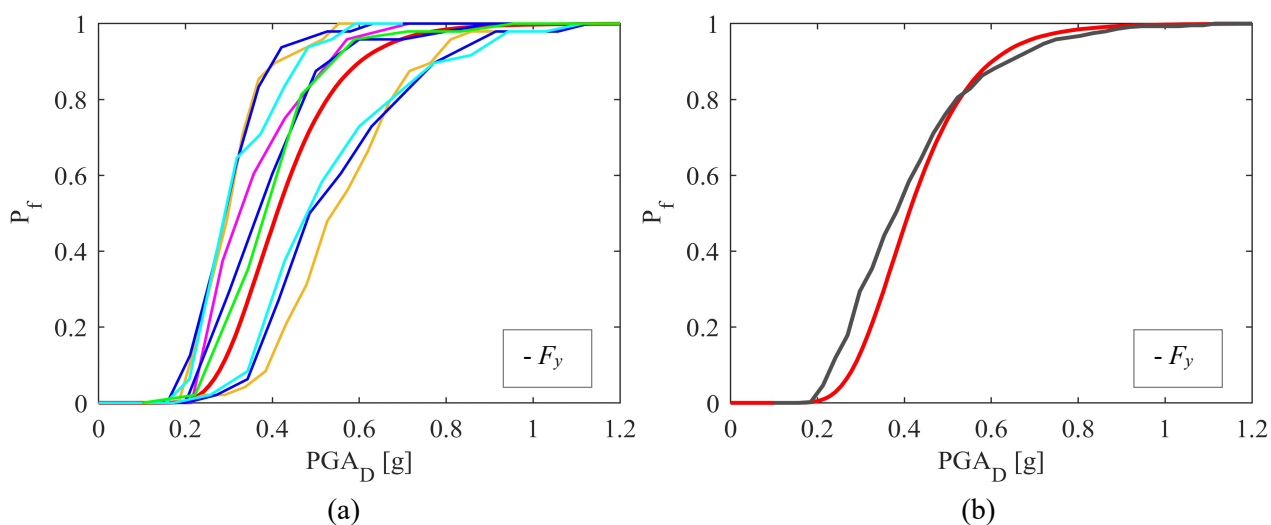


Figure 6.99: Fragility curves in *y*-direction (-  $F_y$ ) over the attainment of the LS limit state (Unit 3): comparison between (a) the AS-D and the 9 AD-I groups and (b) the AS-D and the AS-I.

- *y*-direction, over the attainment of the LS limit state (Unit 4)

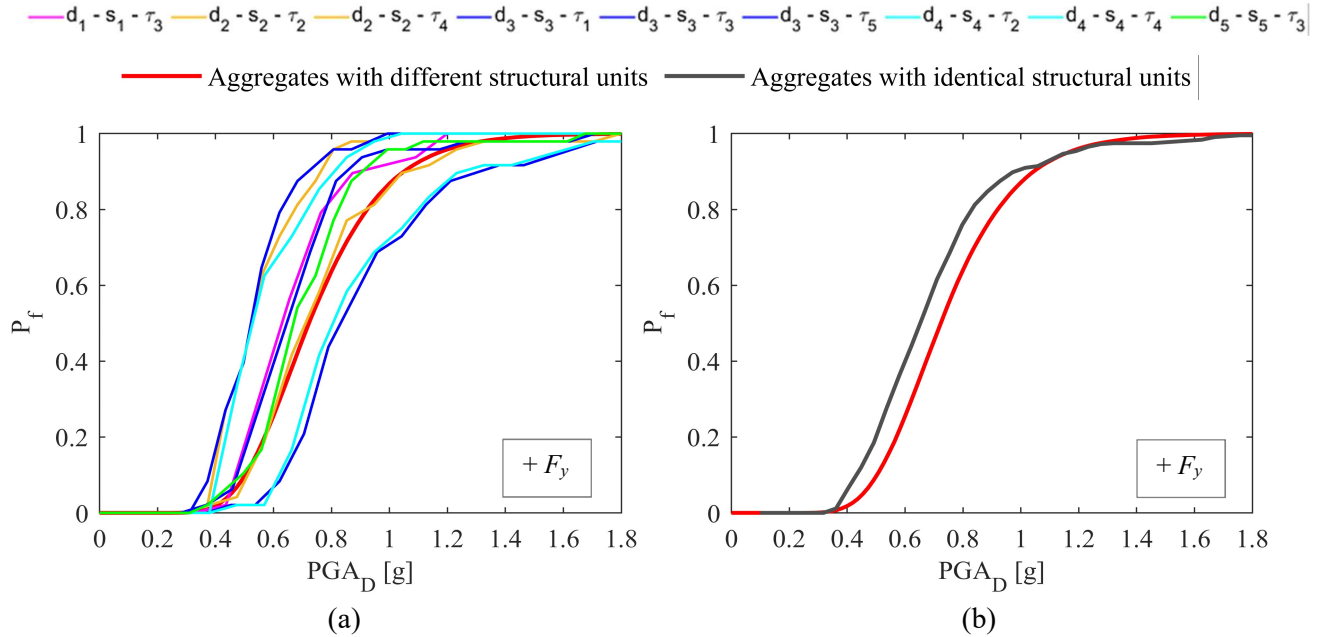


Figure 6.100: Fragility curves in *y*-direction ( $+F_y$ ) over the attainment of the LS limit state (Unit 4): comparison between (a) the AS-D and the 9 AD-I groups and (b) the AS-D and the AS-I.

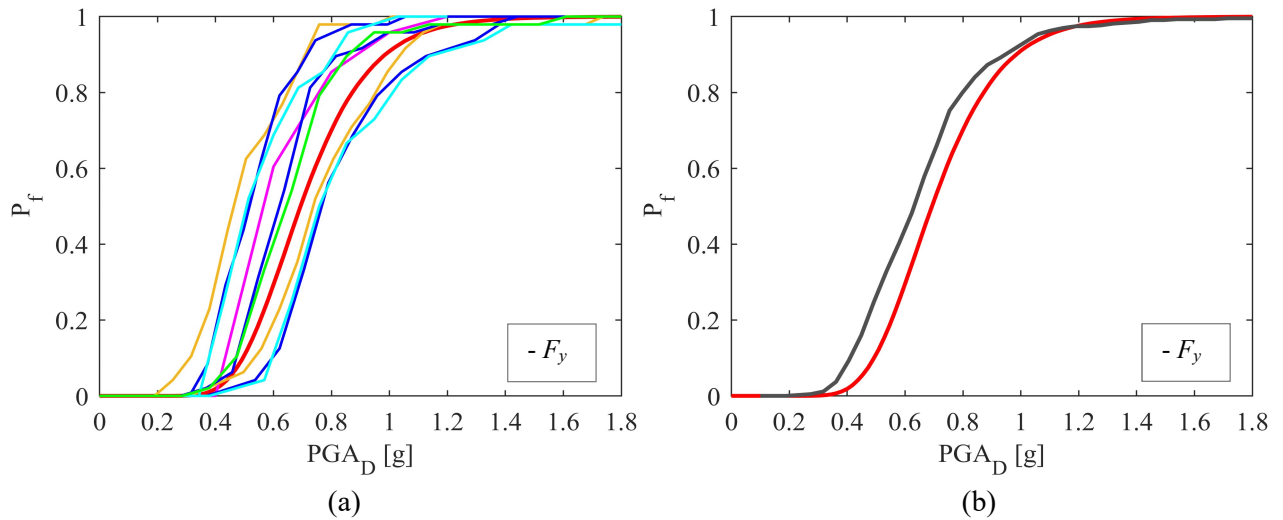


Figure 6.101: Fragility curves in *y*-direction ( $-F_y$ ) over the attainment of the LS limit state (Unit 4): comparison between (a) the AS-D and the 9 AD-I groups and (b) the AS-D and the AS-I.



## **7. SEISMIC FRAGILITY OF STONE MASONRY STRUCTURES: CASE STUDIES IN SEIXAL, PORTUGAL**

---

## 7.1 Introduction

The second application of this thesis is focused on the seismic fragility assessment of stone masonry structures, carried out during my abroad period in Guimarães, Portugal, country where the masonry structures in aggregate represent a very common structural typology, as in Italy, and in some cases, the structural units along the aggregates are characterized by structural and geometrical heterogeneities (Bernardini et al., 2018).

The study of masonry structures belonging to the old historic centres, in particular those enclosed in aggregates, is very often subjected to the consideration of all the possible variabilities and uncertainties involved in the problem. For this reason, this Section starts from a parametric study, considering some structural and geometrical variabilities, referred to some structural typologies sited in a village in the south of Portugal.

The Portuguese historical centres are very often characterized by a big heterogeneous distribution of buildings, due to the unbridled urban growth and to the necessity to fill all the possible urban spaces. Sometimes, catastrophic events, like the earthquakes, lead to the need to requalify or to rebuild the historical centres. It is the case of the old city centre of Seixal, located about 25 km south of Lisbon, in Portugal, which was severely affected by the 1755 Lisbon earthquake. Such an event was in the origin of a deep and long reconstruction process, which profoundly shaped the image of the city. This process led to the formation of a diversified urban centre characterized by a series of homogeneities and similarities related to the architectural arrangement, the structure and the materials used. Several studies focused on the constructive and structural characterization of the buildings in the old city centre of Seixal have been carried out in the last years (Ferreira et al., 2013; Santos et al., 2013; Ferreira et al., 2016), allowing for the identification of the most prevalent structural typologies in the city. In particular, Santos et al. (2013) have identified four main building typologies, ordered from the most to the less representative: narrow front buildings, wide front buildings, row buildings and simple ground floor buildings.

This Chapter aims to study the seismic vulnerability and fragility of the most representative one (the narrow front buildings). Thus, starting from the individuation of this building typology, a parametric study taking into account the uncertainty and the variation of some parameters is presented and discussed herein, allowing to define the variability of these buildings within the study area. Four different parameters - the number of floors, the inter-

storey eight, the type of slabs and the type of internal walls - have been selected and combined in order to obtain 36 different structural typologies, which were subsequently analysed by means of non-linear static analyses with TreMuri software.

It is noticed the presence of both isolated buildings and aggregate structures in Seixal (Vicente et al., 2010a), and, as already discussed in the previous Sections, it is a common simplification in civil engineering practice to analyse the seismic behaviour of a building considering it as an isolated structural unit, even when it belongs to an aggregation of buildings. For this reason, this work aims to analyse and compare the seismic response of the 36 obtained structural typologies as isolated units and that referred to the aggregations of identical structural units in row, allowing to show the differences in the seismic responses when the buildings are affected by the actions of the adjacent ones.

Moreover, the comparison in terms of PGA corresponding to the attainment of the life safety limit state ( $PGA_C$ ) is also performed considering 50 different seismic actions for each of the 36 structural typologies, derived from the 50 accelerograms referred to real earthquakes showed in Section 5.4. The actual obtained values of the PGA were used to obtain the fragility curves. A second set of fragility curves were further obtained and compared with the previous one, resorting to a statistical approach with Gaussian distributions, by means of Monte Carlo method (Section 5.6).

## **7.2 Identification of the structural typologies**

As already mentioned, the structural typology used in this Section is based on the most representative of four building typologies previously identified and characterised by Santos et al. (2013). This typology, originally designated by the authors as “narrow front buildings”, presents a very simple, rectangular and small plan organised in a band layout, three vertical openings alignments are present in the main façade and the number of floors is not more than 3. The structure is made by stone masonry; most of these buildings presents timber slabs and the roof structure is always pitched and made by timber (Ferreira et al., 2016).

Figure 7.1 shows the architectural characteristics of some masonry structures, belonging to the “narrow front buildings” typology, individuated by the authors.



Figure 7.1: Architectural plans and front views of some “narrow front buildings” (adapted from Santos et al. (2013)).

In this work, a building was modelled as prototype of the “narrow front buildings” typology, obtained according to the geometrical and structural characteristics observed in these type of buildings. The model object of the study is showed in Figure 7.2: since it represents a prototype, it was obtained trying to converge the main characteristics of different buildings in a unique model, representative of the “narrow front buildings”.

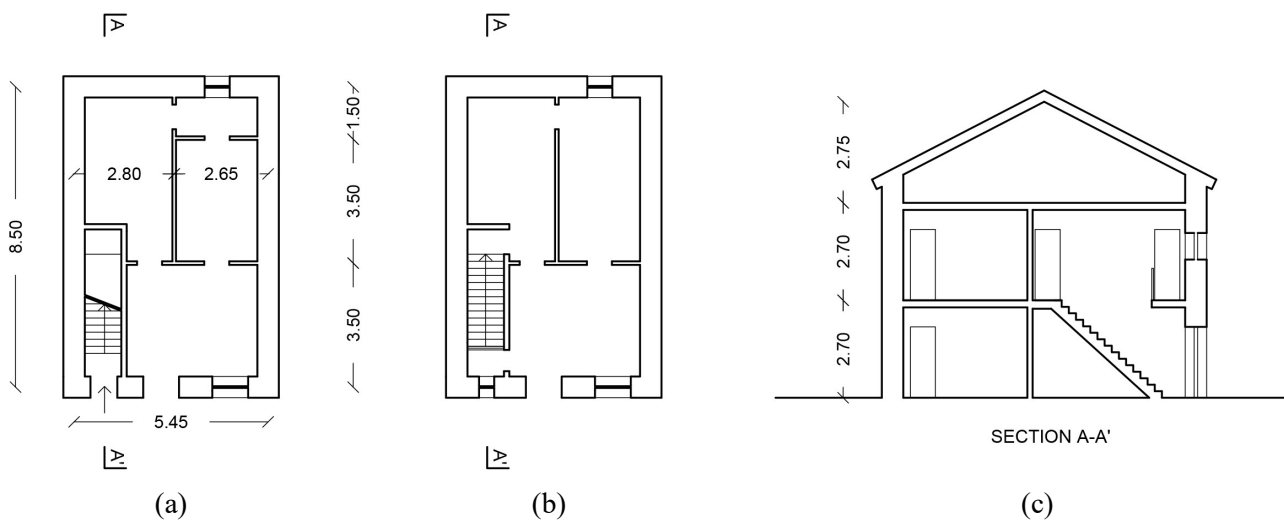


Figure 7.2: (a) Architectural ground floor plan, (b) architectural first floor plan and (c) Section A-A’.

Therefore, in order to taking into account the variability of the building in the city, 4 different parameters were chosen: the number of floors, the inter-storey height, the type of the slabs and the type of the internal walls. The variations considered in each one of these parameters are presented in Table 7.1.

Table 7.1: Variation considered for the structural and geometrical properties.

NUMBER OF FLOORS			INTERSTOREY HEIGHT			TYPE OF SLABS		TYPE OF INTERNAL WALLS	
1	2	3	2.5 m	2.7 m	3.0 m	Concrete slabs	Timber slabs	Clay brick walls	“Tabique” walls

From the variation and the combination of the parameters identified in Table 7.1 it was then possible to obtain 36 different structural typologies. Figure 7.5 illustrates the logic-tree diagram used to obtain the different structural typologies.

The distribution of the parameters provides buildings with 1, 2 or 3 floors, each one of these with 3 different inter-storey heights (2.5 m, 2.7 m, 3.0 m), resulting in 9 buildings. In turn, based on Ferreira et al. (2016), each one of these can have either concrete slabs with *tabique* walls or clay brick walls, or timber slabs with *tabique* walls or clay brick walls.

In Figure 7.5, each building is identified with an acronym, where the first symbol indicates the number of floors of the building (1, 2 or 3); the second symbol indicates the inter-storey height expressed in meters (2.5, 2.7 or 3.0); the third symbol indicates the type of slabs, where “C” stands for concrete slabs and “T” stands for timber slabs; and the forth symbol indicates the type of internal walls, where “T” stands for *tabique* walls and “B” stands for clay brick walls.

According to Ferreira et al. (2016), most of the horizontal structures of these buildings are timber slabs composed by rectangular cross-section beams with around 0.10 m x 0.10 m and timber planks with a thickness of about 0.03 m. Despite not very common, it is possible to find some concrete slabs in the old city centre of Seixal, typically composed of classic hollow-core structures, reason why they were also considered herein. As to the pitched roof structures, they were considered as being made of timber beams of around 0.10 m x 0.10 m cross section and a timber plank 0.03 m thick, covered by ceramic tiles.

The external masonry walls were considered the same for all the buildings, being constituted by irregular fragments of limestone, randomly distributed and linked by lime mortar, sand and earth, with the thickness equal to 0.60 m (Figures 7.3(a) and (b)). The most common

internal walls are the *tabique* walls, which are usually made of vertical timber boards with 0.10 or 0.15 m of width and horizontal laths filled in the gaps by rubble masonry. With a total thickness of about 0.10 m, *tabique* walls may also present diagonal boards. Figure 7.4(a) shows an example of *tabique* wall present in a building in Seixal and Figure 7.4(b) shows an existing *tabique* wall present in one of the buildings constructed in Lisbon after the 1755 earthquake, under the plan of the Marquis of Pombal, later known as “Pombalino” buildings (Appleton, 2003; Lopes et al., 2014). It was also considered the possibility of the internal walls be made of a single layer of clay bricks with a total thickness of 0.125 m, though less frequently seen in the old city centre of Seixal.



Figure 7.3: External aspect of some of the most common limestone masonry walls in Seixal (Ferreira et al., 2016).



Figure 7.4: Internal masonry *tabique* walls: (a) “narrow front building” in Seixal (Ferreira et al., 2016) and (b) “Pombalino” building in Lisbon (Appleton, 2003; Lopes et al., 2014).

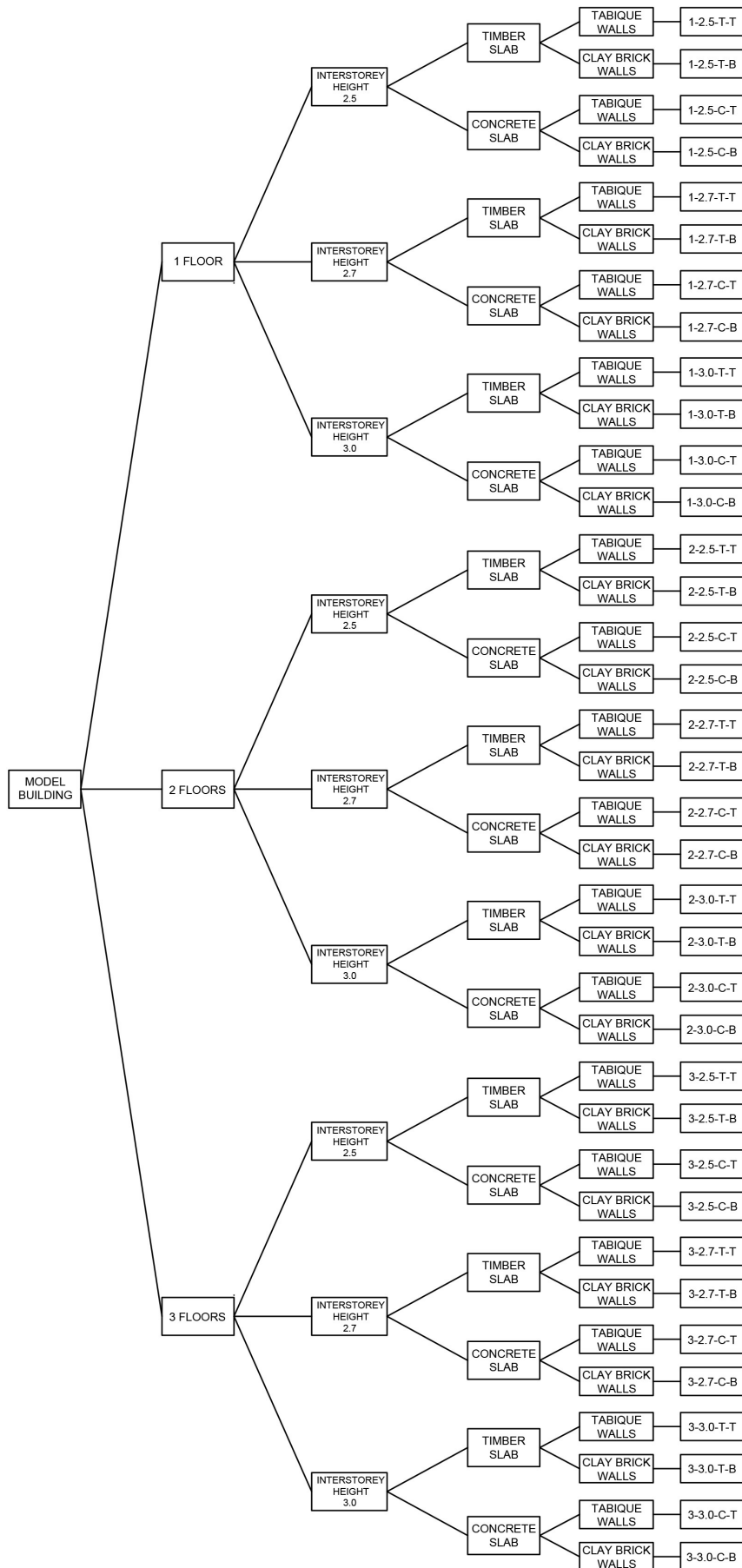


Figure 7.5: Logic-tree diagram built used to obtain the 36 different structural typologies analysed.

### 7.3 Numerical modelling of the structures

Since this work aims to compare the seismic fragility of isolated masonry buildings with the fragility of those enclosed in aggregate, both models are illustrated in Figures 7.6 and 7.7. As in the previous Sections, the structures were modelled with TreMuri software and using the same settings of analysis.

As an example, Figures 7.6(a) and (b) show respectively the plan view of the structural ground floor and the 3D model of the isolated structural unit “2-2.7-T-B”, i.e., the structural typology with 2 floors, inter-storey height equal to 2.7 m, timbers slabs and *tabique* walls.

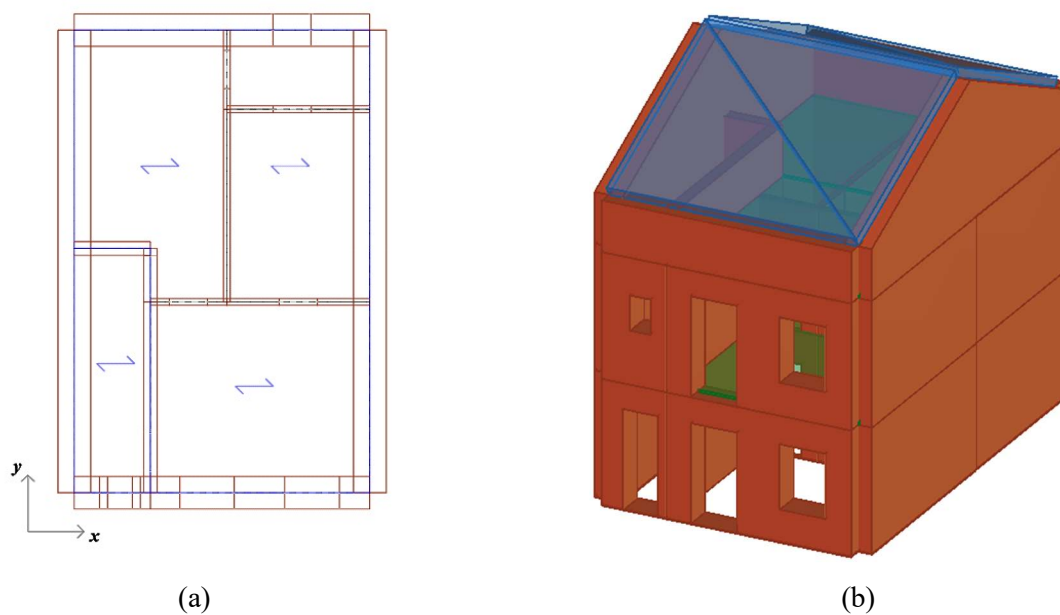


Figure 7.6: (a) Structural ground floor plan of the model “2-2.7-T-B” and (b) 3D structure of the model “2-2.7-T-B”.

Similarly, Figures 7.7(a) and (b) present the plan view of the ground floor and the 3D model of the aggregate resulting from the association of the 5 structural units “2-2.7-T-B”. As can be seen in Figure 7.7(a), the single structural unit was aggregated in row and the common walls between adjacent buildings do not have a doubled thickness, because from the investigations on the building typologies in the city it was noticed the presence of aggregate structures with single thickness of adjacent walls.

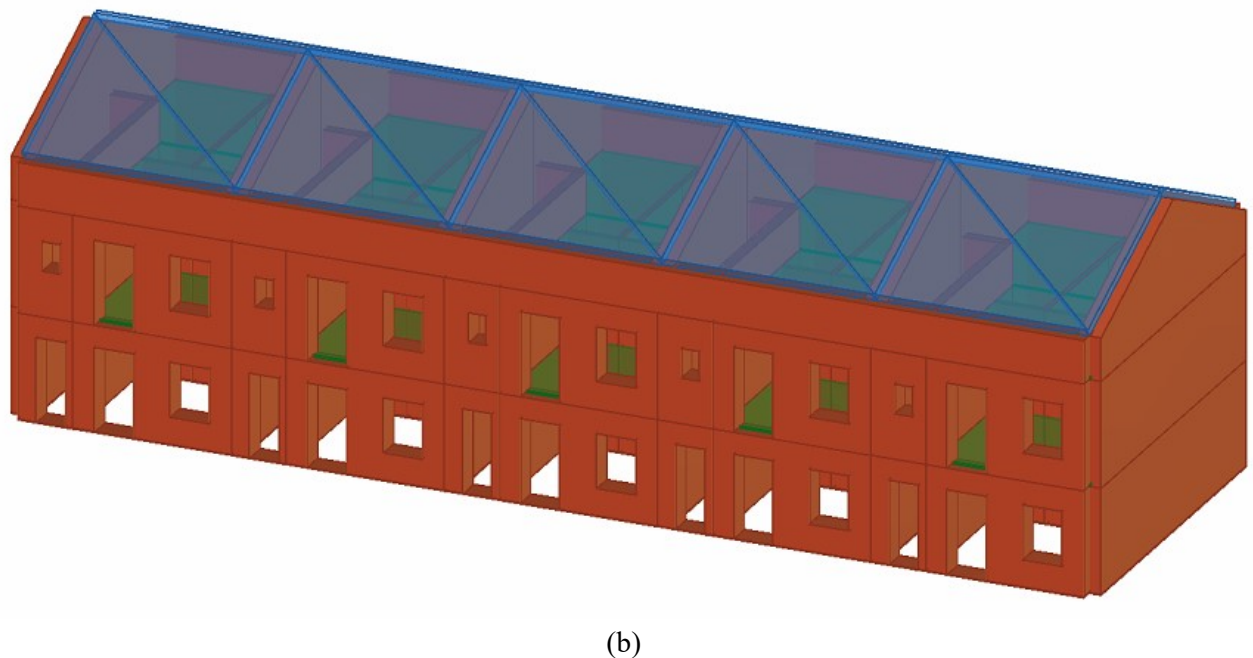
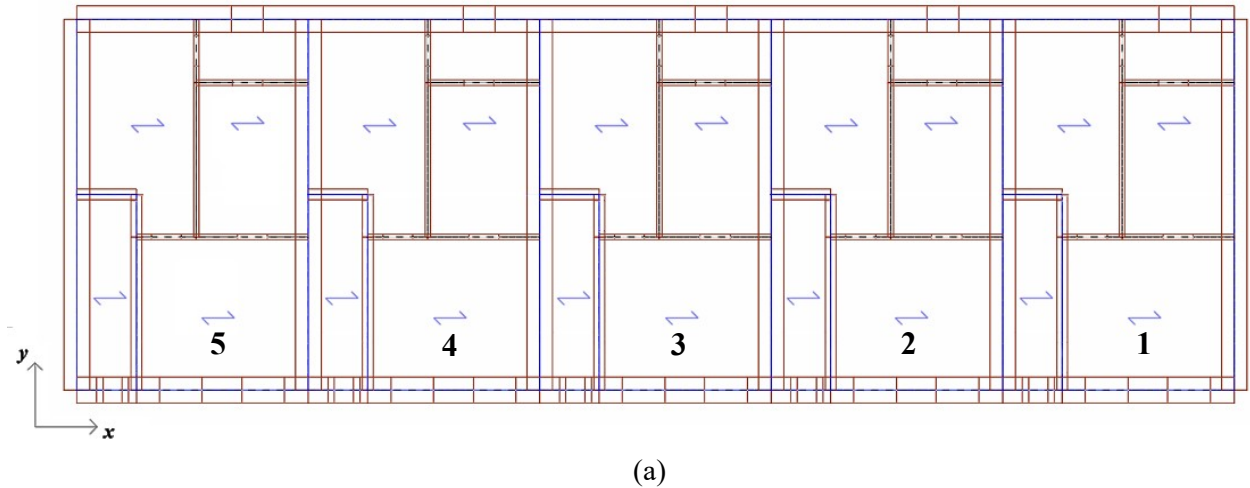


Figure 7.7: (a) Structural ground floor plan of the aggregate model “2-2.7-T-B” and (b) 3D structure of the aggregate model “2-2.7-T-B”.

### 7.3.1 Mechanical and geometrical properties of the masonry walls

The mechanical and geometrical properties of the external walls were defined based on the results obtained from an experimental campaign carried out by Vicente et al. (2010b), involving flat-jack and dynamic tests, which were crosschecked and validated from the comparison with other experimental tests performed in buildings with similar construction and structural characteristics, as well as from the values reported in the Italian Code (NTC, 2008).

Similarly, the mechanical properties of the clay brick internal walls were defined according to the Italian Code. In order to consider just one layer of bricks, the thickness of these walls

was set equal to 0.125 m; the walls around the staircase are modelled as clay brick internal walls with 0.25 m (two layers of bricks) in all the 36 defined models, to make more rigid that part of the buildings.

The timber *tabique* walls have 0.10 m of thickness. These walls are modelled in TreMuriRicerca (Lagomarsino et al., 2008) program following the equivalent frame model approach and considering an equivalent thickness of 0.04 m (Pires, 2013), corresponding to the average thickness of the vertical board. The behaviour of the panels is modelled by non-linear beam elements with lumped (concentrated) inelasticity and by assuming a bi-linear force-deformation constitutive law. The elastic branch is directly determined by the shear and flexural stiffness, computed based on the geometric and mechanical properties of the element (as presented in Figure 4.10 for the case of masonry elements). Their behaviour is determined from the comparison between the acting shear force ( $V$ ) and the ultimate shear force ( $V_u$ ) considering only shear failure modes. The hypothesis of having flexural failure modes is disregarded taking into account that these walls were constructed directly on top of the timber floors (i.e. there is no continuity between floors). Despite these considerations, the *tabique* walls have been considered in the numerical models in order to have a comparable distribution of the vertical loads in the buildings. The *tabique* walls mechanical properties were defined according to the experimental results from compression and shear tests performed by Rebelo et al (2016) in typologically similar walls.

The mechanical and geometrical properties of the three types of walls considered in the models, respectively the compressive strength ( $f_m$ ), the shear strength ( $\tau$ ), the elastic modulus ( $E$ ), the shear modulus ( $G$ ) and the thickness ( $s$ ), are given in Table 7.2.

Table 7.2: Mechanical and geometrical properties of the masonry walls.

<b>MASONRY WALLS</b>	$f_m$ (MPa)	$\tau$ (MPa)	<b>E</b> (GPa)	<b>G</b> (GPa)	$s$ (m)
Limestone external walls	1.00	0.025	1.00	0.25	0.60
Clay brick walls	2.40	0.06	1.20	0.40	0.125
“Tabique” walls	0.56	0.01	0.13	0.002	0.04

### 7.3.2 Mechanical and geometrical properties of the slabs

The slabs were modelled as orthotropic membranes, with chosen equivalent thickness ( $t$ ).

The hollow-core concrete slabs were modelled considering reinforced concrete joists, alternated with perforated bricks and a continuous layer of concrete above. The total thickness

of the structural slabs is equal to 0.25 m. Since the concrete layer is fixed equal to 0.05 m, the software establish an equivalent thickness equal to 0.05 m.

Main timber beams and a timber plank above make the timber slabs. Since the shortage of detailed information about the geometry of the structural elements, according to Maio et al. (2017) a similar timber slab was chosen, with a cross section of the main timber beams 0.10 m x 0.10 m, spanned in 0.40 m. The timber plank above was chosen equal to 0.03 m. According to Maio et al. (2017) the equivalent thickness in the software was defined equal to 0.05 m and the mechanical properties were chosen according to the New Zealand Guidelines (NZSEE, 2015). The structure of the roof is the same of the timber slabs: it is pitched and covered by roof brick tiles (Ferreira et al., 2016).

The mechanical and geometrical properties of the slabs, respectively the main slab modulus of elasticity ( $E_1$ ), the secondary slab modulus of elasticity ( $E_2$ ), the slab shear modulus ( $G$ ), the equivalent thickness ( $t$ ), are given in Table 7.3.

Table 7.3: Mechanical and geometrical properties of the slabs.

SLABS	$E_1$ (GPa)	$E_2$ (GPa)	$G$ (GPa)	$t$ (m)
Hollow-core concrete slab	30.00	15.00	12.50	0.05
Timber slab	7.00	3.50	0.009	0.05

## 7.4 Push-over analyses

Several non-linear static analyses were performed in order to obtain the structural capacity for each of the 36 models (isolated structural units and aggregate structures), using TreMuri software. The two orthogonal directions of the seismic action were considered ( $x$ ,  $y$ ) and an uniform load pattern (i.e. proportional to mass) was assigned, because it resulted more conservative than the load pattern proportional to the first vibration mode. As presented in Figure 7.6(a), the  $x$ -direction is that parallel to the short side of the buildings, the  $y$ -direction is the perpendicular one, as in the previous Sections. Since according to the Italian code (NTC, 2018) the LS limit state is reached when the maximum total shear of the model decreases of the 20%, the last points of the pushover curves are referred to this decrement. As shown in Figures 7.6 and 7.7 the buildings have a more regular plan shape and the distribution of the openings is more symmetric in the masonry panels, with respect to those sited in Bologna. Thus, since the results have shown differences not relevant, in the following only the capacity

curves related to the positive seismic actions ( $+F_x$  and  $+F_y$ ) are reported. The results referred to the negative seismic actions ( $-F_x$  and  $-F_y$ ) are given in Appendix C.

- *x-direction*

At first, the 36 models were considered as isolated structural units. Then, 36 aggregations of identical structural units were assembled in row and horizontal positive forces in  $x$ -direction ( $+F_x$ ) were applied. As an example, Figures 7.8(a) and (b) present respectively the curves related to the 6 isolated structural units (ISU) with 2 floors and timber slabs (“2-2.5-T-T”; “2-2.7-T-T”; “2-3.0-T-T”; “2-2.5-T-B”; “2-2.7-T-B”; and “2-3.0-T-B”) and to the 6 aggregate structures (AS), with the same identical structural units, aggregated in row. Following the same logic, Figures 7.9(a) and (b) show respectively the curves related to the 6 isolated structural units with 2 floors and concrete slabs (“2-2.5-C-T”; “2-2.7-C-T”; “2-3.0-C-T”; “2-2.5-C-B”; “2-2.7-C-B”; and “2-3.0-C-B”) and the 6 aggregations of the same identical structural units, aggregated in row. In all cases, the curves are reported in terms of total shear divided by the total mass ( $V/M$ ) and the displacement obtained as average, weighted on the masses, of the node displacements in the top of the buildings ( $d$ ).

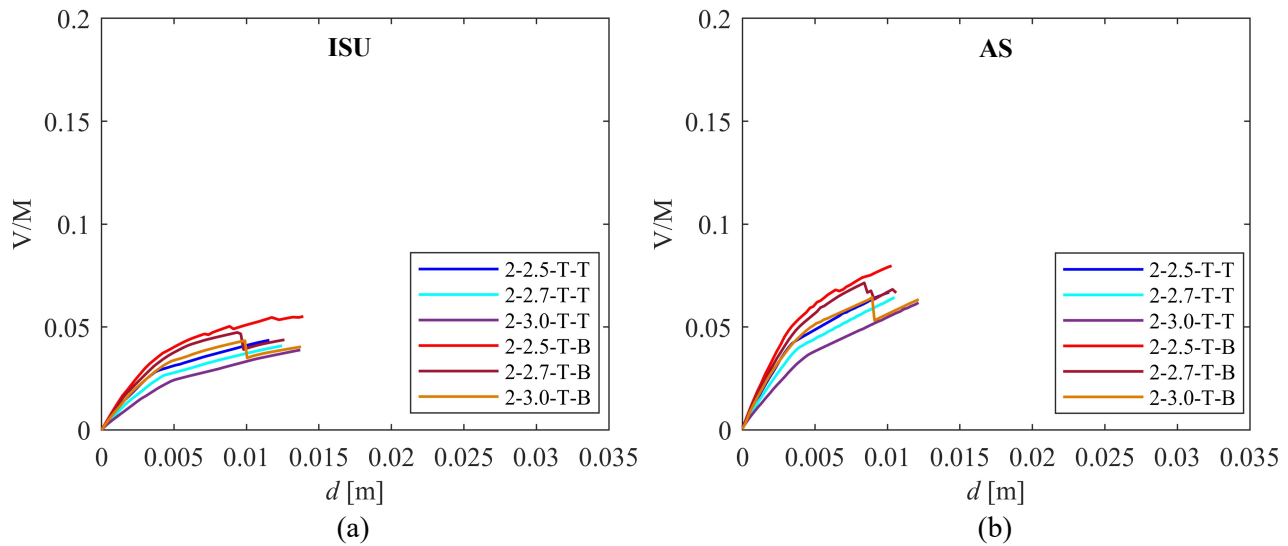


Figure 7.8:  $x$ -direction push-over curves of the buildings with 2 floors and timber slabs: (a) Isolated structural units and (b) Aggregate structures.

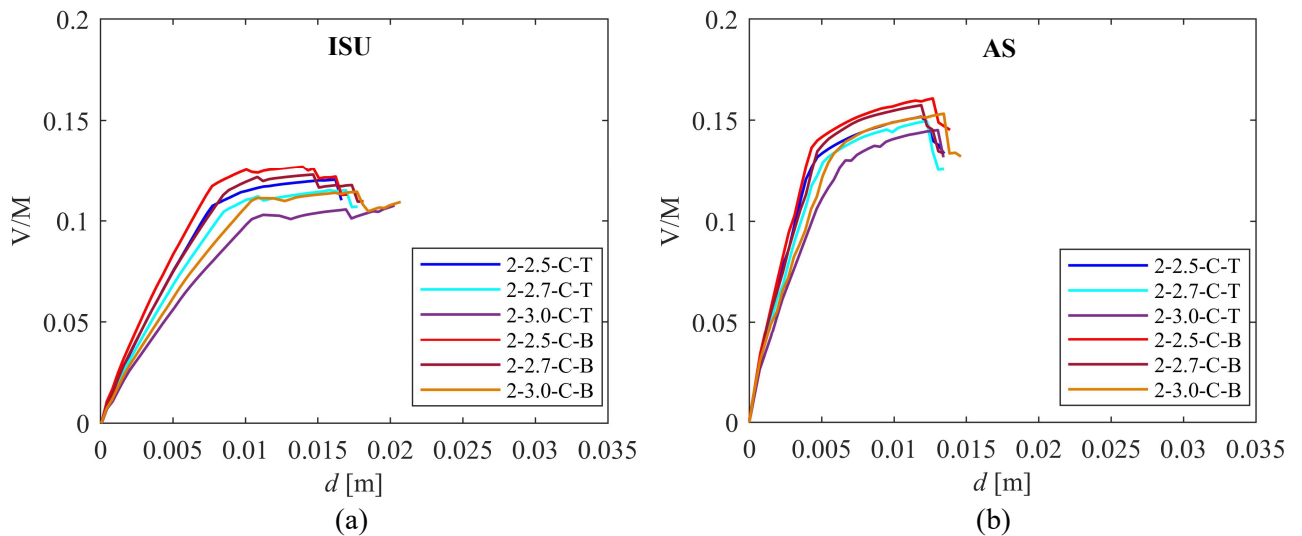


Figure 7.9:  $x$ -direction push-over curves of the buildings with 2 floors and concrete slabs: (a) Isolated structural units and (b) Aggregate structures.

Since the buildings with lower height are stiffer, the curves corresponding to the structural units with 2.5 m of inter-storey height present higher capacity than those with 2.7 m and 3.0 m. Furthermore, the buildings with the same inter-storey height and the same type of slabs show different structural capacity depending on the type of internal walls. As can be seen in these Figures, the presence of *tabique* walls leads to a reduction in the capacity of the buildings. Moreover, considering the global behaviour of the structures, if the identical structural units are aggregated in row it is possible to observe an increment in terms of capacity, which can be explained by the fact that the aggregation process results in the increase of the walls alignment in  $x$ -direction. The curves also highlight the greater capacity of the buildings with concrete slabs, comparing with those with timber slabs: the orientation of the slabs in  $x$ -direction and the different way to transmit the loads lead to greater differences in terms of capacity in this direction, with respect to the  $y$ -direction, as shown in the following. As in the clay brick masonry buildings sited in Bologna, the geometrical configuration of the walls in  $x$ -direction, in particular the considerable presence of openings, make the flexural collapse the main failure mechanism of the masonry walls in this direction. Since the differences between buildings with timber and concrete slabs are significant, as an example Figures 7.11 and 7.13 give the failure mechanisms of the walls in  $x$ -direction of the isolated structural “2-2.7-T-B” and “2-2.7-C-B” models, respectively, referred to the points in the push-over curves corresponding to the same displacement (Figures 7.10(b) and 7.12(b)).

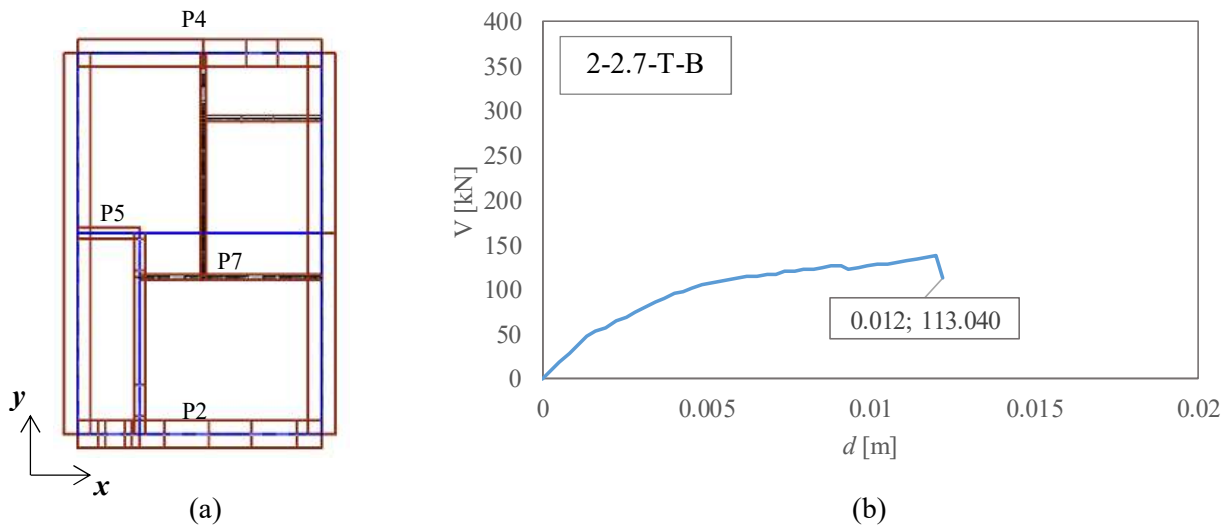


Figure 7.10: (a) Indication of the masonry walls in  $x$ -direction; (b) Point of the capacity curve ( $+F_x$ ) related to the collapse of the walls P5 and P7 for the "2-2.7-T-B" model.

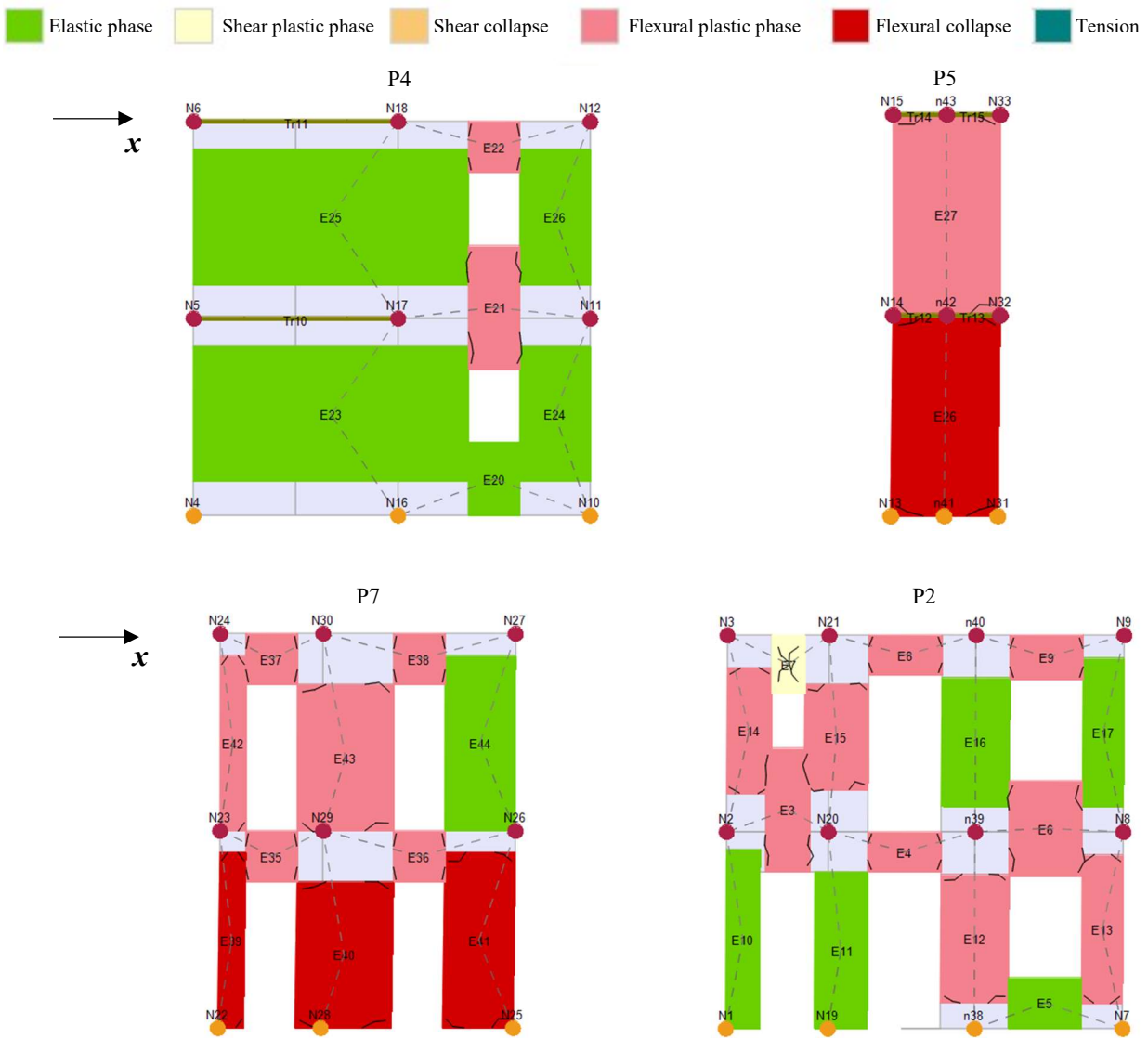


Figure 7.11: Failure mechanisms of the masonry walls considering a seismic action in  $x$ -direction ( $+F_x$ ) for the "2-2.7-T-B" model.

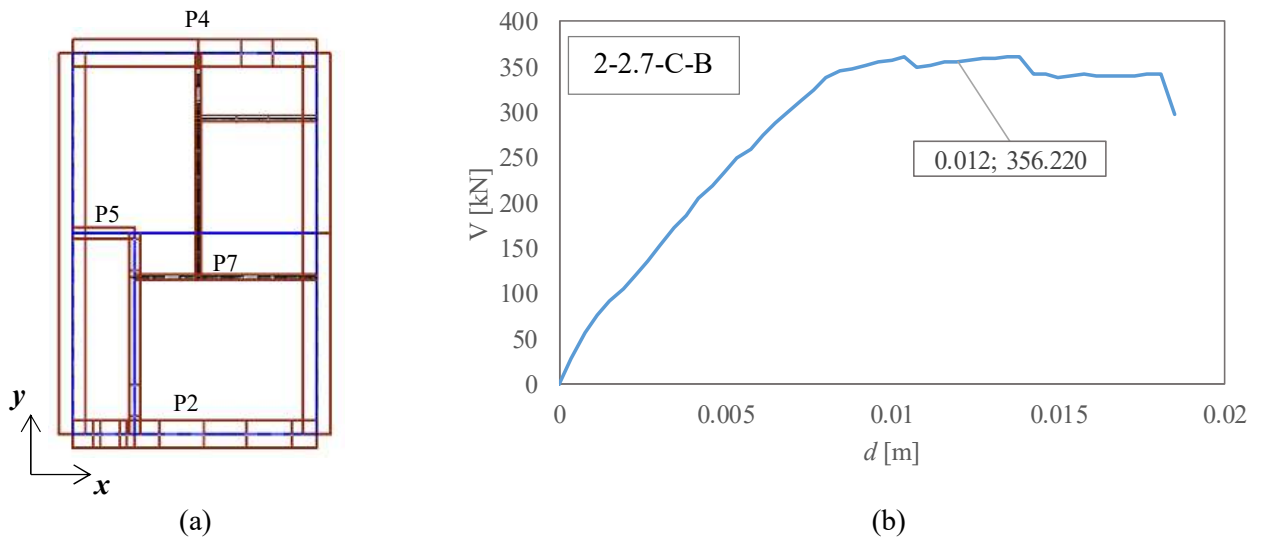


Figure 7.12: (a) Indication of the masonry walls in  $x$ -direction; (b) Point of the capacity curve ( $+F_x$ ) related to the collapse of the wall P2 for the "2-2.7-C-B" model.

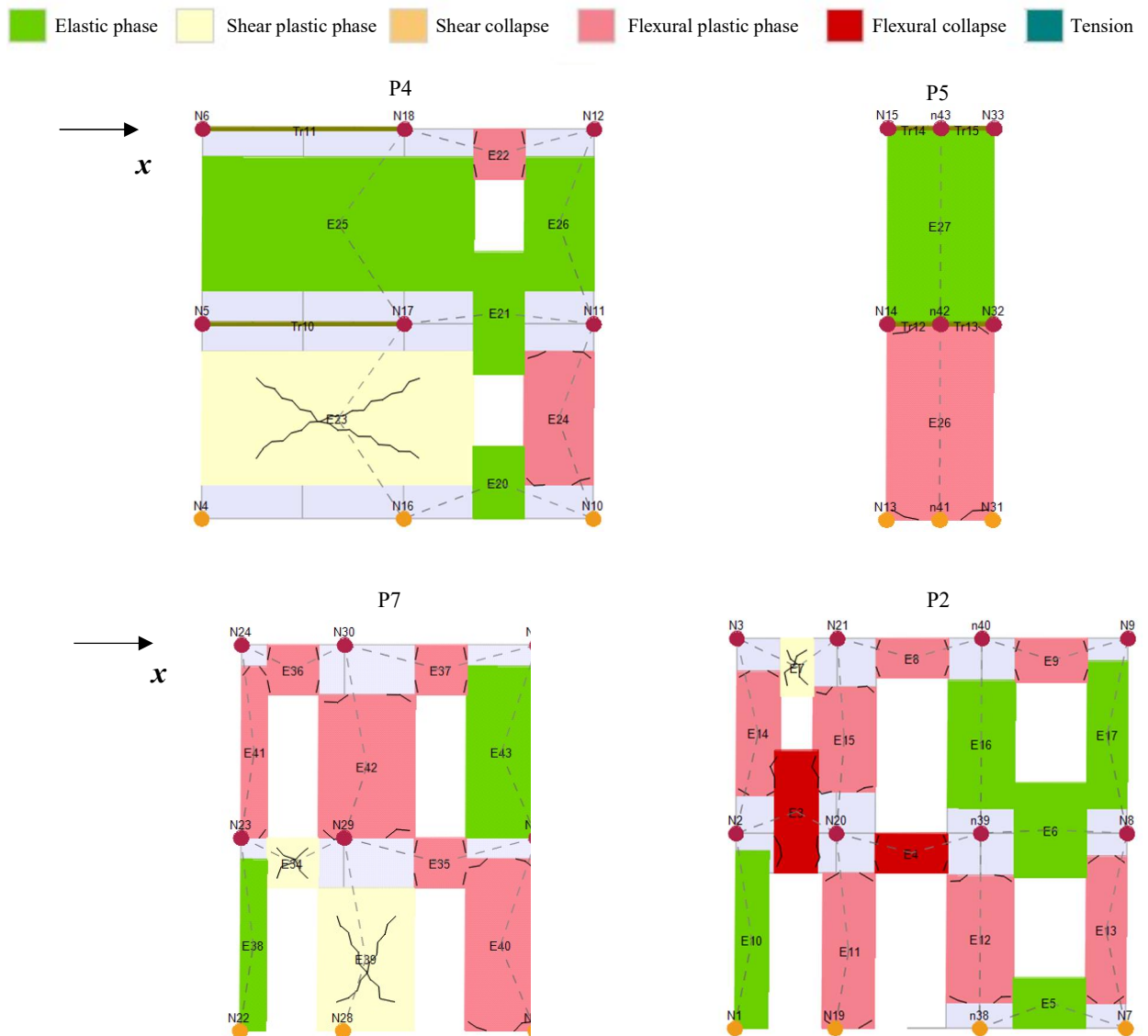


Figure 7.13: Failure mechanisms of the masonry walls considering a seismic action in  $x$ -direction ( $+F_x$ ) for the "2-2.7-C-B" model.

The failure mechanisms confirm the lower capacity of the buildings with timber slabs, as the flexible slabs with a very low stiffness (Table 7.3) lead to a distribution of the forces proportional to the masses decreasing the total capacity. Thus, Figure 7.11 shows that the last point of the capacity curves corresponds to the flexural failure of the internal walls in  $x$ -direction P5 and P7. Otherwise, Figure 7.13 shows that in correspondence of the point corresponding to the failure of the “2-2.7-T-B” model, the masonry walls of the “2-2.7-T-B” are still in the plastic field, except for the spandrels E3 and E4 of the wall P2, collapsing for greater values of the forces with respect to the “2-2.7-T-B” model. These comparisons highlight that the greater stiffness of the slabs allows to distribute the loads proportionally to the stiffness of the elements, contributing to increase the total capacity of the buildings.

Figures 7.14(a) and 7.15(a) show all the 36 isolated structural unit models with timber and concrete slabs, respectively, distinguishing the buildings according the number of floors; Figures 7.14(b) and 7.15(b) are referred to the aggregations of identical structural units.

The curves highlight the differences in terms of stiffness and ductility, if different number of floors are considered. Since the lowest height and the configuration of the resisting walls, the 1-floor buildings are the most rigid: it is possible to notice that the slope of the curves increases with the increment of the number of floors, highlighting the decrement of the stiffness for the buildings with 2 and 3 floors, respectively.

Otherwise, the ductility increases with the increment of the number of floors: the 3-floors buildings experience greater displacements, with respect to the 2-floors and the 1-floor buildings, due to the greater total height.

The curves highlight the decrement of the structural capacity with the increment of the number of floors and that the presence of timber slabs decreases the global capacity of the buildings, compared with the ones with concrete slabs. Thus, a decrement of the collapse PGA is expected if the total number of floors increases and if timber slabs are present.

In Appendix C the curves related to the application of negative forces ( $-F_x$ ) are reported, showing the slightly decrement of the vulnerability due to the asymmetry on the position of the openings in the masonry walls in  $x$ -direction (Figures 7.11 and 7.13), nevertheless being not so remarkable contrary to the case of the clay brick masonries sited in Bologna.

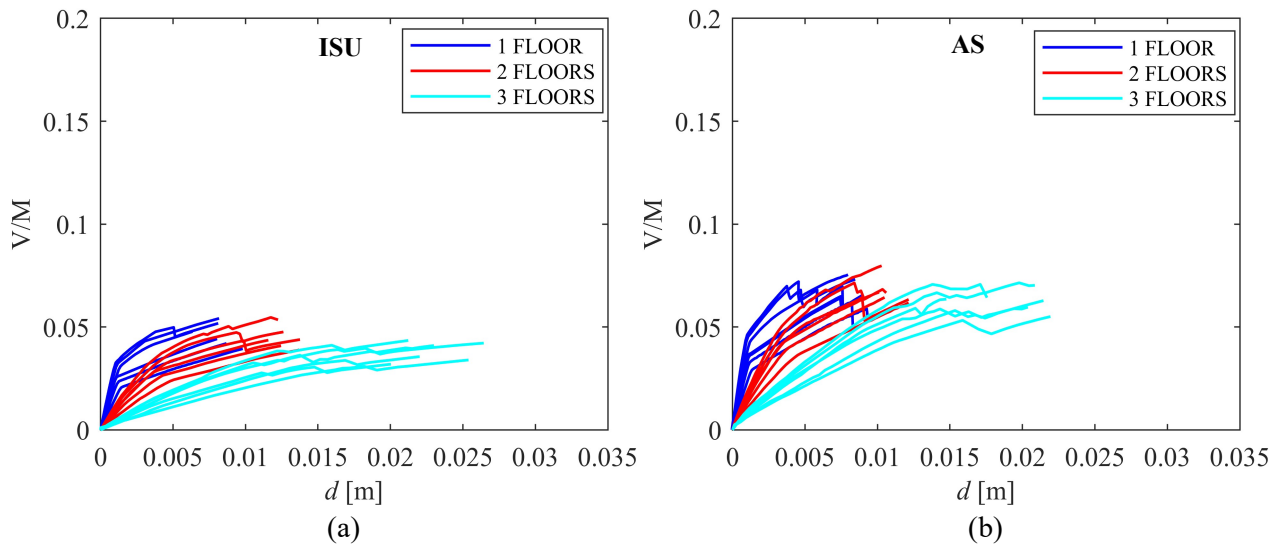


Figure 7.14:  $x$ -direction push-over curves of the buildings with timber slabs: (a) Isolated structural units and (b) Aggregate structures.

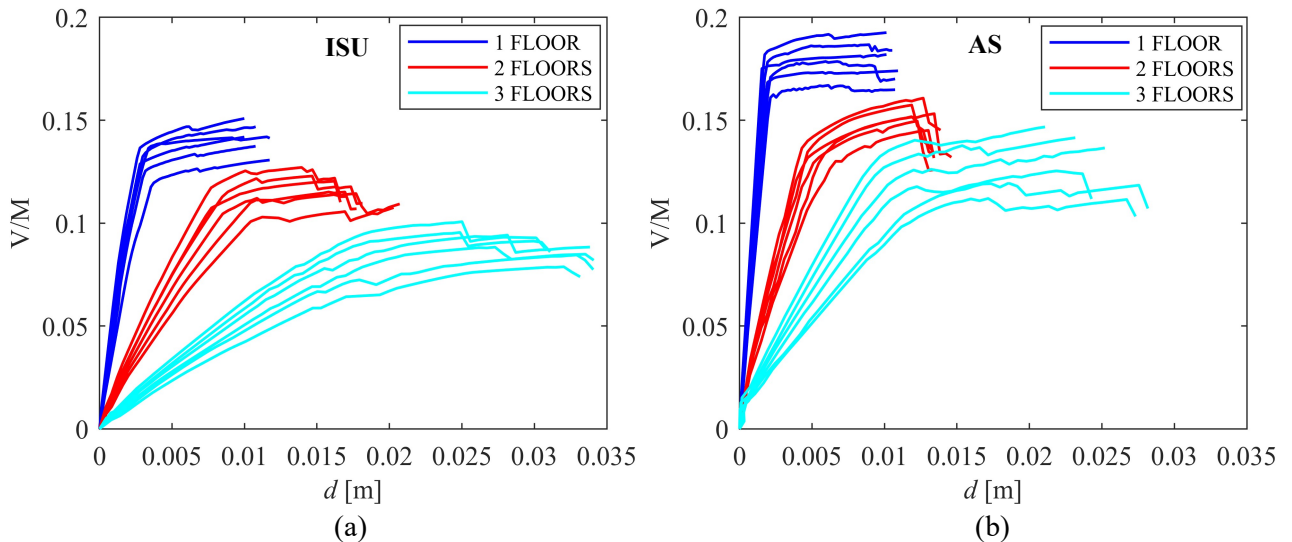


Figure 7.15:  $x$ -direction push-over curves of the buildings with concrete slabs: (a) Isolated structural units and (b) Aggregate structures.

-  $y$ -direction

The same analyses referred to the 36 models were performed applying horizontal positive forces in  $y$ -direction ( $+F_y$ ). Also in this case, as an example, Figure 7.16(a) shows the curves related to the 6 isolated structural units with 2 floors and timber slabs (“2-2.5-T-T”; “2-2.7-T-T”; “2-3.0-T-T”; “2-2.5-T-B”; “2-2.7-T-B”; and “2-3.0-T-B”) and the figure 7.16(b) shows the 6 aggregations of the same identical structural units in row. Figure 7.17(a) shows the curves related to the 6 isolated structural units with 2 floors and concrete slabs (“2-2.5-C-T”; “2-2.7-C-T”; “2-3.0-C-T”; “2-2.5-C-B”; “2-2.7-C-B”; and “2-3.0-C-B”) and Figure 7.17(b) shows the 6 aggregations of the same identical structural units in row.

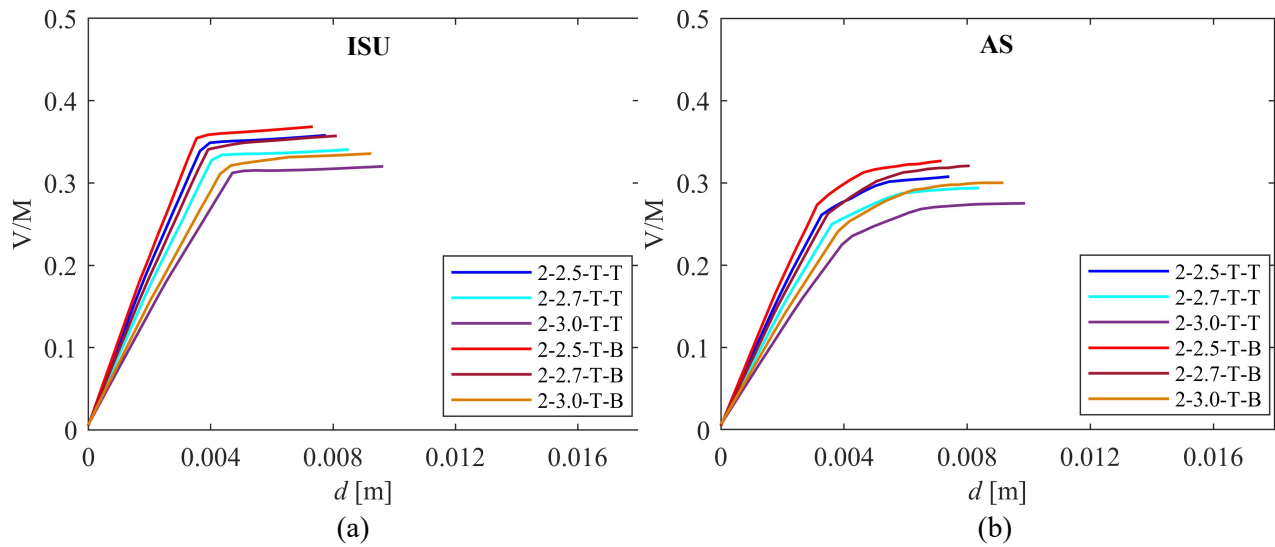


Figure 7.16:  $y$ -direction push-over curves of the buildings with 2 floors and timber slabs: (a) Isolated structural units and (b) Aggregate structures.

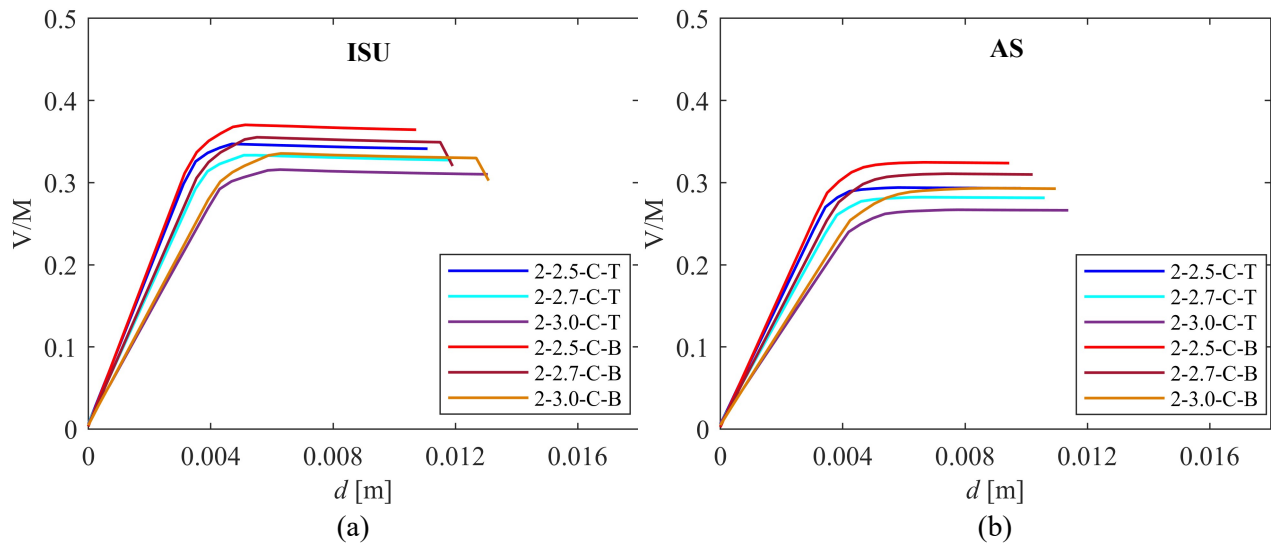


Figure 7.17:  $y$ -direction push-over curves of the buildings with 2 floors and concrete slabs: (a) Isolated structural units and (b) Aggregate structures.

Figures 7.16 and 7.17 highlight the same results of the previous ones, but it is possible to notice that the same buildings exhibit greater capacity in  $y$ -direction, due to the arrangement and the geometry of the walls in this direction: they are longer and with a reduced presence of openings (Figures 7.19 and 7.21).

The remarkable differences are noticed in the global behavior of the aggregate structures in  $y$ -direction: in this case, the aggregation of identical structural units leads to a different geometrical configuration, causing a decrement of the structural capacity: the walls in  $y$ -direction are the same of the ones of the isolated structural units and they are in common with the adjacent buildings, receiving the load of the slabs by two different sides. Moreover, some

torsional effects, decreasing the structural capacity, affect the structures. As in the application to the clay brick buildings sited in Bologna, a decrement of the collapse PGA is expected if identical structural units are aggregated in row, considering the seismic action in  $y$ -direction. It is also possible to notice that the differences between timber slabs and concrete slabs are not so remarkable in terms of capacity, as the case of the seismic action in  $x$ -direction, because in the  $y$ -direction the most contribute against the seismic action is due to the resisting walls in that direction: the contribute of the slabs is higher in  $x$ -direction, considering the orientation of the main beams of the slabs. The differences are more pronounced in terms of displacements, due to the presence of the rigid slabs allowing to distribute the forces in such a way to reach the failure of the walls for higher values of displacement.

As in the application to the clay brick buildings sited in Bologna, the stocky masonry walls in  $y$ -direction with a reduced number of openings lead to the attainment of the shear failure as dominant failure mechanism. Figures 7.19 and 7.21 give the failure mechanisms of the walls in  $y$ -direction of the isolated structural “2-2.7-T-B” and “2-2.7-C-B” models, respectively, referred to the points in the push-over curves corresponding to the same displacement (Figures 7.18(b) and 7.20(b)). In  $y$ -direction the failure mechanisms confirm the lower capacity of the buildings with timber slabs, as well. Thus, Figure 7.18(b) shows that the last point of the capacity curve corresponds to the shear failure of the external wall in  $y$ -direction P3. Otherwise, Figure 7.21 shows that in correspondence of the point corresponding to the failure of the “2-2.7-T-B” model, the masonry walls of the “2-2.7-C-B” are still in the plastic field, except for the little piers E33, E47 and E49, representing the weaker elements: the other piers reach the shear failure for higher values of displacements. Figures 7.18(b) and 7.20(b) show that the curves are comparable in terms of maximum total shear, as the orientation of the slabs does not affect a lot the results, leaving the most contribute against the seismic action to the resisting walls in  $y$ -direction.

In Appendix C the curves related to the application of negative forces ( $-F_y$ ) are reported, showing that they are comparable with those related to the  $+F_y$  forces, leading to almost the same results, due to the limited presence of openings in the masonry walls in  $y$ -direction (Figures 7.19 and 7.21) and being not so remarkable, as in the case of the clay brick masonries sited in Bologna.

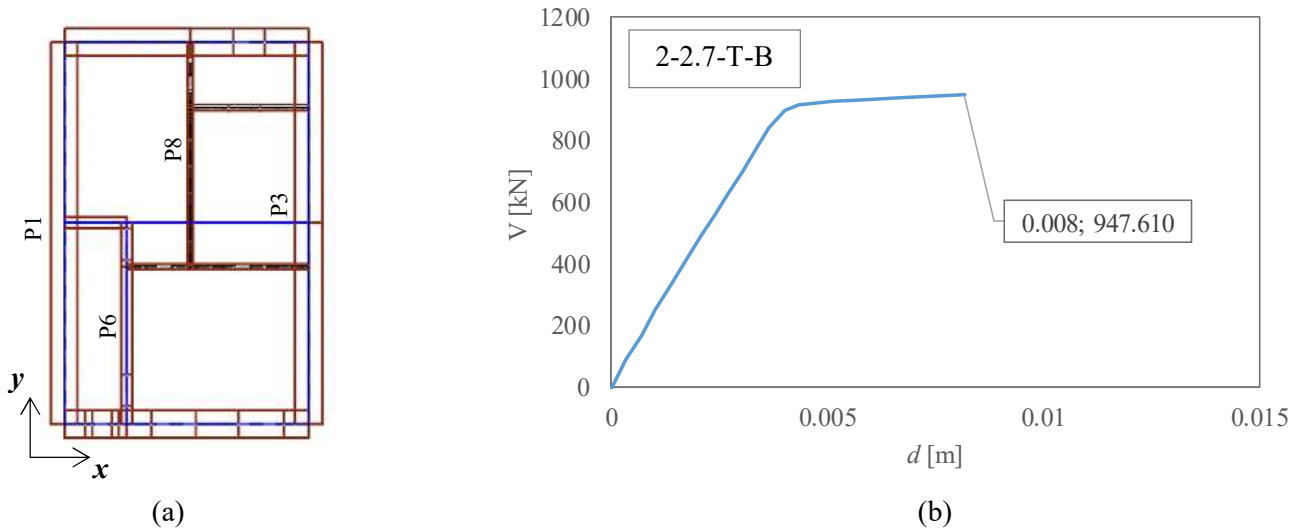


Figure 7.18: (a) Indication of the masonry walls in  $y$ -direction; (b) Point of the capacity curve ( $+F_y$ ) related to the collapse of the wall P3 for the “2-2.7-T-B” model.

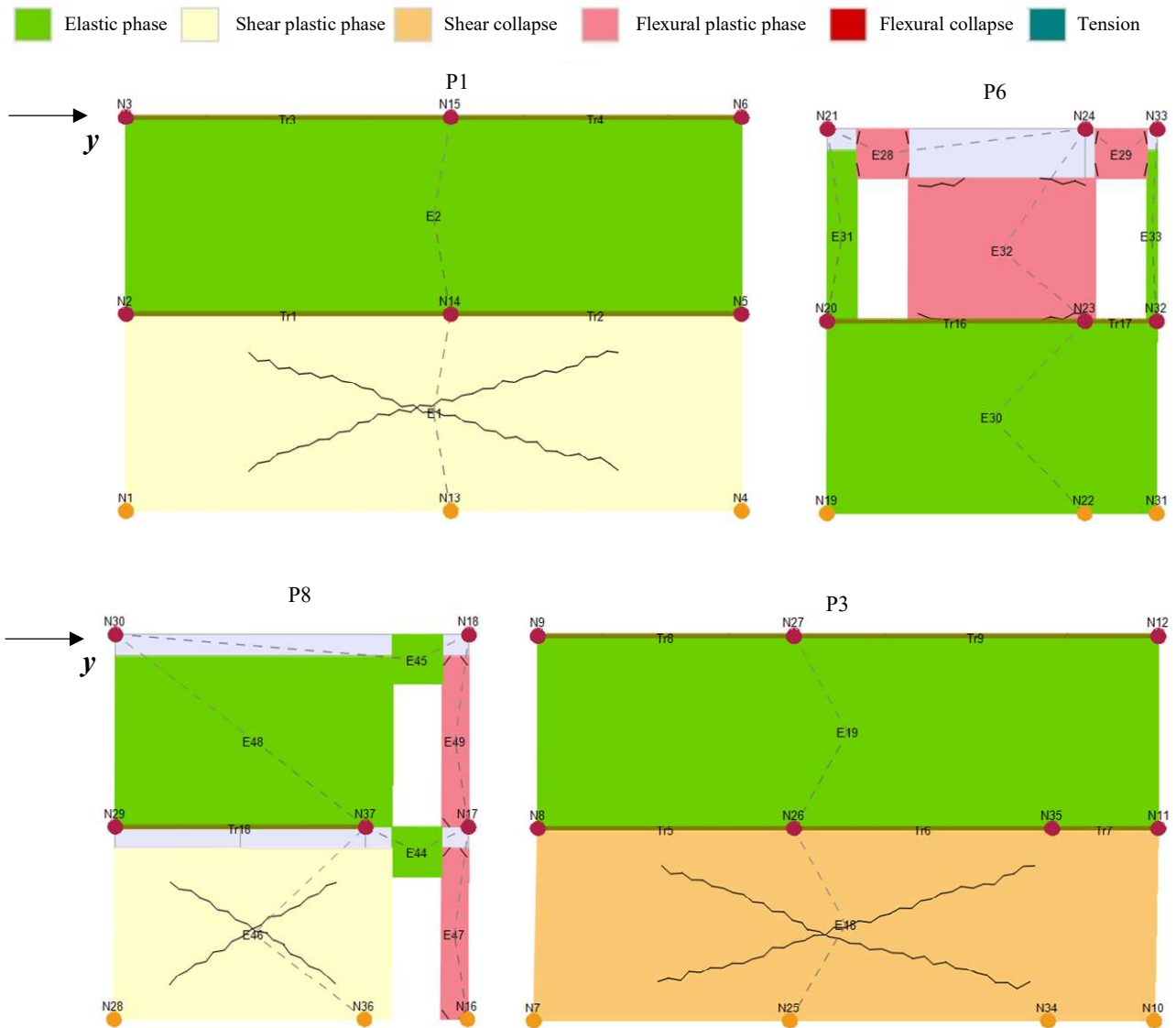


Figure 7.19: Failure mechanisms of the masonry walls considering a seismic action in  $y$ -direction ( $+F_y$ ) for the “2-2.7-T-B” model.

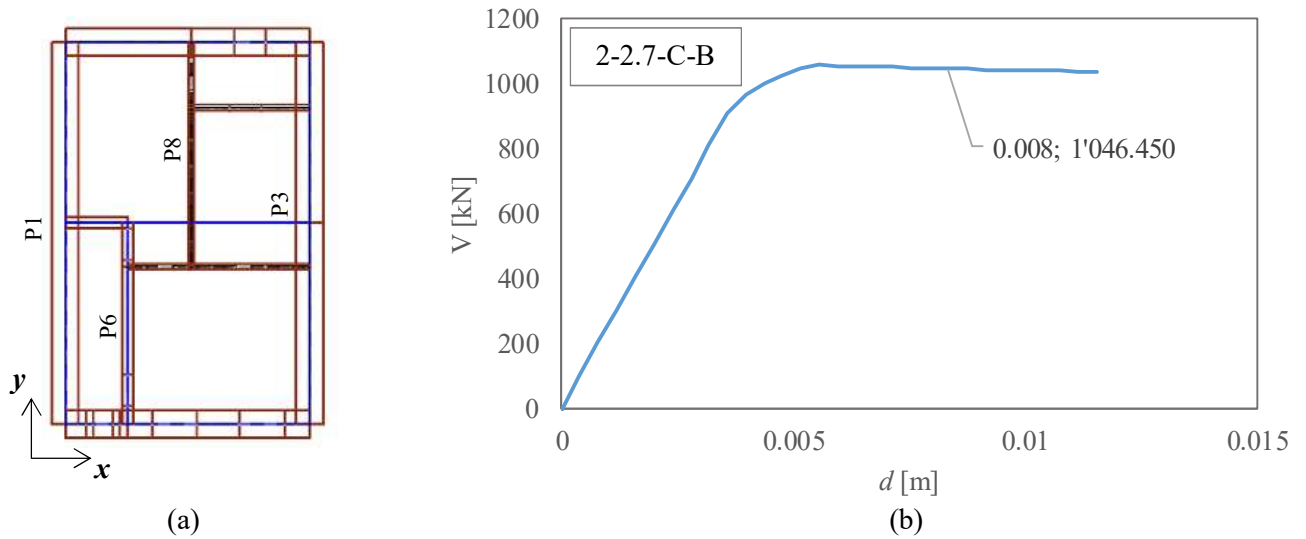


Figure 7.20: (a) Indication of the masonry walls in  $y$ -direction; (b) Point of the capacity curve ( $+F_y$ ) related to the collapse of the walls P6 and P8 for the “2-2.7-C-B” model.

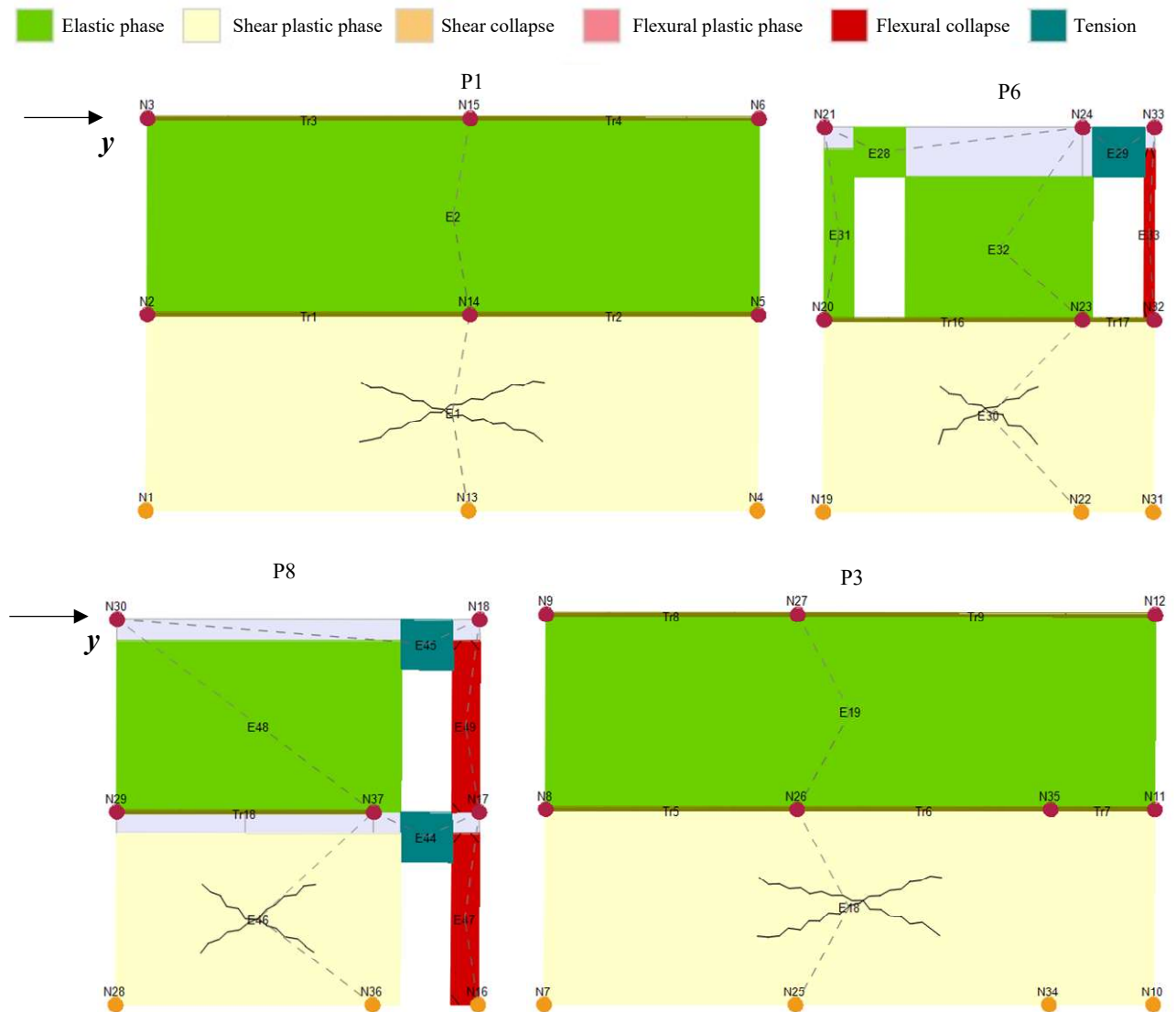


Figure 7.21: Failure mechanisms of the masonry walls considering a seismic action in  $y$ -direction ( $+F_y$ ) for the “2-2.7-C-B” model.

Figures 7.22(a) and 7.23(a) show all the 36 isolated structural unit models with timber and concrete slabs, respectively, distinguishing the buildings according the number of floors; Figures 7.22(b) and 7.23(b) are referred to the aggregations of identical structural units.

The same considerations, in terms of stiffness and ductility, can be also done for the  $y$ -direction; as well, the structural capacity increases as the number of floors decreases, considering the seismic action in  $y$ -direction.

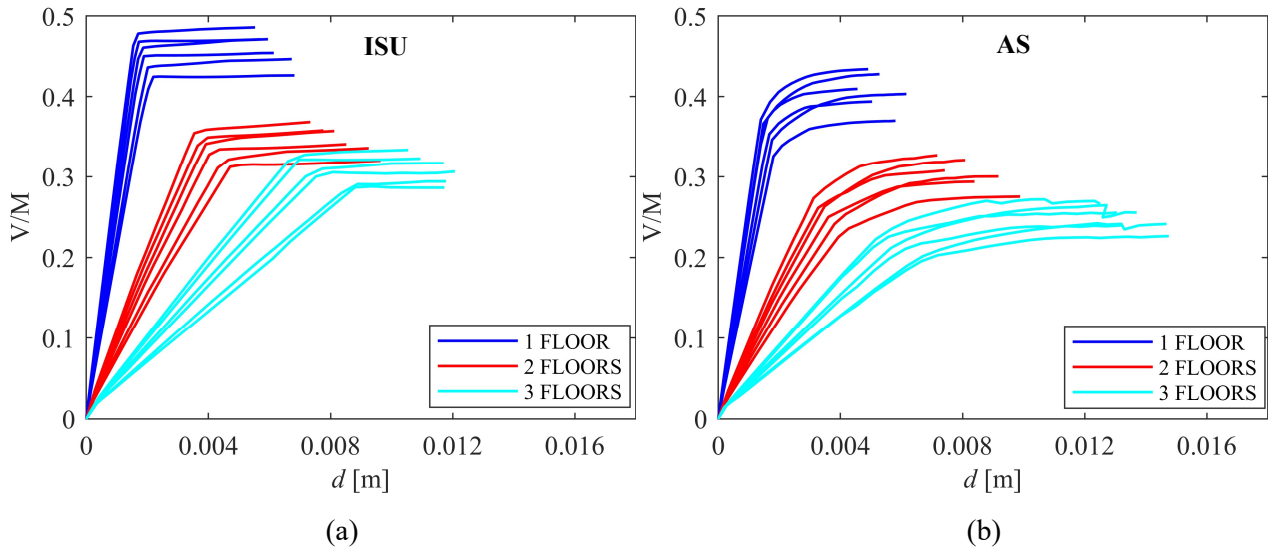


Figure 7.22:  $y$ -direction push-over curves of the buildings with timber slabs: (a) Isolated structural units and (b) Aggregate structures.

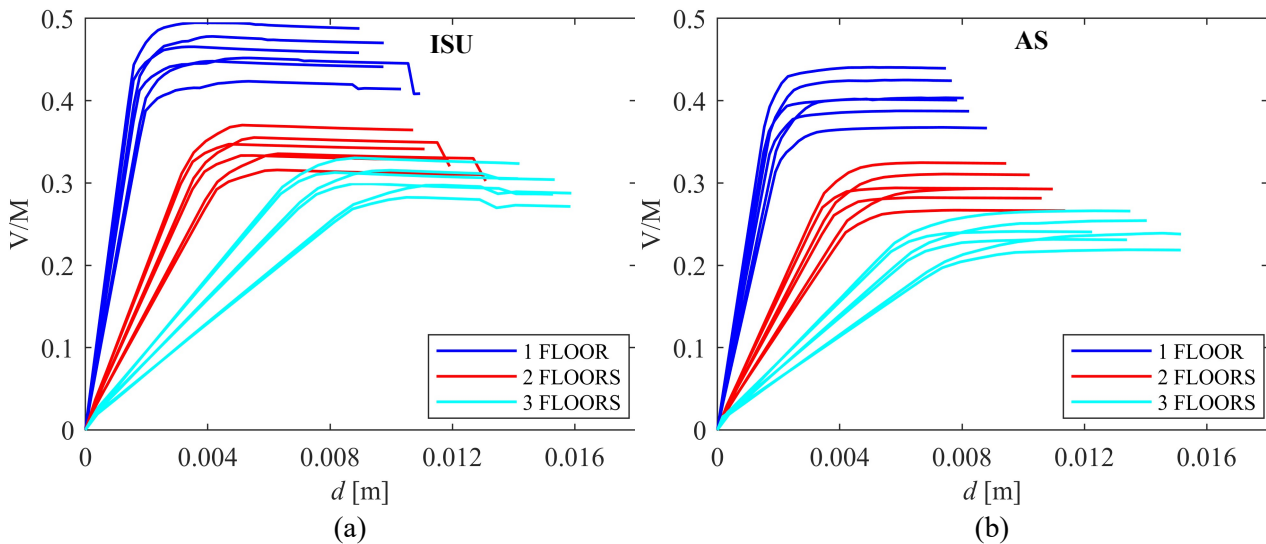


Figure 7.23:  $y$ -direction push-over curves of the buildings with concrete slabs: (a) Isolated structural units and (b) Aggregate structures.

- *y-direction, over the attainment of the LS limit state*

As in the application to the clay brick buildings sited in Bologna, the analyses over the attainment of the LS limit state were performed, in order to evaluate the seismic response of the various structural units, according to their relative position along the aggregate structure. The different geometrical configuration in *y*-direction allows to exhibit different levels of vulnerability of the different structural units along the aggregate structure and if the attainment of the life safety limit state is considered as limit for the analysis of the whole aggregate structure, not all the masonry walls of the structural units have reached the failure for shear and most of them are still in the plastic field. Therefore according to the procedure applied in the previous Sections, the analyses over the attainment of the life safety limit state were performed, to allow each structural unit to reach the failure for shear and to get a kind of vulnerability classification of the structural units that first attain the collapse for shear.

As it is recognized, the type of slabs has a direct influence on the attainment of the shear failure for the masonry walls of the different structural units. This is also observed in this analysis, where, as can be seen in Figure 7.24, the reinforced concrete slabs lead to a rigid deformation of the structure, which results in the early shear failure of the external Units 1-2 due to the torsional effects. The last points of the push-over curves in Figure 7.23(b) are related to the attainment of the life safety limit state, corresponding to the shear failure of the walls belonging to the Unit 1 and Unit 2. Figure 7.24 shows the deformed configuration of the aggregated model “2-2.7-C-B”, confirming the same results obtained in the clay brick masonry structures sited in Bologna, having the same type of slabs and a similar distribution of the internal walls in plan.

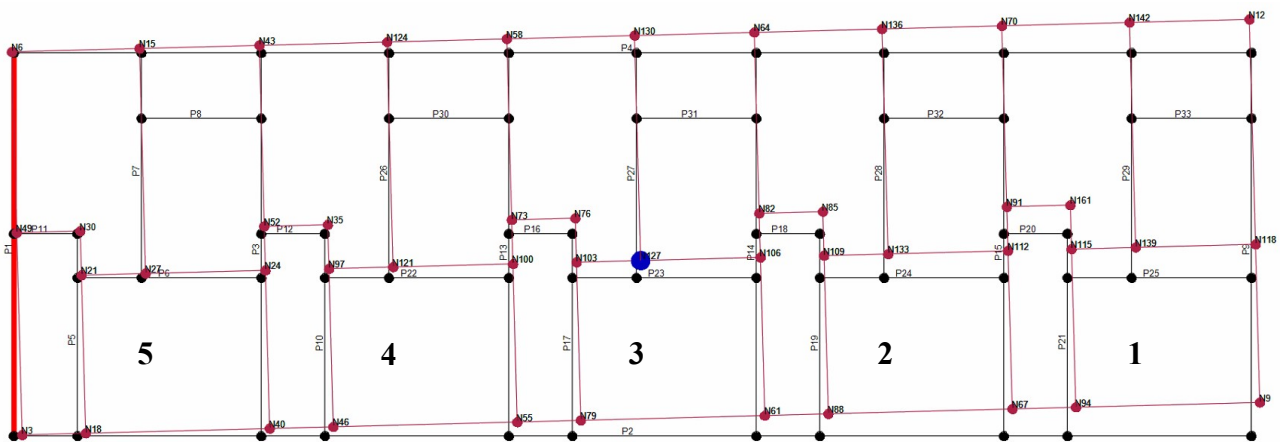


Figure 7.24: Deformed shape of the “2-2.7-C-B” aggregate model.

Contrary to what happen with the reinforced concrete slabs, due to their low stiffness, the timber slabs lead to a distribution of the forces proportional to the masses, allowing a more flexible deformation of the structure. Figure 7.25 illustrates the deformed shape of the aggregate model “2-2.7-T-B”: due to the different distribution of the forces and according to the influence areas, the internal units are those experiencing larger displacements, with respect to the AS with concrete slabs. Thus, in this aggregate configuration the geometrical distribution of the masonry walls lead the internal Units 3 and 4 to early reach the collapse for shear. The last points of the push-over curves in Figure 7.22(b) are related to the attainment of the LS limit state, corresponding to the shear failure of the walls belonging to the Units 3 and 4.

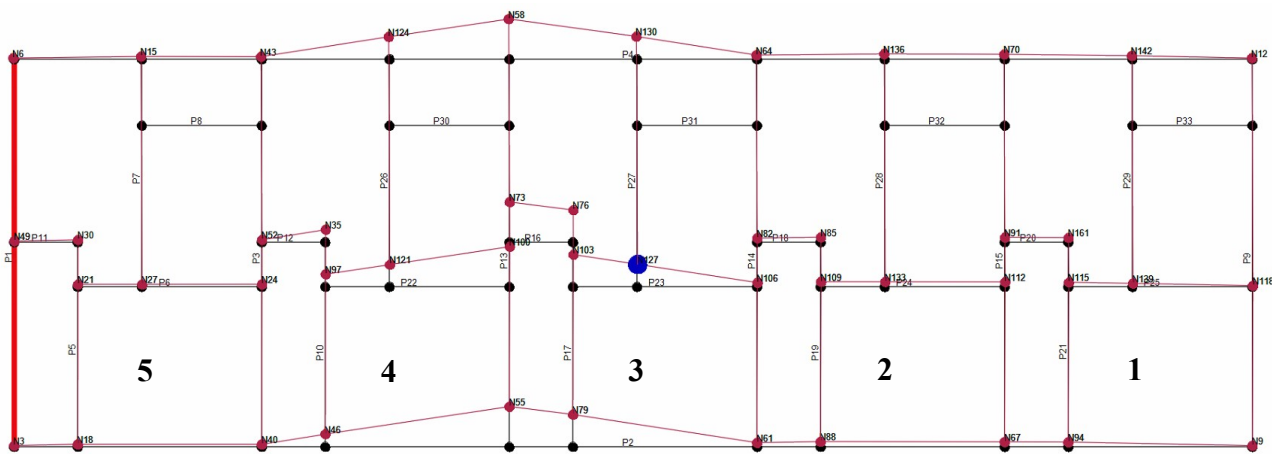


Figure 7.25: Deformed shape of the “2-2.7-T-B” aggregate model.

In order to allow each structural unit to reach the failure for shear, the analyses over the attainment of the LS limit state were performed. Figure 7.26 shows the push-over curves related to the buildings with concrete slabs, distinguished for the number of floors. As identified in this Figure, the first decrement of the shear corresponds to the failure of Unit 1 and Unit 2, the decrement between 0.012 m and 0.02 m is related to the failure of Unit 3 and the last points to that of the Unit 4. Also in this case, it was decided to neglect the failure related to the Unit 5 because the displacements should be so larger to make the results not reliable. These results highlight the different levels of vulnerability referred to the structural units, depending on their position along the aggregate: the vulnerability decreases if more internal units are considering, due to the presence of the rigid slab and to the torsional effects mainly affecting the external Units 1 and 2.

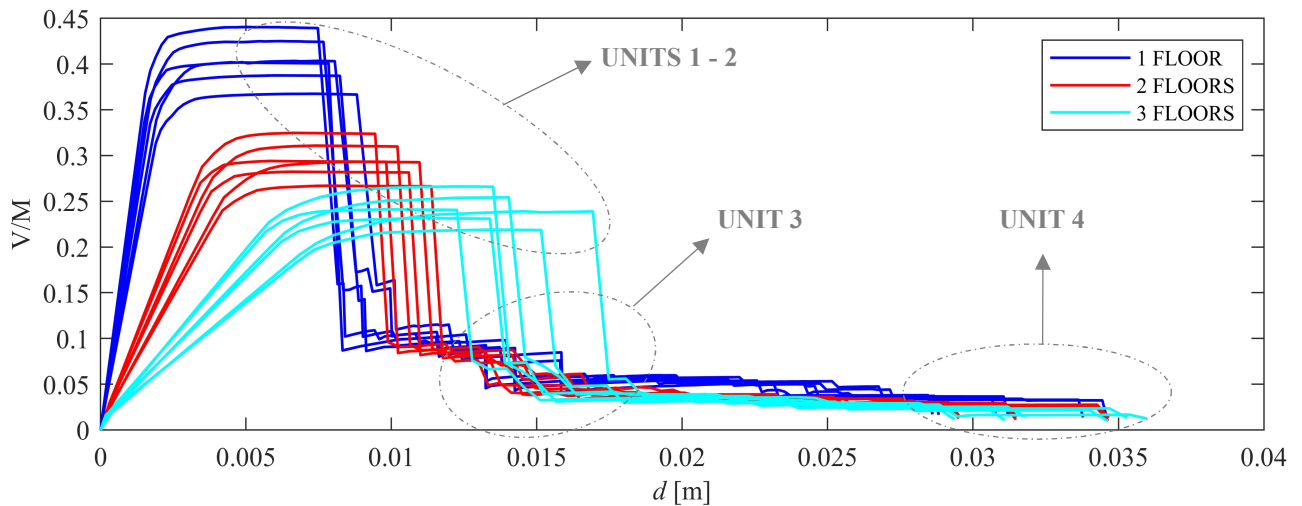


Figure 7.26: Pushover curves of the AS with concrete slabs: analyses over the attainment of the LS limit state.

Figure 7.27 shows the push-over curves related to the buildings with timber slabs, distinguished from the number of floors.

In order to evaluate the structural behaviour of the aggregate with timber floors, the analysis was kept beyond the stop criterion of the push-over analyses. From this analysis it was possible to observe that, in contrast to the other Units 1, 2 and 5, which exhibit very small displacements, Units 3 and 4 keep deforming. In fact, as can be observed in Figure 7.25, Units 3 and 4 behave almost independently, after the achievement of the plastic field and, if the analysis over the attainment of the LS limit state is performed considering the whole aggregate, these two Units continue to move reaching larger values of displacements, with respect to Units 1, 2 and 5, maintaining very small displacements. For this reason, the aggregate structures were disaggregated into the three sub-models presented in Figure 7.28. Thus, the failure of the Units 3 and 4 was analysed considering the whole aggregate, whereas the failure of Units 1 and 2 was evaluated considering only two aggregated structural units (1 and 2) and the failure of Unit 5 was evaluated considering the isolated structural unit. Following this, the final push-over curves given in Figure 7.27 were obtained from the envelopes related to the various failures of the structural units, obtained analysing the three sub-models over the attainment of the LS limit state. As can be seen in Figure 7.27, the first decrement of the shear corresponds to the failure of the Units 3 and 4, the decrement between 0.01 m and 0.0175 m is related to the failure of the Unit 1 and 2 and the last points to that of the Unit 5.

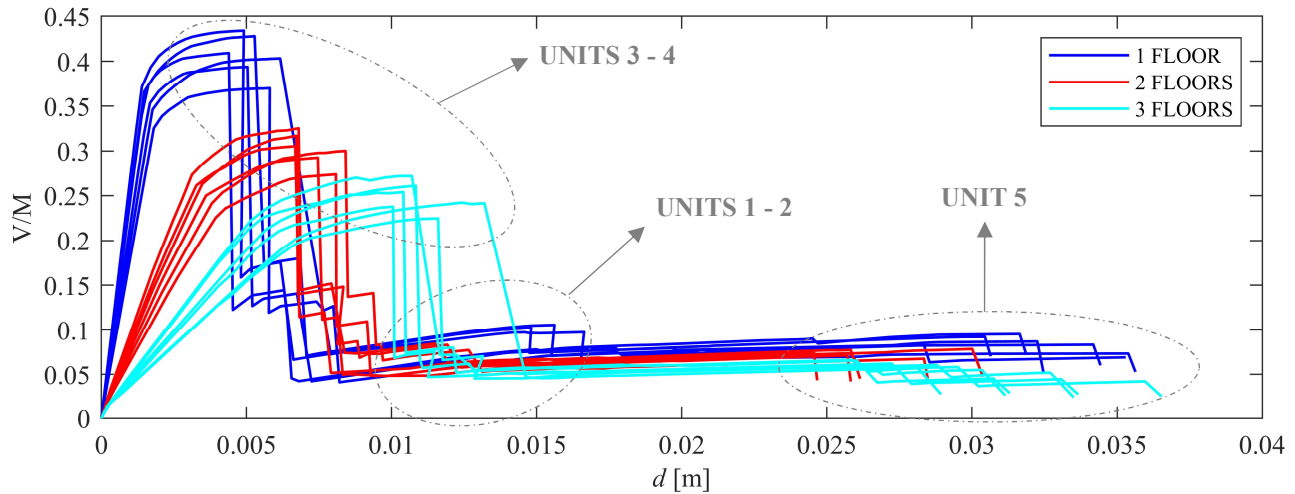


Figure 7.27: Pushover curves of the AS with timber slabs: analyses over the attainment of the LS limit state.

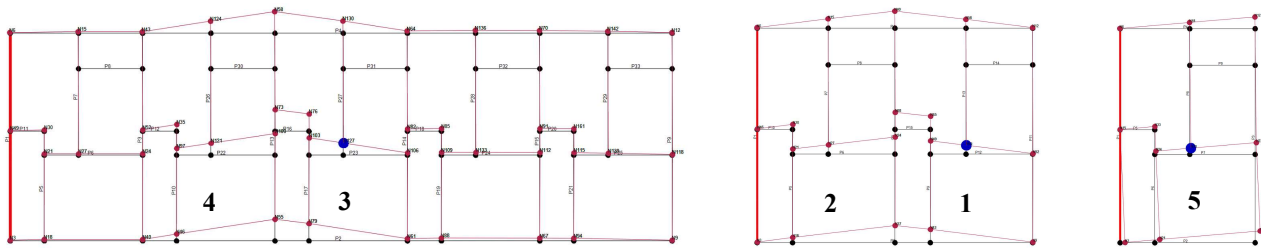


Figure 7.28: Deformed shape of the “2-2.7-C-B” aggregate sub-models.

## 7.5 Fragility curves

As in the application to the clay brick masonries sited in Bologna, the analyses in this Section have as goal the assessment of the seismic fragility referred to the various models obtained. Since the RS statistical method was not applied in this application, all the 50 accelerograms obtained in Section 5.4 were considered for each of the 36 models. Thus, the 50 acceleration and displacement spectra (Figure 5.7) allowed to obtain the 1800 (50x36)  $PGA_C$ , associated to each analysis case. Since both the isolated structural units and the aggregate structures were considered and both  $x$ - and  $y$ -directions of the seismic action were applied, 7200  $PGA_C$  were obtained, considering the attainment of the LS limit state as failure for the models.

As already mentioned, the structural failure is reached when the difference between the structural capacity (C) and the structural demand (D) is less than or equal to zero. The limit state function ( $g$ ), in Equation 7.1, expresses that difference:

$$g = PGA_C - PGA_D \leq 0 \tag{7.1}$$

where  $PGA_C$  is the spectral acceleration corresponding to the attainment of the LS limit state and  $PGA_D$  is the spectral demand acceleration, as in the previous Sections.

The structural capacity is estimated by means of the non-linear static analyses performed in this Section, used to obtain the correspondent values of the  $PGA_C$  and then compared with the  $PGA_D$  values, to plot the fragility curves.

The fragility curves were plotted herein considering all the distributions of the actual  $PGA_C$  obtained from the previous analyses. These curves were compared with those obtained starting from the logarithmic Gaussian distributions, defined from the medium values and the standard deviations of each distribution of  $PGA_C$  and using Monte Carlo method. The comparison allowed to observe that, although they are very similar, the curves obtained with Monte Carlo method presents a more regular shape, according to the considerations explained in Section 5.6. In the following paragraphs, the curves related to the  $x$ - and  $y$ -directions of the seismic action are given in terms of the conditional probability of the structural failure ( $P_f$ ) and the spectral demand acceleration ( $PGA_D$ ).

- *x-direction*

The fragility curves for the  $x$ -direction reveal a high fragility of the buildings analysed, especially those with timber slabs. As can be observed in Figure 7.29(a), the buildings with concrete slabs are lower fragile than the buildings with timber slabs and the curves (blue and red) are considerably spaced due to the orientation of the slabs in  $x$ -direction and their different way to distribute the forces. The fragility curves also show that the aggregation of identical structural units in row in  $x$ -direction leads to a decrement in terms of fragility, confirming what it was expected from the results in terms of capacity. Figure 7.29(b) shows the curves obtained with Monte Carlo method; it is possible to notice that they are comparable. The continuous lines are referred to the isolated structural units (ISU) and the dashed lines to the aggregate structures (AS).

The beneficial contribution of the aggregation in terms of  $PGA_C$  is also evident in the fragility curves presented in Figure 7.30(a) where the buildings are distinguished according to the number of floors: the curves related to the buildings with just one floor show that their greater stiffness considerably decreases their fragility with respect to the higher buildings with two and three floors. Finally, Figure 7.30(b) distinguishes the buildings according the type of the internal walls, confirming as the presence of the clay brick internal walls contributes to decrease the total fragility. These latter Figures only show the curves obtained with Monte

Carlo method, considering that them and the ones obtained with the actual values of the  $PGA_C$  are comparable showing the same results.

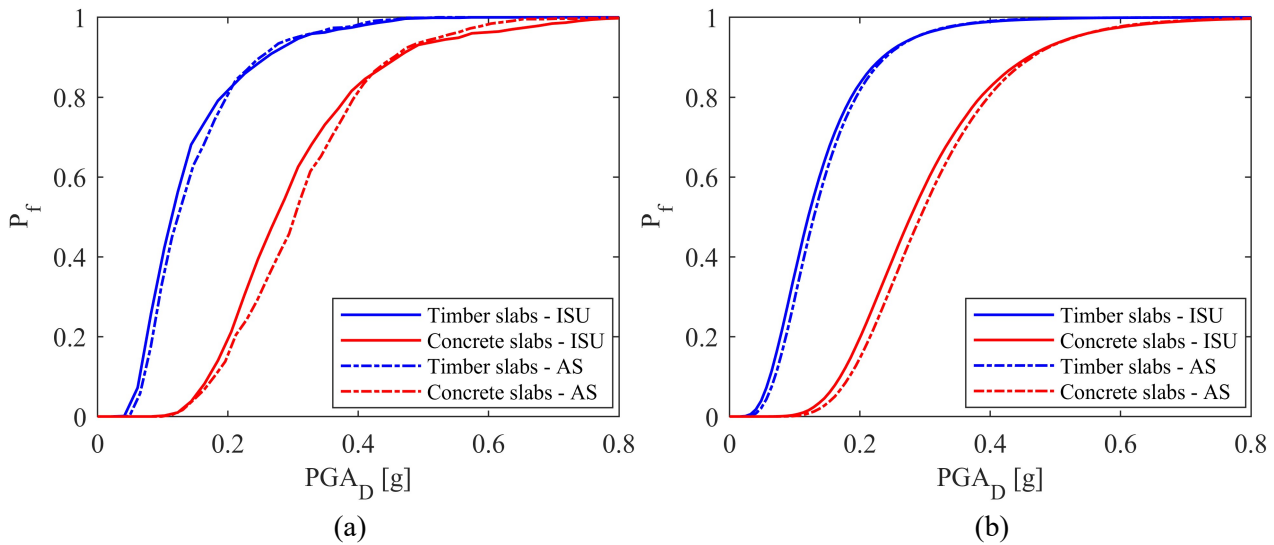


Figure 7.29: Fragility curves of all the models in  $x$ -direction, distinguished according to the type of slabs: (a) actual PGA; (b) Monte Carlo method.

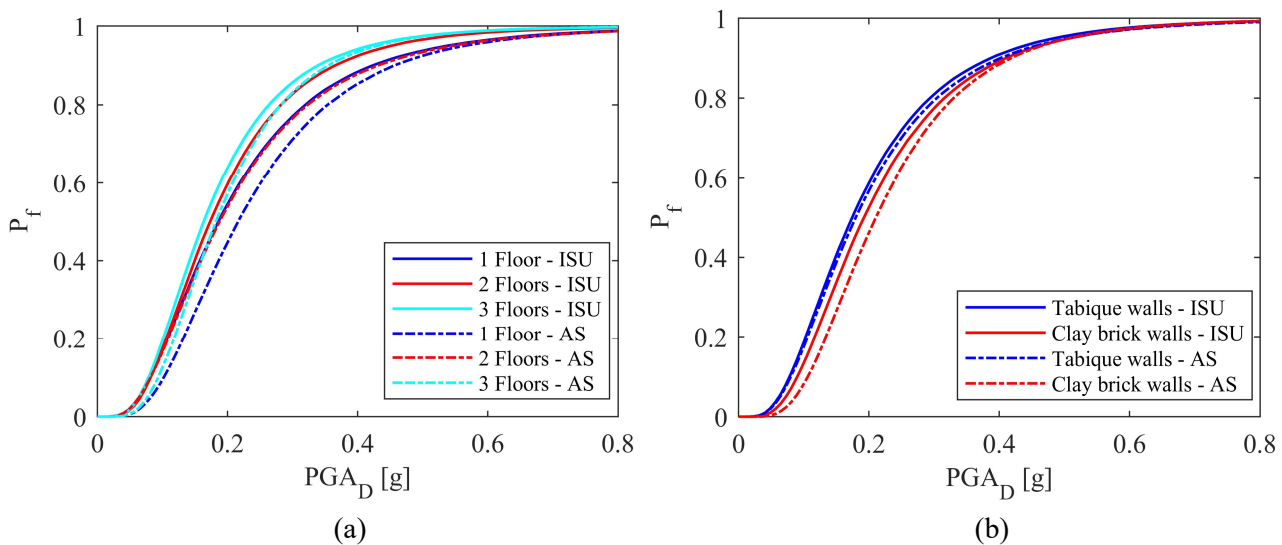


Figure 7.30: Fragility curves of all the models in  $x$ -direction using Monte Carlo method: (a) distinguished according to the number of floors; (b) distinguished according to the type of internal walls.

-  $y$ -direction

Following the same presentation and the analysis scheme, Figures 7.31(a) and (b) present the final fragility curves obtained for the  $y$ -direction, distinguished according to the type of slabs: the presence of the concrete slabs leads to a decrement of the fragility, but the differences with the timber slabs curves are not so remarkable as in  $x$ -direction, because of the orientation of the slabs. As can be observed in these Figures, when considering the  $y$ -direction, the fragility curves reveal less levels of fragility than those related to the seismic action in  $x$ -

direction. This can be explained by the arrangement and the geometry of the walls in this direction: they are mainly stone resisting walls with the biggest thickness and the longest length and most of them are without openings. Like in the previous case, Figures 7.32(a) and (b) show the same comparisons in terms of number of floors and type of internal walls: the fragility increases as the number of the floors increases and it decreases with the presence of the clay brick walls instead of the *tabique* walls. As explained above, the aggregation leads to a decrement of the capacity in the  $y$ -direction and consequently to an increment of the fragility, due to the torsional effects and the contribution of the other adjacent structural units, affecting the global response against a seismic action in  $y$ -direction.

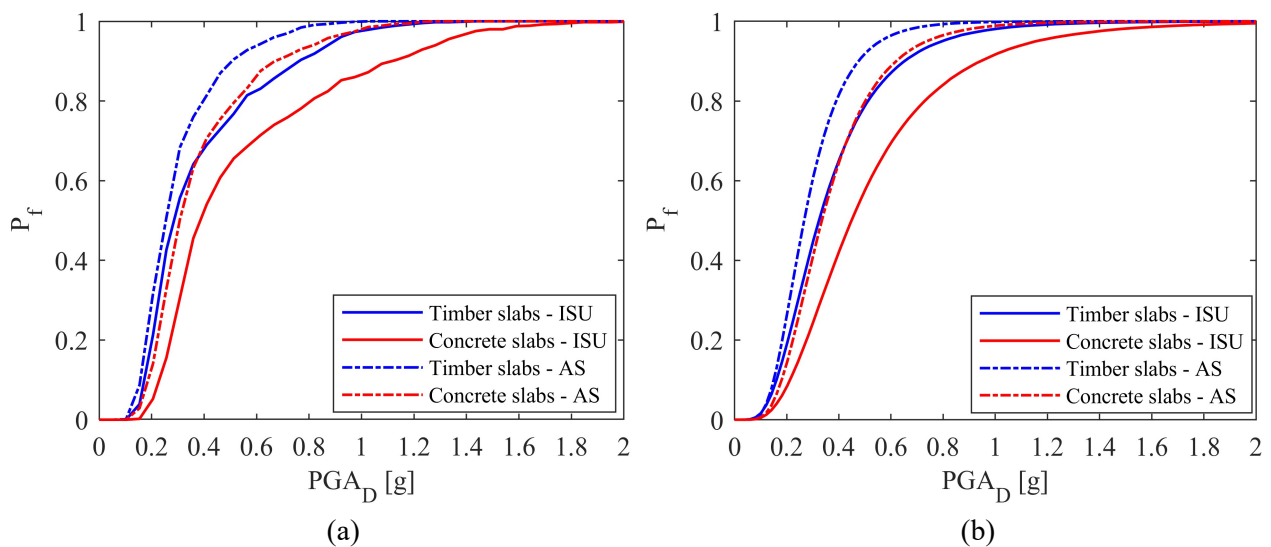


Figure 7.31: Fragility curves of all the models in  $y$ -direction, distinguished according to the type of slabs: (a) actual PGA; (b) Monte Carlo method.

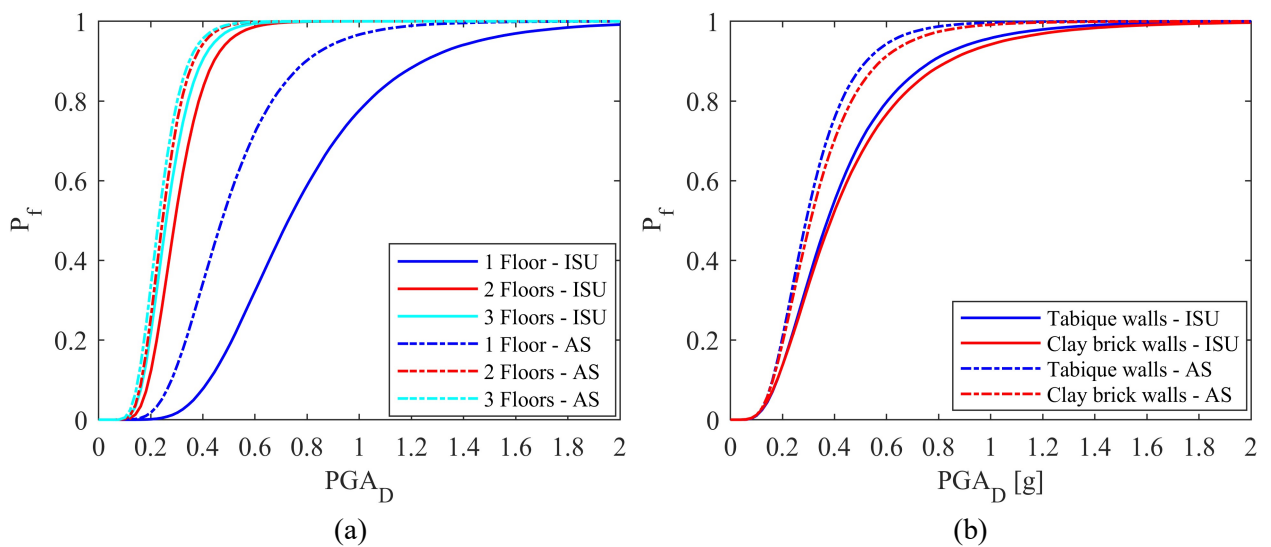


Figure 7.32: Fragility curves of all the models in  $y$ -direction using Monte Carlo method: (a) distinguished according the number of floors; (b) distinguished according the type of internal walls.

- *y-direction, over the attainment of the LS limit state*

The analysis over the attainment of the life safety limit state, considering a seismic action in *y*-direction, led to a differentiation between the aggregate structures with concrete slabs and the ones with timber slabs, because the stiffness and the distribution of the forces change according to the type of the slabs: different levels of vulnerability were found between the structural units, depending on their position along the aggregate structures. Figure 7.33(a) allows to obtain a hierarchy of failure of the various Units along the aggregate structures with concrete slabs. The curves confirm the results obtained by the non-linear analyses, highlighting how the presence of the rigid slab causes some torsional effects mainly affecting the external Units 1 and 2, whose walls are the first to reach the shear failure. Continuing the analyses over the attainment of the life safety limit state it is possible to allow the other units to reach the shear failure, experiencing larger displacements. The curves in Figure 7.33(a) show that the most fragile Units are the external ones 1 and 2 and that the fragility increases respectively in the Unit 3 and Unit 4. Figure 7.33(b) shows the fragility curves related to the aggregate structures with timber slabs: the presence of the flexible slabs leads to a different distribution of the forces, according to the influence areas and the distribution of the masses; the torsional effects are reduced and the forces allow the more central units (Unit 3 and 4) to exhibit larger displacements and their walls to first reach the shear failure. Continuing the analyses over the attainment of the LS limit state it was showed that the global structure model is not able to give the shear failure of the other Units along the aggregate. Thus, since the Units 3 and 4 behave almost independently, the model was disaggregated in three sub-models, allowing to obtain the shear collapse of the Units 1 and 2 (considering only 2 Units) and of the Unit 5 (considering the isolated structural unit), as already shown in Section 7.4. The curves in Figure 7.33(b) allows to obtain a hierarchy of failure of the various Units along the aggregate structures with timber slabs, showing that the most fragile Units are the 3 and 4, followed by the Unit 1 and 2 and finally by the Unit 5.

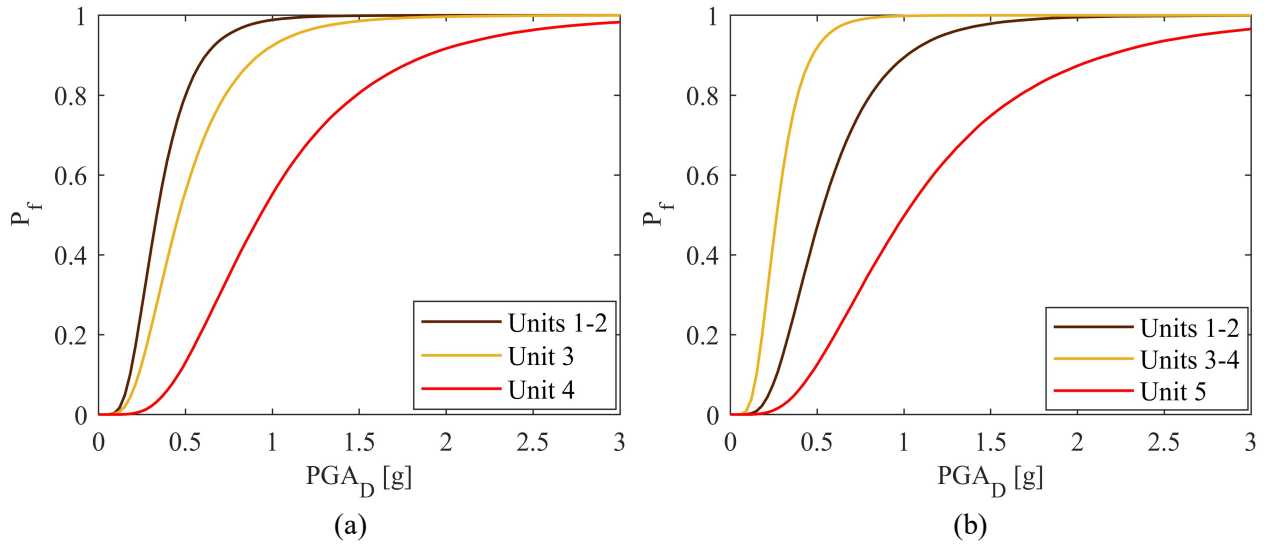


Figure 7.33: Fragility curves of the AS using Monte Carlo method: analyses over the LS limit state in buildings with (a) concrete slabs and (b) timber slabs.



## **8. CONCLUSIONS**

---

## 8.1 Summary

The research work presented in this thesis aimed to assess the seismic vulnerability and fragility of unreinforced masonry aggregate structures, sited in the historic centres. The analyses were focused on the comparison between the seismic behaviour of masonry structural units, considered at first as isolated, with that referred to aggregations in row of those similar or identical structural units. The main goal was to show the advantages and disadvantages the masonry structural unit obtains in the aggregation process, considering two different and orthogonal directions of the seismic action and the variation of its position along the aggregate structure.

The first part of the work was focused on the seismic vulnerability and fragility assessment of clay brick masonry buildings, sited in Bologna, in Italy. Due to a limited availability of the mechanical and geometrical characteristics of the structures in question, the analyses were carried out with the Response Surface (RS) statistical method, taking into account the variabilities and uncertainties involved in the problem. At first, the selected clay brick masonry structure was considered as isolated, performing a set of non-linear static analyses whose data were used to calibrate the Response Surface model. The results of the RS allowed to obtain a relation between the chosen variables and the PGA corresponding to the attainment of the LS limit state, chosen as response parameter, also highlighting the differences considering two orthogonal directions of the seismic action. It was showed that the parameter most influencing the seismic response is the shear strength ( $\tau$ ) of the resisting masonry walls, followed by the geometrical properties of the structure, showing as the arrangement and the geometry (mainly the thickness) of the masonry walls are determining factors in the seismic performance of unreinforced masonry buildings. Moreover, since in this type of analysis the seismic response is mainly governed by the in-plane behaviour of the walls in the considered direction of the seismic action, considerable differences were found between the two directions, due to the different configurations of the masonry walls. In particular, the  $x$ -direction is the weaker, because of the several number of openings, allowing the prevalence of the flexure as main failure mechanism. In the orthogonal  $y$ -direction the masonry walls stockier and with a reduced presence of openings, allowing the prevalence of the shear as main failure mechanism, lead to the attainment of higher values of the collapse PGA and, consequently, to a lower fragility, showed in the plots of the fragility curves obtained.

Furthermore, the different disposition of the openings in the masonry walls makes some of their parts weaker against the seismic action, leading to different seismic performances if positive ( $+F_x$  or  $+F_y$ ) or negative ( $-F_x$  or  $-F_y$ ) seismic forces are considered.

Afterwards, identical structural units chosen by the Response Surface generated simulations are aggregated, in order to compare the fragility referred to the isolated structural unit and the one referred to the entire aggregate structure. The results showed an increment on the values of the collapse PGA, aggregating identical isolated structural units and considering the seismic action in  $x$ -direction: the length of the walls about 5 times that of the walls of the isolated structural unit and the dominance of the flexure as main global collapse mechanism lead to a decrement of the fragility. On the contrary, in  $y$ -direction the different geometrical properties of the resisting walls and the torsional effects deriving from the aggregation of structural units in row cause an increase of the vulnerability, because the external units are affected by torsional effects decreasing the values of the  $PGA_C$  obtained. Higher values of the collapse PGA are associated to the internal structural units along the aggregate structure, obtained continuing the analyses over the attainment of the LS limit state and allowing the walls of the more internal units to reach the shear collapse. These analyses allowed to make a hierarchy of collapse of the various structural units along the aggregate, for the presence of the rigid slabs: the fragility curves show a decrement of the fragility if more internal units are considered.

Finally, the fragility of the masonry aggregates with different structural units (AS - D) was compared with the one of the aggregates with identical structural units (AS - I), generated using the medium values of the distributions of the chosen variables. The comparison showed that it is not possible to define unique seismic behaviours because of the differences in the structural units; but, in general, the ratio between the distance of the masonry walls ( $d$ ) and the thickness of the walls ( $s$ ) of the various structural units is one of the parameters most influencing the differences in the seismic response, compared with the ratio referred to the walls of AS - I, having a unique values of  $d/s$ . The fragility curves obtained showed that, for these specific aggregate configurations, generated with randomly selections of the geometric parameters ( $d$  and  $s$ ), the fragility of the AS - I is higher than the fragility of the AS - D. In fact, the cases of AS - D having structural units with  $d$  and  $s$  greater than those of the identical

structural units along the AS - I are more than the 50% of the total cases, justifying the greater fragility of the AS - I with respect to the AS - D.

The second part of this work was focused on the seismic vulnerability and fragility assessment of a weaker type of structures: the unreinforced limestone masonries, sited in Seixal, in Portugal. In this case, it was not necessary to adopt statistical methodologies, as information on the geometrical and mechanical characteristics of the selected buildings were already available. The analysis involved the assessment of the most prevalent structural typologies individuated in the historic centre, considering the variability of a set of structural and geometrical parameters, individuating 36 different structural configurations, whose seismic performance behaviours were studied by means of non-linear static analyses. The methodology applied was then the same: the seismic behaviour of these structural configurations, analysed as isolated structural units, is compared with their structural performance when enclosed in aggregate, obtaining similar results, compared with the buildings in Bologna, in terms of fragility and considering two directions of the seismic action, due to the similar geometrical configuration of the masonry walls. The results also showed how the variation of the chosen structural and geometrical parameters greatly affects the seismic response. Thus, the fragility curves related to the buildings with just one floor showed that their greater stiffness considerably decreases their fragility with respect to the higher buildings with two and three floors and the fragility curves related to the type of the internal walls highlight as the presence of the *tabique* internal walls contributes to increase the total fragility. However, the presence of different type of slabs, concrete or timber, gives the greatest contribute on the differences in the seismic response: the presence of the concrete slabs confirms the results already discussed for the clay brick masonries sited in Bologna; otherwise, the different way to distribute the forces of the timber slabs greatly increases the fragility of the buildings, especially in *x*-direction, being the direction of orientation of the slabs. Furthermore, the presence of the timber slabs changes the hierarchy of collapse obtained for the various structural units along the aggregates with concrete slabs: the torsional effects are reduced and the distribution of the forces allows the more central units (Unit 3 and 4) to exhibit larger displacements and their walls to first reach the shear failure, behaving almost independently. Disaggregating the whole aggregate in sub-models, it is possible to

obtain the shear collapse of the Units 1 and 2 (considering only 2 Units) followed by that of the Unit 5 (considering the isolated structural unit).

## **8.2 Future works**

In future applications it is suggested to consider a greater and different variability between the masonry structural units along the row aggregates, taking also into account some mechanical differences, besides the geometrical ones. Moreover, among other types of geometrical differences, the consideration of different total heights and interstorey-heights between the structural units should be an interesting aspect to analyse, to show how the presence of slabs at different heights affects the seismic performances.

Among the variabilities related to the parameters of the analyses, the limit thresholds of the drift for shear and flexure mechanism should have a considerable dispersion, influencing the results related to the evaluation of the ultimate displacement of unreinforced masonry structures. For this reason, it is expected to consider this uncertainty in the future analyses of seismic fragility assessment of these type of structures.

Furthermore, since only the analysis of the in-plane masonry walls was carried out in this work, it is suggested to verify the activation of the possible local mechanisms, activating the out-of-plane behaviour of the masonry walls, with the selected seismic actions.

Finally, it is suggested to perform more accurate non-linear dynamic analyses in order to validate the reliability of the methodology applied in this thesis on unreinforced masonry structures.



---

## References

- Alexandris, A. P., Protopapa, E., and Psycharis, I. (2004). Collapse mechanisms of masonry buildings driven by the distinct element method. In *13th World Conference on Earthquake Engineering*. Vancouver, Canada.
- Appleton, J. (2003). *Reabilitação de Edifícios Antigos. Patologias e tecnologias de intervenção*. Amadora: Edições Orion (In Portuguese).
- Asteris, P. G., Chronopoulos, M. P., Chrysostomou, C. Z., Varum, H., Plevris, V., Kyriakides, N., and Silva, V. (2014). Seismic vulnerability assessment of historical masonry structural systems. *Engineering Structures*, 62–63, 118–134.
- ATC-13. (1985). *Earthquake damage evaluation data for California. Report*. Applied Technology Council, Redwood City, Country of San Mateo.
- ATC-40. (1995). *Seismic Evaluation and retrofit of concrete buildings. Report*. Applied Technology Council, Redwood City, Country of San Mateo.
- Barbieri, G., Biolzi, L., Bocciarelli, M., Fregonese, L., and Frigeri, A. (2013). Assessing the seismic vulnerability of a historical building. *Engineering Structures*, 57, 523–532.
- Battaglia, L., Buratti, N., and Savoia, M. (2018). Fragility analysis of masonry structural units by response surface method. In *10th International Masonry Conference*. Milan, Italy.
- Battaglia, L., Buratti, N., and Savoia, M. (2019). Seismic fragility assessment of masonry structural units and masonry aggregates. In *13th North American Masonry Conference*. Salt Lake City, Utah.
- Bernardini, C., Maio, R., Boschi, S., Ferreira, T. M., Vicente, R., and Vignoli, A. (2018). The seismic vulnerability assessment of a stone masonry building enclosed in aggregate. In *16th European Conference on Earthquake Engineering*. Thessaloniki, Greece.
- Birkmann, J. (2007). Risk and vulnerability indicators at different scales: Applicability, usefulness and policy implications. *Environmental Hazards*, 7(1), 20–31.
- Borri, A., Cangi, G., and De Maria, A. (2007). Studio sulla vulnerabilità sismica del patrimonio edilizio. Il centro storico di Gubbio. In *XII Congresso Nazionale ANIDIS 'L'ingegneria sismica in Italia'*. Pisa, Italy. (In Italian).
- Box, G. E. P., and Draper, N. R. (n.d.). *Empirical Model-Building and Response Surfaces*. John Wiley and Sons (Ed.).
- Box, G. E. P., and Wilson, K. B. (1951). On the Experimental Attainment of Optimum Conditions. *Journal of the Royal Statistical Society*, 13(1), 1–45.
- Buratti, N. (2008). *Assessment of Seismic Safety : Response Surface Approach and Accelerogram*. PhD Thesis. University of Bologna, Italy.
- Buratti, N., Ferracuti, B., and Savoia, M. (2006). Seismic fragility of existing RC structures by response surface method. In *First European Conference on Earthquake Engineering and Seismology*. Geneva, Switzerland.

- Buratti, N., Ferracuti, B., and Savoia, M. (2007). A response surface approach with random block effects for seismic fragility assessment of r.c. structures. In *10th International conference on application of statistics and probability in civil engineering (ICASP)*. Tokyo, Japan.
- Buratti, N., Ferracuti, B., and Savoia, M. (2010). Response Surface with random factors for seismic fragility of reinforced concrete frames. *Structural Safety*, 32(1), 42–51.
- Calderini, C., Cattari, S., and Lagomarsino, S. (2009). In-plane strength of unreinforced masonry piers. *Earthquake Engineering and Structural Dynamics*, 38(2), 243–267.
- Calvi, G. M., Pinho, R., Magenes, G., Bommer, J. J., Restrepo-Vélez, L. F., and Crowley, H. (2006). Development of seismic vulnerability assessment methodologies over the past 30 years. *ISET Journal of Earthquake Technology*, 43(3), 75–104.
- Campos Costa, A., Sousa, M. L., and Carvalho, A. (2008). Seismic Zonation for Portuguese National Annex of Eurocode 8. In *14th World Conference on Earthquake Engineering*. Beijing, China.
- Carvalho, A., Zonno, G., Franceschina, G., Bilé Serra, J., and Campos Costa, A. (2008). Earthquake shaking scenarios for the metropolitan area of Lisbon. *Soil Dynamics and Earthquake Engineering*, 28(5), 347–364.
- Casciati, F., and Faravelli, L. (1991). *Fragility analysis of complex structural system*. John Wiley and Sons (Ed.).
- Casti, J. L. (1990). *Searching for certainty*. William Morrow, New York, New York City.
- Cattari, S., and Lagomarsino, S. (2013). Masonry Structures. In *Developments in the field of displacement based seismic assessment* (pp. 151–200). IUSS Press (Ed.).
- Celik, O. C. (2007). *Probabilistic Assessment of Non-Ductile Reinforced Concrete Frames Susceptible To Mid-America Ground Motions Probabilistic Assessment of Non-Ductile Reinforced Concrete Frames Susceptible To Mid-America*. PhD Thesis. Georgia Institute of Technology, Atlanta, Georgia, USA.
- Ceroni, F., Pecce, M., Lignola, G. P., and Ramaglia, G. (2013). Valutazione di vulnerabilità a scala territoriale: modelli e applicazioni a casi reali di edifici in muratura. In *XV Congresso Nazionale ANIDIS 'L'ingegneria sismica in Italia*. Pisa, Italy. (In Italian).
- Cocco, G., D'Aloisio, A., Spacone, E., and Brando, G. (2019). Seismic Vulnerability of Buildings in Historic Centers: From the “Urban” to the “Aggregate” Scale. *Frontiers in Built Environment*, 5:78.
- Commentary to the NTC 2008. (2009). *Circolare 2 febbraio 2009, n. 617 Istruzioni per l' applicazione delle “ Norme tecniche per le costruzioni ” di cui al D . M . 14 gennaio 2008*. Rome, Italy: Italian Ministry of Infrastructure and Transportation. (In Italian).
- Commentary to the NTC 2018. (2019). *Circolare 21 Gennaio 2019, n. 7 Istruzioni per l'applicazione delle “ Norme tecniche per le costruzioni ” di cui al D . M . 17 Gennaio 2018*. Rome, Italy: Italian Ministry of Infrastructure and Transportation. (In Italian).
- Der Kiureghian, A. (1996). Structural reliability methods for seismic safety assessment: A review. *Engineering Structures*, 18(6), 412–424.

- Der Kiureghian, A., and Ditlevsen, O. (2009). Aleatory or epistemic? Does it matter? *Structural Safety*, 31, 105–112.
- Ditlevsen, O., and Madsen, H. O. (1996). *Structural reliability methods*. John Wiley and Sons (Ed.).
- Doherty, K., Griffith, M. C., Lam, N., and Wilson, J. (2002). Displacement-based seismic analysis for out-of-plane bending of unreinforced masonry walls. *Earthquake Engineering and Structural Dynamics*, 31(4), 833–850.
- Donà, M., Carpanese, P., Follador, V., and Da Porto, F. (2019). Derivation of mechanical fragility curves for macro-typologies of italian masonry buildings. In *7th ECCOMAS Thematic Conference on Computational Methods in Structural Dynamics and Earthquake Engineering*. Crete, Greece.
- Erberik, M. A. (2008). Generation of fragility curves for Turkish masonry buildings considering in-plane failure modes. *Earthquake Engineering and Structural Dynamics*, 37(3), 397–405.
- Eurocode 8. (2004). *EN 1998-1:2004. Design of structures for earthquake resistance*. European Committee for Standardization.
- Eurocódigo 8. (2009). *EN 1998-1:2009. Projecto de estruturas para resistência aos sismos Parte 1: Regras gerais, acções sísmicas e regras para edifícios*. (In Portuguese).
- Fajfar, P. (2000). A Nonlinear Analysis Method for Performance-Based Seismic Design. *Earthquake Spectra*, 16(3), 573–592.
- Faravelli, L. (1989). Response-Surface Approach for Reliability Analysis. *Journal of Engineering Mechanics*, 115(12), 2763–2781.
- FEMA. (2003). *Multi-hazard loss estimation methodology, earthquake model, HAZUS-MH MRI technical manual*. Report. Federal Emergency Management Agency (FEMA). Washington, D.C.
- FEMA. (2009). *Unreinforced Masonry Buildings and Earthquakes. Developing successful risk reduction programs*. FEMA P-774. Report. Federal Emergency Management Agency (FEMA). Washington, D.C.
- Ferreira, T. M., Santos, C., Vicente, R., and Mendes da Silva, J. A. R. (2016). Structural and architectural characterisation of old building stocks: case study of the old city centre of Seixal, Portugal, rebuilt after the Great 1755 Lisbon earthquake. *Engineering Structures and Technologies*, 7(3), 126–139.
- Ferreira, T. M., Vicente, R., Mendes da Silva, J. A. R., Varum, H., and Costa, A. (2013). Seismic vulnerability assessment of historical urban centres: Case study of the old city centre in Seixal, Portugal. *Bulletin of Earthquake Engineering*, 11(15), 1753–1773.
- Ferretti, F. (2018). *Experimental and numerical investigations on the shear behavior of existing masonry structures*. PhD Thesis. University of Bologna, Italy.
- Formisano, A., Mazzolani, F., Florio, G., and Landolfo, R. (2010). A quick methodology for seismic vulnerability assessment of historical masonry aggregates. In *COST Action C26: Urban Habitat Constructions under Catastrophic Events*. Naples, Italy.
- Franchin, P., Lupoi, A., Pinto, P. E., and Schotanus, M. I. J. (2003a). Response surface for seismic

- fragility analysis of RC structures. In *Applications of Statistics and Probability in Civil Engineering*. San Francisco, CA.
- Franchin, P., Lupoi, A., Pinto, P. E., and Schotanus, M. I. J. (2003b). Seismic Fragility of Reinforced Concrete Structures Using a Response Surface Approach. *Journal of Earthquake Engineering*, 7(1), 45–77.
- Franchin, P., Lupoi, A., Pinto, P. E., and Schotanus, M. I. J. (2004). Seismic Fragility Analysis of RC Structures, Use of Response Surface for a Realistic Application. In *13th World Conference on Earthquake Engineering*. Vancouver, Canada.
- Galasco, A., Lagomarsino, S., and Penna, A. (2006). On the use of pushover analysis for existing masonry buildings. In *First European Conference on Earthquake Engineering and Seismology*. Geneva, Switzerland.
- Gardoni, P., Der Kiureghian, A., and Mosalam, K. M. (2002). Probabilistic capacity models and fragility estimates for reinforced concrete columns based on experimental observations. *Journal of Engineering Mechanics*, 128(10), 1024–1038.
- Gardoni, P., Mosalam, K. M., and Der Kiureghian, A. (2003). Probabilistic seismic demand models and fragility estimates for RC bridges. *Journal of Earthquake Engineering*, 7(Special issue 1), 79–106.
- Giovinazzi, S., and Lagomarsino, S. (2001). Una metodologia per l'analisi di vulnerabilità sismica del costruito. In *X Congresso Nazionale "L'Ingegneria Sismica in Italia" - ANIDIS*. Matera and Potenza, Italy. (In Italian).
- Graziotti, F., Magenes, G., Penna, A., and Fontana, D. (2012). Experimental cyclic behaviour of stone masonry spandrels. In *15th World Conference on Earthquake Engineering*. Lisbon, Portugal.
- Grünthal, G. (1998). *European Macroseismic Scale 1998 (EMS 1998)*. Council of Europe, *Cahiers du Centre Européen de Géodynamique et de Sismologie*. (Volume 15).
- Guerrini, G., Graziotti, F., Penna, A., and Magenes, G. (2017). Improved evaluation of inelastic displacement demands for short-period masonry structures. *Earthquake Engineering and Structural Dynamics*, 46(9), 1411–1430.
- Gülkan, P., and Sözen, M. (1999). Procedure for determining seismic vulnerability of buildings structure. *ACI Structural Journal*, 96(3), 336–342.
- Hajibabaei, M., Hosseini, K. A., and Ghayamghamian, M. R. (2012). A New Method for Assessing the Seismic Risk Index of Urban Fabrics. In *15th World Conference on Earthquake Engineering*. Lisbon, Portugal.
- Hill, M., and Rossetto, T. (2008). Comparison of building damage scales and damage descriptions for use in earthquake loss modelling in Europe. *Bulletin of Earthquake Engineering*, 6(2), 335–365.
- Hwang, H. H. M., and Jaw, J. W. (1990). Probabilistic damage analysis of structures. *Journal of Structural Engineering (United States)*, 116(7), 1992–2007.
- Khuri, A. I., and Cornell, J. A. (1996). *Response surfaces: design and analyses*. Marcel Dekker, New

- York, New York City.
- Kircher, C. A., Nassar, A. A., Kustu, O., and Holmes, W. T. (1997a). Development of building damage functions for earthquake loss estimation. *Earthquake Spectra*, 13(4), 663–682.
- Kircher, C. A., Reitherman, R. K., Whitman, R. V., and Arnold, C. (1997b). Estimation of earthquake losses to buildings. *Earthquake Spectra*, 13(4), 703–720.
- Laboratório Nacional de Engenharia Civil. (2012). *Earthquake risk scenarios for selected European cities – Lisbon metropolitan area. Report*. Lisbon, Portugal.
- Lagomarsino, S. (2006). Vulnerability Assessment Of Historical Buildings. In *Assessing and Managing Earthquake Risk* (pp. 135–158). Springer Nature (Ed.).
- Lagomarsino, S., and Cattari, S. (2014). Fragility Functions of Masonry Buildings. *Geotechnical, Geological and Earthquake Engineering*, 27, 111–156.
- Lagomarsino, S., Cattari, S., Abbati, S. D., and Ottonelli, D. (2014). Seismic Assessment of Complex Monumental Buildings in Aggregate : the Case Study of Palazzo Del Podesta ' in Mantua ( Italy ). In *SAHC2014 – 9th International Conference on Structural Analysis of Historical Constructions*. Mexico City, Mexico.
- Lagomarsino, S., and Magenes, G. (2006). Evaluation and Reduction of the Vulnerability of Masonry Buildings. In *4th National Conference on Earthquake Engineering -ANIDIS*. Milan, Italy.
- Lagomarsino, S., Penna, A., Galasco, A., and Cattari, S. (2008). User Guide of TREMURI: Seismic Analysis Program for 3D Masonry Buildings. *User Guide*. Genoa, Italy.
- Lagomarsino, S., Penna, A., Galasco, A., and Cattari, S. (2013). TREMURI program: An equivalent frame model for the nonlinear seismic analysis of masonry buildings. *Engineering Structures*, 55, 1787–1799.
- Lamego, P., Lourenço, P. B., Sousa, M. L., and Marques, R. (2017). Seismic vulnerability and risk analysis of the old building stock at urban scale: application to a neighbourhood in Lisbon. *Bulletin of Earthquake Engineering*, 15(7), 2901–2937.
- Lemos, J. V. (2007). Discrete element modeling of masonry structures. *International Journal of Architectural Heritage*, 1(2), 190–213.
- Lopes, M., Meireles, H., Cattari, S., Bento, R., and Lagomarsino, S. (2014). Pombalino Constructions: Description and Seismic Assessment. In *Structural Rehabilitation of Old Buildings, Building Pathology and Rehabilitation* (pp. 187–233). Springer (Ed.).
- Lourenço, P. B. (1996). *Computational strategies for masonry structures. PhD Thesis*. Delft University of Technology, Netherlands.
- Lourenço, P. B. (2002). Computations on historic masonry structures. *Progress in Structural Engineering and Materials*, 4(3), 301–319.
- Lourenço, P. B. (2014). Masonry Structures, Overview. In *Encyclopedia of Earthquake Engineering*. Springer (Ed.).
- Lourenço, P. B., Mendes, N., Ramos, L. F., and Oliveira, D. V. (2011). Analysis of masonry structures

- without box behavior. *International Journal of Architectural Heritage*, 5(4–5), 369–382.
- Lourenço, P. B., Rots, J. G., and Blaauwendraad, J. (1995). Two approaches for the analysis of masonry structures. *Heron*, 40(4), 313–340.
- Lupoi, G., Franchin, P., Lupoi, A., and Pinto, P. E. (2006). Seismic fragility analysis of structural systems. *Journal of Engineering Mechanics*, 132(4), 385–395.
- Magenes, G., and Calvi, G. M. (1997). In-plane seismic response of brick masonry walls. *Earthquake Engineering and Structural Dynamics*, 26(11), 1091–1112.
- Magenes, G., and Penna, A. (2009). Existing masonry buildings: general code issues and methods of analysis and assessment. *Eurocode 8 Perspectives from the Italian Standpoint*, 3, 185–198.
- Maio, R. (2013). *Seismic vulnerability assessment of old building aggregates*. PhD Thesis. University of Aveiro, Portugal.
- Maio, R., Estêvão, J. M. C., Ferreira, T. M., and Vicente, R. (2017). The seismic performance of stone masonry buildings in Faial island and the relevance of implementing effective seismic strengthening policies. *Engineering Structures*, 141(2017), 41–58.
- Mann, W., and Muller, H. (1982). Failure of shear-stressed masonry. An enlarged theory, tests and application to shear walls. In *Proceedings of the British Ceramic Society: Engineering with Ceramics*. Stoke-on-Trent, UK.
- Marino, S., Cattari, S., and Lagomarsino, S. (2019). Are the nonlinear static procedures feasible for the seismic assessment of irregular existing masonry buildings? *Engineering Structures*, 200(2019), 109700.
- McGuire, R. K. (2004). *Seismic Hazard and Risk Analysis*. 1st edn. Earthquake Engineering Research Institute. Oakland, CA: Earthquake Engineering Research Institute.
- Mendes, N. (2012). *Seismic assessment of ancient masonry buildings: Shaking table tests and numerical analysis*. PhD Thesis. University of Minho, Guimarães, Portugal.
- Mendes, N. (2014). Masonry Macro-block Analysis. In *Encyclopedia of Earthquake Engineering*. Springer (Ed.).
- Milošević, J., Cattari, S., and Bento, R. (2019). Definition of fragility curves through nonlinear static analyses: procedure and application to a mixed masonry-RC building stock. *Bulletin of Earthquake Engineering*, 18(2), 513–545.
- Morandi, P., Albanesi, L., and Magenes, G. (2019). In-Plane Cyclic Response of New Urm Systems with Thin Web and Shell Clay Units. *Journal of Earthquake Engineering*.
- Mosalam, K. M., Ayala, G., White, R. N., and Roth, C. (1997). Seismic fragility of LRC frames with and without masonry infill walls. *Journal of Earthquake Engineering*, 1(4), 693–720.
- NTC. (2008). *Norme tecniche per le costruzioni*. Decreto Ministeriale. Rome, Italy: Italian Ministry of Infrastructure and Transportation. (In Italian).
- NTC. (2018). *Norme Tecniche per le Costruzioni*. Decreto Ministeriale. Rome, Italy: Italian Ministry of Infrastructure and Transportation. (In Italian).

- NZSEE. (2015). *Assessment and improvement of the structural performance of buildings in earthquake*. Wellington, New Zealand: New Zealand Society for Earthquake Engineering.
- Orduña, A. (2003). *Seismic assessment of ancient masonry structures by rigid blocks limit analysis*. PhD Thesis. University of Minho, Guimarães, Portugal.
- Penna, A., Morandi, P., Rota, M., Manzini, C. F., Da Porto, F., and Magenes, G. (2014). Performance of masonry buildings during the Emilia 2012 earthquake. *Bulletin of Earthquake Engineering*, 12(5), 2255–2273.
- Pinto, P. E., Giannini, R., and Franchin, P. (2004). *Seismic reliability analysis of structures*. IUSS Press (Ed.). Pavia, Italy.
- Pires, A. (2013). *Análise de Paredes de Tabique e de Medidas de Reforço Estrutural; Estudo Numérico*. MSc Thesis. Universidade do Porto, Porto (In Portuguese).
- Pitilakis, K., Crowley, H., Kaynia, A. M., and Facilities, C. (2014). SYNER-G: Typology Definition and Fragility Functions for Physical Elements at Seismic Risk. *Geotechnical, Geological and Earthquake Engineering*, 27.
- Porter, K., Kennedy, R., and Bachman, R. (2007). Creating fragility functions for performance-based earthquake engineering. *Earthquake Spectra*, 23(2), 471–489.
- Power, M., Chiou, B., Abrahamson, N., Bozorgnia, Y., Shantz, T., and Roblee, C. (2008). An overview of the NGA project. *Earthquake Spectra*, 24(1), 3–21.
- Power, M., Chiou, B., Abrahamson, N., and Roblee, C. (2006). The “Next Generation of Ground Motion Attenuation Models” (NGA) project: an overview. In *8th U.S. National Conference on Earthquake Engineering*. San Francisco, CA.
- Prajapati, S., AlShawa, O., and Sorrentino, L. (2015). Out-of-plane behaviour of single-body unreinforced-masonry wall restrained by a flexible diaphragm. In *5th ECCOMAS Thematic Conference on Computational Methods in Structural Dynamics and Earthquake Engineering*. Crete Island, Greece.
- Priestley, M. J. N. (1998). Displacement-based approaches to rational limit states design of new structures. In *11th European Conference on Earthquake Engineering*. Rotterdam, Netherlands.
- Rajashekhar, M. R., and Ellingwood, B. R. (1993). New look at the response surface approach for reliability analysis. *Structural Safety*, 12(3), 205–220.
- Ramos, L. F., and Lourenço, P. B. (2004). Modeling and vulnerability of historical city centers in seismic areas: A case study in Lisbon. *Engineering Structures*, 26(9), 1295–1310.
- Rathje, E. M., Kottke, A. R., and Trent, W. L. (2010). Influence of input motion and site property variabilities on seismic site response analysis. *Journal of Geotechnical and Geoenvironmental Engineering*, 136(4), 607–619.
- Rebelo, A., Guedes, J. M., Quelhas, B., and Ilharco, T. (2016). Assessment of the mechanical behaviour of tabique walls through experimental tests. In *2nd International Conference on Historic Earthquake-Resistant Timber Frames in the Mediterranean Region*. Lisbon, Portugal.
- ReLUIIS - Dipartimento di Protezione Civile. (2009). Schede illustrative dei principali meccanismi di

- collasso locali negli edifici esistenti in muratura e dei relativi modelli cinematici di analisi. In *Linee Guida per la Riparazione e il Rafforzamento di elementi strutturali, Tamponature e Partizioni*. (In Italian).
- Rodriguez-Marek, A., Rathje, E. M., Bommer, J. J., Scherbaum, F., and Stafford, P. J. (2014). Application of single-station sigma and site-response characterization in a probabilistic seismic-hazard analysis for a new nuclear site. *Bulletin of the Seismological Society of America*, 104(4), 1601–1619.
- Rossetto, T., and Elnashai, A. (2003). Derivation of vulnerability functions for European-type RC structures based on observational data. *Engineering Structures*, 25(10), 1241–1263.
- Rosti, A., Rota, M., Magenes, G., and Penna, A. (2019). A procedure for seismic risk assessment of Italian masonry buildings. In *7th ECCOMAS Thematic Conference on Computational Methods in Structural Dynamics and Earthquake Engineering*. Crete, Greece.
- Rota, M., Penna, A., and Magenes, G. (2010). A methodology for deriving analytical fragility curves for masonry buildings based on stochastic nonlinear analyses. *Engineering Structures*, 32(5), 1312–1323.
- S.T.A. DATA. (2013). Manuale d'uso 3muri (Release 11.5.0.4 ) - Commercial version. *User Guide*. (In Italian).
- Santos, C., Ferreira, T. M., Vicente, R., and Mendes da Silva, J. A. R. (2013). Building typologies identification to support risk mitigation at the urban scale - Case study of the old city centre of Seixal, Portugal. *Journal of Cultural Heritage*, 14(6), 449–463.
- Schotanus, M. I. J., Franchin, P., Lupoi, A., and Pinto, P. E. (2004). Seismic fragility analysis of 3D structures. *Structural Safety*, 26(4), 421–441.
- Schuëller, G. I., Pradlwarter, H. J., and Koutsourelakis, P. S. (2004). A critical appraisal of reliability estimation procedures for high dimensions. *Probabilistic Engineering Mechanics*, 19(4), 463–474.
- Searle, S. R., Casella, G., and McCulloch, C. E. (1992). Variance Components. *Twin Research and Human Genetics: The Official Journal of the International Society for Twin Studies*, 14(1), 25–34.
- Shawa, O. A., De Felice, G., Mauro, A., and Sorrentino, L. (2012). Out-of-plane seismic behaviour of rocking masonry walls. *Earthquake Engineering and Structural Dynamics*, 41(5), 949–968.
- Shinozuka, M., Feng, M. Q., Lee, J., and Naganuma, T. (2000). Statistical analysis of fragility curves. *Journal of Engineering Mechanics*, 126(12), 1224–1231.
- Simões, A. G. (2018). *Evaluation of the seismic vulnerability of the unreinforced masonry buildings constructed in the transition between the 19th and 20th centuries in Lisbon, Portugal*. Universidade de Lisboa. Instituto Superior Técnico, Portugal.
- Simões, A. G., Bento, R., Lagomarsino, S., Cattari, S., and Lourenço, P. B. (2019a). Fragility Functions for Tall URM Buildings around Early 20th Century in Lisbon. Part 1: Methodology and Application at Building Level. *International Journal of Architectural Heritage*.

- Simões, A. G., Bento, R., Lagomarsino, S., Cattari, S., and Lourenço, P. B. (2019b). Fragility Functions for Tall URM Buildings around Early 20th Century in Lisbon, Part 2: Application to Different Classes of Buildings. *International Journal of Architectural Heritage*.
- Simões, A. G., Milošević, J., Meireles, H., Bento, R., Cattari, S., and Lagomarsino, S. (2015). Fragility curves for old masonry building types in Lisbon. *Bulletin of Earthquake Engineering*, 13(10), 3083–3105.
- Singhal, A., and Kiremidjian, A. S. (1996). Method for probabilistic evaluation of seismic structural damage. *Journal of Structural Engineering*, 122(2), 1459–1467.
- Singhal, A., and Kiremidjian, A. S. (1997). *A Method for Earthquake Motion - Damage Relationships With Application To Reinforced Concrete Frames*. National Center for Earthquake Engineering Research.
- Sorrentino, L., Cattari, S., Da Porto, F., Magenes, G., and Penna, A. (2018). Seismic behaviour of ordinary masonry buildings during the 2016 central Italy earthquakes. *Bulletin of Earthquake Engineering*, 17(10), 5583–5607. <https://doi.org/10.1007/s10518-018-0370-4>
- Tomažević, M. (1999). *Earthquake-resistant design of masonry buildings*. (I. C. P. (Ed.), Ed.).
- Turnšek, V., and Čačovič, F. (1971). Some experimental results on the strength of brick masonry walls. In *2nd International Brick Masonry Conference*. Stoke-on-Trent, UK.
- Turnšek, V., and Sheppard, P. (1980). The shear and flexural resistance of masonry walls. In *International Research Conference on Earthquake Engineering*. Skopje, North Macedonia.
- Tyagunov, S., Stempniewski, L., Grünthal, G., Wahlström, R., and Zschau, J. (2004). Vulnerability and Risk Assessment for Earthquake Prone Cities. In *13th World Conference on Earthquake Engineering*. Vancouver, Canada.
- Vamvatsikos, D., and Allin Cornell, C. (2002). Incremental dynamic analysis. *Earthquake Engineering and Structural Dynamics*, 31(3), 491–514.
- Vanin, F., Zaganelli, D., Penna, A., and Beyer, K. (2017). Estimates for the stiffness, strength and drift capacity of stone masonry walls based on 123 quasi-static cyclic tests reported in the literature. *Bulletin of Earthquake Engineering*, 15(12), 5435–5479.
- Veneziano, D., Casciati, F., and Faravelli, L. (1983). Method of seismic fragility for complicated systems. In *2nd CNSI Specialistic meeting on probabilistic method in seismic risk assessment for NPP*. Livermore, CA.
- Vicente, R., Mendes da Silva, J. A. R., Varum, H., Santos, C., and Ferreira, T. M. (2010a). Caracterização construtiva do edificado. In *Caderno de apoio à avaliação do risco sísmico e de incêndio nos núcleos urbanos antigos do Seixal. Report*. Coimbra, Portugal (In Portuguese).
- Vicente, R., Mendes da Silva, J. A. R., Varum, H., Santos, C., and Ferreira, T. M. (2010b). Ensaios in situ caracterização mecânica e Identificação dinâmica. In *Caderno de apoio à avaliação do risco sísmico e de incêndio nos núcleos urbanos antigos do Seixal. Report*. Coimbra, Portugal (In Portuguese).
- Vicente, R., Parodi, S., Lagomarsino, S., Varum, H., and Silva, J. A. R. M. (2011). Seismic

- vulnerability and risk assessment: Case study of the historic city centre of Coimbra, Portugal. *Bulletin of Earthquake Engineering*, 9(4), 1067–1096.
- Wen, Y. K. (2001). Reliability and performance-based design. *Structural Safety*, 23(4), 407–428.
- Wen, Y. K., Ellingwood, B. R., and Bracci, J. (2004). *Vulnerability function framework for consequence-based engineering. Mid-America earthquake center project. Report.*
- Whitman, R. V., Anagnos, T., Kircher, C. A., Lagorio, H. J., Lawson, R. S., and Schneider, P. (1997). Development of a national earthquake loss estimation methodology. *Earthquake Spectra*, 13(4), 643–661.
- Yi, T. (2004). *Experimental investigation and numerical simulation of an unreinforced masonry structure with flexible diaphragms.* Georgia Institute of Technology, Georgia.
- Yüccemen, M. S., Özcebe, G., and Pay, A. C. (2004). Prediction of potential damage due to severe earthquakes. *Structural Safety*, 26(3), 349–366.

### Sitography

PEER Ground Motion Database: <https://ngawest2.berkeley.edu>

Geological maps of Portugal: <https://www.lneg.pt>

## Appendix A

In this work the data of the PEER Ground Motion Database (<https://ngawest2.berkeley.edu>) were used for the selection of the accelerograms. Table A.1 gives details related to the recordings of the earthquakes selected for the site of Bologna, Table A.2 for the site of Seixal. “Accelerogram Number” is used to indicate the accelerograms used in this work; “Record Sequence Number” (RSN) is a unique ID number used in the database; “HC” is the type of the horizontal component of the seismic action (H1 or H2); “ $M_w$ ” is the moment magnitude; “ $E_{JB}$ ” is the epicentral Joyner-Boore distance; “ $V_{S30}$ ” is the shear wave velocity. Furthermore, the name of the Earthquake, the year and the name of the recording station are listed in Table A.1 and Table A.2.

Figures from A.1.1 to A.1.48 show the accelerograms selected for the site of Bologna and Figures from A.2.1 to A.2.50 show the accelerograms selected for the site of Seixal.

Table A.1: Ground-motion selections for the site of Bologna.

Accelerogram Number	RSN	Earthquake Name	Year	Station Name	HC	$M_w$	$E_{JB}$ (km)	$V_{S30}$ (m/s)
1	602	Whittier Narrows-01	1987	Burbank - N Buena Vista	H1	5.99	20.37	271.4
2	652	Whittier Narrows-01	1987	Lakewood - Del Amo Blvd	H2	5.99	22.40	234.9
3	543	Chalfant Valley-01	1986	Benton	H2	5.77	24.25	271.4
4	314	Westmorland	1981	Brawley Airport	H1	5.90	15.28	208.7
5	638	Whittier Narrows-01	1987	LA - N Westmoreland	H1	5.99	15.34	315.1
6	634	Whittier Narrows-01	1987	LA - Fletcher Dr	H2	5.99	11.07	446.0
7	547	Chalfant Valley-01	1986	Zack Brothers Ranch	H1	5.77	6.07	271.4
8	664	Whittier Narrows-01	1987	N Hollywood - Coldwater Can	H2	5.99	28.37	446.0
9	616	Whittier Narrows-01	1987	El Monte - Fairview Av	H1	5.99	0.75	308.6
10	133	Friuli, Italy-02	1976	San Rocco	H1	5.91	14.37	659.6
11	650	Whittier Narrows-01	1987	La Puente - Ringrove Av	H1	5.99	10.24	308.6
12	683	Whittier Narrows-01	1987	Pasadena - Old House Rd	H1	5.99	8.03	455.4
13	649	Whittier Narrows-01	1987	La Habra - Briarcliff	H1	5.99	14.17	361.2
14	637	Whittier Narrows-01	1987	LA - N Figueroa St	H1	5.99	6.00	405.2
15	628	Whittier Narrows-01	1987	LA - Centinela St	H2	5.99	28.00	234.9
16	596	Whittier Narrows-01	1987	Beverly Hills - 12520 Mulhol	H2	5.99	25.91	545.7
17	620	Whittier Narrows-01	1987	Glendale - Las Palmas	H1	5.99	14.68	446.0
18	642	Whittier Narrows-01	1987	LA - W 70th St	H2	5.99	16.77	294.2
19	544	Chalfant Valley-01	1986	Bishop - LADWP South St	H2	5.77	23.38	271.4
20	632	Whittier Narrows-01	1987	LA - Cypress Ave	H1	5.99	8.56	446.0
21	641	Whittier Narrows-01	1987	LA - Saturn St	H1	5.99	20.35	308.7
22	614	Whittier Narrows-01	1987	Downey - Birchdale	H1	5.99	14.90	245.1
23	705	Whittier Narrows-01	1987	West Covina - S Orange Ave	H1	5.99	6.42	308.6
24	696	Whittier Narrows-01	1987	Sun Valley - Sunland	H1	5.99	26.71	271.4
25	640	Whittier Narrows-01	1987	LA - S Grand Ave	H2	5.99	14.46	308.6
26	697	Whittier Narrows-01	1987	Sunland - Mt Gleason Ave	H1	5.99	24.82	446.0
27	2390	Chi-Chi, Taiwan-02	1999	TCU078	H2	5.90	13.94	443.0
28	136	Santa Barbara	1978	Santa Barbara Courthouse	H1	5.92	0.00	515.0
29	649	Whittier Narrows-01	1987	La Habra - Briarcliff	H2	5.99	14.17	361.2
30	544	Chalfant Valley-01	1986	Bishop - LADWP South St	H1	5.77	23.38	271.4
31	668	Whittier Narrows-01	1987	Norwalk - Imp Hwy, S Grnd	H1	5.99	14.37	270.2
32	632	Whittier Narrows-01	1987	LA - Cypress Ave	H2	5.99	8.56	446.0
33	594	Whittier Narrows-01	1987	Baldwin Park - N Holly	H1	5.99	4.34	308.6
34	147	Coyote Lake	1979	Gilroy Array #2	H2	5.74	8.47	270.8

## Appendix A

35	633	Whittier Narrows-01	1987	LA - E Vernon Ave	H1	5.99	10.50	308.6
36	619	Whittier Narrows-01	1987	Garvey Res. - Control Bldg	H1	5.99	0.36	468.2
37	135	Santa Barbara	1978	Cachuma Dam Toe	H1	5.92	23.75	438.3
38	645	Whittier Narrows-01	1987	LB - Orange Ave	H2	5.99	19.80	270.2
39	694	Whittier Narrows-01	1987	Studio City - Coldwater Can	H1	5.99	26.91	294.2
40	626	Whittier Narrows-01	1987	LA - 116th St School	H2	5.99	18.23	301.0
41	706	Whittier Narrows-01	1987	Whittier Narrows Dam upstream	H1	5.99	2.60	298.7
42	154	Coyote Lake	1979	San Juan Bautista, 24 Polk St	H2	5.74	19.46	370.8
43	149	Coyote Lake	1979	Gilroy Array #4	H2	5.74	4.79	221.8
44	633	Whittier Narrows-01	1987	LA - E Vernon Ave	H2	5.99	10.50	308.6
45	622	Whittier Narrows-01	1987	Hacienda Heights - Colima	H1	5.99	9.60	337.0
46	694	Whittier Narrows-01	1987	Studio City - Coldwater Can	H2	5.99	26.91	294.2
47	619	Whittier Narrows-01	1987	Garvey Res. - Control Bldg	H2	5.99	0.36	468.2
48	697	Whittier Narrows-01	1987	Sunland - Mt Gleason Ave	H2	5.99	24.82	446.0

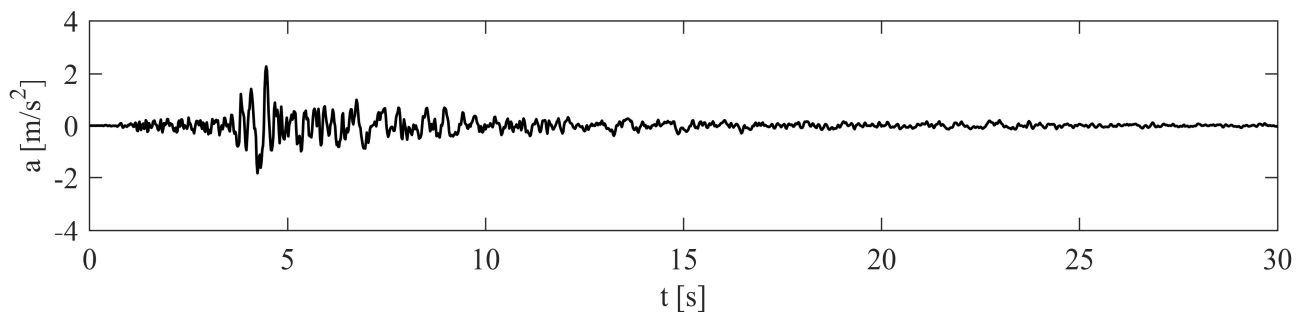


Figure A.1.1: Accelerogram 1 – Bologna.

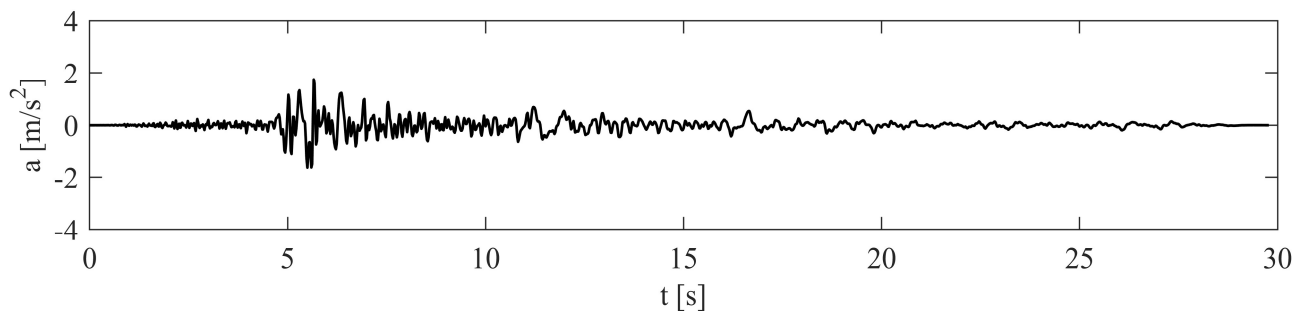


Figure A.1.2: Accelerogram 2 – Bologna.

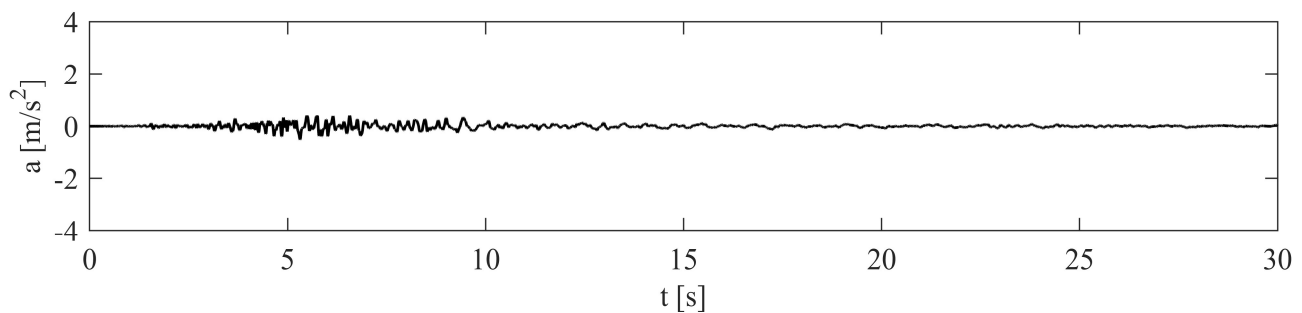


Figure A.1.3: Accelerogram 3 – Bologna.

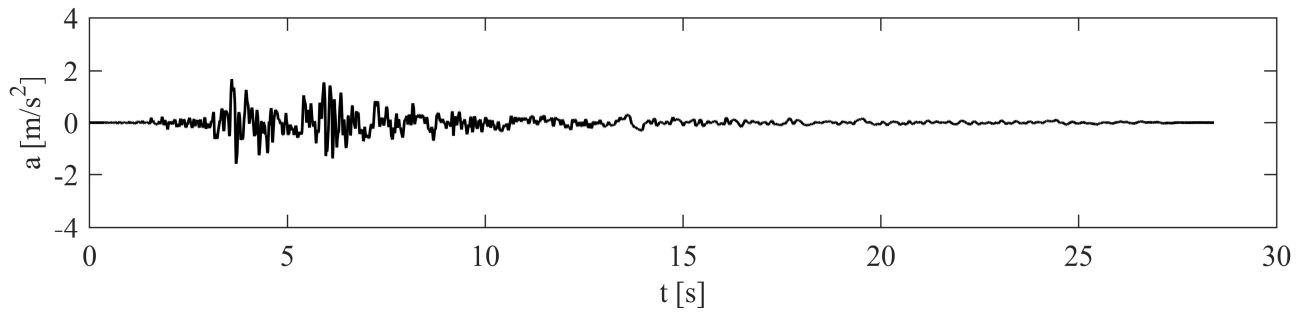


Figure A.1.4: Accelerogram 4 – Bologna.

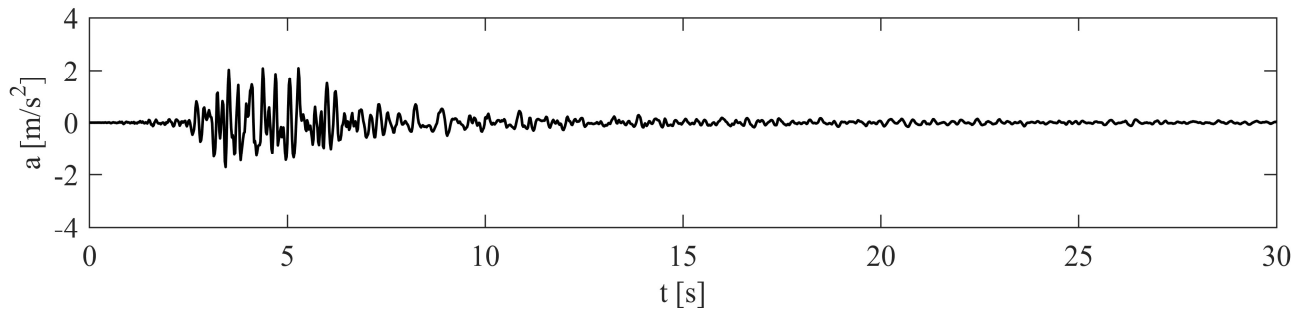


Figure A.1.5: Accelerogram 5 – Bologna.

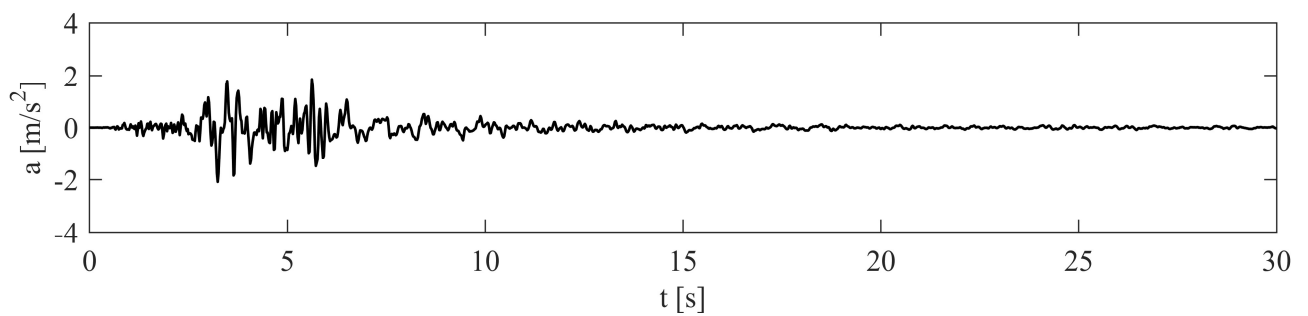


Figure A.1.6: Accelerogram 6 – Bologna.

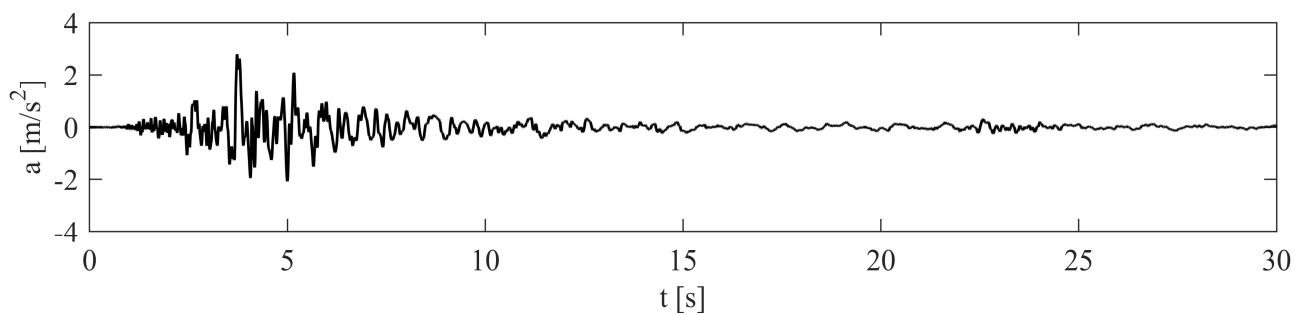


Figure A.1.7: Accelerogram 7 – Bologna.

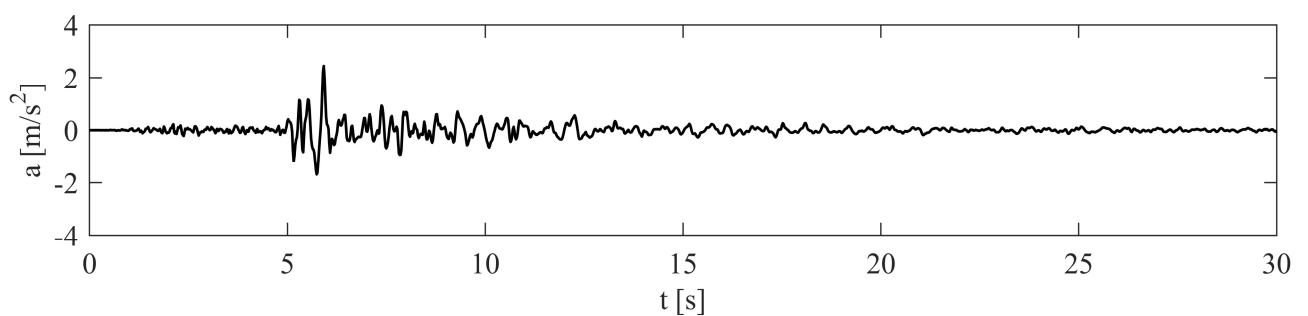


Figure A.1.8: Accelerogram 8 – Bologna.

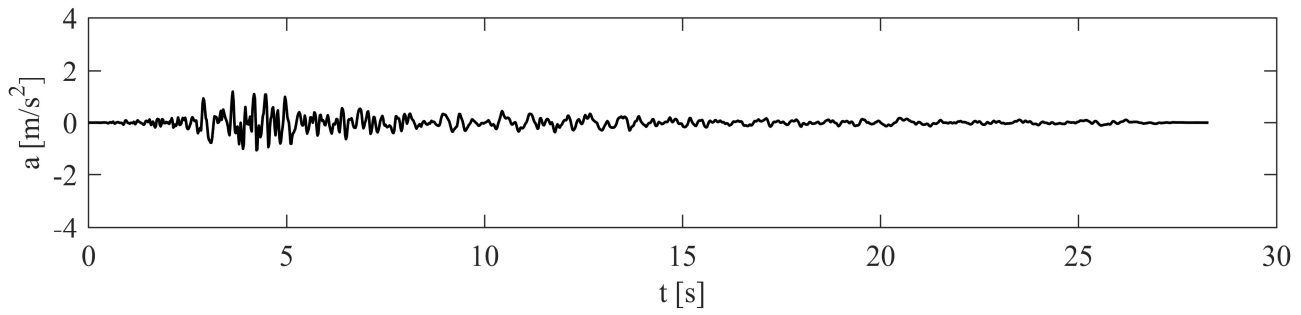


Figure A.1.9: Accelerogram 9 – Bologna.

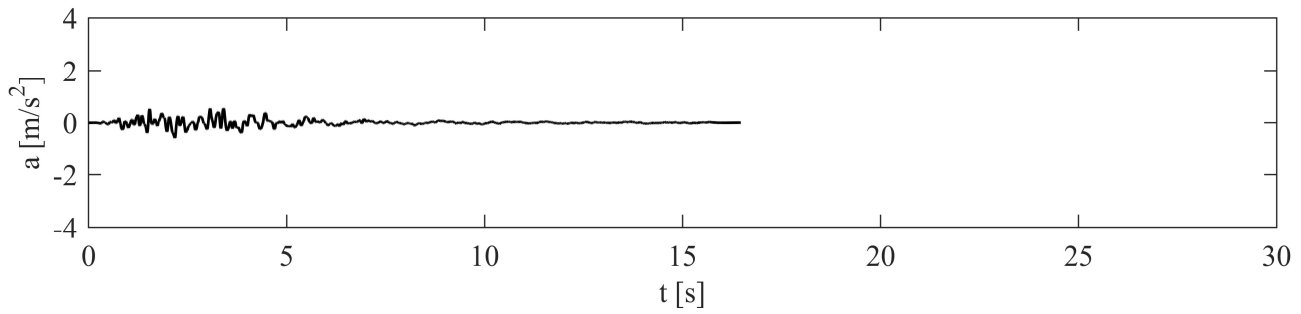


Figure A.1.10: Accelerogram 10 – Bologna.

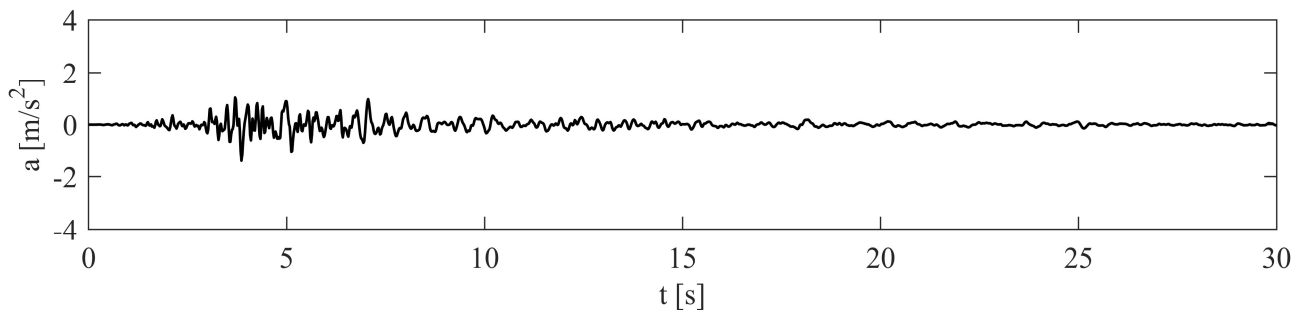


Figure A.1.11: Accelerogram 11 – Bologna.

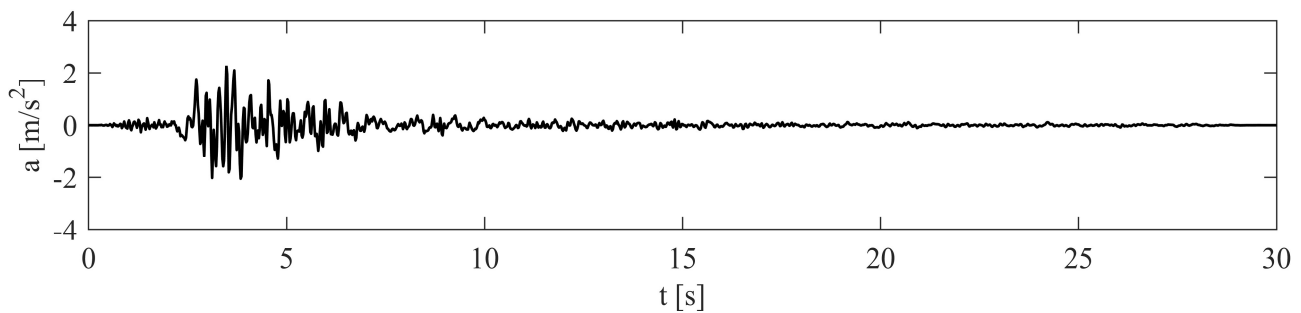


Figure A.1.12: Accelerogram 12 – Bologna.

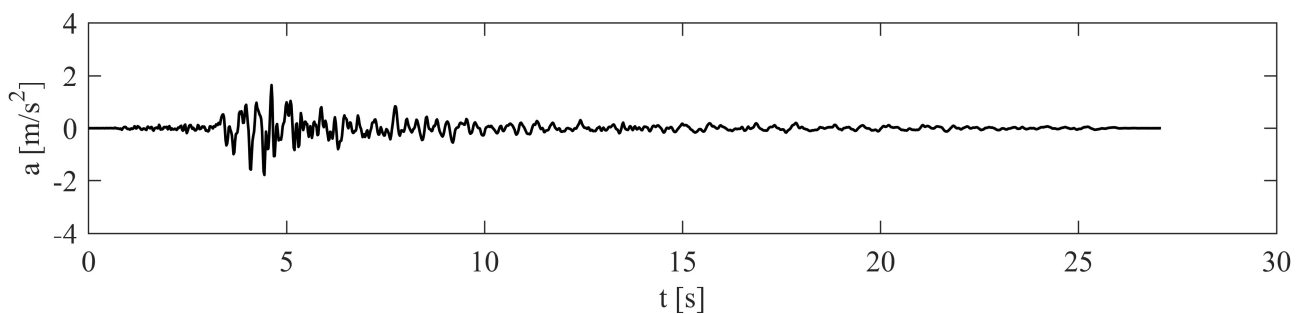


Figure A.1.13: Accelerogram 13 – Bologna.

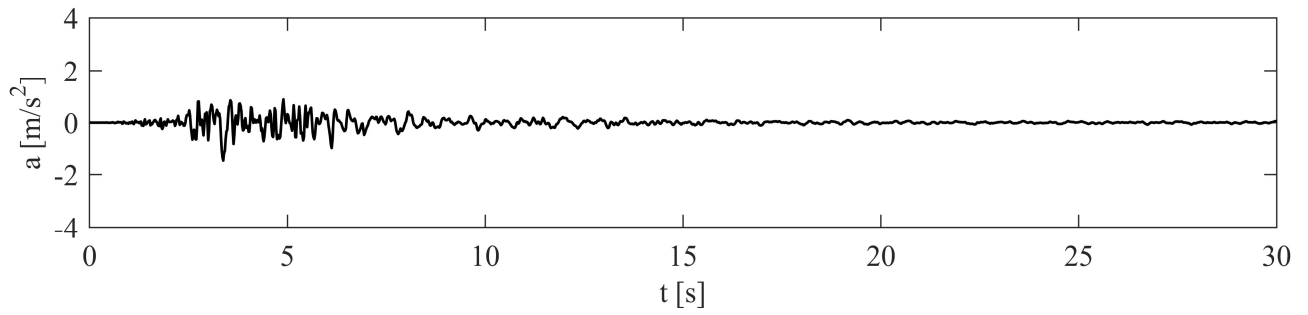


Figure A.1.14: Accelerogram 14 – Bologna.

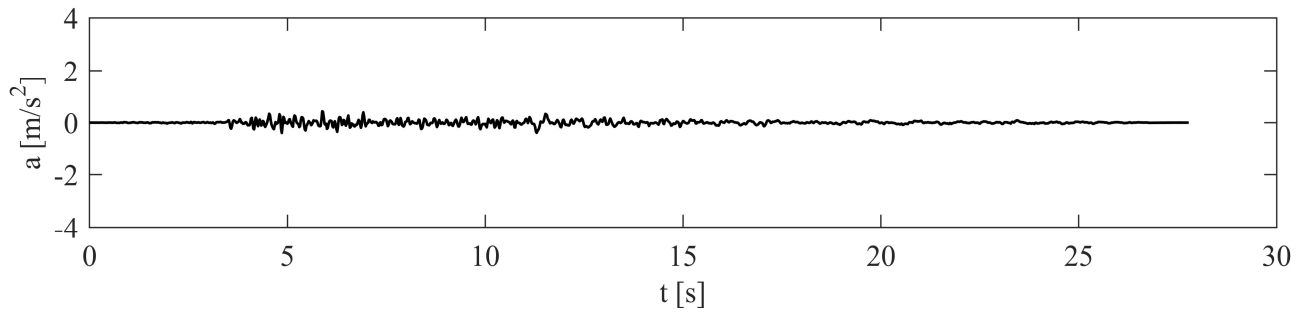


Figure A.1.15: Accelerogram 15 – Bologna.

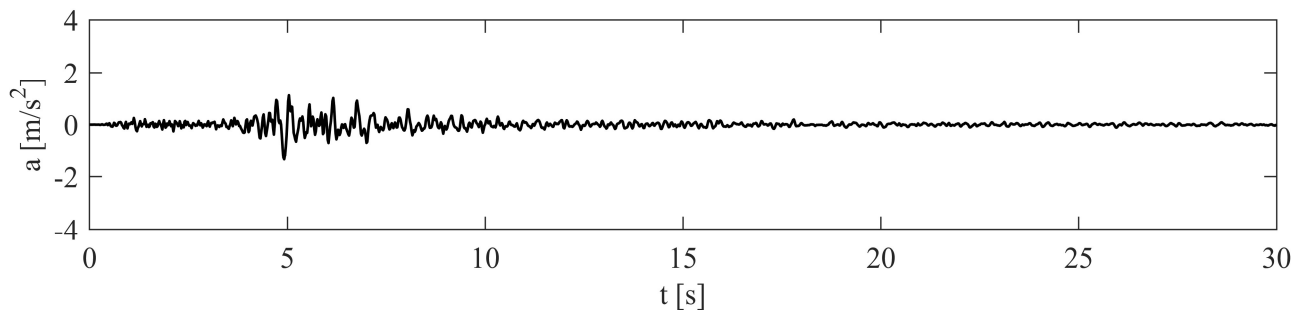


Figure A.1.16: Accelerogram 16 – Bologna.

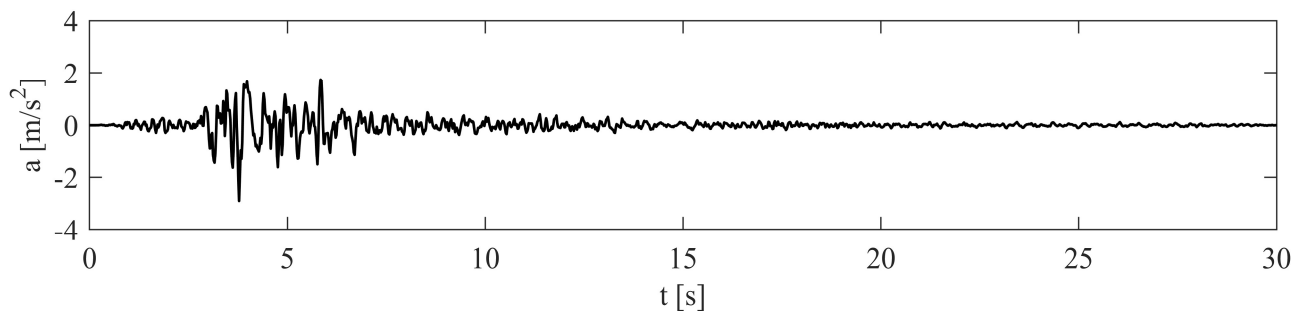


Figure A.1.17: Accelerogram 17 – Bologna.

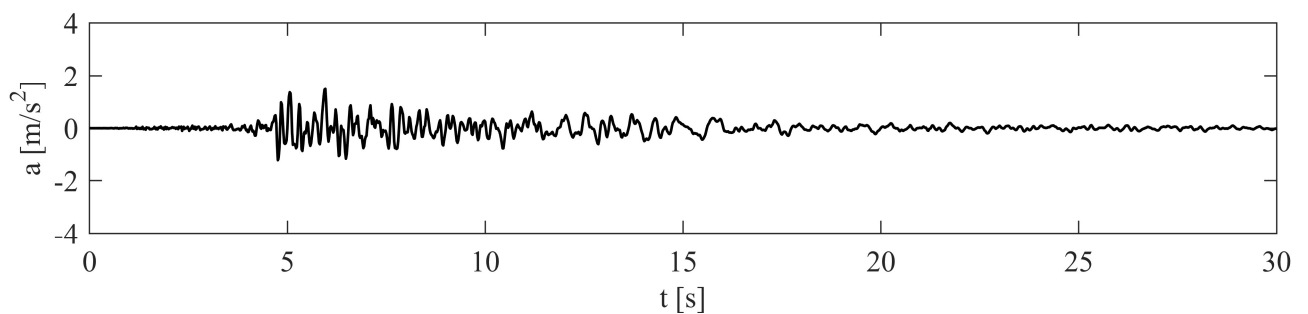


Figure A.1.18: Accelerogram 18 – Bologna.

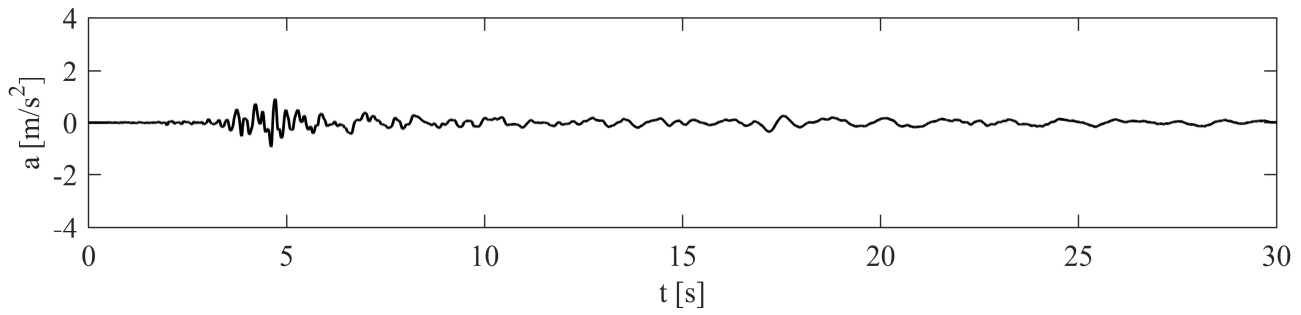


Figure A.1.19: Accelerogram 19 – Bologna.

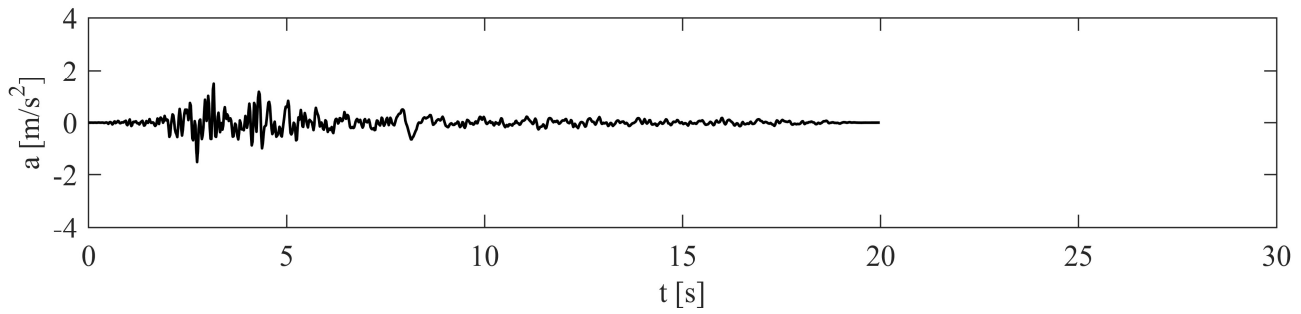


Figure A.1.20: Accelerogram 20 – Bologna.

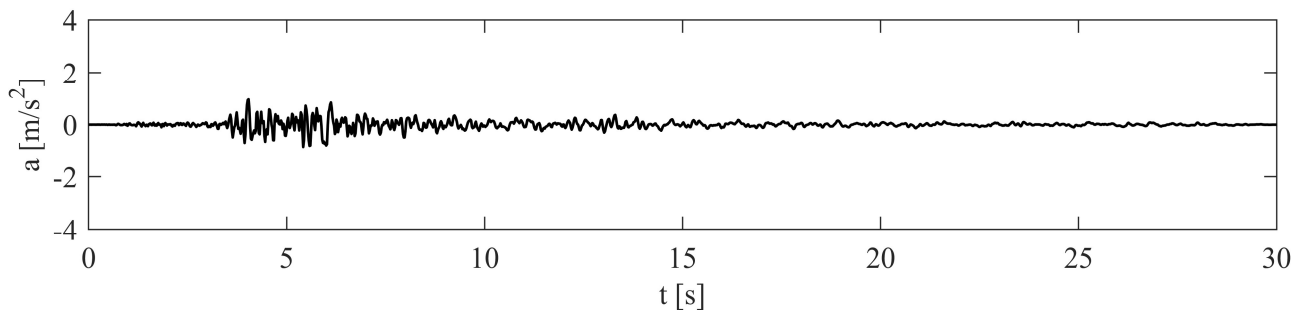


Figure A.1.21: Accelerogram 21 – Bologna.

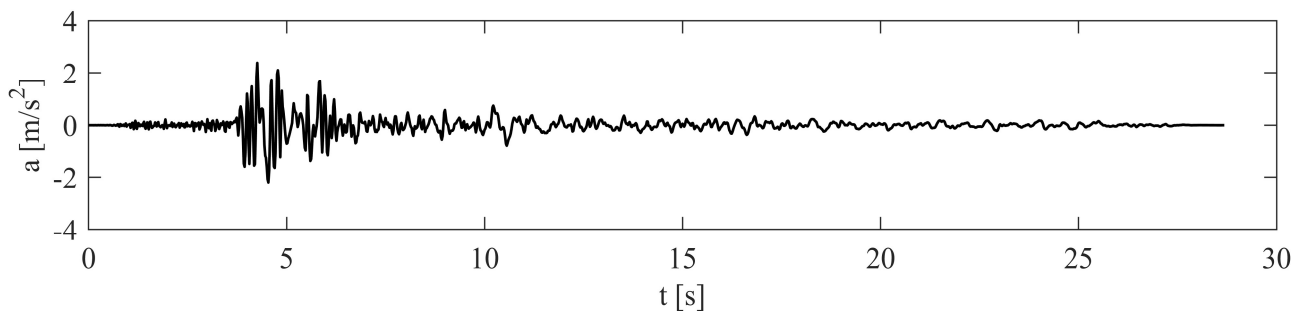


Figure A.1.22: Accelerogram 22 – Bologna.

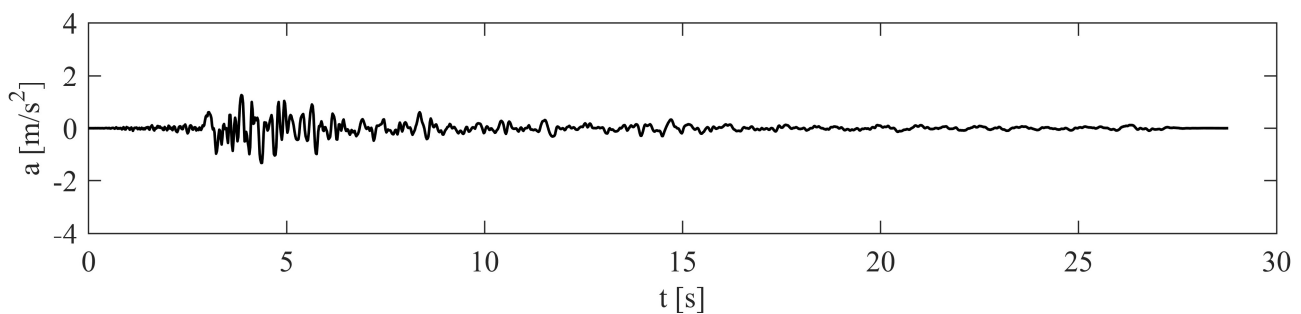


Figure A.1.23: Accelerogram 23 – Bologna.

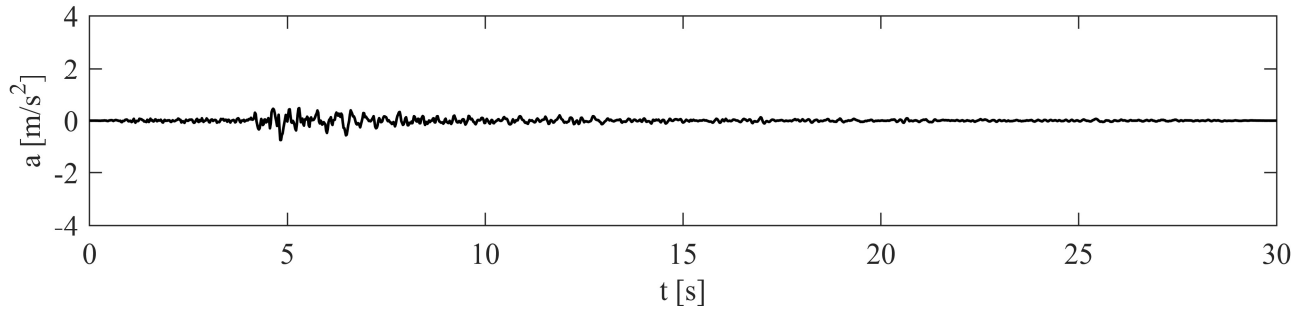


Figure A.1.24: Accelerogram 24 – Bologna.

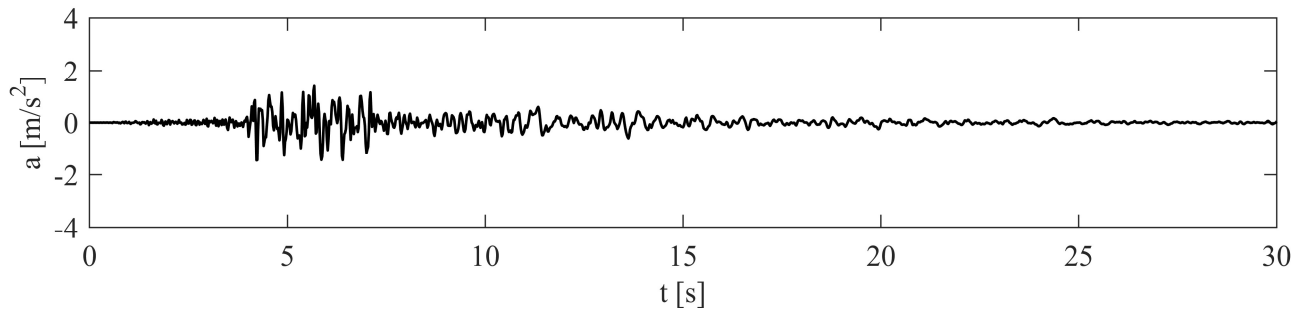


Figure A.1.25: Accelerogram 25 – Bologna.

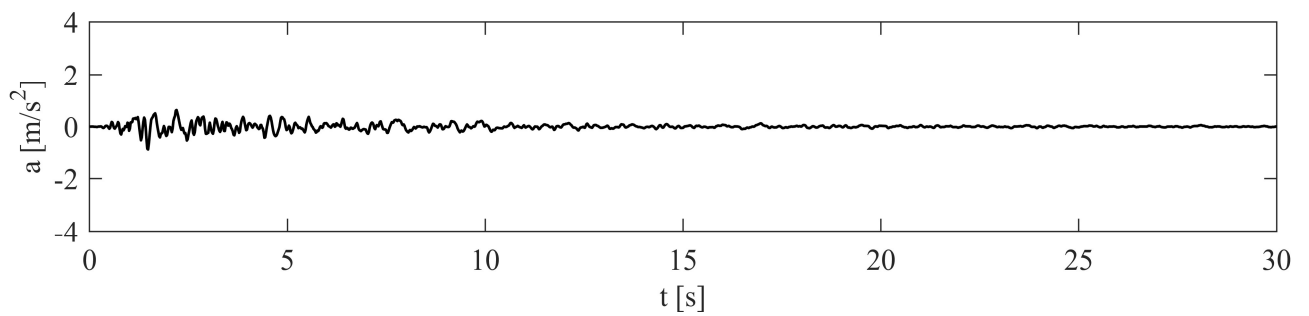


Figure A.1.26: Accelerogram 26 – Bologna.

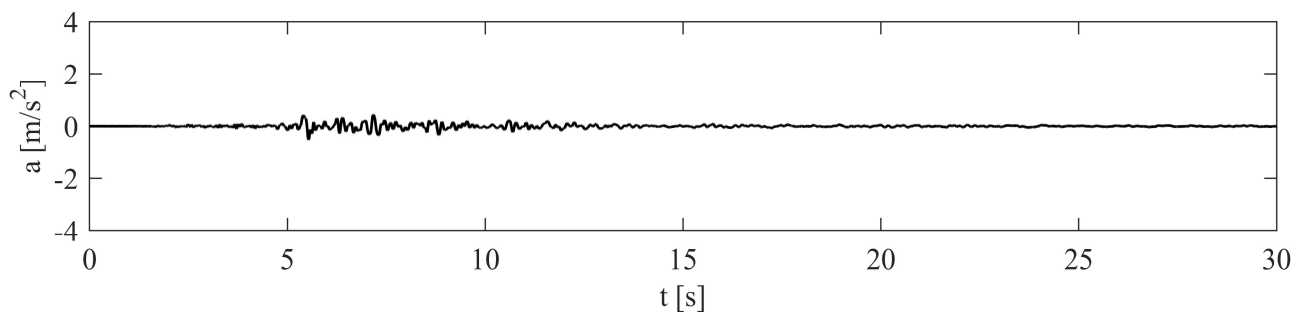


Figure A.1.27: Accelerogram 27 – Bologna.

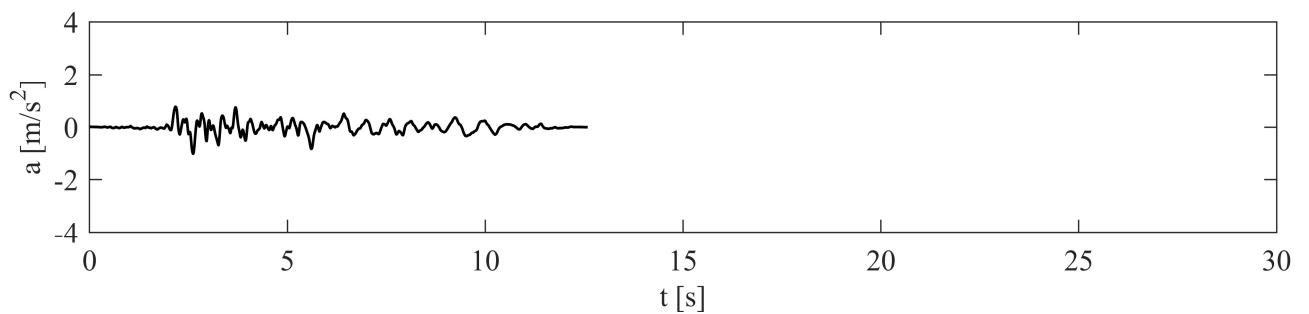


Figure A.1.28: Accelerogram 28 – Bologna.

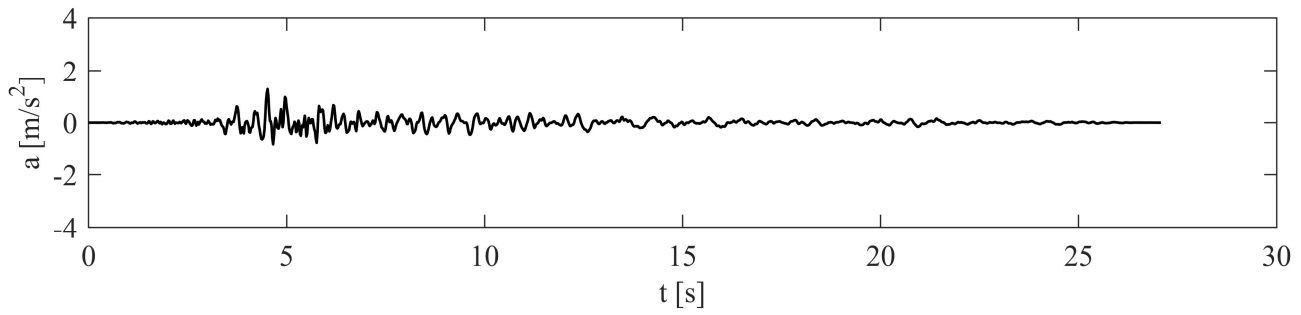


Figure A.1.29: Accelerogram 29 – Bologna.

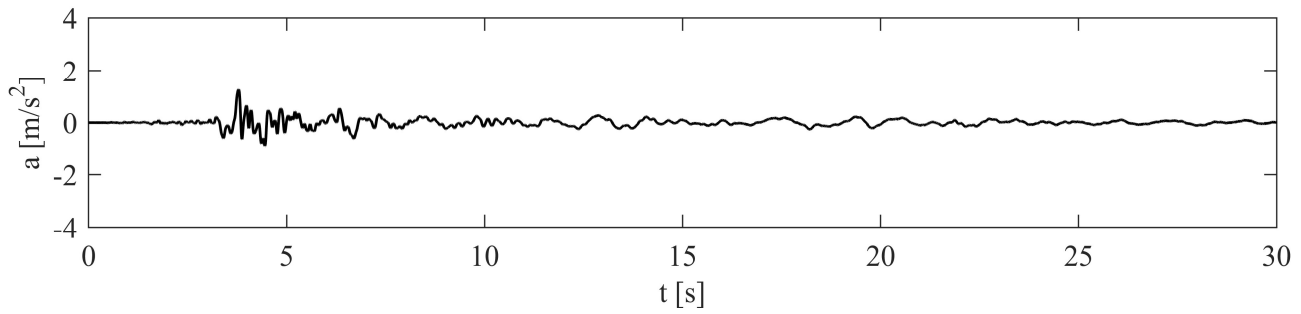


Figure A.1.30: Accelerogram 30 – Bologna.

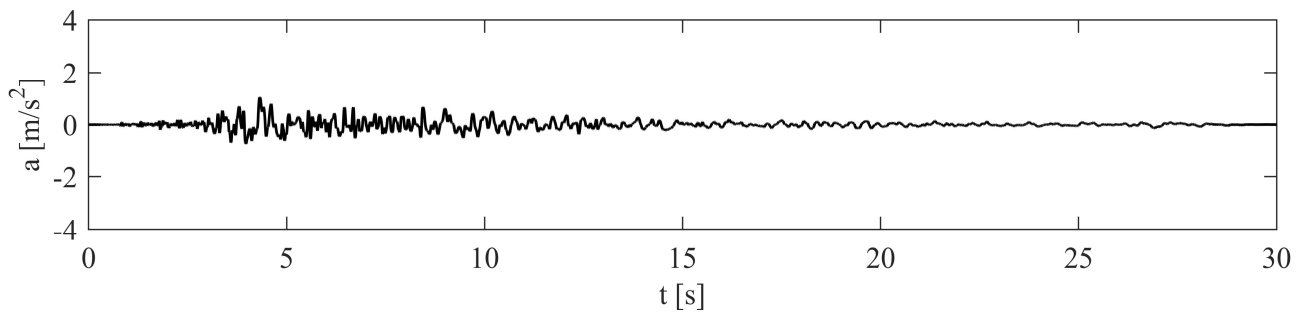


Figure A.1.31: Accelerogram 31 – Bologna.

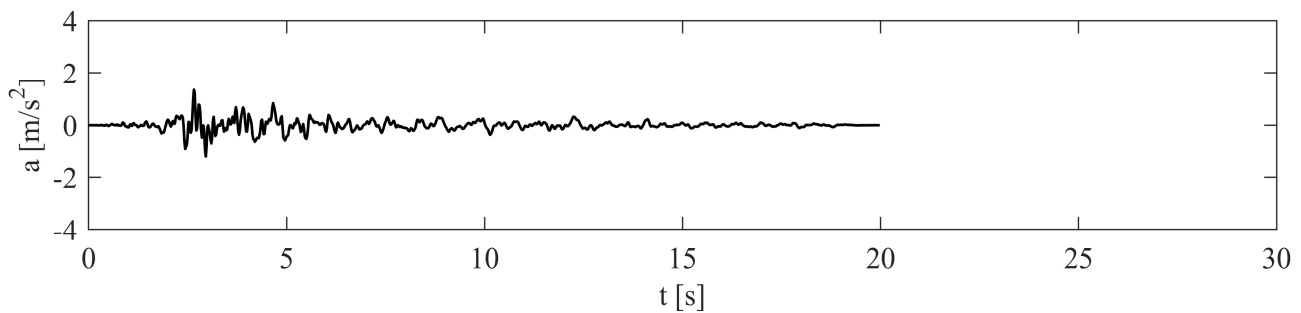


Figure A.1.32: Accelerogram 32 – Bologna.

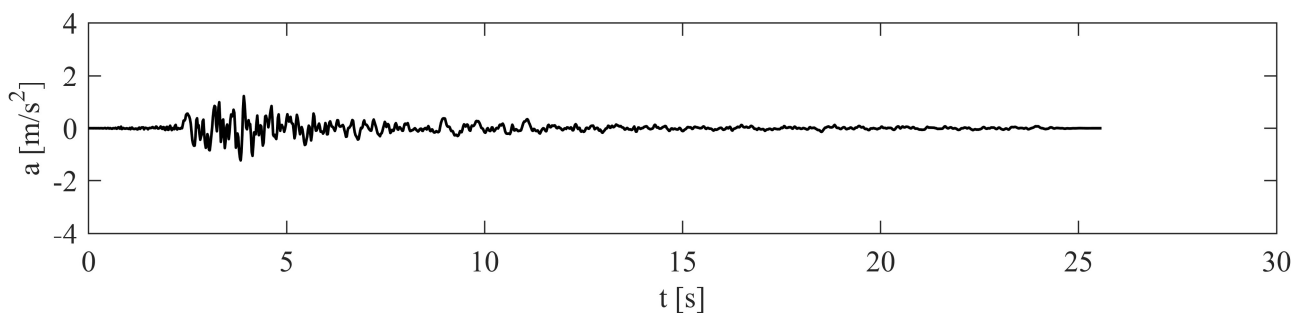


Figure A.1.33: Accelerogram 33 – Bologna.

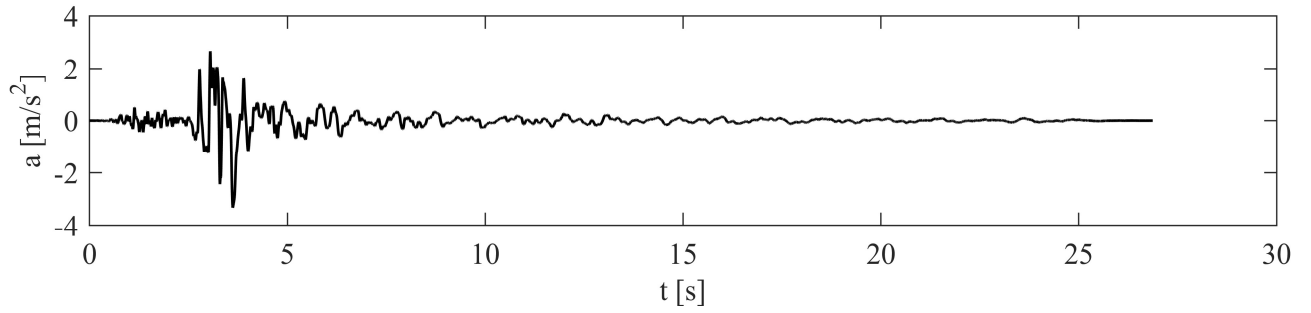


Figure A.1.34: Accelerogram 34 – Bologna.

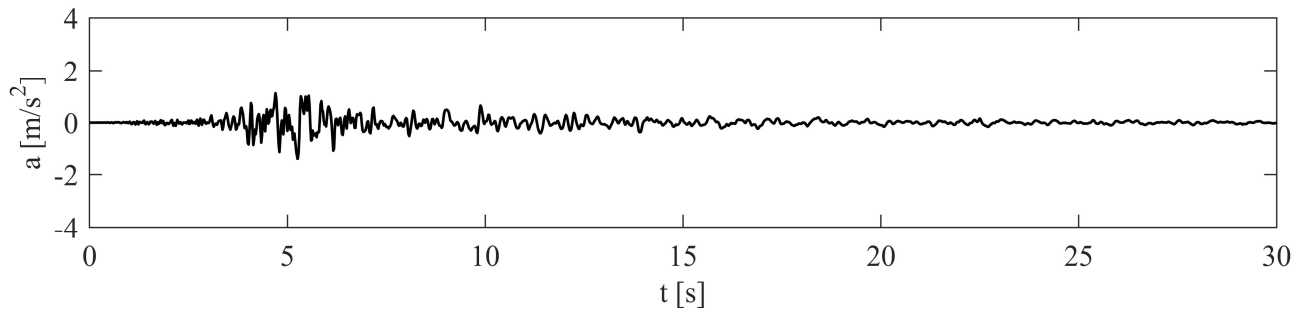


Figure A.1.35: Accelerogram 35 – Bologna.

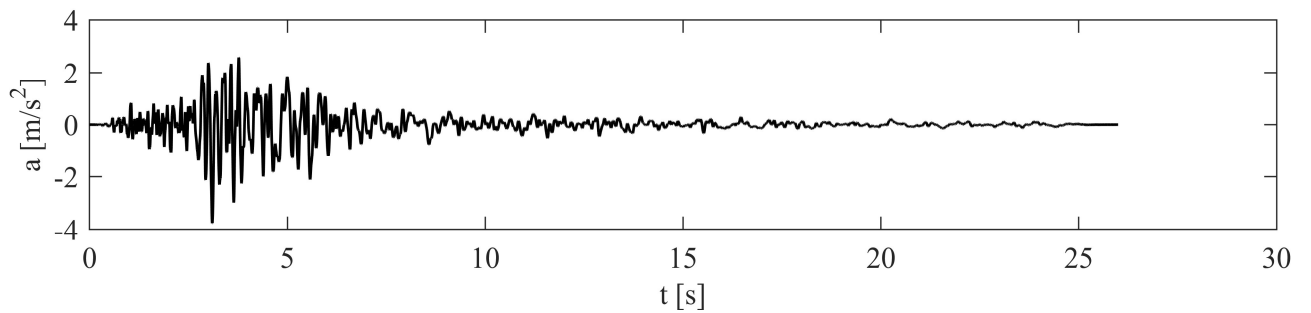


Figure A.1.36: Accelerogram 36 – Bologna.

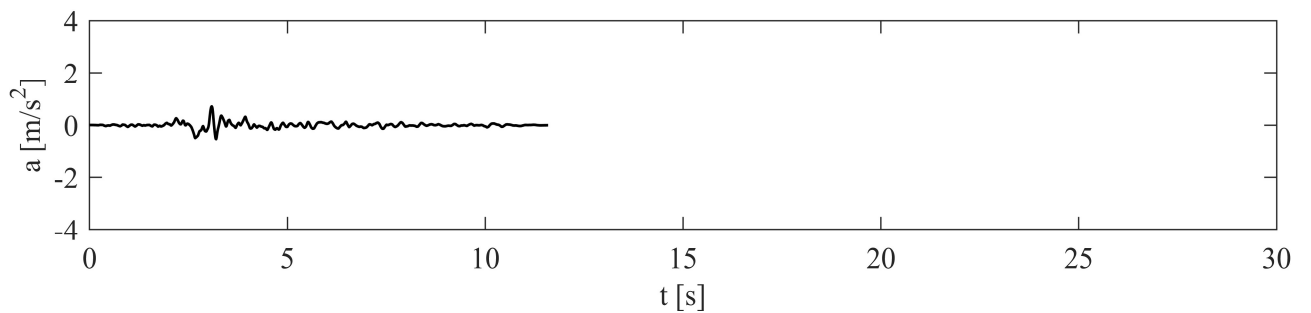


Figure A.1.37: Accelerogram 37 – Bologna.

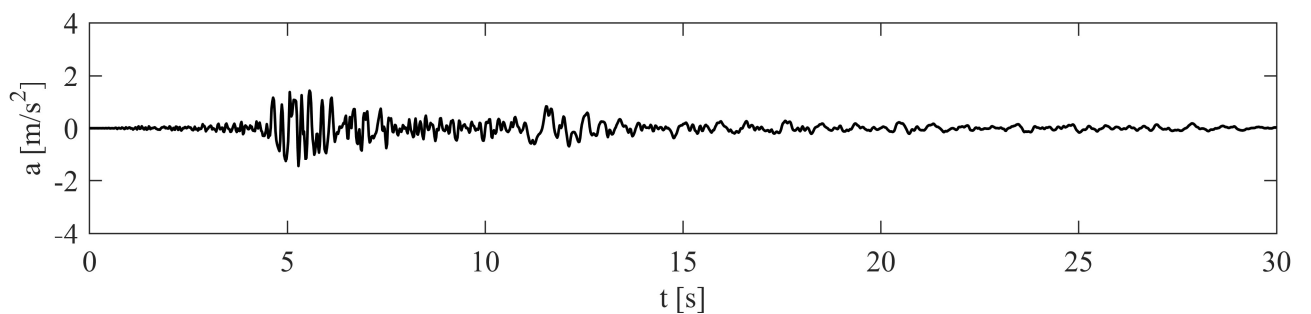


Figure A.1.38: Accelerogram 38 – Bologna.

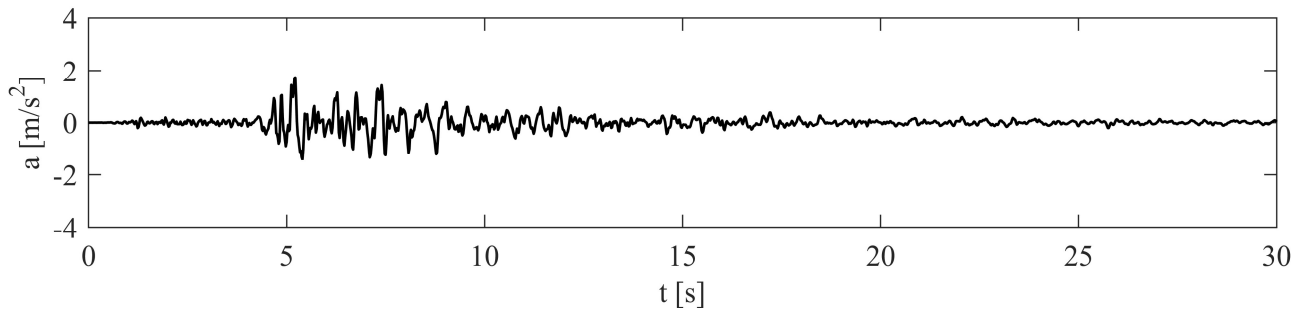


Figure A.1.39: Accelerogram 39 – Bologna.

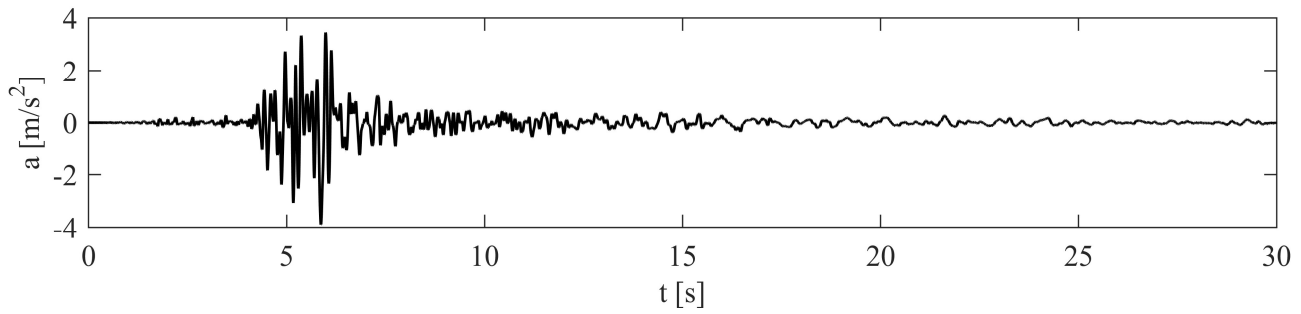


Figure A.1.40: Accelerogram 40 – Bologna.

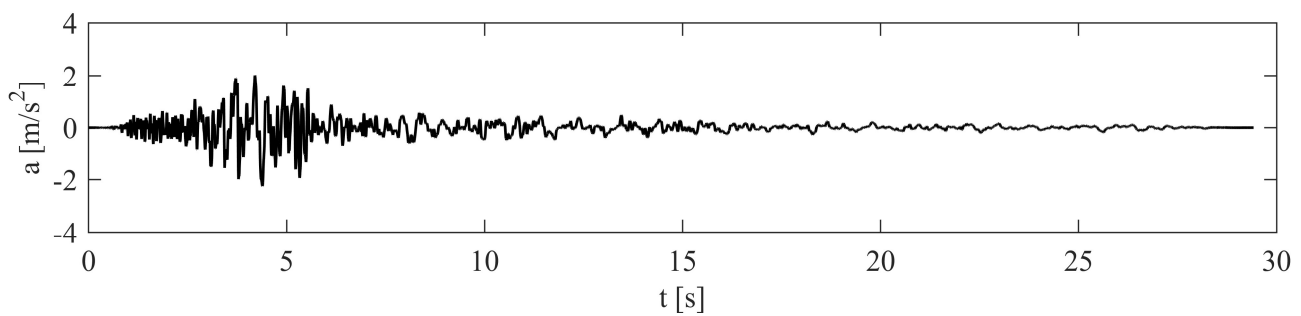


Figure A.1.41: Accelerogram 41 – Bologna.

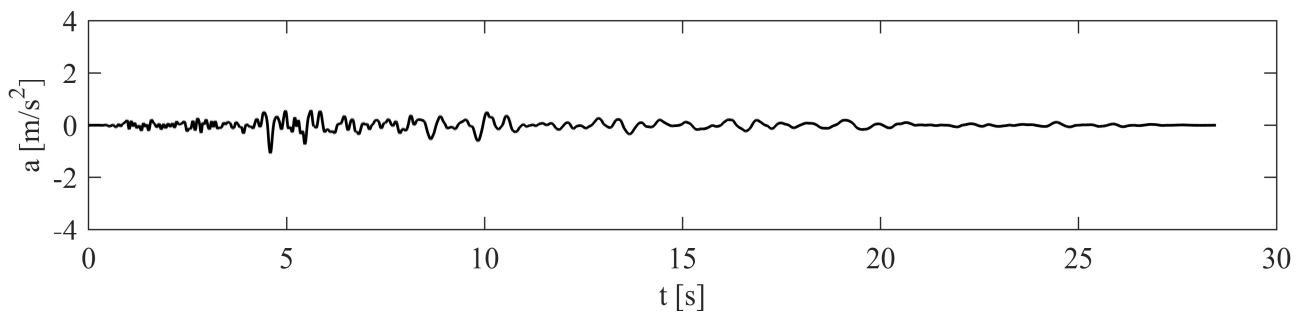


Figure A.1.42: Accelerogram 42 – Bologna.

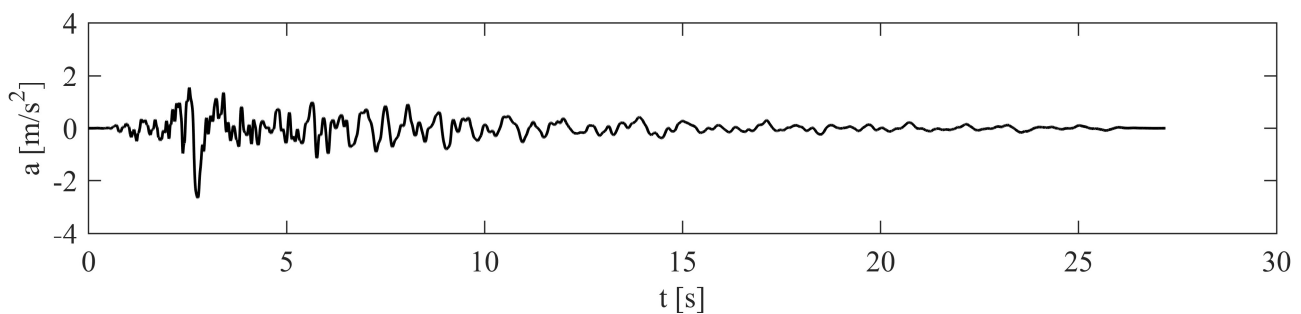


Figure A.1.43: Accelerogram 43 – Bologna.

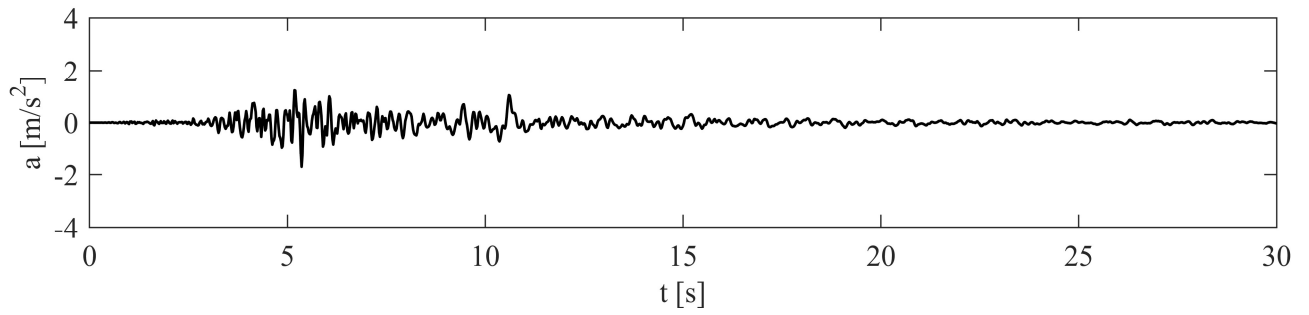


Figure A.1.44: Accelerogram 44 – Bologna.

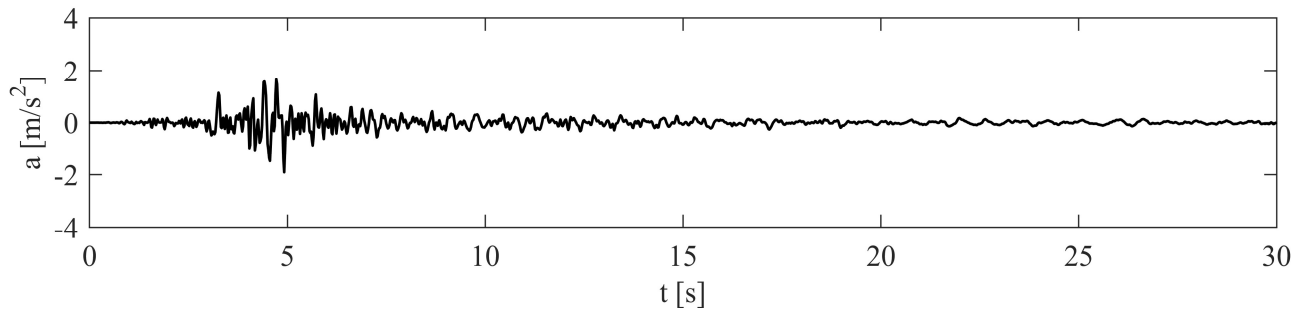


Figure A.1.45: Accelerogram 45 – Bologna.

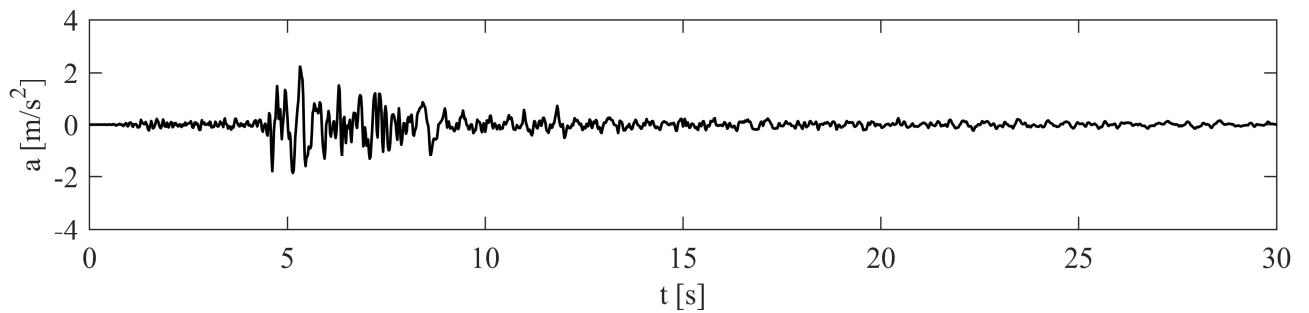


Figure A.1.46: Accelerogram 46 – Bologna.

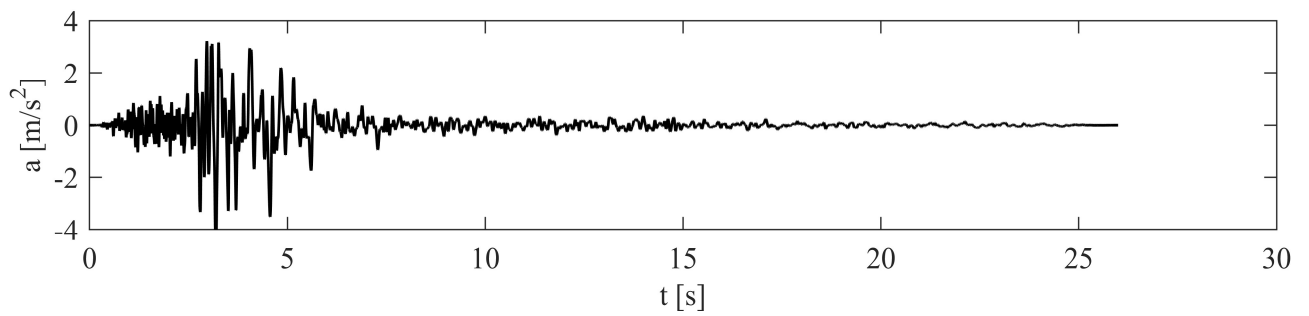


Figure A.1.47: Accelerogram 47 – Bologna.

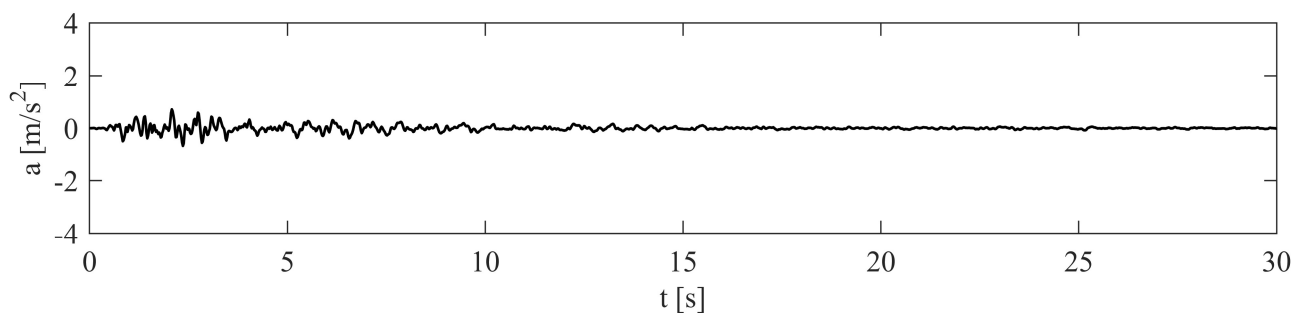


Figure A.1.48: Accelerogram 48 – Bologna.

Table A.2: Ground-motion selections for the site of Seixal.

Accelerogram Number	RSN	Earthquake Name	Year	Station Name	HC	M <sub>w</sub>	E <sub>JB</sub> (km)	V <sub>S30</sub> (m/s)
1	1070	Northridge-01	1994	San Gabriel - E Grand Ave	H2	6.69	38.86	401.4
2	3549	Northridge-01	1994	Monte Nido Fire Station	H1	6.69	15.46	659.6
3	1007	Northridge-01	1994	LA - Univ. Hospital	H2	6.69	32.39	376.1
4	288	Irpinia, Italy-01	1980	Brienza	H2	6.90	22.54	500.0
5	3549	Northridge-01	1994	Monte Nido Fire Station	H2	6.69	15.46	659.6
6	1017	Northridge-01	1994	La Habra - Briarcliff	H2	6.69	58.32	361.2
7	1016	Northridge-01	1994	La Crescenta - New York	H2	6.69	17.81	446.0
8	125	Friuli, Italy-01	1976	Tolmezzo	H1	6.50	14.97	424.8
9	1078	Northridge-01	1994	Santa Susana Ground	H2	6.69	1.69	715.1
10	990	Northridge-01	1994	LA - City Terrace	H1	6.69	35.03	365.2
11	1089	Northridge-01	1994	Topanga - Fire Sta	H1	6.69	10.31	376.1
12	974	Northridge-01	1994	Glendale - Las Palmas	H1	6.69	21.64	446.0
13	974	Northridge-01	1994	Glendale - Las Palmas	H2	6.69	21.64	446.0
14	1010	Northridge-01	1994	LA - Wadsworth VA Hospital South	H1	6.69	14.55	413.8
15	990	Northridge-01	1994	LA - City Terrace	H2	6.69	35.03	365.2
16	1039	Northridge-01	1994	Moorpark - Fire Sta	H2	6.69	16.92	405.2
17	1049	Northridge-01	1994	Pacific Palisades - Sunset	H2	6.69	13.34	446.0
18	952	Northridge-01	1994	Beverly Hills - 12520 Mulhol	H2	6.69	12.39	545.7
19	763	Loma Prieta	1989	Gilroy - Gavilan Coll.	H2	6.93	9.19	729.7
20	1006	Northridge-01	1994	LA - UCLA Grounds	H1	6.69	13.80	398.4
21	288	Irpinia, Italy-01	1980	Brienza	H1	6.90	22.54	500.0
22	1020	Northridge-01	1994	Lake Hughes #12A	H1	6.69	20.77	602.1
23	773	Loma Prieta	1989	Hayward - BART Sta	H2	6.93	54.01	370.8
24	810	Loma Prieta	1989	UCSC Lick Observatory	H1	6.93	12.04	714.0
25	802	Loma Prieta	1989	Saratoga - Aloha Ave	H2	6.93	7.58	370.8
26	809	Loma Prieta	1989	UCSC	H1	6.93	12.15	714.0
27	1089	Northridge-01	1994	Topanga - Fire Sta	H2	6.69	10.31	376.1
28	809	Loma Prieta	1989	UCSC	H2	6.93	12.15	714.0
29	801	Loma Prieta	1989	San Jose - Santa Teresa Hills	H1	6.93	14.18	671.8
30	1009	Northridge-01	1994	LA - Wadsworth VA Hospital North	H1	6.69	14.55	392.2
31	1010	Northridge-01	1994	LA - Wadsworth VA Hospital South	H2	6.69	14.55	413.8
32	810	Loma Prieta	1989	UCSC Lick Observatory	H2	6.93	12.04	714.0
33	1009	Northridge-01	1994	LA - Wadsworth VA Hospital North	H2	6.69	14.55	392.2
34	763	Loma Prieta	1989	Gilroy - Gavilan Coll.	H1	6.93	9.19	729.7
35	1042	Northridge-01	1994	N Hollywood - Coldwater Can	H1	6.69	7.89	446.0
36	1023	Northridge-01	1994	Lake Hughes #9	H2	6.69	24.86	670.8
37	1020	Northridge-01	1994	Lake Hughes #12A	H2	6.69	20.77	602.1
38	1023	Northridge-01	1994	Lake Hughes #9	H1	6.69	24.86	670.8
39	1042	Northridge-01	1994	N Hollywood - Coldwater Can	H2	6.69	7.89	446.0
40	1035	Northridge-01	1994	Manhattan Beach - Manhattan	H1	6.69	33.56	405.2
41	190	Imperial Valley-06	1979	Superstition Mtn Camera	H2	6.53	24.61	362.4
42	769	Loma Prieta	1989	Gilroy Array #6	H2	6.93	17.92	663.3
43	1008	Northridge-01	1994	LA - W 15th St	H2	6.69	25.60	405.2
44	1038	Northridge-01	1994	Montebello - Bluff Rd.	H1	6.69	43.22	405.2
45	1055	Northridge-01	1994	Pasadena - N Sierra Madre	H2	6.69	35.77	455.4
46	587	New Zealand-02	1987	Matahina Dam	H1	6.60	16.09	424.8
47	87	San Fernando	1971	Santa Anita Dam	H2	6.61	30.70	684.9
48	496	Nahanni, Canada	1985	Site 2	H2	6.76	0.00	659.6
49	991	Northridge-01	1994	LA - Cypress Ave	H1	6.69	28.98	446.0
50	801	Loma Prieta	1989	San Jose - Santa Teresa Hills	H2	6.93	14.18	671.8

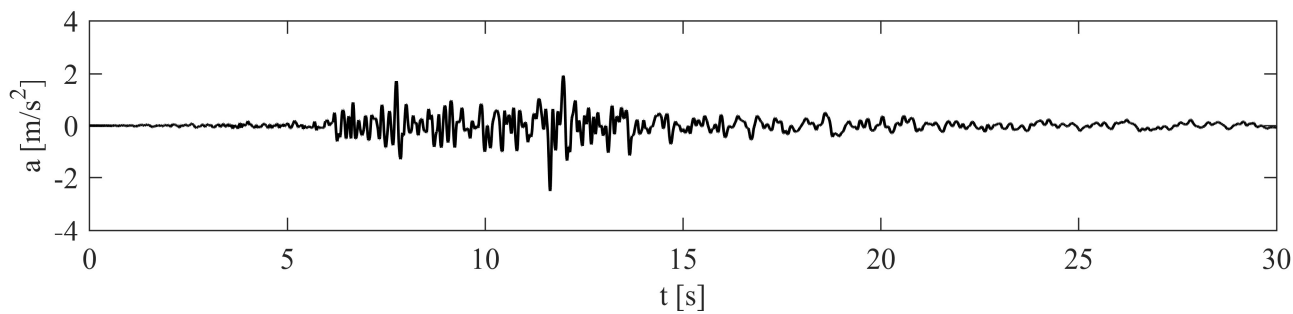


Figure A.2.1: Accelerogram 1 – Seixal.

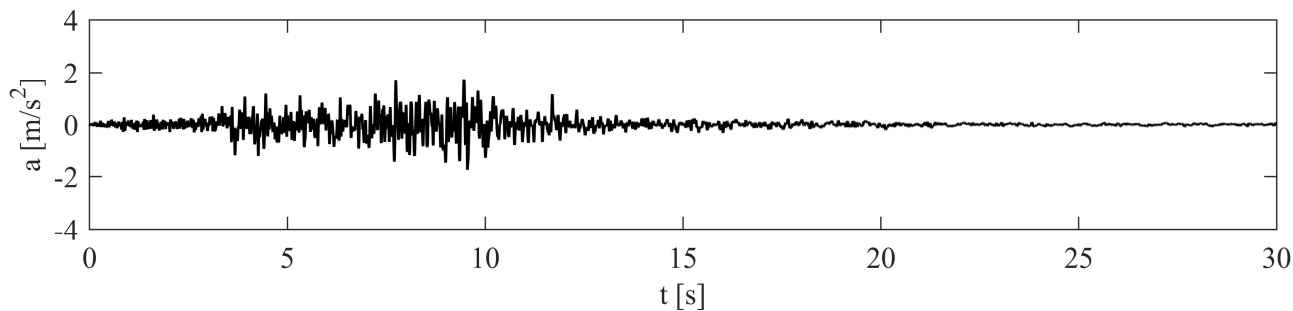


Figure A.2.2: Accelerogram 2 – Seixal.

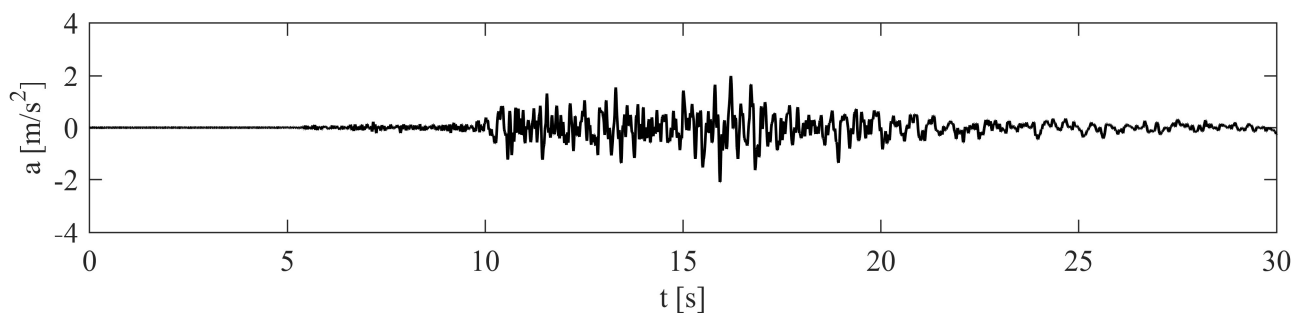


Figure A.2.3: Accelerogram 3 – Seixal.

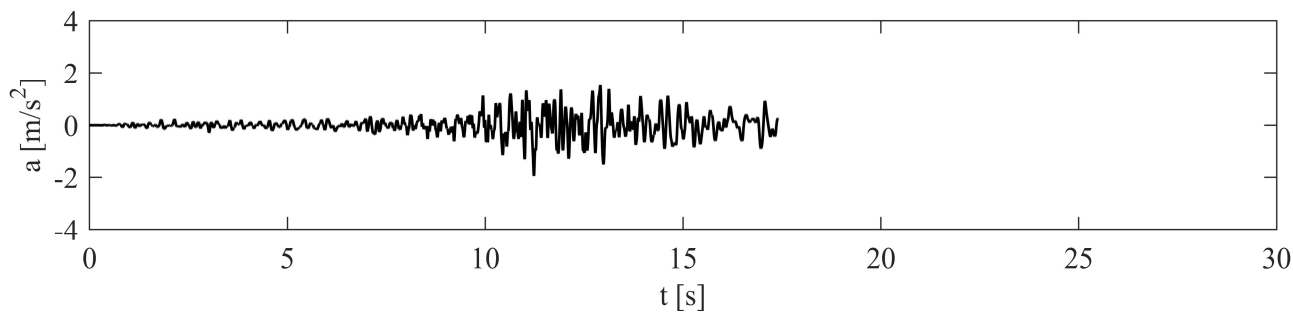


Figure A.2.4: Accelerogram 4 – Seixal.

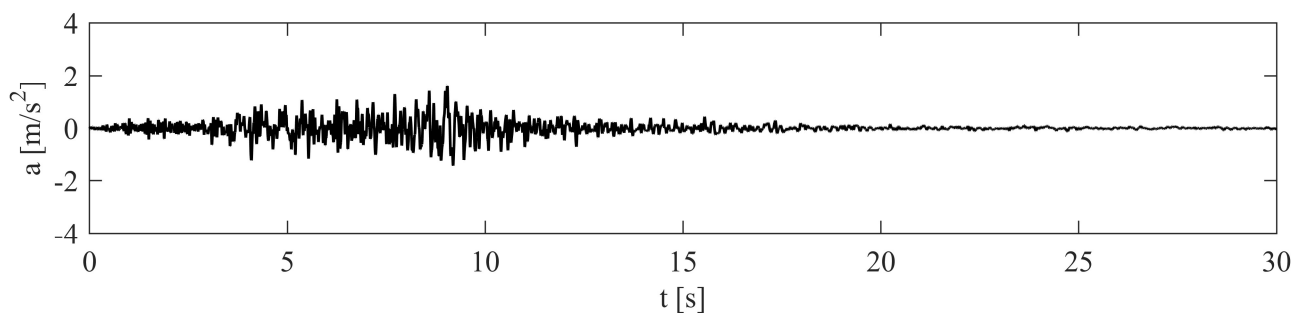


Figure A.2.5: Accelerogram 5 – Seixal.

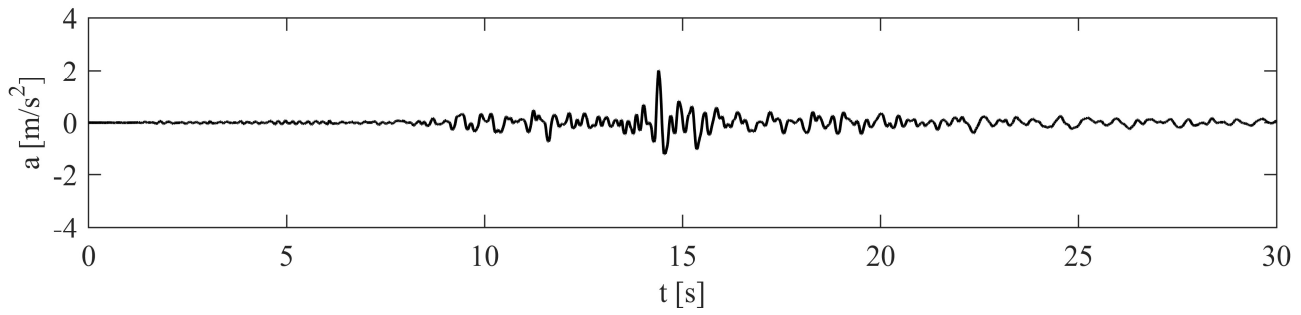


Figure A.2.6: Accelerogram 6 – Seixal.

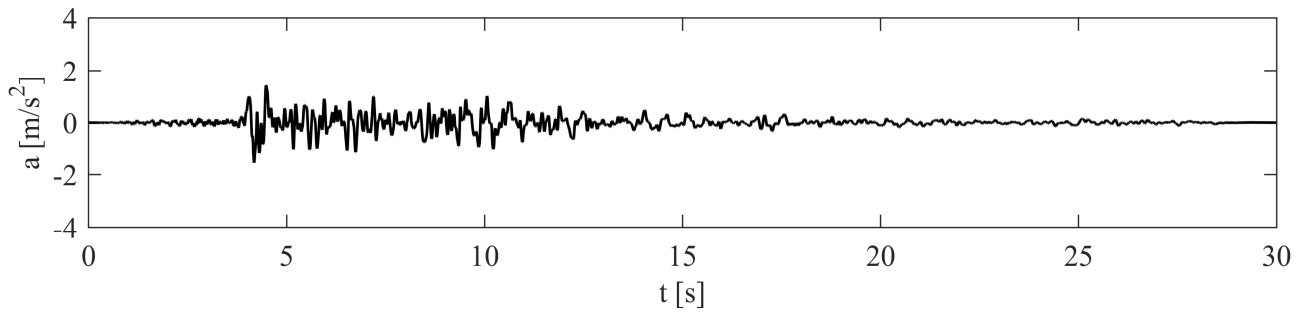


Figure A.2.7: Accelerogram 7 – Seixal.

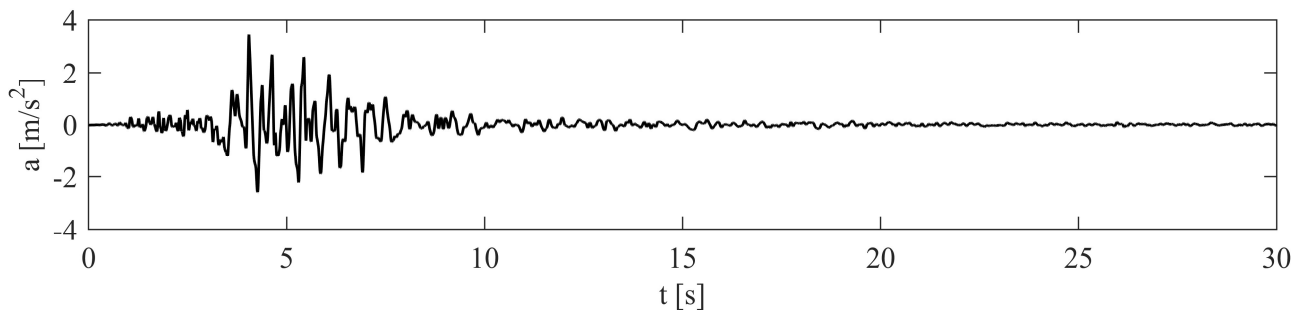


Figure A.2.8: Accelerogram 8 – Seixal.

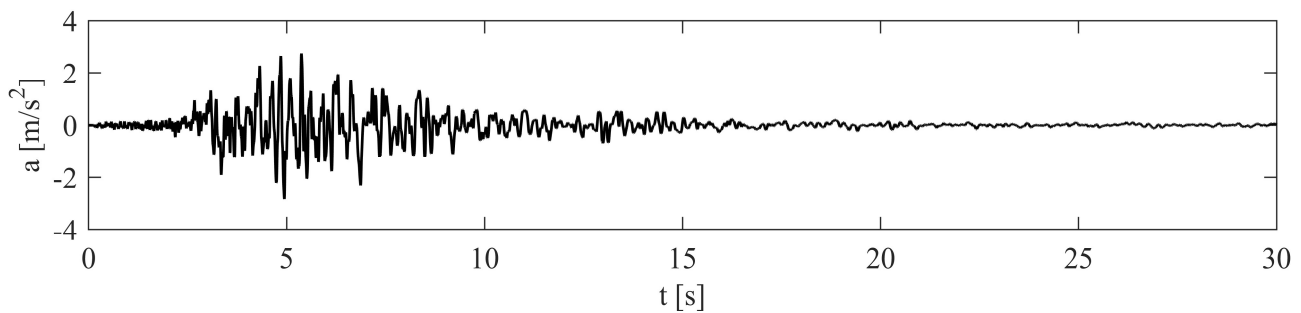


Figure A.2.9: Accelerogram 9 – Seixal.

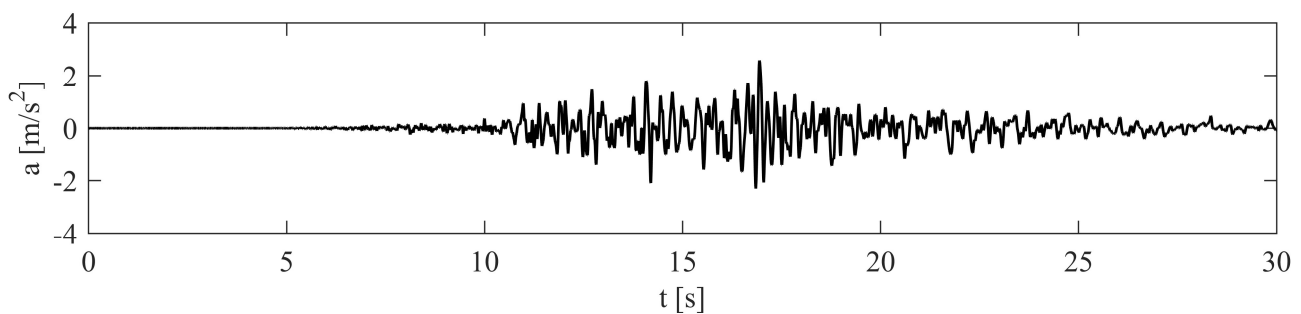


Figure A.2.10: Accelerogram 10 – Seixal.

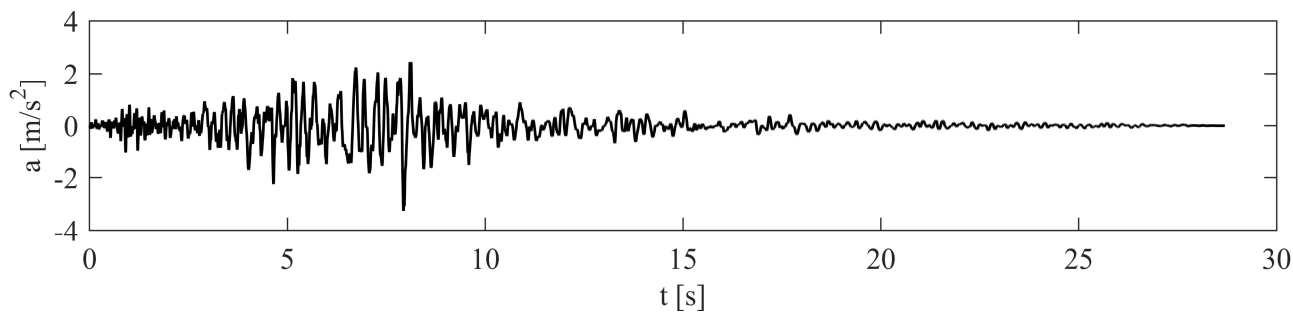


Figure A.2.11: Accelerogram 11 – Seixal.

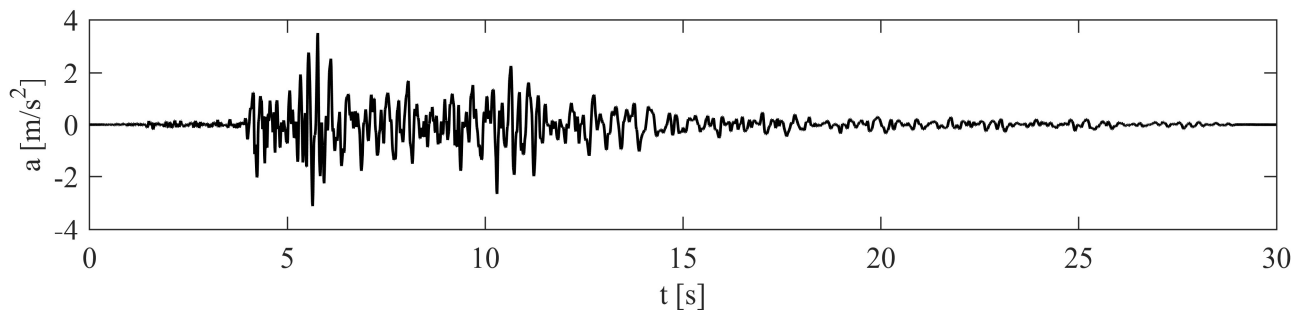


Figure A.2.12: Accelerogram 12 – Seixal.

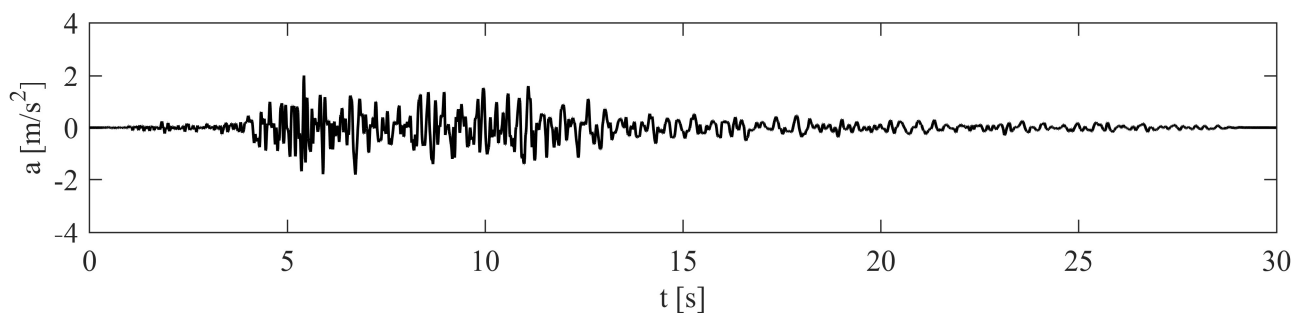


Figure A.2.13: Accelerogram 13 – Seixal.

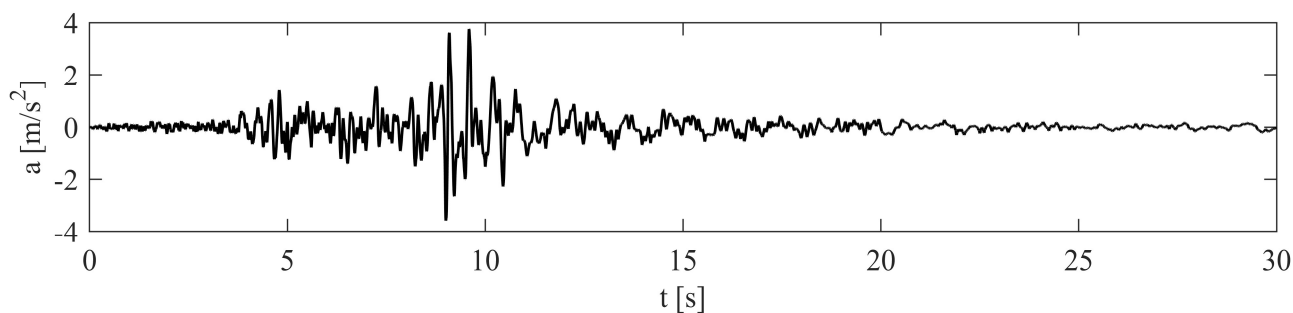


Figure A.2.14: Accelerogram 14 – Seixal.

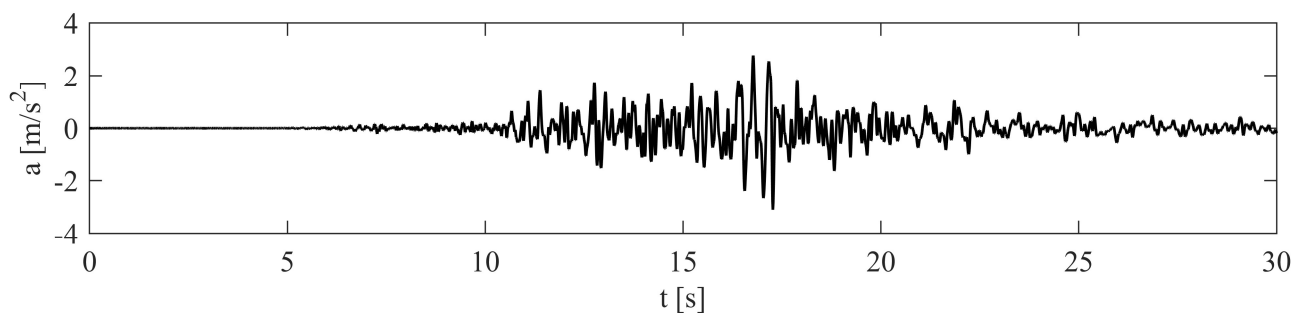


Figure A.2.15: Accelerogram 15 – Seixal.

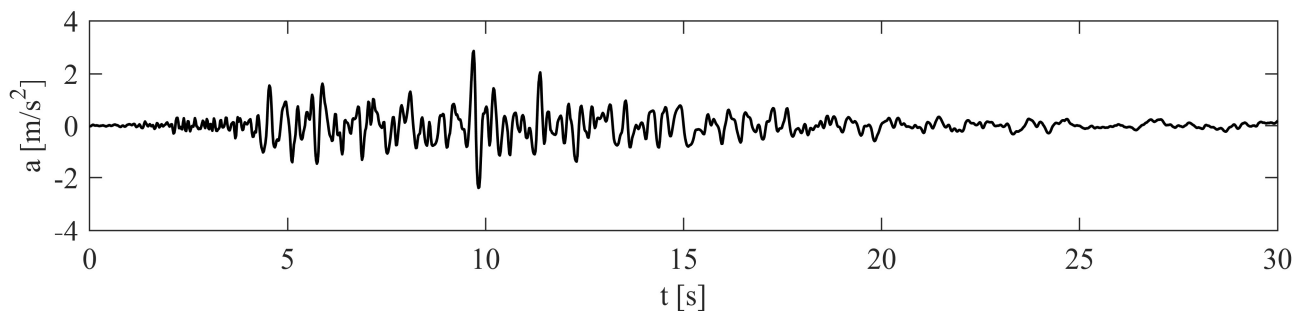


Figure A.2.16: Accelerogram 16 – Seixal.

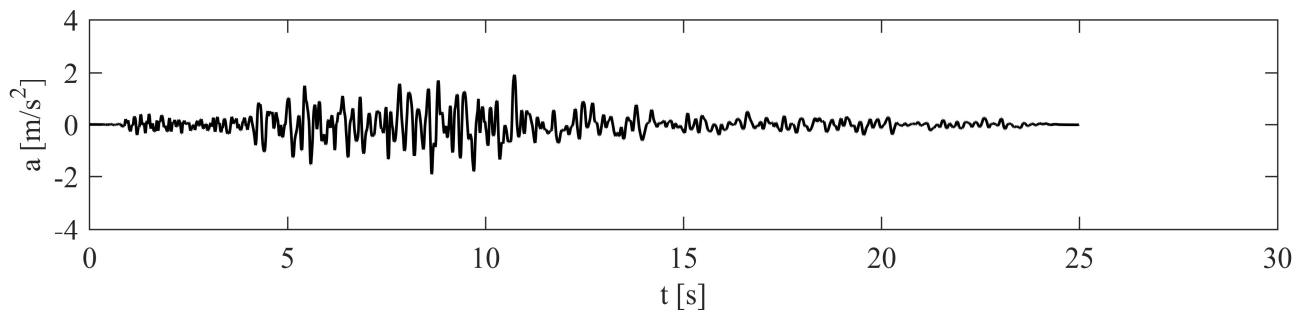


Figure A.2.17: Accelerogram 17 – Seixal.

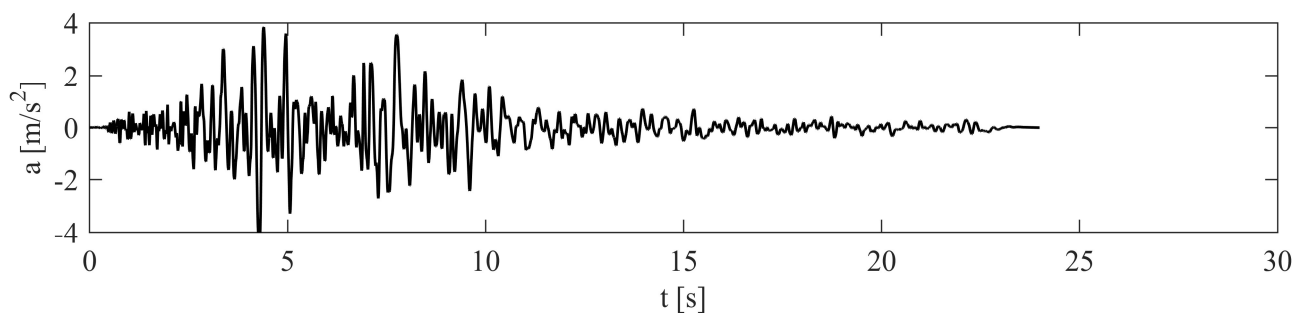


Figure A.2.18: Accelerogram 18 – Seixal.

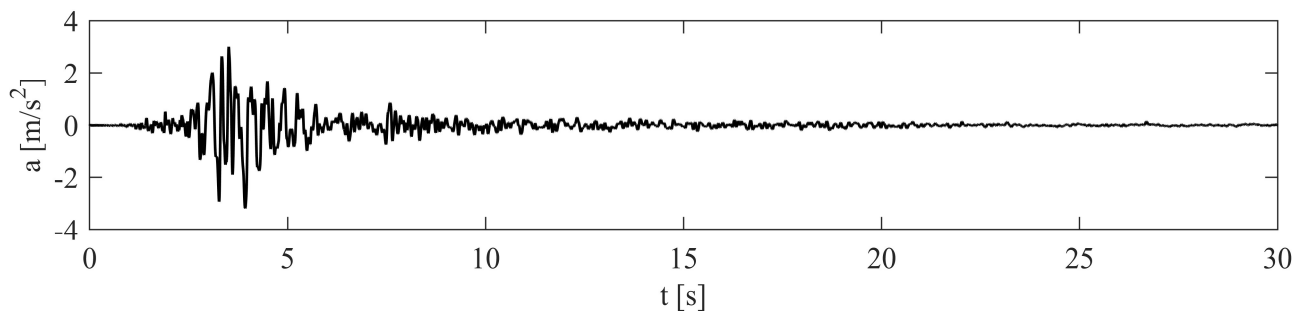


Figure A.2.19: Accelerogram 19 – Seixal.

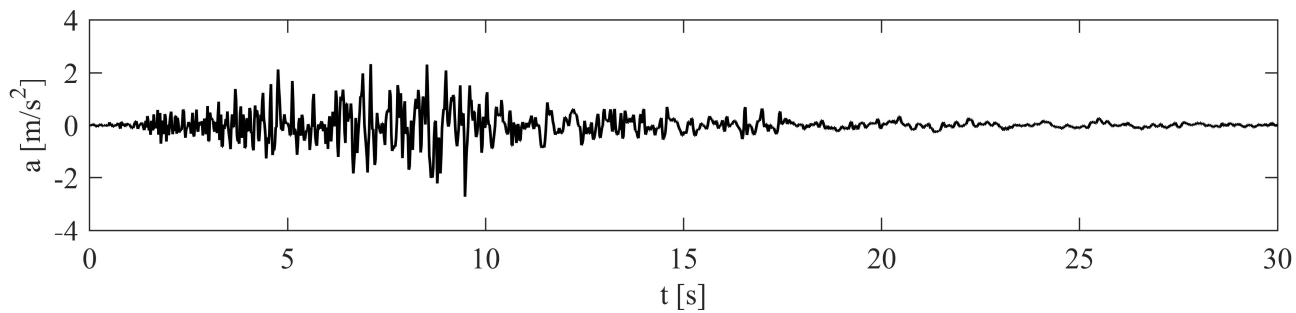


Figure A.2.20: Accelerogram 20 - Seixal

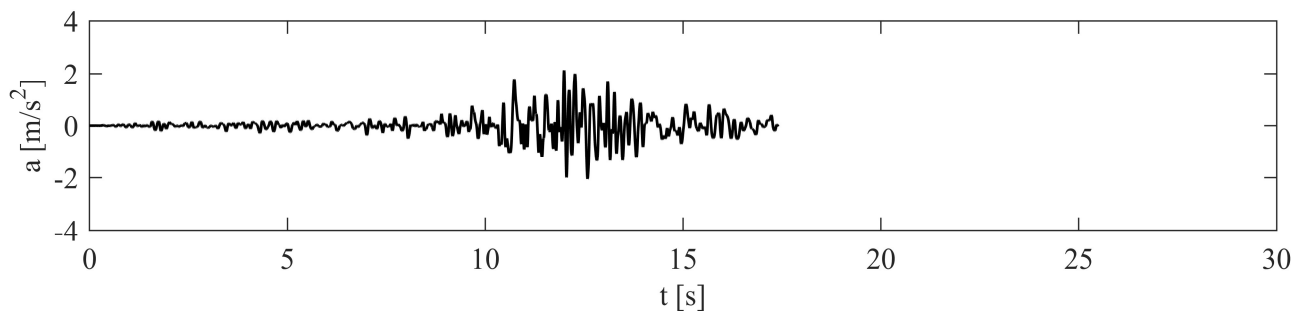


Figure A.2.21: Accelerogram 21 – Seixal.

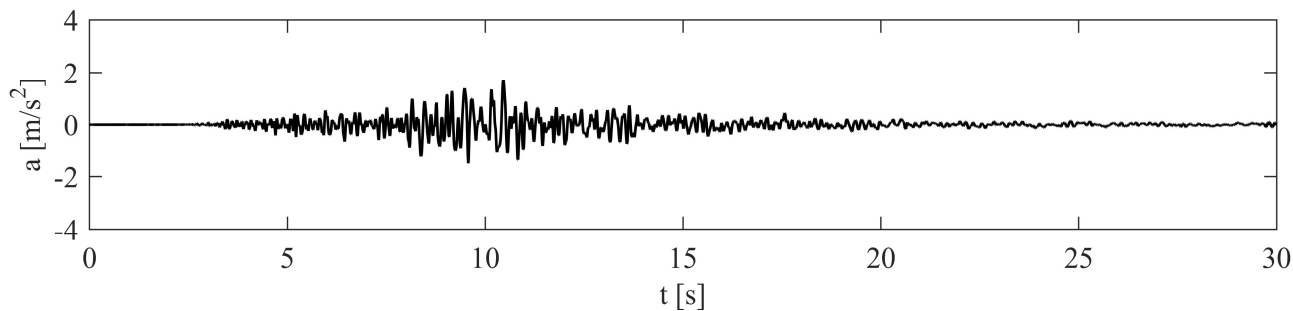


Figure A.2.22: Accelerogram 22 – Seixal.

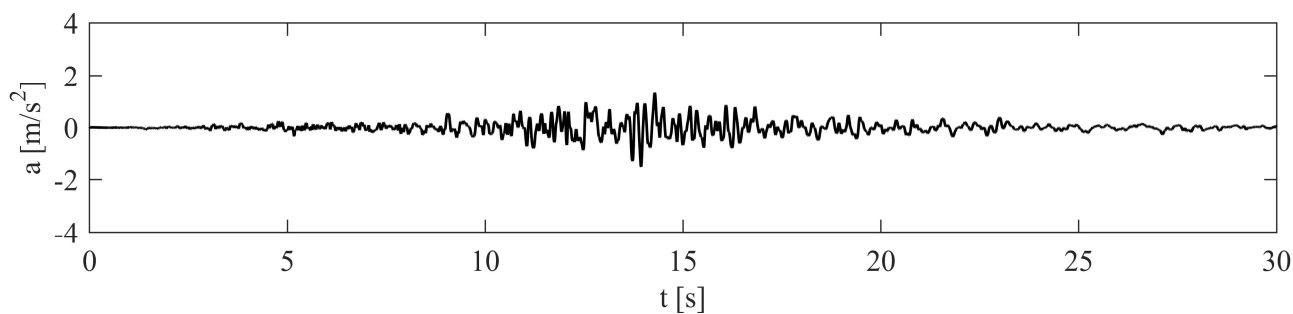


Figure A.2.23: Accelerogram 23 – Seixal.

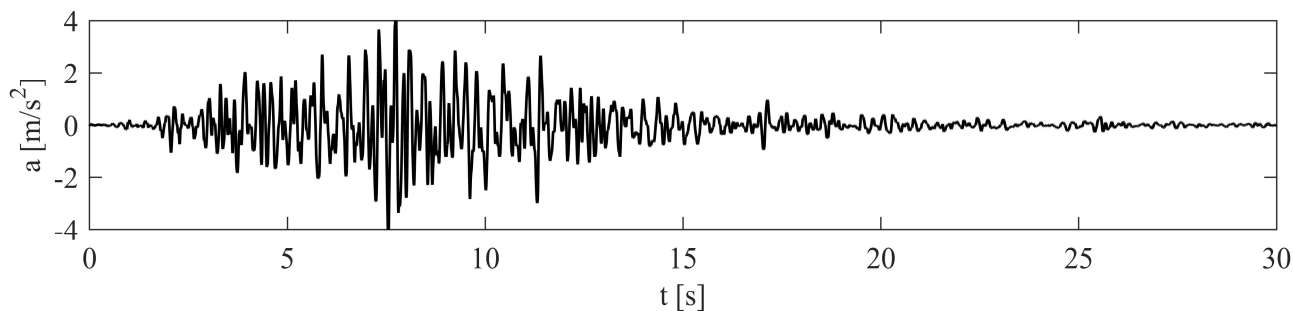


Figure A.2.24: Accelerogram 24 – Seixal.

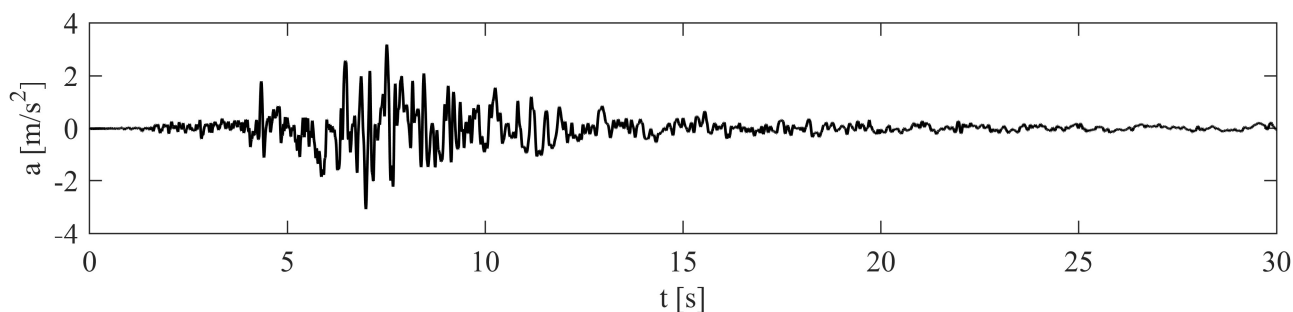


Figure A.2.25: Accelerogram 25 – Seixal.

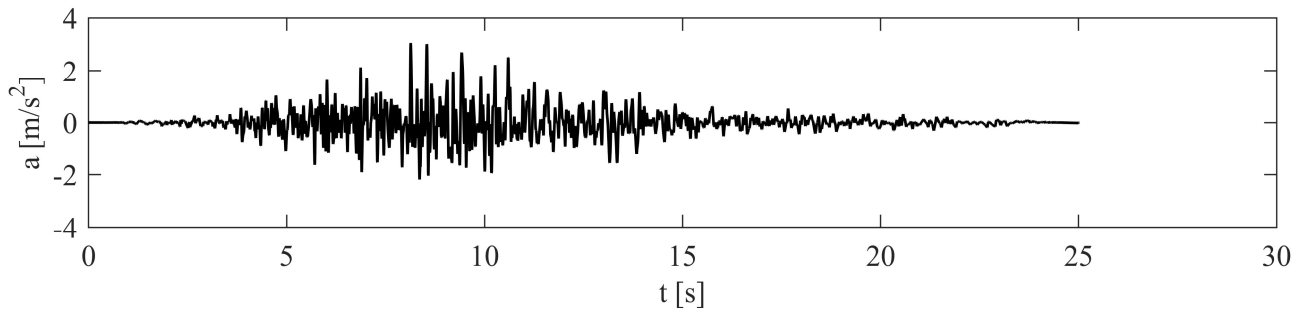


Figure A.2.26: Accelerogram 26 – Seixal.

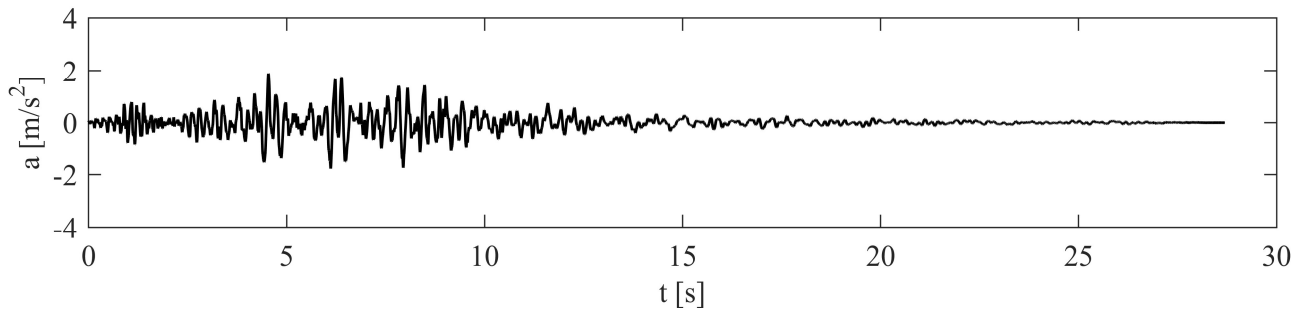


Figure A.2.27: Accelerogram 27 – Seixal.

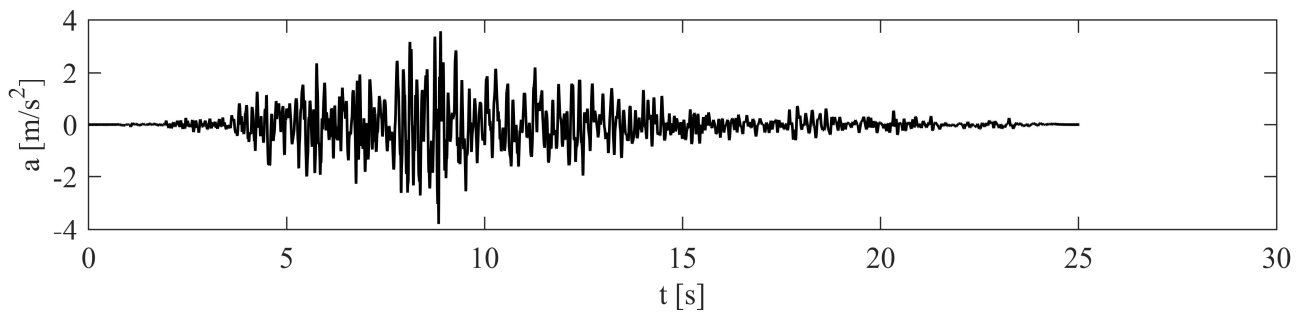


Figure A.2.28: Accelerogram 28 – Seixal.

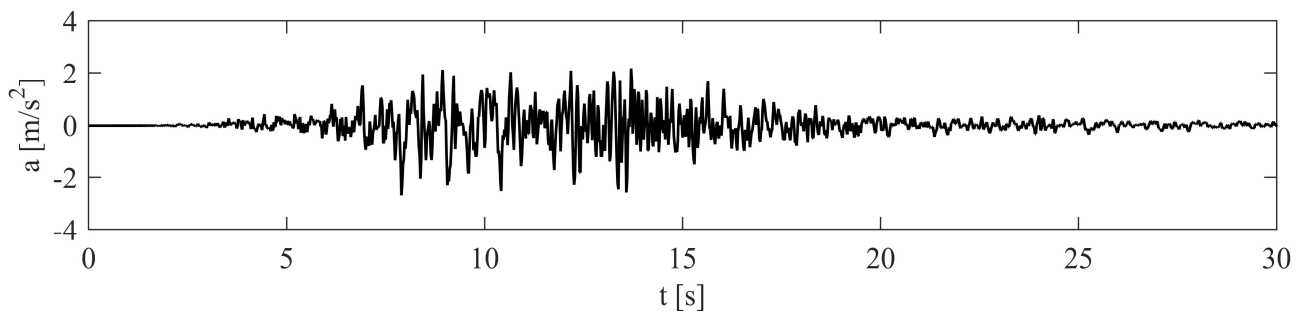


Figure A.2.29: Accelerogram 29 – Seixal.

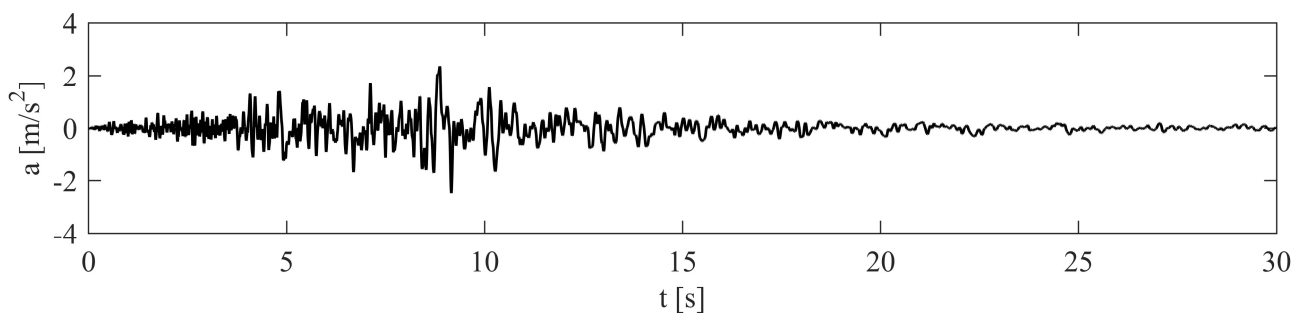


Figure A.2.30: Accelerogram 30 – Seixal.

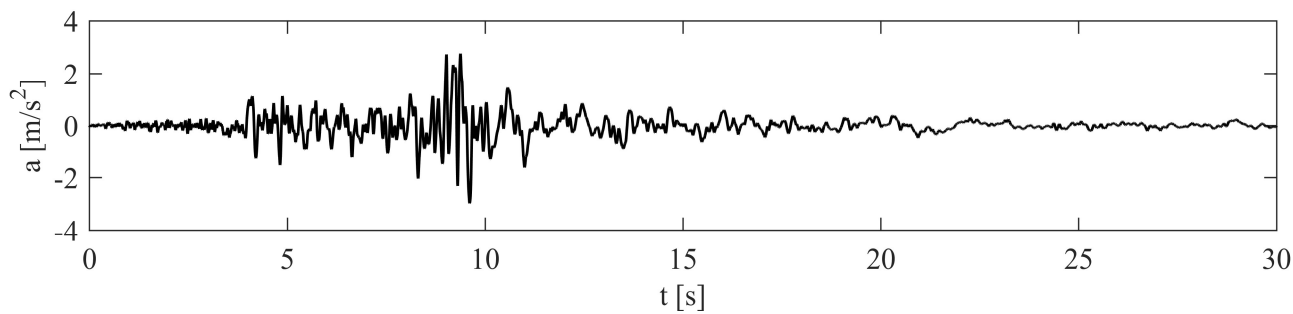


Figure A.2.31: Accelerogram 31 – Seixal.

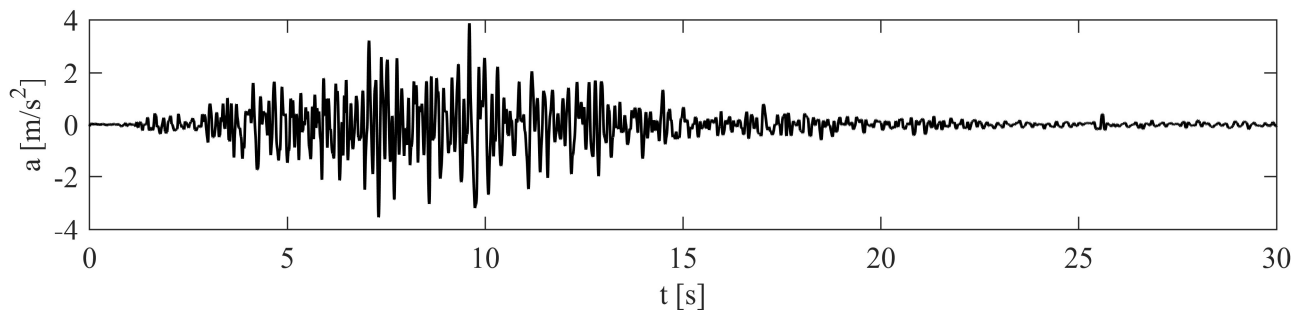


Figure A.2.32: Accelerogram 32 – Seixal.

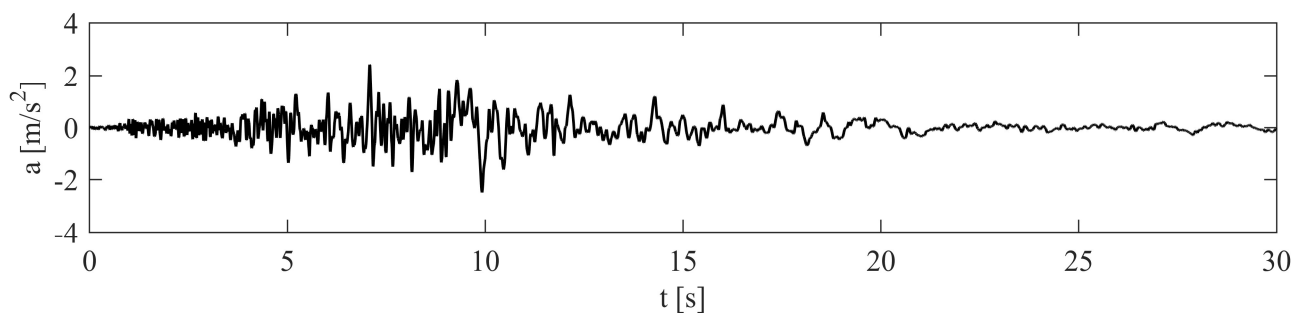


Figure A.2.33: Accelerogram 33 – Seixal.

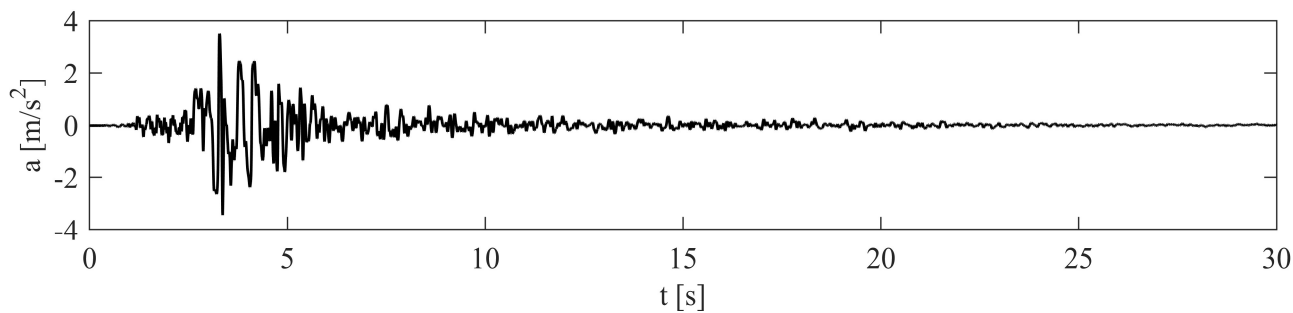


Figure A.2.34: Accelerogram 34 – Seixal.

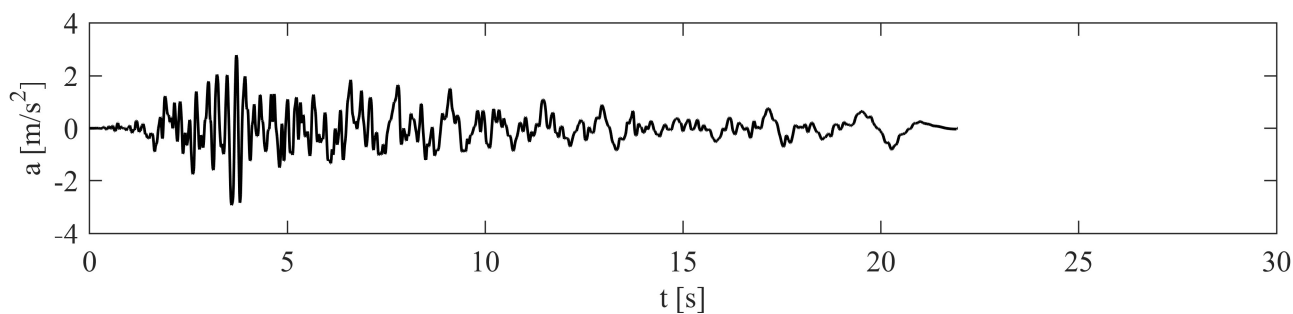


Figure A.2.35: Accelerogram 35 – Seixal.

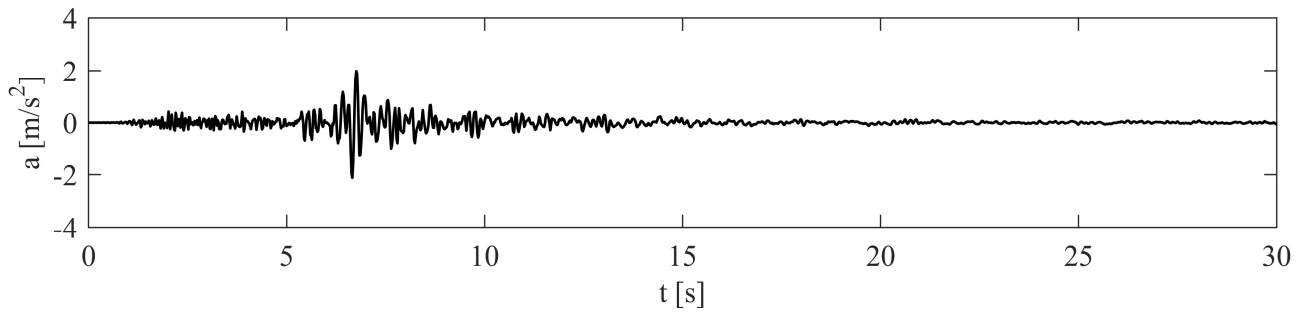


Figure A.2.36: Accelerogram 36 – Seixal.

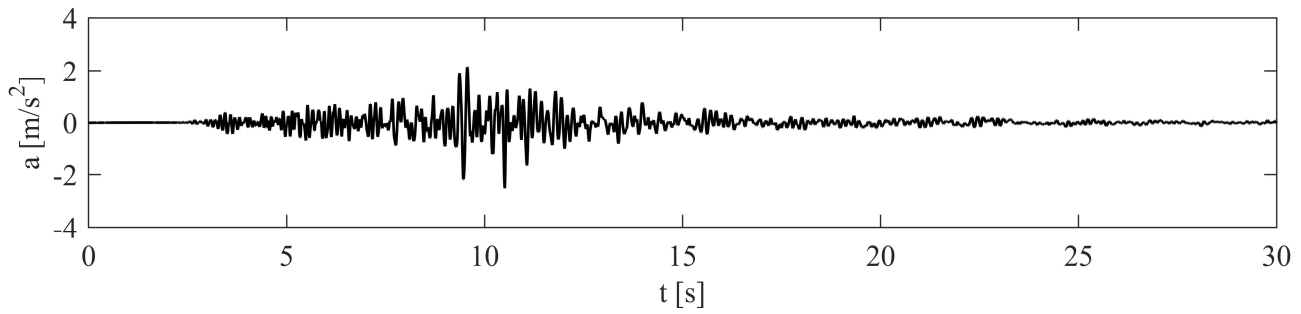


Figure A.2.37: Accelerogram 37 – Seixal.

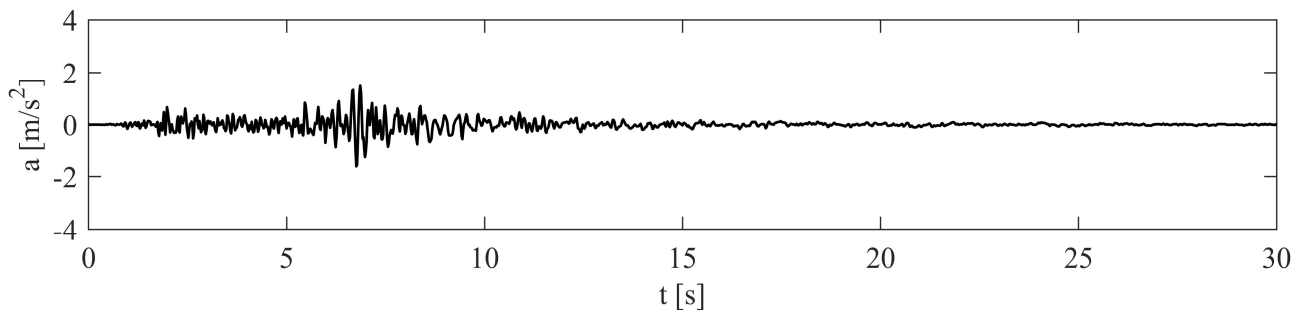


Figure A.2.38: Accelerogram 38 – Seixal.

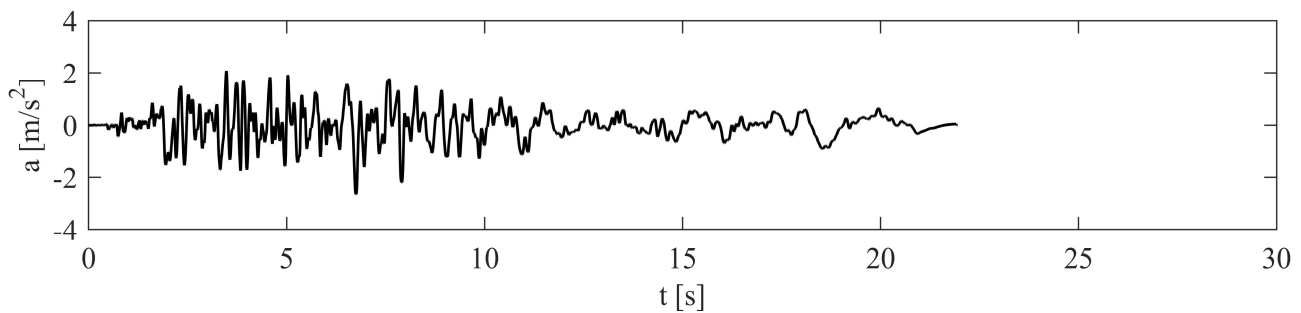


Figure A.2.39: Accelerogram 39 – Seixal.

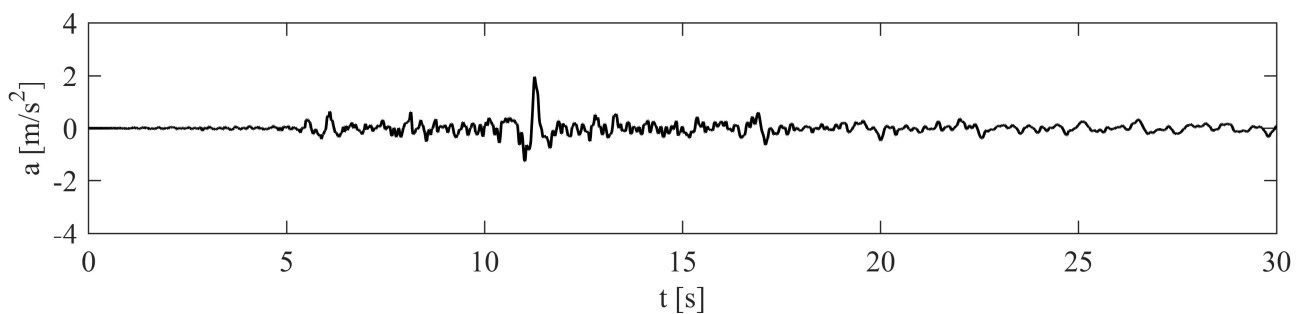


Figure A.2.40: Accelerogram 40 – Seixal.

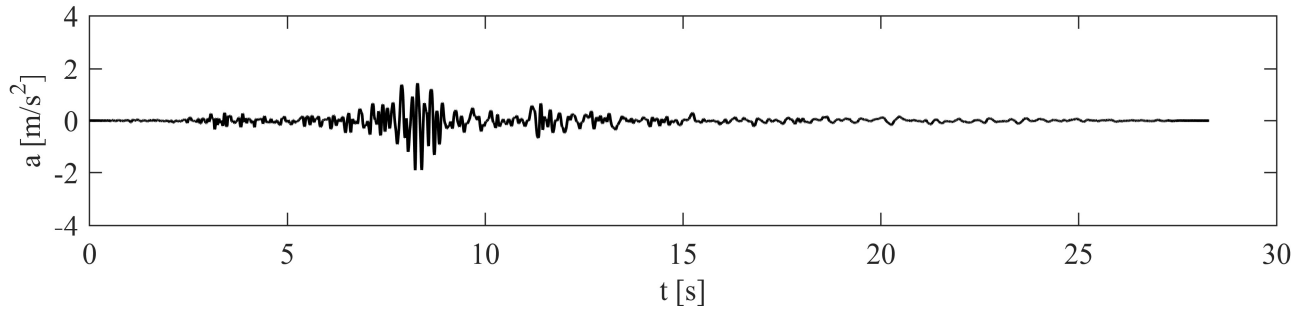


Figure A.2.41: Accelerogram 41 – Seixal.

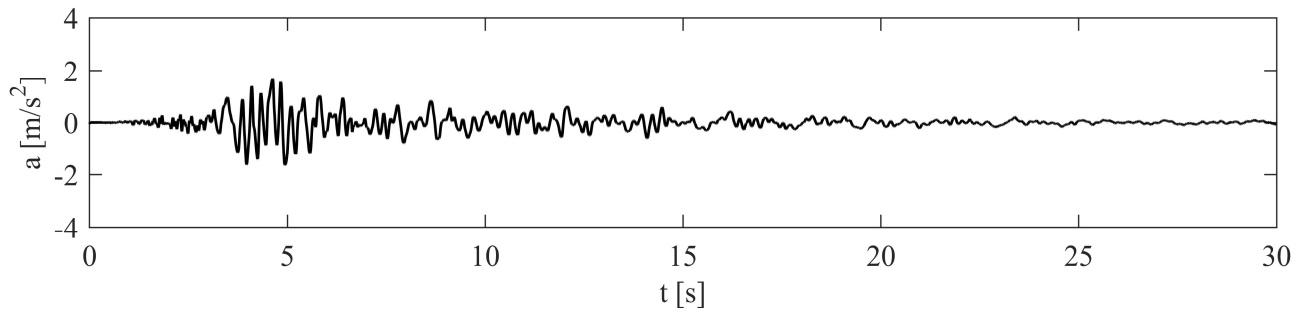


Figure A.2.42: Accelerogram 42 – Seixal.

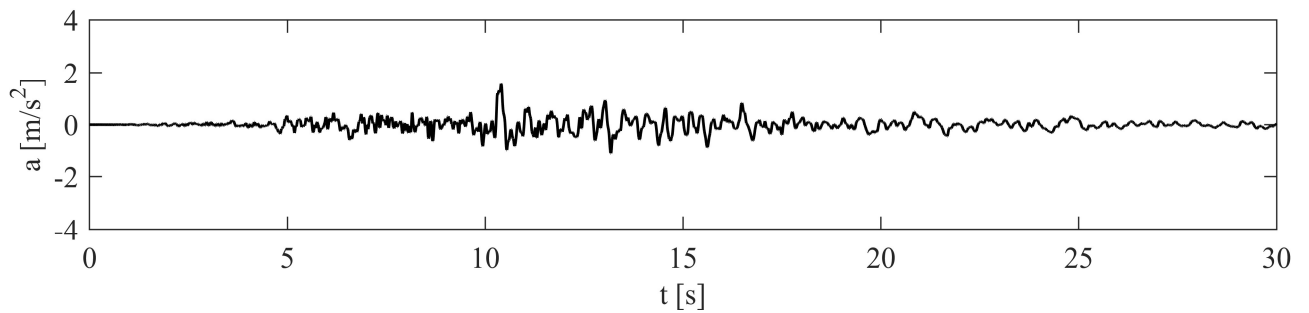


Figure A.2.43: Accelerogram 43 – Seixal.

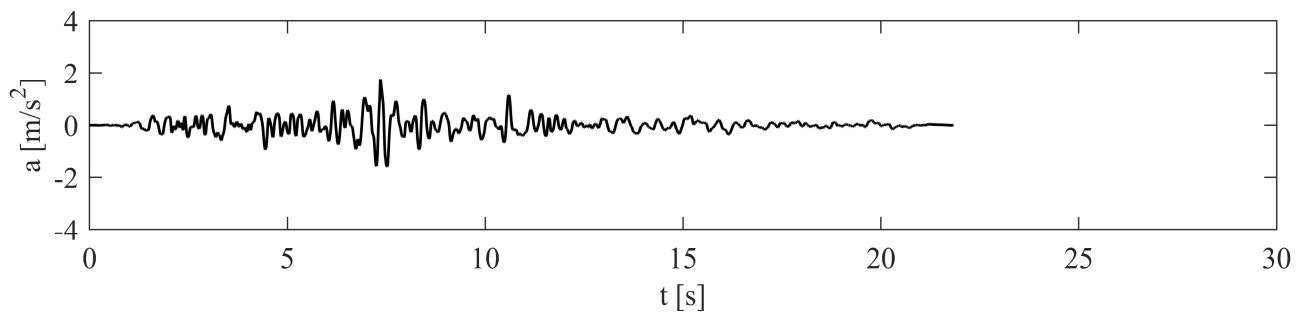


Figure A.2.44: Accelerogram 44 – Seixal.

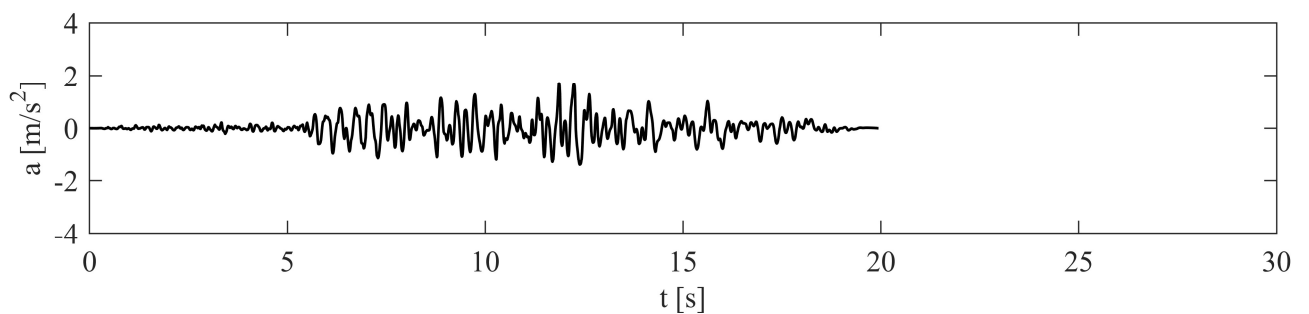


Figure A.2.45: Accelerogram 45 – Seixal.

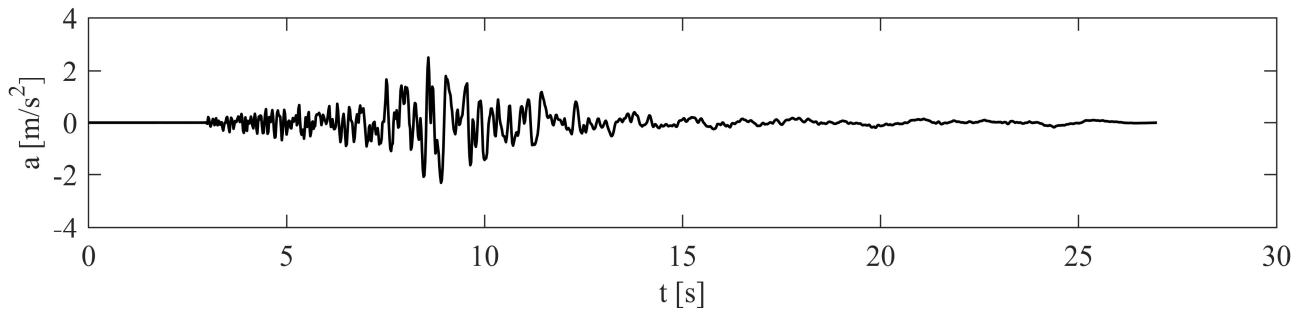


Figure A.2.46: Accelerogram 46 – Seixal.

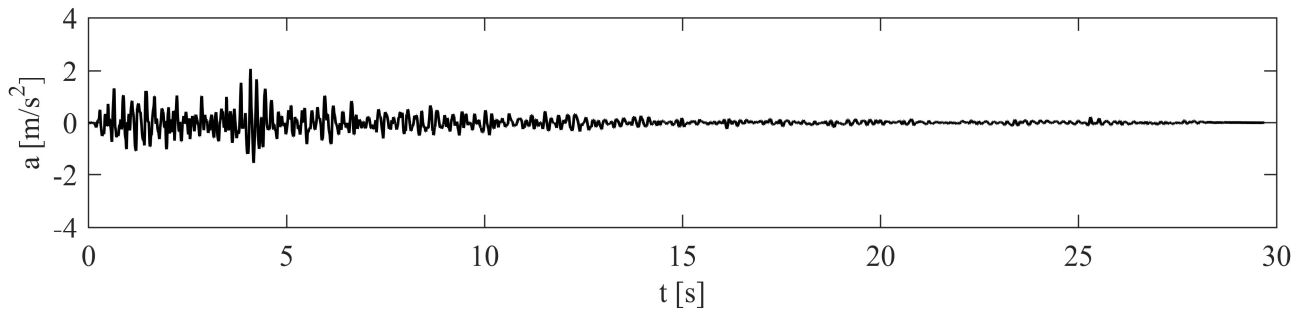


Figure A.2.47: Accelerogram 47 – Seixal.

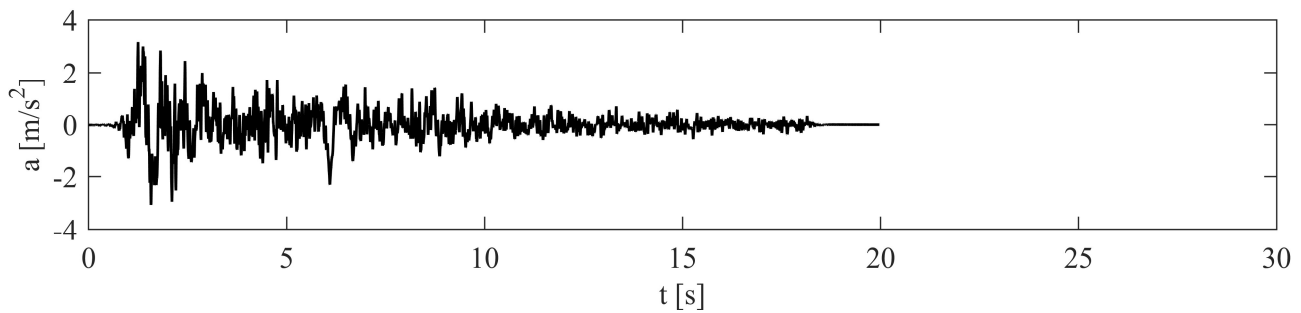


Figure A.2.48: Accelerogram 48 – Seixal.

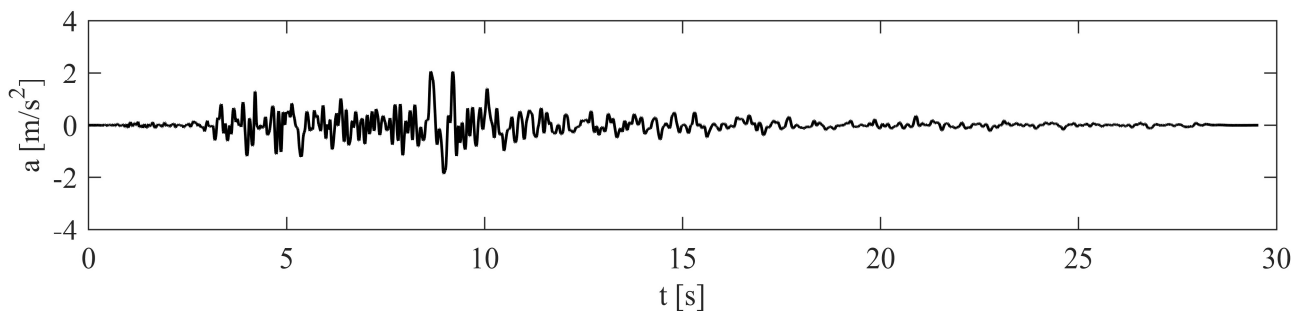


Figure A.2.49: Accelerogram 49 – Seixal.

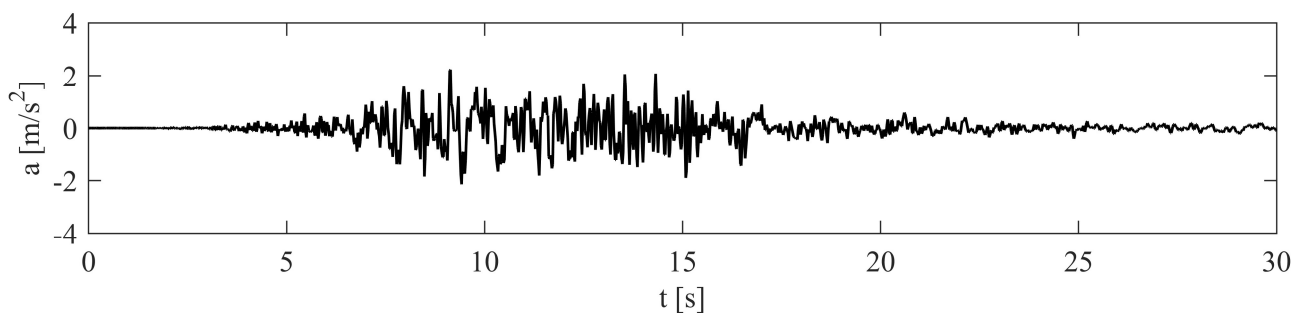


Figure A.2.50: Accelerogram 50 – Seixal.

## Appendix B

Table B.1 gives the design matrix containing the 272 simulations with the combination of the explicit and implicit variables, according to the Design of Experiment Theory and the division in blocks, referred to the Response Surface model in Section 6.2. The values of the explicit variables are reported as coded variables: masonry shear strength ( $x_1 = \tau$ ), slab elastic modulus ( $x_2 = E_1$ ), distance between external walls in  $x$ -direction ( $x_3 = d$ ). The implicit variables are given with the number of the blocks: 48 blocks ( $\delta_{\text{sis}}$ ) for the uncertainty of the seismic action and 8 blocks ( $\delta_{\text{geom}}$ ) for the uncertainty of the geometrical properties of the walls.

Table B.1: Design matrix of the Isolated Structural Unit RS model in Section 6.2.

Simulation	$x_1 = \tau$	$x_2 = E_1$	$x_3 = d$	$\delta_{\text{sis}}$	$\delta_{\text{geom}}$
1	1	1	1	1	1
2	-1	-1	1	1	1
3	-1	1	1	2	1
4	1	-1	1	2	1
5	1	1	-1	2	1
6	-1	-1	-1	2	1
7	1	-1	-1	1	1
8	-1	1	-1	1	1
9	1.33	0	0	3	1
10	-1.33	0	0	3	1
11	0	1.33	0	3	1
12	0	-1.33	0	3	1
13	0	0	0	1	1
14	0	0	0	2	1
15	0	0	0	3	1
16	0	0	1.33	3	1
17	0	0	-1.33	3	1
18	1	1	1	4	1
19	-1	-1	1	4	1
20	-1	1	1	5	1
21	1	-1	1	5	1
22	1	1	-1	5	1
23	-1	-1	-1	5	1
24	1	-1	-1	4	1
25	-1	1	-1	4	1
26	1.33	0	0	6	1
27	-1.33	0	0	6	1
28	0	1.33	0	6	1
29	0	-1.33	0	6	1
30	0	0	0	4	1
31	0	0	0	5	1
32	0	0	0	6	1
33	0	0	1.33	6	1
34	0	0	-1.33	6	1
35	1	1	1	7	2
36	-1	-1	1	7	2
37	-1	1	1	8	2
38	1	-1	1	8	2
39	1	1	-1	8	2
40	-1	-1	-1	8	2
41	1	-1	-1	7	2
42	-1	1	-1	7	2
43	1.33	0	0	9	2
44	-1.33	0	0	9	2
45	0	1.33	0	9	2
46	0	-1.33	0	9	2
47	0	0	0	7	2
48	0	0	0	8	2

## Appendix B

49	0	0	0	9	2
50	0	0	1.33	9	2
51	0	0	-1.33	9	2
52	1	1	1	10	2
53	-1	-1	1	10	2
54	-1	1	1	11	2
55	1	-1	1	11	2
56	1	1	-1	11	2
57	-1	-1	-1	11	2
58	1	-1	-1	10	2
59	-1	1	-1	10	2
60	1.33	0	0	12	2
61	-1.33	0	0	12	2
62	0	1.33	0	12	2
63	0	-1.33	0	12	2
64	0	0	0	10	2
65	0	0	0	11	2
66	0	0	0	12	2
67	0	0	1.33	12	2
68	0	0	-1.33	12	2
69	1	1	1	13	3
70	-1	-1	1	13	3
71	-1	1	1	14	3
72	1	-1	1	14	3
73	1	1	-1	14	3
74	-1	-1	-1	14	3
75	1	-1	-1	13	3
76	-1	1	-1	13	3
77	1.33	0	0	15	3
78	-1.33	0	0	15	3
79	0	1.33	0	15	3
80	0	-1.33	0	15	3
81	0	0	0	13	3
82	0	0	0	14	3
83	0	0	0	15	3
84	0	0	1.33	15	3
85	0	0	-1.33	15	3
86	1	1	1	16	3
87	-1	-1	1	16	3
88	-1	1	1	17	3
89	1	-1	1	17	3
90	1	1	-1	17	3
91	-1	-1	-1	17	3
92	1	-1	-1	16	3
93	-1	1	-1	16	3
94	1.33	0	0	18	3
95	-1.33	0	0	18	3
96	0	1.33	0	18	3
97	0	-1.33	0	18	3
98	0	0	0	16	3
99	0	0	0	17	3
100	0	0	0	18	3
101	0	0	1.33	18	3
102	0	0	-1.33	18	3
103	1	1	1	19	4
104	-1	-1	1	19	4
105	-1	1	1	20	4
106	1	-1	1	20	4
107	1	1	-1	20	4
108	-1	-1	-1	20	4
109	1	-1	-1	19	4
110	-1	1	-1	19	4
111	1.33	0	0	21	4
112	-1.33	0	0	21	4
113	0	1.33	0	21	4
114	0	-1.33	0	21	4
115	0	0	0	19	4
116	0	0	0	20	4
117	0	0	0	21	4
118	0	0	1.33	21	4
119	0	0	-1.33	21	4
120	1	1	1	22	4
121	-1	-1	1	22	4
122	-1	1	1	23	4
123	1	-1	1	23	4
124	1	1	-1	23	4

125	-1	-1	-1	23	4
126	1	-1	-1	22	4
127	-1	1	-1	22	4
128	1.33	0	0	24	4
129	-1.33	0	0	24	4
130	0	1.33	0	24	4
131	0	-1.33	0	24	4
132	0	0	0	22	4
133	0	0	0	23	4
134	0	0	0	24	4
135	0	0	1.33	24	4
136	0	0	-1.33	24	4
137	1	1	1	25	5
138	-1	-1	1	25	5
139	-1	1	1	26	5
140	1	-1	1	26	5
141	1	1	-1	26	5
142	-1	-1	-1	26	5
143	1	-1	-1	25	5
144	-1	1	-1	25	5
145	1.33	0	0	27	5
146	-1.33	0	0	27	5
147	0	1.33	0	27	5
148	0	-1.33	0	27	5
149	0	0	0	25	5
150	0	0	0	26	5
151	0	0	0	27	5
152	0	0	1.33	27	5
153	0	0	-1.33	27	5
154	1	1	1	28	5
155	-1	-1	1	28	5
156	-1	1	1	29	5
157	1	-1	1	29	5
158	1	1	-1	29	5
159	-1	-1	-1	29	5
160	1	-1	-1	28	5
161	-1	1	-1	28	5
162	1.33	0	0	30	5
163	-1.33	0	0	30	5
164	0	1.33	0	30	5
165	0	-1.33	0	30	5
166	0	0	0	28	5
167	0	0	0	29	5
168	0	0	0	30	5
169	0	0	1.33	30	5
170	0	0	-1.33	30	5
171	1	1	1	31	6
172	-1	-1	1	31	6
173	-1	1	1	32	6
174	1	-1	1	32	6
175	1	1	-1	32	6
176	-1	-1	-1	32	6
177	1	-1	-1	31	6
178	-1	1	-1	31	6
179	1.33	0	0	33	6
180	-1.33	0	0	33	6
181	0	1.33	0	33	6
182	0	-1.33	0	33	6
183	0	0	0	31	6
184	0	0	0	32	6
185	0	0	0	33	6
186	0	0	1.33	33	6
187	0	0	-1.33	33	6
188	1	1	1	34	6
189	-1	-1	1	34	6
190	-1	1	1	35	6
191	1	-1	1	35	6
192	1	1	-1	35	6
193	-1	-1	-1	35	6
194	1	-1	-1	34	6
195	-1	1	-1	34	6
196	1.33	0	0	36	6
197	-1.33	0	0	36	6
198	0	1.33	0	36	6
199	0	-1.33	0	36	6
200	0	0	0	34	6

## Appendix B

201	0	0	0	35	6
202	0	0	0	36	6
203	0	0	1.33	36	6
204	0	0	-1.33	36	6
205	1	1	1	37	7
206	-1	-1	1	37	7
207	-1	1	1	38	7
208	1	-1	1	38	7
209	1	1	-1	38	7
210	-1	-1	-1	38	7
211	1	-1	-1	37	7
212	-1	1	-1	37	7
213	1.33	0	0	39	7
214	-1.33	0	0	39	7
215	0	1.33	0	39	7
216	0	-1.33	0	39	7
217	0	0	0	37	7
218	0	0	0	38	7
219	0	0	0	39	7
220	0	0	1.33	39	7
221	0	0	-1.33	39	7
222	1	1	1	40	7
223	-1	-1	1	40	7
224	-1	1	1	41	7
225	1	-1	1	41	7
226	1	1	-1	41	7
227	-1	-1	-1	41	7
228	1	-1	-1	40	7
229	-1	1	-1	40	7
230	1.33	0	0	42	7
231	-1.33	0	0	42	7
232	0	1.33	0	42	7
233	0	-1.33	0	42	7
234	0	0	0	40	7
235	0	0	0	41	7
236	0	0	0	42	7
237	0	0	1.33	42	7
238	0	0	-1.33	42	7
239	1	1	1	43	8
240	-1	-1	1	43	8
241	-1	1	1	44	8
242	1	-1	1	44	8
243	1	1	-1	44	8
244	-1	-1	-1	44	8
245	1	-1	-1	43	8
246	-1	1	-1	43	8
247	1.33	0	0	45	8
248	-1.33	0	0	45	8
249	0	1.33	0	45	8
250	0	-1.33	0	45	8
251	0	0	0	43	8
252	0	0	0	44	8
253	0	0	0	45	8
254	0	0	1.33	45	8
255	0	0	-1.33	45	8
256	1	1	1	46	8
257	-1	-1	1	46	8
258	-1	1	1	47	8
259	1	-1	1	47	8
260	1	1	-1	47	8
261	-1	-1	-1	47	8
262	1	-1	-1	46	8
263	-1	1	-1	46	8
264	1.33	0	0	48	8
265	-1.33	0	0	48	8
266	0	1.33	0	48	8
267	0	-1.33	0	48	8
268	0	0	0	46	8
269	0	0	0	47	8
270	0	0	0	48	8
271	0	0	1.33	48	8
272	0	0	-1.33	48	8

Table B.2 gives the design matrix containing the 384 simulations with the combination of the explicit and implicit variables, according to the selection of the values of the explicit variable and the division in blocks, referred to the Response Surface model in Section 6.3. The values of the explicit variable  $s$  are given with the real assumed values ( $X_1 = s$ ); the implicit variable  $\delta_{\text{sis}}$  is given with the number of the blocks: 48 blocks ( $\delta_{\text{sis}}$ ) for the uncertainty of the seismic action.

Table B.2: Design matrix of the Response Surface models in Section 6.3.

Simulation	$X_1 = s$	$\delta_{\text{sis}}$
1	0.50	1
2	0.40	1
3	0.375	1
4	0.30	1
5	0.25	1
6	0.20	1
7	0.15	1
8	0.125	1
9	0.50	2
10	0.40	2
11	0.375	2
12	0.30	2
13	0.25	2
14	0.20	2
15	0.15	2
16	0.125	2
17	0.50	3
18	0.40	3
19	0.375	3
20	0.30	3
21	0.25	3
22	0.20	3
23	0.15	3
24	0.125	3
25	0.50	4
26	0.40	4
27	0.375	4
28	0.30	4
29	0.25	4
30	0.20	4
31	0.15	4
32	0.125	4
33	0.50	5
34	0.40	5
35	0.375	5
36	0.30	5
37	0.25	5
38	0.20	5
39	0.15	5
40	0.125	5
41	0.50	6
42	0.40	6
43	0.375	6
44	0.30	6
45	0.25	6
46	0.20	6
47	0.15	6
48	0.125	6
49	0.50	7
50	0.40	7
51	0.375	7
52	0.30	7
53	0.25	7
54	0.20	7
55	0.15	7
56	0.125	7

## Appendix B

57	0.50	8
58	0.40	8
59	0.375	8
60	0.30	8
61	0.25	8
62	0.20	8
63	0.15	8
64	0.125	8
65	0.50	9
66	0.40	9
67	0.375	9
68	0.30	9
69	0.25	9
70	0.20	9
71	0.15	9
72	0.125	9
73	0.50	10
74	0.40	10
75	0.375	10
76	0.30	10
77	0.25	10
78	0.20	10
79	0.15	10
80	0.125	10
81	0.50	11
82	0.40	11
83	0.375	11
84	0.30	11
85	0.25	11
86	0.20	11
87	0.15	11
88	0.125	11
89	0.50	12
90	0.40	12
91	0.375	12
92	0.30	12
93	0.25	12
94	0.20	12
95	0.15	12
96	0.125	12
97	0.50	13
98	0.40	13
99	0.375	13
100	0.30	13
101	0.25	13
102	0.20	13
103	0.15	13
104	0.125	13
105	0.50	14
106	0.40	14
107	0.375	14
108	0.30	14
109	0.25	14
110	0.20	14
111	0.15	14
112	0.125	14
113	0.50	15
114	0.40	15
115	0.375	15
116	0.30	15
117	0.25	15
118	0.20	15
119	0.15	15
120	0.125	15
121	0.50	16
122	0.40	16
123	0.375	16
124	0.30	16
125	0.25	16
126	0.20	16
127	0.15	16
128	0.125	16
129	0.50	17
130	0.40	17
131	0.375	17
132	0.30	17

---

133	0.25	17
134	0.20	17
135	0.15	17
136	0.125	17
<hr/>		
137	0.50	18
138	0.40	18
139	0.375	18
140	0.30	18
141	0.25	18
142	0.20	18
143	0.15	18
144	0.125	18
<hr/>		
145	0.50	19
146	0.40	19
147	0.375	19
148	0.30	19
149	0.25	19
150	0.20	19
151	0.15	19
152	0.125	19
<hr/>		
153	0.50	20
154	0.40	20
155	0.375	20
156	0.30	20
157	0.25	20
158	0.20	20
159	0.15	20
160	0.125	20
<hr/>		
161	0.50	21
162	0.40	21
163	0.375	21
164	0.30	21
165	0.25	21
166	0.20	21
167	0.15	21
168	0.125	21
<hr/>		
169	0.50	22
170	0.40	22
171	0.375	22
172	0.30	22
173	0.25	22
174	0.20	22
175	0.15	22
176	0.125	22
<hr/>		
177	0.50	23
178	0.40	23
179	0.375	23
180	0.30	23
181	0.25	23
182	0.20	23
183	0.15	23
184	0.125	23
<hr/>		
185	0.50	24
186	0.40	24
187	0.375	24
188	0.30	24
189	0.25	24
190	0.20	24
191	0.15	24
192	0.125	24
<hr/>		
193	0.50	25
194	0.40	25
195	0.375	25
196	0.30	25
197	0.25	25
198	0.20	25
199	0.15	25
200	0.125	25
<hr/>		
201	0.50	26
202	0.40	26
203	0.375	26
204	0.30	26
205	0.25	26
206	0.20	26
207	0.15	26
208	0.125	26

## Appendix B

209	0.50	27
210	0.40	27
211	0.375	27
212	0.30	27
213	0.25	27
214	0.20	27
215	0.15	27
216	0.125	27
217	0.50	28
218	0.40	28
219	0.375	28
220	0.30	28
221	0.25	28
222	0.20	28
223	0.15	28
224	0.125	28
225	0.50	29
226	0.40	29
227	0.375	29
228	0.30	29
229	0.25	29
230	0.20	29
231	0.15	29
232	0.125	29
233	0.50	30
234	0.40	30
235	0.375	30
236	0.30	30
237	0.25	30
238	0.20	30
239	0.15	30
240	0.125	30
241	0.50	31
242	0.40	31
243	0.375	31
244	0.30	31
245	0.25	31
246	0.20	31
247	0.15	31
248	0.125	31
249	0.50	32
250	0.40	32
251	0.375	32
252	0.30	32
253	0.25	32
254	0.20	32
255	0.15	32
256	0.125	32
257	0.50	33
258	0.40	33
259	0.375	33
260	0.30	33
261	0.25	33
262	0.20	33
263	0.15	33
264	0.125	33
265	0.50	34
266	0.40	34
267	0.375	34
268	0.30	34
269	0.25	34
270	0.20	34
271	0.15	34
272	0.125	34
273	0.50	35
274	0.40	35
275	0.375	35
276	0.30	35
277	0.25	35
278	0.20	35
279	0.15	35
280	0.125	35
281	0.50	36
282	0.40	36
283	0.375	36
284	0.30	36

---

285	0.25	36
286	0.20	36
287	0.15	36
288	0.125	36
<hr/>		
289	0.50	37
290	0.40	37
291	0.375	37
292	0.30	37
293	0.25	37
294	0.20	37
295	0.15	37
296	0.125	37
<hr/>		
297	0.50	38
298	0.40	38
299	0.375	38
300	0.30	38
301	0.25	38
302	0.20	38
303	0.15	38
304	0.125	38
<hr/>		
305	0.50	39
306	0.40	39
307	0.375	39
308	0.30	39
309	0.25	39
310	0.20	39
311	0.15	39
312	0.125	39
<hr/>		
313	0.50	40
314	0.40	40
315	0.375	40
316	0.30	40
317	0.25	40
318	0.20	40
319	0.15	40
320	0.125	40
<hr/>		
321	0.50	41
322	0.40	41
323	0.375	41
324	0.30	41
325	0.25	41
326	0.20	41
327	0.15	41
328	0.125	41
<hr/>		
329	0.50	42
330	0.40	42
331	0.375	42
332	0.30	42
333	0.25	42
334	0.20	42
335	0.15	42
336	0.125	42
<hr/>		
337	0.50	43
338	0.40	43
339	0.375	43
340	0.30	43
341	0.25	43
342	0.20	43
343	0.15	43
344	0.125	43
<hr/>		
345	0.50	44
346	0.40	44
347	0.375	44
348	0.30	44
349	0.25	44
350	0.20	44
351	0.15	44
352	0.125	44
<hr/>		
353	0.50	45
354	0.40	45
355	0.375	45
356	0.30	45
357	0.25	45
358	0.20	45
359	0.15	45
360	0.125	45

## Appendix B

---

361	0.50	46
362	0.40	46
363	0.375	46
364	0.30	46
365	0.25	46
366	0.20	46
367	0.15	46
368	0.125	46
369	0.50	47
370	0.40	47
371	0.375	47
372	0.30	47
373	0.25	47
374	0.20	47
375	0.15	47
376	0.125	47
377	0.50	48
378	0.40	48
379	0.375	48
380	0.30	48
381	0.25	48
382	0.20	48
383	0.15	48
384	0.125	48

---

Table B.3 gives the design matrix containing the 176 simulations with the combination of the explicit and implicit variables, according to the Design of Experiment Theory and the division in blocks, referred to the Response Surface model in Section 6.4. The values of the explicit variables are reported as coded variables: masonry shear strength ( $x_1 = \tau$ ) and distance between external walls in  $x$ -direction ( $x_3 = d$ ). The implicit variables are given with the number of the blocks: 48 blocks ( $\delta_{\text{sis}}$ ) for the uncertainty of the seismic action, 40 blocks ( $\delta_d$ ) for the uncertainty of the distance between the walls in  $x$ -direction and 40 blocks ( $\delta_s$ ) for the uncertainty of the thickness of the walls.

Table B.3: Design matrix of the Response Surface models in Section 6.3.

Simulation	$x_1 = \tau$	$x_2 = d$	$\delta_{\text{sis}}$	$\delta_d$	$\delta_s$
1	1	1	1	4	4
2	-1	1	2	4	4
3	1	-1	2	2	2
4	-1	-1	1	2	2
5	0	0	1	3	3
6	0	0	2	3	3
7	0	0	3	3	3
8	1.33	0	3	3	3
9	-1.33	0	3	3	3
10	0	1.33	3	5	5
11	0	-1.33	3	1	1
12	1	1	4	4	4
13	-1	1	5	4	4
14	1	-1	5	2	2
15	-1	-1	4	2	2
16	0	0	4	3	3
17	0	0	5	3	3
18	0	0	6	3	3
19	1.33	0	6	3	3
20	-1.33	0	6	3	3
21	0	1.33	6	5	5
22	0	-1.33	6	1	1
23	1	1	7	9	9
24	-1	1	8	9	9
25	1	-1	8	7	7
26	-1	-1	7	7	7
27	0	0	7	8	8
28	0	0	8	8	8
29	0	0	9	8	8
30	1.33	0	9	8	8
31	-1.33	0	9	8	8
32	0	1.33	9	10	10
33	0	-1.33	9	6	6
34	1	1	10	9	9
35	-1	1	11	9	9
36	1	-1	11	7	7
37	-1	-1	10	7	7
38	0	0	10	8	8
39	0	0	11	8	8
40	0	0	12	8	8
41	1.33	0	12	8	8
42	-1.33	0	12	8	8
43	0	1.33	12	10	10
44	0	-1.33	12	6	6
45	1	1	13	14	14
46	-1	1	14	14	14
47	1	-1	14	12	12
48	-1	-1	13	12	12
49	0	0	13	13	13
50	0	0	14	13	13
51	0	0	15	13	13

## Appendix B

52	1.33	0	15	13	13
53	-1.33	0	15	13	13
54	0	1.33	15	15	15
55	0	-1.33	15	11	11
56	1	1	16	14	14
57	-1	1	17	14	14
58	1	-1	17	12	12
59	-1	-1	16	12	12
60	0	0	16	13	13
61	0	0	17	13	13
62	0	0	18	13	13
63	1.33	0	18	13	13
64	-1.33	0	18	13	13
65	0	1.33	18	15	15
66	0	-1.33	18	11	11
67	1	1	19	19	19
68	-1	1	20	19	19
69	1	-1	20	17	17
70	-1	-1	19	17	17
71	0	0	19	18	18
72	0	0	20	18	18
73	0	0	21	18	18
74	1.33	0	21	18	18
75	-1.33	0	21	18	18
76	0	1.33	21	20	20
77	0	-1.33	21	16	16
78	1	1	22	19	19
79	-1	1	23	19	19
80	1	-1	23	17	17
81	-1	-1	22	17	17
82	0	0	22	18	18
83	0	0	23	18	18
84	0	0	24	18	18
85	1.33	0	24	18	18
86	-1.33	0	24	18	18
87	0	1.33	24	20	20
88	0	-1.33	24	16	16
89	1	1	25	24	24
90	-1	1	26	24	24
91	1	-1	26	22	22
92	-1	-1	25	22	22
93	0	0	25	23	23
94	0	0	26	23	23
95	0	0	27	23	23
96	1.33	0	27	23	23
97	-1.33	0	27	23	23
98	0	1.33	27	25	25
99	0	-1.33	27	21	21
100	1	1	28	24	24
101	-1	1	29	24	24
102	1	-1	29	22	22
103	-1	-1	28	22	22
104	0	0	28	23	23
105	0	0	29	23	23
106	0	0	30	23	23
107	1.33	0	30	23	23
108	-1.33	0	30	23	23
109	0	1.33	30	25	25
110	0	-1.33	30	21	21
111	1	1	31	29	29
112	-1	1	32	29	29
113	1	-1	32	27	27
114	-1	-1	31	27	27
115	0	0	31	28	28
116	0	0	32	28	28
117	0	0	33	28	28
118	1.33	0	33	28	28
119	-1.33	0	33	28	28
120	0	1.33	33	30	30
121	0	-1.33	33	26	26
122	1	1	34	29	29
123	-1	1	35	29	29
124	1	-1	35	27	27
125	-1	-1	34	27	27
126	0	0	34	28	28
127	0	0	35	28	28

128	0	0	36	28	28
129	1.33	0	36	28	28
130	-1.33	0	36	28	28
131	0	1.33	36	30	30
132	0	-1.33	36	26	26
133	1	1	37	34	34
134	-1	1	38	34	34
135	1	-1	38	32	32
136	-1	-1	37	32	32
137	0	0	37	33	33
138	0	0	38	33	33
139	0	0	39	33	33
140	1.33	0	39	33	33
141	-1.33	0	39	33	33
142	0	1.33	39	35	35
143	0	-1.33	39	31	31
144	1	1	40	34	34
145	-1	1	41	34	34
146	1	-1	41	32	32
147	-1	-1	40	32	32
148	0	0	40	33	33
149	0	0	41	33	33
150	0	0	42	33	33
151	1.33	0	42	33	33
152	-1.33	0	42	33	33
153	0	1.33	42	35	35
154	0	-1.33	42	31	31
155	1	1	43	39	39
156	-1	1	44	39	39
157	1	-1	44	37	37
158	-1	-1	43	37	37
159	0	0	43	38	38
160	0	0	44	38	38
161	0	0	45	38	38
162	1.33	0	45	38	38
163	-1.33	0	45	38	38
164	0	1.33	45	40	40
165	0	-1.33	45	36	36
166	1	1	46	39	39
167	-1	1	47	39	39
168	1	-1	47	37	37
169	-1	-1	46	37	37
170	0	0	46	38	38
171	0	0	47	38	38
172	0	0	48	38	38
173	1.33	0	48	38	38
174	-1.33	0	48	38	38
175	0	1.33	48	40	40
176	0	-1.33	48	36	36



# Appendix C

This appendix gives the results related to the analyses in the buildings sited in Seixal, object of the Chapter 7, considering the negative actions ( $-F_x$  and  $-F_y$ ) of the seismic action.

## Push-over curves

$-F_x$

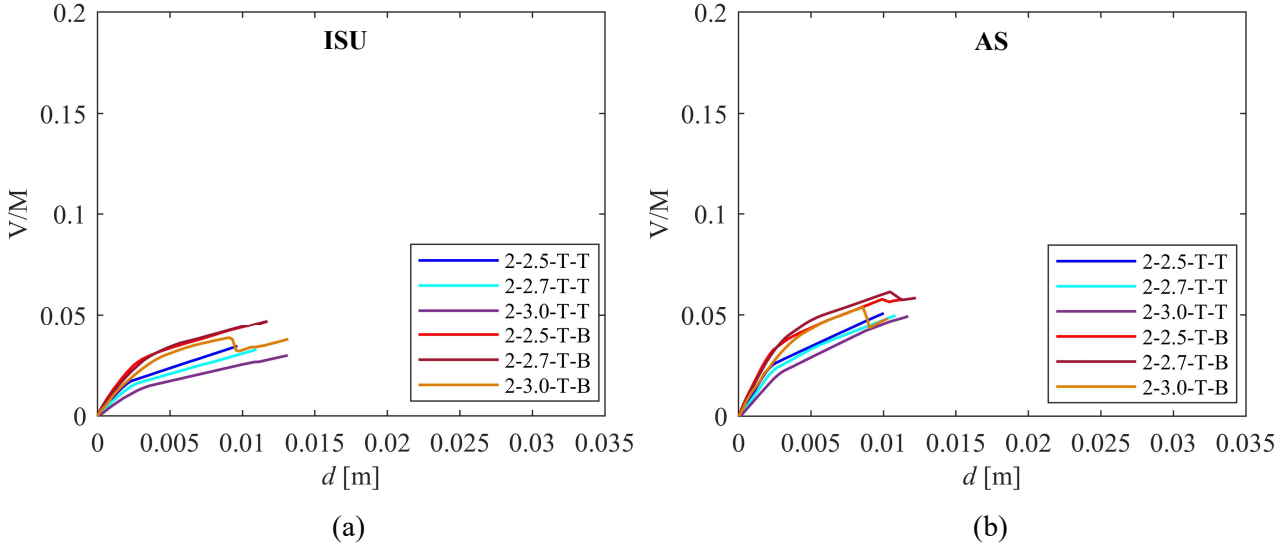


Figure C.1:  $x$ -direction ( $-F_x$ ) push-over curves of the buildings with 2 floors and timber slabs: (a) Isolated structural units and (b) Aggregate structures.

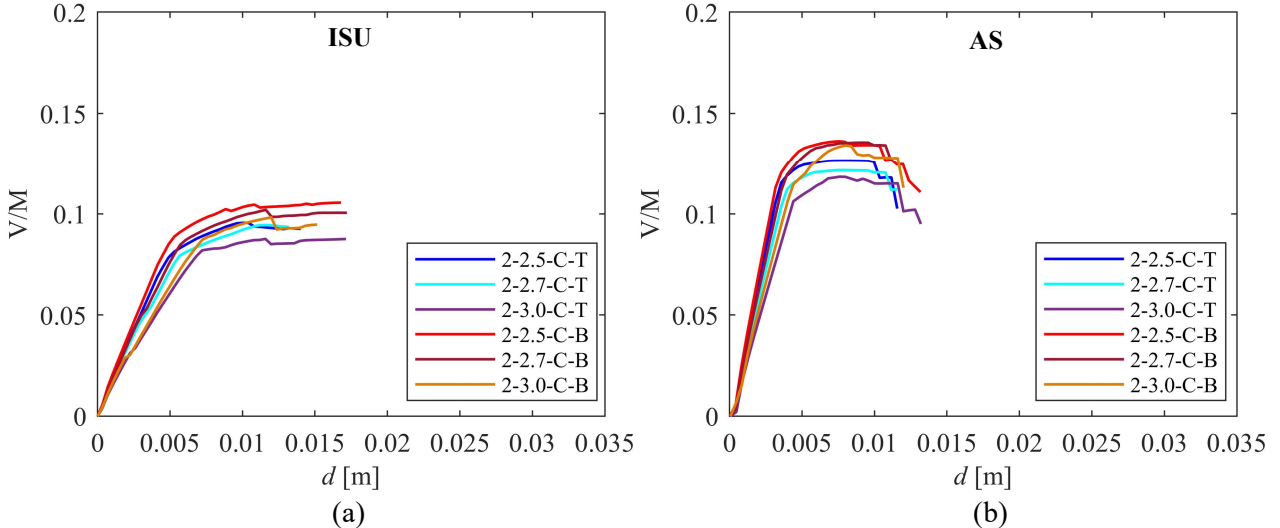


Figure C.2:  $x$ -direction ( $-F_x$ ) push-over curves of the buildings with 2 floors and concrete slabs: (a) Isolated structural units and (b) Aggregate structures.

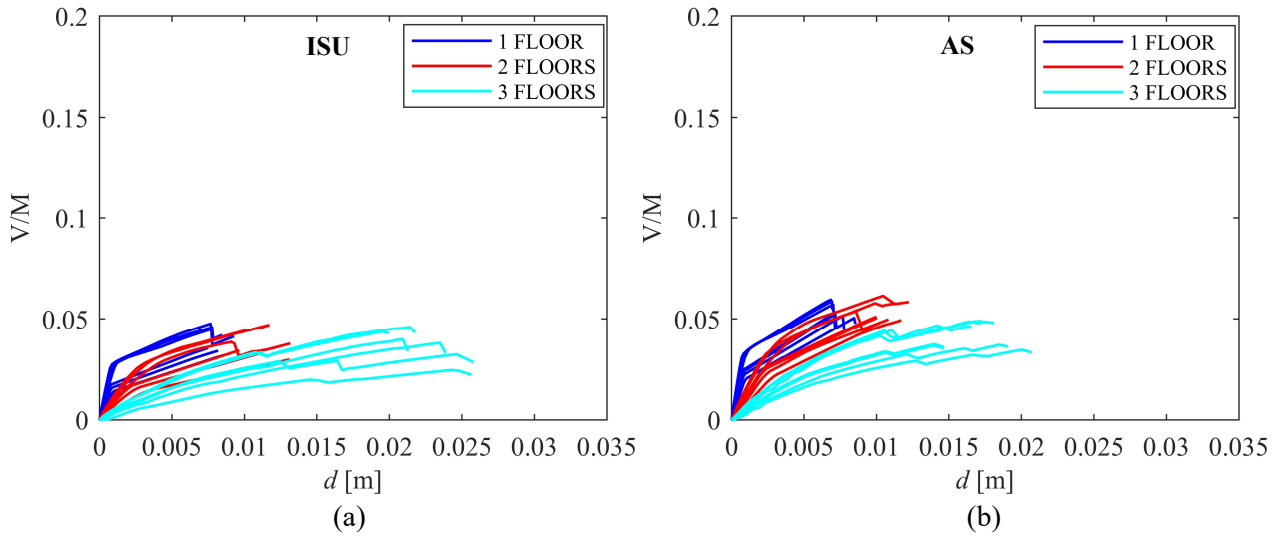


Figure C.3:  $x$ -direction ( $-F_x$ ) push-over curves of the buildings with timber slabs: (a) Isolated structural units and (b) Aggregate structures.

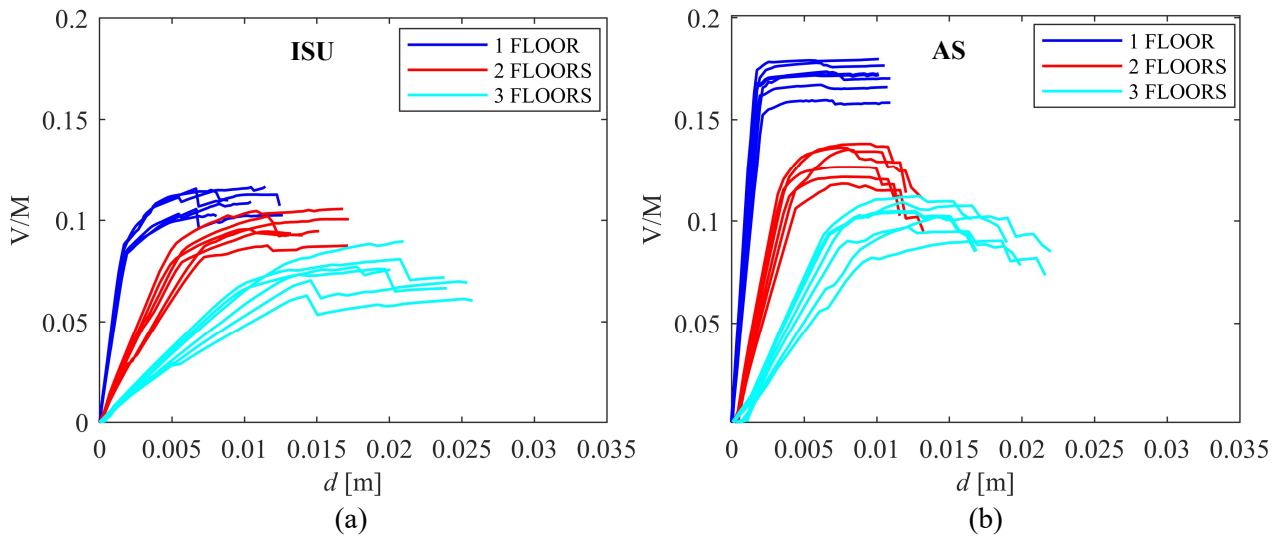


Figure C.4:  $x$ -direction ( $-F_x$ ) push-over curves of the buildings with concrete slabs: (a) Isolated structural units and (b) Aggregate structures.

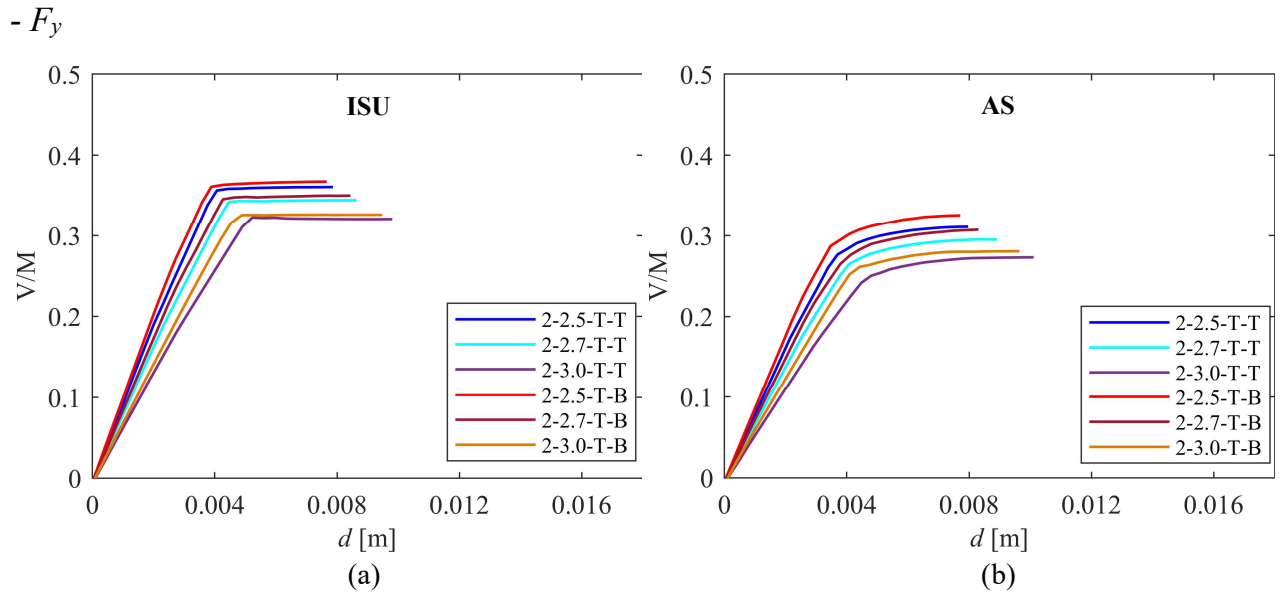


Figure C.5:  $y$ -direction ( $-F_y$ ) push-over curves of the buildings with 2 floors and timber slabs: (a) Isolated structural units and (b) Aggregate structures.

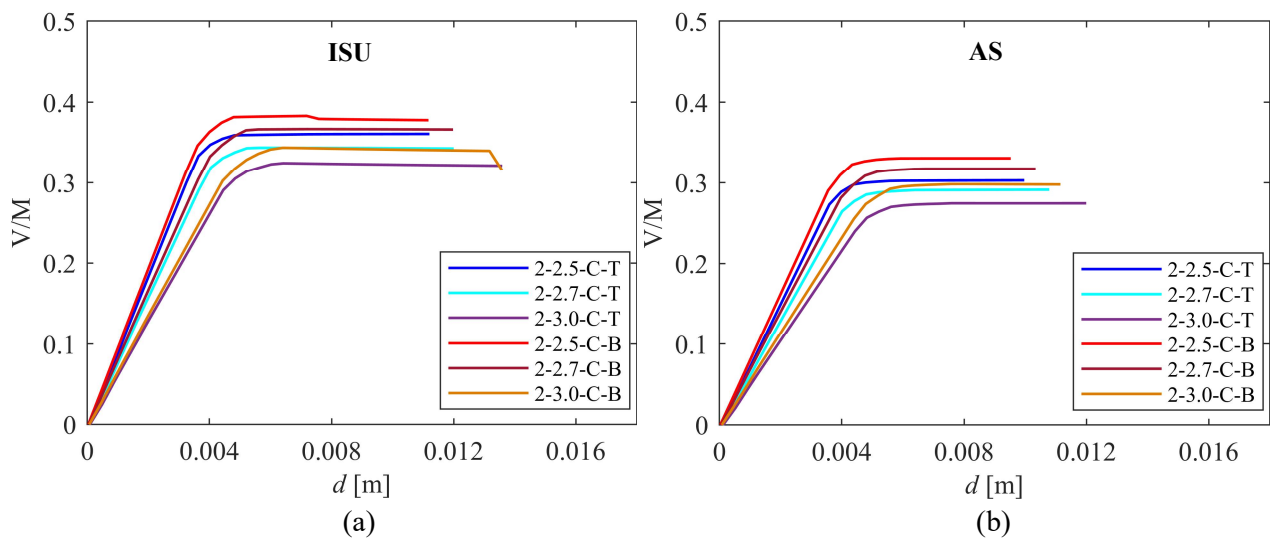


Figure C.6:  $y$ -direction ( $-F_y$ ) push-over curves of the buildings with 2 floors and concrete slabs: (a) Isolated structural units and (b) Aggregate structures.

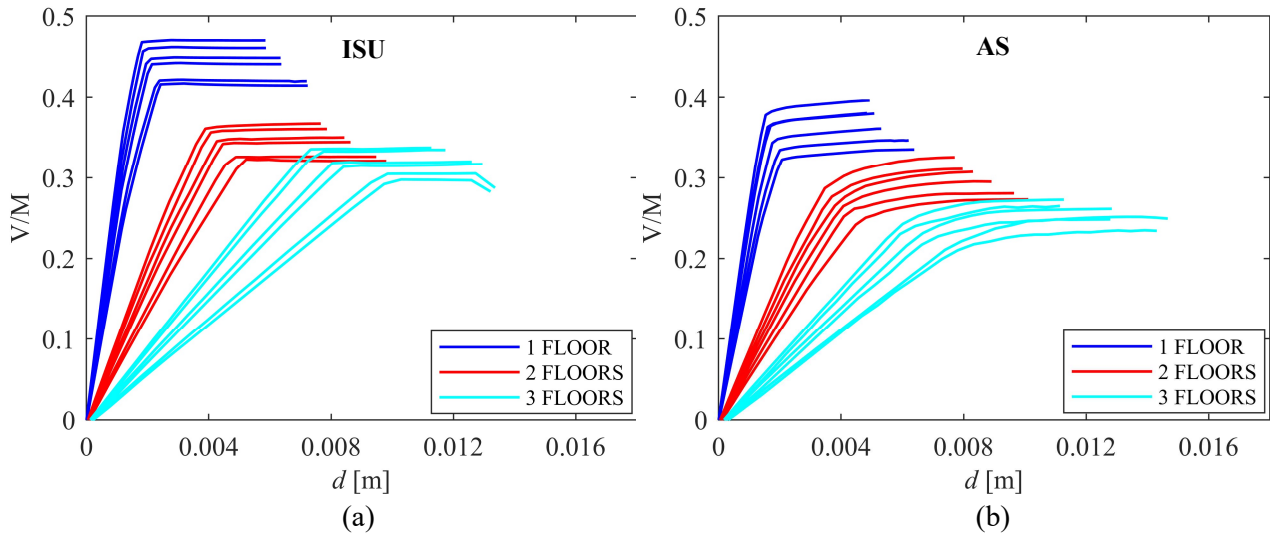


Figure C.7:  $y$ -direction ( $-F_y$ ) push-over curves of the buildings with timber slabs: (a) Isolated structural units and (b) Aggregate structures.

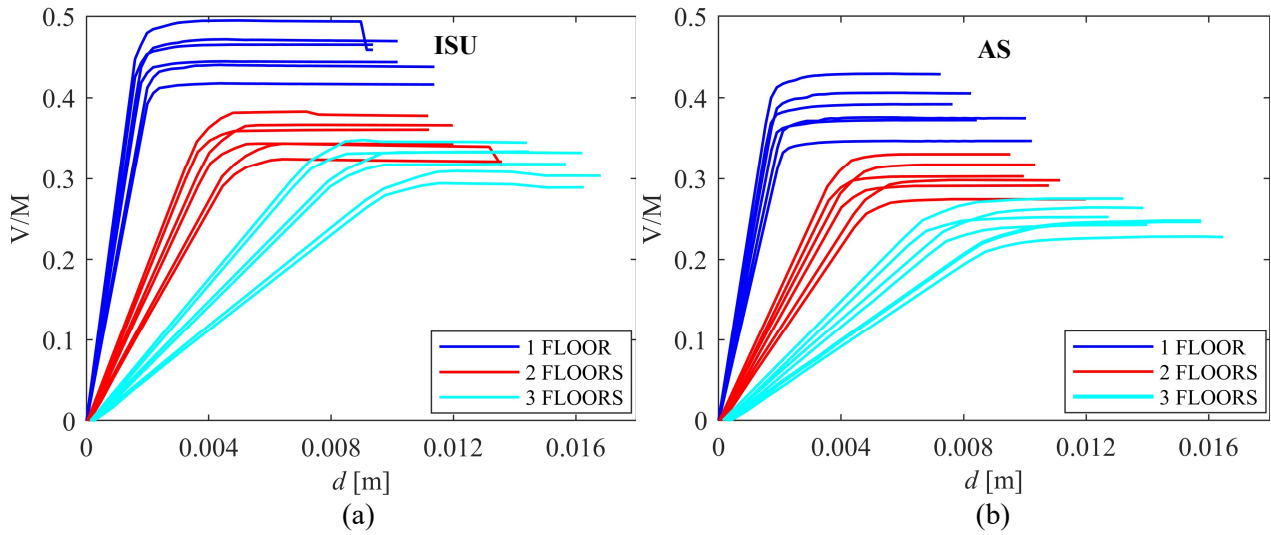


Figure C.8:  $y$ -direction ( $-F_y$ ) push-over curves of the buildings with concrete slabs: (a) Isolated structural units and (b) Aggregate structures.

-  $F_y$ , over the attainment of the LS limit state

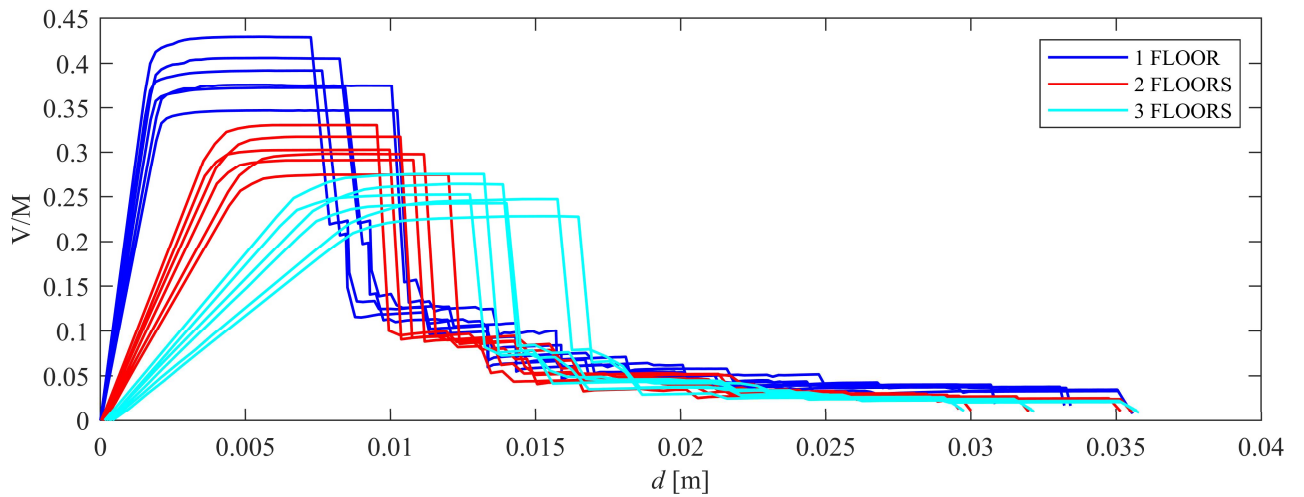


Figure C.9: Pushover curves of the AS with concrete slabs: analyses over the attainment of the LS limit state ( $- F_y$ ).

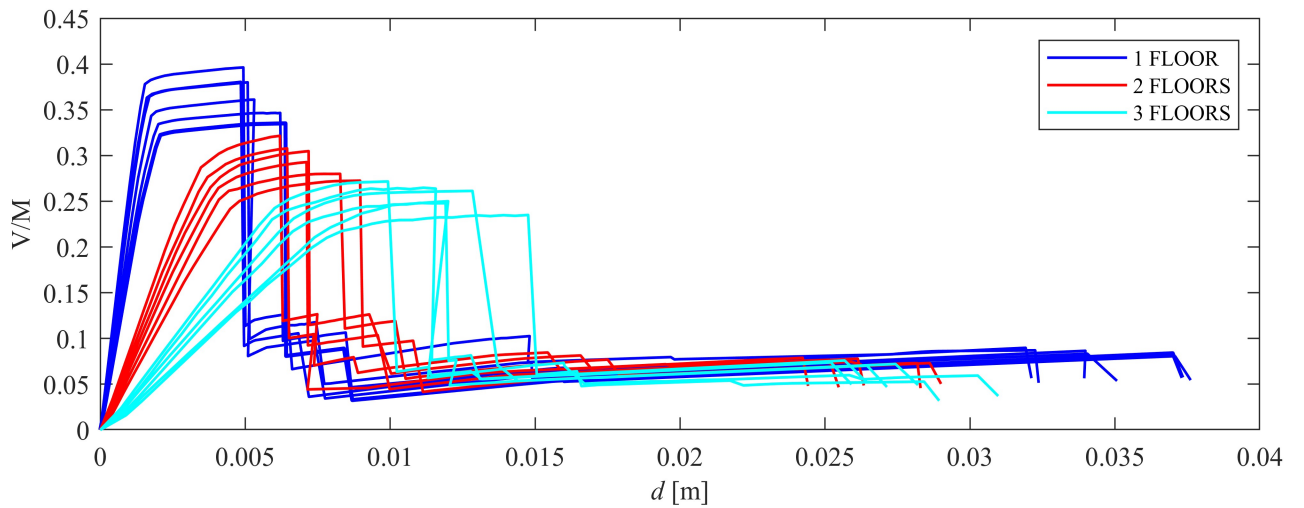


Figure C.10: Pushover curves of the AS with timber slabs: analyses over the attainment of the LS limit state ( $- F_y$ ).

**Fragility curves**

$-F_x$

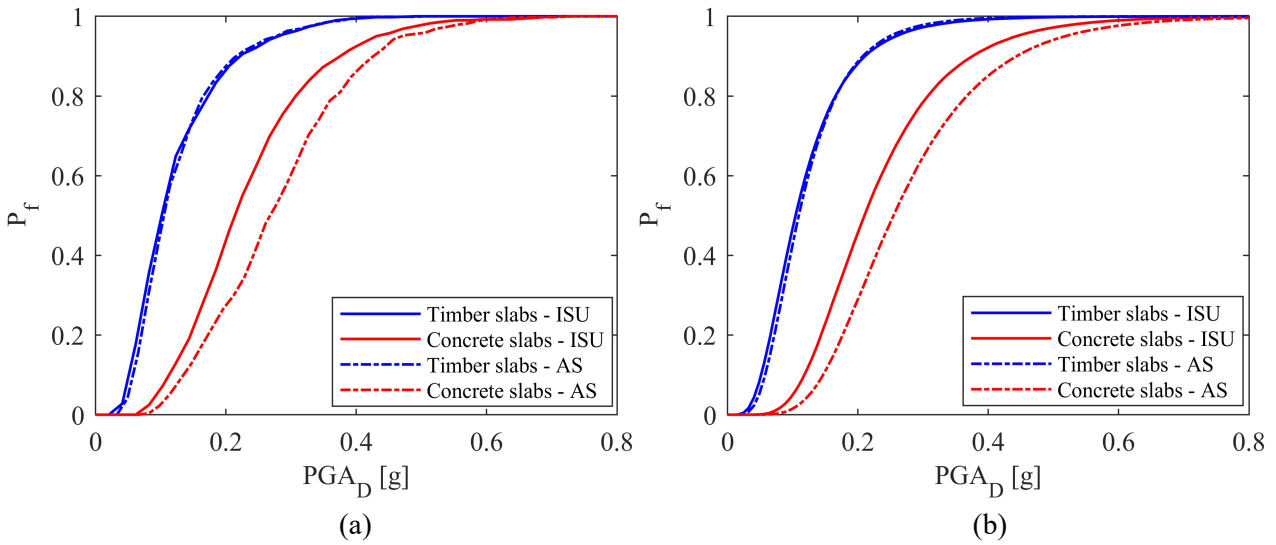


Figure C.11: Fragility curves of all the models in  $x$ -direction ( $-F_x$ ), distinguished according to the type of slabs: (a) actual PGA; (b) Monte Carlo method.

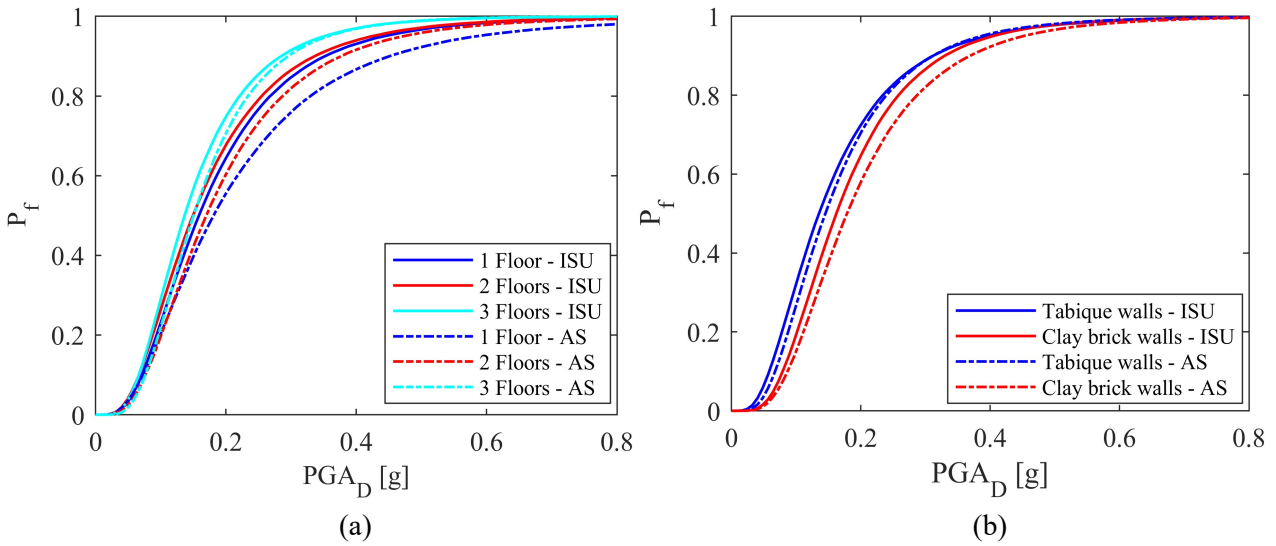


Figure C.12: Fragility curves of all the models in  $x$ -direction ( $-F_x$ ) using Monte Carlo method: (a) distinguished according to the number of floors; (b) distinguished according to the type of internal walls.

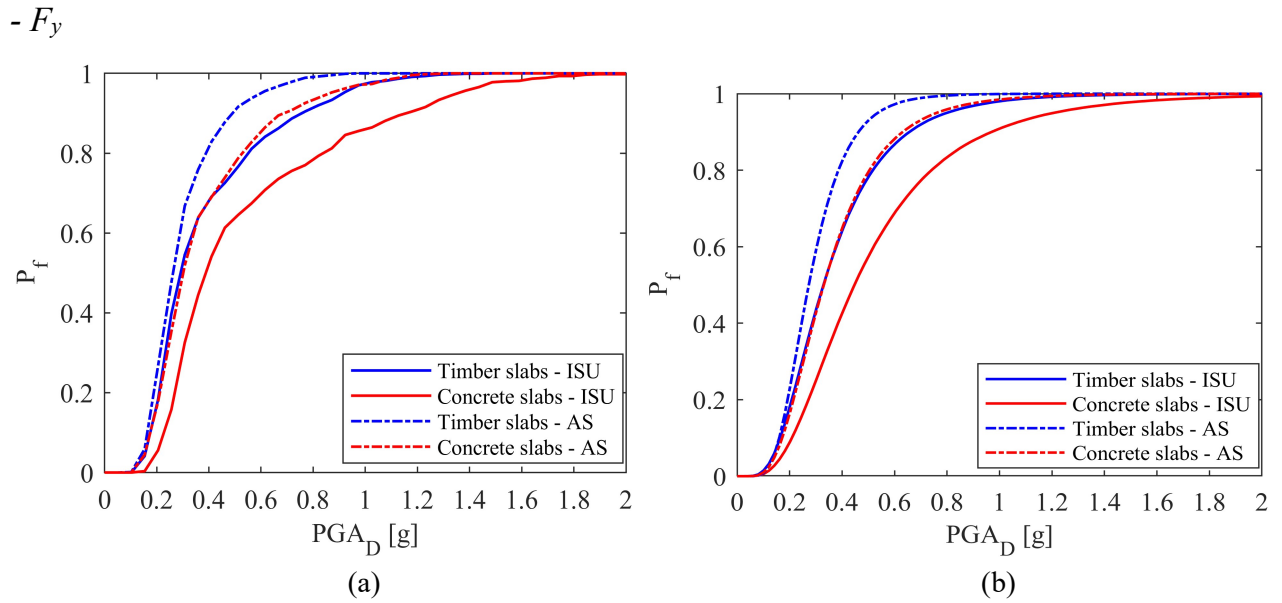


Figure C.13: Fragility curves of all the models in  $y$ -direction ( $-F_y$ ), distinguished according to the type of slabs: (a) actual PGA; (b) Monte Carlo method.

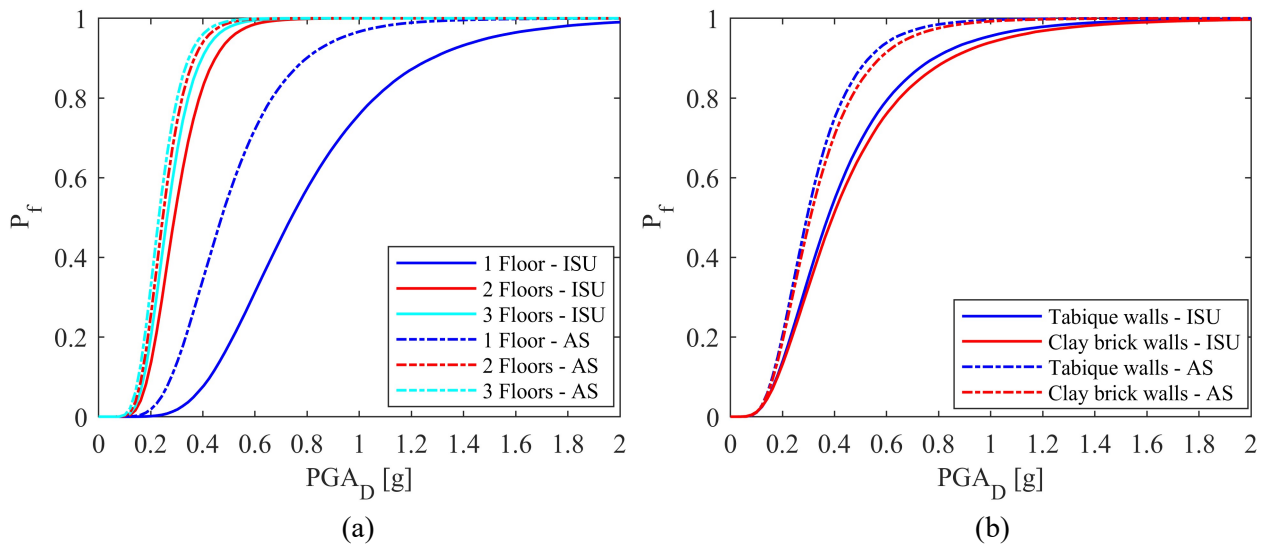


Figure C.14: Fragility curves of all the models in  $y$ -direction ( $-F_y$ ) using Monte Carlo method: (a) distinguished according to the number of floors; (b) distinguished according to the type of internal walls.

-  $F_y$ , over the attainment of the LS limit state

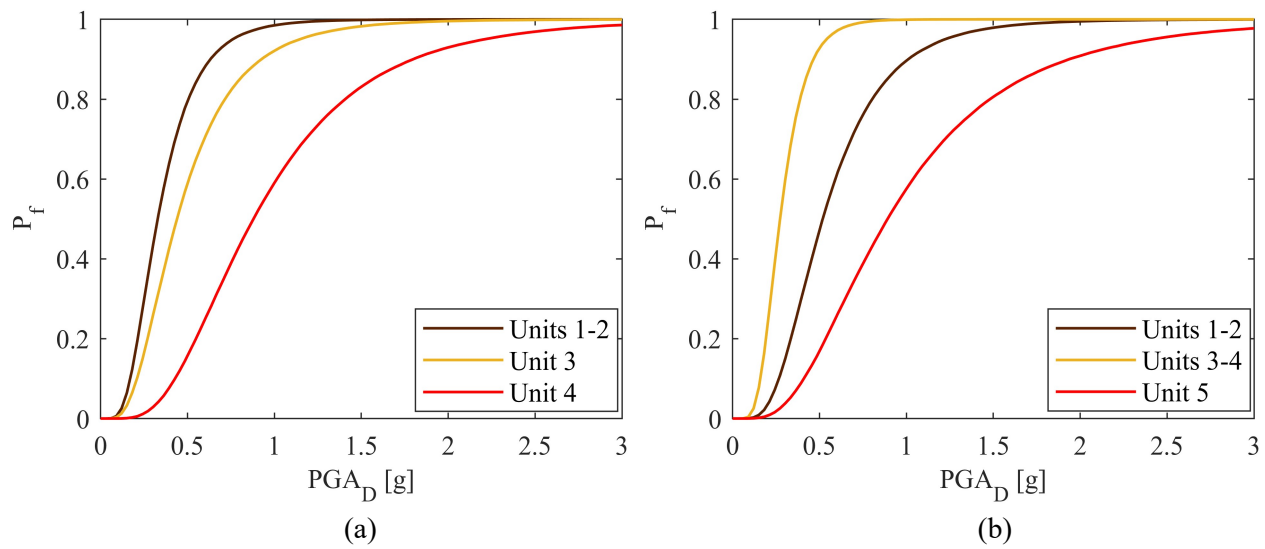


Figure C.15: Fragility curves of the AS using Monte Carlo method: analyses ( $-F_y$ ) over the LS limit state in buildings with (a) concrete slabs and (b) timber slabs.